

ICCEE2019 Proceedings

1. Abdullah Abo Gosh, Alexandria University, Egypt, "Study of Diffusion Controlled Corrosion of Shaft in Agitated Vessels"
2. Ahmed Emara, Alexandria University, Egypt "Toe Drainage Systems for Control of Seepage Through Earth Dams Based on Pervious Foundation"
3. A.M. Ismail, Faculty of Engineering, Alexandria University "Rate of Copper ions removal from Copper Sulfate solution by Cementation on steel turbulence promoters using stirred tank reactor"
4. Hadir Abd-El Moneim, Faculty of Engineering, Alexandria University, "Hydrologic Evaluation of TRMM Multi-satellite Precipitation Analysis Products over Blue Nile Basin"
5. Haroun Hassan, Aswan University, Egypt, "Effect of HHO gas addition on the performance and emissions of SIE"
6. Hossam Alsherbeny, Wastewater Treatment Alexandria Sanitary Drainage Co., "Determination of Wastewater Problems in the Abu Qir Bay and Ways of Risk Reduction"
7. Mariam Eltohamy, Pharos University in Alexandria (PUA), Egypt "Simulating the performance of an industrial packed column in extracting aromatics"
8. Mohamed Ahmed, Alexandria University, Egypt "A Comparative Study of Desalination by Pervaporation and Membrane Distillation using the Sweeping-Air Technique"
9. Mahmoud Souby , Minia University, Egypt, "Cu/C nanofibers decoration for copper substrates as effective strategy for enhancing the surface hydrophobicity"
10. Mai Mohamed Saad, Alexandria University, Egypt, "Hydraulic Simulation of Modern Irrigation Schemes in West Nubaria Region, Egypt"
11. Mostafa Elgedawy, Egyptian Ethylene and Derivatives Company (ETHYDCO), Egypt "Improving the crystallization process of salts on gypsum seeds in ZLD unit"
12. Nada Ward, Alexandria University, Egypt, "Rice-straw: from Waste to Useful Product"
13. Nourhan hassan, Alexandria University, Egypt "Hydrodynamic effect of groins on the estuary exits"
14. O.S. Okwundu, Egypt, japan University of science and Technology (EJUST), "Thermal decomposition of eggshells for quicklime production: the role of egg membrane"
15. Samir Elagamy, Alexandria University, Alexandria, Egypt, "Reinforcing polyhydroxybuterate-co-valertae with agriculture waste to produce a biodegradable composite for packaging and other application"
16. Shaimaa Sadek, Institute of Graduate Studies and Research, Egypt "Desalination of simulated sea water by emulsion liquid membrane using edible oils as liquid membrane"
17. Tahani A. Elbondiral, Egypt, japan University of science and Technology (EJUST) "Analysis of the effectiveness of green roofs to mitigate the urban heat island effect in local outdoor spaces – A review paper"
18. Walaa Elhamamy, Alexandria University, Egypt "Comparison Among Numerous Numerical Alternatives Using Ansys On Open Channel Confluence"
19. Zakari Aretouyap, University of Yaounde, Cameroon "Meteo-parameters variability in the equatorial rainforest"

20. Zakari Aretouyap, University of Yaounde, Cameroon “Inverse slope method for interpreting vertical electrical soundings and characterizing hydraulic and environmental properties of the Adamawa aquifer”
21. Ola Mohammed Ahmed, Alexandria University, Egypt “Living Organisms to Produce Bio-Materials Through Bio-design Strategies”
22. Ashraf Bakkar, Suez University, Egypt “Electrochemical synthesis of photovoltaic thin films: A critical review and a novel approach”
23. Mohamed Antar, KFUPM, Saudi Arabia “Performance of a Two Stage Modified Air Heating HDH System”
24. Youssef Elkhayat, EJUST, Egypt, Life Cycle Assessment of Three High-Performance Glazing Systems
25. Lucienne Basaly, EJUST, Egypt, Effect of the PV Position and Orientation on Improving Thermal Comfort
26. Rania Elghamry, EJUST, Egypt, Effect of Window Orientation and Glass Type on Energy Consumption and Interior Conditions in a Facility
27. Mahacen Abd Elbaset, Helwan University, Egypt, Optimization of Different Parameters of Solar Chimney.
28. Ahmed Tarek, Alexandria University, Egypt “Experimental investigation of a two-bed adsorption cooling system”
29. Nasser Barakat, Minia University, Egypt “NiCo alloy/carbon nanofibers composite as effective non-precious electrocatalyst for PEMFCs and hydrogen production”
30. Islam Mohamed Mousa, Aswan University, Egypt “Theoretical study of influence of the geometric parameters on the performance of Solar Chimney Power Plants”
31. Alaa eldin abdel shafy, EJUST, Egypt, Impact of Hydro Energy upon Multi-Area Interconnected Power Systems via Optimal Fuzzy Logic Load Frequency Controllers.
- 32- Megalaa, Youssef, Helwan University, Cairo, Egypt, Optimization of different Parameters of Solar Chimney
33. Mohammed Khoudary, Aswan University, Egypt Estimation of Groundwater Level Changes Using Finite Differences and GIS before and after the Operation of New Assiut Barrage

Accepted in Key Engineering Materials Journal:

34. Andy Kumi, EJUST, Egypt Biochar Synthesis for Industrial Wastewater Treatment: A Critical Review.
- 35 Hamdiya Orleans, EJUST, Egypt Synthesis, Characterisation, and Performance of Polyaniline (PANI) in Metals Sorption
36. Rehab El-Maghraby Suez University, Egypt, A Study on Bio-Diesel and Jet Fuel Blending for the Production of Renewable Aviation Fuel
37. Rehab El-Maghraby Suez University, Egypt, High Pressure Supercritical Carbon Dioxide Separation from its Mixture with Nitrogen at Different Temperatures
38. Nourwanda Serour, Faculty of Engineering, Alexandria University, Alexandria, Egypt, A Review on Titanium Dioxide Based Nanofluids: Synthesis and Stabilizing Techniques in both “Pure (Single System) and Mixed (Hybrid System) Base Fluids
39. Alaa Ali, EJUST, Egypt Optimal Scheduling of Wood Chips Biomass and Natural Gas Energy Carriers Based on Multi-Objected Particle Swarm Optimization
40. Ahmed Ismail Faculty of Engineering, Alexandria University, Alexandria, Egypt Rate of Copper Ions Removal from Copper Sulfate Solution by Cementation on Steel Turbulence Promoters Using Stirred Tank Reactor
41. Fathy Shokry Pharos University in Alexandria, Egypt The Effect of Using Baffles on the Rate of Mass Transfer of a Cylindrical Stirred Tank React.
42. Hamed Abady, Sohag University, Egypt, Experimental Study on the

Desalination System Using Humidification-Dehumidification Technology

43. Kholoud Madih, EJUST, Egypt Evaluation of Stainless Steel as an Electrocatalyst for Electrooxidation of Urea – Rich Wastewater
44. Esraa Hashem , Removal of Heavy Metals from Wastewater by Ion Exchange Resin Using Pulsation Technique
45. Rehab Ali, City for Scientific Research and Technological Applications, Egypt, Towards Potential Removal of Malachite Green from Wastewater: Adsorption Process Optimization and Prediction
46. Asmaa Nageib, Sohag University, Egypt Effect of Smart Glazing Window on Energy Consumption inside Office Building
47. Ashraf Bakkar, Suez University, Egypt, Electrochemical Synthesis of Silicon and Gallium Arsenide Photovoltaic Thin Films: A Critical Review and a Novel Approach
48. Mahmoud Samy, EJUST, Egypt, Modeling and optimization of photocatalytic degradation of methylene blue using lanthanum vanadate
49. Huda Farid, City for Scientific Research and Technological Applications, Egypt. Superconducting and Electrical Resistivity of HTS Bi-2223 Doped by (SnO:Cr2O3)x Nanoparticles
50. Mohammed Fuseini, EJUST, Egypt, Effects of Doping on Zeta Potential and pH of Polyaniline Colloidal Suspension
51. Rania Osama, EJUST, Egypt, Long-Term Assessment of 1,4-dioxane Uptake via Duckweed with Emphasis on Operational Parameters
52. Ahmed Salman, Effects of Air Temperature on Combustion Characteristics of LPG Diffusion Flame
53. Alaa Adel, Alexandria University, Egypt Numerical Simulation for Falling Film Thickness around Horizontal Tube in MVC and MED Evaporators
54. Sara Zayan,, EJUST, Egypt, Decontamination of Heavy Metals from Wastewater Effluent Using Polypyrrole/Polyvinylpyrrolidone Nanoparticles
55. Essam Hares, EJUST, Egypt, Anodic Aqueous Electrophoretic Deposition of Graphene Oxide on Copper Using Different Cathode Materials
56. Mahmoud Abdelghany Shouman, EJUST, Egypt, Characterization of the Mixing Performance of an Innovative Hepatic Sinusoids-Based Microreactor Using Villermoux–Dushman Protocol
57. Mohammed M.Hamed, Arab Academy for Science & Technology, and Maritime Transport, Giza, Egypt , Different Methods of Water Distribution Network Analysis
58. Marwa Nabil, Advanced Technology and New Materials Research Institute, SRTA-City,Egypt, Micro- Ribbons and Micro-Wires Silica Synthesis Using Bottom-Top Technique
59. Abdallah Youssef, EJUST, Egypt Experimental and Theoretical Studies of Thermophysical Properties of MgO-Water Nanofluid

1-Study of Diffusion Controlled Corrosion of Shaft in Agitated Vessels

A. A. Abo-Gosh*, G.H. Sedahmed, H. A. Farag, D. A. El-Gayar

Department of Chemical Engineering, Faculty of Engineering,
 Alexandria University, Egypt.

E-mail: abdullahabogosh@gmail.com

Abstract

In this study the rate of mass transfer diffusion-controlled corrosion for a rotating shaft in agitated vessel was investigated in absence and presence of suspended inert particles, the system used is dissolution of copper in acidified potassium dichromate solution. Rate of mass transfer was measured under different conditions of the following variables; Impeller rotation speed ranged from (100-800) rpm, Impeller geometry, Concentration of sulfuric acid (0.5-2 M).

Where the rate of mass transfer increased with increasing impeller rotation speed range and increasing of concentration of sulfuric acid (from experimental part k value at 100 rpm for axial shaft =0.166 but k value at 800 rpm for axial shaft =0.295 at 0.5M sulfuric acid) and dimensional analysis method was used to determine an overall mass transfer correlation for the system to be used in designing and operating rotating shafts in agitated vessels.

Keywords: diffusion controlled; corrosion; agitated vessels; mass transfer; suspended particle; rotating shaft.

Introduction

Agitated vessels are used widely in chemical, food, pharmaceutical and metallurgical industries to conduct processes such as mixing, liquid-liquid extraction, solid-liquid and gas-liquid reactions, crystallization and dissolution of salts, ore leaching, wastewater treatment, fermentation, etc. In the majority of these operations corrosive solutions are used which limit the life time of the agitated vessel and its accessories beside contaminating the contents of the agitated vessel with corrosion products. Corrosion of copper diffusion control proceeds much rapidly than corrosion of iron. The main Idea of this paper was to the study corrosion rate of copper under acidic conditions and thus we can estimate the corrosion rate of steels that assist in design and maintenance of mixing equipment. In the corrosion of iron diffusion control process is very slow (takes months) so we used a faster process represented by corrosion of copper by dichromate techniques.

The theory of metal corrosion includes two concurrent reactions, specifically an anodic reaction during which the metal dissolves ($M \rightarrow M^{2+} + 2e$), and a cathodic reaction where a depolarizer (such as dissolved oxygen) is reduced ($1/2 O_2 + H_2O + 2e \rightarrow 2OH^-$). These two reactions are heterogeneous, involving a mass transfer step. The metal ions should diffuse away from the metal surface; meanwhile, dissolved oxygen has to diffuse from the bulk of the solution to the surface of the corroding metal in the pH range 4-10 which is frequently used in practice [1]. Under certain conditions, dissolved oxygen and dissolved metal ions have to diffuse across a porous film of corrosion product, e.g., an oxide covering the metal surface [2]. So the proposed technique was for the measurement of the mass transfer coefficient in the mass transfer step between a liquid and a solid surface, an example is the copper dissolution method [3]. The method comprises the contact of a solution of sulphuric acid containing potassium dichromate with a copper surface. The dichromate anion acts as an oxidizing agent and oxidises the copper according to the following overall equation:



Previous work in this fields include mass transfer in case of flow induced corrosion of the bottom of cylindrical agitated vessels [4], Mass and heat transfer enhancement at the wall of cylindrical agitated vessel by turbulence promoters [5], Mass transfer at the impellers of agitated vessels in relation to their flow-induced corrosion [6] and Mass transfer controlled corrosion of copper shaft in agitated vessels. The aim of this work is to investigate the corrosion of a rotating shaft made of copper and immersed in acidic solutions of potassium dichromate using two types of impellers (as turbulence promoters) and different concentrations of H₂SO₄.

Experimental technique

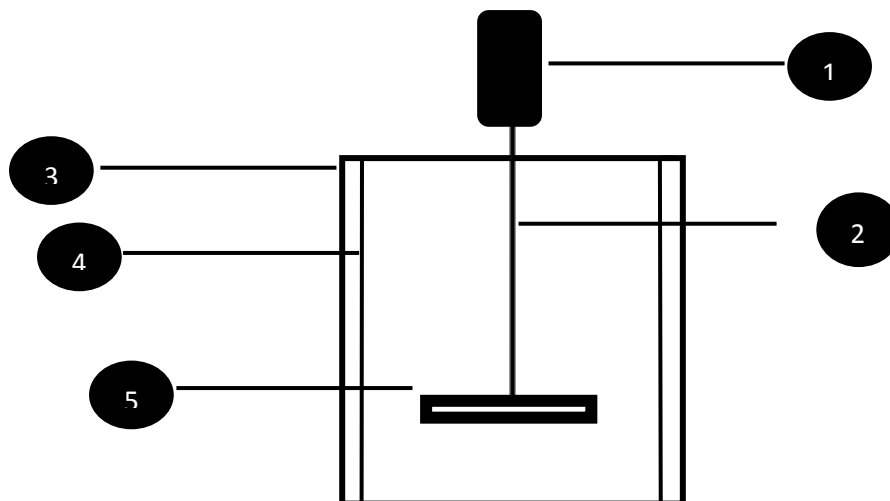


Figure (1) Experimental setup; (1) Electrical motor; (2) shaft made of pure copper; (3) cylindrical plexiglass container; (4) plexiglass baffle; (5) stainless steel impeller covered by epoxy (four blade 45° or 90° pitched turbine)

Materials used in this work were K₂Cr₂O₇, H₂SO₄, ferrous ammonium sulfate and diphenylamine as indicator [7]. Where it is K₂Cr₂O₇ was always 0.003 M but H₂SO₄ was 0.5, 1 and 2 M, ferrous ammonium sulfate was used for balt titration and diphenylamine as indicator [8].

The Experimental setup consisted of plexiglass cylindrical container of 15.2 cm inside diameter and 25 cm height [9]. The vessel had four baffles and was agitated with four blade 45° and 90° pitched turbine impeller (axial flow impeller and radial flow impeller) of 5cm diameter made of Stainless steel impeller coated by epoxy, shaft made from pure copper and using Electrical motor for rotating motion. The procedures steps were :

1. Make solution 2.5L of dichromate, sulphric acid with distilled water
2. Prepared ferrous ammonium sulphate solution with distillated water for analysis (0.01N).
3. Immerse the shaft in the solution about 80 min and operate the motor at speed from (100–800) rpm for each run.
4. Draw 5ml every 10 min for analysis.

Residual dichromate concentration in the sample was determined by titration against standard ferrous ammonium sulphate using diphenylamine as indicator. Diphenylamine was prepared with concentrated sulphric acid by using 1gm of diphenylamine with 55ml of concentrated sulphric acid.

Solution density and viscosity were determined by using a density bottle and an Ostwald viscometer, respectively. The diffusivity of dichromate was taken from the previous work in this fields and the physical properties were adjusted to the solution temperature, which ranged from 25 to 30 °C.

The Variables studied in this process were:

1. Rpm (velocity of rotating) (100 – 800).
2. Concentration of sulphuric acid (0.5 – 2) M.
3. Types of impeller (geometry of impeller 45° or 90°)

Table 1 – Physical properties of the solutions used at 25 °C.

| Solution composition | Density (ρ) g/cm ³ | Viscosity (μ) poise | Diffusivity $D = 10^6$ cm ² /s | Schmidt no Sc |
|--|--------------------------------------|---------------------------|---|---------------|
| 0.003 M K ₂ Cr ₂ O ₇ + 0.5 M H ₂ SO ₄ | 1.0267 | 0.00978 | 9.927 | 960 |
| 0.003 M K ₂ Cr ₂ O ₇ + 1 M H ₂ SO ₄ | 1.0606 | 0.0107 | 9.07 | 1113 |
| 0.003 M K ₂ Cr ₂ O ₇ + 2 M H ₂ SO ₄ | 1.1178 | 0.01217 | 7.98 | 1364 |

Results and discussion

For the present batch reactor the rate of diffusion controlled reaction is given by [10]:

$$Q \frac{dC}{dt} = kAC \quad (1)$$

Which integrates to,

$$Q \ln C_0/C = kAt \quad (2)$$

Where:

Q: solution volume (Lit).

C₀, C: initial reactant concentration and concentration at any time t, respectively (K mol/cm³).

K: K liquid phase mass transfer coefficient (cm/s)

A: shaft area cm².

The mass transfer coefficient k was determined under different conditions from the dichromate concentration-time data by plotting $\ln C_0/C$ vs time, the slope of the resulting straight line (kA/Q) was used to calculate the mass transfer coefficient (Figs. 2 and 3)

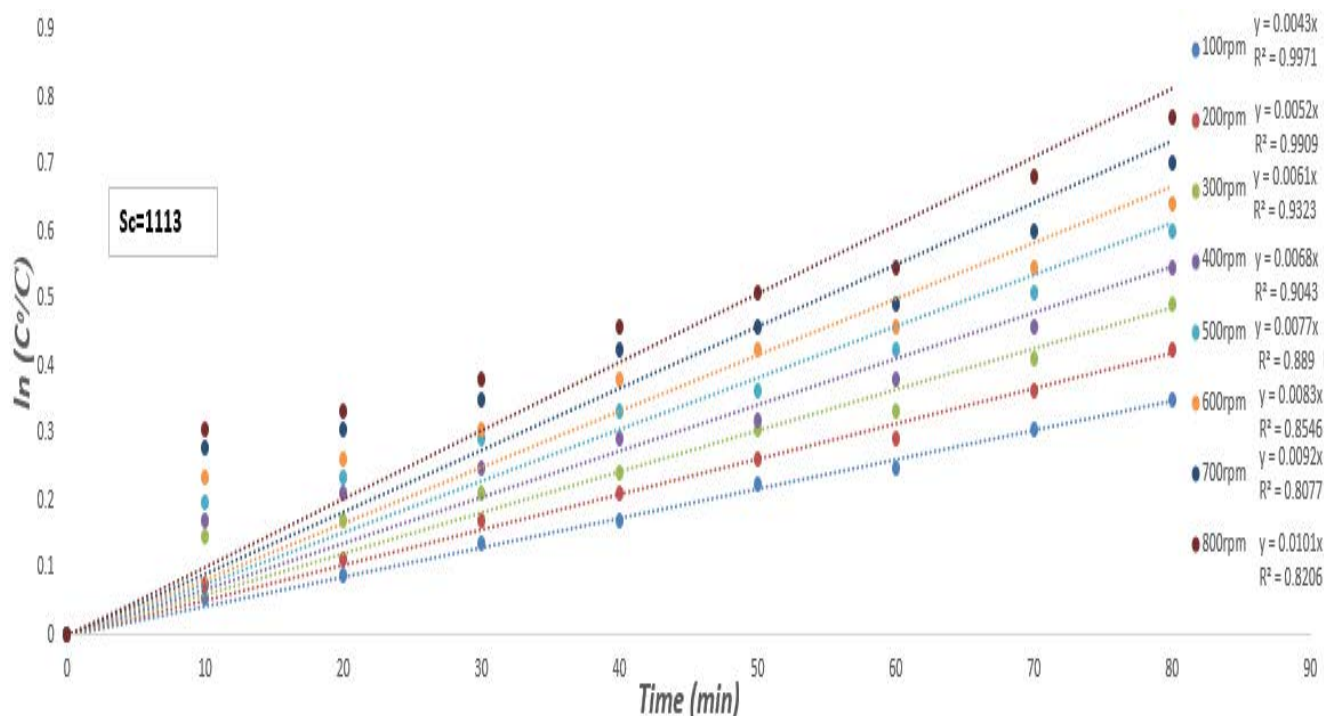


Fig (2) typical plot of $\ln(C_0/C)$ vs t at different rotational speeds; axial shaft 45° pitched blade turbine; 1M H₂SO₄

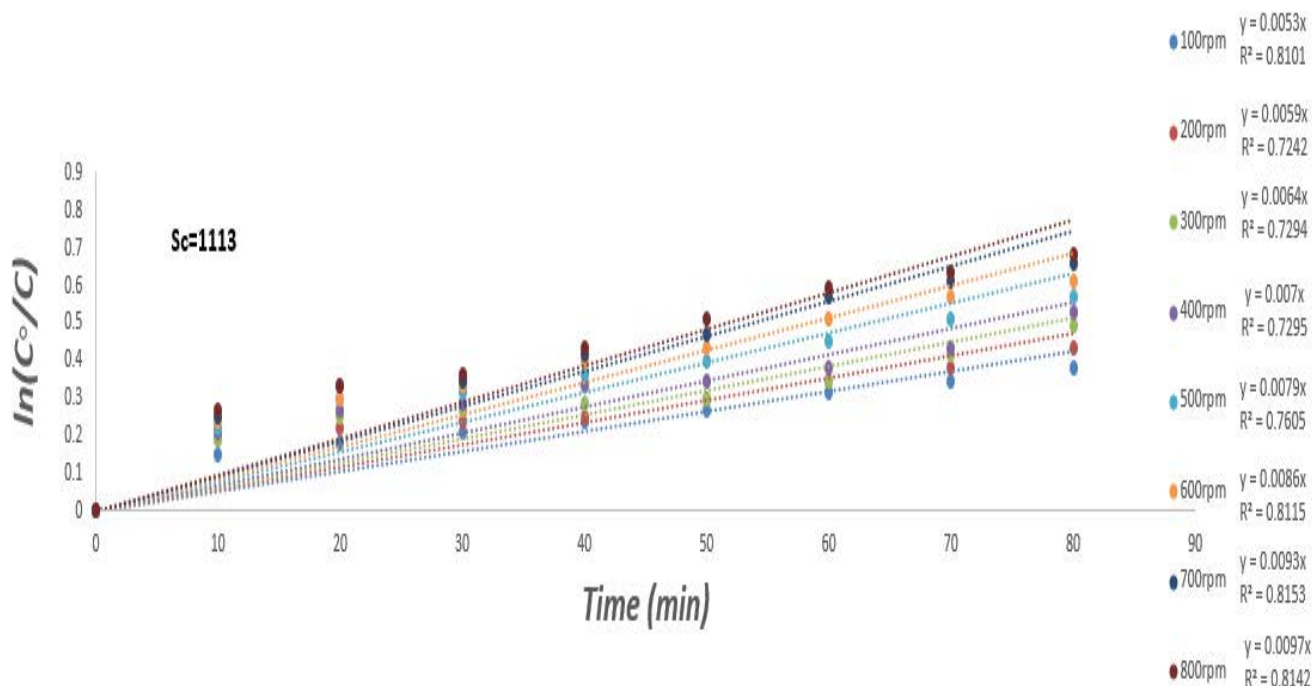


Fig (3) typical plot of $\ln(C^\circ/C)$ vs t at different rotational speeds; radial shaft 90° pitched blade turbine; 1M H₂SO₄.

The increase in the mass transfer coefficient at the shaft of with impeller rotation speed; where the k value at 100rpm and axial shaft 0.213 cm/min when that equal 0.502 at 800rpm. Shows the effect of impeller geometry on the mass transfer coefficient at the copper shaft at different impeller rotation speed. The data show that coefficient for a given speed of rotation radial flow impeller produces higher values of mass transfer than axial flow impeller. This may be explained in terms of flow pattern induced by two geometries. In case of the radial flow impeller (90° four blade turbine).

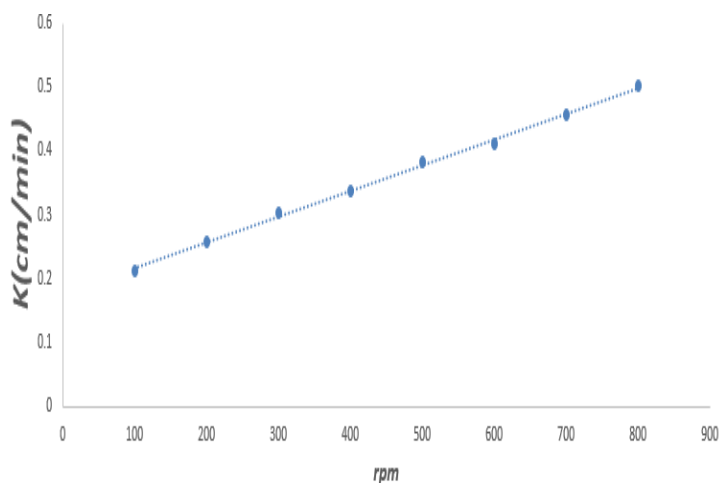


Fig 4 K values vs rpm at 1M H₂SO₄, axial shaft 45° pitched blade turbine

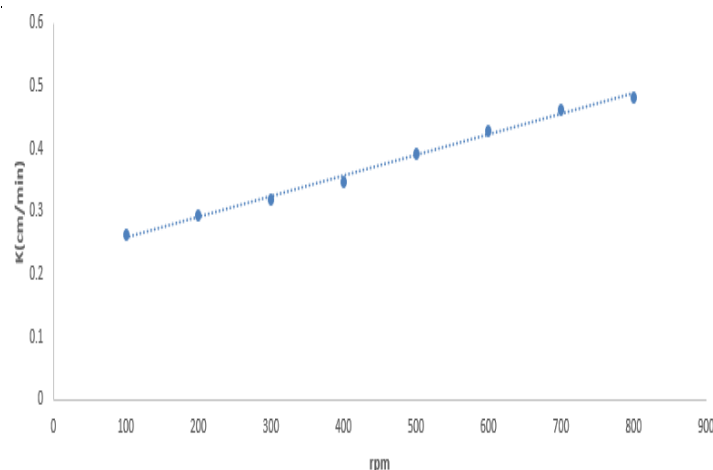


Fig 5 K values vs rpm at 1M H₂SO₄, radial shaft 90° pitched blade turbine

| Axial shaft 45° pitched blade turbine | | Radial shaft 90° pitched blade turbine | |
|---------------------------------------|-------|--|-------|
| rpm | K | rpm | K |
| 100 | 0.213 | 100 | 0.263 |
| 200 | 0.258 | 200 | 0.293 |

| | | | |
|------------|--------------|------------|--------------|
| 300 | 0.303 | 300 | 0.318 |
| 400 | 0.338 | 400 | 0.348 |
| 500 | 0.382 | 500 | 0.393 |
| 600 | 0.412 | 600 | 0.427 |
| 700 | 0.457 | 700 | 0.462 |
| 800 | 0.482 | 800 | 0.502 |

Table 2. K values with Rpm for (axial and radial blade).

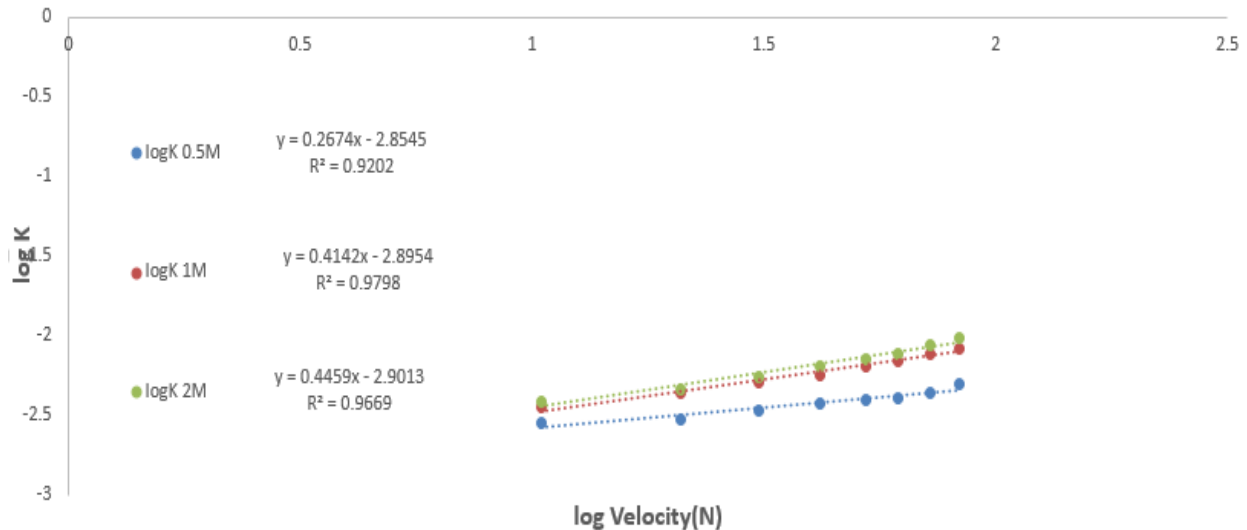


Fig (6) typical plot of log k vs log velocity (N); axial shaft; four 45° blade pitched turbine.

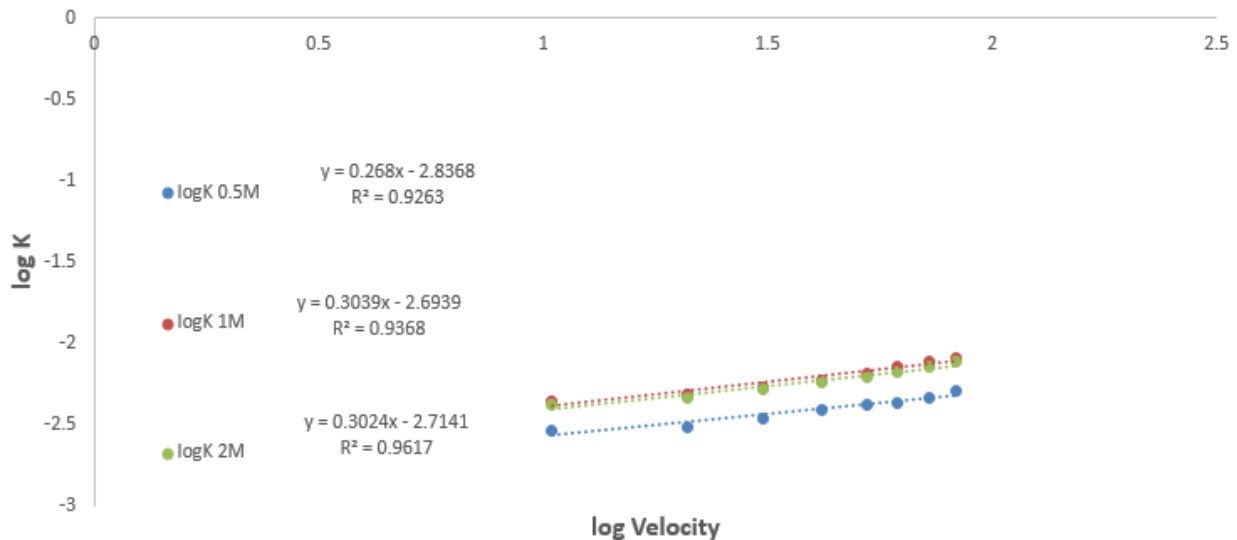


Fig (7) typical plot of log k vs log velocity (N); radial shaft; four 90° blade pitched turbine

Fluid leaves the impeller in the radial direction, separate at the vessel wall into an upward longitudinal stream and a downward stream parallel to the vessel wall and then both stream flows towards the center before they return to the impeller. In case of axial flow impeller (45°pitched blade turbine) the solution leaving the impeller moves downward towards the vessel bottom then moves

radially at the bottom to reach the vessel wall where it moves longitudinally parallel to the wall before it is recycled to the impeller zone. Previous studies on turbulence and velocity distribution in agitated vessels with impellers of different geometries have shown that in case of radial flow impellers the degree of turbulence is high near the wall where the baffles lie while in case of axial flow impellers the degree of turbulence is high in the zone below the impeller which is far away from the baffles (McCabe et al., 1985; Oldshue, 1983; Rushton and Oldshue, 1953; Chudacek, 1985) [11].

The high degree of turbulence at the wall in case of radial flow impeller explains the higher mass transfer coefficient at the baffle compared to the case of axial flow turbine.

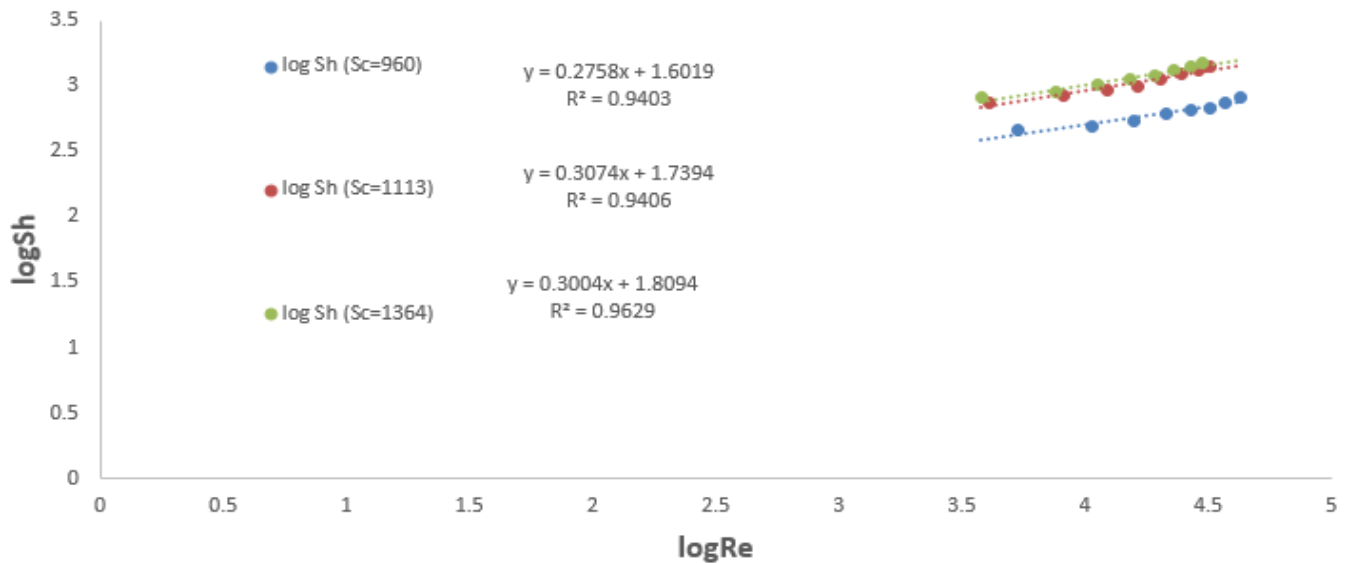


Fig (8) Effect of logRe on logSh for axial flow impeller

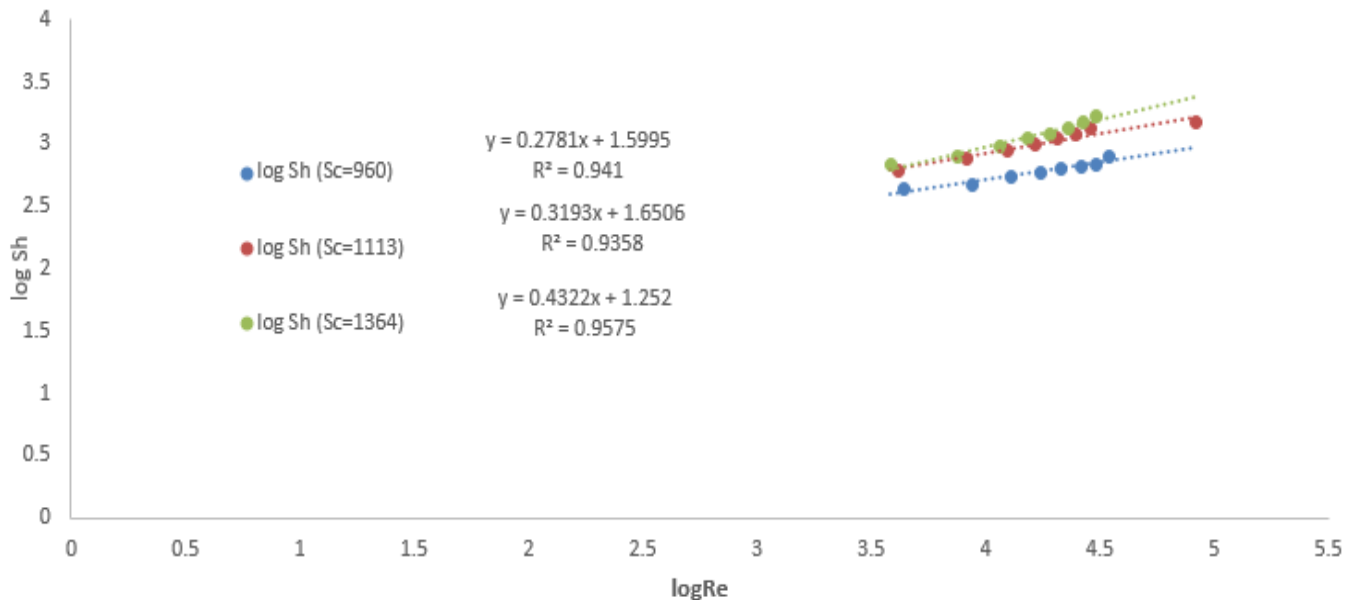


Fig (9) Effect of logRe on logSh for radial flow impeller

Figure (8) choose the effect of logRe on logSh for axial flow impeller. As expected increasing Re increases Sh.

Where: $Sh = K d_s / D$

K liquid phase mass transfer coefficient (cm/s)

d_s shaft diameter (cm)

D diffusion coefficient (cm²/s)

, because increasing Re increases the turbulence and hence increases K (mass transfer coefficient).

The same argument applies for figures (9) effect of $\log Re$ on $\log Sh$ for radial flow impeller.

Comparing the power of Re in case of axial flow impeller (0.307) which is lower than the value of power of Re (0.319). The reason for that is clear from the discussion mentioned after figure (7).

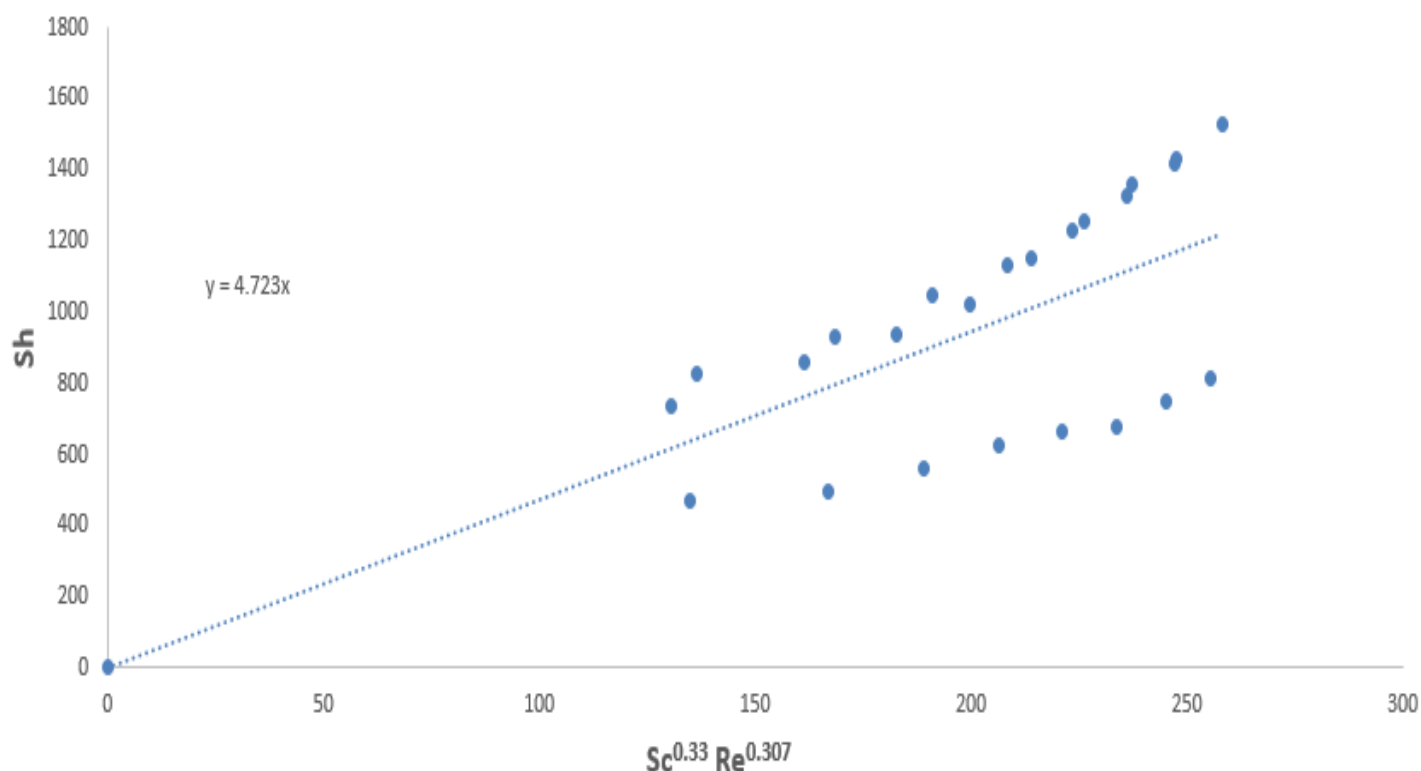


Fig (10) general relation between $Sc^{0.33} Re^{0.307}$ and Sh (for axial flow impeller)

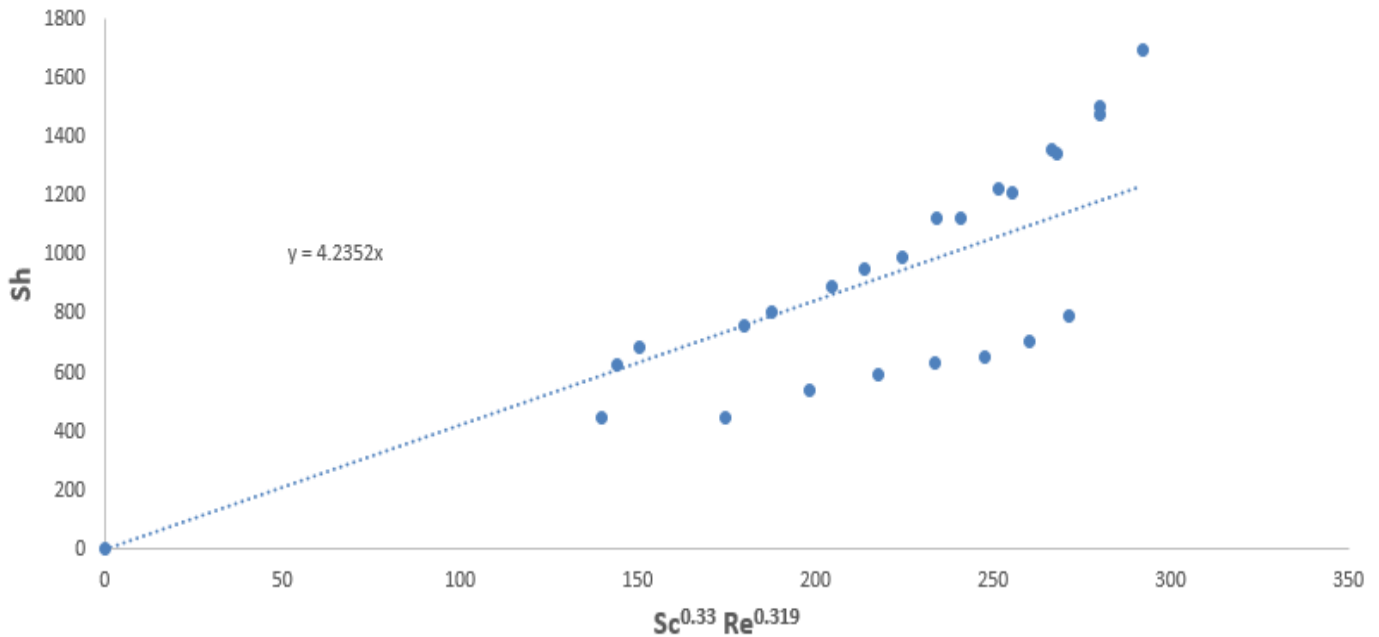


Fig (11) general relation between $Sc^{0.33} Re^{0.319}$ and Sh (for radial flow impeller)

Figures (10, 11) show the general relation between $Sc^{0.33} Re^{0.319}$ and Sh (for radial flow impeller) and $Sc^{0.33} Re^{0.307}$ and Sh (for axial flow impeller). The obtained correlation are

$$Sh = 4.235 Sc^{0.33} Re^{0.319} \quad \text{for radial flow}$$

$$Sh = 4.723 Sc^{0.33} Re^{0.307} \quad \text{for axial flow}$$

The value of Sc in both cases was 1113.

Conclusion

The diffusion controlled corrosion of rotating copper shaft in acidified $K_2Cr_2O_7$ solution of different operating conditions (Rpm and concentration of H_2SO_4) was studied. Two different geometry of impeller (radial and axial flow) were applied.

The result show that radial flow impeller gave higher mass transfer of coefficient. Two different general relation between (Sh, Sc and Re) numbers were obtained.

The obtained relations can be used to predict the corrosion of carbon steel tanks using carbon steel shaft or mixing.

Appendix A. Nomenclature

C_0, C initial reactant concentration and concentration at any time t , respectively (K mol/m³)

d agitated vessel shaft diameter (cm)

d_i impeller diameter (cm)

D diffusion coefficient (cm²/s)

K liquid phase mass transfer coefficient (cm/s)

n impeller rotation speed (r.p.s)

t time (s)

Sc Schmidt number ($\mu/\rho D$)

Sh Sherwood number ($K d/D$)

Re Reynolds number ($\rho d_i^2 n/\mu$)

ρ solution density (g/cm³)

μ solution viscosity (Pa/s) = poise

References

- Fontana, M. G., Corrosion Engineering, McGraw-Hill, New York (1987).
- Zahran, R.R., and Sedahmed, G. H., Effect of drag-reducing polymers on the rate of flow-induced corrosion of metals, Mater Lett, 35, 207-213 (1998).
- Gregory, D. P. and Riddiford, A. C., Dissolution of copper in sulphuric acid solutions, J. Electrochem. Soc., 107, 950-956 (1960).
- El-Shazly, Y.M., and Zahran, R.R., Mass transfer in relation to flow induced corrosion of the bottom of cylindrical agitated vessels, Chemical Engineering and Processing, 43, 745–751(2004) .
- Sedahmed, G.H. and El-Taweel, Y.A., Mass and heat transfer enhancement at the wall of cylindrical agitated vessel by turbulence promoters, Chemical Engineering and Processing, 80, 43–50(2014) .
- El-Gayar , D.A. and Konsowa, A.H., Intensification of the rate of diffusion controlled catalytic and electrochemical reactions in a new stirred tank reactor with a multi cylindrical blade impeller, chemical engineering research and design 109, 607–617 (2016) .
- A.I. Vogel, a Text Book of Quantitative Inorganic Analysis, Longmans, London, 1961.
- A. Findly, J.K. Kitchener, Practical Physical Chemistry, Longmans, London, 1965.
- W.L. McCabe, J.C. Smith, P. Harriot, Unit Operations of Chemical Engineering, McGraw Hill, New York, 1985.
- Walsh, F.C., 1993. A First Course in Electrochemical Engineering The electrochemical consultancy, Hants (U.K).
- McCabe, W.L., Smith, J.C., Harriot, P., 1985. Unit Operations of Chemical Engineering, 4th edn. McGraw Hill, N.Y.
- Findlay, A., Kitchner, J.K., 1965. Practical Physical Chemistry. Longmans, London.
- Fouad, Y.O., Malash, G.F., Zatout, A.A., Sedahmed, G.H., 2013. Mass and heat transfer at an array of vertical tubes in a square stirred tank reactor. Chem. Eng. Res. Des. 91, 234–243.
- Gregory, D.P., Riddiford, A.C., 1960. Dissolution of copper in sulphuric acid. J. Electrochem. Soc. 107, 950–956.
- Gruber, R., Melin, T., 2003a. Mixed convection in the copper dissolution technique of studying mass transfer. Int. J. Heat Mass Transf. 46, 2403–2413.
- Gruber, R., Melin, T., 2003b. Radial mass transfer enhancement in bubble-train flow. Int. J. Heat Mass Transf. 46, 2799–2808.
- Hyman, D., 1962. Mixing and agitation. Adv. Chem. Eng. 3, 119–202.
- Incropera, F.P., Witt, D.P., 1990. Fundamentals of Heat and Mass Transfer, 3rd edn. John Wiley & Sons, N.Y.
- Kato, Y., Kamel, N., Tada, Y., Iwasaki, Y., Nagatsu, Y., Iwata, S., Lee, Y., Koh, S., 2007. Transport phenomena around cylindrical baffles in an agitated vessel measured by an electrochemical method. J. Chem. Eng. Jpn. 40, 611–616.
- Mowena, M., Zatout, A.A., Sedahmed, G.H., 2013. Liquid–solid mass transfer behaviour of a new stirred tank reactor with a packed bed fixed to its wall. Chem. Eng. Technol. 36, 603–610.
- Oldshue, J.Y., 1983. Fluid Mixing Technology. McGraw Hill, N.Y. Rushton, J.H., Oldshue, J.Y., 1953. Mixing—present theory and practice. Chem. Eng. Prog. 49, 161–275.
- Wang, T., Wang, J., Jin, Y., 2007. Slurry reactors for gas-to-liquid processes: a review. Ind. Eng. Chem. Res. 46, 5824–5847.

2-Toe drainage systems for control of seepage through earth dams based on pervious foundation

Ahmed Tarek Emara^{1, a}, Mohammad Ahmad Abourohien^{2, b}, M. Rezk^{3, c}, and M. Aboelela^{4, d}

^{1, 2, 3, 4} Irrigation and Hydraulics Department, Faculty of Engineering, Alexandria University, Alexandria, Egypt. ^aahmed_tarek@alexu.edu.eg, ^bmrohien76@gmail.com, ^cMohamedabdelrazek1953@hotmail.com, ^dmagdyabo@yahoo.com

Abstract. Many dangerous effects may arise due to seepage through earth dams based on pervious foundations. Seepage affects the stability of dam embankment as well as the foundation. To avoid such effects, the dam must be provided with seepage control measures. One of the most common measures, used for this purpose, is draining the seeping water via toe drainage systems. The current paper focuses on the effect of the toe drainage systems on the characteristics of seepage through earth dams based on pervious foundation. Three systems of toe drainage are tested such as; horizontal drainage blanket with pipe drain, drainage banquette, and catch drain. The hydraulic performance of each control measure is analyzed using the numerical solutions, based on the finite element method, to estimate the seepage quantity (q), the height of seepage surface (h), the coordinates of the free surface (h_x), and the exit gradient (I_e). Study is conducted on a physical model with different slopes, for the dam embankment, different conductivities, heights, lengths, and pipe positions for the drainage blanket, different lengths and conductivities for the drainage banquette, and different locations for the catch drain. Results revealed that; the above parameters possess a great effect on the characteristics of seepage through earth dams based on pervious foundations. A comparative study is conducted between the tested toe drainage systems to predict the most efficient measure.

Keywords: Earth Dam, Pipe Drainage, Drainage Banquette, Catch Drain, Seepage Discharge, Finite Element Method

Introduction

Two basic problems arise due to seepage through earth dams. The first deals with stability of dam embankment, as well as the foundation. Soil particles along seepage surface of the downstream slope may be washed out and in turn threaten its stability. The pore water pressure upwardly, acts on the surface of the probable clip circle, accelerates the sliding of downstream slope. The upstream slope may be subjected to sloughing due to rapid draw down. The dam foundation may be also undermined due to excessive gradient especially at the dam toe. The second is concerned with estimation of the amount of seepage discharge, particularly, for storage dams. Both dam embankment and foundation must be safeguard against such dangerous effects. The main objective of toe drainage systems is to allow seepage water to pass without soil particles, and hence safeguard dam slopes from failure. Toe drainage systems may cause some increase in seepage discharge but, in the same time, shift the free surface to be far enough from the downstream slope. This may prevent or reduce the pore water pressure to a large extent, and in turn increase the safety against sliding.

Seepage through earth dams based on pervious foundation was analytically studied in different ways of approach. Some analytical solutions were presented by Pavlovsky [1], Harr [2], Grishin [3], Nedrigy [4], Rozanov [5] and Chugaev [6], Such solutions include various cases of dam embankments with or without seepage control measures.

The considered toe drainage systems, in the present work, are; horizontal blanket with pipe drain, drainage banquette, and catch drain, as shown in Fig (1). The purpose of the present study is to analyze the effect of the toe drainage systems on seepage characteristics, then evaluate the hydraulic performance of each one. Study is conducted on a physical model for a dam embankment having top width $b=10.0$ m, height $H_d=20.0$ m, slope factor $m= 2.25$, base width $B=100$ m, and effective head $H=18.0$ m. A computer software program, based on the finite element technique (Seep/w), is used to define the seepage characteristics; seepage discharge q , height of free surface h , location of the free

surface h_x , and exit gradient at the dam toe I_e . Two assumptions are considered in the present study; (i) the downstream is dry to satisfy the case of maximum effective head (H), and (ii) both embankment and foundation have the same conductivity coefficient (K). The case of seepage through earth dam without toe drainage systems is considered as a reference case to be used as a base of comparison with the other cases of dam with toe drainage systems. Results are presented in a dimensionless form expressing the relative seepage discharge as (q_t/KH), coordinates of the free surface (h_x), the relative height of seepage surface (h/H), for case without drainage systems, and exit gradient at exit ($I_e.B/H$).

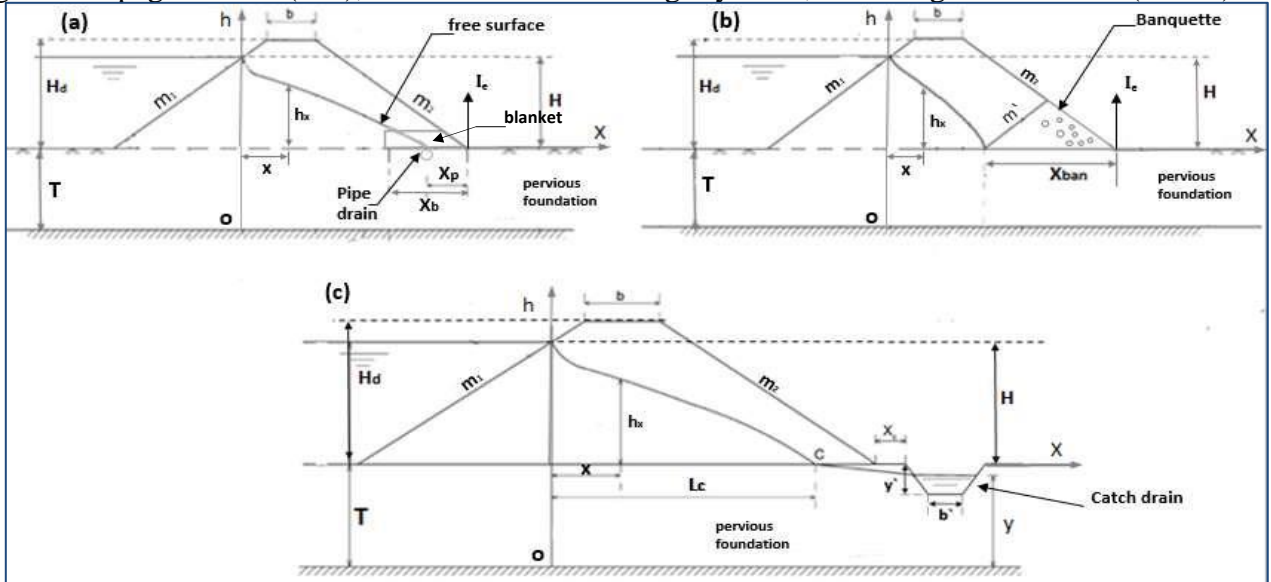


Fig (1) Studied toe drainage systems; a) drainage blanket with pipe drain, b) drainage banquette, and c) catch drain.

1 Determination of the active zone of seepage

To determine the dimensions of the finite element model, the active zone of seepage must be firstly defined. As shown in Fig (2), the seepage field is bounded by both inlet and exit seepage faces of lengths; L_i and L_o as well as the pervious layer depth T . For these purposes, various dimensions for the effective zone were tested as; $L_i/B = L_o/B = 0.25, 0.50, 0.75, 1.0, 1.5, 2.0, 2.5, 3.0$, and $T/B = 0.5, 1.0, 1.5, 2.0, 2.5$, where B is the base width of dam embankment. Applying the software program (Seep/w), the resulted relative values of the seepage discharge q_t/KH are plotted against the tested values of L_i/B , L_o/B , and T/B , as given in Fig (3). It is seen from the figure that, values of $L_i/B = L_o/B = T/B = 2.0$ define the maximum ones after which, nearly, no increase in the seepage discharge. Therefore, such limits, $L_i/B = L_o/B = T/B = 2.0$ will be established to analyze the seepage through earth dams with or without toe drainage systems.

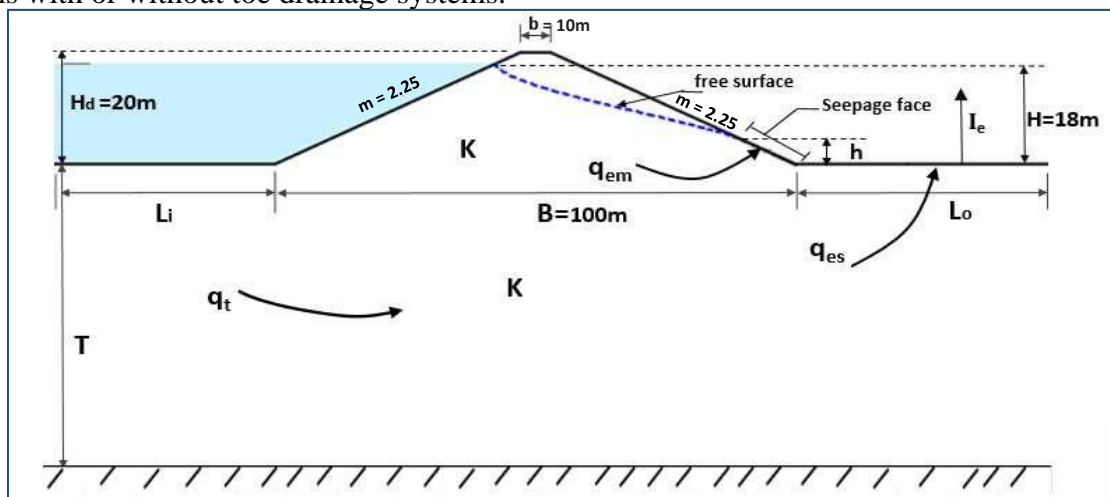


Fig (2) Determination of the active zone of seepage.

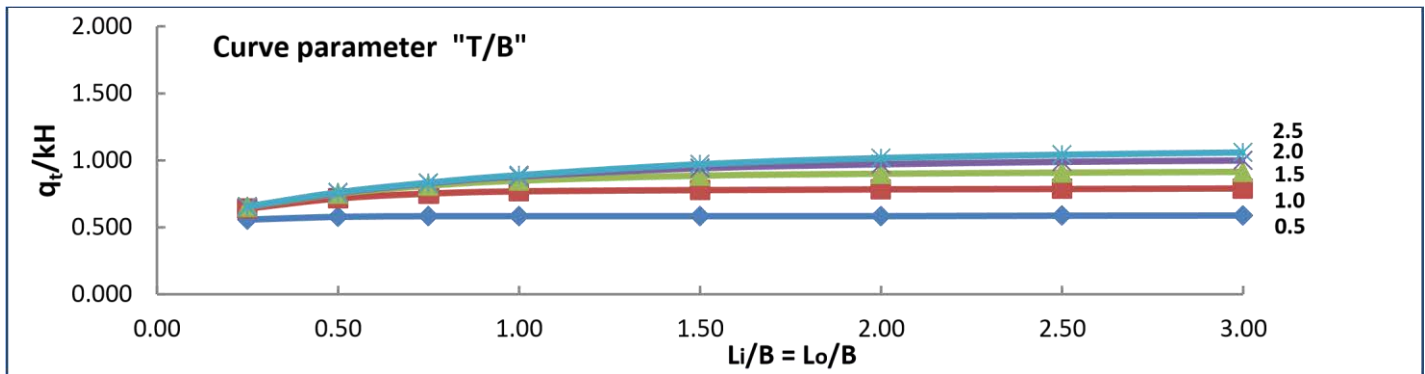


Fig (3) Effect of seepage face lengths and foundation depth on the seepage discharge.

2 Analysis of Results

a. Embankment without toe drainage systems. Such a case is considered as a reference one used to be a base of comparison with other cases of dam with toe drainage systems. Considering a maximum relative head $H/B = 0.18$, slope factor $m = 2.25$, as given in Fig (2) the resulted seepage characteristics are; Total discharge (q_t/KH) = 0.971, Embankment discharge (q_{em}/KH) = 0.149, Escaped discharge (q_{es}/KH) = 0.822, Vertical projection of the seepage face (h/H) = 0.257, and Relative exit gradient ($I_e \cdot B/H$) = 2.33.

It must be noted that, the embankment discharge q_{em} , is that passes through the seepage surface, and may be caught by toe drainage systems if required.

The results of the numerical model, for the reference case, are checked by those obtained using the analytical solution presented in *Grishin* [3], *Nedrigy* [4], *Rozanov* [5], and *Chugaev* [6]. The comparison showed a great agreement between the numerical model and the analytical ones.

b. Effect of slope factor (m). The embankment slopes must be relatively flat to avoid sloughing of the upstream face, due to rapid drawdown, and to safeguard the downstream slope against sliding. *USACE* [7] recommended the embankment slope factor (m) to be between 8.0 - 10.0. Such a range may not be practically unacceptable because this will increase the embankment materials which in turn increase the construction costs. Therefore, different values of slope factor $m = 2.0$ to 10.0 were tested to declare the resulted effect on the relative seepage discharge q_t/KH , as shown in Fig (4). It is seen that values of q_t/KH rapidly decrease up to $m = 4$, beyond which a slight decrease is found up to $m = 7$, after which no decrease occurs in the discharge. Considering an embankment with slope factor $m = 4$, the total discharge is $q_t/KH = 0.95$, resulting a percentage decrease 2% compared to the reference case, where $m = 2.25$. The located free surface for $m = 2.25$ and $m = 4.0$, given in Fig (5), shows a decrease of h/H values from 0.257 to 0.253 with a percentage reduction 1.6%. As for the maximum exit gradient, I_e , obtained just at the toe point, is $I_e = 0.30$ for $m = 4.0$, and $I_e = 0.420$ for $m = 2.25$ giving a percentage decrease = 29%.

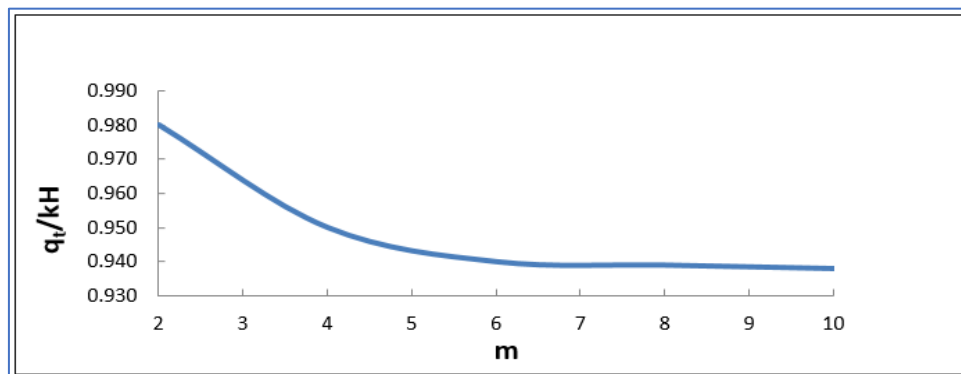


Fig (4) Effect of slope factor “m” on the seepage discharge.

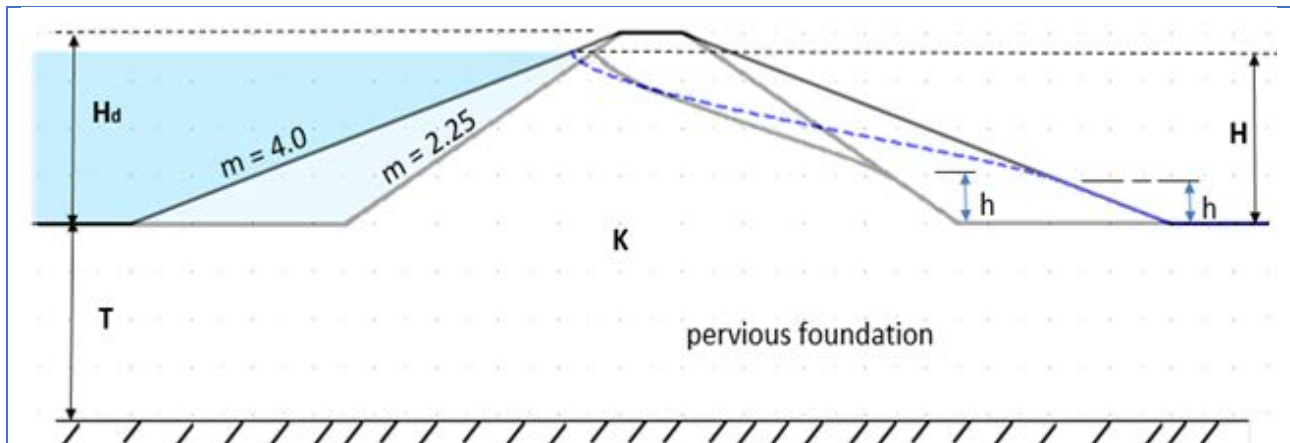


Fig (5) Location of the free surface for $m = 2.25$ and $m = 4.0$.

c. Effect of toe drainage systems. As mentioned above, increasing the slope factor (m) will increase the construction cost and, in the same time, no considerable decrease in values of q_t/KH and h/H is found. Even the value of ($m = 4$) is relatively high with accordance to hydraulic and stability considerations. Therefore, toe drainage systems are used to decrease the slope factor (m) and hence decrease the construction cost. In the present study, the slope factor $m = 2.25$ is established to analyze the performance of the considered toe drainage system. The effect of the considered toe drainage systems, on the seepage discharge, is discussed below.

i. Effect of drainage blanket with pipe drain. Existence of the drainage blanket is essential since acts as a filter allows seepage water to pass through holes of the pipe drain without soil particles. The location of pipe with respect to blanket is at the midpoint of the blanket length as given by *USBR* [8]. The maximum length of blanket (X_b) is taken so that the minimum distance between blanket and the mid-point of the embankment bottom width equals embankment height plus 1.5m *Punmia and Pande* [9]. According to this rule, the maximum available length of blanket, in the present study is $X_b/B = 0.30$. The combined effect of both blanket and drain, on the seepage discharge q_t/KH , includes; thickness (t_b), conductivity (K_b) and length (X_b) of blanket, while for drain; diameter (d_p) and position (X_p). The effect of both blanket height and pipe diameter on the discharge is analyzed considering a relative conductivity, $K_r = K_b/K = 5$, relative length $X_b/B = 0.30$, and pipe position $X_p/B = 0.15$. For this purpose, different values are tested for the relative blanket height t_b/B ranges from 0.15 to 0.40 and pipe diameter $d_p = 0.25 \sim 1.0$ m, as shown in Fig (6). It is found that the minimum value of (t_b/H) giving the maximum discharge q_t/KH , for all pipe diameters, is $t_b/H = 0.275$. The validity of such value is checked using other values of K_r , X_b , X_p for the blanket as well as various values for embankment height (H_d), slope (m), and head (H). It is found that the obtained relative thickness of blanket $t_b/H = 0.275$ is valid. Therefore, it can conclude that, the minimum relative height of blanket, that gives the maximum discharge is $t_b/H = 0.275$.

The effect of blanket conductivity is studied using values of K_r ranges from 0.0 to 20.0 considering $d_p = 0.50$ m, $X_b/B = 0.30$, $X_p/B = 0.15$, and $t_b/H = 0.275$. The results plotted in Fig (7) declare that the discharge rapidly increase up to $K_r = 2$, after which a slight increase is found up to $K_r = 15$ beyond which nearly no increase in the discharge. Hence, the minimum relative conductivity after which nearly no increase in the discharge is $K_r = 15$.

It can state that the most effective relative conductivity is $K_r = 2.0$.

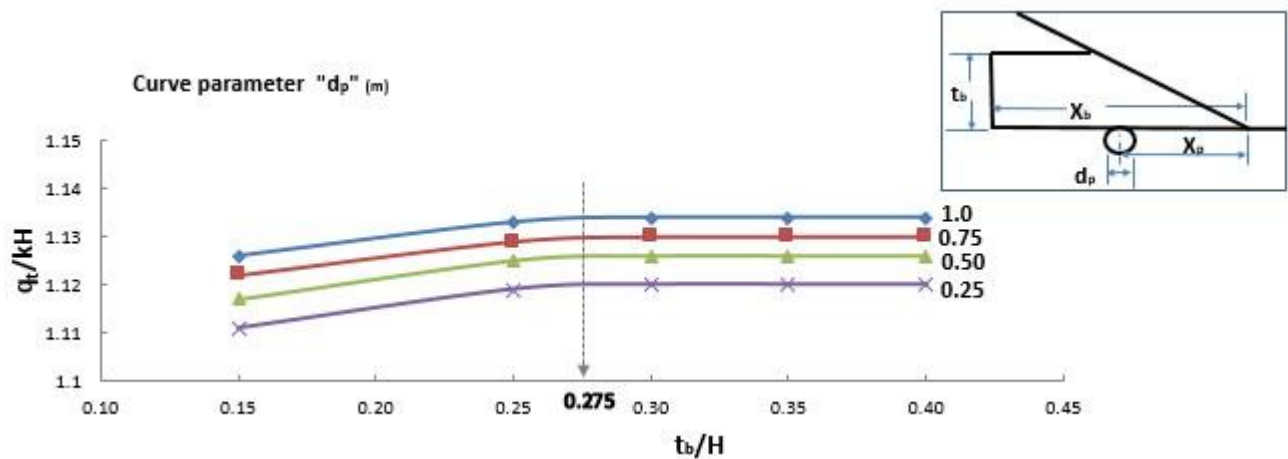


Fig (6) Effect of both blanket thickness and pipe diameter on the discharge.

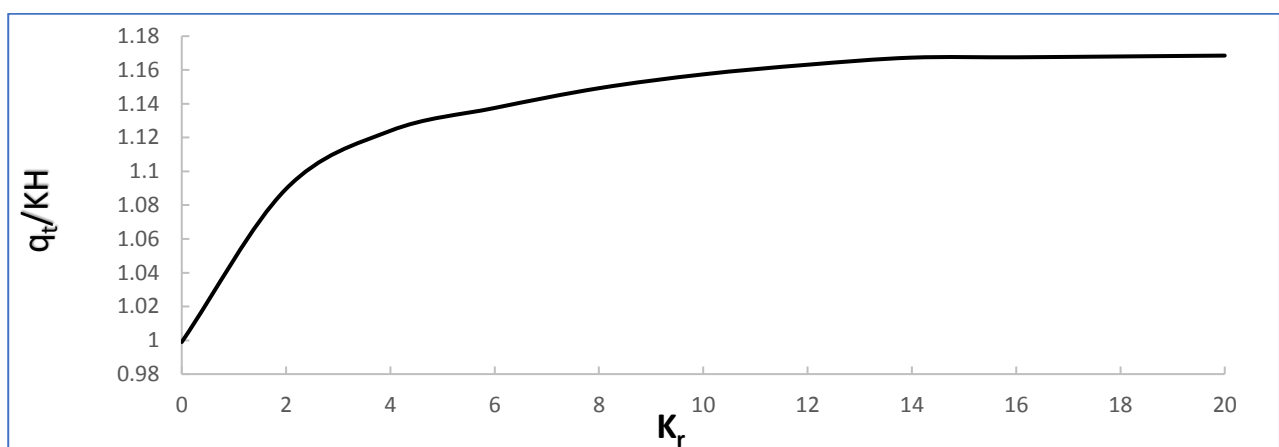


Fig (7) Effect of blanket relative conductivity on the discharge.

The effect of blanket length X_b on the seepage discharge and location of the free surface is analyzed using values of X_b/B varies from 0.10 to 0.30. Considering $K_r = 2, 5, 10, 15$, $d_p = 0.50$ m, and $X_p/X_b = 0.50$, results are graphically presented as shown in Fig (8). It is obvious that both total and pipe discharge increases as X_b increases, for all values of K_r . On contrast, the escaped discharge q_{es}/KH decreases by increasing both X_b and K_r .

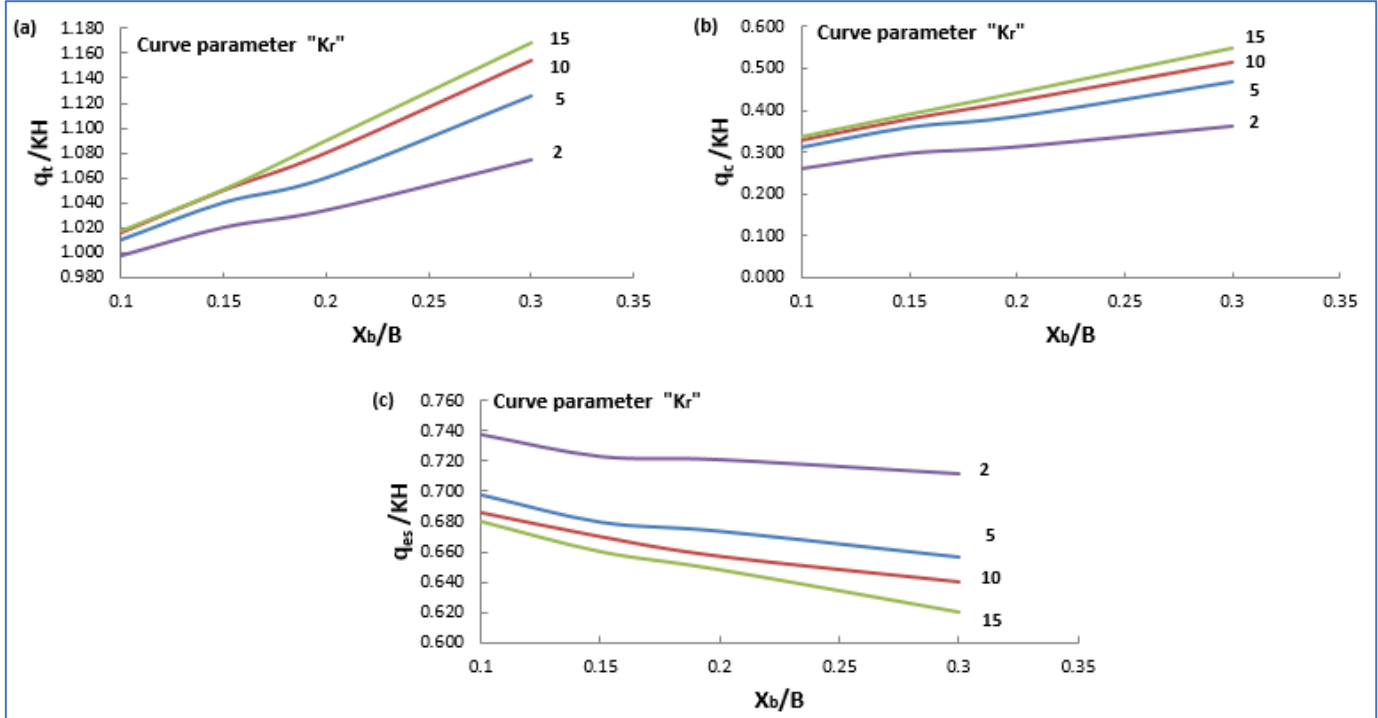


Fig (8) Effect of blanket length on the discharge; a) total discharge, q_t , b) pipe discharge, q_c , and c) escaped discharge q_{es} .

Regarding to the effect of pipe position on both the discharge and the location of free surface, various position for the pipe drain was tested as X_p/B ranges from 0.00 to 0.30, taking in consideration values of $X_b/B = 0.30$, $d_p = 0.50$ m, and $K_r = 2, 5, 10, 15$, as given in Fig (9). The results show that the total discharge increases as X_p/B increases. As for the pipe discharge, it increases as X_p/B increases up to $X_p/B = 0.10$, then a slight increase is existed, meanwhile, the escaped discharge decreases for values of $X_p/B \leq 0.10$, after which a slight increase is found. As a result, the minimum relative position of the pipe drain giving the minimum escaped discharge is $X_p/B = 0.10$ or $X_p/X_b = 0.33$.

Considering $K_r = 10$, another approach is behaved to express the effect of pipe position X_p , with respect to blanket length X_b , on the discharges q_t/KH , q_c/KH , and q_{es}/KH for values of $X_b/B = 0.10, 0.20, 0.30$, as shown in Fig (10). It is seen that the minimum relative position of pipe drain, giving the minimum escaped discharge, is $X_p/X_b = 0.33$ which represents a value of $X_b/B = 0.10$ as obtained above. Such behavior is the same for $K_r = 2, 5$ and 15 . It means that the relative conductivity has no effect on the minimum position of pipe $X_p/X_b = 0.33$. It can conclude that the position of pipe at the outer third of blanket length gives the maximum pipe discharge. Figure (10-b) reveals that location of pipe at $X_p/X_b = 0.00$ gives a minimum discharge $q_c/KH = 0.20$ whatever the value X_b/B , this means that no discharge entering the pipe from the embankment, only from the foundation. Considering $K_r = 2, 5, 10, 15$, $d_p = 0.50$ m, $t_b/H = 0.275$, and $X_p/X_b = 0.33$, the effect of the drainage blanket, with a pipe drain, on the shape of the free surface is given in Fig (11).

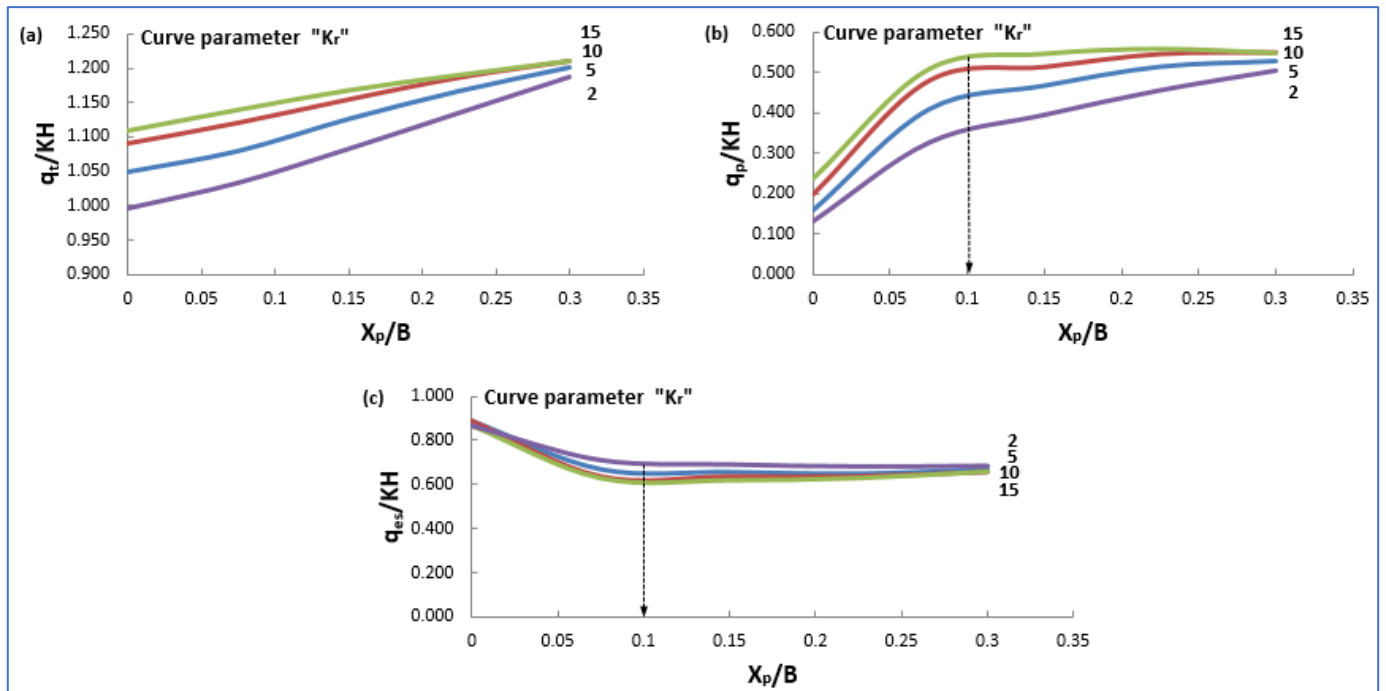


Fig (9) Effect of pipe position on the discharge; a) total discharge, q_t , b) pipe discharge, q_c , and c) escaped discharge q_{es} .

The maximum relative exit gradient $I_e \cdot B/H$ is found for $X_b/B = 0.30$, and $X_p/B = 0.10$, as 1.92, 1.55, 1.25, 1.11 for $K_r = 2, 5, 10, 15$, respectively. Such values show a decrease of the maximum exit gradient by 18 % for $K_r = 2$, 34 % for $K_r = 5$, 46 % for $K_r = 10$, and 52 % for $K_r = 15$, compared to the reference case.

ii. Effect of drainage banquette. Drainage banquette has the same objective as in drainage blanket. Effect of drainage banquette; length and conductivity are performed using constant values of $m = 2.25$, $H/B = 0.18$, and the slope of banquette $m' = 1.0$. For this purpose, different relative conductivities $K_r = 2, 5, 10, 15$ and different relative lengths for the banquette $X_{ban}/B = 0.10, 0.15, 0.20, 0.25$, and 0.30 are tested to declare the resulting effect on the seepage discharges q_t , q_{es} , q_c .

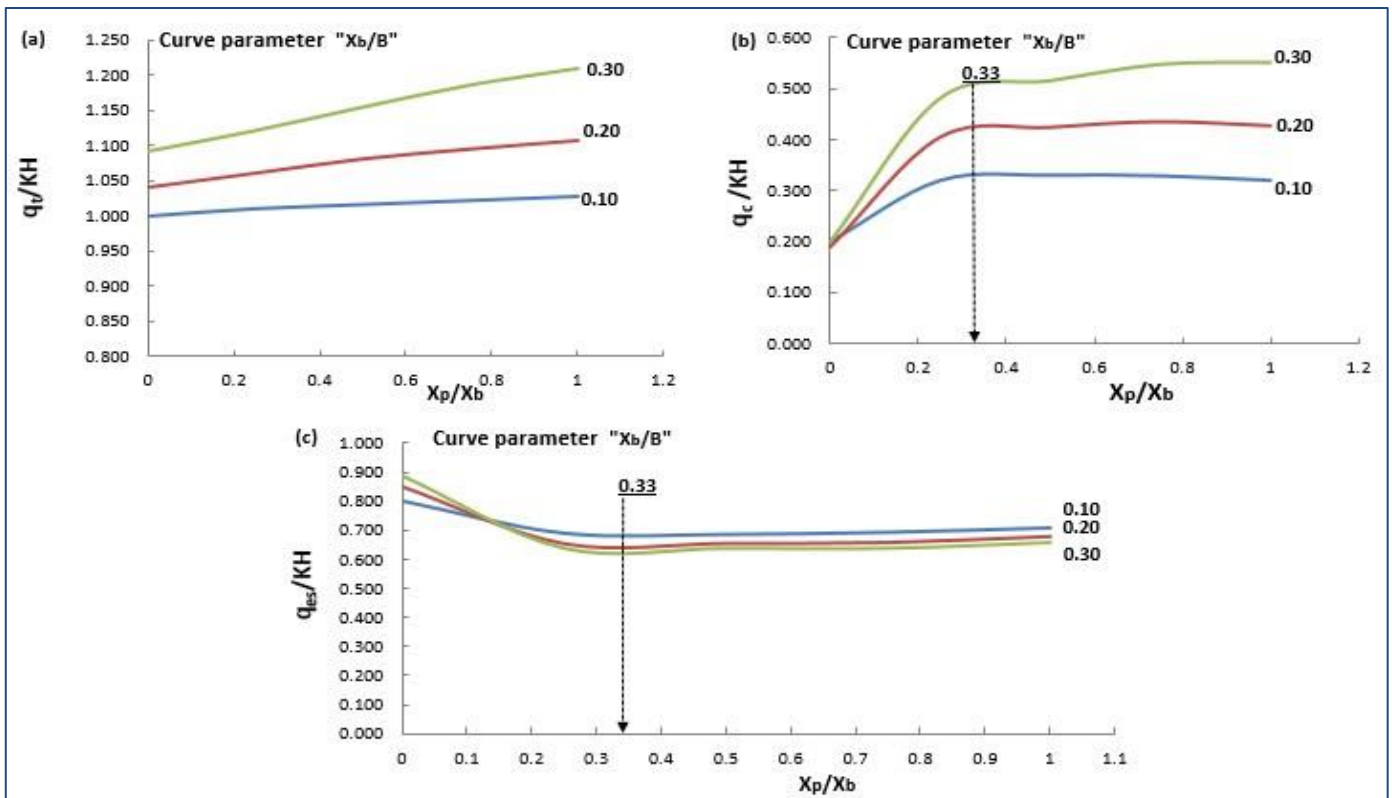


Fig (10) Effect of pipe position related to blanket width on the discharge; a) total discharge, q_t , b) pipe discharge, q_c , and c) escaped discharge q_{es} .

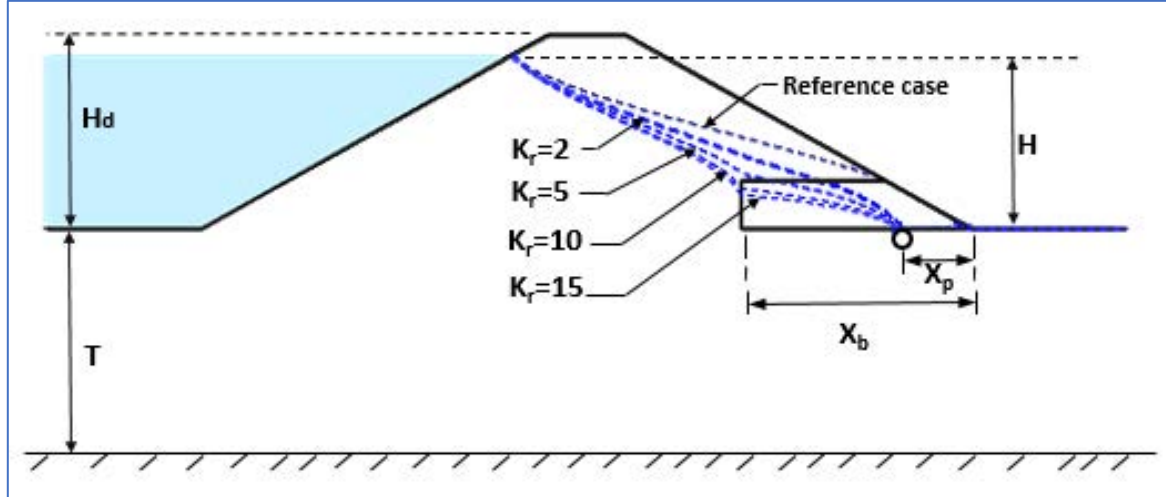


Fig (11) Effect of the drainage blanket with a pipe drain on the shape of the free surface.

Figure (12) shows the variation of seepage discharge due to variation of both X_{ban} , and K_r . It is seen that both values of q_t/KH and q_c/KH increases while q_{es}/KH decreases as X_{ban}/B increases. It is clear also that q_c/KH and q_{es}/KH have the same value when $X_{ban}/B = 0.22$, beyond which the effect of banquette length is being higher and in turn the blanket efficiency increases. The percentage increase in the total discharge, related to the reference case, $\Delta q_t/KH$ due to increasing X_{ban}/B is presented in Fig (13). It is seen that the relative conductivity has no effect.

On the other hand, Fig (14) shows the effect of banquette on the free surface. The effect of the relative conductivity is vanished in this case due to the absence of tail water.

Considering $X_b/B = 0.30$, the resulted maximum relative exit gradient I_e . $B/H = 0.688$ with a percentage decrease of 71% compared to the reference case.

iii. Effect of catch drain. Constant values for the catch drain cross section such as bottom width $b' = 2.0$ m, side slopes 2:1, and depth $y' = 10$ m, are considered. The effect of catch drain location behind the dam embankment X_c/B is analyzed using values of $H/B = 0.18$, and $m = 2.25$. Various values of the relative distance $X_c/B = 0.0, 0.02, 0.04, 0.06, 0.08$, and 0.1 are chosen to get the effect on the seepage discharges, as shown in Fig (15). Both total discharge q_t/KH , and catch discharge q_c/KH decrease with increasing X_c/B . With respect to the escaped discharge, it decreases as X_c/B increases up to $X_c/B = 0.06$ after which, a steep increase is found. This refers to that, at this value $X_c/B = 0.06$ the free surface just touches the embankment at its toe point. For values of $X_c/B > 0.06$, the free surface intersects the downstream slope resulting a seepage surface height h more than that for the reference case, and hence the catch drain becomes useless, as shown in Fig (16). The effect of X_c/B on value of the relative depth of water in the drain y/T is given in Fig (17). The figure shows that the relative y/T has a slight decrease for $X_c/B \leq 0.02$, then it being constant up to $X_c/B = 0.06$ after which, it decreases again. It can state that the effect of X_c/B on y/T is being small.

3 Comparison between the tested toe drainage systems

a. Seepage discharges. A comparison between the maximum relative discharges obtained using the different toe drainage systems is illustrated in Table 1, considering the following conditions: i) $X_b/B = X_{ban}/B = 0.30$, ii) $X_p/B = 0.10$, iii) $X_c/B = 0.00$, and iv) $K_r = 2, 15$ for the blanket with pipe drain and drainage banquette. As given in Table 1, the percentage increase in the total discharge (q_t/KH) ranges from 8~26%, while the percentage decrease in the escaped discharge (q_{es}/KH) ranges from 15~80%. The sign (*) denotes the embankment discharge.

b. Exit gradient. Considering $X_b/B = X_{ban}/B = 0.30$, $X_p/B = 0.10$, and $K_r = 2, 15$, the relative exit gradient I_e . B/H along the exit face is calculated at relative distance X_i/B up to 1.0. Results are shown in Fig (18). It is seen that the exit gradient steeply decreases up to $X_i/B = 0.10$, after which a slight decrease is obtained. The exit gradient using banquette gives the minimum values compared to the drainage blanket with pipe drain. Table 2 shows a comparison between values of the maximum relative exit gradient $I_{e \max}$. B/H resulted using the toe drainage systems.

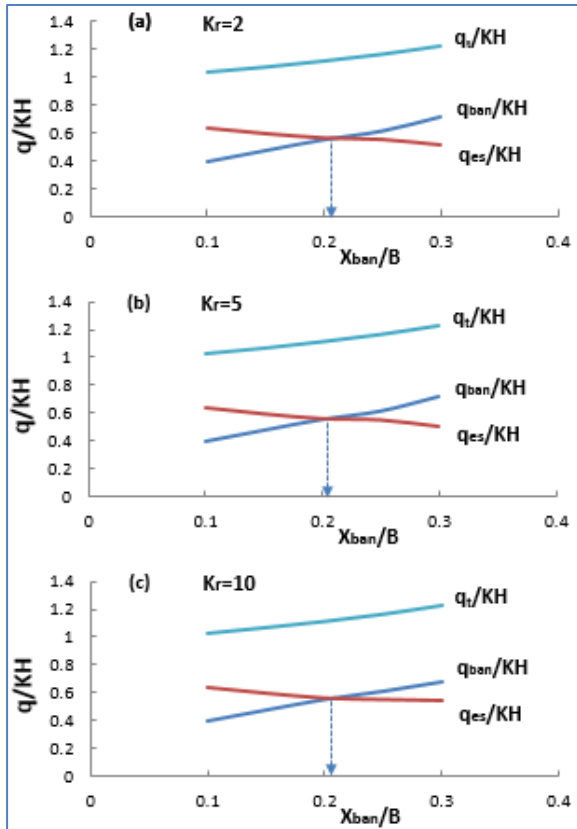


Fig (12) variation of seepage discharge due to variation of both X_{ban} , and K_r .

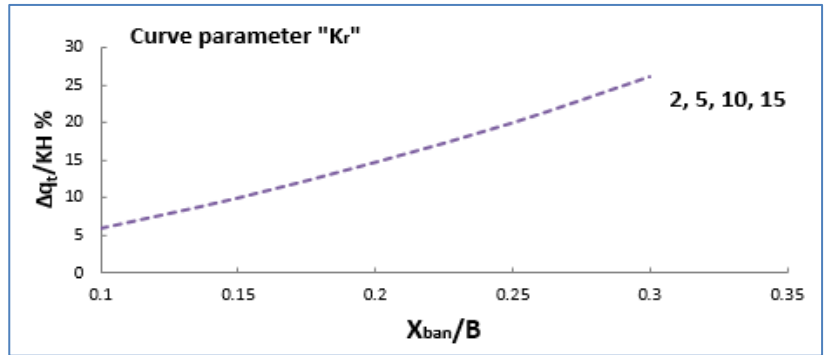


Fig (13) Percentage increase in the total discharge, related to the reference case, due to increasing banquette relative length.

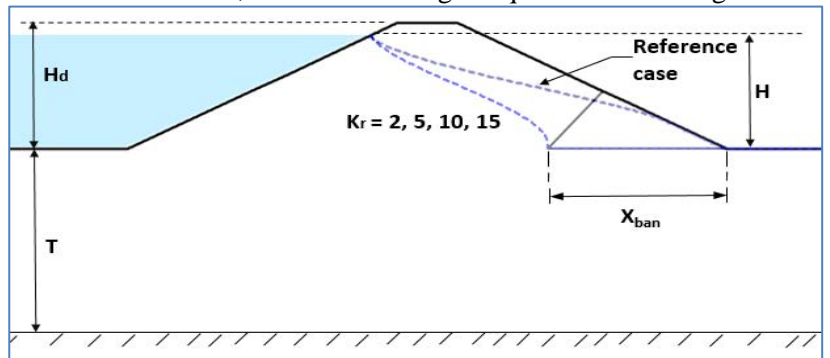


Fig (14) Effect of banquette on the free surface.

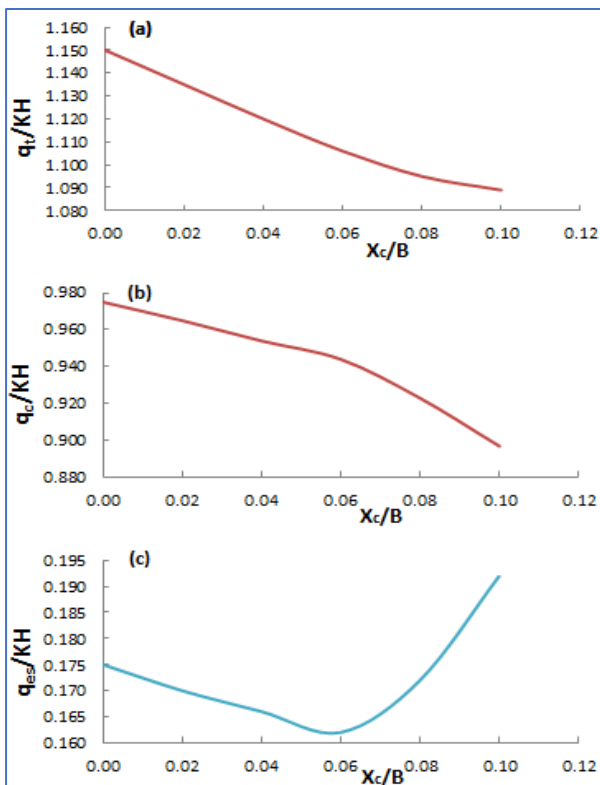


Fig (15) effect of catch drain location on the seepage discharges; a) total discharge, b) catch discharge, and c) escaped discharge.

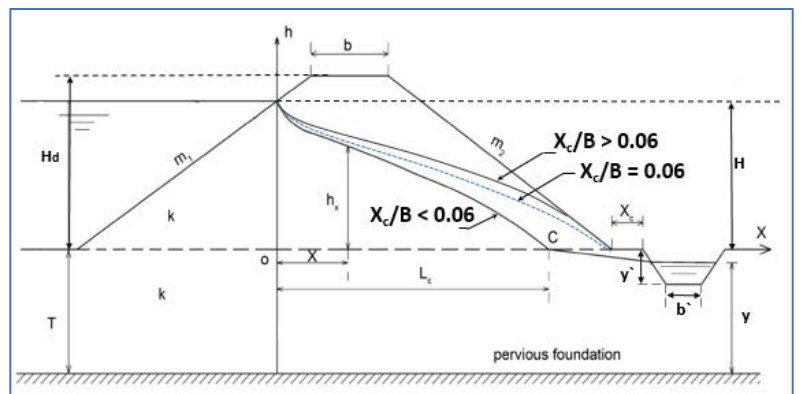


Fig (16) Effect of the catch drain on the shape of the free surface.

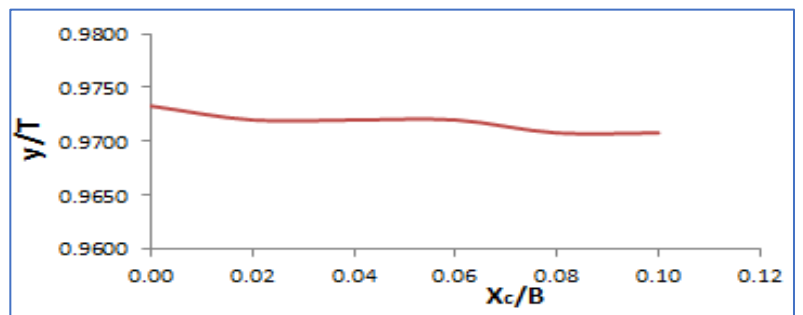


Fig (17) Effect of catch drain position on the drain water level.

Table 1. Comparison between the maximum relative discharges of the toe drainage systems.

| Discharges | Reference Case | Drainage blanket with pipe drain | | % Dev. | Drainage banquette | | % Dev. | Catch drain $X_c/B=0.0$ | % Dev. |
|-------------|----------------|----------------------------------|------------|---------|--------------------|------------|---------|----------------------------|--------|
| | | $K_r = 2$ | $K_r = 15$ | | $K_r = 2$ | $K_r = 15$ | | | |
| q_t/KH | 0.971 | 1.050 | 1.150 | 8→18 | 1.220 | 1.220 | 26 | 1.150 | 18 |
| q_c/KH | 0.149 * | 0.350 | 0.525 | | 0.714 | 0.716 | | 0.975 | |
| q_{es}/KH | 0.822 | 0.700 | 0.625 | -15→-24 | 0.506 | 0.504 | -38→-39 | 0.175 | -79 |

*→ Embankment discharge.

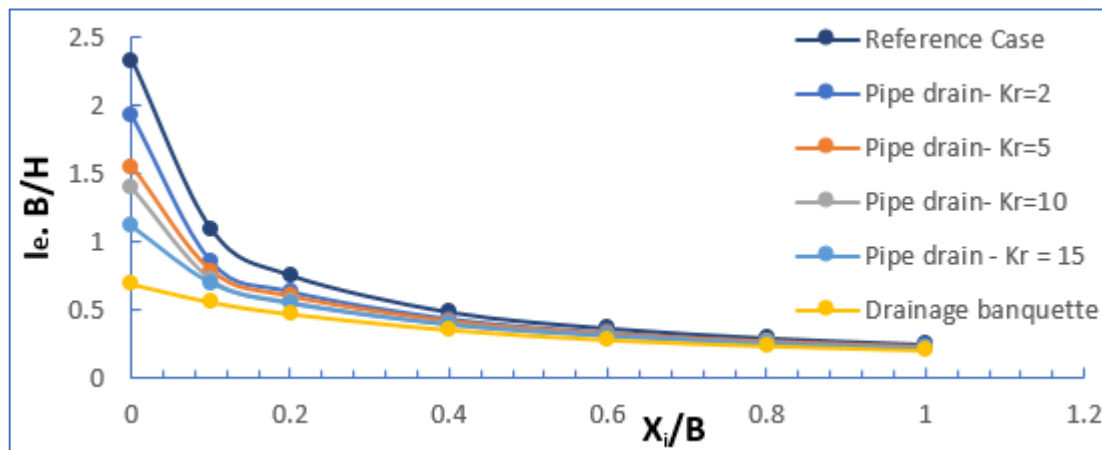


Fig (18) Variation of relative gradient ($I_e. (B/H)$) with relative distance (X_i/B) for blanket with pipe drain, banquette, and the reference case

Table (2). Comparison between the maximum relative exit gradient of the toe drainage systems.

| Maximum exit gradient | Reference Case | Drainage blanket with pipe drain | | % Dev. | Drainage banquette | | % Dev. |
|-----------------------|----------------|----------------------------------|------------|------------|--------------------|------------|--------|
| | | $K_r = 2$ | $K_r = 15$ | | $K_r = 2$ | $K_r = 15$ | |
| $I_e. B/H$ | 2.33 | 1.92 | 1.11 | - 18→ - 52 | 0.688 | 0.688 | - 71 |

4 Conclusions. The current study focuses on evaluation of the hydraulic performance of the tested toe drainage systems used as a control measures to protect earth dams, based on pervious foundation. The study is analyzed using the software program based on the finite element method (Seep/w). As a result, the main conclusions could be arranged as follows:

1. The tested toe drainage systems cause an increase in the total discharge by about 26%, but in the same time make the free surface to be far enough from the downstream slope to a large extent.
2. The minimum relative thickness of blanket giving the maximum discharge is $t_b/H = 0.275$.
3. The minimum position of the pipe drain giving minimum escaped discharge is at the outer third of the blanket length.
4. The most effective relative conductivity is $K_r = 2$, and the maximum relative conductivity after which no effect on the seepage discharge is $K_r = 15$.
5. The banquette conductivity has no effect considering the dry D.S condition.
6. The maximum location of the catch drain with respect to dam base width is $X_c/B = 0.06$, to ensure that the free surface will totally be within the dam embankment.
7. The considered toe drainage systems decrease the maximum exit gradient to a about 71%.

References

- [1] Pavlovsky, N. N. (1931). Seepage through Earth Dams. Leningrad, Russia.
- [2] Harr, M. E. (1962). Groundwater and Seepage. McGraw-Hill Book Company, New York.
- [3] Grishin, M. M. (1982). Hydraulic Structures. Mirpublishers, Moscow.
- [4] Nedrigy, V. P. (1983). Hydraulic Structures. Gostroyzdat, Moscow.
- [5] Rozanov, N. N. (1983). Earth Dams, Strouizdat, Moscow.
- [6] Chugaev, R. R. (1985). Hydraulic Structures part (I) (In Russian). Agropromizdate, Moscow, Russia.
- [7] U. S. Army Corps of Engineering. (1986). Seepage Analysis and Control for Dam. Washington, D.C. 20134-1000.
- [8] USBR (1977). Design of Small Dams, Water Resources Technical Publication.
- [9] Punmia, B. C. and B. B. L. Pande (1983). Irrigation and Waterpower Engineering, Standard Publishers distributors, Naisarak, Delhi, India.

3- Rate of Copper ions removal from Copper Sulfate solution by Cementation on steel turbulence promoters using stirred tank reactor

A. M. Ismail¹, M. S. Mansour¹, D. Elgayar¹, and Y. H. Farid²

¹Chemical Engineering Department, Faculty of Engineering, Alexandria University

²Basic Science Department, Alexandria Higher Institute for Engineering and Technology

ahmed.mah.ismail@gmail.com

Abstract

The present study is concerned with the removal rate of Copper ions Cu⁺⁺ from wastewater by cementation of copper from copper sulfate solution on a horizontal steel sheet placed at the bottom of a square stirred tank reactor and fitted with square steel turbulence promoters.

The variables studied were solution concentration, rotation speed, impeller geometry, promoter diameter and distance between promoters. The rate of mass transfer was found to increase with the rotational speed and decreased with the increase of distance between promoters. The data were correlated with the dimensionless equation: $Sh = 0.23 Sc^{1/3} Re^{0.49}$

Keywords: Mass transfer, cementation, wastewater, copper, stirred tank, turbulence promoters

1 Introduction

In the recent years, the water contamination by heavy metals in both surface and ground water raised the environmental alert for many scientist and engineers due to their toxicity and impact on human and aquatic life [1]. Copper is one of the heavy metals which requires humans to have homeostatic capabilities to regulate copper in the system. Effects such as severe dermal, eye, and inhalation irritation are noticed by acute toxicity studies. Acute toxicity describes the adverse effect of a substance that result either from single exposure or from multiple exposures in a short period of time [2]. Copper, which is considered detrimental to marine life and biological treatment for wastewater could be found in many wastewater sources. Copper plumbing is a major source in the household being responsible for a minimum of 40% to 50% of the copper wastewater load in the United States [3].

On the other hand, copper could be detected in many of the industrial wastewater effluents sources including printed circuit board manufacturing, metal finishing industry e.g. pickling of copper and its alloys, electroplating and electro-less plating, electro polishing, paint manufacturing, wood preservatives and printing operations. In addition, the natural factors include soil erosion, volcanic activities, urban run offs and aerosols particulate [4-5]. Scientist since long time invent and develop many technologies leading to the removal of copper from wastewater streams. The most famous and important methods were adsorption, chemical precipitation, ion exchange, reverse osmosis and electro dialysis [6-10]. Each of the mentioned methods has drawbacks. For example, adsorption, reported as it has limited applications to certain concentrations of copper ions [11], chemical precipitation may result in a complex formation, Ion exchange and reverse osmosis, consumes a high power in addition to the high cost [12].

Finally, the electro dialysis process needs more efforts to be used efficiently at the industrial scale [13]. Cementation is used as a general term to describe the process whereby a metal is precipitated from a solution of its salts by another electropositive metal by spontaneous electrochemical reduction to its elemental metallic state. A consequent oxidation of a sacrificial metal for the recovery of more expensive and nobler dissolved metal species present in aqueous solutions is needed [14]. Cementation is one of the most effective and economic techniques for recovering toxic or valuable metals from industrial waste solutions [15]. The process has been largely used in industry for a long time, not only in hydrometallurgy but also in the purification of stream and wastewater [16].

Cementation method has some merits, such as recovery of metals in relatively pure metallic form, simple control requirements, low energy consumption and is in general low cost process. On the other hand, the main limitations of the technique are excess sacrificial metal consumption [17].

The main aim of the present work is to study the rate of cementation of copper from diluted copper sulfate solution on steel turbulence promoters by using stirred tank reactor. The studies revealed that increasing the rotational speed of the stirred tank reactor gave a sensible increase of the copper cementation rate [18], effect also of other parameters such as solution concentration, the impeller geometry, different promoters diameter and the distance between promoters on cementation rate were studied.

2 Methods

The apparatus as shown in figure (1) consists of a two liters squared stirred tank reactor with a side length of 10 Cm, with a height of 15 Cm, is fitted with a multi speed agitating motor and insulated with Teflon. Two different impeller geometries were used (i) 90° flat plate turbine and (ii) 45° pitch blade turbine. The tank reactor base is fitted with square steel turbulence promoters. The square steel turbulence promoter diameters are 0.5, 0.75, 1 and 1.5 Cm with a distance between promoters of 0.5, 0.75, 1 and 1.5 Cm respectively. Distance between the turbine impeller and the squared tank reactor bottom base is equal to 3.5 Cm.

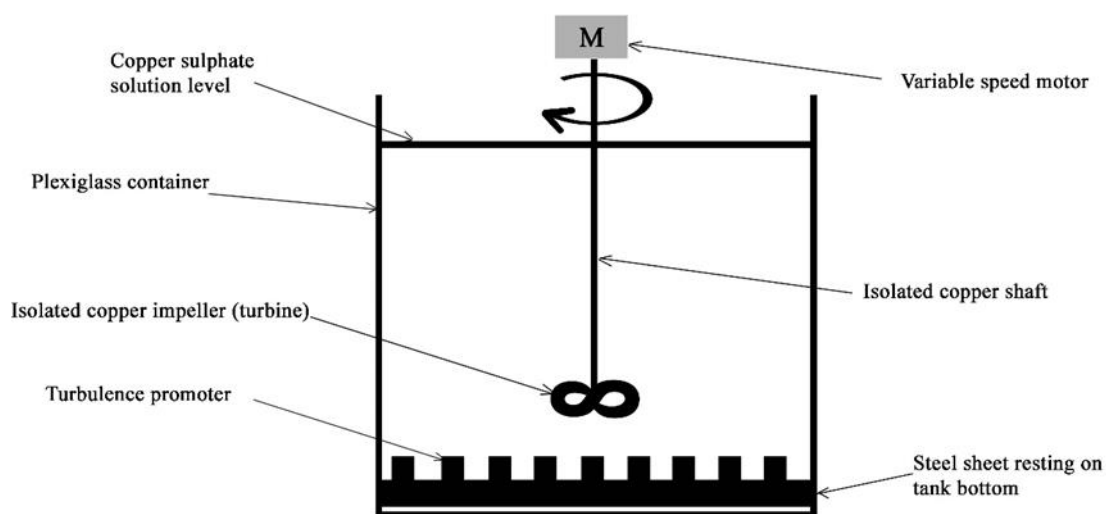


Figure (1) Experimental apparatus

Before each run a stock solution of copper sulfate was prepared by dissolving the copper sulfate analytical reagent in distilled water. The desired experimental concentrations were obtained by successive dilutions with distilled water. The pH of the solution was adjusted by adding 0.1N hydrochloric acid solution each experiment. The pH- meter was used to measure the pH of the solutions. The analytical determination of copper sulfate solutions was carried out by iodometry using standard solution of sodium thiosulfate [19].

Experimental Procedure:

Copper solutions were prepared from the stock solution by successive dilution to the desired concentrations. In each run 1500 ml of synthetic solution were placed in the reactor cell. The pH of the solutions was adjusted by adding 0.1 N hydrochloric acid solutions for each experiment. Before

each run shaft rotation speed was adjusted at the required value, rotation speed was measured by an optical tachometer. A typical experiment runs lasts 45 minutes, where 5 ml samples were collected every 5 minutes from fixed location and analyzed for the percentage removal of copper ions. The rate of copper removal was determined under different parameters [20]. Table (1) shows the physical properties of the solutions at 25°C.

| CuSO ₄ Conc. | ρ (g/cm ³) | μ (g/cm s) (poise) | D (cm ² /s)×10 ⁶ | Sc |
|-------------------------|-----------------------------|---------------------------|--|------|
| 0.025 M | 1.0065 | 0.984043 | 6.24 | 1566 |
| 0.05 M | 1.013 | 0.984043 | 5.94 | 1635 |
| 0.1 M | 1.0259 | 0.984043 | 5.44 | 1763 |

Table (1): Physical properties of CuSO₄ solution at 25°C

3 Results and discussion

For the batch reactor used in the present work, the rate of diffusion-controlled copper cementation on the square promoters is presented by the following equation

$$-Q \frac{dC}{dt} = kAC$$

Which upon integration yields

$$Q \ln(C_0/C) = kAt$$

Where Q is the solution volume in cubic centimeters, C₀, C are initial concentration and concentration at time t, of copper sulfate solution respectively, k is the mass transfer coefficient, and A is the area of the steel plate in addition to the turbulence promoters.

A plot of $\ln(C_0/C)$ verses t gives a straight line of a slope kA/Q from which k can be calculated which expresses the rate of cementation. Figure (1) shows the effect of the rotational speed on the mass transfer coefficient (rate of cementation). It is clear that the rate of cementation increased by increasing rotational speed [18, 21, 22].

Figure (1) a and b shows the effect of increasing the rotation speed on the rate of cementation

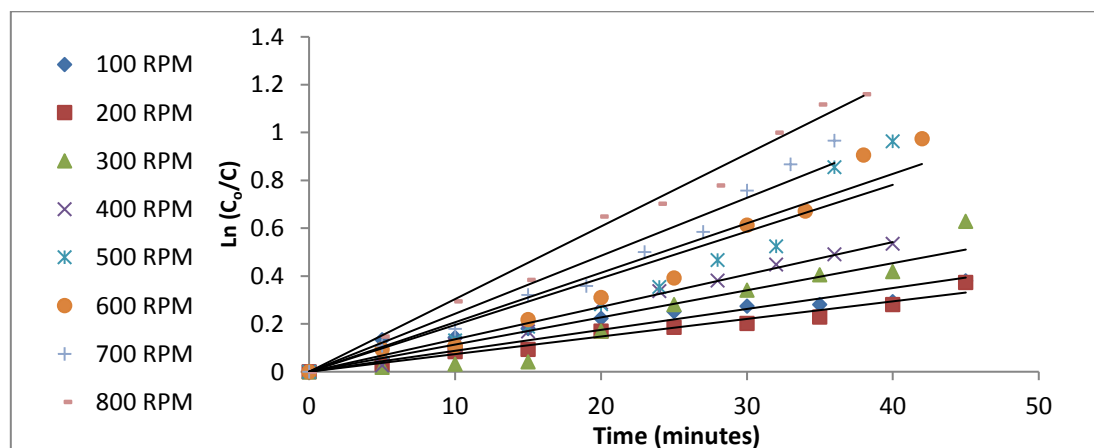


Figure 1 (a) Rate of cementation by various RPM, copper sulfate concentration 0.05M, angle 45°

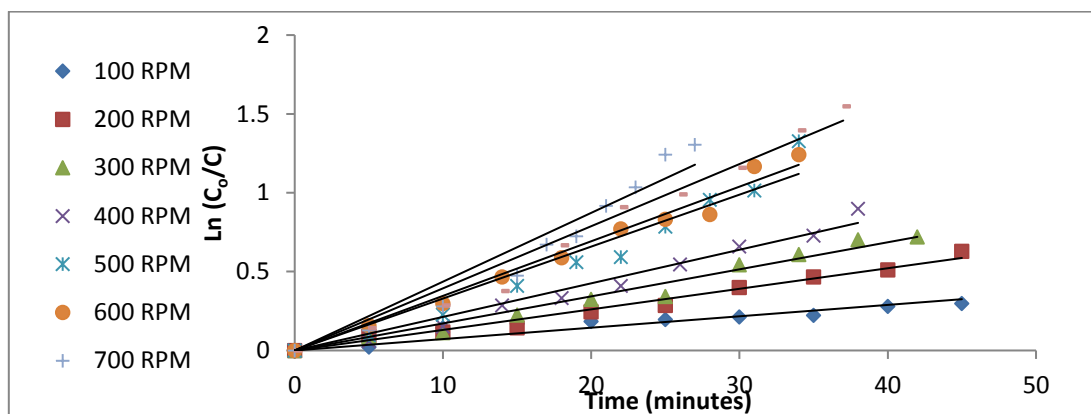


Figure 1 (b) Rate of cementation by various RPM, copper sulfate concentration 0.05M, angle 90°

The impeller geometry used 90° flat plate turbine and 45° pitch plate turbine to enhance the cementation process as shown in figures (1) a & b.

Three different concentrations of copper sulfate studied were used in this work 0.1 M, 0.05 M and 0.025 M of $\text{CuSO}_4 \cdot 5\text{H}_2\text{O}$ [18 , 22].

Figures (2) (3) (4) shows the effect on cementation for the three concentrations.

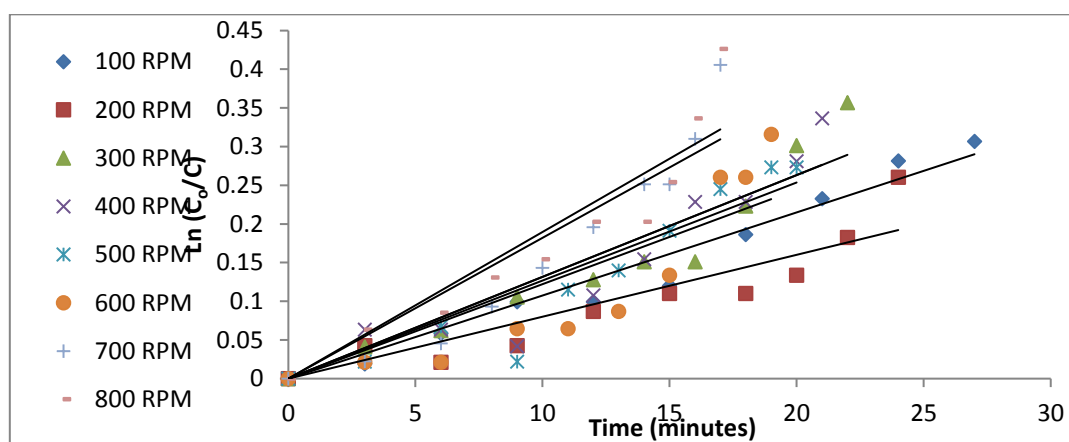


Figure (2) Rate of cementation at copper sulfate concentration 0.1M angle 90°

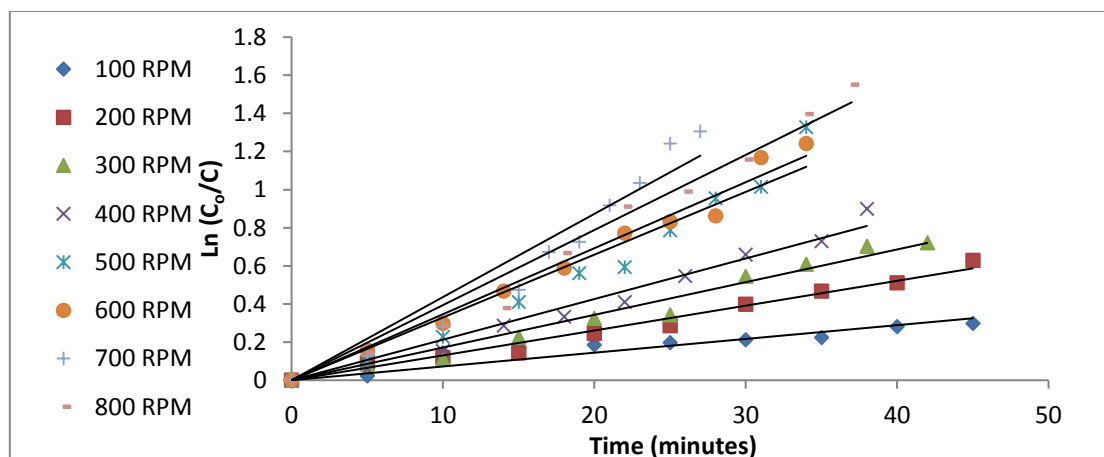


Figure (3) Rate of cementation at copper sulfate concentration 0.05M angle 90°

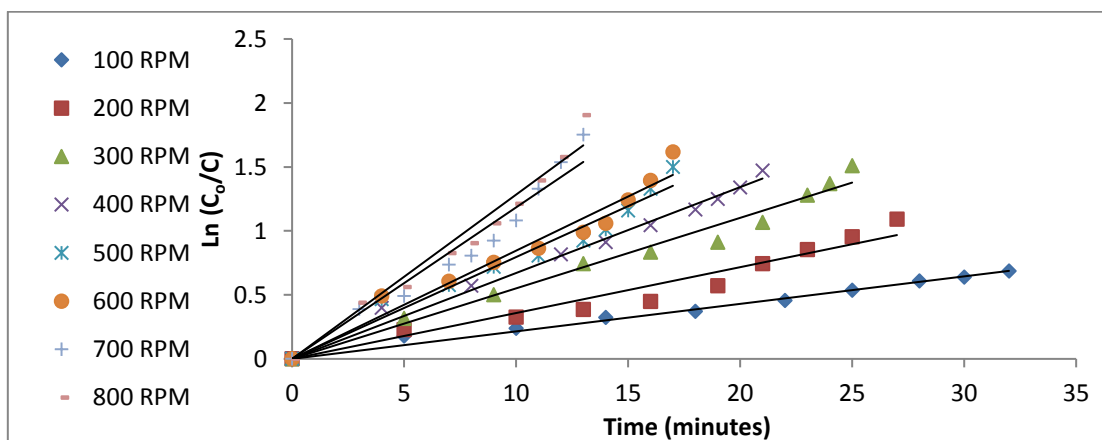


Figure (4) Rate of cementation at copper sulfate concentration 0.025M angle 90°

The square steel turbulence promoters (de) used is: 0.5 Cm, 0.75 Cm, 1 Cm and 1.5 Cm, where $de = 4 \times \frac{\text{cross sectional area}}{\text{perimeter}}$ and the distance between promoters: 0.5 de, 0.75 de, 1 de and 1.5 de, where de is the equivalent diameter [23].

Figures (5)a,b,c&d show the effect of various promoters at 0.025M copper sulfate concentration & impeller geometry of 90°.

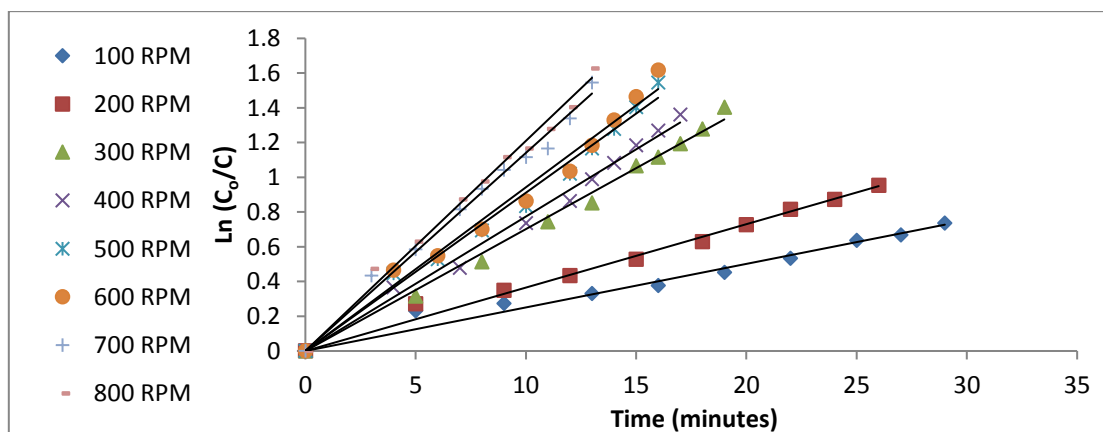


Figure (5.a) Rate of cementation at copper sulfate on square steel sheet promoter 0.5 Cm

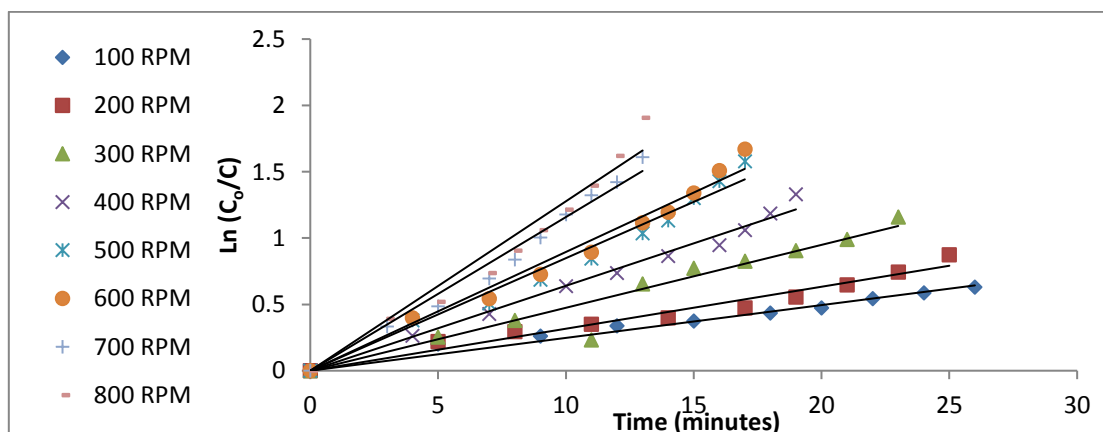


Figure (5.b) Rate of cementation of copper sulfate on square steel sheet promoter 0.75 Cm

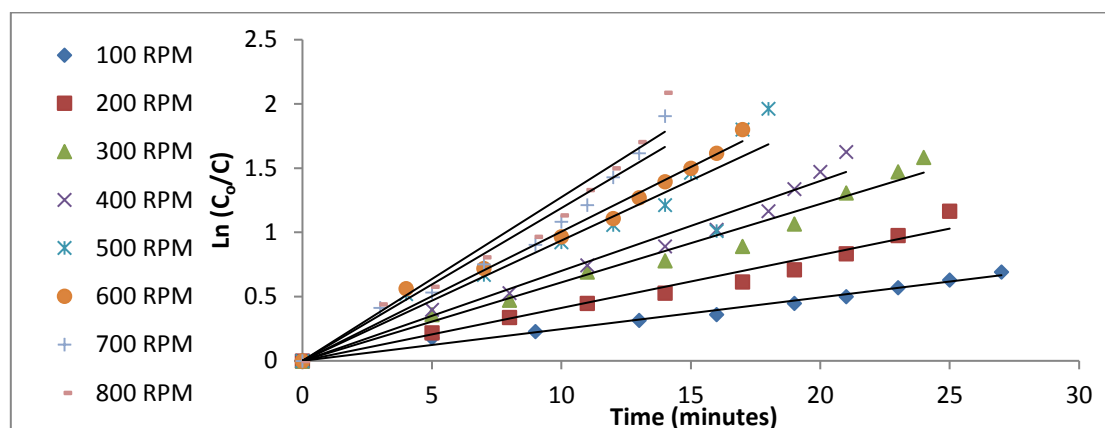


Figure (5.c) Rate of cementation of copper sulfate on square steel sheet promoter 1 Cm

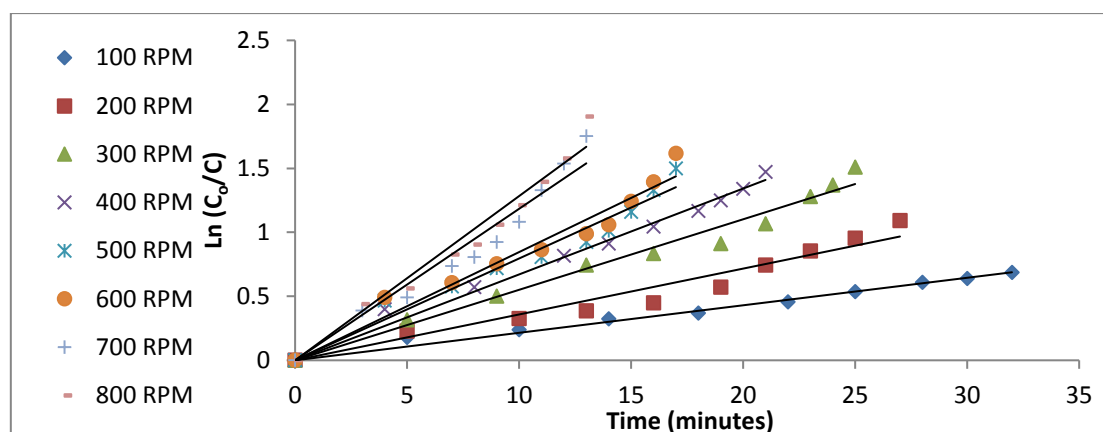


Figure (5.d) Rate of cementation of copper sulfate on square steel sheet promoter 1.5 Cm

As mentioned, during this study a various number of promoters used to evaluate the effect of using different promoters with different height and distance between each promotor.

Figures (6) a & b shows the effect of using promoters with reference to use smooth plate in the cementation process.

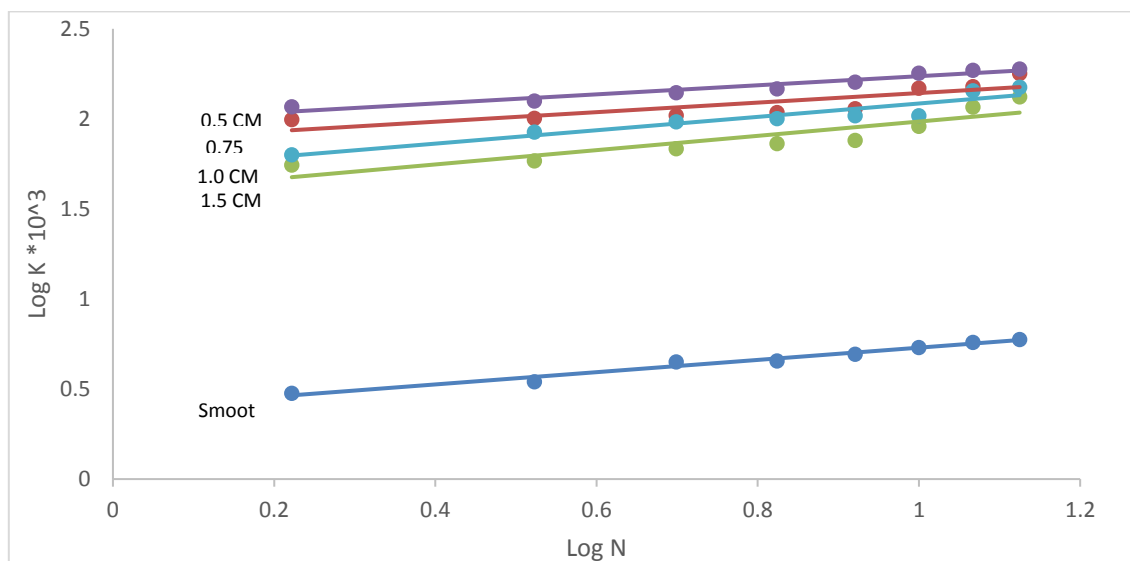


Figure (6.a) plot of Log K vs Log N among various surface roughness @ conc 1.0N Geometry 90°

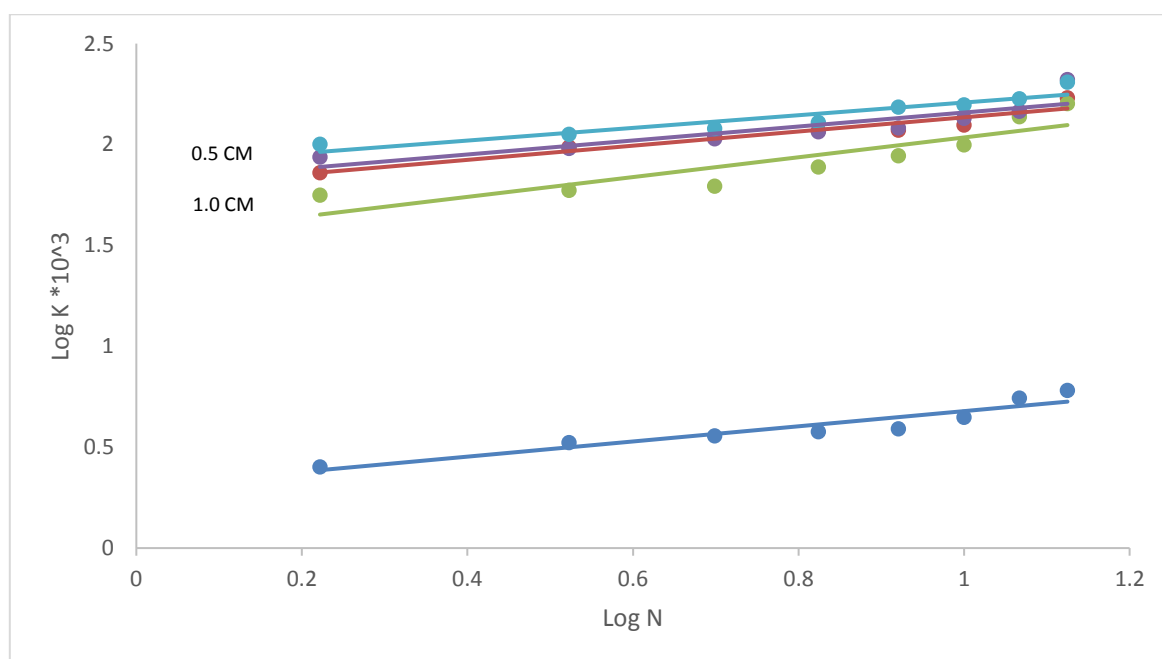


Figure (6.b) plot of Log K vs Log N among various surface roughness @ conc 1.0N Geometry 45°

The mass transfer coefficient, K, for copper cementation on the square steered tank reactor was correlated to other parameters by the dimensionless equation

$$Sh = a Sc^{1/3} Re^a$$

Where,

Sh is Sherwood number, $Sh = Kd_e/D$;

Sc is Schmidt number, $Sc = \mu/\rho D$;

Re is the Reynolds number, $Re = \rho N d^2 / \mu$;

K is the mass transfer coefficient;

ρ is the density of the solution;

μ is the viscosity of the solution;

D is the diffusivity of copper ions;

V is the impeller linear velocity;

The constants a & α were determined using the present experimental data. Following previous experimental and theoretical mass transfer studies, the value of Schmidt exponent was fixed at 0.33 [24] by the following equation:

Figure (7) shows constant α determination and figure (8) shows constant a determination.

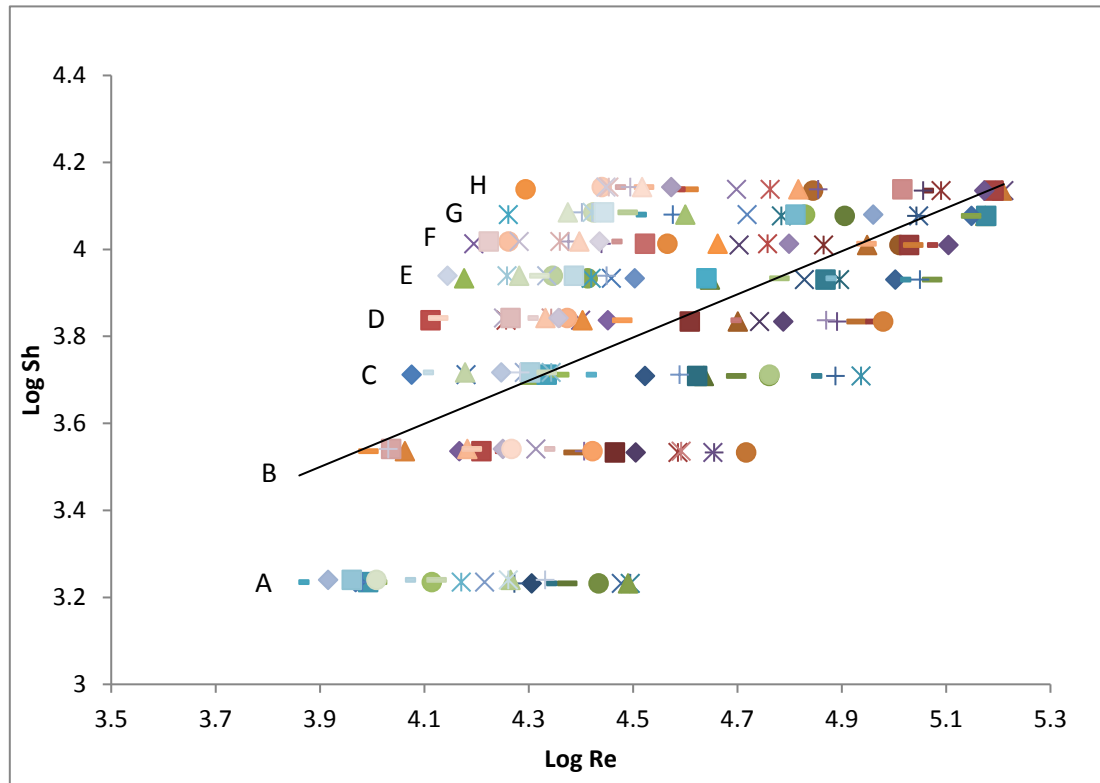


Figure (7) Effect of Log Re on Log Sh Constant α

- Values of group A represents different values of Log Re vs log Sh at 100 RPM
- Values of group B represents different values of Log Re vs log Sh at 200 RPM
- Values of group C represents different values of Log Re vs log Sh at 300 RPM
- Values of group D represents different values of Log Re vs log Sh at 400 RPM
- Values of group E represents different values of Log Re vs log Sh at 500 RPM
- Values of group F represents different values of Log Re vs log Sh at 600 RPM
- Values of group G represents different values of Log Re vs log Sh at 700 RPM
- Values of group H represents different values of Log Re vs log Sh at 800 RPM

By using the values of constants α & β , the value of constant a could be obtained as follow
 $\text{Log Sh} = \log a + \log (\text{Sc}^{1/3} \text{Re}^{0.23})$

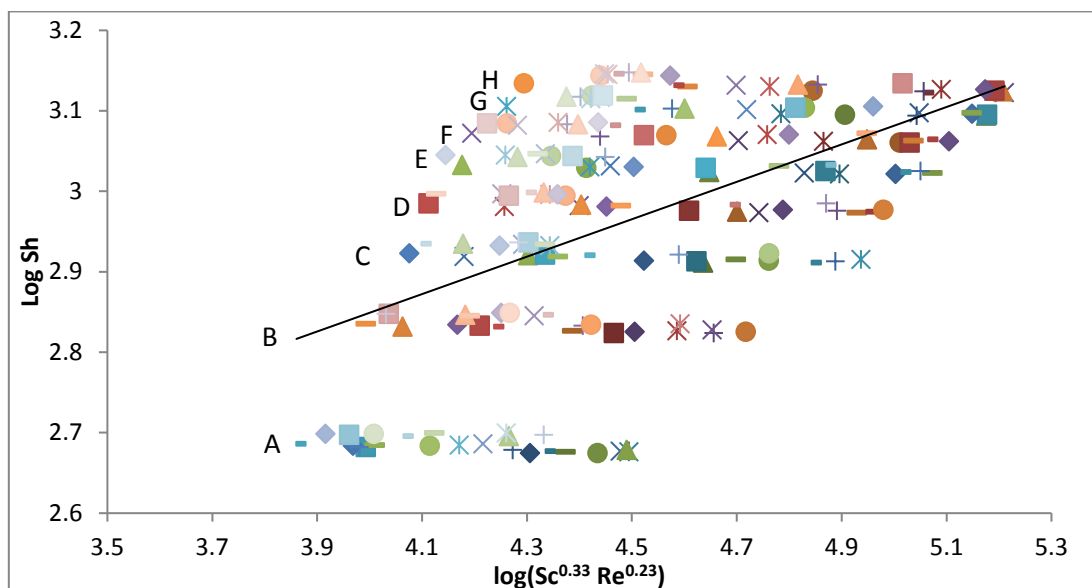


Figure (8) Effect of Log (Sc Re) on Log Sh Constant a

- Values of group A represents different values of Log (Sc Re) vs log Sh at 100 RPM
- Values of group B represents different values of Log (Sc Re) vs log Sh at 200 RPM
- Values of group C represents different values of Log (Sc Re) vs log Sh at 300 RPM
- Values of group D represents different values of Log (Sc Re) vs log Sh at 400 RPM
- Values of group E represents different values of Log (Sc Re) vs log Sh at 500 RPM
- Values of group F represents different values of Log (Sc Re) vs log Sh at 600 RPM
- Values of group G represents different values of Log (Sc Re) vs log Sh at 700 RPM
- Values of group H represents different values of Log (Sc Re) vs log Sh at 800 RPM

The present data for the conditions: $1566 < Sc < 1736$, $1704 < Re < 13900$, fit the equation
 $Sh = 0.23 Sc^{1/3} Re^{0.49}$

4 Conclusions

Cementation of copper from copper sulfate dilute solution on horizontal steel sheet at the bottom of stirred tank reactor and fitted with square steel turbulence promoters shown to be an efficient process which achieves a high rate of copper removal from the solution. The present study shows that the rate of cementation increased with the increase of the rotational speed. Also the rotation angle when 45° is used the cementation degree enhanced. But the promoters when the wide spacing distances were used the removal degree are less and increased with the narrow spacing promoters. In addition, future studies should use higher concentrations of copper sulfate to determine the effect of the concentration on the removal of copper from the copper sulfate solution.

References

1. Abdel-Aziz M. Production of copper powder from wastewater containing $CuSO_4$ and alcoholic additives in a modified stirred tank reactor by cementation. Hydrometallurgy. 2011;109(1-2):161-7.
2. Aronson D, Printup H, Shuler K, Howard P, Boethling RS. Chemical Fate Half-Lives for Toxics Release Inventory (TRI) Chemicals. SRC TR 98-008, Prepared for US Environmental Protection Agency, Washington, DC; 1998.
3. Tjadraatmadja G, Diaper C. Sources of critical contaminants in domestic wastewater-. 2006.
4. Akpor OB, Ohiobor GO, Olaolu TD. Heavy metal pollutants in wastewater effluents: sources, effects and remediation. Advances in Bioscience and Bioengineering. 2014;2(4):37-43.
5. Senophiyah-Mary J., Thomas T., Loganath R., Meenambal T. Removal of Copper from Bioleachate of E-Waste Using Orange Activated Carbon (OAC) and Comparison with

Commercial Activated Carbon (CAC). Waste Valorisation and Recycling. Springer, Singapore. 2019; pp 373-383

6. Morcali MH, Zeytuncu B, Baysal A, Akman S, Yucel O. Adsorption of copper and zinc from sulfate media on a commercial sorbent. *Journal of Environmental Chemical Engineering*. 2014;2(3):1655-62.
7. Alonso-González O, Nava-Alonso F, Jimenez-Velasco C, Uribe-Salas A. Copper cyanide removal by precipitation with quaternary ammonium salts. *Minerals Engineering*. 2013;42:43-9.
8. Wen J-J, Zhang Q-X, Zhang G-Q, Cao Z-Y. Deep removal of copper from cobalt sulfate electrolyte by ion-exchange. *Transactions of Nonferrous Metals Society of China*. 2010;20(8):1534-40.
9. Cséfalvay E, Pauer V, Mizsey P. Recovery of copper from process waters by nanofiltration and reverse osmosis. *Desalination*. 2009;240(1-3):132-42.
10. Peng C, Liu Y, Bi J, Xu H, Ahmed A-S. Recovery of copper and water from copper-electroplating wastewater by the combination process of electrolysis and electrodialysis. *Journal of hazardous materials*. 2011;189(3):814-20.
11. Salam OEA, Reiad NA, ElShafei MM. A study of the removal characteristics of heavy metals from wastewater by low-cost adsorbents. *Journal of Advanced Research*. 2011;2(4):297-303.
12. Bilal M, Shah JA, Ashfaq T, Gardazi SMH, Tahir AA, Pervez A, et al. Waste biomass adsorbents for copper removal from industrial wastewater—a review. *Journal of Hazardous Materials*. 2013;263:322-33.
13. Bukhari AA. Investigation of the electro-coagulation treatment process for the removal of total suspended solids and turbidity from municipal wastewater. *Bioresource technology*. 2008;99(5):914-21.
14. Rahman HHA, Wahed EMA. Removal of nickel ions by cementation on zinc from NiSO₄ solution in presence of accelerator non-toxic organic compounds. *Hydrometallurgy*. 2012;129:111-7.
15. Ahmed I, El-Nadi Y, Daoud J. Cementation of copper from spent copper-pickle sulfate solution by zinc ash. *Hydrometallurgy*. 2011;110(1-4):62-6.
16. Makhlofii L, Saidani B, Hammache H (2000) Removal of lead ions from acidic aqueous solutions by cementation on iron. *Wat Res Pergamon* 34 : 2517-2524.
17. Demirkiran N, Kunkul A (2011) Recovering of copper with metallic aluminum. *Trans Nonferrous Met Soc China* 21: 2778-2782.
18. Sulka GD, Jaskula M (2002) Study of the kinetics of the cementation of silver ions onto copper in a rotating cylinder system from acidic sulphate solutions. *Hydrometallurgy* 64: 13-33.
19. J. W. Patterson, "Wastewater Treatment Technology", 3rd edition Michingan, U.S.A., Ann. Arbor Science Publishers, Inc. (1978).
20. M. Sittig, "Pollutant Removal Handbook", 1st. Edn, London. Moyes. Data Corporation (1973).
21. El-Batouti, Mervette, " Removal of copper metal by cementation using a rotating iron cylinder", *Journal of colloid and interface science*, 2005;283(1), 123-129.
22. Dönmez, Bünyamin Sevim, Fatih Saraç, Hanifi, "A kinetic study of the cementation of copper from sulphate solutions onto a rotating aluminum disc", *Journal of Hydrometallurgy*, 1999;53(2), 145-154.
23. G.H.Sedahmeda, Y.A.El-Taweela, M.H.Abdel-Azizab, H.M.El-Naqearaa, " Mass and heat transfer enhancement at the wall of cylindrical agitated vessel by turbulence promoters", *Chemical Engineering and Processing: Process Intensification*, 2014; 80, 34-50.
24. Helal M., Farag H., Mansour M, Fouad Y. "Expremental study of the diffusion controlled of copper in the bottom of a jet stirred reactor", *Brazillian Journal of Chemical Engineering*, 2018;35(1), 101-11

4- Hydrologic Evaluation of TRMM Multi-satellite Precipitation Analysis Products over Blue Nile Basin

Hadir Abd-El Moneim^{†1}, Mohamed Reda Soliman², Hossam M. Moghazy³

¹ M.Sc. Student, Faculty of Engineering, Alexandria University.

² Assistant Professor, Faculty of Engineering, Alexandria University, Egypt.

³ Professor of Irrigation Engineering and Drainage, Faculty of Engineering, Alexandria University, Egypt

[†]E-mail: hadir_eng@yahoo.com

Abstract

This study focuses on comprehensive evaluating the Tropical Rainfall Measuring Mission (TRMM) Multi-satellite Precipitation Analysis (TMPA) products in the Blue Nile River basin. Both TRMM 3B42V7 and TRMM 3B42RT were evaluated using categorical metrics (Probability of Detection (POD), False Alarm Ratio (FAR), equitable threat score (ETS) and Frequency Bias) and statistical indicators (Root Mean Square Error (RMSE), Mean Absolute Error (MAE), Relative Bias (RE), and Correlation Coefficient (CC)) at dekadal (10 days) and monthly time step. Furthermore, Hydro-BEAM (Hydrological River basin Environmental Assessment Model) a fully distributed model used to assess their ability to predict streamflow over the Blue Nile basin. The Hydrological monthly simulation was calibrated and validated at Khartoum station for the period (2001-2007) for daily and monthly scale. Generally, results show that TRMM 3B42V7 had a better performance than TRMM 3B42RT for both statistical analysis and hydrological simulation. This performance indicates that TRMM 3B42V7 can be used for hydrological and overall water management applications in this area.

Keywords: Hydro-BEAM, TRMM 3B42V7, TRMM 3B42RT, Blue Nile, Hydrological Model

Introduction

Precipitation is a crucial input for hydrologists to apply hydrological simulations, and water resources analysis, especially ungauged or sparse precipitation gauge networks regions, such as Blue Nile river basin. Over the last few decades, the satellite precipitation products are starting to provide alternatives for estimating precipitation data and also pose new challenges for hydrologists in understanding and applying the remotely-sensed information[1], such as TMPA[2], CMORPH[3], and PERSIANN[4]. Several previous studies TRMM precipitations products have been evaluated and used widely in hydrological applications in various regions like [1,5–8]. Other studies have been conducted to validated TRMM precipitations products such as [9–14]. Furthermore, few studies have been evaluated their accuracy and over Ethiopian highland, such as [15–19], While their ability to predict streamflow is evaluated by [20,21].

Most of recent studies focused on the evaluation of satellite precipitation products over Upper Blue Nile river and central of Ethiopia. However, there is no comprehensive evaluation and hydrological application studies over the Blue Nile river basin. Consequently, the main aim of this study is to evaluate the performance of two precipitation products (TRMM 3B42V7, and TRMM 3B42RT) using statistical analysis at dekadal (10 days) and monthly time scales. Moreover, assess the improvement of the version 7 of 3B42 comparing by TRMM 3B2RT. On the other hand, assessment the capability of two precipitation products to predict the streamflow through hydrological simulations for the period (2001-2007) based on distributed model (Hydro-BEAM) at daily and monthly scales.

5 Study Area and Datasets

5.1. Study Area

The Blue Nile River is one of the principal tributaries of the Nile River which originates from the Ethiopian highlands, flowing into northwest Sudan, and when it meets at Khartoum the White Nile to form the Main Nile. It considered the vital tributary of the Nile River because it provides a major part of about 60 % of the Nile flow. The drainage area of the Blue Nile is estimated at about 325000 Km²[22].

The watersheds of the Basin have a range of sizes, slopes, topography, climatic patterns, geological formations, drainage patterns, vegetation cover, soils, and anthropogenic activities. The catchment topography is divided into two different features; the first is the flat topography in the lowlands in Sudan, and the second one is the rugged topography, in the Ethiopian highlands where the high steep mountainous region combined cover about 65% of the Basin area [23]. The Ethiopian plateau is

concentrated at elevations of 2000-3000 m, with several peaks up to 4000 m or more as shown in **Fig. 1(a)** [1].

Rainfall over the Blue Nile Basin varies significantly with altitude and is considerably greater in the Ethiopian highlands than on the Plains of Sudan. Rainfall ranges from nearly 2,000 mm/yr in the highlands of Ethiopia to less than 200 mm/yr at the junction with the White Nile, as shown **Fig. 1(b)** [24]. The highest mean annual temperatures occur in the northeastern clay plains of Sudan. In Sudan, the daily minimum and maximum temperatures in January are 14°C and 33°C, and those in May are 24°C and 44°C, respectively. The area located in the Ethiopian highlands is characterized by lower minimum mean monthly temperatures that range between 3°C and 21°C occur between December and February, as shown **Fig. 1(c)** [3]. Evapotranspiration spatial distributions are similar to rainfall and temperature with considerable variations across the basin and higher correlation with altitude, as shown **Fig. 1(d)** [3].

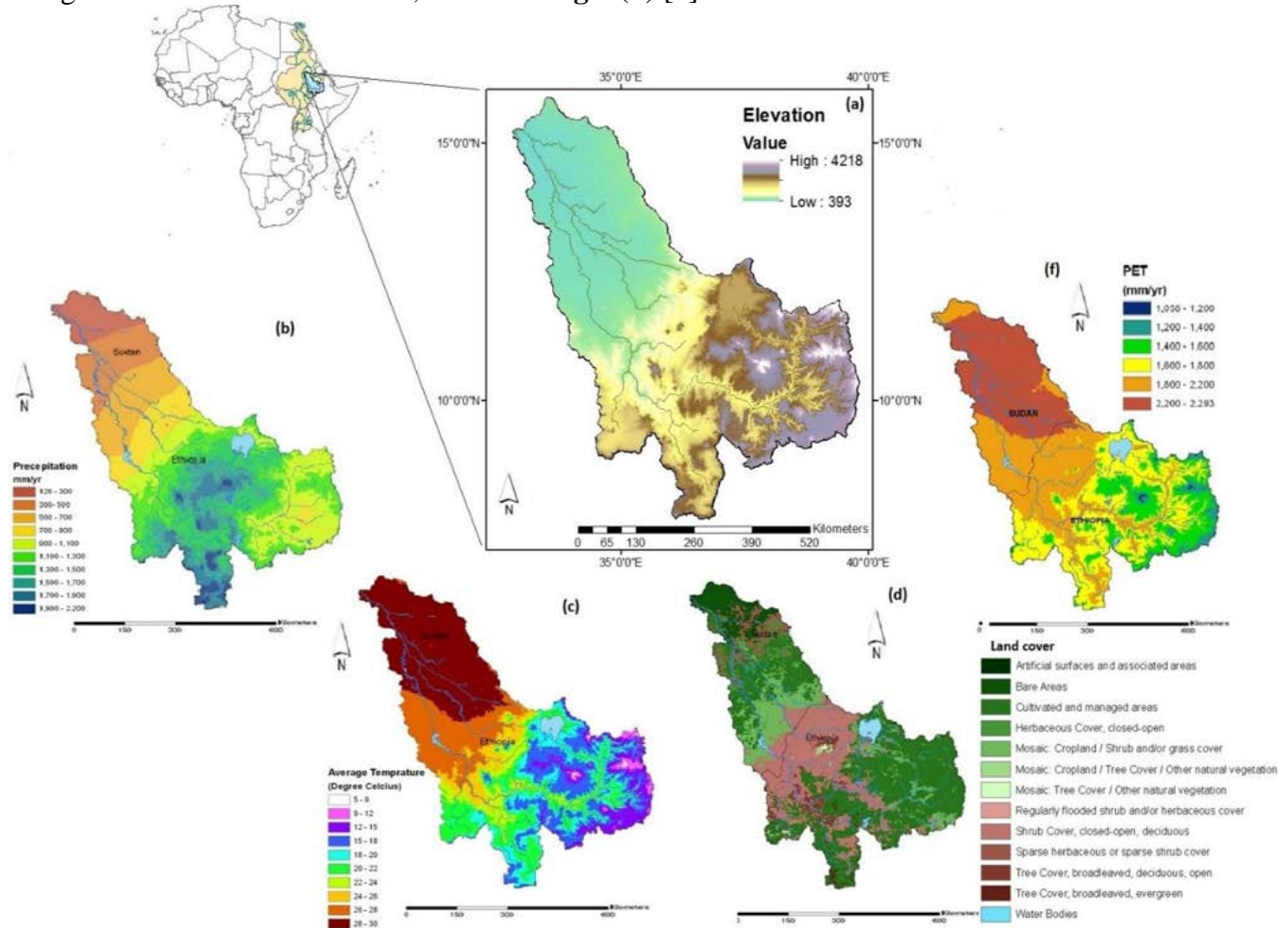


Figure 1(a) Location of Blue Nile basin in Ethiopia and (right) the DEM map of Blue Nile basin; (b) average annual precipitation distribution over Blue Nile basin, (c) average annual temperature distribution over Blue Nile basin, (d) soil type and (f) average annual Evapotranspiration distribution over Blue Nile Basin.

5.2. Datasets

5.2.1. Measured data

Observed data is a pivotal tool to evaluate the two satellite precipitation products. For this reason, 30 daily rain gauges are obtained from the National Meteorological Agency of Ethiopia and 15 monthly rain gauges from the Ministry of water resources and irrigation of Egypt for the period 2001 to 2007. Furthermore, daily measured discharge at Khartoum station (outlet of the basin) for the same period.

5.2.2. TRMM satellite precipitation products

The Tropical Rainfall Measurement Mission (TRMM) precipitation was developed by the National Aeronautics and Space Administration (NASA) and the National Space Development Agency (NSDA). It was obtained from the TRMM Multisatellite precipitation analysis (TMPA) algorithm which combines Infrared (IR) and Passive Microwave (PM) data retrievals [2,25]. TMPA precipitation products are available in two versions: near-real-time version (3B42RT) (three-hourly) and post-real-time research version (3B42) (three-hourly and daily), covering the range of latitude 50°S–50°N and longitude 180°W–180°E. The main difference between the two versions is the use of monthly rain gauge data for bias adjustment in the research product[6]. 3B42RT product is available starting from 1 March 2000, however, the 3B42V7 dataset is available from January 1998 till present. In the current study, both products are evaluated against rain gauges observations. All these datasets used are downloaded from <https://giovanni.sci.gsfc.nasa.gov/giovanni/>.

6 Methods

6.1. Statistical indicators

Several statistical indices are used to qualitatively evaluate the performance of TRMM precipitation products against rain gauge observations and their influence on streamflow simulation. Continuous statistical metrics include the root mean square error (RMSE), Pearson correlation coefficient (CC) and relative BIAS (BIAS) for rainfall amount evaluation. The formulas are given by:

$$RMSE = \sqrt{\frac{\sum_{i=1}^n (P_i - G_i)^2}{n}} \quad (1)$$

$$BIAS = \frac{\sum_{i=1}^n (P_i - G_i)}{\sum_{i=1}^n G_i} \times 100\% \quad (2)$$

$$CC = \frac{\sum_{i=1}^n (G_i - G_i') (P_i - P_i')}{\sqrt{\sum_{i=1}^n (G_i - G_i')^2 \sum_{i=1}^n (P_i - P_i')^2}} \quad (3)$$

Where P_i and G_i are the i th values of the TRMM precipitation products and rain gauges observation data, respectively, P_i' and G_i' are their mean values, respectively, and n is the total number of time steps. The rain gauge measurements and TRMM precipitation products are considered fully consistent without uncertainty if the amount of RMSE, and $BIAS = 0$ and $CC = 1$, which means higher CC, and lower RMSE represent the higher accuracy of products.

Moreover, four categorical statistical metrics were applied to measure the correspondence between the satellite precipitation products and rain gauge observations, including the probability of detection (POD), false alarm ratio (FAR) equitable threat score (ETS), and Frequency Bias (FB). The ideal values of POD, FAR, FB, and ETS are 1, 0, 1, and 1, respectively.

$$POD = \frac{H}{H + M} \quad (4)$$

$$FAR = \frac{F}{H + F} \quad (5)$$

$$FBI = \frac{H + M}{H + F} \quad (6)$$

$$ETS = \frac{H - \text{hits}}{H + M + F - \text{hits}} \quad (7)$$

$$\text{hits} = \frac{(H + M)(H + F)}{H + M + F + Z}$$

where H is the observed rainfall correctly detected (hits), M is the observed rainfall not detected (misses) and F is the rainfall detected but not observed.

For hydrologic model simulation, CC, BIAS and the Nash–Sutcliffe coefficient of Efficiency (NSE) [26] were used to assess the performance of the hydrological model simulation and observation. The perfect result occurs with $\text{NSE} = 1$, $R^2 = 1$, and $\text{Bias} = 0\%$.

$$\text{NSE} = 1 - \frac{\sum_{i=1}^n (Q_{\text{obs}} - Q_{\text{sim}})^2}{\sum_{i=1}^n (Q_{\text{obs}} - Q'_{\text{sim}})^2} \quad (8)$$

Where i , and n is the total number of time steps. Q_{obs} and Q'_{obs} are the observed streamflow and averaged of observed streamflow, respectively, Q_{sim} and Q'_{sim} are the simulated streamflow and averaged of the simulated streamflow respectively.

6.2. Hydrological Model (Hydro_BEAM)

A physically-based distributed hydrological model Hydro-BEAM (Hydrological River basin Environmental Assessment Model) has been used in this study to investigate the potential of the TRMM products through the streamflow simulation. It was originally developed by Kojiri et al. [27] to assess water quantity, water quality, sediment, reservoir operations, and the impacts of climate change and anthropogenic activity, such as [28,29]. However, all of these applications were limited to environments with humid conditions until the model was later modified for flash flood simulations in the arid wadis [30,31] and semi-arid basins [32,33].

The model consists of meshed cells with multi-layers. The cells are given by discretizing a river basin into square elements. Each of the mesh cells has a hydrological structure of Layer A to D, which is represented by a combination of one surface layer and three subsurface layers, in the vertical direction as shown in **Fig. 2**. Horizontal discharges from Layer A, B, C, and D flow into a river. In this study, the model consists of three layers A, B and C while layer D which represents deeper seepage and long-term groundwater storage is not considered in this analysis. It consists of: (1) the watershed modeling is processed using Geographical Information System (GIS) technique, (2) Surface runoff and stream routing modeling based on the kinematic wave approximation, (3) transmission losses modeling is estimated by using Walter's equation [34], (4) Canopy interception losses, and (5) Groundwater modeling based on the linear storage model. The watershed is divided into meshed cells with multi-layers and each mesh contains information such as surface runoff, land use, slope direction, and the absence/ presence of a channel [35]. According to Abd-El Moneim et al.[36], the spatial resolution used in this study for the Blue Nile basin is (5 km × 5 km).

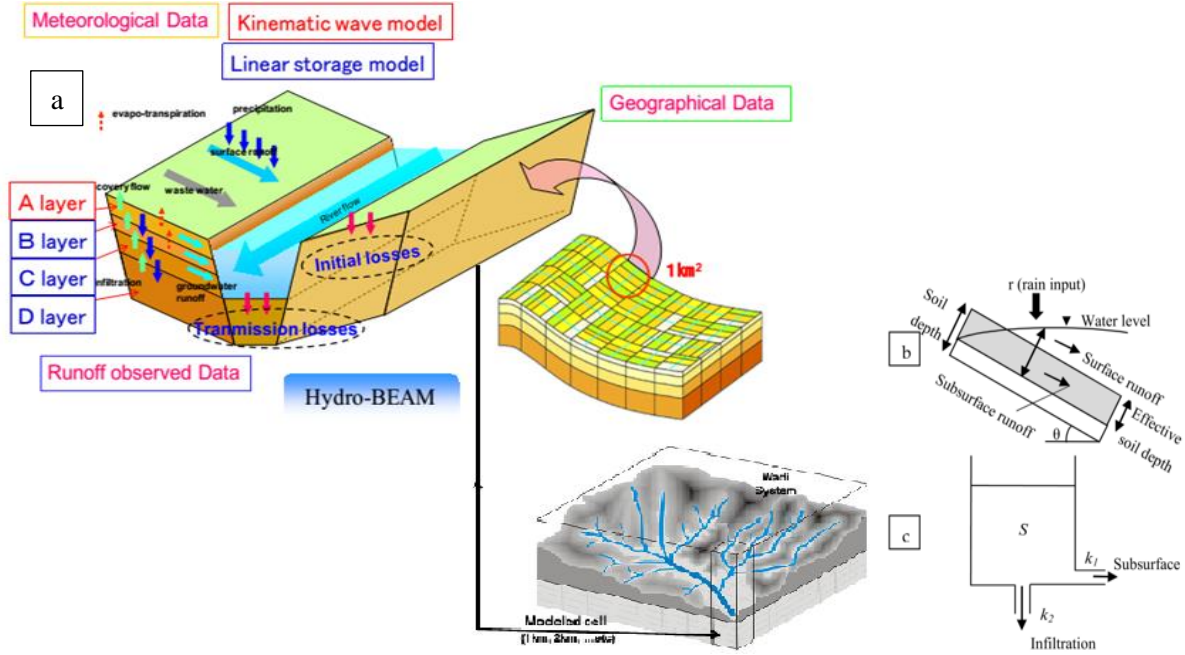


Figure 2 Conceptual representation of Hydro-BEAM (a) Hydro-BEAM basic structure; (b) surface layer kinematic wave model; (c) simple representation of subsurface storage tank layers[33,35].

Blaney–Criddle method has been used to calculate potential evapotranspiration (ET_o) in the model as follows [37]:

$$ET_o = p(0.46T_{mean} + 8.13) \quad (9)$$

Where ET_o potential evapotranspiration (mm/day), T_{mean} average Temperature ($^{\circ}C$) and p is mean daily percentage of annual daytime hours. According to the approximate latitude of the study area and the number of degrees north or south of the equator, we can determine the value of p from [37]. In this study, daily temperature and daily Radiation datasets are obtained from the Climate Forecast System Reanalysis (CFSR). The datasets were available to download from [https:// globalweather.tamu.edu/#pubs](https://globalweather.tamu.edu/#pubs).

Stream routing and surface runoff are calculated using integrated kinematic wave runoff approximation assuming the river channel cross-section as triangle Eq (10,11,12,13).

$$\frac{\partial h}{\partial t} + \frac{\partial q}{\partial x} = fr \quad (10)$$

$$q = \alpha(h - d)^{\frac{5}{3}} + ah \quad (h > d) \quad (11)$$

$$q = ah \quad (12)$$

$$\text{When } \begin{cases} h \geq d \\ h \leq d \end{cases}, d = \lambda D$$

$$\alpha = \frac{\sqrt{\sin \theta}}{n}, a = Ks \frac{\sin \theta}{\gamma} \quad (13)$$

Where, h : is the water depth (m), q : is the discharge per unit length of flow [$m^3/m.s$], r : is input effective rainfall intensity (m/s), which corresponds to the sum of rainfall infiltration into the soil after extracting evapotranspiration losses, f : is the direct runoff ratio, which is equal to the soil saturation ratio in the upper soil, layer A (0–1). x is the distance from the upstream edge, and α , m is constant concerning frictions, λ : is the porosity, D is the thickness of layers (m), and d is the saturation poundage(m).

To predict the base flow process more realistically, a multi-layer linear storage function model is applied to the B and C layers of Hydro-BEAM. The continuity equation and dynamic equation of the linear storage function model are as follows [36]:

$$\frac{dS}{dt} = I - O \quad (14)$$

$$O = kS \quad (15)$$

Where, S: is water storage (m), I: is inflow (m/s), O: is outflow (m/s), k: is the runoff coefficient (1/s).

7 Results and discussion

7.1. Evaluation TRMM precipitation products at the dekadal temporal scale

The daily precipitation data were aggregated to dekadal total precipitation for both rain gauge observation data and the daily TRMM precipitation products. Overall, both products show good agreement with rain gauge observation at dekadal timescale, as listed in **Table 1**. **Fig. 3** illustrates scatter plots of TRMM precipitation products against rain gauge observation data. TRMM 3B42V7 exhibits better performance than TRMM 3B42RT with the highest correlation (CC=0.96), and the lowest BIAS and RMSE 1.89%, 10.67 mm/dekad, respectively. However, TRMM 3B42RT shows good performance with CC=0.94 and RMSE=17.29 mm/dekad. Meanwhile, it appears high underestimation rainfall with a negative value of bias, on the contrary, TRMM 3B42V7 shows a little overestimation rainfall against rain gauge observation data.

Table 1 Summarize of statistical indicators at dekadal and monthly timescales

| Time Scale | Precipitation products | Mean | RMSE | BIAS | CC | POD | FAR | FB | ETS |
|------------|------------------------|-------|-------|--------|------|------|------|------|------|
| Dekadal | rain gauge | 33.58 | - | - | - | - | - | - | - |
| | TRMM 3B42V7 | 34.22 | 10.67 | 1.89 | 0.96 | 0.91 | 0.15 | 1.09 | 0.68 |
| | TRMM 3B42RT | 24.98 | 17.29 | -25.16 | 0.94 | 0.66 | 0.05 | 0.69 | 0.51 |
| Monthly | rain gauge | 85.33 | - | - | - | - | - | - | - |
| | TRMM 3B42V7 | 88.02 | 12.88 | 3.15 | 0.99 | - | - | - | - |
| | TRMM 3B42RT | 70 | 29.68 | -17.42 | 0.97 | - | - | - | - |

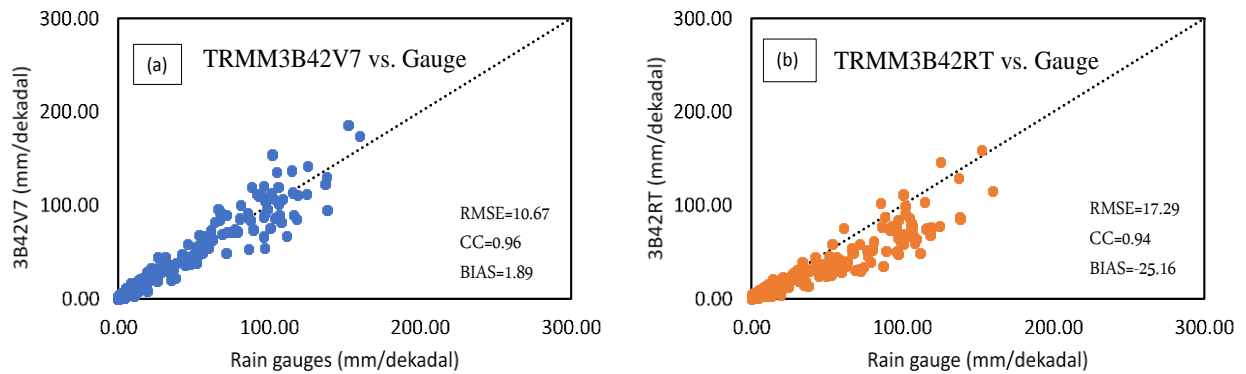


Figure 3 Scatter plots of dekadal precipitation between TRMM precipitation products and rain gauge observation data in the Blue Nile basin during 2001-2007

For the categorical statistics, four statistical indicators are used to evaluate the capability of the TRMM precipitation products to detect precipitation events. In this study, the rainfall events are classified into five different categories (1, 10, 50, 100, and 150 mm/dekad) as shown in **Fig. 4**. Generally, both products show better for the first and the second groups than other groups. TRMM 3B42V7 still remains the same which shows the perfect performance than TRMM 3B42RT for all statistical metrics except FAR, where it appears worse FAR scores than TRMM 3B42RT at dekadal. The mean value of TRMM3B42V7's POD is 0.91 (range from 0.69 at 100 mm/dekad to 1.0 at 150 mm/dekad), FB is 1.09 (range from 0.94 at 50 mm/dekad to 1.50 at 150

mm/dekad), and ETS is 0.68 (range from 0.51 at 100 mm/dekad to 0.85 at 50 mm/dekad). On contrast, the mean value of TRMM3B42RT's POD is 0.66 (range from 0.25 at 100 mm/dekad to 0.99 at 1 mm/dekad), FB is 0.69 (range from 0.29 at 100 mm/dekad to 1.05 at 1 mm/dekad), and ETS is 0.51 (range from 0.22 at 100 mm/dekad to 0.75 at 10 mm/dekad). However, false alarm ratio of TRMM 3B42RT is lower than TRMM 3B42V7 with mean value 0.05 (range from 0 at 50 mm/dekad and 150 mm/dekad to 0.14 at 100 mm/dekad), meanwhile, the mean value of TRMM 3B42V7 is 0.15 (range from 0.03 at 50 mm/dekad to 0.33 at 150 mm/dekad). These results show that TRMM 3B42V7 can capture the correct magnitude of intense rainfall for different rainfall thresholds at dekadal scale.

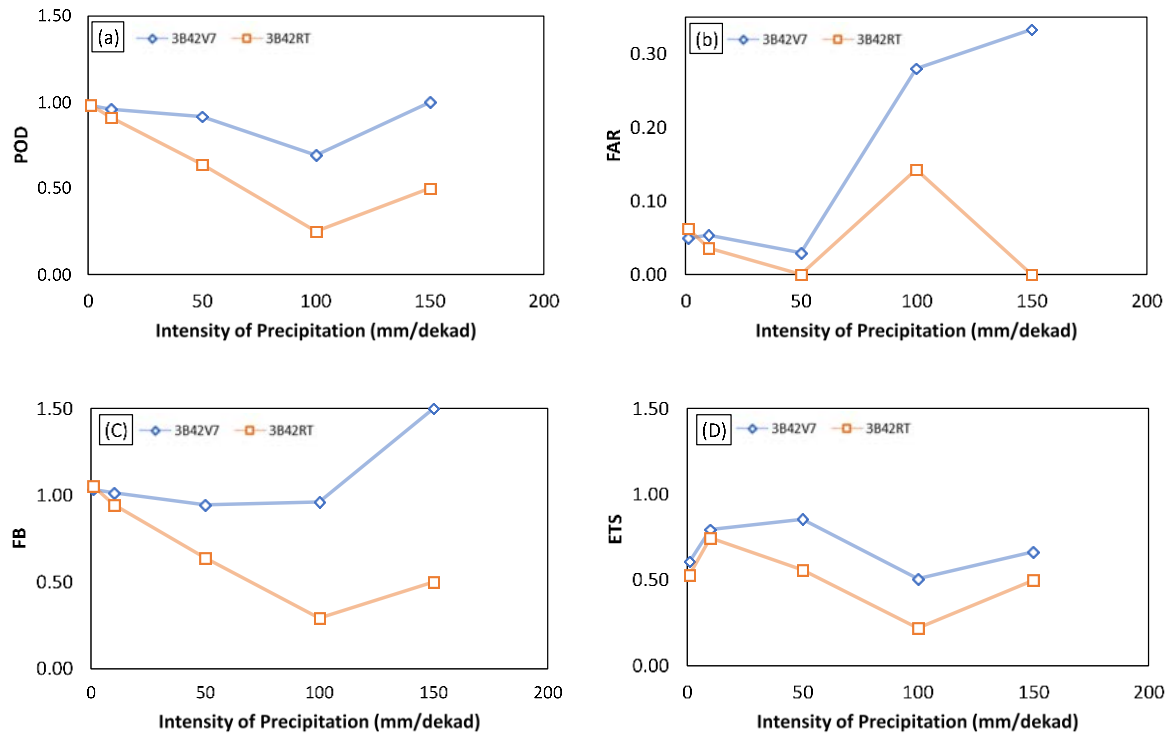


Figure 4 (a) POD, (b) FAR, (c) Frequency Bias and (d) ETS of TRMM precipitation products against rain gauge observations data at the thresholds of 1 mm/month, 10 mm/month, 50 mm/month, 100 mm/month and 150 mm/dekad over Blue Nile basin for the period 2001–2007.

7.2. Evaluation TRMM precipitation products at a monthly temporal scale

This section presents statistics evaluating and comparing the monthly TRMM precipitation products against monthly rain gauge observations data. the monthly data are accumulated from daily data for both TRMM precipitation products and rain gauge measurements. **Table 1** summaries all statistical indices. **Fig. 5** shows a scatter plot comparing monthly TRMM precipitation products with monthly rain gauge observations data. It is evident that despite the slight improvement of bias and correlation coefficient TRMM 3B42RT still has unperformed than TRMM 3B42V7. Meanwhile, TRMM 3B42V7 appears the best performance. Relative bias notices that TRMM 3B42V7 product are overestimated, however, TRMM 3B42RT are underestimated.

Fig. 6 also shows the spatial distribution of statistical indices at monthly scale to provide insights regarding spatial variability. TRMM 3B42V7 correlated very close to rain gauge measurements where most stations are greater than 0.9 (less value at Khartoum=0.72), as shown **Fig. 6(a)**. For BIAS values, most of the stations are mainly varied from -20% to 20. However, three stations (Roseries, Hassa Heissa, and Humera) have a large bias, with a value greater than 0.6, as shown **Fig. 6(b)**. The northwest stations show best RMSE values (ranging between 10 mm and 30 mm),

while, the southeast stations had good agreement with rain gauge observations, with RMSE values varies from 30 mm to 50 mm, as shown **Fig. 6(c)**. On the other hand, TRMM 3B42RT exhibits good correlation with the rain gauge observations, except three stations (CC value less than 0.61), as shown in **Fig. 6(d)**. **Fig. 6(e)** illustrates that TRMM 3B42RT shows great underestimation (-80 % to -20%) at the southeast stations. On contrary, it appears large overestimation at the majority of the northwest stations, with large BIAS value is 189% at Hassa Heissa station. RMSE values mainly varied between 180 mm and 24 mm, imply that TRMM 3B42RT has a large discrepancy with rain gauge observations, as shown **Fig. 6(f)**.

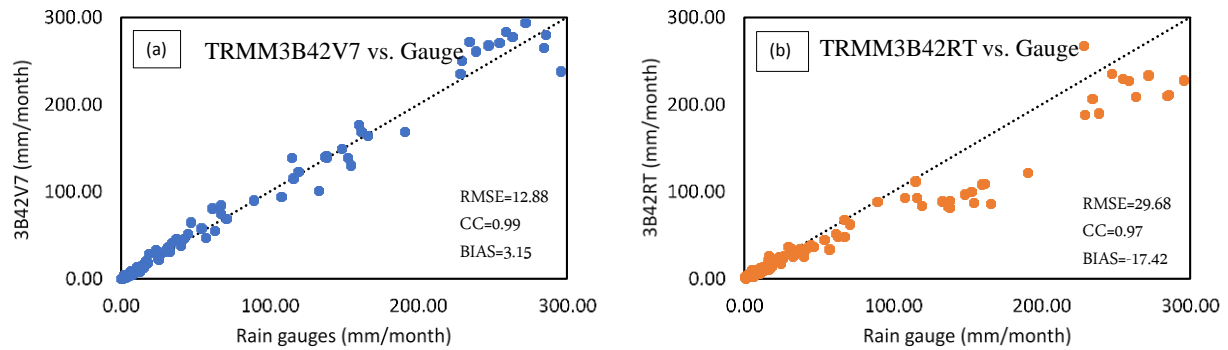


Figure 5 Scatter plots of monthly precipitation between TRMM products and rain gauge observation data in the Blue Nile basin during 2001-2007

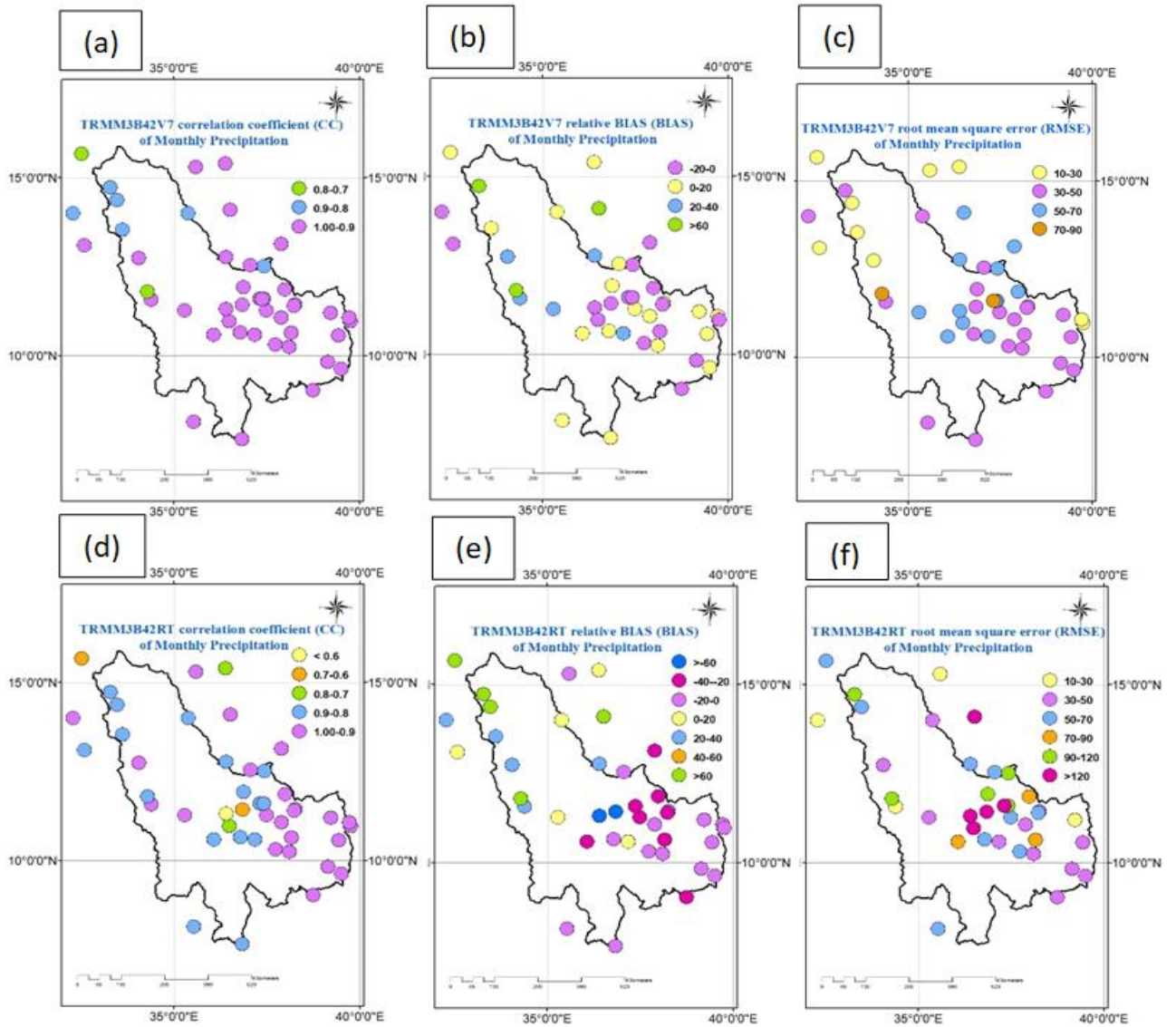


Figure 6 The spatial distribution of the continuous statistical metrics of monthly TRMM products for the period 2001-2007 over the Blue Nile basin

7.3. Hydrological Evaluation

In this part, TRMM precipitation products are evaluated their utility in streamflow simulation by driving the Hydro-BEAM hydrologic model over the Blue Nile basin during the period (2001-2007) for two different timescales (daily and monthly). The period from 2001 to 2003 are used to calibrate the model, and the period from 2004 to 2007 are used for model validation. The summary values of the evaluation criteria for the performance of the model for both calibration and validation periods are shown in **Table 2**. The comparison of simulated and observed streamflow hydrographs in both calibration and validation periods at daily and monthly scales are illustrated in **Fig. 7**. At daily timescale, both TRMM precipitation products show good agreement, with NSE=0.749, and CC=0.870, 0.884, respectively, in the calibration period. However, the NSE and CC values slightly increase in the validation period. In addition, both products exhibit overestimation, with positive relative bias, in the calibration period, while, TRMM precipitation products show underestimation, with negative relative bias in the validation period. On the other hand, TRMM precipitation products show slightly improved at monthly scale. TRMM 3B42V7 appears better performance than TRMM 3B42RT, with NSE=0.878 and 0.851, and CC=0.941, 0.925, respectively, for both calibration and validation periods. Furthermore, TRMM 3B42V7 still shows overestimation in the

calibration period and underestimation in the validation period. On the contrast, TRMM 3B42RT shows overestimation at both calibration and validation. In general, TRMM 3B42V7 simulations are a significant enhancement over TRMM 3B42RT for both statistically and hydrologically evaluation.

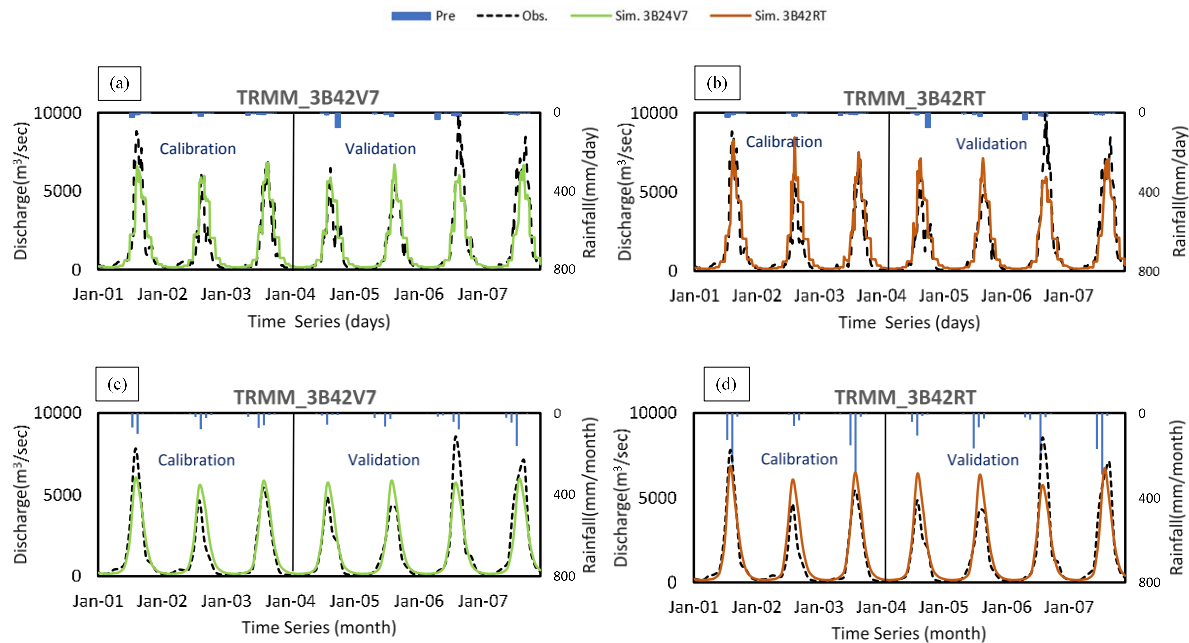


Figure 7 comparison of simulated and observed hydrographs in both calibration and validation periods at the outlet (Khartoum station) of the Blue Nile river basin for the period (2001-2007)

Table 2 Statistical analysis for hydrologic evaluation at daily and monthly timescales

| Time Scale | Precipitation products | Calibration | | | Validation | | |
|------------|------------------------|-------------|-------|--------|------------|-------|--------|
| | | NSE | CC | BIAS | NSE | CC | BIAS |
| Daily | TRMM 3B42V7 | 0.749 | 0.870 | 10.192 | 0.788 | 0.893 | -5.516 |
| | TRMM 3B42RT | 0.749 | 0.884 | 17.415 | 0.785 | 0.887 | -1.219 |
| Monthly | TRMM 3B42V7 | 0.878 | 0.941 | 10.350 | 0.851 | 0.925 | -2.872 |
| | TRMM 3B42RT | 0.873 | 0.950 | 17.314 | 0.838 | 0.915 | 2.946 |

8 Conclusions

In study, two TRMM precipitation products (TRMM 3B42V7 and TRMM 3B42RT) are compared and evaluated against rain gauge measurements data via statistical analysis and hydrological simulation in the Blue Nile river basin for the period (2001-2007). The main findings are summarized into the following:

1. For continuous statistical analysis, TRMM 3B42V7 shows strong performance with rain gauge observed data for both dekadal and monthly timescales, with RMSE=10.67 mm and 12.88 mm, respectively, and best correlation CC=0.96 and 0.99, respectively.
2. TRMM 3B42V7 appears slightly overestimation, however, TRMM 3B42RT exhibits a large underestimation at two timescales.
3. For categorial statistical indices, TRMM 3B42V7 can capture the correct magnitude of intense rainfall for different rainfall thresholds at dekadal time step, with mean POD value=0.91, FB=1.09, and ETS=0.68. on the other hand, TRMM 3B42RT performed well for the rain occurrences were incorrectly detected (FAR=0.05) than TRMM 3B42V7,
4. At monthly scale, spatial distribution map illustrates the variability of spatial for TRMM precipitation products.

5. Hydrological simulations forced by TRMM 3B42V7 better performed than TRMM 3B42RT in both calibration and validation periods.

Generally, this evaluation reveals the TRMM 3B42V7 algorithm has a noticeable improvement from TRMM 3B42RT due to the use of the monthly gauge in bias correction algorithm. The TRMM precipitation products also have great potentiality in hydrological application at daily or monthly time steps, which is particularly promising for water resource management and assessment in sparse rain gauge observed data or ungauged basins in arid and semiarid regions, such as the Blue Nile river basin.

Acknowledgments

This paper is a part of M.sc. Thesis for the first author. The authors thank the late professor Kojiri, Prof. Sumi & Dr. Saber from DPRI for support by sharing the adopted program of Hydro-BEAM. We also thank Dr. Mohammed E. Abou ElHaggag, Ewunetu Tarkegn and Kiduse Teshome for sharing data.

References

1. Xue, X.; Hong, Y.; Limaye, A. S.; Gourley, J. J.; Huffman, G. J.; Khan, S. I.; Dorji, C.; Chen, S. Statistical and hydrological evaluation of TRMM-based Multi-satellite Precipitation Analysis over the Wangchu Basin of Bhutan: Are the latest satellite precipitation products 3B42V7 ready for use in ungauged basins? *J. Hydrol.* **2013**, *499*, 91–99, doi:10.1016/j.jhydrol.2013.06.042.
2. Huffman, G. J.; Bolvin, D. T.; Nelkin, E. J.; Wolff, D. B.; Adler, R. F.; Gu, G.; Hong, Y.; Bowman, K. P.; Stocker, E. F. The TRMM Multisatellite Precipitation Analysis (TMPA): Quasi-Global, Multiyear, Combined-Sensor Precipitation Estimates at Fine Scales. *J. Hydrometeorol.* **2007**, *8*, 38–55, doi:10.1175/JHM560.1.
3. Joyce, R. J.; Janowiak, J. E.; Arkin, P. A.; Xie, P. CMORPH: A Method that Produces Global Precipitation Estimates from Passive Microwave and Infrared Data at High Spatial and Temporal Resolution. *J. Hydrometeorol.* **2004**, *5*, 487–503, doi:10.1175/1525-7541(2004)005<0487:CAMTPG>2.0.CO;2.
4. Sorooshian, S.; Hsu, K.; Gao, X.; Gupta, H. V.; Imam, B.; Braithwaite, D. Evaluation of PERSIANN System Satellite Based Estimates of Tropical Rainfall. *Bull. Am. Meteorol. Soc.* **2000**, *81*, 2035–2046, doi:10.1175/1520-0477(2000)081<2035:EOPSSE>2.3.CO;2.
5. Wang, Z. Evaluating the suitability of TRMM satellite rain- fall data for hydrological simulation using a dis- tributed hydrological model in the Weihe River catchment in China. **2016**, doi:10.1007/s11442-015-1161-3.
6. Tong, K.; Su, F.; Yang, D.; Hao, Z. Evaluation of satellite precipitation retrievals and their potential utilities in hydrologic modeling over the Tibetan Plateau. *J. Hydrol.* **2014**, *519*, 423–437, doi:10.1016/j.jhydrol.2014.07.044.
7. Peng, B.; Shi, J.; Ni-Meister, W.; Zhao, T.; Ji, D. Evaluation of TRMM multisatellite precipitation analysis (tmpa) products and their potential hydrological application at an arid and semiarid basin in china. *IEEE J. Sel. Top. Appl. Earth Obs. Remote Sens.* **2014**, *7*, 3915–3930, doi:10.1109/JSTARS.2014.2320756.
8. Bodian, A.; Dezetter, A.; Deme, A.; Diop, L. Hydrological Evaluation of TRMM Rainfall over the Upper Senegal River Basin. *Hydrology* **2016**, *3*, 15, doi:10.3390/hydrology3020015.
9. Lu, X.; Tang, G.; Wei, M.; Yang, L.; Zhang, Y. Evaluation of multi-satellite precipitation products in Xinjiang , China Evaluation of multi-satellite precipitation products in Xinjiang , China. *Int. J. Remote Sens.* **2018**, *00*, 1–26, doi:10.1080/01431161.2018.1471246.
10. Zhang, C.; Chen, X.; Shao, H.; Chen, S.; Liu, T.; Chen, C.; Ding, Q.; Du, H. Evaluation and Intercomparison of High-Resolution Satellite Precipitation Estimates — GPM , TRMM , and CMORPH in the Tianshan Mountain Area., doi:10.3390/rs10101543.

11. Serrat-Capdevila, A.; Merino, M.; Valdes, J. B.; Durcik, M. Evaluation of the performance of three satellite precipitation products over Africa. *Remote Sens.* **2016**, *8*, doi:10.3390/rs8100836.
12. Tan, M. L.; Ibrahim, A. L.; Duan, Z.; Cracknell, A. P.; Chaplot, V. Evaluation of six high-resolution satellite and ground-based precipitation products over Malaysia. *Remote Sens.* **2015**, *7*, 1504–1528, doi:10.3390/rs70201504.
13. Tan, M. L.; Duan, Z. Assessment of GPM and TRMM precipitation products over Singapore. *Remote Sens.* **2017**, *9*, doi:10.3390/rs9070720.
14. Huang, Y.; Chen, S.; Cao, Q.; Hong, Y.; Wu, B.; Huang, M.; Qiao, L.; Zhang, Z.; Li, Z.; Li, W.; Yang, X. Evaluation of version-7 TRMM multi-satellite precipitation analysis product during the Beijing extreme heavy rainfall event of 21 July 2012. *Water (Switzerland)* **2014**, *6*, 32–44, doi:10.3390/w6010032.
15. Hirpa, F. A.; Gebremichael, M.; Hopson, T. Evaluation of high-resolution satellite precipitation products over very complex terrain in Ethiopia. *J. Appl. Meteorol. Climatol.* **2010**, *49*, 1044–1051, doi:10.1175/2009JAMC2298.1.
16. Worqlul, A. W.; Maathuis, B.; Adem, A. A.; Demissie, S. S.; Langan, S.; Steenhuis, T. S. Comparison of rainfall estimations by TRMM 3B42, MPEG and CFSR with ground-observed data for the Lake Tana basin in Ethiopia. *Hydrol. Earth Syst. Sci.* **2014**, *18*, 4871–4881, doi:10.5194/hess-18-4871-2014.
17. Dinku, T.; Ceccato, P.; Grover-Kopec, E.; Lemma, M.; Connor, S. J.; Ropelewski, C. F. Validation of satellite rainfall products over East Africa's complex topography. *Int. J. Remote Sens.* **2007**, *28*, 1503–1526, doi:10.1080/01431160600954688.
18. Fenta, A. A.; Yasuda, H.; Shimizu, K.; Ibaraki, Y.; Haregeweyn, N.; Kawai, T.; Belay, A. S.; Sultan, D.; Ebabu, K. Evaluation of satellite rainfall estimates over the Lake Tana basin at the source region of the Blue Nile River. *Atmos. Res.* **2018**, *212*, 43–53, doi:10.1016/j.atmosres.2018.05.009.
19. Ayehu, G. T.; Tadesse, T.; Gessesse, B.; Dinku, T. Validation of new satellite rainfall products over the Upper Blue Nile Basin, Ethiopia. *Atmos. Meas. Tech.* **2018**, *11*, 1921–1936, doi:10.5194/amt-11-1921-2018.
20. Bitew, M. M.; Gebremichael, M.; Ghebremichael, L. T.; Bayissa, Y. A. Evaluation of High-Resolution Satellite Rainfall Products through Streamflow Simulation in a Hydrological Modeling of a Small Mountainous Watershed in Ethiopia. *J. Hydrometeorol.* **2012**, *13*, 338–350, doi:10.1175/2011JHM1292.1.
21. Bitew, M. M.; Gebremichael, M. Evaluation of satellite rainfall products through hydrologic simulation in a fully distributed hydrologic model. *Water Resour. Res.* **2011**, *47*, 1–11, doi:10.1029/2010WR009917.
22. Ragab, O.; VALERIANO, O. C. S. Flood Forecasting in Blue Nile Basin Using a Process-Based Distributed Hydrological Model and Satellite Distributed Hydrological Model and Satellite Derived Precipitation Product. In *ASEE 2014 Zone I Conference*; USA, 2014.
23. Gebrehiwot, S. G.; Ilstedt, U.; Gärdenas, A. I.; Bishop, K. Hydrological characterization of watersheds in the Blue Nile Basin, Ethiopia. *Hydrol. Earth Syst. Sci.* **2011**, *15*, 11–20, doi:10.5194/hess-15-11-2011.
24. Awulachew, S. B.; McCartney, M.; Steenhuis, T. S.; Ahmed, A. A. *A review of hydrology, sediment and water resource use in the Blue Nile Basin (IWMI Working Paper 131)*; 2008; Vol. 131;.
25. Guo, R.; Liu, Y. Evaluation of satellite precipitation products with rain gauge data at different scales: Implications for hydrological applications. *Water (Switzerland)* **2016**, *8*, doi:10.3390/w8070281.
26. Nash, J. E.; Sutcliffe, J. V. Riverflow forecasting through conceptual models. part I: A discussion of principle. *J. Hydrol.* **1970**, *10*, 282–290.

27. Kojiri, T.; Tokai, A.; Kinai, Y. Assessment of river basin environment through simulation with water quality and quantity. *Annu. Disaster Prev. Res. Inst. Kyoto Univ* **1998**, *41*, 119–134.
28. Kojiri, T.; Hamaguchi, T.; Ode, M. Assessment of global warming impacts on water resources and ecology of a river basin in Japan. *J. Hydro-Environment Res.* **2008**, *1*, 164–175, doi:10.1016/j.jher.2008.01.002.
29. Sato, Y.; Kojiri, T.; Michihiro, Y.; Suzuki, Y.; Nakakita, E. Assessment of climate change impacts on river discharge in Japan using the super-high-resolution MRI-AGCM. *Hydrol. Process.* **2013**, *27*, 3264–3279.
30. Abdel-Fattah, M.; Kantoush, S.; Sumi, T. Integrated Management of Flash Flood in Wadi System of Egypt: Disaster Prevention and Water Harvesting. *Annu. Disas. Prev. Res. Inst., Kyoto Univ* **2015**, *58*, 485–496.
31. Saber, M.; Hamaguchi, T.; Kojiri, T.; Tanaka, K.; Sumi, T. A physically based distributed hydrological model of wadi system to simulate flash floods in arid regions. *Arab. J. Geosci* **2013**, *58*, 485–496, doi:10.1007/s12517-013-1190-0.
32. Saber, M.; Yilmaz, K. Bias Correction of Satellite-Based Rainfall Estimates for Modeling Flash Floods in Semi-Arid regions: Application to Karpuz River, Turkey. *Nat. Hazards Earth Syst. Sci. Discuss.* **2016**, 1–35, doi:10.5194/nhess-2016-339.
33. Abdel-fattah, M. A Hydrological and Geomorphometric Approach to Understanding the Generation of Wadi Flash Floods A Hydrological and Geomorphometric Approach to. **2017**, doi:10.3390/w9070553.
34. Walters, B. M. O. Transmission losses in a r i d r e g i o n. **1990**, *116*, 129–138.
35. Saber, M. Hydrological Approaches of Wadi System Considering Flash Floods in Arid Regions, Kyoto University, Japan, 2010.
36. Abd-El Moneim, H.; Soliman, M. R.; Moghazy, H. M. Numerical Simulation of Blue Nile Basin using Distributed Hydrological Model. In *11 th International Conference on The Role Of Engineering Towards A Better Environment (RETBE' 17)*; Alexandria, Egypt, 2017.
37. Karamouz, M.; Nazif, S.; Falahi, M. *Hydrology and Hydroclimatology_ Principles and Applications*; CRC Press: U.S., 2013;

5- Effect of HHO gas addition on the performance and emissions of SIE

Haroun Hassan¹, W. A. Aissa^{1,*}, M. Shaban Eissa¹, H. Abdel-Mohsen¹

¹ Mechanical Engineering Department, Faculty of Energy Engineering, Aswan University, Egypt

*waessa@energy.aswu.edu.eg

Abstract. Addition of hydroxy gas (HHO) to a spark-ignition engine (SIE) is an effective method to improve its performance and to reduce the engine emissions. The HHO gas that is generated from water electrolysis has several advantages rather than the gasoline fuel. In the present study, a simple dry fuel cell is manufactured and tested then it is connected to a 183 CC single cylinder air cooled engine (Robin EY 20-3) without any modification in engine intake air system. The engine drives a centrifugal water pump with a maximum delivery flow rate of 520 L/min and total head of 32 m. The engine performance is evaluated under different engine speeds of 1200,1500,2000,2500,3000 and 3500 rpm and fully open water discharge throttle for two cases; without introducing HHO gas and with addition of HHO gas. Different operating parameters are measured such as fuel consumption, pump flow rate, water head, exhaust temperature, intake air mass flow rate and engine emissions including HC and CO. The experimental results show that introducing HHO gas into the intake manifold is more effective in both low and high engine speeds; however, it has an undesirable effect for engine speed around 2000 rpm. Moreover, the average enhancement of engine efficiency, reductions in break specific fuel consumption, reduction in CO and HC emissions are 5.44%, 16.9%, 4.8%, and 5.5%, respectively.

Keywords HHO; gasoline engine; emissions; fuel cell; engine performance.

Introduction

The increasing demand for petroleum fuel associated with limited non-renewable stored quantities has resulted in a huge increase in crude oil prices in the last few years [1]. Many researches focused on finding new effective alternativ sources. HHO gas ; resulted from water electrolyser, is considered to be the best effective solution which can be used hybird with internal combustion engine. Mohamed EL-Kassaby et al. [2] studied the Effect of hydroxy (HHO) gas addition on gasoline engine. ,They reported that HHO gas leads to 10% increase in engine thermal efficiency, 34% reduction of fuel consumption and 18% reduction in NOx emissions. Wang et al. [3] studied the effects of using hydrogen and hydroxy on SI engine at a speed of 1400 rpm. They stated that after hydrogen addition, the fuel flow rate decreased, but it increased with HHO blending. HC emissions decreased, whereas NOx increased with the increase of hydrogen and hydroxy. The CO emissions increased after adding hydrogen but decreased with using hydroxy. Baltacioglu et al. [4] studied the emissions and performance of CI with using of pure hydrogen, biodiesel and HHO gas. They reported that brake power, brake torque, and brake specific fuel consumption increased with HHO addition more than pure hydrogen compared with the diesel fuel, but pure hydrogen gives better values than HHO in engine emissions. Uludamar et al.[5] studied the vibration of a hydroxyl gas generator and diesel engine with different types of biodiesel. They used different values of flow rates of canola, sunflower, and corn biodiesels. They stated that, introducing HHO gas improved the vibration values with a reduction of 1.23%, 2.34%, and 3.54% for HHO-2, HHO-4 and HHO-6 respectively. Baltac M K. [6] constructed electronic control system to generate different hydroxy gas production flow rates with pulse width modulation (PWM) according to the demand of engine operation condition. Al-Rousan and Musmar. [7] studied the effect of anodes-cathodes inter-distances of HHO fuel cell on SI engine. Their results showed that, at 10 mm cathode-anode plates distance hydrocarbons and carbon monoxide emissions reduced to about 40% at different engine speeds. They stated that the 5 mm gap has the highest impact on emission reduction. Ismail et-al. [8] conducted an experiment on a 1500 CC SI engine supplied with 0.375 L/min of HHO gas. They stated that a fuel consumption

reduced by 17%, and a reduction in emissions of CO, HC, and CO₂ 17%, 27%, and 15% respectively was achieved. Yilmaz et al. [9] studied the effect of HHO production on CI engine by using different electrolytes such as KOH, NaOH & NaCl with an electronic control unit (PWM) in order to control the production rate of the gas. Changwei Ji et al. [10] investigated the effect of hydrogen addition on the performance of a methanol engine at the condition of part load and lean conditions. They used dual-fuel injection system at engine speed of 1400 rpm with two hydrogen volume fractions in the intake air of 0% and 3%. The results showed that brake efficiency enhanced after the hydrogen addition besides, HC and CO emissions reduced. Bari and Esmaeil. [11] studied the effect of H₂/O₂ addition resulted from water electrolysis process on the thermal efficiency of a CI engine; they stated that, under constant engine speed and variable load and amount of H₂/O₂ mixture. Results showed that by using 4.84%, 6.06%, and 6.12%, total diesel equivalent of H₂/O₂ mixture, the engine brake thermal efficiency increased from 32.0% to 34.6%, 32.9% to 35.8% and 34.7% to 36.3% at 19 kW, 22 kW and 28 kW, respectively. Leading to a 15.07%, 15.16% and 14.96% fuel reductions and a decrease in HC, CO₂ and CO emissions whereas NO_x emission increased. In this study, a simple fuel dry cell was manufactured and tested then connected to a small gasoline engine to investigate the effect of HHO gas on the engine performance and emissions.

2. Experimental set up

2.1. HHO generator

The cell used in this experiment is a dry fuel cell shown in Fig. 1, it has 21 plates (made of stainless steel-grade 316L) 12 × 12 × 0.1 cm thickness. Stainless steel has good electric conductivity and it can resist rust formation. The distance between plates is limited to 2 mm by insulator rubber gasket, and the cover plate 15 × 15 × 2 cm thickness is made of reinforced wood, another two plates of stainless steel 15 × 15 × 2 cm thickness are located between the two ends of the plates arrangement and the cover plate for pipe connections. The plates are arranged as shown in Fig. 1 in alternate form (+, 4N, -), where (+) represents the positive electrode, (N) is neutral, and (-) is the negative electrode. Current flows from the negative through the neutral plates to the positive plate [2] and the cell has two ports; one for HHO gas exit and the second port is located in the bottom of the cell for water feed. The two ports are connected to a separation tank; Fig. 2. HHO gas generated in the cell, flows up with some water droplets to the separation tank, water droplets fall in the bottom of the separation tank and flows back to the cell, and HHO gas will be delivered from separation tank to a small water tank called bubbler to achieve safe cell operation and avoid fire flash back of the engine. The electrolyte used is NaOH with a concentration of 10g/L of distilled water to increase the conductivity of water.

The cell is tested before it is connected to the engine, and it is allowed to run for about 3.5 hours and the production rate, current drawn and water temperature were measured. Then the cell is connected to the engine.

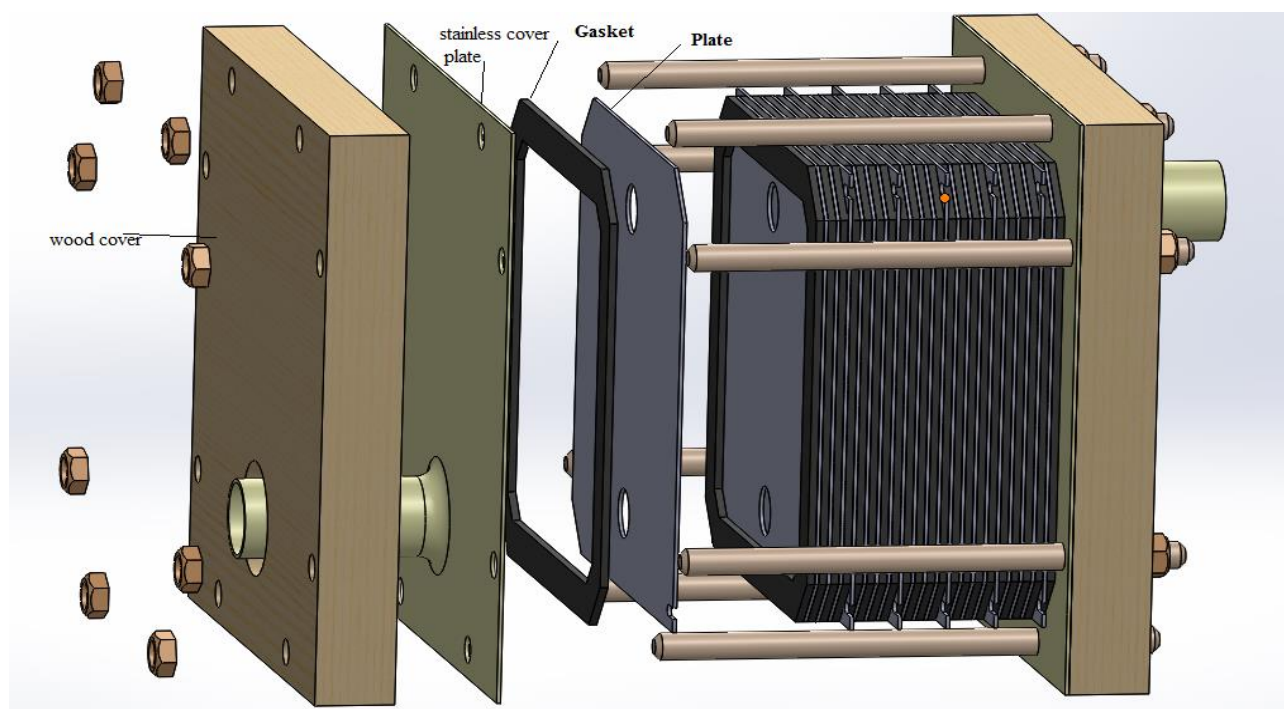


Fig. 1. HHO dry fuel cell construction

2.2. Engine test rig

Fig.2. shows the experiment test rig. The engine used in this experiment is (Robin EY 20-3) single cylinder air cooled whose specification are listed in table 1 and the load used is a centrifugal pump whose specifications are listed on table 2. The test is carried out under different engine speeds of 1200, 1500, 2000, 2500, 3000 and 3500 rpm and fully open pump water discharge. The test is done for two cases. First, the engine run without HHO gas in order to compare the performance of the engine with and without the cell, then the cell is connected to the intake air manifold without any modifications in engine constructions. Many engine parameters were measured such as fuel consumption by self built inclined manometer, exhaust temperature by (Infra red) IR, water flow rate , water head , engine speed by tachometer and engine emissions by Beckman 530 gas analyzer.

Table 1 Engine specifications.

| | |
|---------------|--------------------------|
| Engine model | EY20-3D |
| Engine type | 4-cycle, single cylinder |
| Fuel system | Carburetor |
| Bore × stroke | 67x 52mm |
| Max. power | 5.0 HP @ 4000 rpm |
| Max. torque | 9.3 N.M @ 2800 rpm |

Table 2 Pump specifications.

| | |
|------------------------------|--------------|
| Model | PTG210 |
| Type | Centrifugal |
| Suction × Delivery Diameters | 50.8×50.8 mm |
| Maximum Delivery Volume | 520L/min |
| Total Head | 32m |
| Suction Head | 8m |

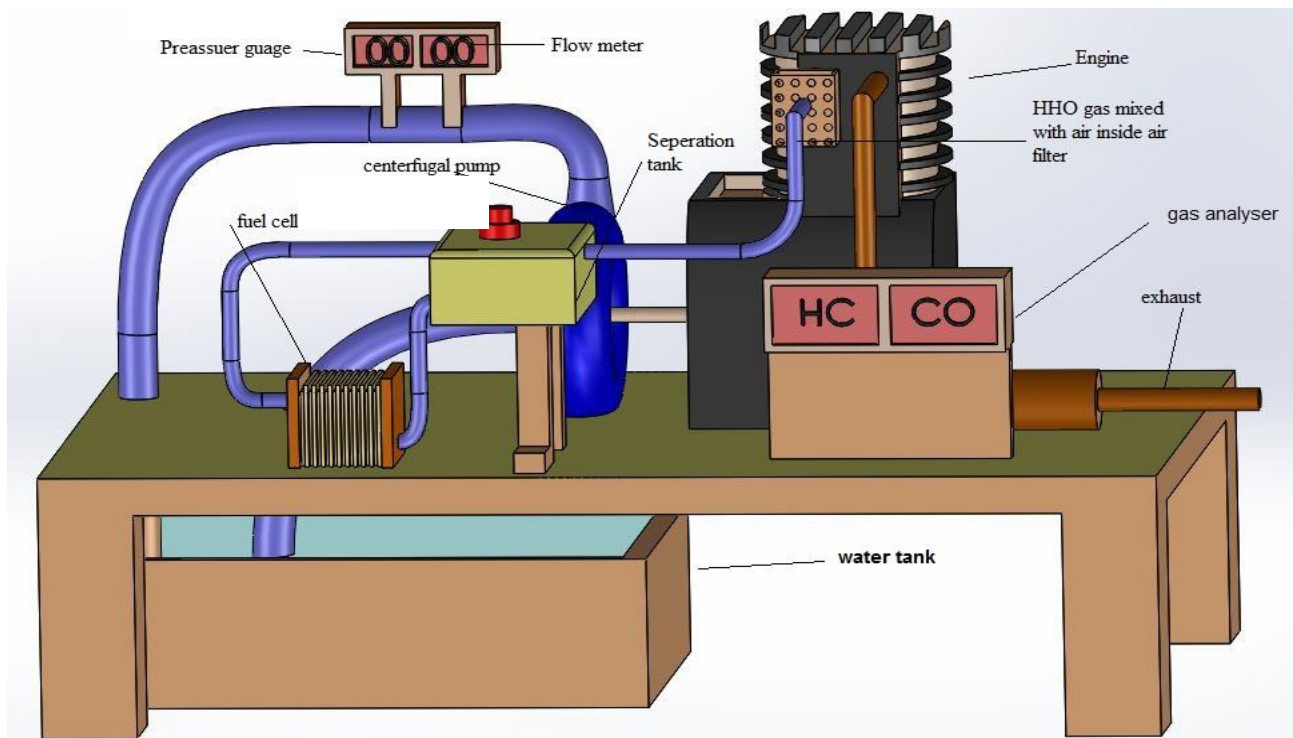


Fig. 2. Experiment test rig

3. Results and discussion

3.1. HHO generator

As mentioned, the cell must be tested separately without the engine before it is connected to the intake air of the engine. Fig. 3. shows the production rate of HHO gas over 210 minutes of cell operation, the production rate increases with time, it reaches 0.14 L/min at the end of operation time because of the increase in electric current drawn; Fig. 4 which shows the variation of current drawn with time. The amount of produced HHO depends on the current flows. Increasing the current leads to a subsequent increase in the production rate. However, this has a side effect on water temperature as shown in Fig. 5. Part of the electric power is consumed in water heating which increases the water temperature. The reason is the ionic conductivity of electrolyte and surface reaction [12].

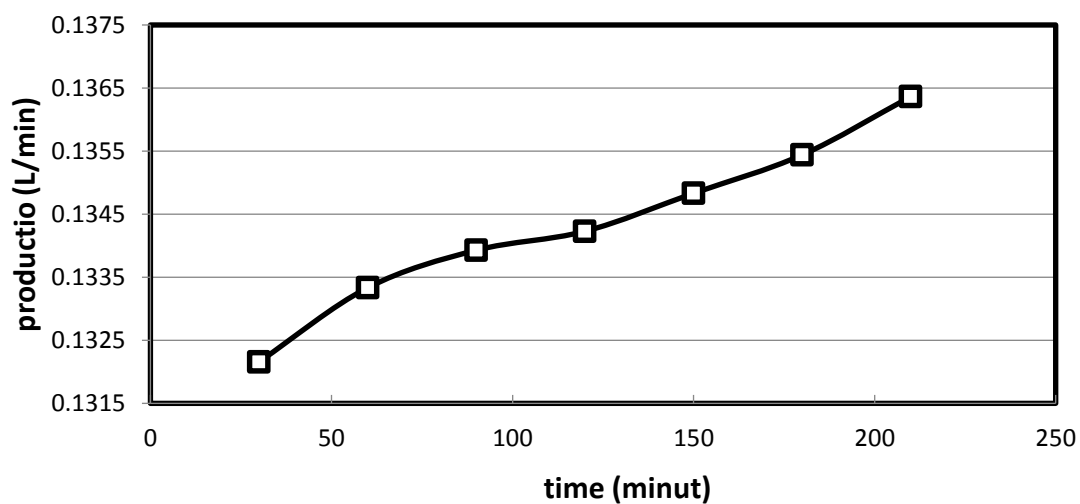


Fig. 3. HHO production rate over time

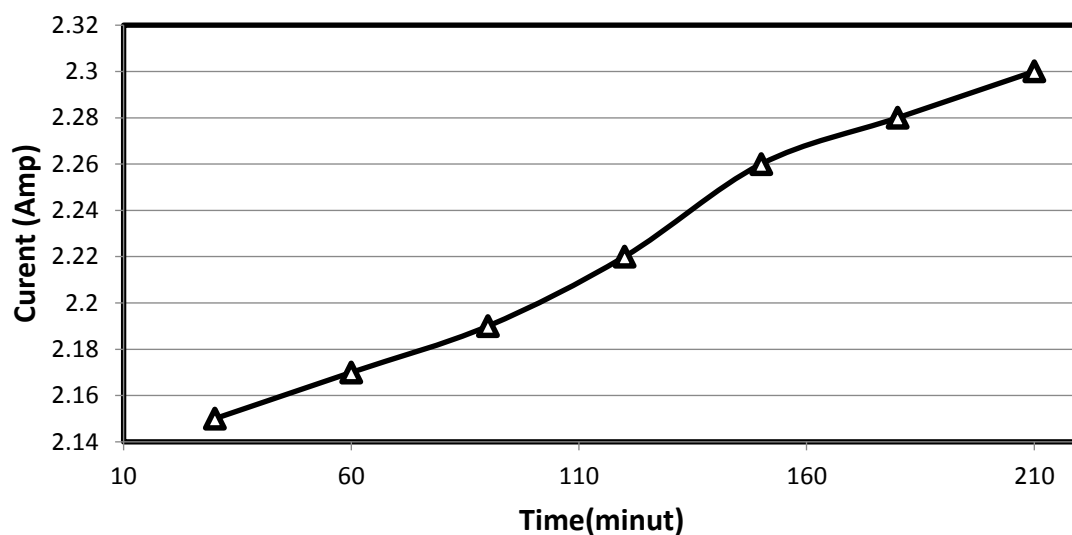


Fig. 4. Variation of drawn cell current with time

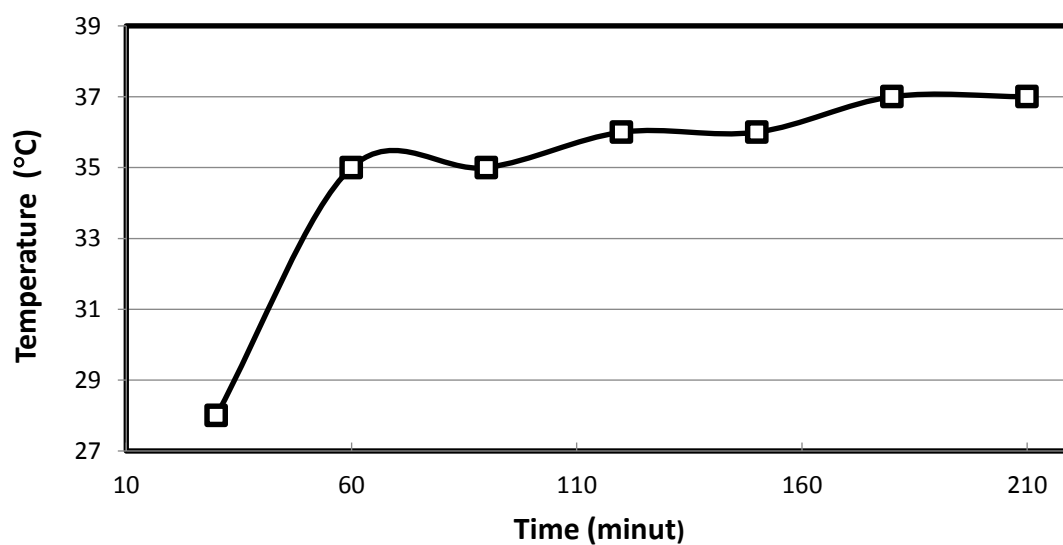


Fig. 5. Variation of cell temperature with time

3.2. Engine performance

Figs. 6. and 7. show the effect of HHO gas addition on the efficiency and B.S.F.C respectively of the engine, the general trend of the curve shows an improvement in engine efficiency for different engine speeds but it has an undesirable effect for engine speed around 2000 rpm. HHO gas enhances the average thermal efficiency by 5.44% and reduces the break specific fuel consumption by 16.9%.

Engine thermal efficiency and B.S.F.C are representing the economics of the engine, HHO gas enhances these two parameters because HHO gas has several advantages rather than the gasoline fuel, it increases the octane rating of any fuel. "octane rating" means how much the fuel can be compressed before it ignites [8], while increasing the octane rating the thermal efficiency increases because the combustion will be much closer to the top dead center of the cylinder [1]

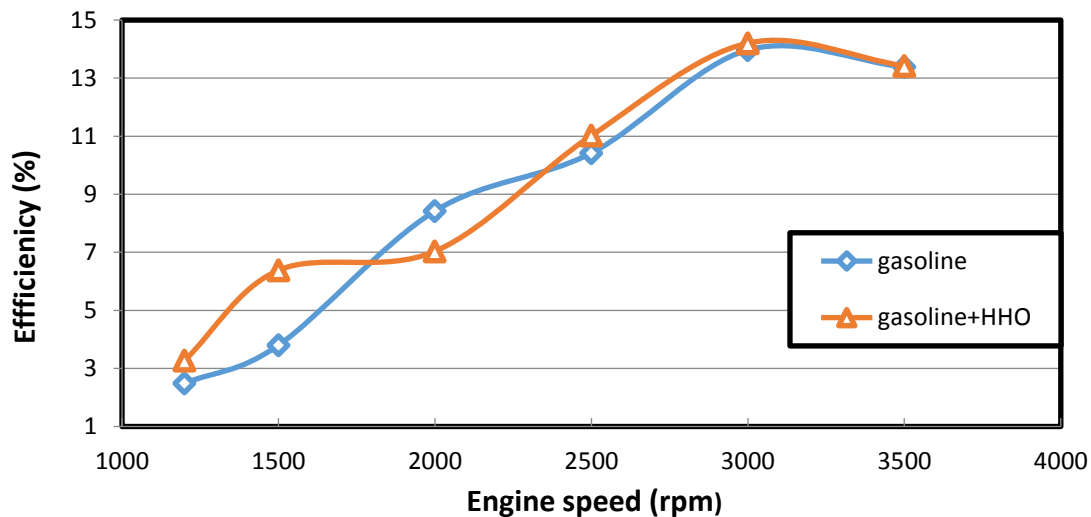


Fig. 6. Variation of thermal efficiency with engine speed.

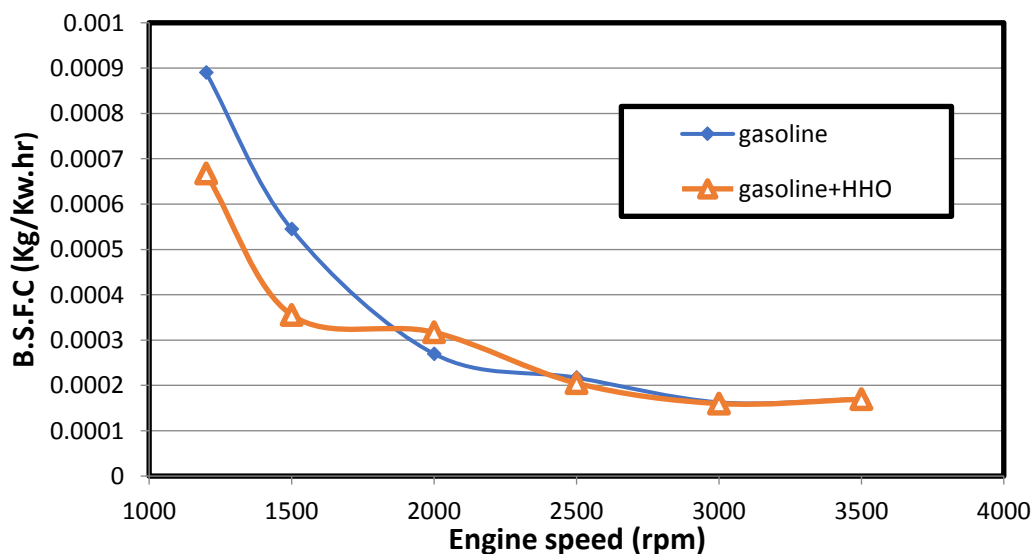


Fig. 7. Effect of HHO gas on break specific fuel consumption for different engine speeds

3.3. Engine emissions

Introducing HHO gas into gasoline engine has a significant effect on engine exhaust emissions. Fig. 8. shows the variations of CO with engine speed ,generally there is a reduction of 4.8% in CO, but for the speeds near 2000 rpm the engine became un steady and gives undesirable effect. If the 2000 rpm was excluded, the average reduction will be 20.8%. Fig. 9. shows the variation of HC with engine speed , an average reduction of 5.5 % were obtained and the average reduction will be 13.6 if the value of 2000 rpm was excluded. The reduction of engine emissions is a result of the good chemical structure of HHO gas rather gasoline, hydrogen and oxygen exists in HHO as two atoms per combustible unit with independent cluster, while gasoline fuel consists of thousands of large molecules of hydrocarbons [2] .In addition, HHO gas has a higher flame velocity than gasoline.

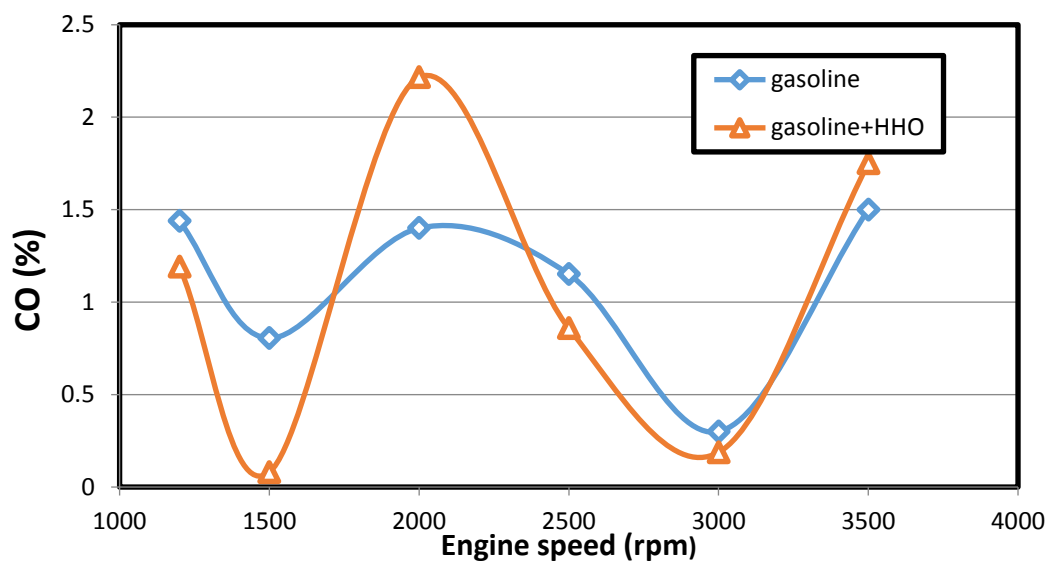


Fig. 8. Effect of HHO gas on CO emissions

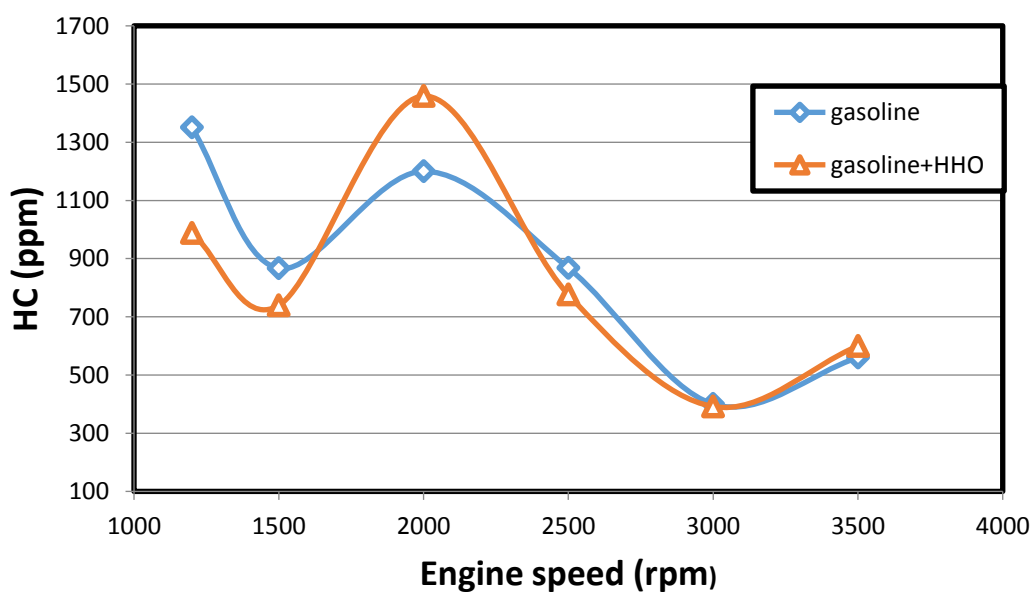


Fig. 9. Effect of HHO gas on HC emissions

4. Conclusions

A simple fuel dry cell was manufactured and tested, then it is connected to a 183 CC single cylinder air cooled engine (Robin EY 20-3) to study the effect of HHO gas on the performance and emissions of SI engines, the following conclusions were obtained

1. HHO gas increased the thermal efficiency by 5.44%, and reduced the break specific fuel consumption by 16.9%.
2. HC and CO emission reduced by 4.8%, and 5.5%, respectively.
3. HHO gas introduced to the intake manifold of the engine without any change in engine system.

References

- [1] Al-Rousan A A 2010 Reduction of fuel consumption in gasoline engines by introducing HHO gas into intake manifold *Int. J. Hydrogen Energy* **35** 12930–5
- [2] El-kassaby M M, Eldrainy Y A, Khidr M E and Khidr K I 2016 Effect of hydroxy (HHO) gas addition on gasoline engine performance and emissions *Alexandria Eng. J.* **55** 243–51
- [3] Wang S, Ji C, Zhang J and Zhang B 2011 Comparison of the performance of a spark-ignited gasoline engine blended with hydrogen and hydrogen-oxygen mixtures *Energy* **36** 5832–7
- [4] Baltacioglu M K, Arat H T, Özcanli M and Aydin K 2016 Experimental comparison of pure hydrogen and HHO (hydroxy) enriched biodiesel (B10) fuel in a commercial diesel engine *Int. J. Hydrogen Energy* **41** 8347–53
- [5] Uludamar E, Tosun E, Tüccar G, Yıldızhan Ş, Çalık A, Yıldırım S, Serin H and Özcanlı M 2017 Evaluation of vibration characteristics of a hydroxyl (HHO) gas generator installed diesel engine fuelled with different diesel–biodiesel blends *Int. J. Hydrogen Energy* **42** 23352–60
- [6] Baltac M K 2018 ScienceDirect A novel application of pulse width modulation technique on hydroxy gas production
- [7] Al-rousan A A and Musmar A 2018 ScienceDirect Effect of anodes-cathodes inter-distances of HHO fuel cell on gasoline engine performance operating by a blend of HHO *Int. J. Hydrogen Energy* **43** 19213–21
- [8] Ismail T M, Ramzy K, Abelwhab M N, Elnaghi B E, Abd El-Salam M and Ismail M I 2018 Performance of hybrid compression ignition engine using hydroxy (HHO) from dry cell *Energy Convers. Manag.* **155** 287–300
- [9] Yilmaz A C, Uludamar E and Aydin K 2010 Effect of hydroxy (HHO) gas addition on performance and exhaust emissions in compression ignition engines *Int. J. Hydrogen Energy* **35** 11366–72
- [10] Ji C, Zhang B and Wang S 2013 Enhancing the performance of a spark-ignition methanol engine with hydrogen addition *Int. J. Hydrogen Energy* **38** 7490–8
- [11] Bari S and Esmail M M 2010 Effect of H₂ / O₂ addition in increasing the thermal efficiency of a diesel engine *Fuel* **89** 378–83
- [12] Masjuki H H, Ruhul A M, Mustafi N N, Kalam M A, Arbab M I and Rizwanul Fattah I M 2016 Study of production optimization and effect of hydroxyl gas on a CI engine performance and emission fueled with biodiesel blends *Int. J. Hydrogen Energy* **41** 14519–28

6- Determination of Wastewater Problems in the Abu Qir Bay and Ways of Risk Reduction

Hossam Abdel wakil Alsherbeny
General Director, Alexandria Sanitary Drainage Co.
halsherbeny@gmail.com

Abstract

Abu Qir Bay coastal zone, located between Abu Qir city and Rosetta city, near the western side of the Rosetta branch of the River Nile. Abu-Qir Bay is considered as *an Estuary*; it extends for about 50 km from El- Montazah in the west to Rosetta mouth of the Nile River in the east and extends northward to about 40 km in the Mediterranean Sea. The maximum depth of the Bay reaches 16 m, while the surface area is about 500 km² with water volume of 4.3 km³.

The present work aims to will determine several parameters to achieve levels of pollution in Abo Qir bay, Alexandria, Egypt. This could be realized by determination of organic loads and nutrient in the bay to minimize the environmental impact on the receiving ecosystem. Abu Qir Bay receives different pollutants discharged through three main openings namely; El-Tabia pumping station, Outlet of Lake Edku (Boughaz El-Maddya). Rosetta mouth of the Nile River.

Along the coast of Abu-Qir Bay, there exist about 22 different factories representing four major categories of industrial wastes which are: food processing and canning, paper industry, fertilizers industry, textile manufacturing. Elements of the Problem: Direct Industrial wastewater disposal into water bodies (Abo Qir bay, Amia drain and Tabia). Deterioration of Public sewerage system. Increasing levels of groundwater. Deterioration of sewers pipeline. Presence of several random sewerage connections constructed in non-scientific and engineering way, especially in the nearest sea areas.

Keywords: Abu qir bay, pollution sources, amia drain, tabia pump station, boughaz el- maadyah,

Introduction

The Abu Qir bay receives 6 million m³/day as: 2 M m³/day from Amia drain through Tabia pump station, 3.5 M m³/day from Maadia opening, 300000 m³/day from Rasheed drain, 8000 m³/day direct discharge from Abo Qir Fertilizer Company, 2500 m³/day from Abo Qir power station, some industrial discharge from petroleum and gas companies at Edko, some discharge from Maadia opening and agricultural and domestic discharge from Edko and Bersik.

Abo Qir Bay Pollution Sources

Amia Drain consists of: - Agricultural discharge from Kafr El-Dawar, Abo Qir, Tarh and Tabia as all agricultural drains dispose into it. -In addition to discharge of the random zones and non-served areas from Behira Governorate. Amia drain receives Organic load resulting from wastewater of random areas and not served which discharges to Amia drain then to Abo Qir bay (from Behira Governorate and Abo Qir), as follows: -150 ton COD. - 95 ton BOD. -60 Ton TSS.

Along the coast of Abu-Qir Bay, there exist about 22 different factories representing four major categories of industrial wastes which are: food processing and canning, paper industry, fertilizers industry and textile manufacturing. The wastes of these industries are of either organic or inorganic nature and are pumped to the sea through El-Tabia pumping station; it pumps out an average amount of 1.5–2.0 million m³ of polluted water per day.

West Zone of Abo Qir bay and the main industries disposing their effluents into it. Industrial Companies that discharges directly into Amia drain then to Abo Qir through Tabia pump station: - National paper company. - Kaha for preserved foods Co. - Agrokim for Agricultural Chemicals co. - Chemics for pesticides co. -Nasr for drying agricultural. West Zone of Abo Qir bay and the main industries disposing their effluents into it. Industrial Companies that discharges directly into

Abo Qir Bay at Alexandria Governorate -Abo Qir for Fertilizers co. -Abo Qir power station. - 60 Ton TSS.

In addition to discharge of four big companies at Kafr El-Dawar with rate of 95000 m³/day, consists of: -43 ton/day COD. -26 ton/day BOD. -25 ton/day TSS. These are: - Misr for artificial silk. - Dye and chemicals company (Asma dye). - ElBida dyeing company. - Egypt for textile and winning. Abo Qir bay extends 50 km, starting from Tabia north east Alexandria to Nile river (Rosseta branch) at Behira Governorate. The total area of the bay is about 500 km² with shore line of about 50 km.

Problem addressed

The problem associated with the current study, the Abo Qir Bay has become a hot spot area due to stress from discharged wastewaters, requiring permanent monitoring of its water quality and inhabiting biota. The seasonal variability in the quantity and quality of these wastes and their dispersion is of great importance in the dynamics of the hydrographic conditions, nutrient concentrations and plankton density in the bay. This means that the growth of planktonic organisms in Abu Qir Bay is stimulated directly and indirectly by nutrients and may be inhibited by the discharged pollutants.

The first clear effect of such variations was shown in the hydrographic conditions, particularly water transparency, dissolved oxygen and salinity. The southwestern bay was characterized by low water transparency all year round, due to the mixing processes. Although chlorophylla was generally high, dissolved oxygen was usually low. The low oxygenation of the coastal waters in Abu Qir Bay has been a characteristic feature for a long time. This results mainly from oxygen consumption in the oxidation of a heavy organic matter load in the bay, particularly in the southwestern part which is directly exposed to industrial and domestic wastes and characterized by intensive plankton production.

Direct Industrial wastewater disposal into water bodies (Abo Qir bay, Amia drain and Tabia), deterioration of Public sewerage system, vertical and horizontal housing extensions in random areas and increasing levels of groundwater. Create unpleasant sea shore conditions, affecting different touristic activities and affecting fishery activities.

Objectives

The proposed study will determine several parameters to achieve levels of pollution in Abo Qir bay, Alexandria, Egypt. This could be realized by determination of organic loads and nutrient in the bay. Determination the specific pollution to achieve the levels of parameters according to law 48 to 1982 belongs to the discharges to surface water.

Study area

The selected area of study known as Abu Qir Bay, is a semicircular shallow basin lying at 35 km to the east of Alexandria city between Abu Qir Peninsula (west) and the Rosetta branch of the Nile (east), with a shoreline about 50 km long. It lies between 30° 4' - 30° 21' East and 31° 16' - 31° 30' North. The bay is relatively shallow with a depth ranging from less than one meter along the coast, increasing gradually away from the shore to reach a maximum depth of about 15 m. The bay has a surface area of about 360 km², its mean depth is 12 m and the volume of water is about 4.32 km³. The amount of freshwater discharged into the bay is estimated as 2130 x 10⁶ m³/y. The mean concentrations of hydrographic parameters, nutrients and metals recorded in the bay waters



Fig. (1): Abu Qir Bay

Abu Qir Drain receives and discharges industrial wastewaters from 22 different factories of food processing and canning, paper industry, fertilizer industry, and textile manufacturing. Besides, 15000 m³ /day of industrial wastes are discharged directly into the bay. The major industrial activities affecting the quality of Abu Qir Bay are located in EL-Tabia and Kafr EL-Dawar regions.

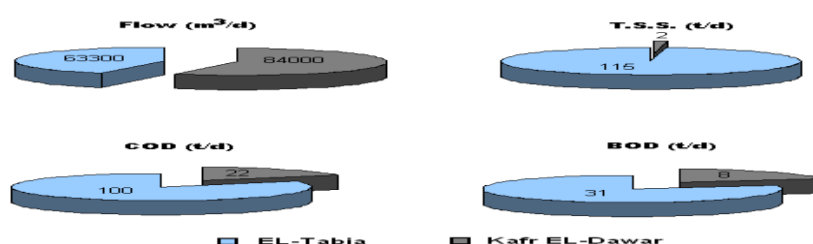


Fig. (2): Contributions of the industrial areas to the flowrate, total suspended solids TSS, COD and BOD in Abu Qir Bay.

Table 1. Sources of various pollutants in Abu-Qir Bay:

| Source | Types of pollution, | Rate of Discharge |
|----------------------------------|--|---|
| El-Tabia Outfall | Food processing and canning, paper, fertilizers industry and textiles manufacturing. | 1.5-2 million m ³ /day |
| Maadia outlet of Idku Lagoon | Drainage water from agricultural usually contains pesticides. | 1.5-2 million m ³ /day |
| Rosetta branch of the River Nile | Fresh water discharged carries Agricultural waste from cultivated lands. | 2-5 x 10 ⁹ m ³ /year, |

Abo Qir sewerage system problems

Abo Qir wastewater treated at ETP, The wastewater resulting from Abo Qir treated East treatment plant so far from Abo Qir area.

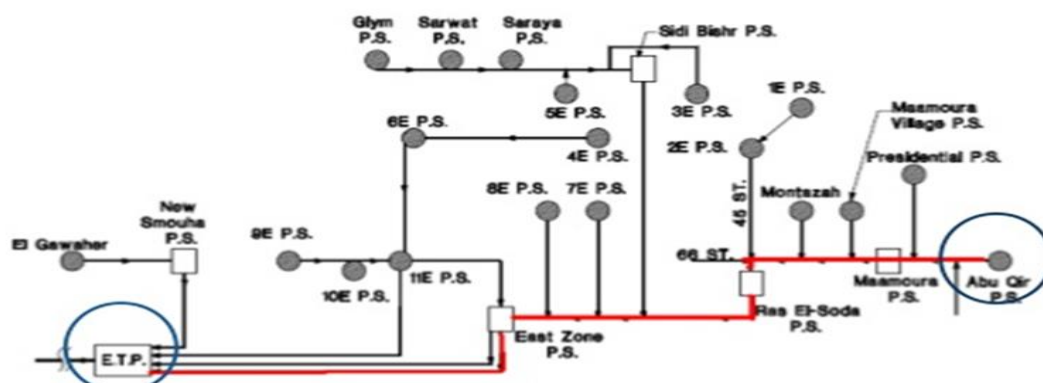


Fig. (3): The wastewater resulting from Abo Qir treated East treatment plant so far from Abo Qir area.

Abo Qir bay pollution risk

The pollution of Abu-Qir Bay region induced a panic oxidative stress in fish living in this area. This indicates that the industrial wastewater treatment in this area is not adequate to avoid the hazardous effects of such pollutants.



Fig. (4): Mass death of fish as a result of industrial pollution in Tabia area.

Due to stress from discharged wastewaters, the Bay has become a hot spot area; requiring permanent monitoring of its water quality and inhabiting biota. The seasonal variability in the quantity and quality of these wastes and their dispersion is of great importance in the dynamics of the hydrographic conditions, nutrient concentrations and plankton density in the bay. This means that the growth of planktonic organisms in Abu Qir Bay is stimulated directly and indirectly by nutrients and may be inhibited by the discharged pollutants.

The first clear effect of such variations was shown in the hydrographic conditions, particularly water transparency, dissolved oxygen and salinity. The southwestern bay was characterized by low water transparency all year round, due to the mixing processes. Although chlorophylla was generally high, dissolved oxygen was usually low.

The low oxygenation of the coastal waters in Abu Qir Bay has been a characteristic feature for a long time. This results mainly from oxygen consumption in the oxidation of a heavy organic matter load in the bay, particularly in the southwestern part which is directly exposed to industrial and domestic wastes and characterized by intensive plankton production.

Effect on the buildings on the new random housing areas, especially at Toson zone and loss of agricultural land. High cost of applying solutions to avoid high groundwater levels. Amplifying the impacts of sea rise in the area. Create expected dramatic industrial pollution

Site Description

Wastewater Sampling Site

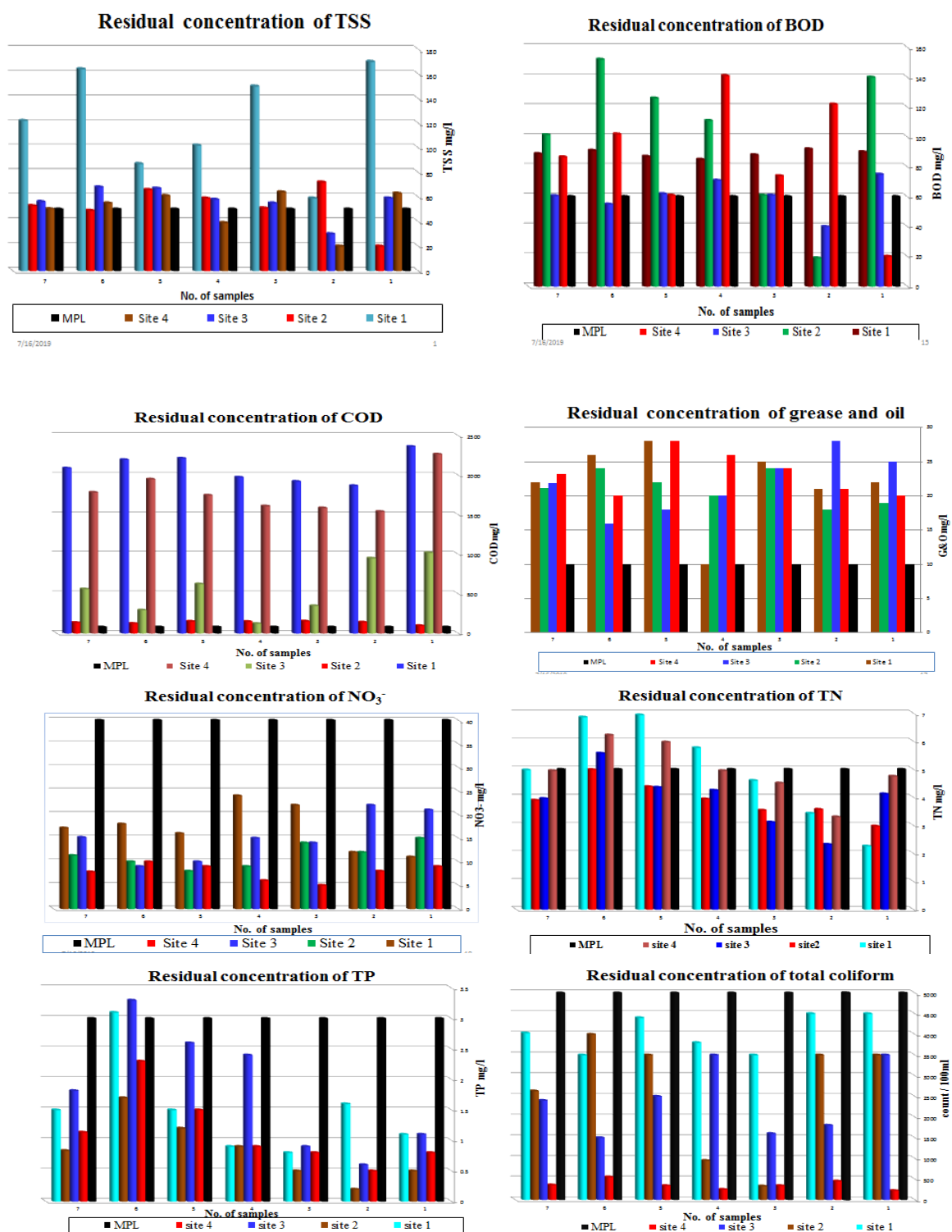
During the present study, wastewater samples were harvested from the four points includes, Rosetta branch of the River Nile, Maadia outlet of Idku Lake, El-Tabia outfall and abo qir beach, Alexandria, Egypt, as shown in fig. (5).

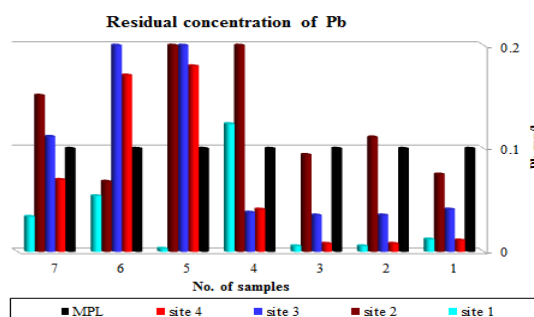
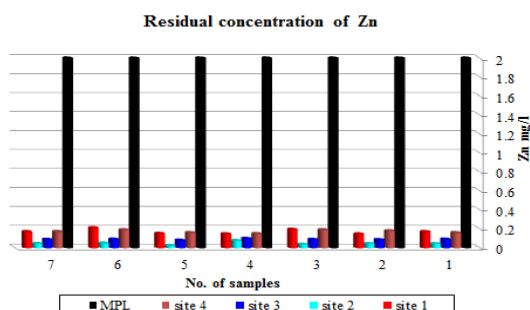
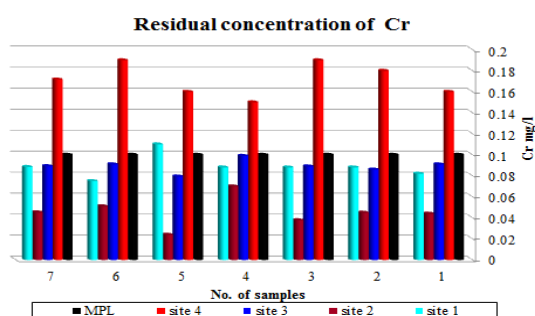
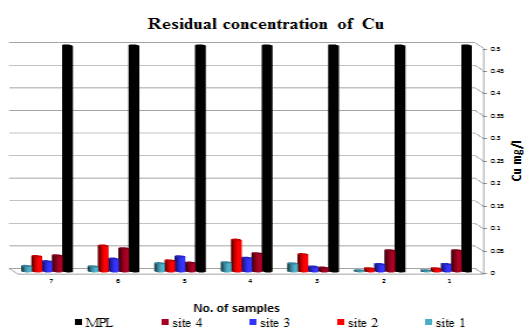
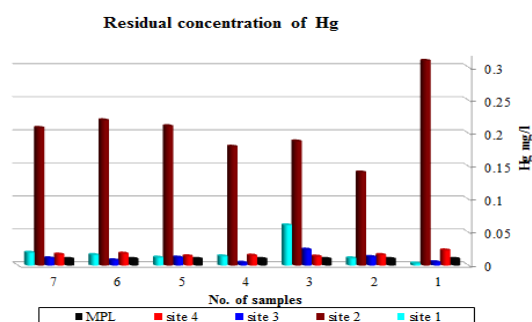
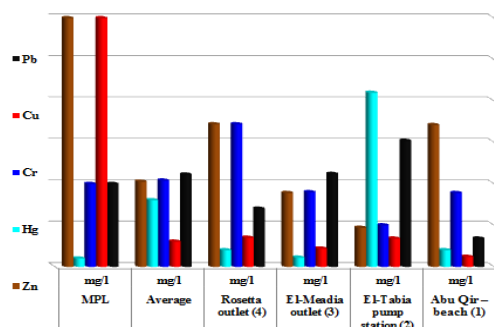
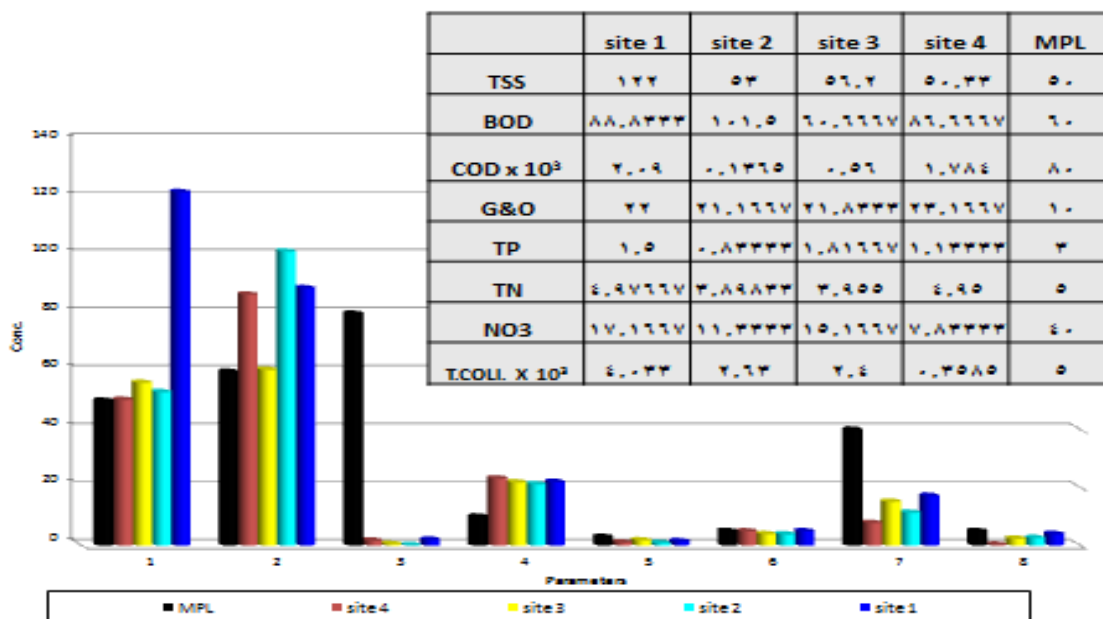


Fig. (5): Samples Collection sites

Results

Data Collection and Analysis





Conclusions

This study discussed level of pollution in abo qir bay to determine problems and ways of risk reduction. Many problems of natural water pollution are attributed to sanitary sewage, organic industrial and agricultural wastes. The suspended solids (TSS) and the biological oxygen demand (BOD₅), in addition to the chemical oxygen demand (COD), are the three major characteristics determining the pollution levels in wastewater. The maximum permissible limits (MPLs) of these

indicators are specified nationally by laws and regulations to provide a safe protection to the environment and receiving water surfaces.

The temperature usually influences the rate of all chemical and biochemical reactions. However, the effect of temperature in the present work was not considered as a variable, as the temperatures ranged between 18-30 °C, and all the work was carried out under the prevailing room temperature, which ranged between 20-25°C.

During the present study, wastewater samples were collected from the four points includes Abo qir beach, El-Tabia outfall, Maadia outlet and Rosetta branch of the River Nile, of Idku Lake, Alexandria, Egypt.

Results obtained during the present study can be summarized in the following points:

1. Analysis the organic load where BOD₅ average recorded 89, 101.5, 60.7, 86.7 mg/l respectively. The MPL of 60 mg/l.
2. Analysis the organic load where COD average recorded 2090, 136.5, 560, 1784 mg/l respectively. The MPL of 80 mg/l.
3. Level of total phosphorous TP recorded an average of 1.5, .633, .1.82, 1.133 mg/l compared to MPL of 5 mg/l. Also the effluent contained ammonia (NH₃-N) content with an average of 17.2, 11.3, 15.16, 7.83 mg/l (MPL=3.0 mg/l).
4. The TSS recorded 122, 53, 56.2, 50.33 mg/l respectively, (MPL, 60 mg/l).
5. Total Nitrogen (TN) recorded 4.98, 3.9, 3.96, 4.95 mg/l respectively, (40 mg/l (MPL)
6. Total Coliform recorded 4033, 2630, 2400, 359 count/100 ml respectively, (MPL 5000 cont /100 ml)
7. The heavy metal (Hg) represent high level in El-Tabia pump station, were recorded 0.21 mg/l (MPL, 0.005 mg/l).
8. The heavy metal (Cr) represent high level in Rosetta branch of the River Nile, were recorded 0.17 mg/l (MPL, 0.09 mg/l).
9. The heavy metal (Pb) represent high level in El-Tabia pump station, were recorded 0.15 mg/l (MPL, 0.09 mg/l).

Recommendation

1. Effective industrial wastewater control program.
2. Upgrading old and low capacity public sewerage systems.
3. Long-term program for groundwater reduction.
4. Minimizing different impacts resulting from groundwater high level problems through appropriate and specific best management practices.
5. Abo Qir domestic wastewater must be pumped to the Maaamora wastewater treatment plant.

References

- [1] Water Encyclopedia: Domestic, Municipal, and Industrial Jack Keeley (Editor) Janet Lehr (Associate Editor), July 2005.
- [2] Corbitt, R. A. "Wastewater Disposal." In Standard Handbook of Environmental Engineering, edited by R. A. Corbitt. New York: McGraw-Hill, 1990.
- [3] Junkins, R., K. Deeny, and T. Eckhoff. The Activated Sludge Process: Fundamentals of Operation. Boston: Butterworth Publishers, 1983.
- [4] CIWEM. Handbook of UK Wastewater Practice, Activated Sludge Treatment CIWEM1997, p13.
- [5] Water Pollution Control Federation and American Society of Civil Engineers Manual of Practice FD-13 Aeration WPCF/ASCE 1988, p30
- [6] Principal Contractors and Grantees Include ABBA Susa, Harza, UNICEF, and Planning Development Collaborative (PADCO). FY 2004 Program & FY 2005 Program: No Obligations are planning for FY2005.
- [7] USAID / EGYPT'S Democracy and Governance Annual Program Statement from Flow year (FY) 2005, Arabic Version.
- [8] USAID / EGPT'S Democracy and Governance Annul Program Statement (APS) for TY 2005.

- [9] Principal Contractors and Grantes Include ABBA Susa, Harza, UNICEF, and Planning Development Collaborative (PADCO). FY 2004 Program & FY 2005 Program: No Obligations are planning for FY2005.
- [10] US clean water Act of 1977 pl 95-217, the Water Quality Act of 1987 2nd Edition Water Pollution Control Federation, 1990.
- [11] Catherine Taylor and Joseph Yahner, Pipeline, Fall 1997, Vol. 18, No. 4 .Donjones. Agricultural Engineering, Purdue University and Alan Dunn, Indiana State, Department of Health.
- [12] Typical Municipal Wastewater Characteristics Metcalf and Eddy, Inc. 1991, Wastewater Engineering Treatment.
- [13] Environmental Inquiry Cornell, University and Penn State University 2005.
- [14] Borough of Edinboro, John R. Marchese, Assistant Super intending, Wastewater Treatment Facility 301 Water Street, Edinboro PA. 16412, 2003.
- [15] The Standard Methods for the Examination of Water and Wastewater, (APHA, 1998).
- [16] Arab Republic of Egypt, Alex. General Organization for Sanitary Drainage Volume 1, Operation and Maintenance Manual for, East Treatment Plant. Nov. 2004, ABB Susa Inc. OM&T.
- [17] Albertson O.E. , and R.N. Okay. “Trickling Filters need to Breath too” Presented at the Low Water Pollution Control Federation, Des Moines, June 1988.
- [18] Wastewater treatment Plant, Columbia, Missouri, 28 August, 2004, City of Columbia.
- [19] American Public Health. (1998). Standard methods for examination of water & wastewater. 20th ed., 4(75-155) Washington, D.C.}.
- [20] Metcalf and Eddy, Inc. 1991. Wastewater Engineering Treatment, Disposal, and Reuse. 3rd ed. McGraw-Hill, Inc

7- Simulating the performance of an industrial packed column in extracting aromatics

Mariam Eltohamy^{a,†}, Hassan A. Farag^b, Mona E. Osman^c

^a Chemical Engineering Department, Faculty of engineering, Alexandria University, Alexandria, Egypt

^b Chemical Engineering Department, Faculty of engineering, Alexandria University, Alexandria, Egypt

^c City for Scientific Research and Technological Applications, SRTA City, Borg el-Arab, Alexandria, Egypt.

† corresponding author: Mariam Alaa eldein Eltohamy, E-mail: eltohamy.mariam@gmail.com

Abstract

A two-dimensional model was developed to simulate the performance of an industrial packed column used to extract aromatics from lube oil fraction using N-Methyl-2pyrrolidone (NMP). The model was numerically solved using a MATLAB code. The effect of operational variables such as voidage of the packing, the flow rates of both dispersed and continuous phases, and dispersed phase holdup on the extraction of aromatics from lube oil and hydrodynamic parameters were studied. It was found that the dispersed phase holdup showed a remarkable effect on extraction of aromatics. Also by increasing flow rates of both dispersed and continuous phases, concentration of aromatics in dispersed phase (lube oil) decreased. On increasing column height, the mass transfer increased between the two phases. On decreasing the voidage of the bed, the extraction efficiency of the aromatics by NMP increased due to the increasing of the rate of mass transfer. This work has provided valuable model for the prediction of the extraction efficiency in a random packed extraction column. The results of the mathematical model gave a good agreement with actual industrial data for the removal of aromatics from lube oil cut fraction. This model can be successively applied to predict different extraction efficiencies when using different values of flow rates, voidage of the bed and dispersed phase holdup inside the column.

Keywords: simulation, lubricating oil, solvent extraction, random packed column

Introduction

In the method of producing lubricating mineral oil, the removal of aromatic hydrocarbons from vacuum distillates is required to enhance many lubricating properties. The residue from the crude oil part distillation (long residue) is transferred to a vacuum distillation column and separated into completely different lube oil cuts, characterized by their boiling range and viscosity. For several years, many works have been centered on trying to find selective solvents for aromatics extraction from hydrocarbon mixtures. A good solvent needs to maximize variations in properties between the liquid phases to reduce the loss of oil [1].

For many years a good deal of attention has been paid to the selective solvents used to extract aromatic compounds from organic compound mixtures. One among the solvents used extensively for this purpose is furfural. Because of some difficulties in using furfural attempts are made to exchange it with alternative solvents like N-methyl-2-pyrrolidone. The benefits of using this solvent (NMP) rather than furfural for the extraction of aromatic compounds from hydrocarbon mixtures (lube-oil cut) are as follows: Lower energy consumption in the lube-oil extraction units; Lower solvent-to-oil ratio in the lube-oil extraction units and Lower toxicity. [2].

The design and simulation of solvent extraction processes are performed mostly by totally empirical ways requiring experimental information sometimes not available. Such approach is sometimes expensive as a result of massive experimental determination is required. Rigorous modeling of the extraction method would be an acceptable tool to simulate changes in operation conditions or feed quality, and thus to properly describe the liquid-liquid equilibrium (LLE) established within the extraction operation.

In the analysis and therefore the quest for an understanding of a physical system, generally, the formulation and use of a mathematical model that is thought to explain the system is an essential step. That is, a mathematical model is formulated (as a system of equations) that is thought to

quantitatively define the inter relationships between phenomena that determine the characteristics of the physical system. The mathematical model is sometimes tested against observations of the physical system, and if the agreement is taken into account acceptable, the model is then taken as an illustration of the physical system. The solution of the model equations is commonly a challenge. Typically, in science and engineering this involves the integration of systems of partial differential equations (PDEs) [3].

The packed columns find a wide application like contactor for liquid-liquid systems such as solvent extraction. In the literature, the modeling of this type of equipment received much less attention in comparison with the plate columns. Berenice Blanco (2000) studied a dynamic model which described the mass transfer in a liquid-liquid extraction column filled with a structured packing. The system used was toluene-acetone-water as the availability of its physical data [4]. Amir Hossein Mehrkesh et al. (2010) discussed an artificial neural network (ANN) to have a simulation model to predict the rotating disc contactor (RDC) performance during the extraction of aromatic hydrocarbons from lube oil cuts, to get a lubricating base oil using furfural as solvent [5]. Seyed Mousa Fakhr (2012) used a mathematical modeling approach to obtain a simulation model to predict the performance of an industrial rotating disc contactor (RDC) in the extraction of lubricating base oils by using furfural [6].

9 Methods

2.1 Basic concept of modeling

Modeling the packed tower for a liquid-liquid extraction process using mass correlations and with regard to the hydrodynamic behavior and geometrical properties of the column could be useful for:

1. Investigation of the possibility of increasing production of high quality base oils by adjusting and optimizing the different operational parameters, such as dispersed phase holdup, solvent/feed ratio, and packing effective area.
2. Determination of the appropriate concentration gradient in the column.
3. Determination of the impact of physical properties of the extraction solvent on the extraction productivity.

For the production of lubricating base oil in a solvent extraction process, lube oil cut (as feed) and NMP (as solvent) should be blended well enough to reach the maximum yield of extraction. In this study, operating data from the field data of the Oil Company (one of the largest base oil producer in Egypt) were used for calculating the parameters and validating the model. The characteristics of the packed column are as follows: column diameter, 5 m; height of packing, 1 m; column height, 20 m; feed entry, (bottom); solvent entry, (top) filled with Raschig rings of 2.45 cm diameter. The physical properties of the used lube oil cut and NMP are listed in Table 1 and the characteristics of random packing are represented in Table 2.

Table 1. Typical physical properties of the system lube-oil cut and NMP.

| Physical Properties of the system (NMP/Lube-oil cut) | | |
|--|------|-------|
| Dispersed Phase | | |
| Viscosity, cSt , 40o c | | 57.6 |
| 100o c | 7.25 | |
| Density, g/cm ³ | | 0.850 |

| | |
|---------------------------|------|
| Sulfur, weight % | 1.84 |
| Aromatics, weight % | 40 |
| Distillation, ASTM D-2887 | |
| OC AT % Volume, IBP | 377 |
| 5 | 414 |
| 10 | 424 |
| 30 | 440 |
| 50 | 450 |
| 70 | 460 |
| 90 | 477 |
| 95 | 485 |
| EP | 517 |

Continuous Phase

| | |
|------------------------------|----------------------------------|
| Formula | C ₅ H ₉ NO |
| Density, g/cm ³ | 1.028 |
| Molecular Weight, g/mol | 99.133 |
| Interfacial Tension, dyne/cm | 24 |
| Viscosity, cP at 66 °C | 1.66 |

Table2. Characteristics of random packing

| Ceramic Raschig Ring | |
|---|--------|
| Nominal size, mm (in) | 25 (1) |
| Wall thicken, mm | 3.6 |
| Voidage ϵ | 0.71 |
| Interfacial area a_p , m ² /m ³ (ft ² /ft ³) | 19 |

2.2 Extraction Column Modeling

The mathematical model is based on a differential element of the column with the assumptions that:

- The dispersed phase velocity, v_d , is constant ,i.e., independent of z and r .
- The radial fluid velocity is zero.
- Constant axial dispersion coefficient E_z and a constant radial dispersion coefficient E_r .

A material balance by applying the dispersion model [7] on a differential element of the column and within the absence of any reaction, results in the transient global differential equation that models the column behavior, taking into consideration axial and radial dispersions:

$$-\phi v_d \frac{\partial y}{\partial z} + E_z \phi \frac{\partial^2 y}{\partial z^2} + E_r \phi \frac{\partial}{\partial r} \left(r \frac{\partial y}{\partial r} \right) - K_{od} a (y - y^*) = \phi v_d \frac{\partial y}{\partial t} \quad (1)$$

$$\text{With equilibrium equation: } y^* = m x \quad (2)$$

A material balance on the lower part of the column gives:

$$(1 - \Phi) v_c x + \phi v_d y_e = \phi v_d y + (1 - \phi) v_c x_s \Phi \quad (3)$$

$$\text{And } x = \frac{\phi v_d}{1 - \phi v_c} (y - y_e) + X_s \quad (4)$$

By replacing equations (2) and (4) in (1) we have:

$$-\phi v_d \frac{\partial y}{\partial z} + E_z \phi \frac{\partial^2 y}{\partial z^2} + E_r \phi \frac{\partial}{\partial r} \left(r \frac{\partial y}{\partial r} \right) - K_{od} a (\alpha y + \beta) = \phi V_d \frac{\partial y}{\partial t} \quad (5)$$

$$\text{With: } \alpha = 1 - m \frac{\phi v_d}{1 - \phi v_c} \quad \beta = m \frac{\phi v_d}{1 - \phi v_c} y_e - m X_s \quad (6)$$

Boundary conditions used to solve the differential equation are:

$$\text{At } z = 0 \text{ (at outlet), } y = y_e \text{ and at } z = H, \frac{\partial y}{\partial z} = 0 \quad (7)$$

The axial symmetry imposes the following boundary conditions in the radial direction:

$$\text{At } r = 0, \quad \frac{\partial y}{\partial r} = 0 \quad (8)$$

$$\text{On the wall, at } r = R, \quad \frac{\partial y}{\partial r} \Big|_{r=R} = -\frac{K_{od}}{E_r} (y - y_\infty) \quad (9)$$

With y_∞ : mole fraction obtained at an infinite height of the column.

10 Results and discussion

Solving the differential equation of a specific case is obtained using MATLAB software. We will therefore study the impact of dispersion on the concentration profiles along the column.

The results obtained in this work are compared with those obtained from refinery in Egypt of an extraction packed column in the treatment of the system: lube oil/ N-Methyl-2 pyrrolidone (NMP).

We used the same data and same operating conditions of the column: a packed column of 20 m height and 2.7 m diameter, filled with ceramic Raschig rings of 2.54 cm diameter with an interfacial area of 190 m²/m³ and a void fraction of 0.71. From literature we used some auxiliary equations to calculate the parameters of the model equation where the dispersed phase holdup ϕ was proposed by analytical model by Seibert & Fair (1988)[8].

3.1 Axial dispersion effect:

The differential equation obtained for our case was solved taking into account axial dispersion only, which can be summarized in the following differential equation:

$$E_z \phi \frac{\partial^2 y}{\partial z^2} - \phi v_d \frac{\partial y}{\partial z} - K_{od} a (\alpha y + \beta) = 0 \quad (10)$$

E_z : the coefficient of axial dispersion in the dispersed phase expressed as a dimensionless number of Peclet number (Pe_d) calculated according to the operating point considered: V_c , V_d

The boundary conditions used are as follows:

$$\text{At } z = 0 \text{ (at outlet), } y = y_e \text{ and at } z = H, \frac{\partial y}{\partial z} = 0 \quad (11)$$

In steady state, the change in mole fraction along the column is shown on the graph in Fig.1.

Where mole fraction of solute in dispersed phase (lube oil phase) decreases with the height of the column.

To study the impact of axial dispersion on the profile of the mole fraction along the column, we have a tendency to compare. For the latter case the differential equation is simplified and an analytical solution giving the variation of mole fraction as a function of the column height is given by:

$$y = \left(y_e + \frac{\beta}{\alpha} \right) \exp \left(-\frac{K_{od} a \alpha}{v_d \phi} z \right) - \frac{\beta}{\alpha} \quad (12)$$

The values obtained are shown in Table 3. From these results, the mole fraction of solute increases slightly in the presence of axial dispersion along the column, but its effect is considered negligible and even vanishes when approaching the exit of the column. The relative error between calculated value from refinery data of the mole fraction and calculated one at the column outlet is: 1.7 %

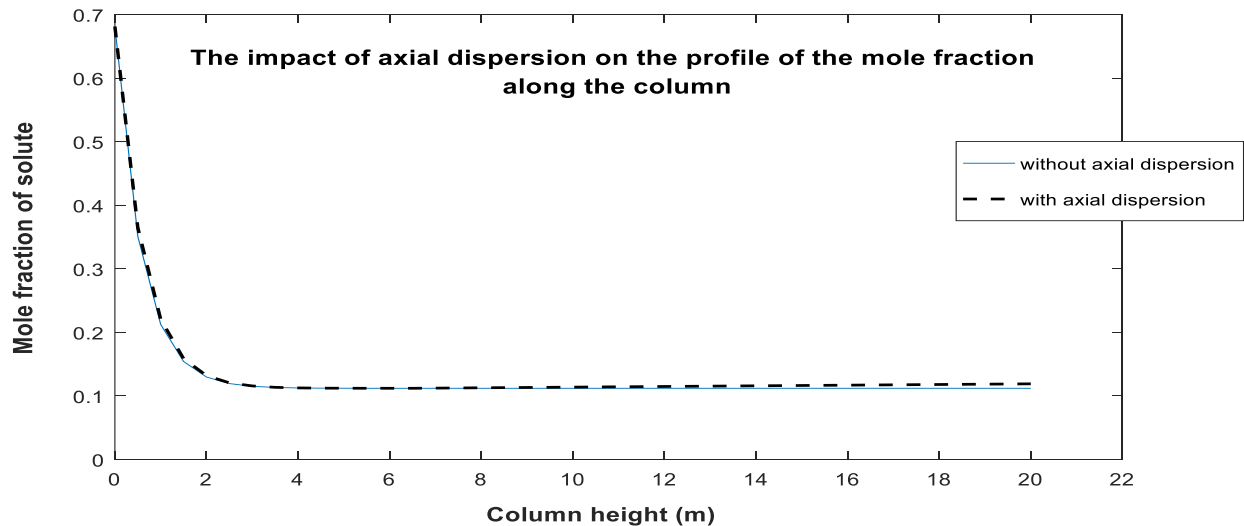


Fig. 1: The impact of axial dispersion on the concentration profile of the mole fraction of solute along the column

3.2 Effect of dispersed phase holdup:

The dispersed phase holdup is an essential parameter for the design and scale-up of columns. Values of the holdup can be used to determine the flooding velocity, and it is entirely related to the interfacial area available for mass transfer.

This parameter provides an indication about the capacity of the random packing; higher is this value higher is the space inside the packing bed free for the passage of the fluids

Fig.2 shows the effect of dispersed phase holdup on mole fraction of aromatic hydrocarbons in dispersed phase.

The dispersed phase holdup (ϕ) is defined as the volume fraction of the extraction column that is occupied by the disperse phase:

$$\phi = \frac{V_d}{V_d + V_c} \quad (13)$$

Generally speaking, it is clear from Fig (2.a) that by increasing dispersed phase holdup will increase the mole fraction of aromatics of lube oil.

At a certain value of dispersed phase holdup, decreasing column height will increase the mole fraction of aromatic in dispersed phase and at the outlet the effect of packing height on holdup is in agreement with previous investigators.[9]

The mass transfer of LLE column is directly connected to the drop phase holdup within the tower. The main function of the packing is to supply an increased flow path length respectively more residence time for the drop phase. Coalesced drops are re-dispersed at the sharp edges of the packing and also the residence time distribution of each phase ought to be kept as narrow as possible (plug flow) by minimizing any axial back mixing effect and to supply more contact area between the two phases. As shown in Fig (2.e), at height $z = 20$ m (actual operating value) the dispersed phase holdup has no effect on mole fraction of aromatics.

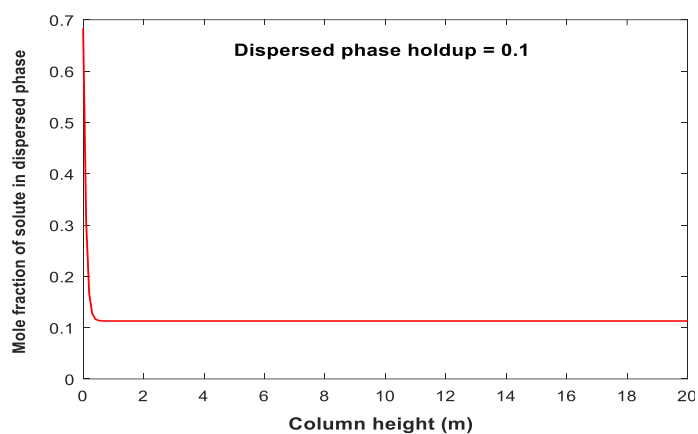


Fig (2.a)

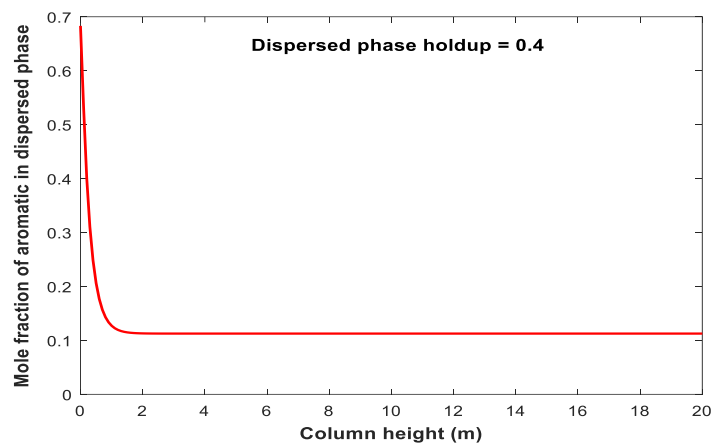


Fig (2.b)

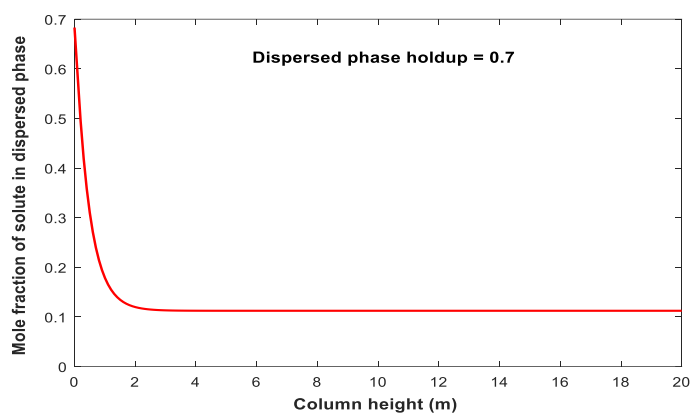


Fig (2.c)

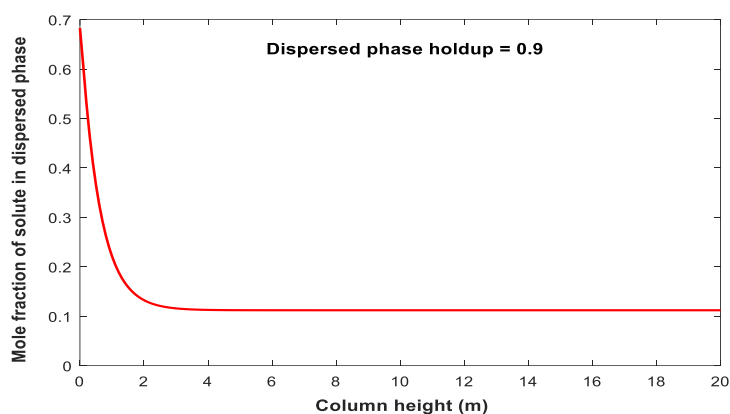


Fig (2.d)

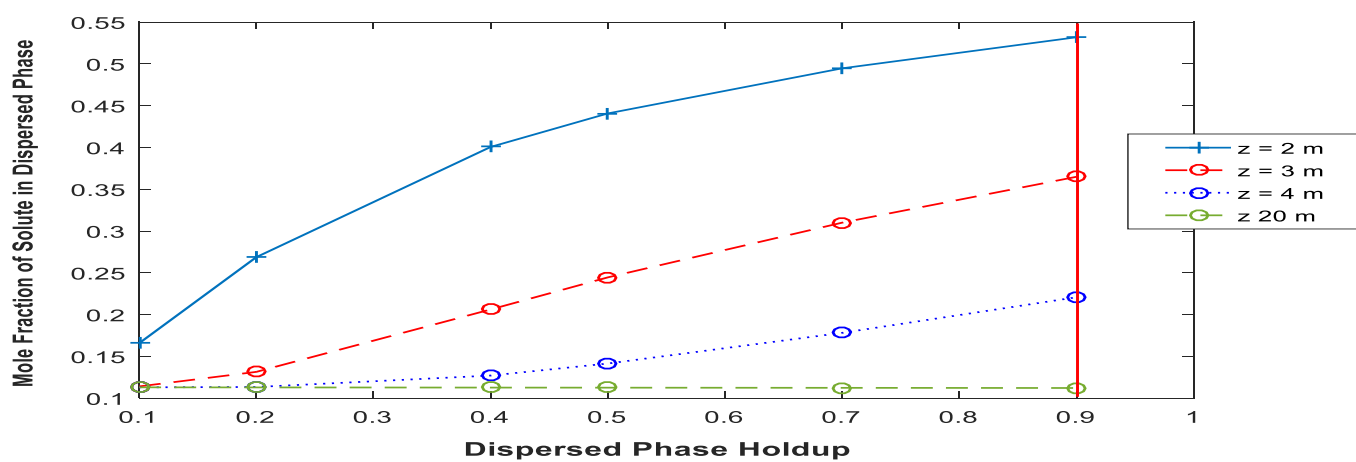


Fig (2.e)

Fig. 2: Effect of dispersed holdup on mole fraction of aromatics at different heights of the packed column

3.3 Effect of dispersed phase flow rate:

According to the definition of the dispersed phase holdup, when the dispersed phase flow rate and the number of dispersed phase droplets increase, the value of holdup will increase. The effect of the dispersed phase flow rate on the performance of the extraction column is found to be appreciable as shown in Fig 3 (a,b,c,d). Many literature show that the mass transfer coefficient varies directly with phase flow rate and is more influenced by the dispersed phase flow rate than by the continuous phase rate [10]. This may be attributed to the increased holdup associated with the increased drop population at higher dispersed phase flows. This can also be due to less residence time (on increasing flow rate) and hence less chance for the solvent to extract the aromatics.

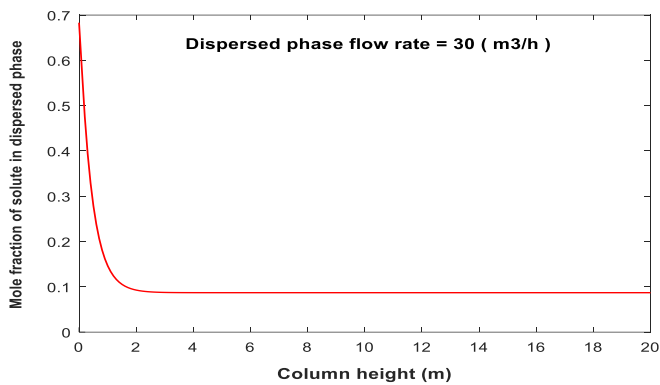


Fig (3.a)

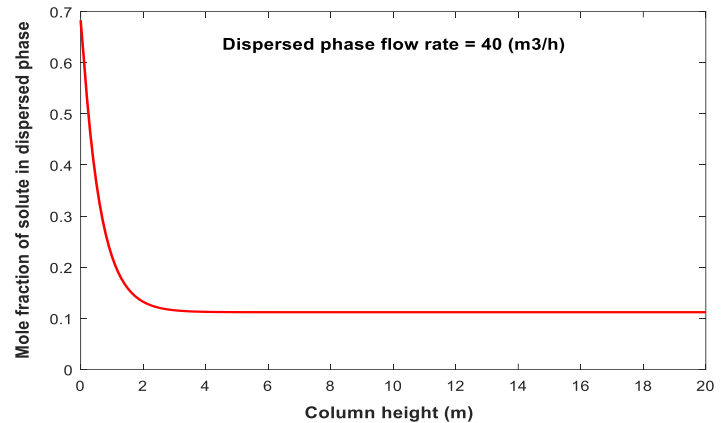


Fig (3.b)

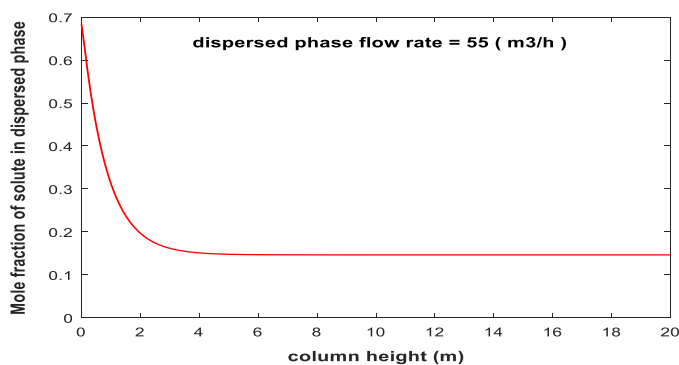


Fig (3.c)

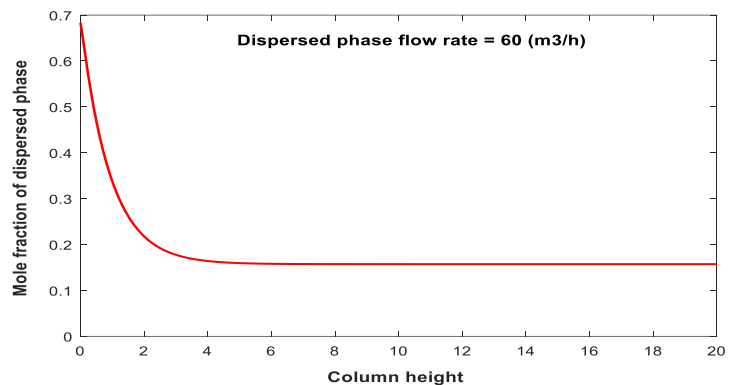


Fig (3.d)

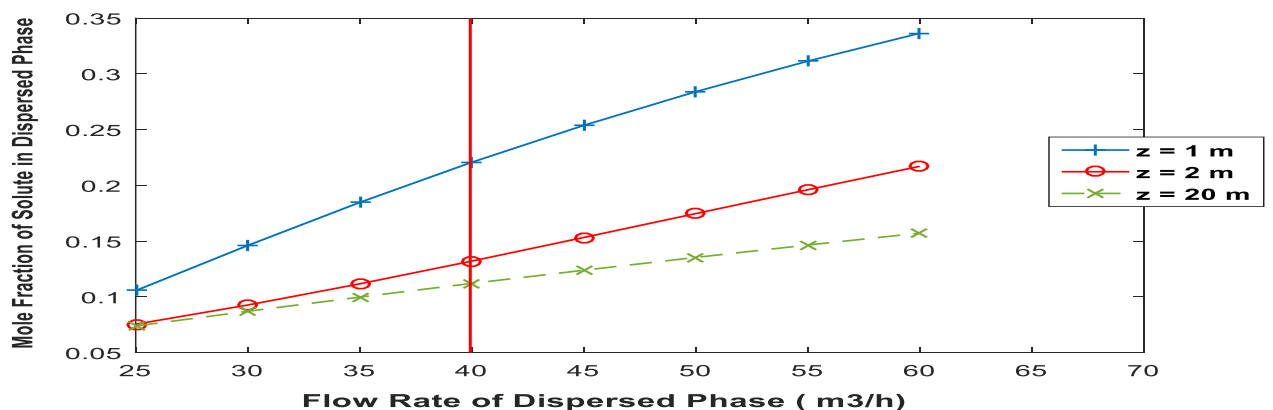


Fig. 3: Effect of dispersed flow rate on mole fraction of aromatics at different heights of the packed column

3.4 Effect of continuous phase flow rate

By increasing the continuous phase flow rate, the drag force between the dispersed droplets and continuous phase increases, that the droplets movement will be limited and the residence time and consequently the holdup will increase (overall efficiency increases). Fig.4 reveals the effect of the continuous phase flow rate on the mole fraction of aromatics at exit.

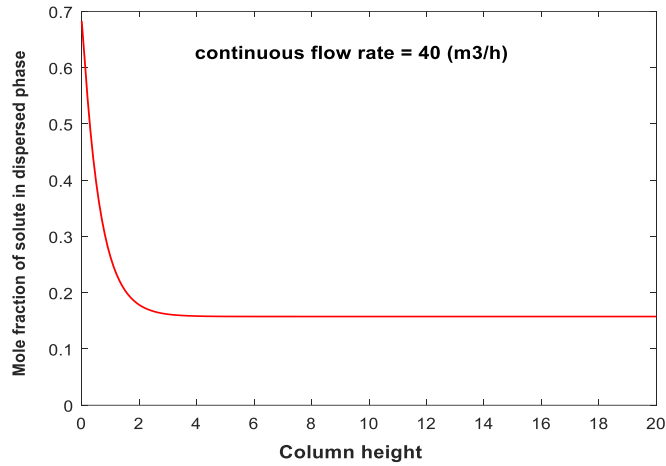


Fig (4.a)

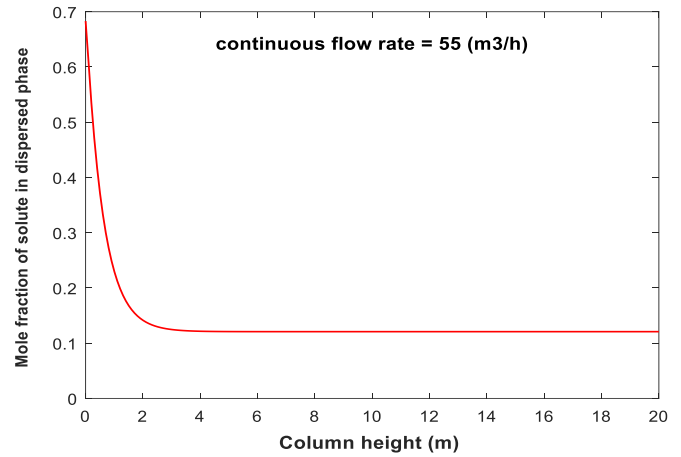


Fig (4.b)

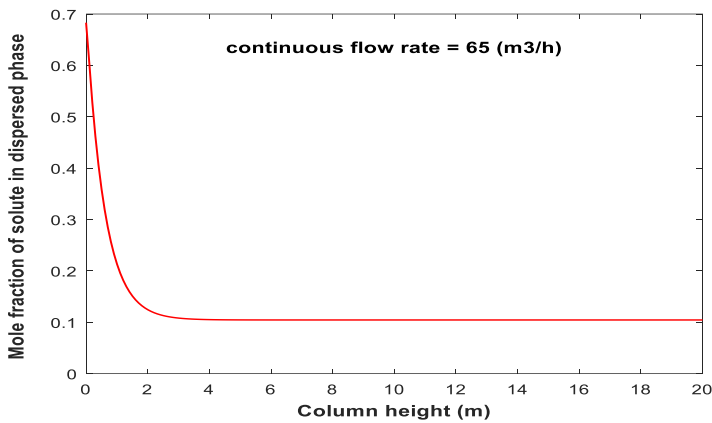


Fig (4.c)

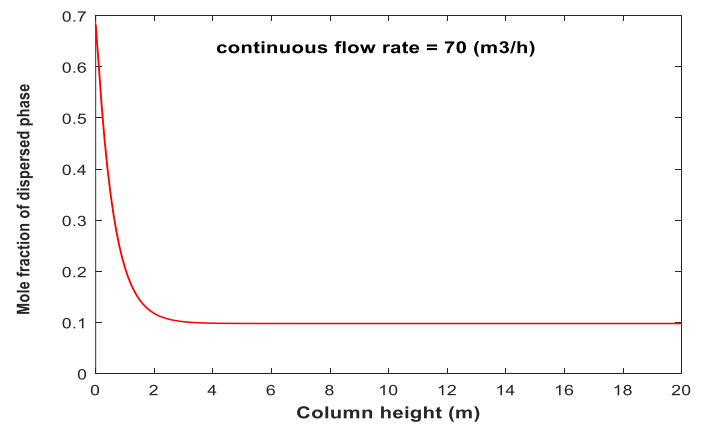


Fig (4.d)

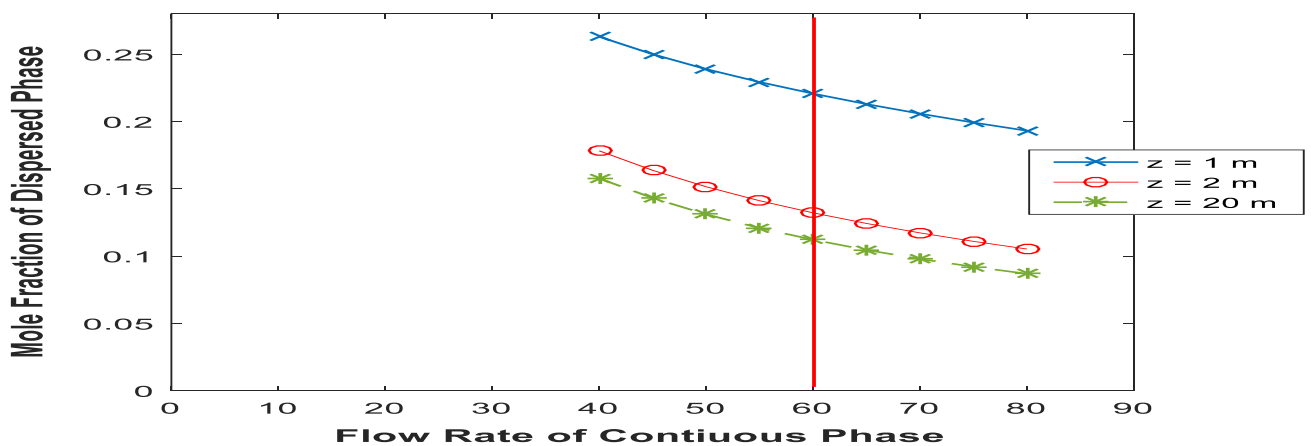


Fig. 4: Effect of continuous flow rate on mole fraction of aromatics at different heights of the packed column

3.5 Effect of packing on extraction efficiency

A lot of literature has proved that often the maximum effective manner of enhancing mass transfer is achieved by improving mixing and settling of droplets in liquid-liquid extraction this can be implemented to lube systems by using internals (packings). Even though, such retrofits are normally accomplished to increase capability, they also have been used to increase separation efficiency. Packing material promotes mass switch between the continuous and dispersed phases with the aid of forcing the phases to pass through interstices of the packings causing the dispersed phase droplets to follow a tortuous path through the packed bed[11].

Packing surface area a_p defined as the geometrical surface area offered by one cubic meter of packing (using SI units):

$$a_p = \frac{S_p}{V_p} \quad (14)$$

This factor is a difficult estimation of the packing efficiency: the higher this value is, the better is the surface area to be had for the liquid to wet the packing and higher is the anticipated rate of the mass-transfer. To attain a higher a_p it is necessary to decrease the packing element's size d_p . the present study has been carried out to examine the effect of packing voidage and interfacial area on extraction of aromatics from lube-oil. These observations clearly indicate that there is a great role of packing in the lube system. The packing may improve mole fraction of solute and improve quality, which is only possible by better separation efficiencies. Improvement in mole fraction of solute in the case of ceramic Raschig ring packing as shown in fig (5), is the result of the fact that it enhances the degree of turbulence of the continuous phase, hinders the movement of the drops of dispersed liquid, and continually distorts their shape resulting in exposure of fresh surface to contact with the liquid. It is clear that for voidage less than 0.71 the effect of voidage on the mole fraction is negligible. On the other hand for voidage greater than 0.71 and as expected decreasing packing height increases mole fraction of aromatics at exit. Again this can be due to less contact area supplied by the packing on decreasing height of the packed bed.

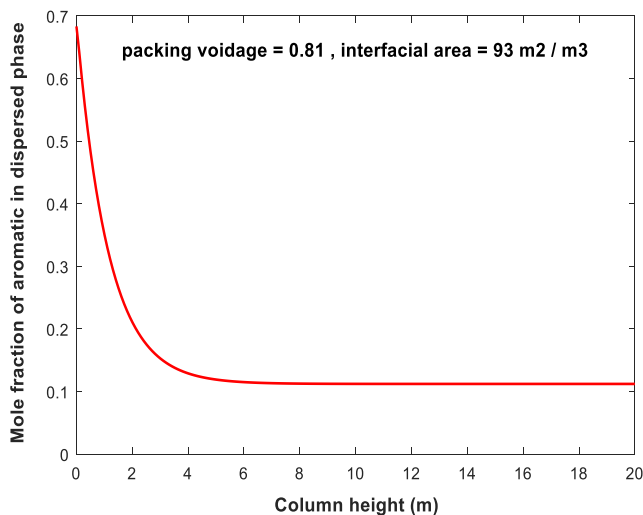


Fig (5.a)

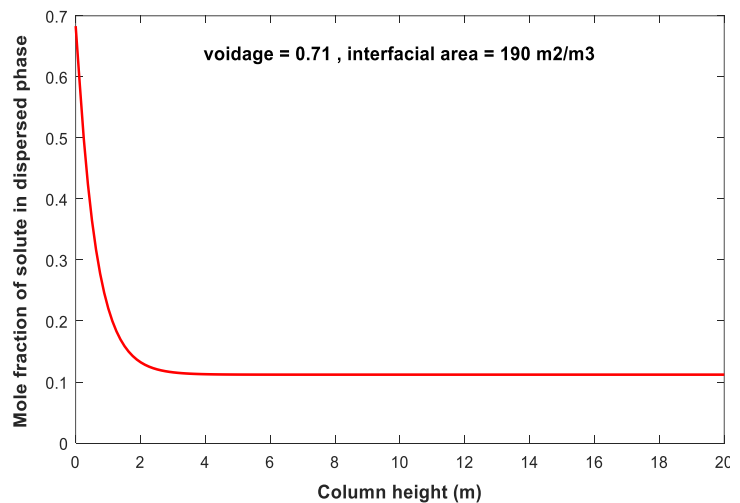


Fig (5.b)

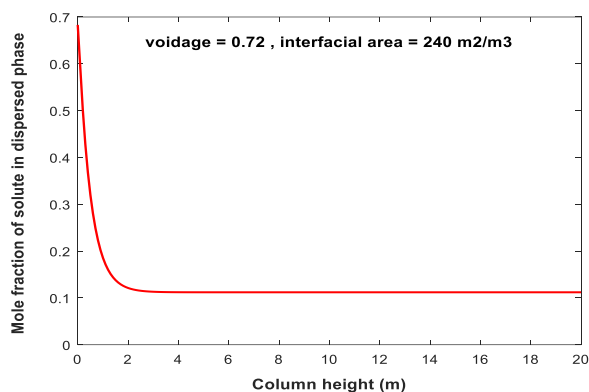


Fig (5.c)

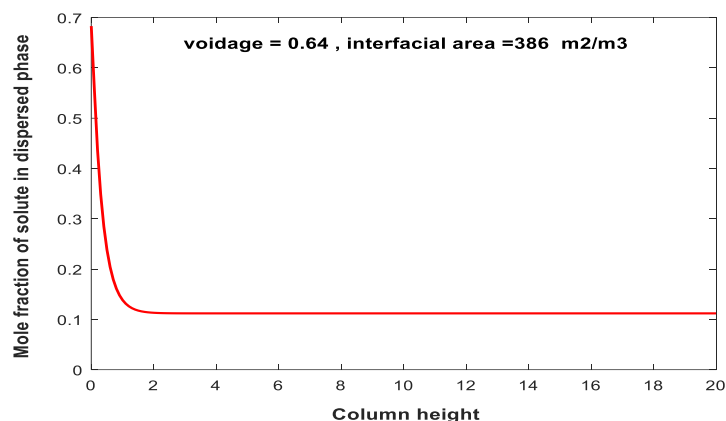


Fig (5.d)

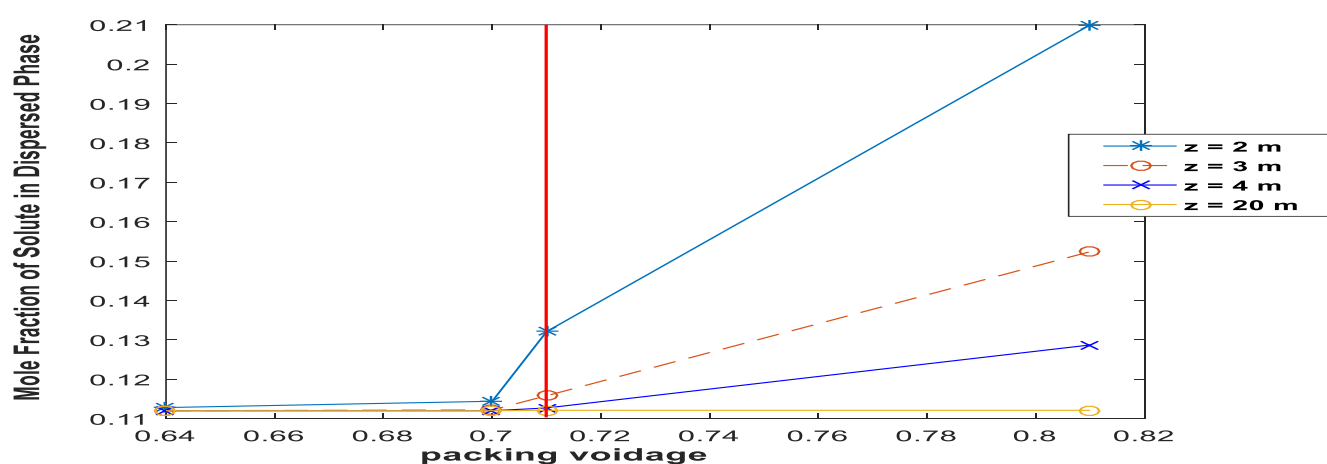


Fig. 5: Effect of voidage and interfacial area of Raschig rings on mole fraction of aromatics

Conclusions

In this work we presented a numerical model that simulates a packed column of liquid-liquid extraction. The calculation of the industrial scale column serving to the extraction of aromatics from lube oil with N-methyl-2-pyrrolidone (NMP). The work is based on real plant data. It is a simple, easy to handle model composed by one equation for steady state physical extraction with auxiliary equations from literature for parameters calculation. The two-dimensional model with neglecting the radial dispersion is best which governs the behavior of the column away from the flooding point. The effects of operational variables, such as the flow rates of the dispersed and continuous phases and dispersed phase holdup, on the extraction of aromatics from lube-oil and hydrodynamic parameters were studied. We also revealed the effect of axial dispersion on the profile of the mole fraction along the column. It was found that the dispersed phase holdup showed important effect on extraction of aromatics at specific height of the column and with unremarkable effect beyond this value while, the two phases flow rates of dispersed and continuous revealed that by increasing dispersed and continuous flow, mole fraction of aromatic in dispersed phase (lube-oil) decreased and by decreasing the height of packed column at a certain value of both phase flow (operating value) showed increasing in percentage of aromatic in raffinate. By increasing the height of column the two phase flow rates of dispersed and continuous changed in such a way that the mass transfer increased. In addition, the extraction efficiency was influenced by the interfacial area and the voidage of the packing. Finally, this work has provided valuable model for the prediction of the extraction efficiency in a random packed extraction column. Good agreement between predictions and field data causes these correlations to be

recommended for the studying the operation parameters effect on extraction efficiency and consequently for the final selection of the column. The model deviation is 1.7 %, so the accuracy of the model is very good.

NOTATION

a: interfacial area (m^2/m^3)

E_r : radial dispersion coefficient (m^2/s)

E_z : axial dispersion coefficient (m^2/s)

H: column height (m)

K_{0d} : global mass transfer coefficient (m/s)

m: distribution coefficient

r: radial coordinate (m)

R: column radius (m)

t: time (s)

v: phase superficial velocity (m/s)

x: continuous phase mole fraction

y: dispersed phase mole fraction

z: axial coordinate (m)

vd, vc: the volumes of the disperse and continuous phases respectively

d_p : nominal diameter of the packing (m)

S_p : surface of the packing (m^2)

V_p : volume of the packing (m^3)

Greek letters

α : constant

β : constant

ϕ : dispersed phase holdup

ε : Void fraction of packing

σ : surface tension (dyne/cm)

μ : liquid viscosity (cP)

ρ : liquid density (g/cm^3)

Indices

c: continuous phase

e: at inlet

d: dispersed phase

s: at outlet

References

- [1] B. Coto, R. van Grieken, J. L. Peña, and J. J. Espada, "A model to predict physical properties for light lubricating oils and its application to the extraction process by furfural," *Chemical Engineering Science*, vol. 61, no.13, pp. 4381–4392, 2006.
- [2] G. Reza Vakili, H. Modarress and G. Ali Mansoori, "Thermodynamic Modeling and Experimental Studies of Dearomatization Process from a Complex Petroleum Fraction," *Separation Science and Technology*, vol. 35, no. 5, pp. 743–757, 2000.
- [3] W. E. Schiesser, G. W. Griffiths, "A Compendium of Partial Differential Equation Models," Cambridge University Press, New York, 2009.
- [4] B. Blanco, H. Elman, R. Salazar, and M. Berberian, "Dynamic Simulation of the Concentration Profiles in a Liquid-Liquid Extraction Tower," 2000.
- [5] A. H., Hajimirzaee, S., Hatamipour, M. S., "Artificial Neural Network for Modeling the Extraction of Aromatic Hydrocarbons from Lube Oil Cuts. *Chemical Engineering*," *Chemical Engineering Technology*, vol. 34, no. 3, pp. 459–464, 2011.
- [6] S. M. Fakhr, T. Tavakkoli and M. Sadegh, "Mathematical modeling of RDC column in extraction of base oil and computing of the energy saving," *C. Technology*, 2012.
- [7] N. Outili and A. Meniai, "Two Dimensionnal Model for Extraction Packed Column Simulation using Finite Element Method," vol. 5, no. 5, pp.422–426, 2011.
- [8] A. F. Seibert and J. R. Fair, "Hydrodynamics and Mass Transfer in Spray and Packed Liquid-Liquid Extraction Columns," pp. 470–481, 1988.
- [9] R.M. SÁ, L.M.N. GÓIS and C.F. Cavalcanti, "Dispersed Phase Holdup in A liquid-liquid Extraction Column," *Latin American Applied Research*, vol. 40, pp. 373–376 2010.
- [10] A. F. Seibert, J. L. Humphrey, and J. R. Fair, "Separation Science and Technology Evaluation of Packings for Use in Liquid-Liquid Extraction Columns," no. December 2014, pp. 37–41.
- [11] R. S. Kaushik, M. Srivastava, M. Kumar, S. Mandal, N. N. Bahuguna, R. Sharma, M. Anwar and M. O. Garg, "Evaluation of Different Packings in Lube Extraction System," *Petroleum Science and Technology*, pp. 437–44, 2005.

8- A Comparative Study of Desalination by Pervaporation and Membrane Distillation using the Sweeping-Air Technique

Mohamed A.S. Ibrahim^{†1}, Mostafa K. Roshdy¹, Shaaban A. Noseir¹, Mahmoud M. Elewa², Mervette El Batouti³, Mona M. Naim¹

¹Chem. Eng. Dept., Fac. of Eng., Alexandria University, Alexandria, Egypt

²Arab Academy for Science and Technology and Maritime Transport, Alexandria, Egypt

³Fac. of Sci., Alexandria University, Alexandria, Egypt

[†]E-mail: ma6722247@gmail.com

Abstract

In the present work a comparison between pervaporation (PV) and membrane distillation (MD) applied to desalinate saline water using the sweeping-air technique was conducted. PV and MD are young members of the membrane desalination techniques which have not yet been commercialized, and which employ hydrophilic and hydrophobic membranes in respective order. A lab-scale unit of the sweeping-air configuration, was devised and constructed for carrying out the experiments. Especially tailored hydrophilic membranes of which cellulose acetate (CA) constituted the polymer matrix, were used in desalination by PV, while hydrophobic PTFE membranes (Sterlitechcorp, USA) were used in the MD experiments. CA membranes were fabricated by casting using the phase inversion technique, in which a casting assembly of our design was used. Variables investigated included type of membrane, pore size of PTFE membrane, casting solution composition of CA, feed solution concentration, temperature of feed, and temperature of condenser cooling water. Scanning electron microscopy examination of the membranes was conducted to reveal their morphologies. Results showed that MD gave a higher flux and an outstanding percent salt rejection, and that the flux varied directly with the feed temperature and inversely with the cooling water temperature. Moreover, the pore size of the PTFE membrane only slightly affected the performance of the desalination process. The optimum results arrived at were 11.52 l/m²h and SR% = 99.89, and 6.39 l/m²h and SR% = 99.83 when applying MD and PV respectively. In addition, both techniques were able to desalinate saline solutions of extremely high salinity reaching 135g/l and produce potable water in one stage.

Keywords: Membrane distillation, Pervaporation, Sweeping-air technique, PTFE membrane, Cellulose acetate membrane, Desalination

1. Introduction

Water shortage is a worldwide problem which is facing numerous countries, particularly the MENA region. This scarcity has led to rapid technology developments aiming at wastewater reclamation and seawater desalination. Currently, however, reverse osmosis (RO) stands out as the most efficient way for producing fresh water from seawater, with an average salinity of 3.5%, due to its high salt rejection over 99.5% and modular size. However, the driving force for RO process is the pressure difference between the feed and permeate sides across the RO membrane, which in order to overcome the high osmotic pressure, entails a very high feed pressure to be able to force water from the concentrated salt solution to the permeate side. Therefore, a typical water production rate for seawater RO desalination process is only 50%, which not only limits the productivity of RO, but also produces highly concentrated brine that causes environmental issues due to dumping into the sea.

To address this problem, novel membrane technologies have been proposed to increase the water production rate and avoid the seawater pollution problem. In this regards membrane distillation (MD) and pervaporation (PV) have been lately explored as substitutes for RO, due to the permeating species being vapor instead of water since the driving force in these two cases is the water vapor partial pressure difference. Moreover, both technologies rely on moderate feed water temperatures instead of high operating pressures. However, membranes applied in MD and PV

for desalination need to be hydrophobic and hydrophilic in respective order. To this end, hydrophobic membranes are known to suffer from severe fouling problem and the formation of NaCl crystal on the membrane surface which may also deteriorate the separation efficiency. On the other hand, hydrophilic membranes, used in PV, are less liable to foul. However, although many research works have been done to solve these two issues, there are no industrial applications for desalination, to the best of our knowledge, neither by MD nor by PV.

Few research groups have lately explored the possibility of using PV for seawater desalination. Separation by PV is based on the solution-diffusion model which is similar to RO, in which a liquid mixture first absorbs on the feed side of the PV membrane and then diffuses across the membrane and subsequently desorbs at the permeate side. Thus, due to the difference in solubility and diffusivity of each component of the liquid mixture in the membrane material, the PV membrane is able to selectively permeate one component over others to separate the mixture. However, similar to MD process, the driving force can be supplied either by applying vacuum or a sweeping gas in the permeate side. Hence, a highly concentrated salt solution can be dehydrated. Right now, PV technology has been industrially applied in dehydration of organic solvent dehydrations, and removal of volatile organics from aqueous solutions. In both processes, the separated matter is the minor part of the mixture. Therefore, the membrane flux need not be very high. For instance, a typical water flux for a PV dehydration membrane ranges from 100-1000 g/m²h. Since the water fluxes of RO and MD processes are 60-70 L/m²h, it would seem that PV is not a practical technology for desalination. However, considering that the water concentration in the liquid mixture for dehydration processes is normally less than 5 wt%, while in seawater desalination process it is higher than 95 wt%, therefore when applying a PV membrane in desalination, the water vapor driving force would be 20 times higher. Therefore, applying a hydrophilic membrane in desalination may yield good salt rejection with impressive water flux. Moreover, both MD and PV require only moderate temperatures for heating which can be easily obtained via renewable energy such as solar energy coupled with a solar thermal energy storage system for operation during the night or when inclement weather prevails.

PV has been extensively used for separation or concentration of mixtures of aqueous–organic liquids, e.g. dehydration of alcohols [1-3]. It has also been widely used in the separation of azeotropic mixtures [4], separation of water from organic solvent [5], removal of trace organics from water [6], and separation of organic mixtures [7]. However, there are only limited studies on the application of this technology in water desalination [8-10,17]. PV of an aqueous salt solution can be regarded as separation of a pseudo-liquid mixture containing free water molecules and bulkier hydrated ions formed by dissociation of the salt in water. Membranes used in previous studies on PV desalination include sulphonated polyethylene [11], quaternized polyethylene [12], polyetherimide and polyether ester [13] in which fluxes were very low, although the PV temperature was in the region of 40–82 °C. The feed temperature was a crucial parameter due to the increase in diffusivity and reduction in viscosity that occurs on heating. However, the inherent permeability of the membrane polymer is also extremely important [14]. Gong et al. [15] successfully prepared super hydrophilic nano-hybrid membrane by in situ ultraviolet irradiation of titanium dioxide (TiO₂) nano-particles embedded in polyelectrolyte complexes, in which the TiO₂ precursor solution was dynamically filtered through a layer-by-layer-assembled poly(ethylene-imine)/poly(acrylic acid) multi-layer under a specific pressure. The permeate flux was, however, only 865 g/m² h. The preparation of hybrid polymer super-hydrophilic films has not proven to be feasible, as the uniform dispersion of TiO₂ nano-particles in the polymer is very difficult. Also, novel inorganic–polymer hybrid membranes were prepared [16] by incorporation of nano-TiO₂ into regenerated cellulose by phase inversion and were tested in the separation of caprolactam–water mixtures by PV.

Cho et al. [17] have achieved ion rejection of over 99.9% combined with a water flux of 1.9 kg/m² h at 69°C for synthetic sea water tested using a NaA zeolite membrane. Ultrapure water

has also been produced from North Sea water using a hydroxyl sodalite PV membrane with ion rejection greater than 99.99% [18]. Although the mechanism of transport and ion rejection remains controversial, several research groups have established that PV through zeolite membranes shows great promise for desalination applications [19-22]. Currently, the most popular zeolite membranes for PV applications are synthetic thin-film zeolite membranes supported on porous substrate [23-27]. Several major factors restrict their application to industrial desalination, however, including strict requirements for the structural properties of the support materials. Poor chemical and physical compatibility between the available support materials and the zeolite layer increases the cost of production and the presence of defects formed during membrane preparation. Other concerns, including fragile thin surface layers and tedious synthesis procedures, also reduce the feasibility of applying thin-film membranes. Hydrophilic ion-exchange membranes based on sulfonated polyethylene hollow fibers were manufactured by Korin et al. [28], the membranes' suitability for a water PV process was studied for possible application in water desalination. In a study by Korngold and Korin [29], sweeping-air PV through a hydrophilic anion-exchange hollow fiber membrane and through a porous hydrophobic hollow fiber was investigated. Ben Hamouda et al. [30] prepared hydrophobic dense PEBAX membrane and their suitability for desalination of brine by PV was studied. The effects of brine inlet temperature (28–54°C) and NaCl concentration in the feed brine (0–3.5 mol/l) were determined. A water flux of 1.3–7 g m⁻² h⁻¹ was obtained using this type of membranes. The authors found that the optimal specifications for their membrane was a thickness of 100 µm and an operating temperature of 50°C that provide a water flux of 7 g m⁻² h⁻¹ in the permeate side. Quinones-Bolanos et al. [31] studied the suitability of a homogeneous hydrophilic dense membrane in PV, for reusing brackish and/or contaminated waters. Xie et al. [32] prepared hybrid polymer inorganic membranes by cross-linking PVA, maleic acid (MA), and silica via an aqueous sol-gel route. Zwijnenberg et al. [33] described details of a solar driven PV process for the production of desalinated water from highly contaminated waters. Drobek et al. [34], prepared Silicalite-1 (S-1) and ZSM-5 membranes by secondary growth on tubular ceramic supports which were tested using a PV setup for the desalination of aqueous solutions containing NaCl in concentrations corresponding to brackish (0.3–wt.%), sea (3.5 wt.%) and brine (7.5–15 wt.%) water. The pervaporative salts rejection and water flux characteristics of the NaA zeolite membrane in sea water were investigated by Cho et al. [17]. Liang et al. [35] prepared a three-layer thin-film nano-fibrous PV composite (TFNPVC) membrane by sequential deposition using electrospraying/electrospinning. Heat treatment is believed to be an important step in controlling the morphology and properties of polymer-based membranes. In a study by Xie et al. [36], hybrid organic-inorganic membrane based on PVA, MA, and tetraethyl orthosilicate (TEOS) was synthesized via a sol-gel route. Sweeping air PV is simpler than vacuum PV, and there is limited literature citing the application of separations by PV using sweeping air, particularly desalination. In case of vacuum PV, the costs are much higher than in the case of sweeping air as regards to the necessity of liquid nitrogen which is costly and not safe to use in the condensation step, and it is also more complicated compared to sweeping air in which air is available at no cost and condensation is effected at 0–2°C (using only an ice-water bath).

2. Methods

The aim of the present work is to compare between desalination by PV and MD using a sweeping-air unit designed and fabricated in our lab, in which novel hydrophilic cellulose-based membranes fabricated by the phase inversion method are to be used in the PV experiments, and in which ready-made PTFE membranes are to be used in the MD experiments. Several variables are to be investigated for their effect on the flux of the product water and its salinity, and finally the two techniques are to be compared, pointing out the prominent findings for each technique. The main factors to be studied include solution concentration (C_i) and pervaporation temperature (T_{pv}), which are followed by computation of the separation factor (α) and pervaporation separation

index (PSI). The morphology of the membrane is to be determined via examination by scanning electron microscopy (SEM), and finally, the activation energy (E_a) for permeation through the membrane is to be determined through application of the Arrhenius law.

2.1. Materials

For PV, cellulose acetate powder (CA) (product of Panreac, Egypt), acetone (A), dimethyl phthalate (DMP), and dimethyl formamide (DMF) (products of Adwic, Egypt), glycerol (G), maleic acid (MA) and sodium chloride (products of El-Nasr Chemicals, Egypt) and sodium hydroxide (product of Chemajet, Egypt) were all used as received. For MD, PTFE membranes (product of Sterlitech corp, USA) of different pore sizes were used as received in the MD experiments.

2.2. Methods

2.2.1. Preparation of casting solution

CA powder and MA powder were added to a wide-mouthed glass-stoppered bottle, then dissolved in a mixture of solvents including DMF, D, A, and DMP in different weight proportions. The mixture was mixed manually using a glass rod until all the CA dissolves, then the membrane solution was left overnight, in the tightly sealed bottle, until complete removal of air bubbles.

2.2.2. Casting of membranes

The solution was cast on a smooth uniform glass plate of a casting assembly equipped with a doctor's blade, then was immersed in distilled water contained in a tray, for 60 min, to effect coagulation, during which the membrane changed from transparent color to white. It was detached slowly from the glass sheet and steeped in a distilled water bath, ready for deacetylation.

2.2.3. Deacetylation of membranes

The membranes were subjected to complete deacetylation by steeping them for 24 h in an aqueous alkaline bath consisting of 1% sodium hydroxide and 20% sodium chloride, at room temperature. The membranes were then washed by repetitive steeping in distilled water followed by decantation then stored in distilled water for later use in the PV experiments.

2.2.4. Test cell

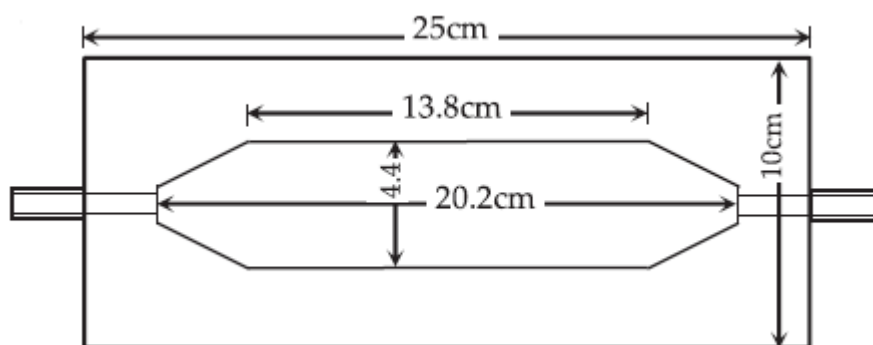


Figure 8 : A Schematic diagram of PV cell

The cell consisted of two identical plexiglass parallel-piped halves. Each cell half contained a compartment consisting of hexagonal grooves (length 20.2 cm, width 4.4 cm, and depth 1.5 cm) as shown in Fig. 1. Before operation, the two cell halves were firmly held together with a set of six bolts and nuts such that the membrane completely separated the two halves. Rubber gaskets placed all around the grooves functioned as liquid seals and prevented leakage during operation. The cell was then clamped horizontally, such that the salt solution is made to flow above the membrane, ready for operation.

2.2.5. Experimental setup

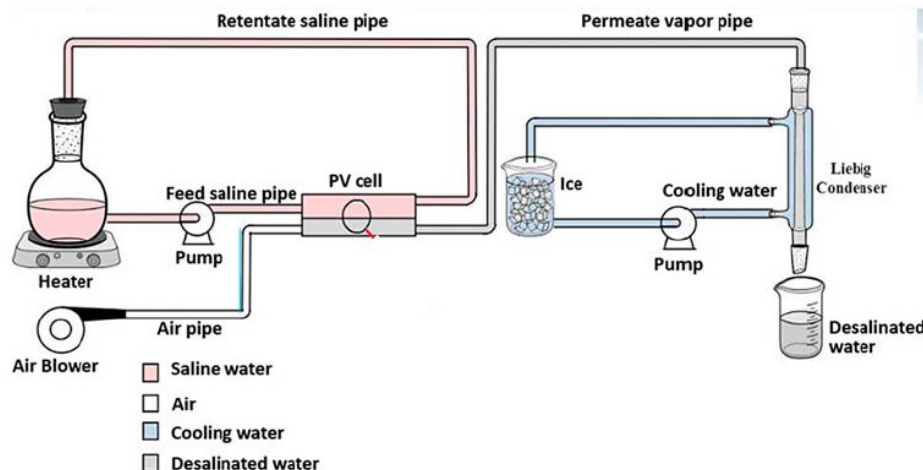


Figure 9 : A Schematic of the pervaporation (PV) setup

Fig. 2 illustrates a schematic diagram of the setup which consists of the PV cell, feed solution flask, electric heater, and saline-water pump, constituting the heating circuit; and a cooling water pump, a long Liebig condenser, and an ice-water bath, constituting the cooling circuit. The last once-through route is that of the purge air provided by an air blower, which sweeps the permeating vapor from the downstream of the cell and forces it to pass through the condenser, where it is condensed into water drops that are collected in a receiver flask.

2.2.6. Procedure

The PV membrane was placed in the test cell, then the latter was closed tightly by the bolts and nuts, placed horizontally and the whole unit was connected. Two liters of sodium chloride solution were heated to the required temperature, and allowed to recycle through the top compartment of the cell. The pump and blower were operated, and the condensate was collected at half hourly intervals, in the receiving flask, and analyzed for concentration by a conductivity meter, and its volume measured. The solution temperature was also recorded every half hour. Recycling of the solution ensured constancy of its temperature adjacent to the membrane. Each experiment was conducted for six hours at least, after which the experiment was terminated.

2.2.7. Variables Investigated

Numerous factors were investigated for their effect on the productivity and percent salt rejection of the product water, and these were type of membrane, pore size of PTFE membrane, casting solution composition of CA, feed solution concentration, temperature of feed, and temperature of condenser cooling water, as well the presence of support beneath the CA membrane.

2.2.8. PV membrane performance

Performance of PV membrane is determined by the values of J , %SR, α , and PSI as follows, in which:

$$J = Q / (A * t)$$

where J is the flux, Q is the volume of the permeate collected in time t , A is the effective membrane area,

$$\%SR = \frac{(C_i - C_f)}{C_i} * 100$$

where C_i and C_f are the initial and final solution concentration,

$$\alpha = \frac{Y_w/Y_s}{X_w/X_s}$$

where Y and X are the weight of components in the pervaporate and feed, respectively, the suffix w refers to water and s refers to solute, and

$$PSI = J * \alpha$$

2.2.9. Activation energy (E_a)

The dependence of flux on T_{pv} could be expressed by Arrhenius law as follows and from which E_a could be computed:

$$J = A_p \exp(-E_a/RT)$$

where A_p , R , and T are the pre-exponential factor, universal gas constant, and feed temperature in absolute units, respectively. E_a is determined from the plot of $\ln J$ vs. $1/T$. A linear relationship is produced from which E_a is computed from the slope of the straight line.

3 Results and discussion

3.1. Results

The present work dealt with a comparative investigation of desalination by both PV and MD using the sweeping air technique. Different factors were studied for their effect on the flux and salinity of the product water as mentioned earlier.

| Experiment Number | Polymer Type | Solvents | | | | NaCl Ci (g/l) | T_{hot} ($^{\circ}$ C) | T_{cold} ($^{\circ}$ C) | Time (hr) | Membrane | |
|-------------------|--------------------|----------|------|----|---|---------------|---------------------------|----------------------------|-----------|-------------|-------------|
| | | A | DMF | MA | G | | | | | Hydrophilic | Hydrophobic |
| 1 | CB | 13 | 100 | — | 3 | 35 | 70 | 13 | 3.46 | ✓ | — |
| 2 | CAB | 10.5 | 74.5 | 10 | — | 35 | — | — | — | ✓ | — |
| 3 | PTFE (0.1 μ m) | — | — | — | — | 35 | 80 | 13 | 1.25 | — | ✓ |
| 4 | PTFE (0.1 μ m) | — | — | — | — | 35 | 55 | 12 | 1.66 | — | ✓ |
| 5 | PTFE (1 μ m) | — | — | — | — | 35 | 80 | 12 | 2.33 | — | ✓ |
| 6 | PTFE (1 μ m) | — | — | — | — | 35 | 60 | 12 | 2.33 | — | ✓ |
| 7 | PTFE (1 μ m) | — | — | — | — | 96 | 70 | 13 | 3.5 | — | ✓ |
| 8 | PTFE (1 μ m) | — | — | — | — | 101.5 | 60 | 10 | 2.5 | — | ✓ |
| 9 | CA | — | — | — | — | 135 | 71 | 3 | 5.5 | ✓ | — |

Table 3 : Conditions of all experiments conducted in the present work

| Experiment Number | Polymer Type | PV or MD | Feed Solution (g/l) | Permeate | | Flux (L/m ² hr) | Salt Rejection (%) | Notes |
|-------------------|--------------------|----------|---------------------|-------------------|-----------------------------|----------------------------|--------------------|--|
| | | | | Total Volume (ml) | Average Concentration (g/l) | | | |
| 1 | CB | PV | 35 | 409 | 8.94 | 14.3 | 43.3 | A hole in the membrane |
| 2 | CAB | PV | 35 | — | — | — | — | Casting was bad |
| 3 | PTFE (0.1 μ m) | MD | 35 | 103 | 0.6478 | 9.98 | 99.89 | — |
| 4 | PTFE (0.1 μ m) | MD | 35 | 54 | 0.0357 | 3.94 | 99.91 | The work was stopped due to blower maintenance |
| 5 | PTFE (1 μ m) | MD | 35 | 199 | 0.155 | 10.35 | 99.85 | High Temperature |
| 6 | PTFE (1 μ m) | MD | 35 | 99 | 3.31 | 5.15 | 98.84 | Low Temperature |
| 7 | PTFE (1 μ m) | MD | 96 | 209 | 3.84 | 7.2 | 99.71 | High Concentration & Temperature |
| 8 | PTFE (1 μ m) | MD | 101.5 | 110 | 1.4 | 5.333 | 99.79 | High Concentration & low Temperature |
| 9 | CA | PV | 135 | 292 | 5.347 | 6.435 | 99.83 | — |

Table 4 : Results of all experiments conducted in the present work

Table 1 and 2 present the conditions of all the experiments conducted in the present work by the application of both techniques, and the results of each experiment, in respective order. In experiments 1,2 and 9, cellulose butyrate (CB), cellulose acetate butyrate (CAB) and cellulose acetate (CA) were used as the membranes of choice in the PV experiments respectively, while PTFE membranes of various pore sizes were used in the MD experiments.

3.2. Discussion

From expt 1, it is clear that CB proved to be inadequate as the membrane polymer, since it led to a poor salt rejection, though high flux. Furthermore, the membrane was weak and was torn after a few hours of operation. Accordingly the membrane was discarded and not subjected to further investigation. In expt 2, the CAB membrane did not give a uniform membrane, probably due to the presence of the butyrate radical with the other acetyl ester group, and the membrane was full of streaks, and was therefore discarded and not subjected to PV tests. In expt 9 however, in which CA constituted the membrane matrix, and in which C_i was equal to 135g/l which is an exceptionally high concentration the flux was acceptable and the SR% was dramatic (99.83). The reason for this outstanding result was attributed to two reasons, of which the first was due to the well known fact that CA is known to form homogeneous membranes of high tenacity and has therefore been used for decades in desalination by the high pressurized reverse osmosis technique. Secondly, the composition of the casting dope had been optimized previously as stated in the experimental section, such that a PV membrane of outstanding performance was fabricated. It is worth noting that this membrane was fabricated by casting the dope over a polypropylene screen of specific mesh number in order to support the membrane without disturbing its performance. The second part of the present investigation deals with desalination using sweeping air MD. The results are presented in Table 2, expts 3 to 8, in which PTFE membranes were used, under various

conditions. It is clear from expt 3 that the 0.1 microm membrane gave a very high SR% (99.89) when C_i was 35g/l, which proves that MD using this particular membrane is superior to PV with the CA membrane since the flux was almost double that of expt 9 at the same salt rejection. However, it is worth mentioning that hydrophobic membranes generally suffer from more rapid fouling on prolonged usage compared to hydrophilic membranes. Experiment 4, in which the 0.1 μm PTFE membrane was also used, shows a very high SR% (99.91) but unluckily a low flux due to a malfunction in the blower and trying to repair it.

Experiments 5 to 8 in which PTFE membranes of 1 microm pore size were used, under different conditions, show that when a high temperature was used as shown in expt 5, a very high flux (13.355 L/m²h) was obtained as well as an exceptional salt rejection (99.86%). On lowering the feed temperature, however, the flux fell to half its value as shown in expt 6, and the salt rejection slightly declined (98.84%). This observation suggests that MD is preferred at moderate temperatures in the vicinity of 65°C, which suggests that solar heat may be used favourably to heat the feed during operation. In addition, it can be realized that membrane wetting may have initiated after working at higher temperature (80°C). Moreover, the membrane after expt 5, was left in a horizontal manner with some solution above it which might have probably assisted in partial wetting, thus reducing the membrane's performance.

In expt 7 in which C_i was increased to 96g/l and T_f was high, the flux was decreased appreciably than expt 5, in which the membrane was still unused, but the salt rejection was still high which might be due to partial pore blocking overnight as mentioned earlier. The following experiment (expt 8) C_i was increased all the more to 101.5g/l, so as expected the flux decreased to 5.333 L/m²h. However, the SR% remained high (99.71), as the previous experiments (5 and 7), being all above 99.71.

3.2.1. Effect of pore size on flux and SR%

As shown in figure 3, experiments 3 & 5 were taken as an example for the effect of membrane pore size on the flux and SR%. It has been concluded that increasing the pore size from 0.1 to 1 μm improves the permeate productivity while SR% remains approximately constant but we should take into account the probability of membrane wetting with increasing the pore size.

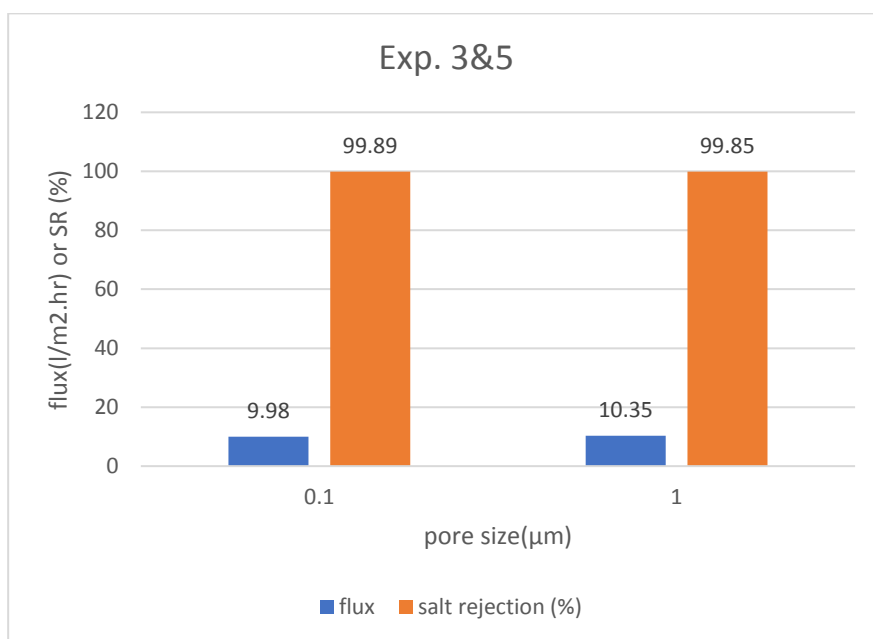


Figure 10 : The effect of pore size on flux and SR%

3.2.2. Effect of initial feed concentration on SR%

As shown in figure 4, experiments 6 & 7 were taken as an example for the effect of initial feed concentration on the SR% when 1 μ m PTFE membrane is used. It has been concluded that increasing the initial concentration of feed from 35 to 96 g/l increases the SR% by ~ 1%.

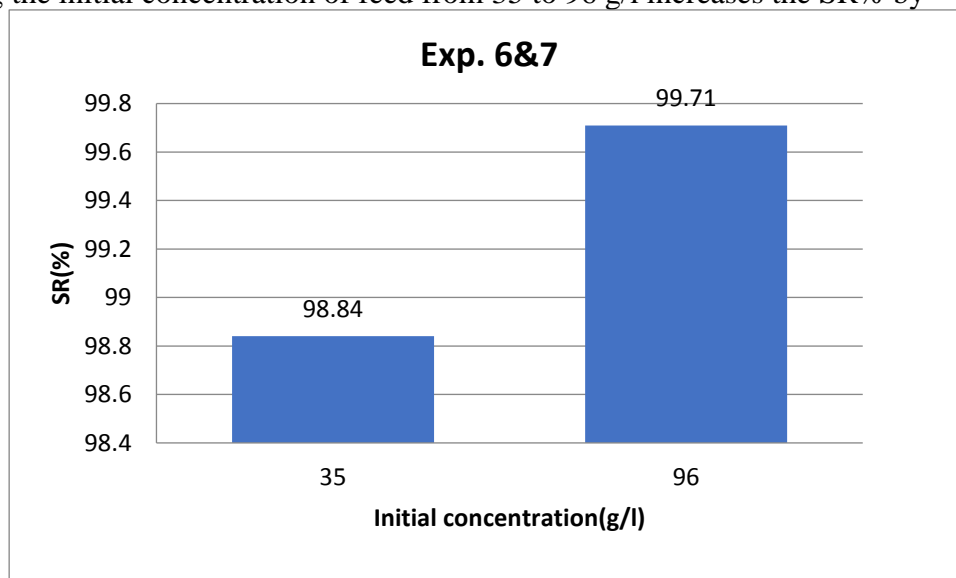


Figure 11 : effect of initial feed concentration on SR%

3.2.3. Effect of feed temperature on flux and SR%

As shown in figure 5, experiments 5 & 6 were taken as an example for the effect of feed temperature on the flux and SR% when 1 μ m PTFE membrane is used. It has been concluded that increasing the feed temperature by 20 degrees leads to doubling the flux and improving the SR% because of increasing the water vapor partial pressure difference which is considered the driving force for the process.

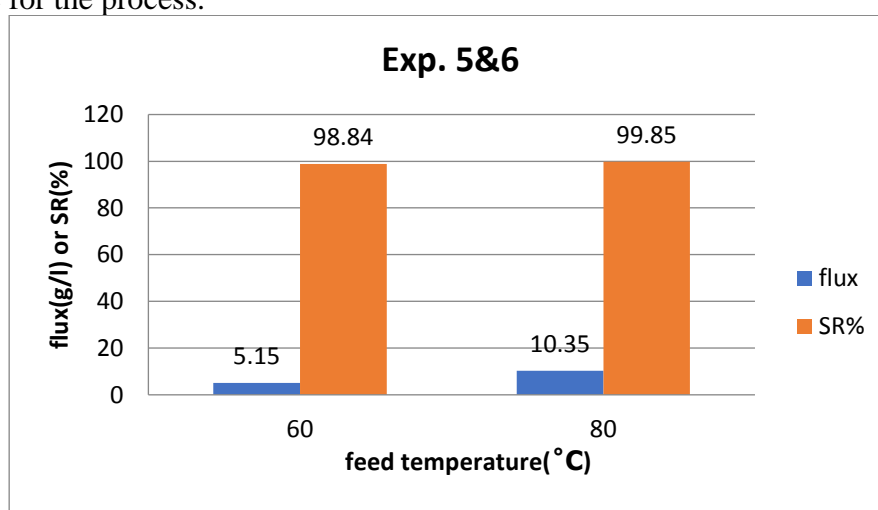


Figure 12 : effect of feed temperature on flux or SR%

3.2.4. Effect of cooling water temperature on the permeate salinity

As shown in figure 6, experiments 7 & 8 were taken as an example for the effect of cooling water temperature on the permeate salinity. It has been concluded that decreasing the cooling water temperature improves the permeate water quality and then improves the SR%.

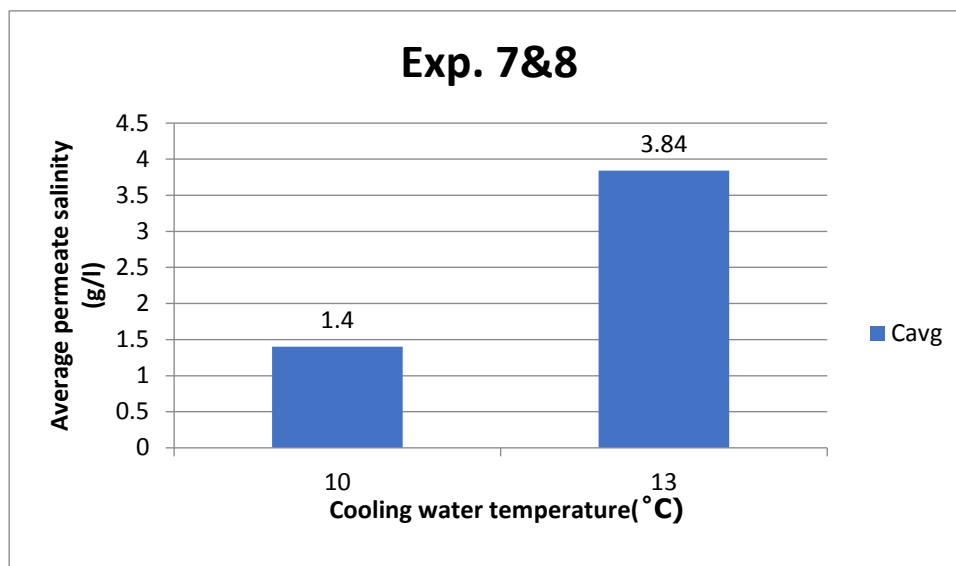


Figure 13 : effect of cooling water temperature on the permeate salinity

Figure 7 shows a scanning electron microscope for the pervaporation membrane which consists of: i) A dense skinned layer used as primary filtration barrier and, ii) A thick and more porous understructure that serves as support structure. It may be either homogeneous or heterogeneous and it is characterized by a density change given by the membrane material across the cross sectional area.

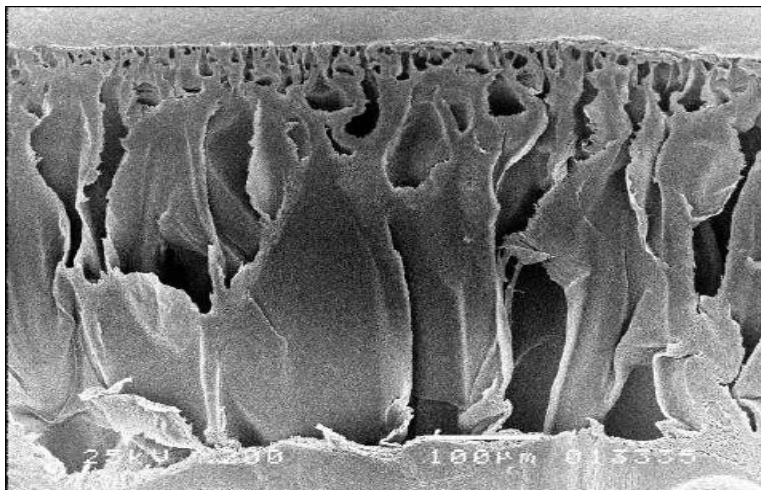


Figure 14 : SEM for asymmetric membrane used for pervaporation with magnification of 200×

4 Conclusions

From the present work it has been concluded that MD might be preferred to PV as regards flux. However, the salt rejections in both cases are comparable, when CA is used in PV, and PTFE in MD, and are both above 99.8. But it has been proven that PTFE is susceptible to fouling and pore blocking more than the hydrophilic regenerated CA membrane. It was also found that PTFE membranes can be used in desalinating concentrated brines three times the concentration of seawater, producing almost potable water in one stage, and the flux decreased in direct proportionality to the initial concentration. However, the SR% remained extremely high in all cases. It was also found that both pore sizes studied were comparable, but the 1.0 microm pore sized membrane sgave a relatively higher flux.

Acknowledgements

Special thanks go to our main supervisor Prof. Dr. Mona M. Naim for her patience, understanding, guidance, and most of all the encouragement she has given us during our graduate studies.

References

- [1] Hu, S. Y., Zhang, Y., Lawless, D. & Feng, X. □□□□ Composite membranes comprising of polyvinylamine-poly(vinyl alcohol) incorporated with carbon nanotubes for dehydration of ethylene glycol by pervaporation. *Journal of Membrane Science* 417–418, 34–44.
- [2] Kuila, S. B. & Ray, S. K. □□□□ Separation of isopropyl alcohol–water mixtures by pervaporation using copolymer membrane: analysis of sorption and permeation. *Chemical Engineering Research and Design* 91 (2), 377–388.
- [3] Pandey, R. P. & Shahi, V. K. □□□□ Functionalized silica–chitosan hybrid membrane for dehydration of ethanol/water azeotrope: effect of cross-linking on structure and performance. *Journal of Membrane Science* 444, 116–126.
- [4] Luyben, W. L. □□□□ Control of a column/pervaporation process for separating the ethanol/water azeotrope. *Industrial & Engineering Chemistry Research* 48 (7), 3484–3495.
- [5] Lu, Y. & Chen, J. □□□□ Optimal design of multistage membrane distillation systems for water purification. *Industrial & Engineering Chemistry Research* 50 (12), 7345–7354.
- [6] Knight, R. L., Kadlec, R. H. & Ohlendorf, H. M. □□□□ The use of treatment wetlands for petroleum industry effluents. *Environmental Science & Technology* 33 (7), 973–980.
- [7] Smitha, B., Suhanya, D., Sridhar, S. & Ramakrishna, M. □□□□ Separation of organic–organic mixtures by pervaporation—a review. *Journal of Membrane Science* 241 (1), 1–21.
- [8] Kuznetsov, Y. P., Kruchinina, E. V., Baklagina, Y. G., Khripunov, A. K. & Tulupova, O. A. □□□□ Deep desalination of water by evaporation through polymeric membranes. *Russian Journal of Applied Chemistry* 80 (5), 790–798.
- [9] Ben Hamouda, S., Boubakri, A., Nguyen, Q. T. & Ben Amor, M. □□□□ PEBAX membranes for water desalination by pervaporation process. *High Performance Polymers* 23 (2), 170–173.
- [10] Swenson, P., Tanchuk, B., Gupta, A., An, W. & Kuznicki, S. M. □□□□ Pervaporative desalination of water using natural zeolite membranes. *Desalination* 285, 68–72.
- [11] Korin, E., Ladizhensky, I. & Korngold, E. □□□□ Hydrophilic hollow fiber membranes for water desalination by the pervaporation method. *Chemical Engineering and Processing: Process Intensification* 35 (6), 451–457.
- [12] Korngold, E., Korin, E. & Ladizhensky, I. □□□□ Water desalination by pervaporation with hollow fiber membranes. *Desalination* 107 (2), 121–129.
- [13] Quiñones-Bolaños, E., Zhou, H., Soundararajan, R. & Otten, L. □□□□ Water and solute transport in pervaporation hydrophilic membranes to reclaim contaminated water for micro-irrigation. *Journal of Membrane Science* 252 (1–2), 19–28.
- [14] Xie, Z., Ng, D., Hoang, M., Duong, T. & Gray, S. □□□□ Separation of aqueous salt solution by pervaporation through hybrid organic–inorganic membrane: effect of operating conditions. *Desalination* 273 (1), 220–225.
- [15] Gong, L., Zhang, L., Wang, N., Li, J., Ji, S., Guo, H., Zhang, G. & Zhang, Z. □□□□ In situ ultraviolet-light-induced TiO₂ nanohybrid superhydrophilic membrane for pervaporation dehydration. *Separation and Purification Technology* 122, 32–40.
- [16] Zhu, T., Lin, Y., Luo, Y., Hu, X., Lin, W., Yu, P. & Huang, C. □□□□ Preparation and characterization of TiO₂-regenerated cellulose inorganic–polymer hybrid membranes for dehydration of caprolactam. *Carbohydrate Polymers* 87 (1), 901–909.
- [17] C.H. Cho, K.Y. Oh, S.K. Kim, J.G. Yeo, P. Sharma, Pervaporative seawater desalination using NaA zeolite membrane: Mechanisms of high water flux and high salt rejection, *J. Membr. Sci.* 371 (2011) 226–238.
- [18] S. Khajavi, J.C. Jansen, F. Kapteijn, Production of ultra pure water by desalination of seawater using a hydroxy sodalite membrane, *J. Membr. Sci.* 356 (2010) 52–57.

- [19] M.C. Duke, J. O'Brien-Abraham, N. Milne, B. Zhu, J.Y.S. Lin, J.C. Diniz da Costa, Seawater desalination performance of MFI type membranes made by secondary growth, *Sep. Purif. Technol.* 68 (2009) 343–350.
- [20] W. An, P. Swenson, L. Wu, T. Waller, A. Ku, S.M. Kuznicki, Selective separation of hydrogen from C1/C2 hydrocarbons and CO₂ through dense natural zeolite membranes, *J. Membr. Sci.* 369 (2011) 414–419.
- [21] S. Khajavi, J.C. Jansen, F. Kapteijn, Performance of hydroxy sodalite membranes as absolute water selective materials under acidic and basic conditions, *J. Membr. Sci.* 356 (2010) 1–6.
- [22] M. Kazemimoghadam, T. Mohammadi, Synthesis of MFI zeolite membranes for water desalination, *Desalination* 206 (2007) 547–553.
- [23] S.-L. Wee, C.-T. Tye, S. Bhatia, Membrane separation process—Pervaporation through zeolite membrane, *Sep. Purif. Technol.* 63 (2008) 500–516.
- [24] W. An, P. Swenson, L. Wu, T. Waller, A. Ku, S.M. Kuznicki, Selective separation of hydrogen from C1/C2 hydrocarbons and CO₂ through dense natural zeolite membranes, *J. Membr. Sci.* 369 (2011) 414–419.
- [25] X. Chen, X. Lin, P. Chen, H. Kita, Pervaporation of ketone/water mixtures through silicalite membrane, *Desalination* 234 (2008) 286–292.
- [26] R.W. Baker, *Membrane Technology and Applications*, second ed., John Wiley and Sons, England, 2004.
- [26] Q. Liu, R.D. Noble, J.L. Falconer, H.H. Funke, Organics/ water separation by pervaporation with a zeolite membrane, *J. Membr. Sci.* 117 (1996) 163–174.
- [9] Q. Liu, R.D. Noble, J.L. Falconer, H.H. Funke, Organics/ water separation by pervaporation with a zeolite membrane, *J. Membr. Sci.* 117 (1996) 163–174.
- [27] H. Ahn, Y. Lee, Pervaporation of dichlorinated organic compounds through silicalite-1 zeolite membrane, *J. Membr. Sci.* 279 (2006) 459–465.
- [28] E. Korin, I. Ladizhensky, E. Korngold, Hydrophilic hollow fiber membranes for water desalination by the pervaporation method, *Chem. Eng. Process.* 35 (1996) 451–457.
- [29] E. Korngold, E. Korin, Air sweep water pervaporation with hollow fiber membranes, *Desalination* 91 (1993) 187–197.
- [30] S. Ben Hamouda, A. Boubakri, Q.T. Nguyen, M. Ben Amor, PEBAX membranes for water desalination by pervaporation process, *High Perform. Polym.* 23 (2011) 170–173.
- [31] E. Quin˜ ones-Bolan˜ os, H. Zhou, R. Soundararajan, L. Otten, Water and solute transport in pervaporation hydrophilic membranes to reclaim contaminated water for micro-irrigation, *J. Membr. Sci.* 252 (2005) 19–28.
- [32] Z. Xie, D. Ng, M. Hoang, T. Duong, S. Gray, Separation of aqueous salt solution by pervaporation through hybrid organic–inorganic membrane: Effect of operating conditions, *Desalination* 273 (2011) 220–225.
- [33] H.J. Zwijnenberg, G.H. Koops, M. Wessling, Solar driven membrane pervaporation for desalination processes, *J. Membr. Sci.* 250 (2005) 235–246.
- [34] M. Drobek, C. Yacou, J. Motuzas, A. Julbe, L. Ding, J.C. Diniz da Costa, Long term pervaporation desalination of tubular MFI zeolite membranes, *J. Membr. Sci.* 415–416 (2012) 816–823.
- [35] B. Liang, K. Pan, L. Li, E.P. Giannelis, B. Cao, High performance hydrophilic pervaporation composite membranes for water desalination, *Desalination* 347 (2014) 199–206.
- [36] Z. Xie, M. Hoang, D. Ng, C. Doherty, A. Hill, S. Gray, Effect of heat treatment on pervaporation separation of aqueous salt solution using hybrid PVA/MA/TEOS membrane, *Sep. Purif. Technol.* 127 (2014) 10–17.

9- Cu/C nanofibers decoration for copper substrates as effective strategy for enhancing the surface hydrophobicity.

M. Souby^{1,a}, Mohamed R. O. Ali^{2,b}, Ramadan Bassiouny^{3,c},
N. A. Barakat^{4,d}, Ibrahim M. El Moghazy^{5,e}.

^{1,2,3,5}Mechanical Power Engineering and Energy Department ,Faculty of Engineering , Minia university , Minia . 61519, Egypt.

⁴Chemical Engineering Department , Faculty of Engineering , Minia university , Minia . 61519, Egypt.

^amahmoudsouby1992@gmail.com, ^bmohamedroali@mu.edu.eg, ^cramadan.b@mu.edu.eg, ^dnasbarakat@yahoo.com, ^eelmoghazy@yahoo.com

Abstract

Hydrophobic coated surfaces are used in many energy conversion and utilization of thermal systems, especially in pool boiling systems which leads to energy and material saving , surgical tools, medical equipments and textiles. In this study , a novel technique was used to fabricate hydrophobic Nano structured coatings on copper substrates .A solution contains a mixture of poly vinyl alcohol (PVA) and copper acetate was electrospun and the produced Nano fibers are collected on copper substrates. Three polished surfaces were coated with different electrospinning time (5, 15, and 30 min). Hereafter, the samples will be coded as S5, S15 and S30 respectively. The coated substrates were dried under vacuum for 24 hrs, and then calcined at 850 oC under vacuum. SEM, XRD, EDX, TEM are reported. Contact angles are measured for all surfaces to be 70o, 80.1o, and 115o, 102o for polished, S5, S15 and S30 surfaces respectively. The Nano structure change the nature of surfaces from hydrophilic to hydrophobic surfaces with high mechanical strength coatings.

Keywords: Hydrophobic coating; Calcination; Carbon Nano fibers; Electrospinning; Cu-incorporated carbon nanofibers.

1. Introduction

Surfaces coated with hydrophobic nanostructured coatings are used in a wide range of applications such as surgical tools [1], medical equipments [2, 3], textiles [4-7] , wear resistant surfaces[8] , material for mold fabrication in the manufacturing of various polymer products [9] and energy conversion and utilization of thermal systems applications such as pool boiling. The benefits of such coatings with hydrophobic nature can leads to heat transfer enhancement in pool boiling and hence lead to energy and material saving [10-13] . Hydrophobic surfaces also are produced for buildings which will never need cleaning [14] . Hydrophobic coatings also can solve the biofilm problems and Legionnaires disease outbreaks which existed in the cooling towers. Biofilms can cause clogging and corrosion so the reduction of such biofilms is important for operational reasons and public health so, an effective hydrophobic coating anti-biofilm strategies are needed in practice [15] . Finally, enhancing surface characteristics especially controlling surface wettability is a crucial parameter in the design of many industrial and daily life applications.

2. Experimental Procedure

2.1 Materials

Poly Vinyl alcohol (PVA, Mw = 82000 g /mol , Loba , Mumbai , India) and copper acetate Tetra hydrate (CuAc, 99.9 Sigma-Aldrich Corporation, St. Louis, MO, USA) were utilized as-received without any additional treatment. The used copper substrates were made from a copper rod obtained from Egyptian Copper Works, Cairo, Egypt.

2.2 Sample Preparation

2.2.1 Polishing

In order to compare the wettability for all surfaces, surfaces with no features must be created. To insure this finishing, a copper rod was cut in to many test sections of 15 mm diameter and 20 mm long, bare copper substrates were polished with emery papers of P400, P600, P800, P1000, P1200, and P2500 successively. After the treatment, the substrates were washed by distilled water and acetone. . Polished surface serve as a base line of all coated surfaces. For all polished surfaces used in this study, a mirror polishing was achieved as shown in Fig. 1, a reflection of a bolt thread can be seen on the surface of polished surface.



Fig .1 a reflection of a bolt thread on polished surface

2.2.2 Electrospinning and Calcination

Electrospinning [16] is used to texture nanofibers on the copper substrates . Electrospinning is a widely used technique for the electrostatic production of nanofibers, during which high voltage electric power is used to make polymer fibers with diameters ranging in nanometer scale. Electrospinning is a relatively simple way of creating nanofiber materials. This process has an extremely attention by many researchers because of its ability to produce fibers on a scale of nanometers which is difficult to achieve using other standard technologies. Fig. 2 displays a schematic illustration of the basic setup of the electrospinning apparatus used in this study. The electro spun sol-gel was formed by mixing of a CuAc solution (20 wt% in water) with a pre-Prepared PVA aqueous solution (10 wt %). The final mixture was adjusted to have 20 wt% of the metallic precursor with respect to the solid polymer. The mixture was vigorously stirred at 50 oC for 5 h. The final prepared solution was placed in a plastic capillary. The formed polymeric nanofibers were collected on the surface of the copper specimen as shown in the figure. The electrospinning process was carried out at 20 kV voltage with a tip-to-collector distance of 25 cm. Three polished surfaces were coated with different electrospinning time (5, 15, and 30 min). Hereafter, the samples will be coded as S5, S15 and S30 for an electrospinning time of 5, 15 and 30 min, respectively. The specimens holding the formed nanofibers were initially dried at 80 oC for 24 h under vacuum. After drying all coated samples under vacuum at 80 oC for a day, all samples are calcined at 850°C for 2 h under vacuum with a heating rate of 3 °C/min. the benefit of calcination is to convert the polymer nano fibers to carbon nano fibers which has a hydrophobic characteristics . Calcination [17] is the process of subjecting a substance to the action of heat, but

without fusion . XRD and EDX revealed that the nano textured coating after calcination for all samples is cu nano particles incorporated carbon nano fibers. Fig. 3, shows the sintering curve.

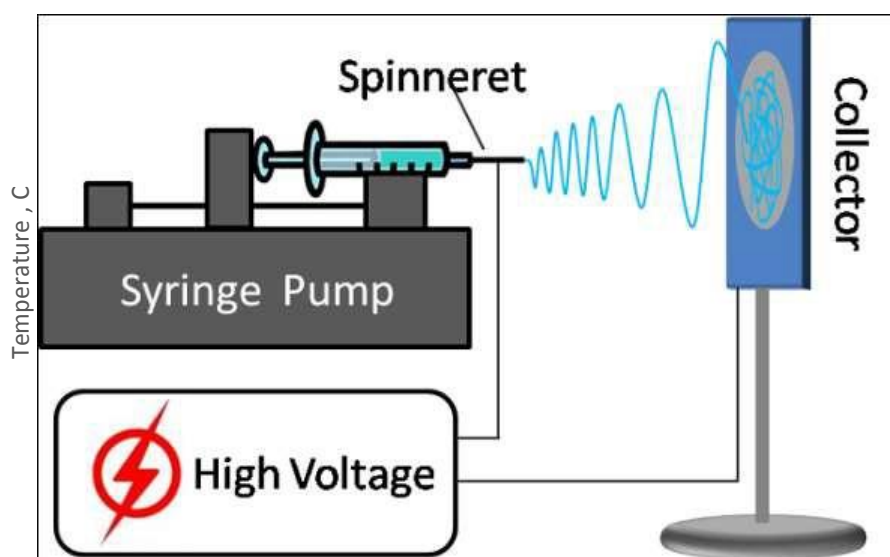


Fig.2 a schematic illustration of the basic setup of the electrospinning apparatus used in this study

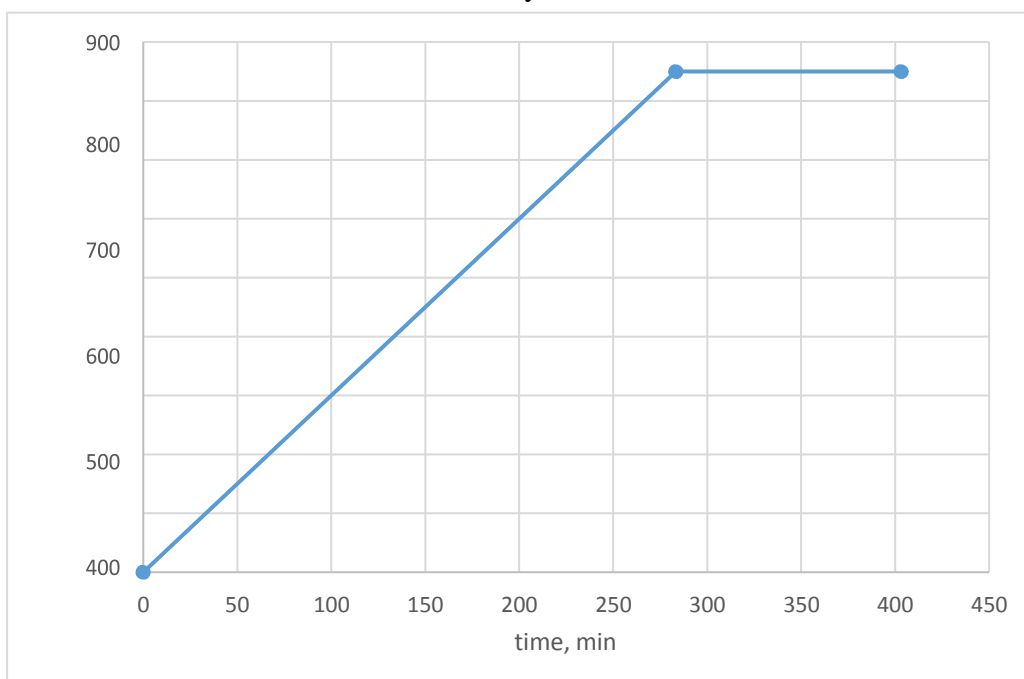


Fig.3 The sintering curve

3. Results and discussion

3.1 Characterization

The surface morphology was studied by scanning electron microscope (SEM) (JSM IT 200, Fine measurements Lab, Minia University, Egypt) equipped with energy-dispersive X-ray (EDX) analysis tool. Information about the phase and crystallinity was obtained by using x-ray diffractometer (XRD) with Cu K α ($\lambda = 1.540 \text{ \AA}$) radiation over Bragg angle ranging from 10° to 90° . High-resolution image and selected area electron diffraction patterns were obtained with transmission electron microscope (TEM) operated at 200 kV equipped with EDX analysis. The electrospinning is the most efficient inorganic nanofibers making technique if the polymer and metallic precursor were properly selected. Overall, metal alkoxides are the best metallic precursors due to the high polycondensation tendency. Besides, metal acetates showed good activity as precursors due to the polycondensation ability [18, 19]. Fig. 4 displays the SEM image of the

collected nanofibers before the calcination process. As shown, smooth and beads-free nanofibers were obtained.

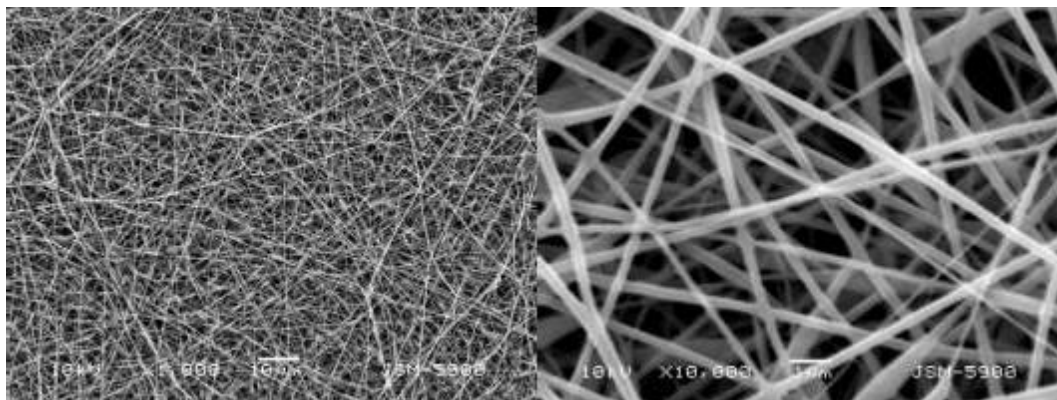


Fig.4 SEM image for the CuAC/PVA electrospun nanofibers.

Fig. 5 shows SEM images of the copper specimens surfaces after the calcination process. Fig. 4A shows the SEM image of the specimen surface coated for 5 min; sample S5. As shown, small amount of nanofibers appeared and a microporous nanostructure. Fig 4B and 4C show the morphology of S15 and S30 samples, respectively. As it can be concluded, increasing the electrospinning time leads to increase the nanofibers density on the surface. It is noteworthy mentioning that we believe the background can be a thin graphite layer merged with the original surface due to containing copper nanoparticles fused with the bulk copper. Fig. 6 displays the EDX analysis of the surface S30. The copper identification peaks clearly appear.

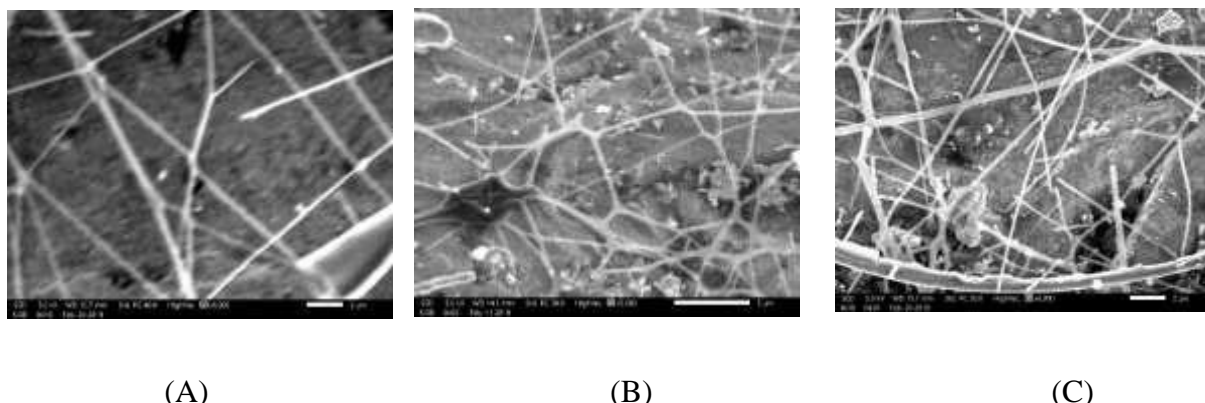


Fig. 5 SEM image for the copper disc surfaces coated by CuAC/PVA nanofibers for 5; (A), 15; (B) and 30; (C) min after the calcination process.

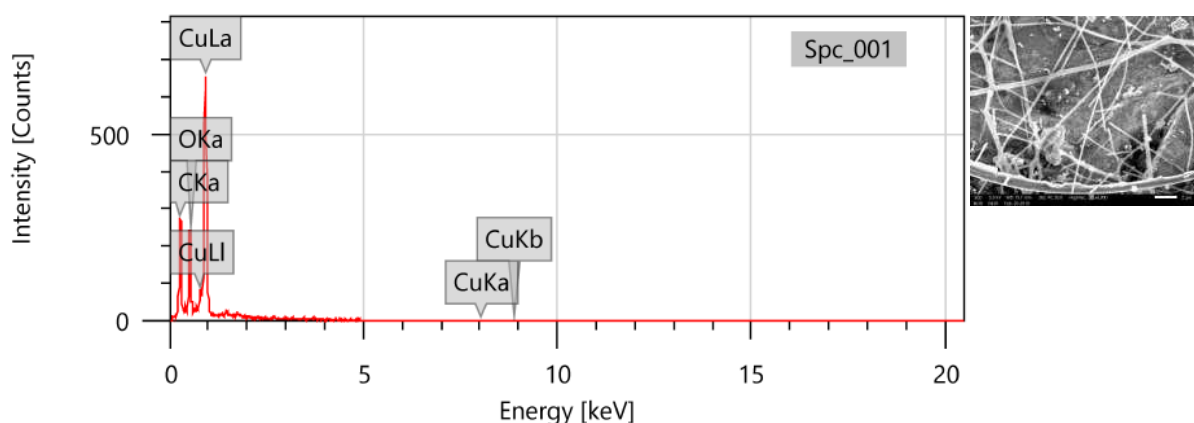


Fig. 6 EDX analysis for a randomly selected area from the sample S30.

Compared to many polymers, the carbon content in the PVA is relatively high. However, it is not commercially used as a precursor of carbon nanofibers fabrication due to the problem of breaking down to volatile compounds before the graphitization Process. However, presence of metal nanoparticles can distinctly overcome this dilemma[20, 21]. Forming of non-zero valent copper Compound is the first impression about the expected outcome from calcination of the copper acetate. Paradoxically, due to the abnormal decomposition of the acetate anion that results in evolving strong reducing gases (CO and H₂), metallic copper is formed. To properly confirm the aforementioned hypothesis, XRD analysis was exploited. Fig. 7 demonstrates the XRD pattern for the obtained nanofibers after the calcination process. The obtained results confirmed formation of pure copper due to appearance the standard peaks representing (111), (200), (220), (311) and (222) crystal plans (JCDPS # 04-0836). Moreover, the appeared broad peak at 2theta value ~ 26o is attributed to formation of graphite phase. The results indicated that the obtained nanofibers composed of zerovalent copper (Sp.Gr Fm3m(225)). The inset demonstrates the TEM image of the obtained nanofibers. The image indicates that the obtained nanofibers compose of amorphous nanofiber matrix embedded crystalline nanoparticles. Accordingly, it can be confidently concluded that the final product is copper nanoparticles-incorporated carbon nanofibers.

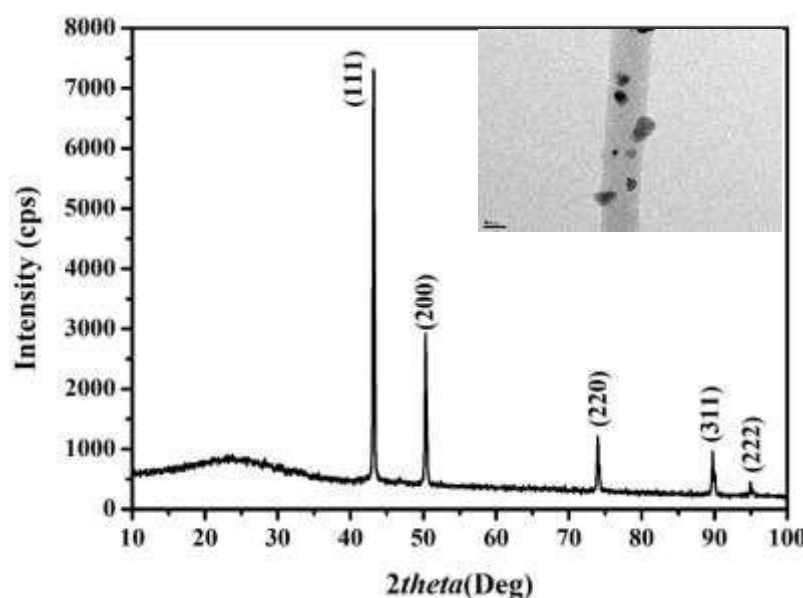


Fig. 7 XRD analysis results the powder obtained from calcination of CuAC/PVA electrospun nanofibers (sample S3) at 850 oC. The inset displays TEM image.

3.2 Wettability Results

The proposed study is to change the Wettability from hydrophilic surfaces to hydrophobic surfaces. The contact angles are measured using a contact angle goniometer. The contact angle of the smooth surface used in this study is measured to be 70o. The Nano structured surfaces in this study revealed hydrophilic structure for S5 and hydrophobic structures for S15 and S30 with a contact angles of 80.65o , 115o , 102o for S5,S15 and S30 respectively .Fig. 8 shows the contact angles for test samples . hydrophilic structure for S5 is expected due to the little amount of collected nano fibers on the copper surface and hence a small amount of micro cavities Smooth surface and S5 have higher wettability but Surfaces S15 and S30 have lower wettability. The hydrophobicity of surfaces S15 and S30 is due to the combined effect of copper Nano

particles and carbon Nano fibers. The nano coating improve the hydrophobicity of the surface by providing numerous micro 3D cavities.

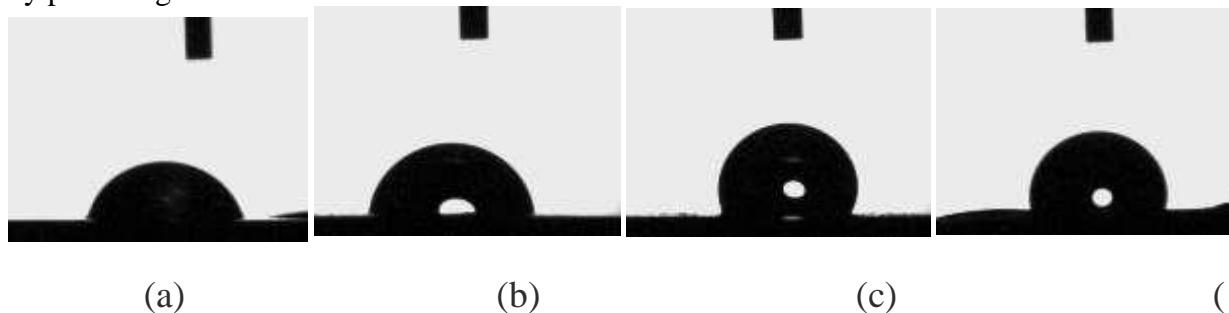


Fig .8 The contact angles of the Nano structured surfaces: (a) for smooth surface, (b), (c) and (d) for S5, S15 and S30 respectively.

Fig. 9 shows the relation between contact angles and electro spinning time. The contact angle increases with the increase of electrospinning time due to the presence of graphite and the 3D micro cavities. So contact angle increases with electrospinning time except for S30. Due to the longtime of electrospinning, a large amount of nano fibers were accumulated and hence the porosity and cavities on the surface decreased compared to surface S15. So S15 is the best hydrophobic surface in this study.

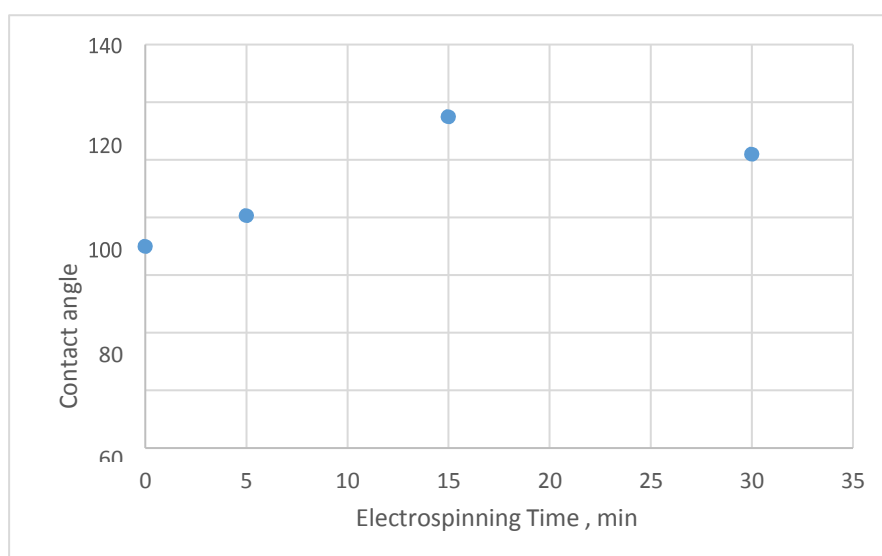


Fig .9 The relation between contact angles and electro spinning time.

SEM revealed that the nanofibers self-sintered and the presence of cu nano particles have a great benefit in enhancing surface characteristics and aiding the attachment between the nano structured coating and the original substrate. Hence, this coatings can be expected as a good adhesive and a mechanical stable coatings. The proposed nano textured coatings are expected to be valid for many applications.

5. Conclusion

From this experimental study, we can concluded that Cu-nano particles incorporated in carbon nano fibers is a good mechanical stable coating and change the contact angles from 70o, 80.1o, 115o, 102o for polished, S5, S15, S30 respectively .Hence, the surfaces of test samples change from hydrophilic nature to hydrophobic nature with compared to the polished surface except S5 is still hydrophilic due to the little amount of fibers collected on the polished substrate. Contact angles increases with electrospinning time except for S30because of the dense nano fibers collected

.SEM, EDX, TEM, XRD were reported in this study and revealed a good mechanical stable nano structured coatings.

References

- [1] M. C. e. al, "Mammalian cell viability on hydrophobic and superhydrophobic fabrics," Materials Science and Engineering, vol. 99, pp. 241-247, 2019
- [2] b. Juan Meng a, Haiyan Li b, Yaqin Gaoa, He Xub, Hongchen Gu b and Jiang Chang b,c,. "Application of hydrophobic coatings in biodegradable devices" Bio- Medical Materials and Engineering pp. 77-88 2015.
- [3] "Combination of laser patterning and nano PTFE sputtering for the creation a super-hydrophobic surface on 304 stainless steel in medical applications," Surfaces and Interfaces, vol. 8, pp. 219-224, September 2017.
- [4] M. E. Y. a. M. Shateri-Khalilabad*, "One-Step Synthesis of Superhydrophobic Coating on Cotton Fabric by Ultrasound Irradiation" Ind. Eng. Chem, vol. 52 pp. 12846-12854, 2013.
- [5] O. D. a. R. Dag, " Application of Nano Coating (SiO₂) on Textile Products" J. Chem. Chem. Eng, pp. 82-85, 2017.
- [6] M. J. e. al, "Nanostructured coatings for super hydrophobic textiles" Bulletin of Materials Science vol. 35, November 2012
- [7] M. J. Virginija Sacevičienė , V. B. , , and a. V. U. Vitalija Čepauskienėb, "Investigation of the wettability of the hydrophobic textile after mechanical treatments," Proceedings of the Estonian Academy of Sciences,, pp. 118-123, 2015.
- [8] "Feasible fabrication of a wear-resistant hydrophobic surface," Applied Surface Science, vol. 463, pp. 923-930, January 2019.
- [9] "Picosecond Laser Surface Texturing of a Stavax Steel Substrate for Wettability Control," Engineering, vol. 4, pp. 816-821, December 2018
- [10] M. Zupančič, M. Steinbücher, P. Gregorčič, and I. Golobič, "Enhanced pool-boiling heat transfer on laser-made hydrophobic/superhydrophilic polydimethylsiloxane- silica patterned surfaces," Applied Thermal Engineering, vol. 91, pp. 288-297, 2015.
- [11] S. S.-R. R.P. Sahu, S. Sinha-Ray, A.L. Yarin, " Pool boiling on nano-textured surfaces comprised of electrically-assisted supersonically solution-blown,copper- plated nanofibers: experiments and theory,," Int. J. Heat Mass Transfer vol. 87, pp. 521–535, 2015.
- [12] S. S.-R. S. Jun, A.L. Yarin, "Pool boiling on nano-textured surfaces," Int. J.Heat Mass Transfer . vol. 62, pp. 99-111, 2013.
- [13] Z. C. e. al, "POOL BOILING HEAT TRANSFER OF WATER ON COPPER SURFACES WITH NANOPARTICLES COATING," Proceedings of the ASME 2017 International Mechanical Engineering Congress and Exposition, November 3-9, 2017 Tampa, Florida, USA.
- [14] M. F. McGuire, Stainless steels for design engineers: Asm International, 2008. [15] I. Turetgen, "Reduction of microbial biofilm formation using hydrophobic nano-silica coating on cooling tower fill material" AFRICAN JOURNALS ONLINE, vol. 41, 2015.
- [16] J. Huang and T. You, "Electrospun nanofibers: from rational design, fabrication to electrochemical sensing applications," in Advances in Nanofibers, ed: IntechOpen, 2013.

- [17] B. Kaur and S. Bhattacharya, "Automotive dyes and pigments," in Handbook of Textile and Industrial Dyeing, ed: Elsevier, 2011, pp. 231-251.
- [18] N. A. Barakat, M. A. Abdelkareem, M. El-Newehy, and H. Y. Kim, "Influence of the nanofibrous morphology on the catalytic activity of NiO nanostructures: an effective impact toward methanol electrooxidation," Nanoscale research letters, vol. 8, p. 402, 2013.
- [19] N. A. Barakat, F. S. Al-Mubaddel, M. R. Karim, M. Alrashed, and H. Y. Kim, "Influence of Sn content on the electrocatalytic activity of NiSn alloy nanoparticles- incorporated carbon nanofibers toward methanol oxidation," International Journal of Hydrogen Energy, vol. 43, pp. 21333-21344, 2018.
- [20] N. A. Barakat, M. H. El-Newehy, A. S. Yasin, Z. K. Ghouri, and S. S. Al-Deyab, "Ni&Mn nanoparticles-decorated carbon nanofibers as effective electrocatalyst for urea oxidation," Applied Catalysis A: General, vol. 510, pp. 180-188, 2016.
- [21] N. A. Barakat, M. Motlak, A. A. Elzatahry, K. A. Khalil, and E. A. Abdelghani, "NixCo1-x alloy nanoparticle-doped carbon nanofibers as effective non-precious catalyst for ethanol oxidation," international journal of hydrogen energy, vol. 39, pp. 305-316, 2014.

10- Hydraulic Simulation of Modern Irrigation Schemes in West Nubaria

Region, Egypt

Mai M. Saad¹, Amr Fleifle² and Hossam M. Moghazy³

1. Researcher, Irrigation and Hydraulics Dept., Faculty of Engineering, Alexandria University
Alexandria, Egypt, e-mail: maimohamed2081985@gmail.com
2. Irrigation and Hydraulics Dept., Faculty of Engineering, Alexandria University 21544,
Alexandria, Egypt
3. Professor of Irrigation Engineering and Drainage, Head of Irrigation and Hydraulics Dept.,
Faculty of Engineering, Alexandria University, Egypt

Abstract

Nowadays, water and its supply raise problems of strategic importance and great complexity, being considered one of the keys to sustainable human development. The use of modern irrigation systems is increased to safe water facing the problem of water scarcity. The main objective of this research is to compare different irrigation methods based on a parametric evaluation system. The comparison was applied on an area of 5,000 feddans as a case study in West Nubaria Region. A hydraulic model using water CAD software was developed to optimize the design of modern irrigation system. A combination system of sprinkler and drip irrigation, considering the topography of this region is proposed. Verifying the actual hydraulic design of pipelines and comparing the results with the specific requirements and design assumptions was carried out. Different scenarios were investigated to find out the optimum design. The comparison evaluated the saved irrigation water and the corresponding power using the proposed modern irrigation system.

Keywords: Drip irrigation, Sprinkler irrigation, Modern irrigation, WaterCAD.

5 Introduction

Food security and stability in the world greatly depends on the management of natural resources. Due to the depletion of water resources and an increase in population, the extent of irrigated area per capita is declining and irrigated lands now produce 40% of the food supply. Consequently, available water resources will not be able to meet various demands in the near future and this will inevitably result into the seeking of newer lands for irrigation in order to achieve sustainable global food security. Land suitability, by definition, is the natural capability of a given land to support a defined use. The process of land suitability classification is the appraisal and grouping of specific areas of land in terms of their suitability for a defined use. Water usage has been raising as much as more than twice the rate of population increase in the last century. The situation will be exacerbated as rapidly growing urban areas place heavy pressure on neighboring water resources [1]. Water balance in Egypt is water revenue and water needs. Our main source of revenue is the Nile River and its flows from the Upper Nile, a fixed share of 55.5 billion cubic meters. It is included in the agreement to share the benefits of the construction of the High Dam between Egypt and Sudan in 1959 the revenues also include deep reservoir water estimated about 2 billion cubic meters annually. There are about 1.3 billion meters of rain and flood, and about 0.4 billion cubic meters of seawater desalination, both on the shores of the Red Sea or the Mediterranean on the northern coast and Mars Matruh. The total amount of revenue available in the revenues does not exceed 59 billion cubic meters, while the total use of water annually 78 billion cubic meters, including drinking water, agriculture, industry and all other uses. It is clear that the water shortage is 20 billion meters per year, taking into account the increase in

annual growth rates, with the increasing need for water for national projects and development plans that all rely on water. This imbalance is a candidate for expansion in the coming years. Agriculture is the backbone of Egypt's economy and the largest consumer of fresh water consuming more than 85% of its water resources. Many water policies have been formulated to accommodate the dynamics of water resources and changes in goals and priorities [2]. Irrigation of old lands in Egypt is currently confronted with problems which including the inequitable distribution of water between farmers in the tail-end of branch canal and Mesqas. In addition, there is excessive water wasting and energy cost to current system operations. These problems effect on their production, losses of cultivated land, and low income [3]. The current policy in Egypt aims to develop water resources by increasing water supply (rain, sudden flood harvesting, groundwater development, desalination, etc.), as well as improving water management through several factors, improving water quality, increasing public awareness and international agreements among Nile Basin countries. One of the major forms of development is represented to change irrigation flooded to the modern irrigation. As a result, Programs for the development of the agricultural sector, and expansion of the land reclamation plan which turn now to the installation of means Modern irrigation [4]. The Ministry of Irrigation has launched a plan to rationalize water consumption since 1995 and led to positive results, to rationalize water consumption in all sectors used by it, especially the agricultural sector, which consumes about 85% of Egypt's water resources.

By means of how to irrigate the agricultural land, within the framework of the rationalization of consumption implemented, without wasting any drop of water by irrigation the land at night to consume less water, cultivation of crops that consume small quantities of water, settle the land until the water takes as much as it needs, commitment to irrigation in the role and to the extent of need only and not take the right of others and commitment to modern irrigation systems in the new lands.

We can imagine the amount of water lost as a result of many conventional irrigation methods. When irrigating the plant, the plant benefits only 10% of the amount of water used, while the remaining 90% is lost in (disposing of soil layers - evaporation from soil surface - Plant). Since a large amount of water lost by disposing of the land had to follow modern irrigation methods because of their many advantages such as suitable for irrigation of all crops and vegetables, suitable for high porosity land, increase productivity due to continuous plant nutrition (increase 15-50% by plant type), increase crop production and increase exports, increasing national income and provision of chemical fertilizers (save from 30-50%). [5].

This paper presents the application of modern irrigation in desert lands like West Nubria Region, Egypt instead of the surface irrigation by using (WATERCAD) program in three different scenarios to calculate the actual hydraulic design assumptions of pipelines and pumps then use Excel to calculate the total capital cost and the total annual cost and comparing the results.

6 Methods:

a. Study area:

The study area located in close to EL Nasr Canal and Branch 17 in West Nubria Region, EGYPT .It is proposed that the model for modern irrigation 5000 feddans, Fig (1).

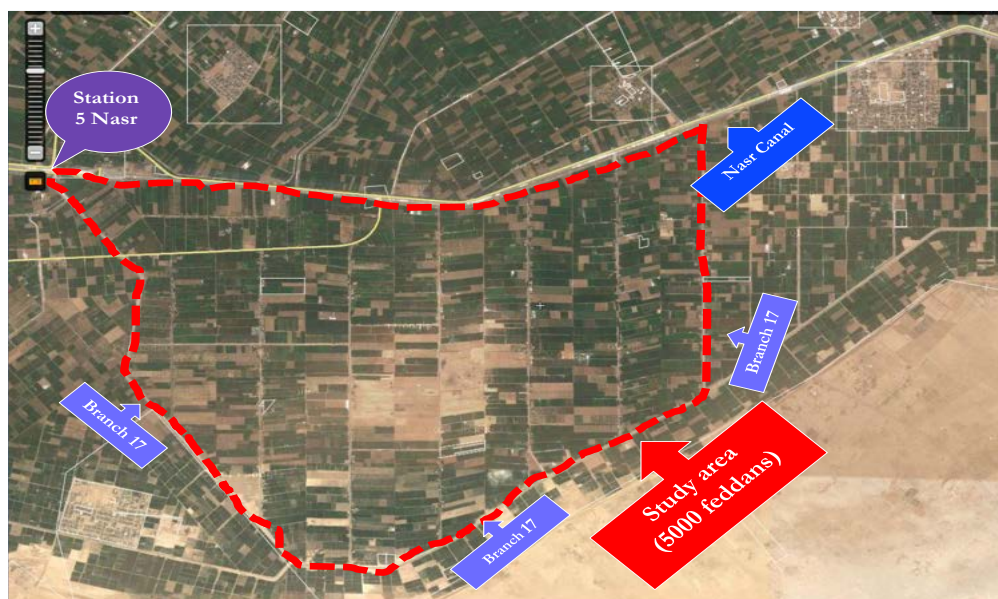


Fig (1): Location of the study area.

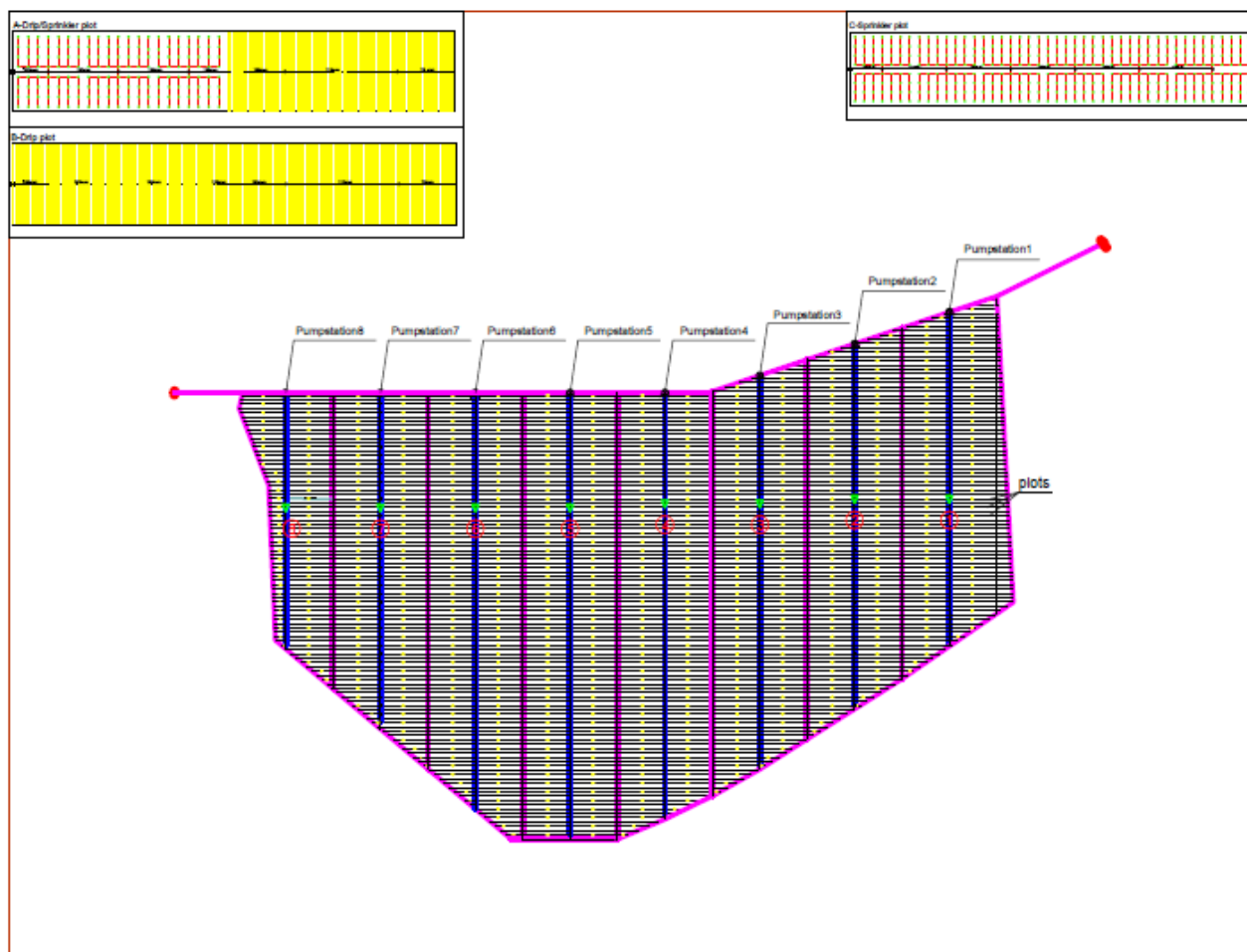


Fig (2): Layout and plots types.

b. Geographical data :

The Advanced Space borne Thermal Emission and Reflection Radiometer (ASTER) Global Digital Elevation Model (GDEM) is concurrently distributed from the Ministry of Economy, Trade, and Industry (METI) Earth Remote Sensing Data Analysis Center (ERSDAC) in Japan and the National Aeronautics and Space Administration (NASA) Earth Observing System (EOS) Data Information System (EOSDIS) Land Processes (LP) Distributed Active Archive Center (DAAC) in the United States. The ASTER GDEM covers land surfaces between 83N and 83S and is comprised of 22,702 1 x 1 tiles. Tiles that contain at least 0.01% land area are included. The ASTER GDEM is distributed as Geo referenced Tagged Image File Format (GeoTIFF) files, and in geographic coordinates (latitude, longitude). The data are posted on a 1 arc-second (approximately 30-m at the equator) grid and referenced to the 1984 World Geodetic System (WGS84)/1996 Earth Gravitational Model (EGM96) geoid. [6]. The location of study area its location ASTGTM2_N30E030_num and its size 30 pixel x 30 pixel.

Then the Global Mapper Program was used to create contour map to verify maximum and minimum level of study area by entering ASTGTM2_N30E030 and Google Earth location of the zone, Fig(3).

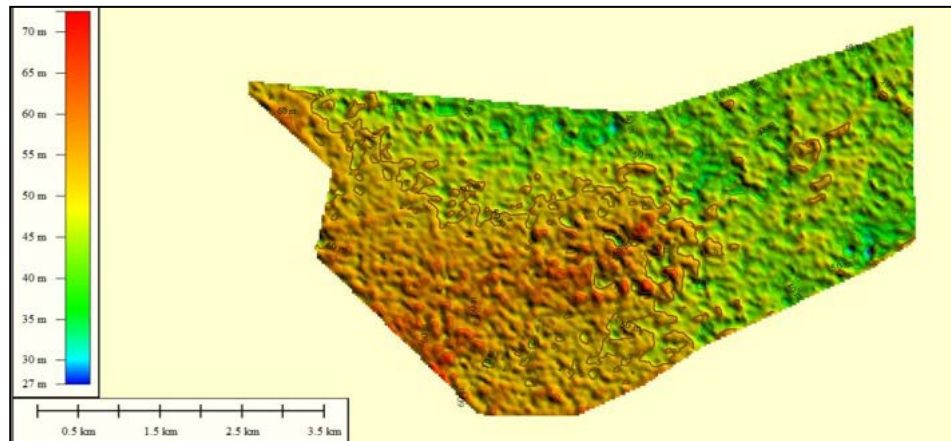


Fig (3): Contour map.

c. Simulation software :

The Geographic Information System (GIS) is taken as an aid to visualize the sources and feeders and conceptualize the entire distribution network. GIS integrates stores, edits, analyzes, shares, and displays geographic information for informing decision making. The topographical elevations of the stand posts, houses and other demand points are obtained from the GIS software. Preliminary GIS analysis using the Quantum GIS Lisboa software is done which included pilot study area water distribution system map digitization, georeferencing, DEM analysis for elevation map generation and attribute table generation are performed for data preparation for Water CAD software. Bentley Water CAD is a multi-platform hydraulic and water quality modeling solution for water distribution systems with advanced interoperability, geospatial model-building, optimization, and asset management tools[7]. The calculation software algorithm which is based on Hydraulic Gradient method, allows the hydraulic analysis of water networks (although it can be used for any Newtonian fluid) determining the pressures at various points in the system, as well as the flow rates, velocities, losses the lines that make the water network, and many other operating parameters derived from the elements present in the system as: Pumps, Control Valves, Tanks, etc. from the physical characteristics of the system and demand conditions previously established. WaterCAD also allows extend its capabilities to issues of long-term management of supply systems including: vulnerability analysis, fire protection analysis, cost estimating energy, hydraulic calibration, optimization, etc. [8].

WaterCAD can use any one of three general forms of the head loss the previous formula the Hazen-Williams formula, the Darcy-Weisbach formula, or the Chezy-Manning formula. Hazen-Williams formula is possibly the most popular head loss equation for water distribution systems, the Darcy-Weisbach formula is more appropriate to laminar flow and to fluids other than water, and the Chezy-Manning formula is more generally used for open channel flow.

Table (1) lists resistance coefficients and flow exponents for each formula. Each formula uses a different pipe roughness coefficient, which must be determined empirically. Lists general ranges of these coefficients for different types of new pipe materials, but a pipe's roughness coefficient can change considerably with age while the Darcy-Weisbach relationship for closed-conduit flows is generally recognized as a more accurate mathematical formulation over a wider range of flow than the Hazen-Williams formulation [9].

Table (1): Pipe head loss formulas

| Formula | Resistance Coefficient (a) | Flow Exponent (b) |
|--------------------------------|------------------------------------|-------------------|
| Hazen- Williams | $4.72C^{-1.85}d^{-4.87} L$ | 1.85 |
| Darcy- Weisbach | $0.0252 f(\epsilon, d, q)d^{-5} L$ | 2.00 |
| Chezy-Manning (full pipe flow) | $4.66 n^2 d^{-5.33} L$ | 2.00 |

Where:

C = Hazen-Williams roughness coefficient

e = Darcy-Weisbach roughness coefficient, m

f = friction factor (dependent on e, d, and q)

d = pipe diameter, m

L = pipe length, m

n= Chezy-Manning coefficient

The Hazen-Williams formula is the most commonly used head loss formula for the hydraulic head lost by water flowing in a pipe due to friction with the pipe walls, is being used for the present study (Bentley System Incorporated, 2012). The Hazen- Williams equation is used for calculating the head loss in the network and the main pipelines and the distribution pipelines are designed based on the required discharge and the velocity of flow using Continuity equation.

$$Q = A V$$

Where:

A = Area of cross section of pipe

V= the velocity of the flow

d. Hydraulic design scenarios :

It was conducted on three scenarios in West Nubaria Region, Egypt as follows:

The first scenario, the network was conducted on 8 mainlines, 8 pump station and 694 plots where area plot was about 8.5 feddans. Plots were divided by 50% to 50% irrigation by sprinkler and drip irrigation. For the network, the maximum velocity in main pipes was (1.49m/s²) and the minimum velocity was (1.10m/s²). Pump station design flow was (0.12m/s³) at design head (45m,50m).The maximum total head in junction was (59.93m) and the minimum total head was (25.97m).

The second scenario, the network was conducted on 8 mainlines, 8 pump station and 694 plots where area plot was about 8.5 feddans. Plots were irrigated by drip irrigation. For the network, the maximum velocity in main pipes was (1.49m/s²) and the minimum velocity was

(1.09m/s²). Pump station design flow was (0.12m/s³) at design head (45m,55m).The maximum total head in junction was (49.44) and the minimum total head was (16.91m).

The third scenario, the network was conducted on 8 mainlines, 8 pump station and 694 plots where area plot was about 8.5 feddans. Plots were irrigated by sprinkler irrigation. For the network, the maximum velocity in main pipes was (1.49 m/s²) and the minimum velocity was (1.08 m/s²). Pump station design flow was (0.12m/s³) at design head (55m,60m).The maximum total head in junction was (59.92m) and the minimum total head was (25.96m).

Table (2) presents the summary of scenarios of the network as follow:

| Scenario | Scenario 1 | Scenario 2 | Scenario 3 |
|---------------------------------------|------------|------------|------------|
| Max. velocity (m/s) | 1.49 | 1.49 | 1.48 |
| Min. velocity (m/s) | 1.10 | 1.09 | 1.08 |
| Head of pump (m) | 55,60 | 45,50 | 55,60 |
| Flow of pump (m/s³) | 0.12 | 0.12 | 0.12 |
| Max. head (m) | 59.93 | 49.44 | 59.92 |
| Min. head (m) | 25.97 | 16.91 | 25.96 |

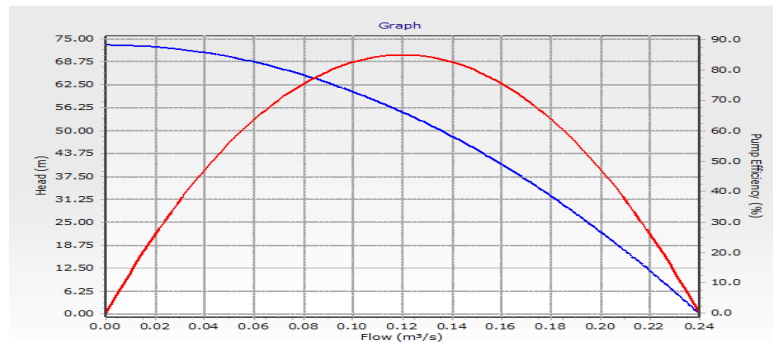


Fig (4): Typical Pump Definition curve

7 Result and Discussion

Results in this study as follows:

In the first scenario, capital cost pipe lines were calculated by the sum of costs of drippers, sprinklers, main pipes, valves & fittings, excavation and backfilling and it was (32,515,792L.E.). Capital cost pump stations were calculated according to the operating flow, the operating head, efficiency of pump, efficiency of motor and total power of pumps, it was (43,619,373 L.E.). Annual operation and maintenance were obtained for pipeline cost and cost of pump station (civil work and electromechanical), it was (850,686 L.E.). Annual electrical power consumption was (1,545,192 L.E.). Annual components were calculated according to lifetimes of pipes, valves, fittings and pump station and it was (7,632,084 L.E.)

In the second scenario, capital cost pipe lines were calculated by the sum of costs of drippers, main pipes, valves & fittings, excavation and backfilling and it was (23,293,553L.E.). Capital cost pump stations were calculated according to the operating flow, pumps, it was (38,769,510 L.E.). Annual operation and maintenance were obtained for pipeline cost and cost of pump station (civil work and electromechanical), and it was (666,316L.E.). Annual electrical power consumption was (1,820,716 L.E.). Annual components were calculated according to lifetimes of pipes, valves, fittings and pump station and it was (5,727,379 L.E.).

In the third scenario, capital cost pipe lines were calculated by the sum of costs of sprinklers, main pipes, Valves & Fittings, excavation and backfilling and it was (45,871,806 L.E.).

Capital cost pump stations costs were calculated according to the operating flow, the operating head, efficiency of pump, efficiency of motor and total power of pumps , it was (43,619,373 L.E.). Annual operation and maintenance were obtained for of pipeline cost and cost of pump station (civil work and electromechanical), it was (984,246L.E.). Annual electrical power consumption was (1,103,708L.E.). Annual components were calculated according to lifetimes of pipes, valves, fittings and pump station and it was (9,780,963 L.E.).

Table (3) presents the details of costs of each mainline of the first Scenario:

| Cost/L.E. | Main line1 | Main Line2 | Main Line3 | Main Line4 | Main Line5 | Main Line6 | Main Line7 | Main Line8 |
|-------------------------------------|------------|------------|------------|------------|------------|------------|------------|------------|
| Pipe lines | 3654872 | 3945646 | 4310594 | 4686294 | 4874144 | 4592369 | 3662864 | 2789010 |
| Pump station | 5329281 | 5329281 | 5329281 | 5632397 | 7081746 | 5632397 | 5329281 | 3955710 |
| Annual Operation and maintenance | 99900 | 102808 | 106457 | 115973 | 135130 | 115034 | 99980 | 75404 |
| Annual Electrical power consumption | 186100 | 186100 | 186100 | 203018 | 270691 | 203018 | 186100 | 124066 |
| Annual Components | 877421 | 924205 | 982922 | 1069676 | 1178822 | 1054565 | 878707 | 665766 |

Table (4) presents the details of costs of each mainline of the second Scenario:

| Cost/L.E. | Main line1 | Main Line2 | Main Line3 | Main Line4 | Main Line5 | Main Line6 | Main Line7 | Main Line8 |
|-------------------------------------|------------|------------|------------|------------|------------|------------|------------|------------|
| Pipe lines | 2618366 | 2829410 | 3088049 | 3357441 | 3492137 | 3290093 | 2626358 | 1991698 |
| Pump station | 4723048 | 4723048 | 4723048 | 5026164 | 6323955 | 5026164 | 4723048 | 3501036 |
| Annual Operation and maintenance | 78017 | 80127 | 82713 | 91167 | 106912 | 90493 | 78096 | 58792 |
| Annual Electrical power consumption | 217519 | 217519 | 217519 | 241688 | 322251 | 241688 | 217519 | 145013 |
| Annual Components | 658041 | 691996 | 733609 | 803260 | 890699 | 792424 | 659327 | 498023 |

Table (5) presents the details of costs of each mainline of the third Scenario:

| Cost/L.E. | Main line1 | Main Line2 | Main Line3 | Main Line4 | Main Line5 | Main Line6 | Main Line7 | Main Line8 |
|-------------------------------------|------------|------------|------------|------------|------------|------------|------------|------------|
| Pipe lines | 5155980 | 5562225 | 6081132 | 6610792 | 6875621 | 6478377 | 5163972 | 3943708 |
| Pump station | 5329281 | 5329281 | 5329281 | 5632397 | 7081746 | 5632397 | 5329281 | 3955710 |
| Annual Operation and maintenance | 114911 | 118974 | 124163 | 135218 | 155144 | 133894 | 114991 | 86951 |
| Annual Electrical power consumption | 132928 | 132928 | 132928 | 145013 | 193350 | 145013 | 132928 | 88619 |
| Annual Components | 1118938 | 1184300 | 1267788 | 1379313 | 1500844 | 1358009 | 1120224 | 851548 |

The Comparison between simulated scenarios indicated that the numerically simulated results of:

1. Pipe lines costs were found the least cost to the second scenario, then the first scenario and the most cost to the third scenario, Fig (5-a).
2. Pump stations costs were found the least cost to the second scenario and the scenario first had as same as results to the third scenario, Fig (5-b).
3. Annual Operation and maintenance costs were found the least cost to the second scenario, then the first scenario and the most cost to the third scenario, Fig (5-c).

4. Annual Electrical power consumption costs were found the least cost to the third scenario, then the first scenario and the most cost to the second scenario, Fig (5-d).
5. Annual Components costs were found the least cost to the second scenario, then the first scenario and the most cost to the third scenario, Fig (5-e).

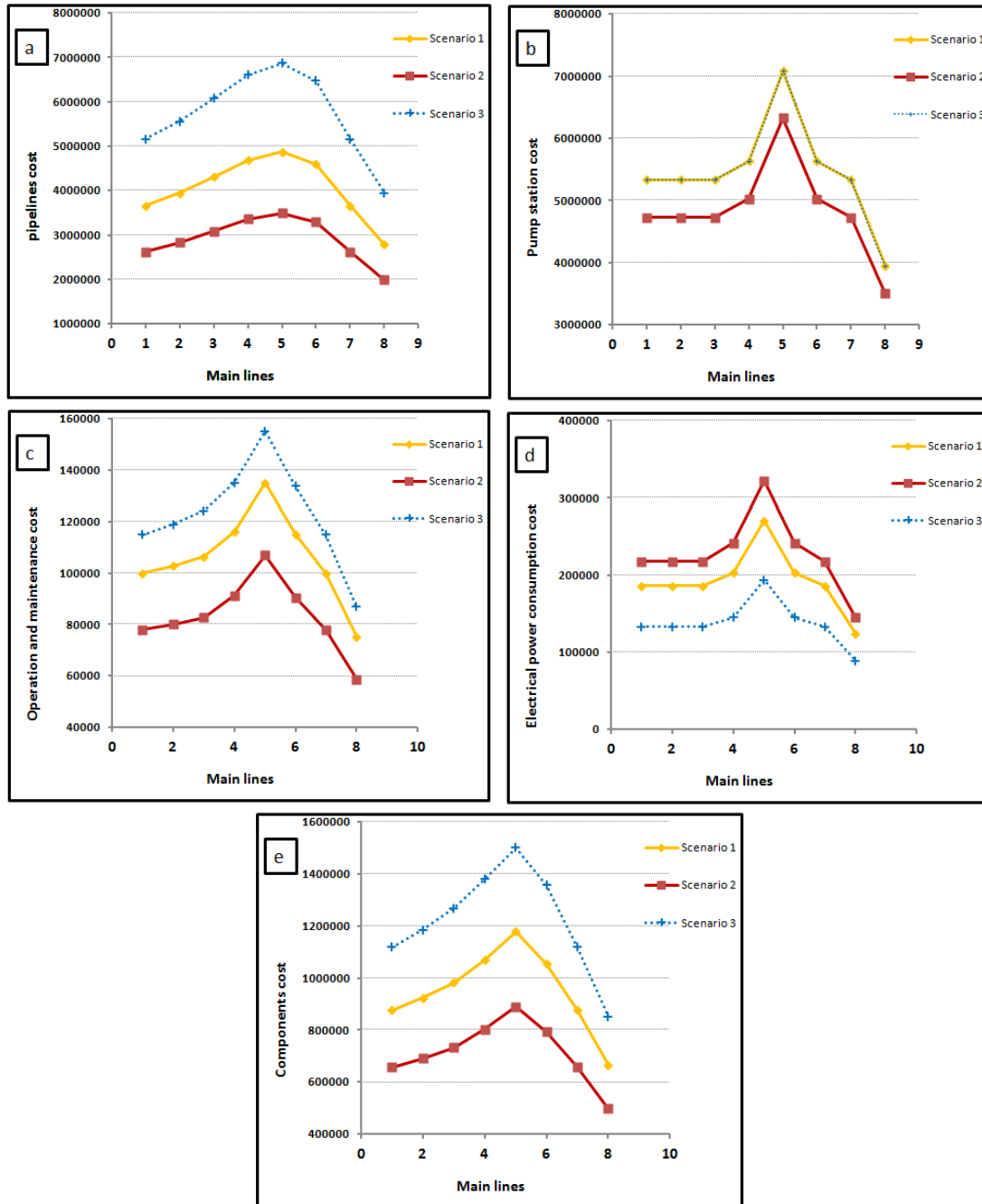


Fig (5): Comparison of costs of three scenarios

Table (6) the summary of Total capital cost of each scenario of the network as follow:

| Scenario | Scenario 1 | Scenario 2 | Scenario 3 |
|--------------------------------------|------------|------------|------------|
| Capital cost Pipelines (L.E.) | 32515792 | 23293554 | 45871806 |
| Capital cost Pump station cost(L.E.) | 43619373 | 38769510 | 43619373 |

| | | | |
|----------------------------------|----------|----------|----------|
| Total Capital Cost (L.E.) | 76135165 | 62063064 | 89491179 |
|----------------------------------|----------|----------|----------|

Table (7) the summary of Total Annual Cost of each scenario of the network as follow:

| Scenario | Scenario 1 | Scenario 2 | Scenario 3 |
|---|-------------------|-------------------|-------------------|
| Annual Operation and maintenance cost(L.E.) | 850686 | 666316 | 984246 |
| Annual Electrical power consumption cost(L.E.) | 1545192 | 1820716 | 1103708 |
| Annual Components cost(L.E.) | 7632084 | 5727379 | 9780963 |
| Total Annual cost (L.E.) | 10027961 | 8214412 | 11868918 |

8 Conclusion

In this study the hydraulic simulation of modern irrigation schemes in West Nubaria area was evaluated using three scenarios. From Water CAD program it was reported that the velocity of pipes were be at range from (1m/s) to (1.5m/s) .The pipes were made from UPVC and their diameters were be at range from (250mm) to (710 mm). The comparison between simulated scenarios indicated that the minimum total capital cost results were found to the second scenario (drip irrigation of total area) and the maximum total capital cost results were found to the third scenario (sprinkler irrigation of total area) and the first scenario (drip irrigation of 50% area and sprinkler irrigation of 50% area) was in between the other scenarios. Although annual electrical power consumption cost of the third scenario (sprinkler irrigation of total area) was the least cost and annual electrical power consumption cost was the most, but its total annual cost was the maximum. So annual cost results were found to the minimum to the second scenario (drip irrigation of total area) and the maximum results were found to the third scenario and (sprinkler irrigation of total area) the first scenario (drip irrigation of 50% area and sprinkler irrigation of 50% area) was in between the other scenarios.

Acknowledgements

Grateful thanks to my husband, my mother in law,all family, specially my parents, my uncle and my friends of Pharos University for their encouragement that made this study possible.

References

1. Food and Agriculture Organization of the United Nations Rome, (2017), FAO , Assessment of Water for Sustainable Food and Agriculture A report produced for the G20 Presidency of Germany.
2. Abu Zeid K. M., Mahmoud A., Rady, M.A. (2007). Water resources management and policies in Egypt. In: Country experiences with water resources management: economic, technical and environmental issues. World Bank Technical Paper No. 175. Washington D.C.
3. Allam. M. N, El Gamal. F, and Hesham.M.(2005). Irrigation systems performance in Egypt”,Options Méditerranéennes : Série B. Etudes et Research, No:52.
4. Mostafa.H., and Fujimoto.N.,(2014). Monitoring and Evaluation of Irrigation Management Projects in Egypt, Japan Agricultural Research Quarterly (JARQ), Vol: 49, No: 2, (pp.111-118).
5. Amer,M.H. , AbdEl-Hafez,S.A., AbdelGhany,M.B. (2017), International Book Market Service Ltd., member of Omniscriptum Publishing Group All rights reserved . Beau Bassin 2017, Water Saving In Irrigated Agriculture in Egypt
6. Earth Remote Sensing Data Analysis Center ASTER GDS User (2011). Aster Gdem 2 Readme Advanced Spaceborne Thermal Emission And Reflection Radiometer (Aster) Global Digital Elevation Model (Ggdem) Version 2.

7. Ramesh et al (2012). Designing a Water Distribution System in a Site Development Project Using WaterGEMS.
8. Pankaj Kumar Roy^{1*}, Ankita Konar¹, Gourab Banerjee¹, Somnath Paul^{1,,} (2015). Development and Hydraulic Analysis of A Proposed Drinking Water Distribution Network Using Water GEMS And GIS; Poll Res. 34 (2) 371-379.
9. Abd El Azim N. F., (2013). Strategic plan for water resources management of El Mahmoudia canal up to the year 2050, Egypt”, Ph.D. Thesis, Alexandria University, Alexandria, Egypt.

11- Improving the Crystallization Process of Salts on Gypsum Seeds in ZLD unit

M. El-Gedawy*, D. A. Elgayar, E-S. Z. El-Ashtoukhy, A. A. Zaatout

Faculty of Engineering, Alexandria University, Alexandria, Egypt

Mostafa El-Gedawy Gaber: **Email:** eng-mostafa.elgedawy@alexu.edu.eg

Abstract

In this study we investigated some factors to improve the crystallization process of wastewater salts on the seeds of calcium sulfate dihydrate (Gypsum), where this system is used in zero liquid discharge unit in a petrochemical plant to reduce the scaling occurs by calcium sulfate on the metal surface of the evaporators and heat exchangers. The benefits of this ZLD unit and this technology are to eliminate wastewater discharge in a friendly way to the environment, the sustainability of water (water recovery). Experiments were done at conditions of temperature 100 °C and a feed mixture of reverse osmosis (RO) reject and softener regeneration waste in a ratio 85:15 respectively. The effect of preheating time, rotational speed & initial gypsum concentration on total suspended solids (TSS) & total dissolved solids (TDS) were examined. The results show that both preheating time and rotational speed do not affect the value of TSS, while the TSS increases by increasing the initial gypsum concentration. The best conditions found for the crystallization process were 7 g/l initial gypsum concentration, 25 RPM rotational speed & without any preheating time before treatment.

Keywords: gypsum, crystallization, Zero Liquid Discharge.

1. Introduction

Calcium sulfate occurs naturally as the mineral gypsum and is the most common sulfate mineral in the environment that has been traditionally extracted from the ground [1]. In the modern world, gypsum is widely used as a constituent in construction materials such as cement or gypsum wallboards [2,3], as well as in the production of biocompatible materials such as bone void fillers [4]. However, calcium sulfate appears as an undesirable by-product, mostly as discard solids and/or as scale, in many industrial processes including wastewater treatment, oil and gas production, desalination, sulfur dioxide removal from coal-fired power plants flue gas [5,6], and during neutralization of free sulfuric acid in hydrometallurgical processes [7-12].

Calcium sulfate scale formation in industrial plants results in reduced production capacity and process efficiency due to decreased equipment volume, heat transfer capacity and material flow, blocked pipelines and corrosion. Calcium sulfate can be precipitated as dihydrate (DH) or gypsum ($\text{CaSO}_4 \cdot 2\text{H}_2\text{O}$) at low temperatures and as hemihydrate (HH) ($\text{CaSO}_4 \cdot 0.5\text{H}_2\text{O}$) or anhydrite (AH) (CaSO_4) at elevated temperatures [13]. A survey conducted in New Zealand showed that more than 90% of heat exchangers were reported to have some sort of fouling [14].

The presence of the fouling layer on the metal heat transfer surface results in primarily two major implications, an increase in heat transfer resistance and the restriction of the flow through the plates of the heat exchanger [15]. Several ways of minimizing the effects of fouling are present such as pretreatment of streams and regular mechanical or chemical cleaning [16].

One of the most common causes of CaSO_4 scale formation in hydrometallurgical processes is the transformation of the metastable CaSO_4 hydrate to the stable one (usual gypsum to anhydrite), as was the case with the Bulong nickel/cobalt plant, and then gradually transforms into anhydrite which has lower solubility under these conditions and consequently results in anhydrite scale formation downstream. Such scaling could result in serious operational problems, particularly in the solvent extraction stage [8,17].

During sulphuric acid neutralization with calcium-containing bases which occurs below 100 °C, first gypsum forms as a metastable phase because of its higher solubility, All calcium sulfate hydrates are relatively insoluble and they are formed wherever calcium and sulfate occur together after the equilibrium of the unstable or metastable hydrate in solution is reached (according to the Ostwald rule)[18].

Theoretically, gypsum is the stable solid phase in water up to 45 – 50 °C, and above that it transforms into anhydrite [19-22]. Transformation of calcium sulfate dihydrate (gypsum) into anhydrous calcium sulfate (anhydrite) proceeds slowly in a manganese sulfate/sulfuric acid medium (36 g Mn²⁺/kg of solution and 36 g H₂SO₄/kg of solution) at 95 °C was studied, the mechanism for the transformation appears to be one of dissolution and reprecipitation. The addition of anhydrite as seed to the process initially accelerates the transformation and contracts the induction period markedly, consistent with expectations for an autocatalytic process [22].

The aim of the present study is to investigate the effect of different factors on the crystallization process of wastewater salts from a mixture of reverse osmosis (RO) reject and softener regeneration waste in a ratio 85:15 respectively from actual wastewater from a petrochemical plant. Those streams are the inlet feed streams for the zero liquid discharge unit, in which we use the seeded brine slurry technology to make the wastewater salts crystallize on the seeds instead of the metal surface of the evaporator and crystallizer. The variables studied were preheating time before adding the wastewater, rotational speed & initial gypsum concentration.

2. Methods and Materials

2.1 Materials

The wastewater used in this study is a mixture of reverse osmosis (RO) reject and softener regeneration waste from actual wastewater from a petrochemical plant, and the chemical analysis of those two waste streams are shown below in Table 1. All chemicals used throughout the experiments and analytical measurements were of analytical grade.

Table 1 – Chemical analysis of feed wastewater streams (RO & Softener)

| | pH - | TSS (ppm) | TDS (ppm) | Cl ⁻ (ppm) | Ca Hardness (ppm) as CaCO ₃ | Mg Hardness (ppm) as CaCO ₃ | M. Alkalinity (ppm) as CaCO ₃ | SiO ₂ (ppm) | SO ₄ ⁴⁻ (ppm) |
|------------------------|-------------|-----------------|--------------|--------------------------|---|---|---|---------------------------|--|
| RO (85 %) | 10.3 | < 2.5 | 14673 | 7140 | - | - | 480 | 15.2 | 3108.6 |
| Softener (15 %) | 6.8 | < 2.5 | 42545 | 23480 | 12840 | 16920 | 80 | 0.55 | 268.4 |

2.2. Experimental setup and measurements

Before the beginning of each run, 100 ml of demineralized water was placed into the unit after mixing with the appropriate amount of gypsum. one liter prepared wastewater from RO reject and Softener regeneration waste in a ratio 85:15 respectively was heated till 100°C. the temperature of the gypsum solution was slowly raised to reach 100°C, then the waste solution was added while keeping mixing at constant RPM. The pH of the solution was measured by a pH meter (370 pH meter Jenway). Samples were drawn (60 ml) during evaporation at fixed volumes of 800 ml, 600

ml, 400 ml & 200 ml during the experiment period using a pipette. TSS (ppm) & TDS (ppm) were measured according to the standard methods [23, 24].

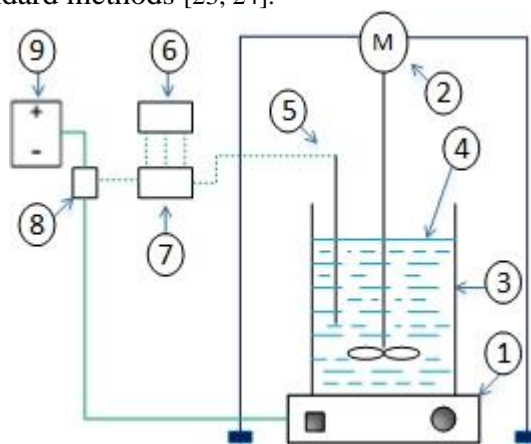


Fig. 1 - Experimental Apparatus

- | | |
|---------------------------|----------------------------|
| 1- Heater | 6- Arduino UNO board |
| 2- Motor | 7- Breadboard |
| 3- Beaker | 8- Relay |
| 4- Wastewater with gypsum | 9- Power supply (220 volt) |
| 5- Temperature sensor | |

3. Results and Discussion

3.1. Effect of Preheating Time

The preheating duration was found to have no significant effect on TSS as presented in Fig.2. A similar study showed that it took a period of (60-80 hours) to notice a transformation in gypsum seeds reflected an increase in the rate of crystallization of calcium sulfate dihydrate. Some residual gypsum is still present in the final stage of the reaction at longer periods (80–120 hours) but the examination of the progress of the reaction to 200 h indicates that conversion was complete [22,25]. This long time of transformation between the solid phase and the solution phase is thought to be due to the slow crystallization kinetics of calcium sulfate dihydrate [26], and while the solid phase may show the reaction is half completed, the calcium sulfate concentration in the solution phase reflects that the process not yet in equilibrium with the solids. This provides some evidence that the transformation involves a dissolution precipitation mechanism [27].

As a result, it is better to start the experiment without preheating duration and the wastewater added immediately after the temperature reaches near 100° C, this condition is optimum for time and energy saving (heater & motor).

As the results are shown in Fig.3. the preheating time does not affect the TDS of the solution, and the TDS values increased as a result of the evaporation process.

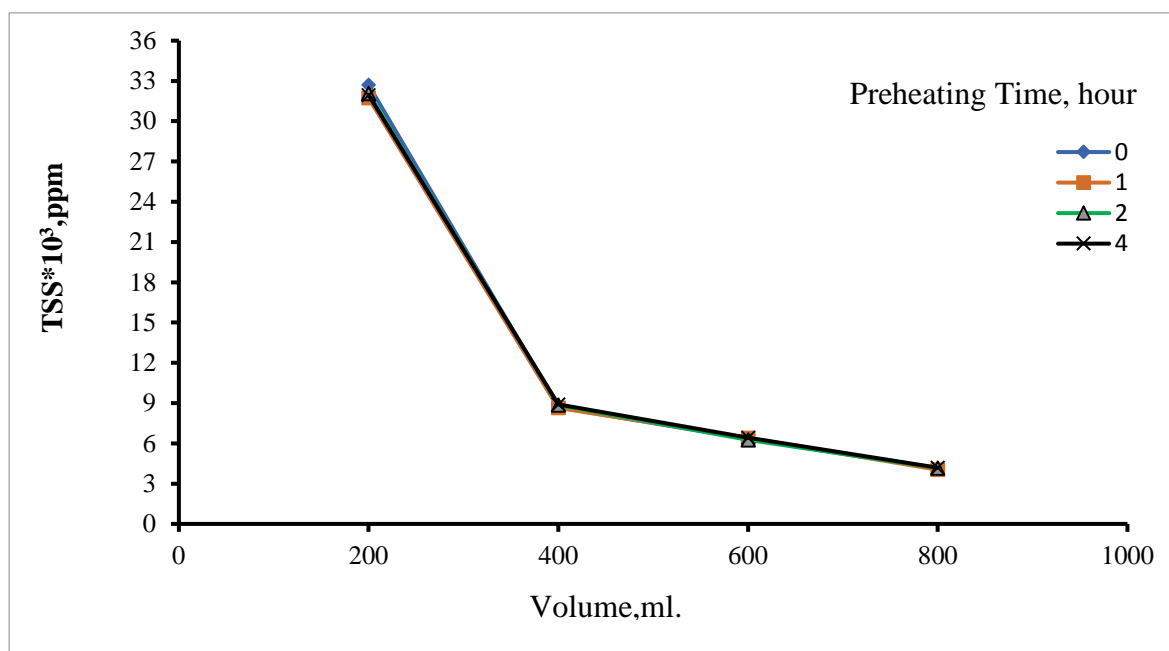


Fig. 2 - Effect of preheating time on TSS (feed ratio = RO 85% & Softener 15%, Temperature = 100 °C, pH = 10, initial gypsum concentration = 7 g/l, rotational speed = 25 RPM)

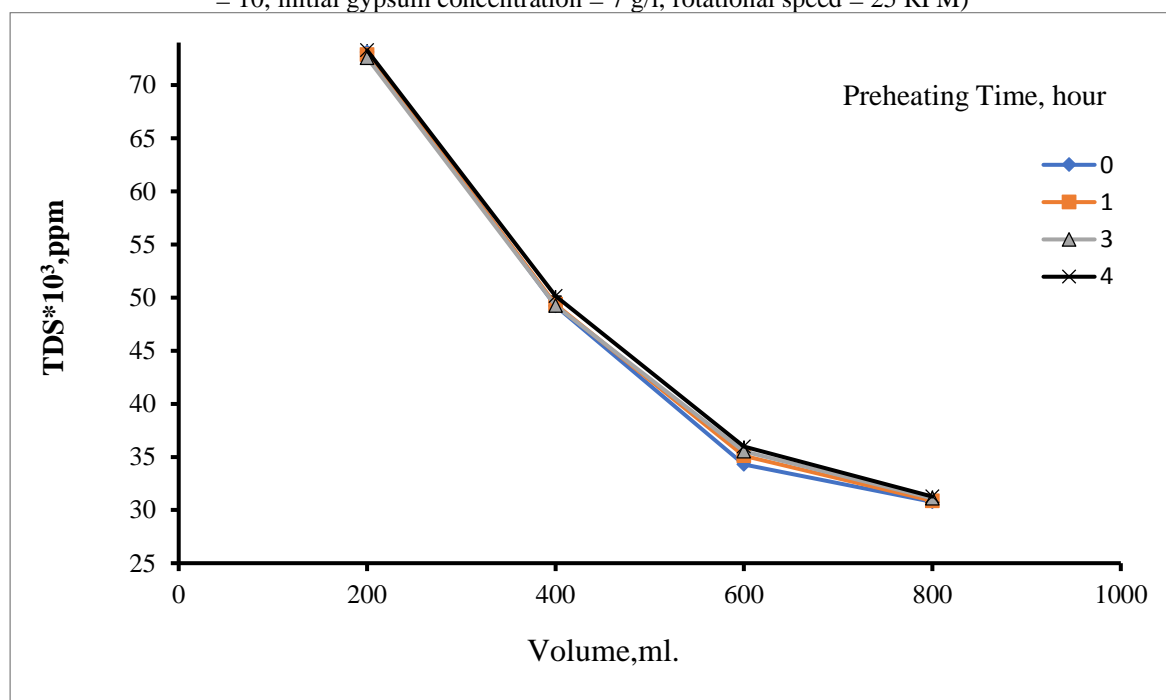


Fig. 3 - Effect of preheating time on TDS (feed ratio = RO 85% & Softener 15%, Temperature = 100 °C, pH = 10, initial gypsum concentration = 7 g/l, rotational speed = 25 RPM)

3.2. Effect of Rotational Speed

A study was established to investigate the role of agitation in the crystallization process of calcium sulfate [28], the precipitated calcium sulfate for mixtures with agitation is more than those without agitation, that agitation is usually disrupted aggregates and salts crystallized on the gypsum seeds [29].

The rotational speed has a minor effect on the value of TSS as shown in Fig.4. These results ascribed to the dispersion effect of salt crystallized on the seeds. The rate of crystallization for crystal growth of calcium sulfate dehydrate is independent of the stirring rate between 25 and 140 RPM [30,31]. The optimum speed was found 25 RPM for good TSS formation and less power consumption (of the motor).

As the results are shown in Fig.5. the rotational speed does not affect the TDS of the solution, and the TDS values increased as a result of the evaporation process.

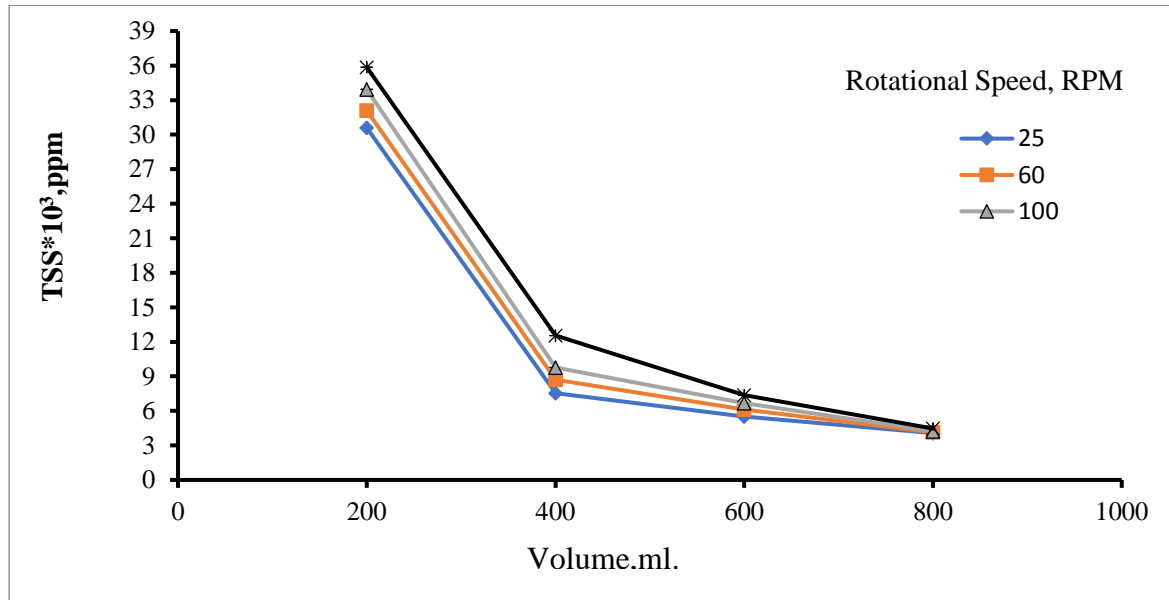


Fig. 4 - Effect of rotational speed on TSS (feed ratio = RO 85% & Softener 15%, Temperature = 100 °C, pH = 10, initial gypsum concentration = 7 g/l, no preheating time)

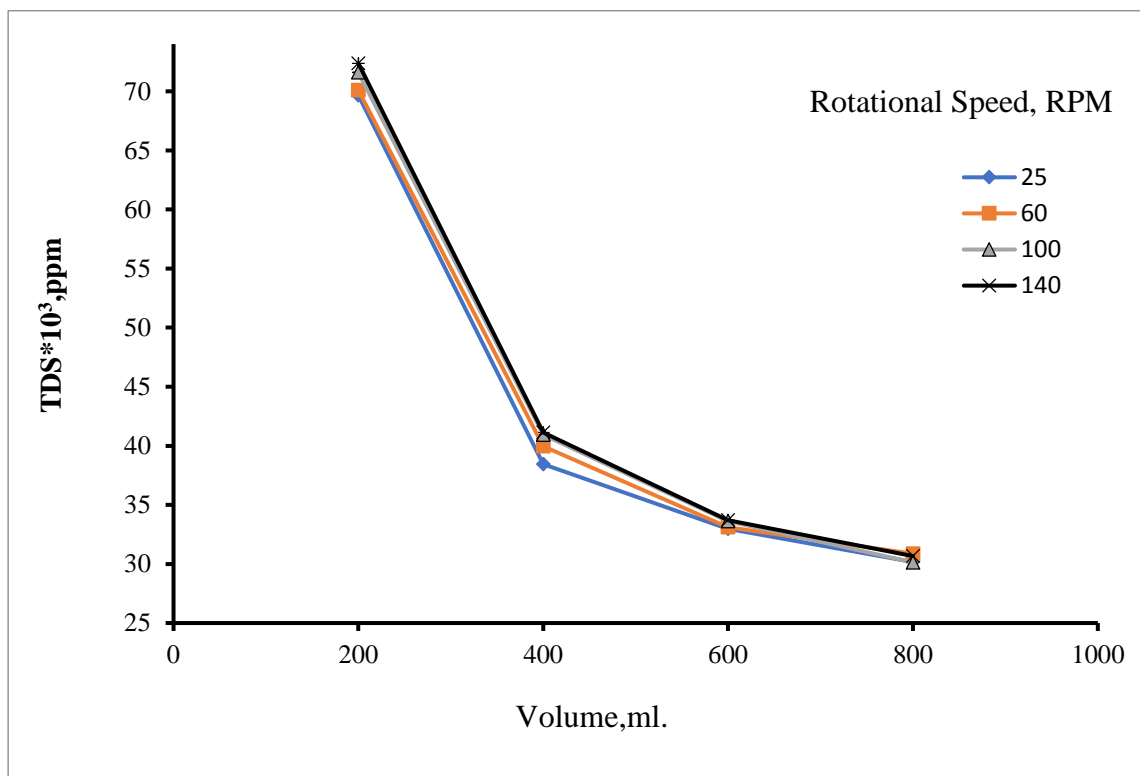


Fig. 5 - Effect of rotational speed on TDS (feed ratio = RO 85% & Softener 15%, Temperature = 100 °C, pH = 10, initial gypsum concentration = 7 g/l, no preheating time)

3.3 Effect of Initial Gypsum Concentration

The effect of initial gypsum concentration on TSS was shown in Fig.6. Starting with no seeds added for crystallization, the value of TSS was low and scales were formed on the inner wall of the beaker. By increasing gypsum seeds, the TSS was increased gradually till 7 g/l gypsum concentration, then the TSS increased remarkably at 9 g/l gypsum concentration. The TSS was noticeable on the gypsum surface and no scale formed on the beaker wall. The optimum amount was found to be 7 g/l and used in all remaining experiments.

The results mentioned above were also confirmed by the fact that additional particles provide additional surface area [32], which is indeed utilized for crystallization. From this observation, it can be deduced that the particles did indeed enhance the rate of nucleation and crystallization by providing a sacrificial surface for calcium sulfate precipitation [33-35]. This suggests that seeds particles provide better control for nucleation and crystal growth as the process was initiated and completed in less time than the unseeded experiment [30].

As the results are shown in Fig.7. the initial gypsum concentration does not affect the TDS of the solution, and the TDS values increased as a result of the evaporation process.

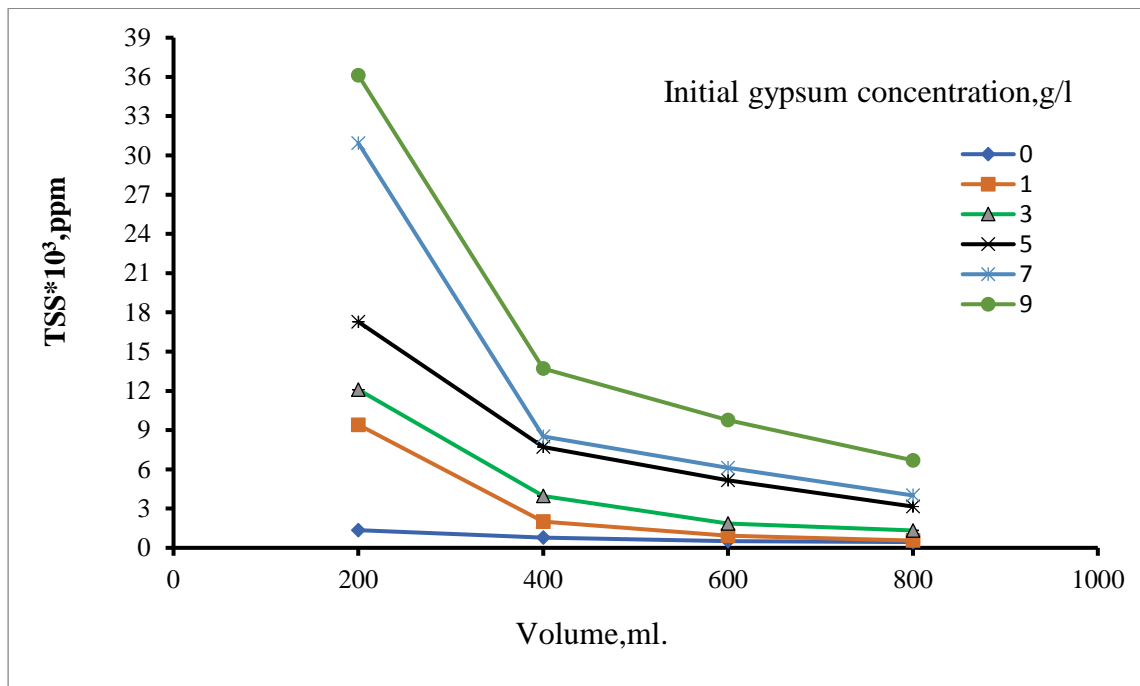


Fig. 6 – Effect of initial gypsum concentration on TSS (feed ratio = RO 85% & Softener 15%, Temperature = 100 °C, pH = 10, no preheating time)

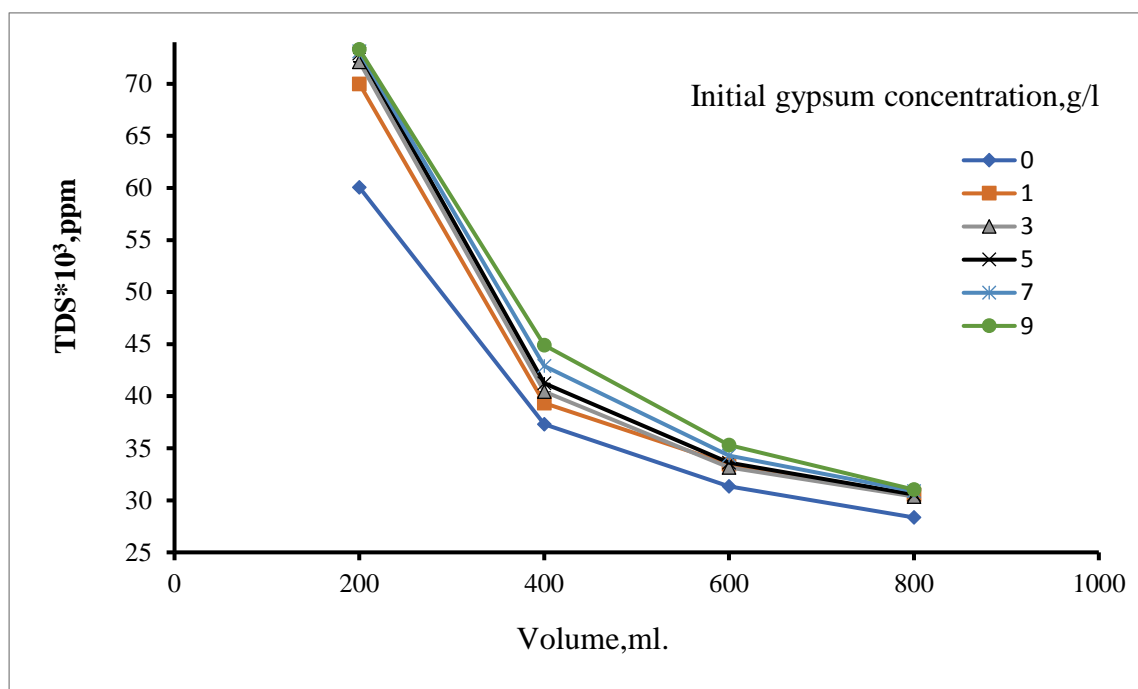


Fig. 7 - Effect of initial gypsum concentration on TDS (feed ratio = RO 85% & Softener 15%, Temperature = 100 °C, pH = 10, no preheating time)

4. Conclusions

Investigating some factors affecting the crystallization process of the salts of actual wastewater from a petrochemical plant, those salts were crystallized on the calcium sulfate (Gypsum) seeds which this technology used to reduce the formation of scale on the inner metal walls of the evaporator. It was found that when the initial amount of gypsum increased the values of TSS increased, the rotational speed has no effect on the value of TSS, also time has no effect of the formation of the TSS and found to be the best as it saves time and power consumption for preheating the solution and for the mixing motor. The best conditions found for the crystallization process were 7 g/l initial gypsum concentration, 25 RPM rotational speed & without any preheating time before treatment.

References

- [1] Hand, R.J., 1997. Calcium sulphate hydrates: a review. Br. Ceram. Trans. 96, 116–120.
- [2] Christensen, A.N., Olesen, M., Cerenius, Y., Jensen, T.R., 2008. Formation and transformation of five different phases in the $\text{CaSO}_4\text{--H}_2\text{O}$ system: crystal structure of the subhydrate $\beta\text{-CaSO}_4\cdot 0.5\text{H}_2\text{O}$ and soluble anhydrite CaSO_4 . Chem. Mater. 20, 2124–2132.
- [3] Solberg, C., Evju, C., Emanuelson, A., Hansen, S., 2002. Crystal structures of cementitious compounds part 3: calcium sulphates. ZKG Int. 55, 94–97
- [4] Doadrio, J.C., Arcos, D., Cabañas, M.V., Vallet-Regí, M., 2004. Calcium sulphate-based cement containing cephalixin. Biomaterials 25, 2629–2635.
- [5] Dathe, H., Jentys, A., Haider, P., Schreier, E., Fricke, R., Lercher, J.A., 2006. On the trapping of SO_x on $\text{CaO--Al}_2\text{O}_3$ -based novel high capacity sorbents. Phys. Chem. Chem. Phys. 8, 1601–1613

- [6] Lee, K., Teong, B., Subhash, M.J., Abdul, R., 2006. Preparation and characterization of CaO/CaSO₄/coal fly ash sorbent for sulfur dioxide (SO₂) removal: part I. *Energ. Source* 28, 1241–1249.
- [7] Dutrizac, J.E., 2002. Calcium sulphate solubilities in simulated zinc processing solutions. *Hydrometallurgy* 65, 109–135.
- [8] Dutrizac, J.E., Kuiper, A., 2006. The solubility of calcium sulphate in simulated nickel sulphate-chloride processing solutions. *Hydrometallurgy* 82, 13–31.
- [9] Adams, J.F., Papangelakis, V.G., 2007. Optimum reactor configuration for prevention of gypsum scaling during continuous acid neutralization. *Hydrometallurgy* 89, 269–278
- [10] Dutrizac, J.E., Kuiper, A., 2008. The solubility of calcium sulphate in simulated copper sulphate electro-refining solutions. *Hydrometallurgy* 92, 54–68.
- [11] Azimi, G., Papangelakis, V.G., 2010. The solubility of gypsum and anhydrite in simulated laterite pressure acid leach solutions up to 250 °C. *Hydrometallurgy* 102, 1–13.
- [12] Ghazal Azimi, Vladimiro G. Papangelakis, 2011. Mechanism and kinetics of gypsum–anhydrite transformation in aqueous electrolyte solutions. *Hydrometallurgy* 108, 122–129.
- [13] Li, Z., Demopoulos, G.P., 2005. Solubility of CaSO₄ phases in aqueous HCl+CaCl₂ solutions from 283 K to 353 K. *J. Chem. Eng. Data* 50, 1971–1982
- [14] Bansal, B., Muller-steinhausen, M., 1993. Crystallization fouling in plate heat exchangers. *J. Heat Transfer* 115 (3), 584–591
- [15] Hewitt, G.F., Shires, G.L., Bott, T.R., 1994. *Basic Theory of Heat Exchangers*, Process Heat Transfer. CRC Press, London, pp.155–158.
- [16] Bohnet, M., 1987. Fouling of heat transfer surfaces. *Chem. Eng. Technol.* 10 (1), 113–125.
- [17] Nofal, P., Allen, S., Hosking, P., Showell, T., 2001. Gypsum Control at Bulong: the Final Hurdle, ALTA 2001: Nickel/Cobalt-7 Technical Proceedings. ALTA Metallurgical Services, Melbourne, pp. 1–17.
- [18] Santen, R.A., 1984. The Ostwald step rule. *J. Phys. Chem.* 88, 5768–5769.
- [19] Nývlt, J., 1997. On the kinetics of solid–liquid–solid phase transformation. *Cryst. Res. Technol.* 32, 695–699.
- [20] Dutrizac, J.E., 2002. Calcium sulphate solubilities in simulated zinc processing solutions. *Hydrometallurgy* 65, 109–135.
- [21] Freyer, D., Voigt, W., 2003. Invited review, crystallization and phase stability of CaSO₄ and CaSO₄-based salts. *Monatsh. Chem.* 134, 693–719
- [22] Farrah, H.E., Lawrance, G.A., Wanless, E.J., 2004. Gypsum-anhydrite transformation in hot acidic manganese sulphate solution. A comparative kinetic study employing several analytical methods. *Hydrometallurgy* 75, 91–98.
- [23] American Public Health Association (APHA) section 2540 C - TDS.
- [24] American Public Health Association (APHA) section 2540 D - TSS.
- [25] Witkamp, G.J., Seckler, M.M., Bruinsma, O.S.L., Van Rosmalen, G.M., 1990. Recrystallization of calcium sulfate in phosphoric acid solutions: batchwise operation. *Journal of Crystal Growth*, 99 (1–4, Pt. 2), 1117–1123.
- [26] Freyer, D., Voigt, W., 2003. Crystallization and phase stability of CaSO₄ and CaSO₄-based salts. *Monatsh. Chem.* 134 (5), 693–719.
- [27] Cruft, E.F., Chao, P.-C., 1970. Nucleation kinetics of the gypsum–anhydrite system. *Symposium Salt* (1), 109–118.
- [28] Meisam Kamalipour, Seyyed Ali Mousavi Dehghani, Ali Naseri, Saeed Abbasi, 2017. Role of agitation and temperature on calcium sulfate crystallization in water injection process. *Journal of Petroleum Science and Engineering* 151, 362–372.

- [29] Li, D., Kaner, R.B., 2006. Shape and aggregation control of nano particles: not shaken,not stirred. J. Am. Chem. Soc. 128 (3), 968–975.
- [30] SUNG-TSUEN LIU and GEORGE H. NANCOLLAS, 1970. The Kinetics of Crystal Growth of Calcium Sulfate Dihydrate Journal Of Crystal Growth 6, 281-289.
- [31] G. H. Nancollas (1973).The Crystal Growth of Sparingly Soluble Salts. Croatica Chemica Acta 45.548.52.
- [32] G. H. NANCOLLAS, M. M. REDDY and F. TSAI., 1973. Calcium Sulfate Dihydrate Crystal Growth in Aqueous Solution at Elevated Temperatures, Journal of Crystal Growth 20, 125—134.
- [33] Shah, U.V., Williams, D.R., Heng, J.Y., 2012. Selective crystallization of proteins using engineered nanonucleants.Cryst. Growth Des.12 (3), 1362–1369.
- [34] W.N. Al Nasser, U.V. Shah, K. Nikiforou, P. Petrou, J.Y.Y. Heng, 2016. Effect of silica nanoparticles to prevent calcium carbonate scaling using an in situ turbidimetre chemical engineering research and design 110, 98–107.
- [35] Mullin, J.W., 1993. Crystallization, 3rd ed. Butterworth-Heinemann, UK.

12- Rice-straw: from Waste to Useful Product

Nada M. Ward[†]1, Esraa M. Kabary1, Heba A. Elmsiry1, Nada M. Elkony1, Mona
M. Naim1 1Chem. Eng. Dept., Fac. of Eng., Alexandria University, Alexandria,
Egypt

[†]E-mail: nadaward499@gmail.com

Abstract

Rice-straw (RS) has been considered an undesirable waste material for long, ever since man grew rice in open fields as a major source of starchy food beside wheat and corn. Farmers considered it a nuisance and burned it on site in the farms to get rid of it, thus polluting the air and environment with black smoke, which caused numerous lung infections and other ailments. Researchers and scientists have recently started to realize that RS could make very valuable and useful products, due to its unique chemical composition, being composed mainly of cellulose, hemicelluloses and lignin. Owing to the rise in wood consumption, the reserves of native woody species have been decreasing, causing the search for new renewable ligno-cellulosic materials that may efficiently meet the demand. This environmental pressure supports research regarding new products and a better utilization of the raw material available. Residue reutilization has been increasing, thus several researches have been investigating the characteristics of particleboards produced with these residues. Furthermore, there is the possibility of combining wood with other ligno-cellulosic materials aiming at obtaining more profitable products and with environmental marketing strategies, without reducing its quality. The particleboard industry in many parts all over the world uses mostly wood shavings from reforested, resulting in a higher quality product due to better control of the homogeneity of raw material. However, a recent alternative for particleboard production may be the use of agro-industrial ligno-cellulosic wastes to replace solid wood particles in the manufacture of composite panels. The aim of the present work was to prepare binderless-boards made from RS, in an effort to avoid its burning in open rice fields which presents an environmental problem due to the polluting smoke that is formed, and which causes a threat to living beings all over the globe and continues to increase gradual global warming. Besides, forestry has led to rapid diminution of wood available for making wooden-based material such as furniture and the like, and therefore alternative means for making such products had to be searched for. Accordingly, this work was directed toward preparing boards/panels via initial grinding of RS then pressing it at various pressures hydraulically to form a cohesive and strong board/panel, without using any adhesive, to replace wooden panels.

Keywords: Rice-straw, Ligno-cellulosic material, Binderless-board, Air-pollution, Hydraulic-pressing

Introduction

Since the beginning of the industrial revolution, the required energy for the developed industries has been extremely increased all around the world [1]. However, ease of access to the fossil fuels during almost two centuries has decreased the available fossil fuel reservoirs, causing the rising prices. Therefore, the energy supply for the future has become one of the most important global problems [2]. On the other hand, combustion of fossil energy carriers like petrol, natural gas and coal has led to the release of CO₂, NO_x and SO_x, which all cause huge environmental problems and adverse effects on human health and ecosystem [3]. Agriculture is not only important from

the economic point of view but even agricultural waste such as wheat straw, rice straw, can play an important role in meeting the growing energy demand of the society in a sustainable manner. In particular, ligno-cellulosic agricultural crops waste has huge unutilized energy generation potential [4]. Rice ranked at third as major agricultural crop grown in the world, in term of total cultivated area of 161.42 million hectare with a gross grain yield production of 678.69 million tons in year 2009. The total estimated dry -duct yield in any biological energy conversion processes [5]. As a matter of fact that the most part of biomass contents (carbohydrates, fats and proteins) in anaerobic digestion process are converted into simple derivatives, which finally transforms into biogas ($\text{CH}_4 + \text{CO}_2$) with the help of different types of anaerobic micro-organisms [4]. Further again, it has been found that biogas-to-electricity is among technologies having increasing production potential on criteria-based evaluation of low carbon power technologies. Therefore, biogas is able to contribute carbon neutral electricity. Moreover, by applying carbon capture and sequestration into biogas-to electricity the negative net CO_2 emissions can be achieved [6].

Nowadays, world faces the energy and environmental crisis due to the depletion of petroleum resources which results in the increasing oil price. This leads to public concerns on adequacy of long term energy supply and also environmental problems due to greenhouse gas release. Biofuel, particular bioethanol is a widely used alternative fuel in many countries which can be produced from renewable resources. Due to controversy on food vs. fuel issue, research on bioethanol production from alternative underused biomass is thus of great interest [7]. Utilization of renewable lignocellulosic materials as feedstock in biorefineries is considered a sustainable approach for production of biofuel and commodity chemicals. Moreover, the uses of agricultural by-products also has benefits on disposal of problematic solid wastes and provides opportunity to improve energy security, reduce the trade deficit, and decrease greenhouse gas emissions, which in overall improve value of agricultural by-products [8]. Lignocellulose materials consist of three primary chemical components: (a) cellulose, a linear homopolymer of glucose which forms into organized microfibril structure, (b) hemicellulose, amorphous heterogenous polymer of pentoses, hexoses, and sugar acids, and (c) lignin, a complex polymer of phenolic compounds which provides shields to external physical, chemical and biological stresses, in addition to other minor components such as ash, and a small amount of proteins. Conversion of lignocellulosic materials into fermentable sugars by enzymatic hydrolysis is an important step for further conversion to biorefinery products by fermentation or catalytic routes. Lignocellulosic materials are highly recalcitrant due to their rigid structure, particular by lignin which acts as physical barrier against hydrolytic enzyme penetration to the biomass microstructure. An effective pretreatment step is required in order to release the carbohydrates from lignin association which will lead to the increasing of fermentable sugars from the enzymatic hydrolysis step [9]. Different pretreatment methods, including physical, chemical, thermal and biological approaches are used to improve the availability of cellulose for enzymatic hydrolysis. Each pretreatment has its own effects on the cellulose, hemicellulose, and lignin fractions, which result in increased digestibility of plant biomass [10]. These include removal of hemicellulose and lignin, increase in biomass accessible surface area, and de-crytallization of cellulose. Alkaline peroxide provides an effective method for delignification and is considered a promising approach for low-energy pretreatment of lignocelluloses under mild conditions [11]. Principle of this method relies on formation of hydroperoxide anion formed in alkaline media which acts as active species in hydrogen peroxide bleaching systems. Decomposition products such as hydroxyl radicals and superoxide anion radicals cause oxidation of lignin structures, which leads to the introduction of carbonyl group,

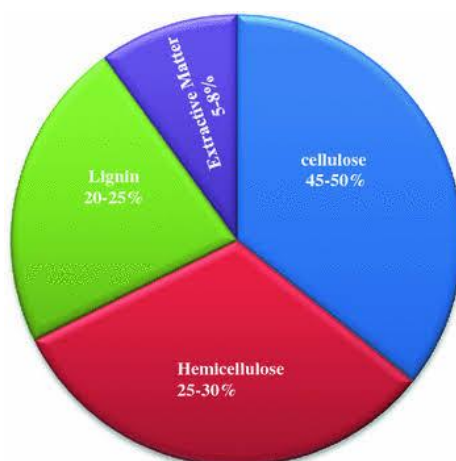
cleavage of some inter-unit bonds and eventually, the dissolution of lignin and hemicelluloses [12].

The chemical composition of rice straw

The chemical composition of rice straw varies between varieties and growing seasons, with higher nitrogen and cellulose contents in early-season rice compared to others (Shen et al., 1998)[13].

Nutritive quality of rice straw

Rice straw consists predominantly of cell walls, comprised of cellulose, hemicellulose, and lignin. To break down these components cellulose, hemicellulose and ligninase are required (Schiere and Ibrahim, 1989)[13]. These enzymes are not produced by the animals themselves but the reticulorumen of ruminants maintains microorganisms that do produce cellulose and hemicellulose. However, lignin cannot be broken down in the rumen due to the lack of ligninase. Even if lignin could be degraded in the rumen it would not provide much energy for the animals. Lignin, however, has important effects on livestock production through effects on degradability and feed intake. Theoretically, lignin located between the cellulose microfibrils is regarded as the most abundant natural aromatic organic polymer that plays a role in resisting compressing forces, providing protection against consumption by insects and mammals, and also inhibiting the rate and degree of microbial degradation (Iiyama et al., 1990)[14]. Silica, one element of the rice cell walls, can be present in high concentrations ranging from 5% to 15%, depending on the rice variety (Vadiveloo, 1992)[14] and the availability of this mineral in the soil (Agbagla-Dohnani et al., 2003)[14]. Silica reduces palatability and the degradability of rice straw in the rumen due to its direct action in preventing colonization by ruminal microorganisms (Bae et al., 1997; Agbagla-Dohnani et al., 2003)[14]. The role of silica on the quality of rice straw was also reviewed by Van Soest (2006), in an attempt to put into perspective the problems of silicon metabolism. Besides cell wall polymers, rumen organisms need other nutrients for growth and metabolism (Hoover, 1986)[14]. Since rice straw does not contain enough sugars, amino acids and minerals for efficient microbial growth, feeding ruminants with only rice straw, without any supplementation of the other required nutrient sources, will result in poor performance of the animals (Doyle et al., 1986)[14]. The combination of low intake, low degradability, low nitrogen content and an unbalanced mineral composition means that rice straw alone may not even meet the animal's maintenance needs. Poor degradability is caused by a series of factors (Schiere and Ibrahim, 1989)[14]. The fiber is very difficult to degrade, which is partly an intrinsic characteristic of the straw fiber. The degradation of the straw fiber is also complicated by the poor functioning of the rumen due to the unbalanced availability of nutrients, the low protein content, the lack of easily available energy and the low content of essential minerals such as P and S. Hence, due to the low degradability and the poor rate of degradation, animals will tend to consume less. The mechanism regulating voluntary intake of low quality feeds, such as rice straw, is still not fully understood. The rumen processing capacity is characterized by rumen fill, the rate of degradation of potentially degradable matter and the rate of passage out of the rumen. Devendra (1997)[14] summarized that the main determinants of intake and degradability of rice straw depend on their morphological characteristics, such as the proportion of the different plant parts (leaves and stems), their chemical composition and the distribution of the different chemical components in the tissues, their relative amounts of cell contents and cell walls and the physical and chemical nature of the cell walls. These factors influence the chewing behavior of animals and the extent of fragmentation in the reticulorumen.



The chemical composition of rice straw

Annual plant materials are promising candidates for alternative lignocellulosic fiber composites. Several annual plant fibers such as flax, hemp, jute, kenaf, bagasse, corn, and bamboo have been the subject of extensive research for the manufacture of non-wood particle and fiberboards (Youngquist et al. 1993, Rowell 2001)[15]. The agro-straw materials are abundant, inexpensive, and readily available sources of lignocellulosic fibers. The basic challenge for board producers is to convert the agricultural straw materials into particle boards, medium density fiberboards or high density fiberboards in a sound technical and economical process (Sauter 1996) [15].

In the morphological structure, straw from wheat and rice is less homogeneous than softwoods or hardwoods. Straw contrary to wood contains a relatively large number of cell elements, that is, fibers, parenchyma cells, vessel elements, and epidermic cells that comprise a high amount of ash and silica. In a cross section, the epidermic cells are the outermost surface cells and are covered by a thin waxy layer. This layer lowers the wet ability of straw with water-based formaldehyde resins. In addition, straw has a quite different chemical composition compared to wood. Straw has a higher content of hemicelluloses, ash, and silica, but a lower content of lignin compared with wood (Sudhakara and Sddhartha 1981)[16].

GENERAL CHARACTERISTICS OF RICE STRAW

Rice straw contains a relatively high proportion of leaf (60%), compared to other cereal straws such as barley (35%), oats (43%) and wheat (20-41%) (Theander and Aman, 1984). Leaves of rice straw contain less NDF than the stems, but more ash and acid-insoluble ash, resulting in a lower *in vitro* dry matter digestibility (IVDMD) of the leaves (50-51%) compared to the stems (61%) (Vadiveloo, 2000)[38]. In goats, Phang and Vadiveloo (1992) observed an *in vivo* dry matter digestibility of 56.2% for rice leaf and 68.5% for the stem. However, treatment with a 4% urea solution for 21 d increased the IVDMD of the leaf fraction more than that of the stem fraction (Vadiveloo, 2000). Since rice straw consists of approximately 60% leaves (Vadiveloo, 1995), which are less degradable than stems, improving the feed value of rice straw should focus on improving the degradability of the leaves[17].

STRATEGIES TO IMPROVE RICE STRAW UTILIZATION

Basically, the key to improving the use of crop residues for ruminants is to overcome their inherent barriers to rumen microbial fermentation. In the case of rice straw, the important factors that restrict bacterial degradation in the rumen are its high levels of lignification and silicification, and its low contents of nitrogen, vitamins and minerals. To improve the feeding value of rice straw, the straw can be treated with different means and methods and other required nutrients can be supplied to the ration of the animal. (after Ibrahim, 1983)[17].

Physical treatment

Crop residues can be ground, soaked, pelleted or chopped to reduce particle size or can be treated with steam or X-rays or pressure cooked. Uden (1988) observed that grinding and pelleting of grass hay decreased dry matter degradability in cows from 73 to 67%, which was mainly due to a decreased fermentation rate (9.4-5.1%/h) and decreased total retention time of the solids from 73 to 54 hours, resulting in an increased intake (Stensig et al., 1994). Liu et al. (1999) reported that the use of steam treatment in a high pressure vessel at different pressures and for a range of different treatment times increased the degradation *in vitro* in rumen fluid after 24 h and the rate of degradation, but could not enhance the potential degradability of the fibrous fractions (NDF, ADF and hemicellulose). Physical treatments of crop residues have received an appreciable amount of research. Many of these treatments are not practical for use on small-scale farms, as they require machines or industrial processing. This makes these treatments in many cases economically unprofitable for farmers as the benefits may be too low or even negative (Schiere and Ibrahim, 1989). However, small machines to grind or chop rice straw may be feasible [17].

Chemical treatment

Chemicals to improve the utilization of rice straw may be alkaline, acidic or oxidative agents. Among these, alkali agents have been most widely investigated and practically accepted for application on farms. Basically, these alkali agents can be absorbed into the cell wall and chemically break down the ester bonds between lignin and hemicellulose and cellulose, and physically make the structural fibers swollen (Chenost and Kayouli, 1997; Lam et al., 2001). These processes enable the rumen microorganisms to attack more easily the structural carbohydrates, enhancing degradability and palatability of the rice straw (Prasad et al., 1998; Shen et al., 1999; Selim et al., 2004). The most commonly used alkaline agents are sodium hydroxide (NaOH), ammonia (NH₃) and urea [17].

NH₃ treatment : Treatment of straw with anhydrous and aqueous ammonia, urea or other ammonia-releasing compounds has been widely investigated to improve degradability (Abou-EL-Enin et al., 1999; Selim et al., 2002; Fadel-Elseed et al., 2003). The principle of ammonia treatment is supposed to be similar to that of NaOH treatment. Ammonia treatment not only increases the degradability of the straw, but also adds nitrogen (Abou- EL-Enin et al., 1999) and preserves the straw by inhibiting mould growth (Calzado and Rolz, 1990). Besides, improvement in degradability of structural carbohydrates, ammonia treatment is an effective means of reducing the amount of supplemental nitrogen, reducing the costs of purchasing protein-rich feedstuffs, and enhancing acceptability and voluntary intake of the treated straw by ruminants. Although comparative studies in improving the energy value of straw have shown that ammonia treatment is less efficient than NaOH (Liu et al., 2002), its use may be more profitable for farmers as the added ammonia serves as a source of nitrogen. In a previous study using sheep, Selim et al. (2004)

treated rice straw packed in polyethylene bags for 4 weeks with gaseous ammonia (3 g NH₃ per 100 g drymatter). The excess was removed before offering the straw to animals. The ammonia treatment increased the N content in the rice straw from 8.16 to 18.4 g kg⁻¹ (CP content increased from 51 to 115 g kg⁻¹). The ammonia treatment slightly decreased the NDF content from 571 to 551 g kg⁻¹, because of dilution with the additional N, but increased the ADF content from 303 to 327 g kg⁻¹, indicating that the cell wall properties were changed. Moreover, the physical strength of ammoniated rice straw was significantly lower than that of the untreated straw. [17].

Urea treatment: Rice straw can also be treated with urea, which releases ammonia after dissolving in water. For practical use by farmers, urea is safer than using anhydrous or aqueous ammonia and also provides a source of nitrogen (crude protein) in which straw is deficient (Schiere and Ibrahim, 1989). Since urea is a solid chemical, it is also easy to handle and transport (Sundstøl and Coxworth, 1984) and urea can be obtained easily in many developing countries. In addition, urea is considerably cheaper than NaOH or NH₃. Vadiveloo (2003) reported that rice varieties with a low degradability responded better to urea treatments than higher quality straw, increasing the *in vitro* dry matter degradability from 45 to 55-62%. Urea treatment may therefore be most suitable for small-scale farmers to improve the quality of straws, particularly varieties showing a low degradability. In the past, numerous investigations involving urea treatment of rice straw, with or without additional supplementation, were performed not only in the laboratory (Reddy, 1996; Shen et al., 1998; 1999; Vadiveloo, 2003) but also in field trials (Prasad et al., 1998; Vu et al., 1999; Akter et al., 2004). Pradhan et al. (1997) showed that addition of Ca(OH)₂ to urea improved the IVDMD. Sirohi and Rai (1995) demonstrated that a combination of 3% urea plus 4% lime at 50% moisture for 3 weeks incubation time was the most effective treatment for improving degradability of rice straw. Using urea is regarded as a practical and available method in livestock production, especially in developing countries, as it is relatively cheap, adds nitrogen to the ration and is relatively safe to work with.

Lime treatment: Lime (CaO/Ca(OH)₂) is a weak alkali agent with a low solubility in water. It has been reported that lime can be used to improve the utilization of straw and also can be used to supplement the ration with calcium, which has been found to be in a negative balance in cattle fed only rice straw (Hadjipanayiotou, 1984; Pradhan et al., 1997; Chaudhry, 1998). Soaking and ensiling are two methods of treating straw with lime. Although lime treatments increase the degradability of straw, the dry matter intake decreases, due to a reduced acceptability of the treated feed by animals. Pradhan et al. (1997) reported that ensiling rice straw with 4 or 6% Ca(OH)₂ showed a higher IVDMD than using 4 or 6% urea. However, mould growth was noticed in the Ca(OH)₂ treated straw. It was suggested that a combination of lime and urea would give better results than urea or lime alone. This combination has the advantage of an increased degradability and an increased content of both calcium and nitrogen. Additive effects of lime and the other alkali agents have been demonstrated (Saadulah et al., 1981; Hadjipanayiotou, 1984). The use of lime may be safer and more cost effective to use than NaOH[17].

Feeding rice straw supplemented with other components

As rice straw is low in nitrogen and difficult to degrade, it is obvious that supplementation of a ration of rice straw with a protein source and a more easily accessible energy source will improve the performance and production of the animals. Supplementation of a ration of rice straw with protein, energy and/or minerals may optimize rumen function, also maximizing utilization of the rice straw and increasing intake. Chenost and Kayouli (1997) emphasized that it is primarily necessary to supply the rumen microorganisms with the nutritive elements needed for self

multiplication as well as for degradation of the cell walls of straw, leading to suitable conditions for maintenance of good cellulolysis. Different supplements can be used, such as concentrates, molasses, multi-nutrient blocks, green leaves, crop residues and locally available by-products. In the case of high-yielding dairy cows, the supplements can be the major part of the ration where fibrous feed only serves to supply the rumen with enough fiber. Warly et al. (1992) showed in a field trial that a ration of rice straw supplemented with soybean meal increased both degradability and intake. Because of the poor quality of untreated rice straw, supplementation easily can increase milk production, as shown for supplementation with cottonseed meal (Wanapat et al., 1996) and with an ureamolasses- multi-nutrient block (Vu et al., 1999; Wanapat et al., 1999; Akter et al., 2004) [17].

Uses of Rice Straw

1. Board Manufacture

Straw has not been utilised before for board production with the use of conventional formaldehyde based resins because its fiber cells are surrounded by a layer of wax/silica. This layer prevents the water based formaldehyde resins - which are widely used today in the industrial fiberboard manufacture – from forming a sufficiently strong bond between the fibers. However, the new technology enables the destruction of the wax/silica layer by using mechanical high shear forces accompanied by a thermal and chemical treatment. This combined chemi-thermo-mechanical process subsequently refines straw and allows the formaldehyde resins to penetrate and adhere the individual straw fibers. The board produced known as strawboard matches MDF (medium density fiberboard from wood) in appearance, surface smoothness and strength.

In overall, the new process has two major advantages:

- It promises to be at least 20% cheaper compared to the existing processes; therefore, possesses the potential to have a huge impact on the market.
- It is an environmentally friendly process by which agricultural residues are recovered and transformed into value-added products[16].



2. Food for Ruminants

In tropical zones in the world, ruminants depend on year-round grazing on natural pastures or the animals are fed with cut grass and crop residues. Most of these areas face seasonal dry periods in which the availability of pasture decreases, and also its quality by a reduction in the content of

digestible energy and nitrogen. Due to the fact that in these areas rice straw is abundantly available from cultivating rice, farmers offer rice straw as the main roughage source to their animals. This is particularly the case in Southeast Asian countries such as Thailand, Vietnam and Indonesia (NARC newsletter, 2004). Feeding only rice straw does not provide enough nutrients to the ruminants to maintain high production levels, due to the low nutritive value of this highly lignified material. The high level of lignification and silicification, the slow and limited ruminal degradation of the carbohydrates and the low content of nitrogen are the main deficiencies of rice straw, affecting its value as feed for ruminants (reviewed by Van Soest, 2006). By treating rice straw with urea or calcium hydroxide or by supplementing rice straw with protein, intake, degradability and milk yield can be enhanced, compared to feeding untreated rice straw alone (Fadel Elseed, 2005; Wanapat et al., 2009). In past years, several studies have been reported on the physical and chemical characterization and utilization of rice straw as ruminant feed (Shen et al., 1998; Abou-El- Enin et al., 1999; Vadiveloo, 2000; 2003) [13].

3. Building Materials

The development of natural material cementitious composites to produce building materials for construction is going for many years. India is one of the largest rice Producing countries and per capita rice consumption is higher than that in any other countries. There are main three biomass byproduct comes from rice viz. rice straw, rice husk and rice bran. Rice straw, rice husk and rice bran are used as feed for cattle, poultry, fish etc. In villages people also use rice straw in cooking and other purpose by burning. After burning a huge amount of rice straw, ash is produced and dumped it as waste which creates an environmental problem though some time it is used in the agricultural land. For decreasing the cost of construction materials and raising environmental concerns, considerable efforts are being taken worldwide to utilize local natural waste and byproduct materials to improve the performance of construction materials. Conventional building materials are beyond the reach of a majority of the world population due to their poor affordability. Rice straw is one of the major agricultural byproduct and available all parts of the world.

During growth, rice plants absorb silica from the soil and accumulate it into their structures. It is this silica, concentrated by burning at high temperatures removing other elements, which make the ash so valuable. Amongst the agricultural waste, rice straw has a very high potential for the production of very effective secondary raw material. It is mainly due to its random availability, very high silica content and relatively low cost. After burning rice straw and husk in controlled temperature and duration using properly small plants, 14.6 % and 22% of mass rice straw and husk respectively are converted into high quality value added ash which unique secondary raw material due to the high amount of silica in the ash .

Rice straw and husk are composed of both organic and inorganic matter. Organic matter consists of cellulose, lignin, hemi cellulose, some proteins and vitamins while the major component of inorganic minerals is silica. The actual composition of rice straw and husk varies with the type of paddy, inclusion of bran and broken rice in the husk, geographical factors, crop season, samples preparation and relative humidity. This is a bio waste from the rice plant. The silica is absorbed from the ground and gathered in the straw where it makes a structure and is filled with cellulose. When cellulose is burned, only silica is left which is grinded to fine powder which is used as pozzolana [18].

4. Enhancing soil quality

Application of crop and plant biomass for improving soil organic matter and enhancing soil quality is well recognized in sustainable agriculture (Carter et al, 1988; Kay, 1998). Recycling of these surplus agricultural byproducts has the advantage to meet nutrient requirements for the crop and expanded use as effective soil amendments. During the last few decades much attention has been paid to the utilization of crop and plant residues as soil amendments as well as to evaluate the effects of existing organic matter on soil physical properties such as soil structure and aggregate stability (Tisdal and Oades, 1982; Debosz et al, 2002), porosity and pore size distribution (Schjonning et al, 2002), bulk density (Gupta et al, 1977) and water holding capacity (Rawls et al, 2003; Miller et al, 2002). Mando et al, 2004 found that farmyard manure and rice straw had higher percentage of water stable aggregates, greater mean weight diameter, higher porosity, lower bulk density, higher available water capacity and higher hydraulic conductivity of saturated soil. Saddiq and Al-Ameer also studied the effect of addition of poultry waste and rice straw on the soil physical properties of clay soil [19].

5. Removal of Heavy Metals

Decontamination of heavy metals in the soil and water around industrial plants has been a challenge for a long time. A number of efficient methods have been developed for the removal of heavy metals from liquid wastes such as precipitation, evaporation, electroplating, ion exchange, membrane processes, etc. However, these methods have several disadvantages such as unpredictable metal ion removal, high reagent requirement, generation of toxic sludge, etc. The removal of heavy metals from our environment especially wastewater is now shifting from the use of conventional adsorbents to the use of biosorbents. Biosorption is a process, which represents a biotechnological innovation as well as a cost effective tool for removing heavy metals from aqueous solutions. The pollutants of concern include uranium, selenium, zinc, arsenic, cadmium, lead, chromium, mercury, gold, silver, copper and nickel. These toxic materials may be derived from mining operations, refining ores, sludge disposal, fly ash from incinerators, the processing of radioactive materials, metal plating, or the manufacture of electrical equipment, pesticides or preservatives, paints, alloys, batteries. Hence, easy, effective, economic and ecofriendly techniques are required for fine-tuning of wastewater treatment. In this present review investigates that the bases for the biosorption, mechanism and its necessity for the removal of heavy metals. Toxic metals are often discharged by a number of industrial processes and this can lead in turn to the contamination of freshwater and marine environment. Heavy metals are major pollutants in marine, ground, industrial and even treated wastewaters. Industrial waste constitutes the major source of various kinds of metal pollution in natural waters. The important toxic metals i.e. Cd, Cu, Zn, Ni, and Pb finds its way to the water bodies through waste waters. Many physico-chemical methods have been proposed for their removal from industrial effluents. Adsorption is an effective purification and separation technique used in industry especially in water and wastewater treatments. Cost is an important parameter for comparing the sorbent materials. Byproducts of soybean and cottonseed hulls, rice straw and sugarcane Bagasse were evaluated as metal ion adsorbents in aqueous solutions[20].

Conclusions

Rice straw has been considered for long a nuisance to the farmers, and was therefore wasted by burning in open fields which polluted the environment intensively. It has been shown in this paper that, recently, it has been realized that rice straw could be used in making useful products such as

1. Boards and panels which can replace wood, which comes from trees that are depleting all around the globe, in making boards of different kinds, which may be used in making tables and chairs,
2. Food for ruminants, by treating rice straw with urea or calcium hydroxide etc. in order to improve the utilization of rice straw by ruminants, or by supplementing rice straw with protein, to enhance intake, degradability and milk yield.
3. Building materials for decreasing the cost of construction materials and raising environmental concerns, considerable efforts are being taken worldwide to utilize local natural waste and byproduct materials to improve the performance of construction materials.
4. Enhancing soil quality whereby utilization of rice straw improves soil physical properties such as soil structure and aggregate stability, porosity and pore size distribution, bulk density and water holding capacity.
5. Removal of heavy metals from wastewater and soil via biosorption with rice straw, which is cheaper than other methods of decontamination.

References

- [1] Cheremisinoff N. (2002). Handbook of water and wastewater treatment technologies. USA: Butterworth-Heinemann.
- [2] Deublein D, Steinhauser A. (2008) Biogas from waste and renewable resources. Wiley-VCH Verlag GmbH & co KGaA.
- [3] Mussgnug JH, Klassen V, Schluter A, Kruse O. (2010). Microalgae as substrate for fermentative biogas production in a combined biorefinery concept. J Biotechnol;150(1):51–6.
- [4] Chandra, R., Takeuchi, H., Hasegawa, T., & Kumar, R. (2012). Improving biodegradability and biogas production of wheat straw substrates using sodium hydroxide and hydrothermal pretreatments. Energy, 43(1), 273–282. doi:10.1016/j.energy.2012.04.029
- [5] Chandra, R., Takeuchi, H., & Hasegawa, T. (2012). Hydrothermal pretreatment of rice straw biomass: A potential and promising method for enhanced methane production. Applied Energy, 94, 129–140. doi:10.1016/j.apenergy.2012.01.027
- [6] Chandra R, Takeuchi H, Hasegawa T. (2012). Methane production from lignocellulosic agricultural crop wastes: a review in context to second generation of biofuel production. J Renewable Sustainable Energy Rev 2012;16:1462e76. doi:10. 1016/j.rser.2011.11.035.
- [7] Gould, J.M. (1984). Alkaline peroxide delignification of agricultural residues to enhance enzymatic saccharification. Biotechnology and Bioengineering, 26, 46-52.
- [8] Martin, N., Anglani, N., Einstein, D., Khrushch, M., Worrell, E., & Price, L. K. (2000). Opportunities to improve energy efficiency and reduce greenhouse gas emissions in the US pulp and paper industry. [9] Alvira, P., Tomás-Pejó, E., Ballesteros, M., & Negro, M. J. (2010). Pretreatment technologies for an efficient bioethanol production process based on enzymatic hydrolysis: a review. Bio resource technology, 101(13), 4851-4861.
- [10] Hendriks, A. T. W. M., & Zeeman, G. (2009). Pretreatments to enhance the digestibility of lignocellulosic Biomass. Bio resource technology, 100(1), 10-18
- [11] Yamashita, Y., Shono, M., Sasaki, C., & Nakamura, Y. (2010). Alkaline peroxide pretreatment for efficient enzymatic saccharification of bamboo. Carbohydrate Polymers, 79(4), 914-920.
- [12] Sun, R., J. Tomkinson, et al. (2000). "Comparative study of hemicelluloses from rice straw by alkali and hydrogen peroxide treatments." Carbohydrate Polymers 42(2): 111-122.

- [13] C. Sarnklong, J. W. Cone*, W. Pellikaan and W. H. Hendriks, Utilization of Rice Straw and Different Treatments to Improve Its Feed Value for Ruminants: A Review, Asian-Aust. J. Anim. Sci. Vol. 23 (2), 2010
- [14] C. Sarnklong, J. W. Cone*, W. Pellikaan and W. H. Hendriks, Utilization of Rice Straw and Different Treatments to Improve Its Feed Value for Ruminants: A Review, Asian-Aust. J. Anim. Sci. Vol. 23 (3), 2010
- [15] Atanu Kumar Das, Rumana Rana, Using of Rice Straw (Oryza Sativa L.) for Better Purposes Fabricating and Mechanical Properties of Fiberboard , researchgate, 2014
- [16] GEORGE MANTANIS, PANAGIOTIS NAKOS, JOCHEM BERNIS, LUC RIGAL, TURNING AGRICULTURAL STRAW RESIDUES INTO VALUE –ADDED COMPOSITE PRODUCTS: A NEW ENVIRONMENTALLY FRIENDLY TECHNOLOGY,
- [17] Sarnklong et al. (2010) Asian-Aust. J. Anim. Sci. 23(5):680-692
- [18] Surajit Munshi, Gopinandan Dey, and Richi Prasad Sharma, Use of Rice Straw Ash as Pozzolan Material in Cement Mortar, IACSIT International Journal of Engineering and Technology, Vol. 5, No. 5, October 2013
- [19] Muneer H Saddiq, Hadie Abd Al-Ameer The effect of rice straw and poultry waste addition on the soil physical properties I- clay soil, RESEARCHES of THE FIRST INTERNATIONAL CONFERENCE (BABYLON AND RAZI UNIVERSITIES) (2011)
- [20] L. Nageswara Raoa , Dr G.Prabhakara, REMOVAL OF HEAVY METALS BY BIOSORPTION–AN OVERALL REVIEW, Journal of Engineering Research and Studies E-ISSN0976-7916 JERS/Vol. II/ Issue IV/October-December, 2011/17-22

13- Hydrodynamic effect of groins on the estuary exits

M. Abd EL-Mooty¹ and N. H. Ali^{†2}

¹ Faculty of Engineering, Hydraulics department ,Alexandria University

² Coastal Research Institute, 15 El Pharaanastreet ElShallat ,Alexandria, Egypt

[†]E-mail: nourhanhassan291@gmail.com

Abstract

The Nile Delta coastal zone faces serious erosion, which observed along some beaches of the Nile Delta coast. In the absence of a sediment supply, after construction of Aswan High Dam (AHD) in 1964 that dramatically decreased both water discharge and sediment transport to the sea. The continued transport of beach sediments by marine processes which include winds, waves, littoral currents, tides, together with Coriolis Effect due to rotation of the earth, towards the east has resulted in dramatic erosion, migration exits of some estuaries to east, and direct their discharge anti-clock wise. Examples of these estuaries are exit of El Burullus lake, west Noubaria drain, Gamasa drain and Kitchener drain. The Egyptian government has implemented many protection structures to protect the eroded areas and stop migration of estuaries' exits by constructing seawalls, jetties, groins, revetments, and detached breakwaters. The presented study concentrates on the hydrodynamic effect of groins on the estuary exits at the Mediterranean coast of the Nile Delta. Gamasa drain is taken as a study case. Depending on Delft 3D, a 2D model is prepared for the study area by using the field measured data, the effect of the earth rotation is obtained. The necessary precautions against Coriolis Effect can be taken by groins at the east side of the estuary, which decrease the effect of littoral processes at the area just eastern exit of estuary. The details of the study are given in the paper.

Keywords: Groins, littoral currents, and Delft 3D.

1 Introduction

The Nile delta coast is a typical wave- and current-dominated environment. The erosion of the Nile Delta coast was first observed in 1898, but accelerated after the construction of the Aswan High Dam (AHD) in 1964. The dam not only decreased the sediment supply but also decreased water discharge to the sea. The Nile Delta shoreline faces serious erosion has been observed along some beaches of the Nile Delta. In the absence of a sediment supply, the continued transport of beach sediments by marine processes which include winds, waves, littoral currents, tides, together with Coriolis Effect due to rotation of the earth, to the east has resulted in dramatic erosion and migration of exits of some estuaries. The eroded sand is generally transported along the shore from the eastern side of estuary outlet move partly offshore and partly eastwards due to the prevailing wave arrived from the northwest (CORI, 1978). Erosion is not the only problem occurring along the Mediterranean coast of Egypt. It is noticed that the exits of some main estuaries tend to migrate in the direction of the littoral sediment transport and direction of their discharge to the sea. The exits of these estuaries tend to move eastward and direct its discharge anti-clock wise due to Coriolis Effect. Examples of these estuaries are exit of El Burullus Lake, west Noubaria drain, Gamasa drain and Kitchener drain, as shown in fig.1. This problem is mitigated by the construction of a series of coastal engineering structures at the rapidly eroding beaches. Many measures have implemented by the Egyptian government, to protect the eroded areas by constructing seawalls, jetties, groins, revetments, and detached breakwaters. While the Nile Delta coast suffers from severe erosion problems, there is shoreline retreat and erosion at zones of down

drift of the structures' lee side. This erosion took place due to the action of the littoral processes (wave, littoral current actions, and Coriolis force). Coriolis force causes water to move anti-clock wise in the northern hemisphere and clock wise in the southern hemisphere (N.H. Ali, 2018). The exits of estuaries tend to migrate eastward due to the direction of the littoral sediment transport and Coriolis force.

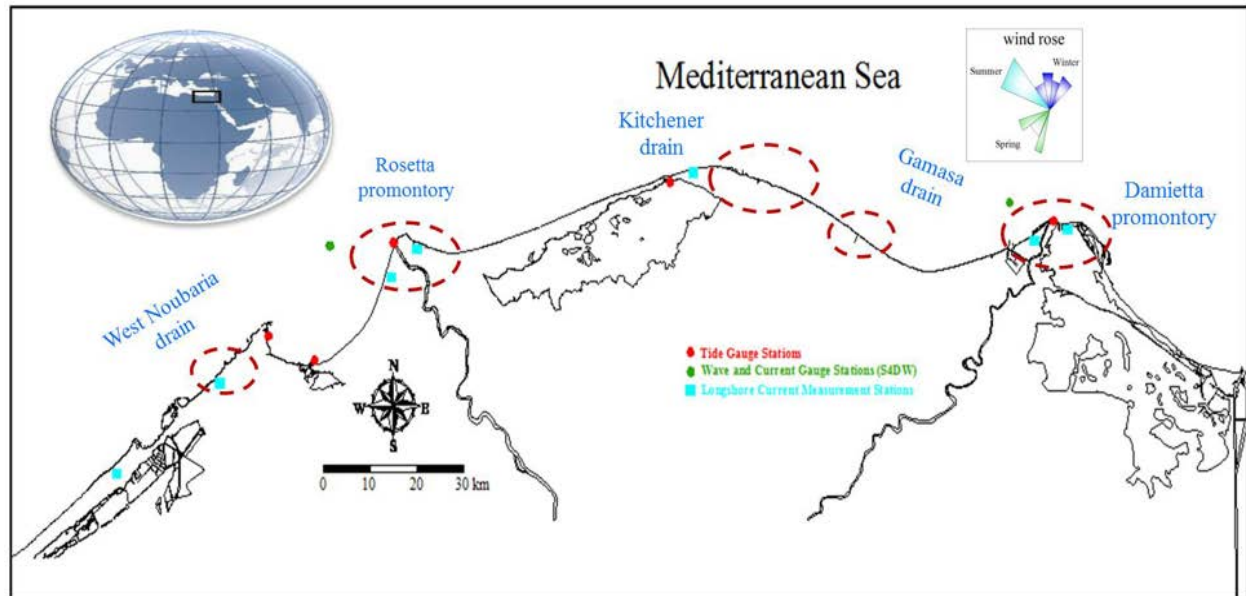


Figure 1. Map of the Nile Delta coast, (wave, current, and tide measurement stations), and examples of estuaries exits.

Gamasa drain is taken as study case. The study area suffering from shoreline retreating and the drain outlet has been moved eastward due to decrease of the discharge water to the sea and the coastal processes. It is noticed that the exit of the drain tends to migrate to the east in the direction of the littoral sediment transport and direction of its discharge to the sea (CORI, 2013).

Groins are cross shore structures built to promote shoreline stabilization. However, the specific impact of these structures on the wave conditions, velocity field nearshore and sediment transport. This paper aims to study the hydrodynamic effect of groins on the estuary exit under the influence of different significant incident-wave heights. the effect of the earth rotation (Coriolis force) and effect maximum wind are obtained in the study.

Two techniques are applied at the study area to achieve that:

- First, analysis of field data.
- Second, numerical modeling by using Delft 3D.

DELFT 3D is a numerical modeling program that is designed to solve non-steady flows and transport phenomena in coastal, river and estuarine areas, which make it an ideal tool for this project. Also one of Standard features for Delft 3D is The effect of the Earth's rotation (Coriolis force), so The Delft2D-Flow and Delft2D-WAVE software have been used in this study (Deltares, 2013).

2 Groins behavior

Groins are cross-shore structures projected to retain sediments from the littoral drift, to attenuate the erosion of specific coastline stretches. The shoreline adjusts to the presence of the obstruction

in littoral sediment transport, and after some time, accretion causes a positive increase in beach width updrift of the groin. Conservation of sand mass then produces erosion and decrease in beach width on the downdrift side of the groin (Basco, 2006), fig.2.

The real impact and dependence of groins on the wave conditions and the velocity field nearshore is still an ongoing field of investigation and thus requires further research. Several authors have been pursuing this aim. Authors like Dean (1978) started understanding wave diffraction and current patterns on the lee-side of groins.

The direction of incident waves is also of particular importance in these kind of studies, as the waves arriving and breaking with different angles relatively to the beach. Authors such as Pattiaratchi et al. (2009) have studied the nearshore current system resulting from the presence of a groin, using surf-zone drifters.

Hence, and to bring further insight on this matter, this work presents a numerical modeling study of groin impact on significant wave height and littoral currents, accounting for different incident wave heights and sea-surface levels.



Figure 2. Protection structures at Gamasa drain exit (groins and jetties) (Google earth maps).

the Coriolis effect prominently in studies of the coastal dynamics, in which it affects prevailing winds and, the rotation of the coastal currents. These effects can be explained in terms of an 'imaginary' force called the Coriolis force. This force causes water to move to the right in the

Northern Hemisphere and to the left in the Southern Hemisphere, (Stull, R., 2011), as shown in fig. 3.

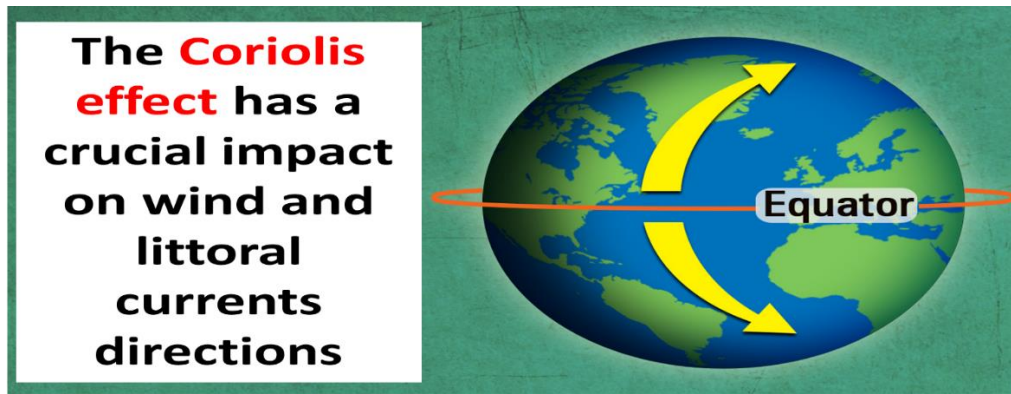


Figure 3. Direction of wind and littoral currents due to Coriolis effect (the Encyclopedia Britannica).

3 Case study (Gamasa drain)

Gamasa drain outlet is located nearly 40km to the west of Damietta Nile branch (fig. 4). The drain was constructed to collect drainage water from the secondary drains distributed over cultivated land of Dakahliaa Governorate. The drain outlet was perpendicular to the shoreline and the flow velocities of drainage water were sufficient to flush the sediment deposited in the drain mouth. The drain outlet has been moved eastward due to decrease of the discharge water to the sea and the coastal processes. The eastward sediment transport causes the accumulation of sediments in drain channel and migration of the outlet eastward. The maximum migration reaches about 1.50 km eastward, (N.H. Ali, 2013).



Figure 4. Migration of Gamasa Drain exit from (2003 to 2019), (Google earth maps).

Fig. 4 shows that exit of drain tend to migrate in the direction of the littoral current. The exit of this drain tends to move eastward. The main reasons for this phenomenon are Coriolis force and the littoral currents caused by the wind waves. The effective direction of the wind is North West. This causes the littoral currents to be from west to east parallel to the shore.

Table 1. show the rate of migration of drain exit towards the east direction from year 2003 to 2008.

Table 1. Rate of migration at exit of Gamasa drain.

| Sector | 2003 | 2006 | 2008 |
|---|-------------|-------------|------------|
| Exit location from the drain centerline (m) | 950 | 1180 | 1500 |
| Rate of migration m/year | 42.5 | 76.7 | 160 |

Two short jetties have been constructed on both sides of the drain outlet to prevent siltation of the drain and to stop the eastward migration of its mouth. The updrift accretion and the downdrift erosion started during the construction phase from 2003 to 2006. The area westward of the western jetty was filled and sediment turned around the jetty. To solve this problem, a dredging project started in July 2008 to create a trapped area of 250*250 m with -5.0 m depth just west of western jetty and to dredge the drain outlet, fig. 2.

Recently, The Egyptian shore protection Authority is implementing several protection projects on the shores of the Mediterranean Sea, with total cost of about 1.80 billion pounds covering the coast of northern Egypt and include project of protection the outlet of Gamasa drain and dredging the drain.

a. Data analysis at the study area

The shoreline changes were studied in the period from 2013 to 2016 in order to conduct the behavior of the shoreline at the study area. The movement pattern indicates that most of sediments eroded from the eastern side of the drain outlet move partly offshore and partly eastwards (Fig. 5.). The survey of the hydrographic profiles has been carried out and completely analyzed by Surfer programme to study the changes of the beach characteristics as shown in Fig. 6.

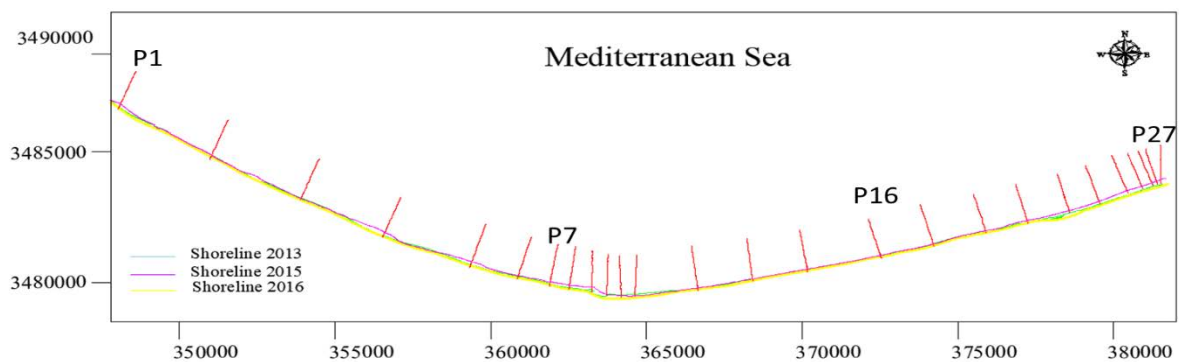


Figure 5. Shoreline changes at Gamasa drain area in period from 2013 to 2016 and shows field profiles

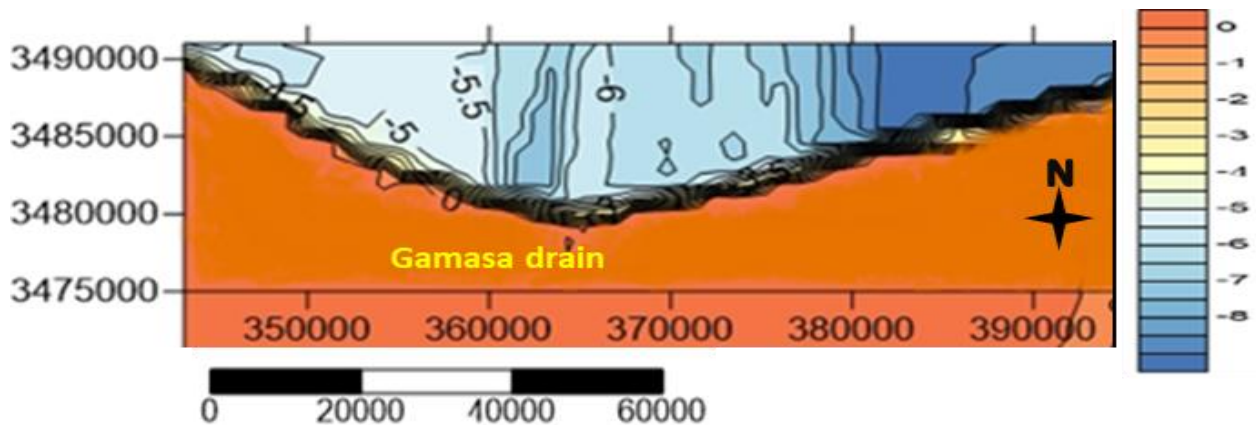


Figure 6. Field bathymetry for the study area for year 2015.

The prevailing direction of wind was mainly from WSW(17.2 %), W(17.2 %) and WNW (10.3 %) at year 2010. The maximum wind speed was (18.6 m/sec) from E with mean value of (2.3 m/sec).

At year 2010, waves had significant wave height of 1.02 m, average wave height of 0.56 m, average peak wave period of 6.3 sec and originated from the NW. The maximum measured wave characteristics are 4.47 m, 5.6 sec., NW for wave height, corresponding wave period and wave direction respectively observed during the winter. During the winter (storm season), monthly significant wave heights vary from 0.50 to 2.16 m with a weighted average of 1.15 m, average peak wave period range from 4.4 to 8.3 sec with a weighted average of 6.70 sec (CORI, 2011).

The maximum current speed is ranging from 33 cm/sec and 91 cm/sec. The minimum current speed is ranging from 10 cm/sec and 23 cm/sec. The average current speed is ranging from 22 cm/sec and 34 cm/sec, as shown in fig. 7. From year 1982 to 2009, the predominant direction is from west to east with percentage ranging from 55% to 74%.

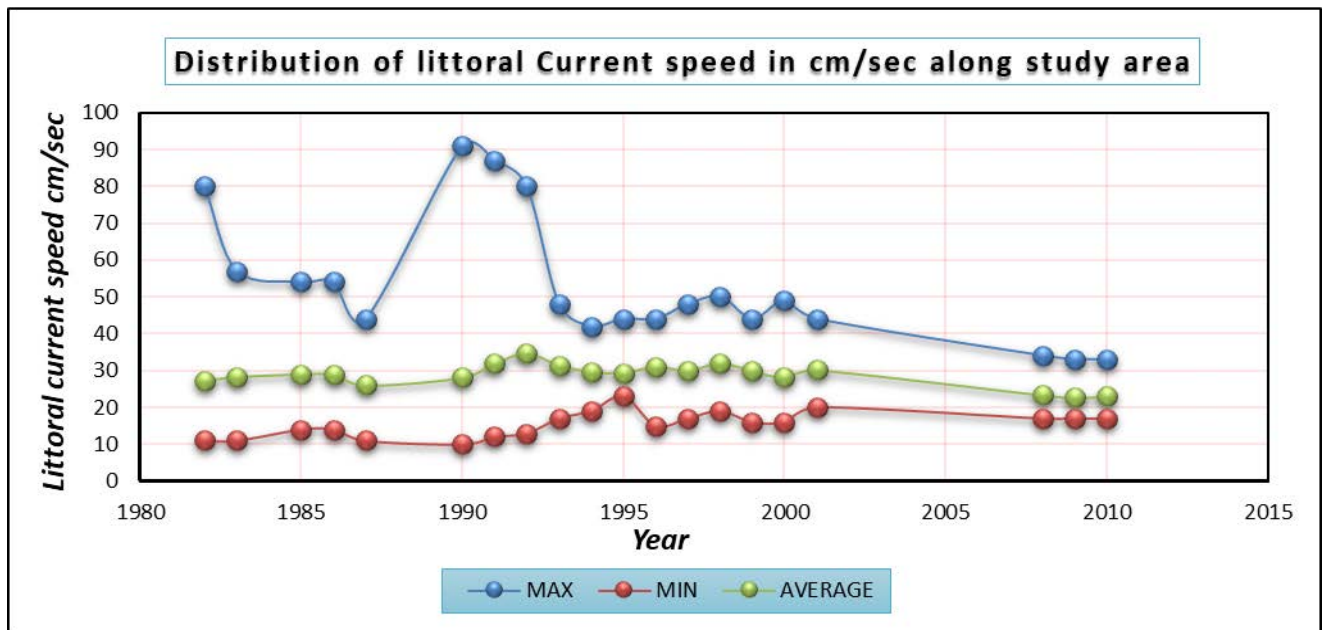


Figure 7. Disribution of littoral current speed in cm/sec along Gamasa drain coast.

At Damietta sea level increases by about 2.5 mm/yr during the period (1990-2010), This indicates that mean sea level appears to be risen about 5.3 cm for the entire period between 1990 and 2010. The sea level variation has been considered one of the most important factors in coastal processes. The average value at the study area is 0.51 m for year 2012, recorded by Coastal Research Institute (CORI, 2011).

The annual discharge of Gamasa drain during the period from 1997 to 2002, which has been recorded by CoRI, shown in Fig. 8. The average annual discharge of the drain, for this period, is about 1646.22 million m³.

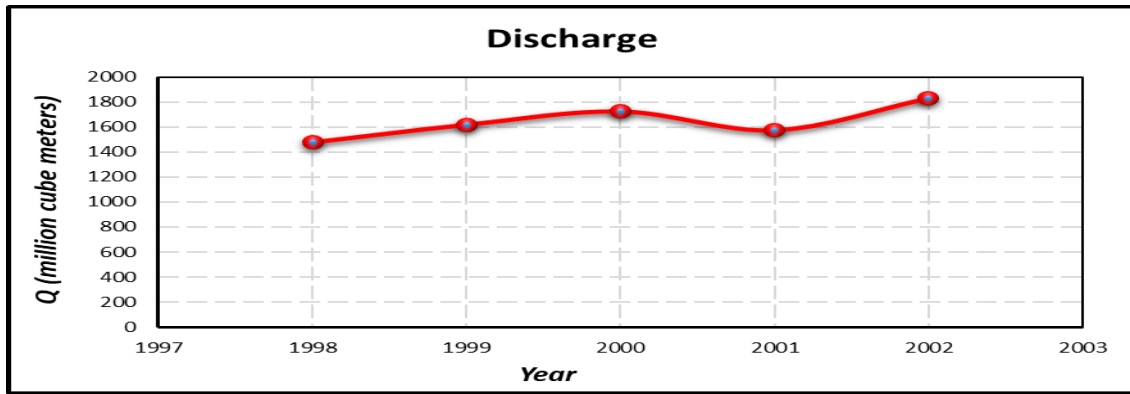


Figure 8. The drainage water discharge of Gamasa drain during period (1997 – 2002).

The sediment of the Gamasa drain coast is composed of quartz, silt, mud, rock fragment of flat stone and heavy minerals. Most of these grains are derived from the coastal erosion along the Nile Delta coast. The mean grain size of sediment ranges from 0.09 to 0.61 mm and overall average 0.25 mm during year 2012.

4 Result of numerical modeling using Delft 3D

Three proposed scenarios have been numerically modeled using Delft 3D, which is based on two dimensional shallow water equation derived from Navier-Stokes equations (Deltares, 2013), as shown in fig. 9. Each scenario has been applied twice in year 2016, without eastern groins, and in year 2019, with eastern groins. Numerical models have been calibrated and validated by adjusting significant wave heights, which have been surveyed by CoRI at 2004, in the eroded zone at onshore observation point. The difference between the two data can be considered acceptable to start the numerical model for the three scenarios. All scenarios simulate for 1 week.

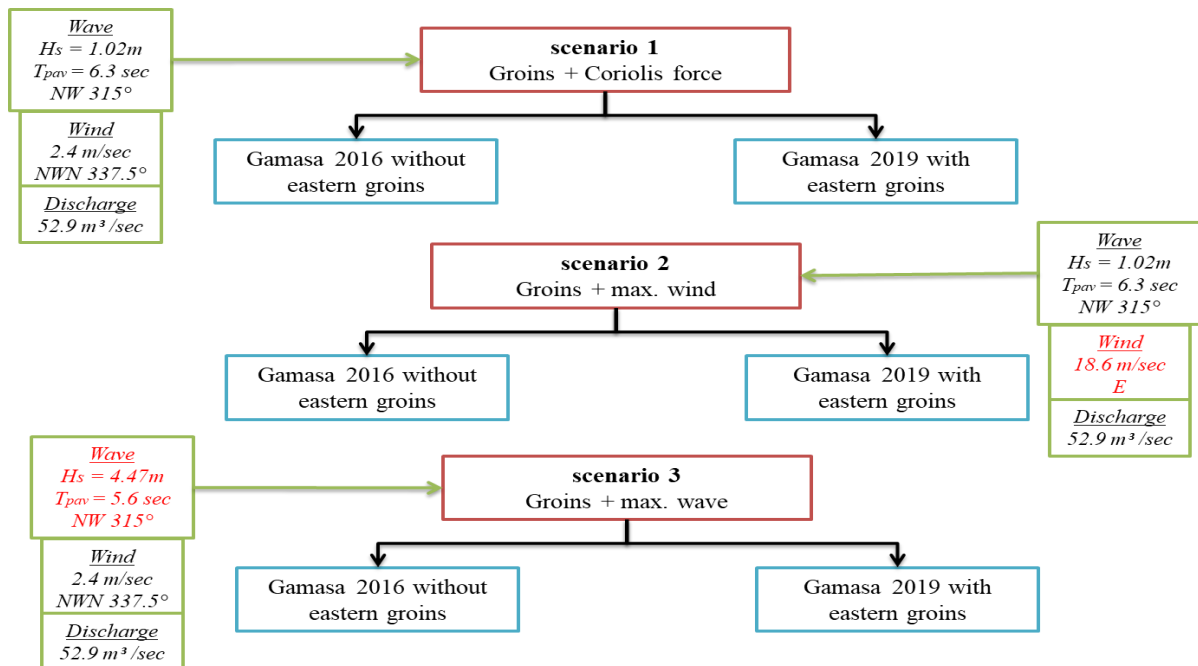


Figure 9. Proposed scenarios to study the hydrodynamic effect of groins at the study area.

For scenario 1, the analysis of the results, which focused on the eastern side of the drain, shows that: The discharge at exit of the drain has deflection in eastern side of drain (fig. 10.). Significant wave heights have range from (0.49 to 0.58m) at end of simulation (fig. 11). For littoral currents values ranges from (0.17 – 0.4 m/s), at end of simulation (fig. 11,12).

For scenario 2, the analysis of the results, shows that: The discharge at exit of the drain has maximum deflection in eastern side of drain (fig. 10.). Significant wave heights have values from (0.61 to 0.92m) at end of simulation (fig. 11). For littoral currents have maximum values ranges from (0.56 – 0.67 m/s) at end of simulation (fig. 11,12).

For scenario 3: The discharge at exit of the drain deflects to east in eastern side of drain (fig. 10). Significant wave heights have maximum range from (1.1 to 1.6 m) at end of simulation (fig. 11). For littoral currents values ranges from (0.38 – 0.52 m/s), at end of simulation (fig. 11,12).

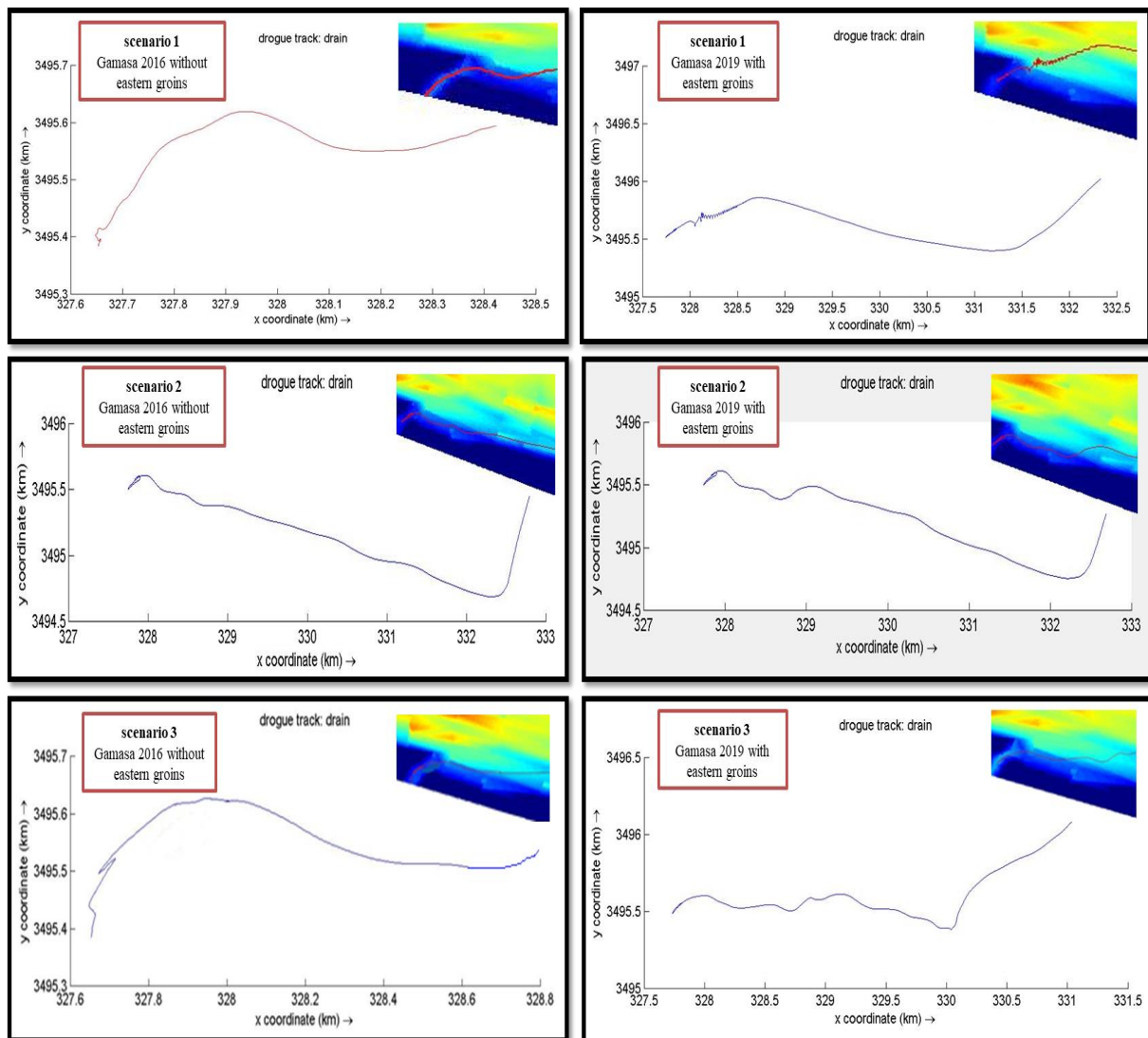


Figure 10. Direction of discharge at exit of Kitchener drain in all scenarios.

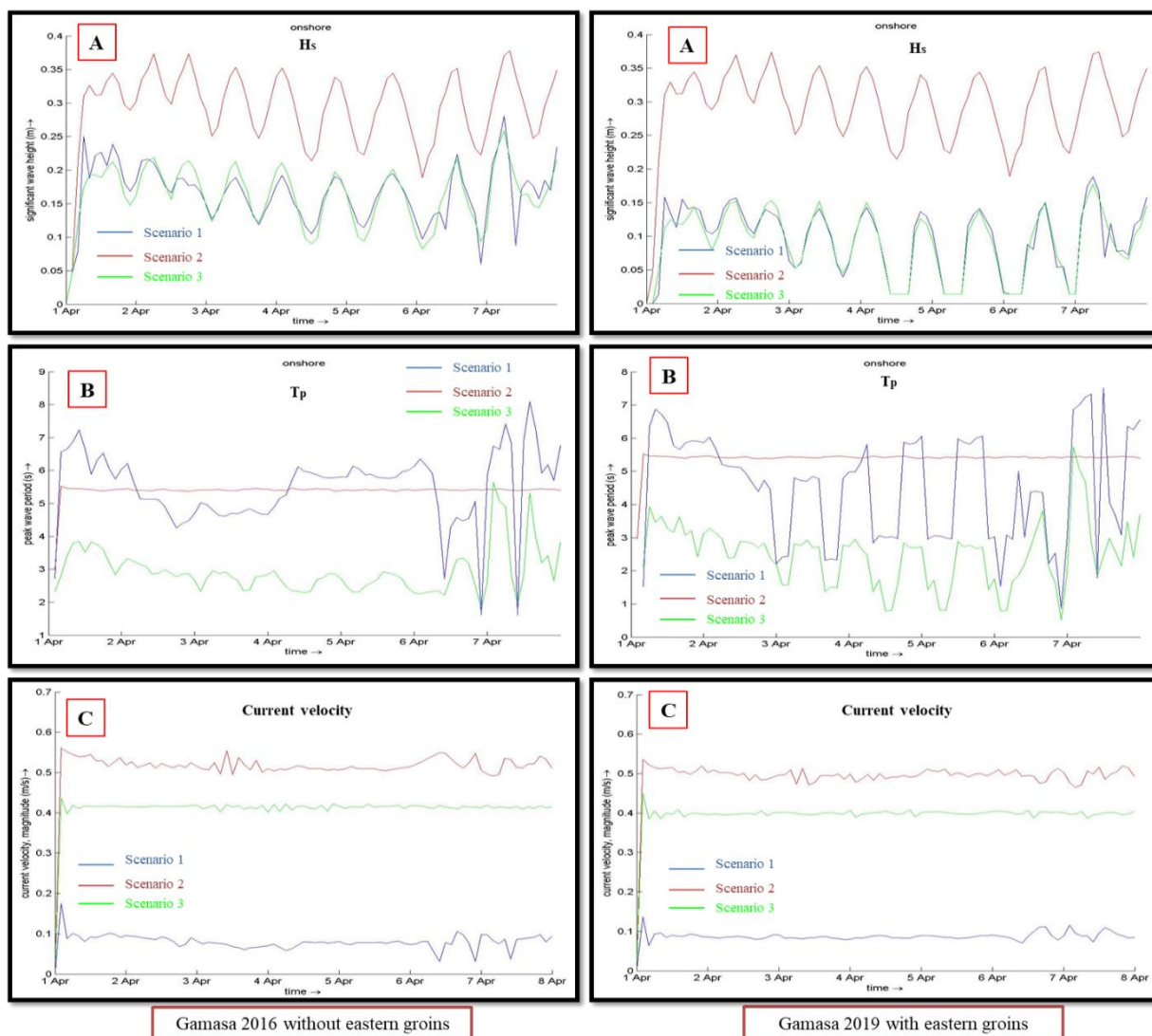


Figure 11. (A-B) wave characteristics (h_s - t_p) and (C) current velocity (cm/s) at onshore point for all scenarios at years (2016-2019).

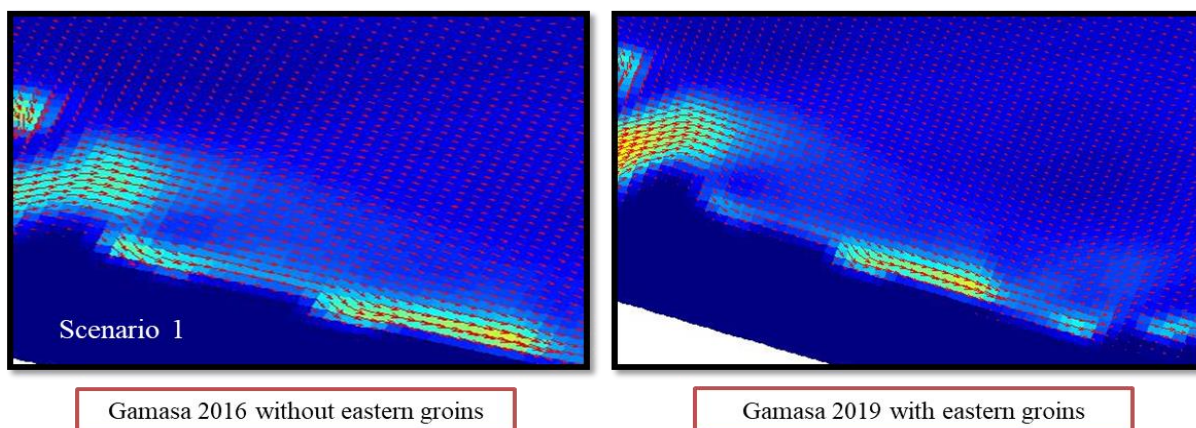


Figure 12. Littoral Current speed at year 2016, 2019.

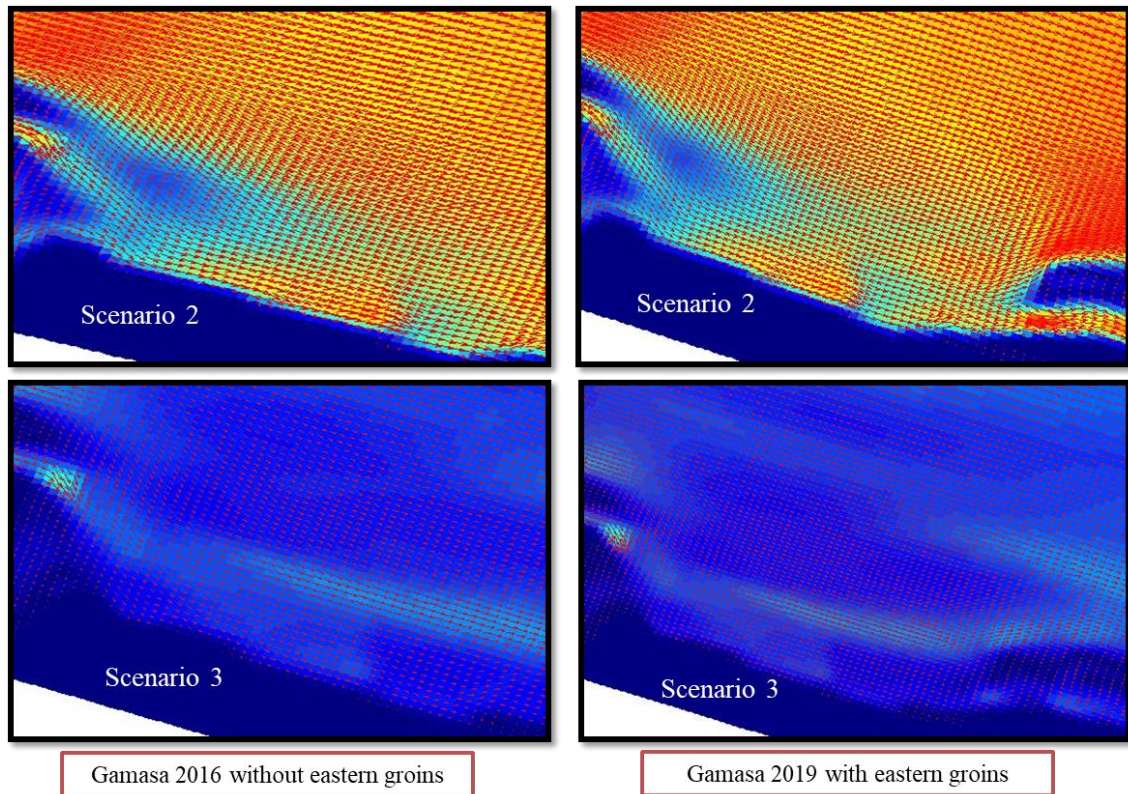


Figure 12. continued Littoral Current speed at year 2016, 2019.

5 Conclusions

The hydrodynamics factors are found to have a greater impact on the nearshore wave conditions than the groin geometry. The variation of significant incident-wave height imparts the greater changes in wave height nearshore, where the groin would be located. The typical tidal range is also important, since a 2 m change in sea surface level can cause great depth changes over bathymetric features and thus influence wave propagation. Although less important, the geometry of the groin should also be considered. The groins at the eastern side of Gamasa drain decrease the effect of littoral processes at the area just eastern drain exit.

The rotation of the earth affects the currents through the Coriolis force, which causes water to move to the right in the Northern Hemisphere and to the left in the Southern Hemisphere. While littoral currents are most significant in causing a littoral movement of beach material which can consist of hundreds of kilometers of sediment, but Coriolis force has significant effect on migration of drains exits

6 Recommendations for future research

1. Study the effect of groins length, at the eastern side, on the migration of the exits, extending further to the lee-side of the groin.

2. The Coriolis force prominently in studies of the coastal dynamics, in which it affects prevailing winds and, it affects the rotation of the coastal currents. These effects can be explained in terms of an 'imaginary' force called the Coriolis force, thus, we should take in consideration the effect of Coriolis force on coastal dynamic factors and in designing of coastal structures in the future.

References

1. CORI/UNESCO/UNDP, 1978. Coastal protection studies. *Final Technical Report, I and II*.
2. N.H. Ali, "Evaluation of Coriolis Factor Effect on Drain Exit Migration at The Sea", *Master of science*, Faculty of Engineering, Alexandria University, 2018.
3. CORI/ Coastal research institute Technical report (2013) on the "Studying Shoreline Changes along El Burullus Coastal Zone, Nile Delta Coast," Technical Progress report during the period (2004 - 2012).
4. Deltares, Delft3d flow user manual. July 2013.
5. Deltares, Delft3D-WAVE User Manual. 2013.
6. Basco, D.R., 2006. "Shore Protection Projects. Coastal Engineering Manual", Washington, DC, U.S. Army Corps of Engineers. Part V—Coastal Project Planning and Design, pp. 59–76.
7. Dean, R.G., 1978. "Coastal structures and their interaction with the shoreline. Application of Stochastic Processes in Sediment Transport. In: Kikkaua, H.W.S.A.H. (Ed.)", Water Resources Publications, Littleton, CO.
8. Pattiaratchi, C., and Woo, M. (2009), "The mean state of the Leeuwin Current system between North West Cape and Cape Leeuwin, J. R. Soc. West". Aust., 92, 221– 241.
9. Stull, R., 2011: "Meteorology for Scientists & Engineers, 3rd Edition." Univ. of British Columbia. 938 pages chapter 9, dynamics. isbn 978-0-88865-178-5
10. N.H. Ali, "Hydrodynamic Study of the Coastal Area at El-manzalaLake", High Diploma Degree, January 2013.
11. CORI/ Coastal Research Institute Technical report (2011) on the "Physical Parameters related to climate change along the Mediterranean coastal zone of Egypt," Technical Progress report (2011).

14- Thermal decomposition of eggshells for quicklime production: the role of egg membrane

O.S. Okwundu^{†1,2}, A.H. El- Shazly^{1,3}, M.F. Elkady^{1,4}.

¹Department of Chemical and Petrochemical Engineering, Egypt-Japan University of Science and Technology (E-JUST), New Borg El-Arab City, Alexandria, Egypt.

²Department of Chemical Engineering, University of Benin, Edo State, Nigeria.

³Chemical Engineering Department, Alexandria University, Alexandria, Egypt.

⁴Fabrication Technology Department, Advanced Technology and New Materials Research Institute (ATNMRI), City of Scientific Research and Technology Applications, Alexandria, Egypt.

[†]E-mail: onyeka.okwundu@eng.uniben.edu

Abstract

Quicklime (CaO) is produced industrially by thermal decomposition of naturally existing calcium carbonates. Eggshell is a renowned source of high purity quicklime. The shell is accompanied by thin layer(s) of organic egg membrane. This study investigates the role of egg membrane in the calcination of waste chicken eggshells for quicklime production. This was achieved via comparison of synthesized materials properties with and without membrane. Two samples of dried waste chicken eggshells were prepared with and without removal of membrane layers respectively. Thermogravimetric analysis (TGA) of

the shell samples suggested a suitable calcination temperature ≥ 800 °C. The samples were each calcined at 700, 800, 900 and 1000 °C then characterized by SEM, XRD and catalyst (EG900). Comparison of EG900 (prepared with membrane) and EG_{nil} (without membrane) was made based on SEM, BET, XRF, XRD, particle size analysis and catalytic activity tests. The results showed no significant alteration in elemental and crystalline composition. Inclusion of membrane resulted to increase in surface area (0.58 to 3.61 m²/g and 0.32 to 2.98 m²/g, after and before calcination, respectively). Use of

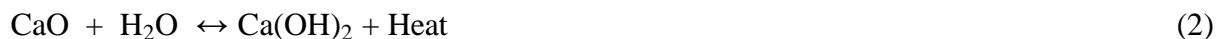
EG900 and EG_{nil}, respectively yielded 95.94 and 96.78 % beef tallow methyl ester. It was concluded that inclusion of egg membrane enhances material's surface area, alters the surface morphology, while only slightly tarnishing its purity and catalytic activity. Economically, membrane removal is unnecessary for biodiesel production.

Keywords: Egg membrane, calcination, eggshell derived CaO, heterogeneous catalysis, biodiesel production

1 Introduction

Calcium is a naturally abundant alkaline earth metal that exists in chemically combined state as trioxocarbonate in limestone, chalk, dolomite and marble, or as tetraoxosulphate in gypsum and plaster of Paris. These minerals are famous and of great value [1]. The ubiquity of calcium is further revealed by its existence in skeletal systems of animals. One important compound of calcium is its oxide (CaO), which is commonly known as quicklime. It is commonly synthesized via decomposition of CaCO₃, contained in the shells of mollusks [2], poultry eggs [3], CaCO₃ rich bones like that of cuttlefish and in reliably larger quantity, from the CaCO₃ rich minerals [4], [5]. The chemical decomposition as described in Equation (1), requires heating (calcination) to about 900 °C for some hours [3]. Even though surface decomposition can occur at lower temperatures, Oates noted that complete conversion only occurs above 900 °C [5].

Δ



Some notable uses of CaO include water treatment, pharmaceuticals, processing of steel from iron ore, cement production, as laboratory reagent for dehydration, precipitation and as a cheap base. Because of its ‘quick’ exothermic reaction with water as represented in Equation (2), quicklime is used alongside suitable pH indicator for aqua-sensing (detection of water in petroleum industry) [6], it was also used as ancient weapon [7]. It is the starting material for synthesis of some products like slaked lime as illustrated in Equation (2). It makes a good binder [8] and also has potentials for use as dielectric in supercapacitors [9]. Quicklime is an economically viable catalyst for fuel production; as it is well known to enhance the pyrolysis of coal [10] and sewage sludge [11], [12], while its use in biodiesel production is well recognized [2], [4]. In some of these applications, quicklime is preferred pure.

One of the most reliable naturally-sourced precursor materials for CaO, with regards to purity, is eggshells – comprising of more than 90 % CaCO_3 [13]. Eggshells is direct waste from food processing and poultry hatcheries; in fact, European Union classifies it as hazardous waste. However, while the shells finds application as animal feed-supplement, fertilizer and even CO_2 capture material [14]; Various types of collagens, amino acids and hyaluronic acid of interest, are contained in the membrane and may be extracted for biomedical, pharmaceutical, dietary or cosmetic applications [15]. In the synthesis of high purity quicklime, for analytical use or for catalysis, egg membranes are removed at times [16], [17], while many atimes, the membrane is included [18], [19]. The role of egg membrane in the preparation of CaO from eggshells has not been clearly established.

Consequently, this study investigates role of egg membrane in quicklime production.

2 Methods

2.1. Search for favorable calcination temperature. Waste white chicken eggshells were reclaimed from a restaurant, and upon arrival to the laboratory, the shells (alongside the accompanying membrane) were sorted, washed, and drained. The shells were dried in D-78532 Binder Oven Dryer (Tuttlingen, Germany), for 24 hours at 110 °C to ease size reduction. The dried shells were milled with Rose GTM-8302 milling system and sieved. Sieved eggshell particles in the size range of 45 to 63 micron (labeled EG) were subjected to thermogravimetric analysis (TGA, Shimadzu) in nitrogen atmosphere at flow rate of 40 mL/min, over platinum cell, from room temperature up to 800 °C (the maximum temperature permissible by the device operator), at heating rate of 5 °C/minute.

The TGA result is shown in Figure 1. The result suggests adequate calcination temperature ≥ 800 °C, since the heated sample did not attain constant temperature within the temperature range of analysis. As a result, the sieved particles in the stated classification, were calcined in 4 batches, using muffle furnace KBF794N1 (Koyo Thermo Systems Co. Ltd., Japan), at: 700, 800, 900 and 1000 °C, respectively, with heating rate of 5 °C/min, for 3 hours. The calcined samples were each, cooled in the humidity chamber at zero humidity and stored air-tight in autoclavable glass bottle [20], [21]. The samples (catalysts) were labeled: EG700, EG800, EG900 and EG1000, with respect to their calcination temperatures.

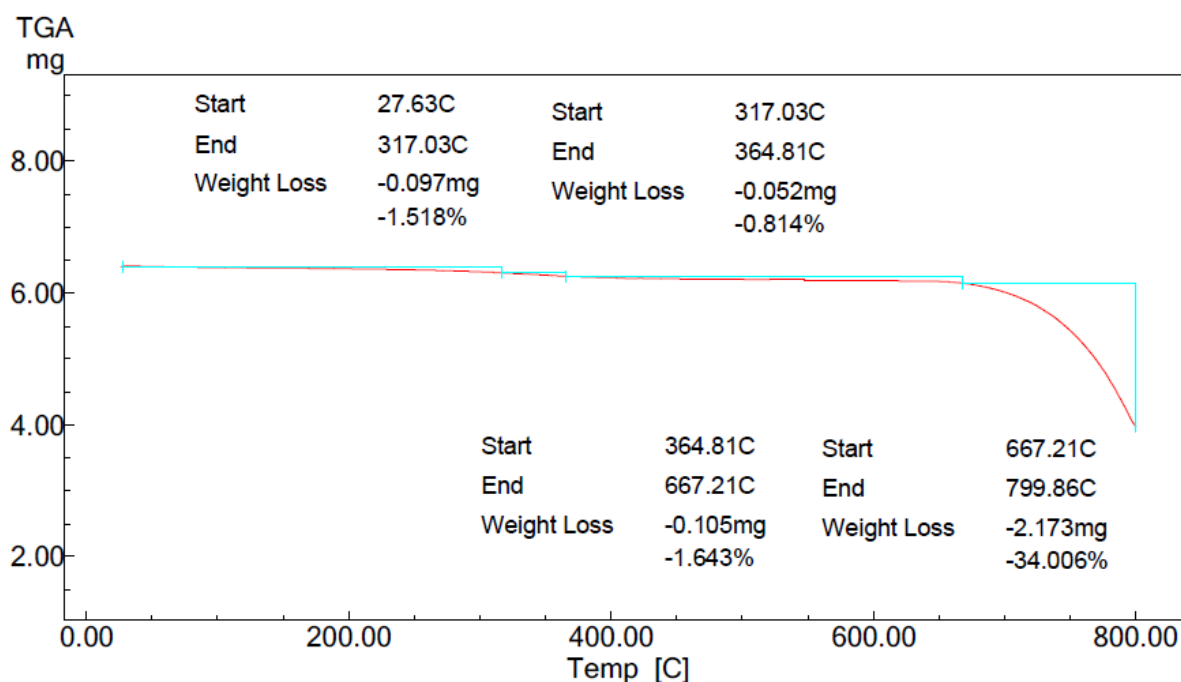


Figure 1: TGA result of eggshell particles in the range of 45 to 63 micron.

EG, EG700, EG800, EG900 and EG1000 were examined for surface morphology using Scanning Electron Microscope (SEM, JEOL JSM-6010LV), and for crystallinity, using X-Ray Diffractometer (XRD, Shimadzu Xlab 6100). The 4 catalysts were each used in transesterification test experiment, at adapted conditions of: 8 wt.% catalyst concentration, methanol to fat ratio of 12:1, at 65 °C, 1500 rpm and reaction times of 10, 60, 150 and 240 minutes [22], [23], to ascertain the best calcination temperature. Raw sieved sample and the sample calcined at the most favorable temperature, were characterized for particle size distribution by Malvern Zetasizer, specific surface area by nitrogen adsorption-desorption using Brunauer-Emmett-Teller (BET) surface area

analyzer, Belsorp II (BEL Japan Inc.), elemental analysis by X-Ray Fluorescence (XRF) Spectrometer (Rigaku NEX CGEDXRF), and used for catalytic test.

Catalysis of beef tallow methanolysis with the best EG-catalyst was optimized in a different study, resulting to catalyst concentration of 5.42 wt.%, at 63 °C, methanol to fat ratio of 16.39 mole/mole, reaction time of 3.38 hours and stirring speed of 1300 rpm [24]. Comparative activity tests for catalysts prepared with and without membrane, were performed at this condition.

2.2. Synthesis of quicklime without membrane. For ease of membrane removal, a crate of raw chicken eggs (with white shell) was purchased from a nearby supermarket and carefully cracked into halves to empty the contents. Resulting eggshells were soaked in water for 2 hrs and then completely stripped of their membranes, before washing, draining and drying. Membrane removal was done by manual peeling and scrubbing with finger [25], [26]. Dried, ceramic mortar-crushed, and calcined (at the established favorable temperature) shell sample was labelled EG_{nil}. This was characterized and tested just like the best EG-catalyst sample.



Figure 2: Eggshell without membrane (EGnil , left) and the removed membrane sheaths (right), just after drying; image by Tecno L9 Plus.

In addition, the excluded membrane sheaths were carefully sorted, washed, dried and calcined as well. Weight of the membrane sample before and after calcination was noted.

2.3. Transesterification catalytic test. Catalyst samples were tested in the methanolysis of low free fatty acid (FFA < 0.5%) beef tallow at specified conditions. Details of biodiesel production methodology, including how FAME yield was calculated, is noted in our earlier reports [3], [24].

3 Results and discussion

3.1. Favorable calcination temperature. Figure 3 shows the XRD spectra of EG-catalyst samples. Peaks were identified by matching with data of Joint Committee on Powder Diffraction

Standards, JCPDS. Obviously there was progressive conversion of trioxocarbonates to oxides with increase in calcination temperature. The observed hydroxide species must have resulted from atmospheric moisture contamination during sampling, according to Equation 2. From the XRD spectra, EG900 and EG1000 were fully developed CaO.

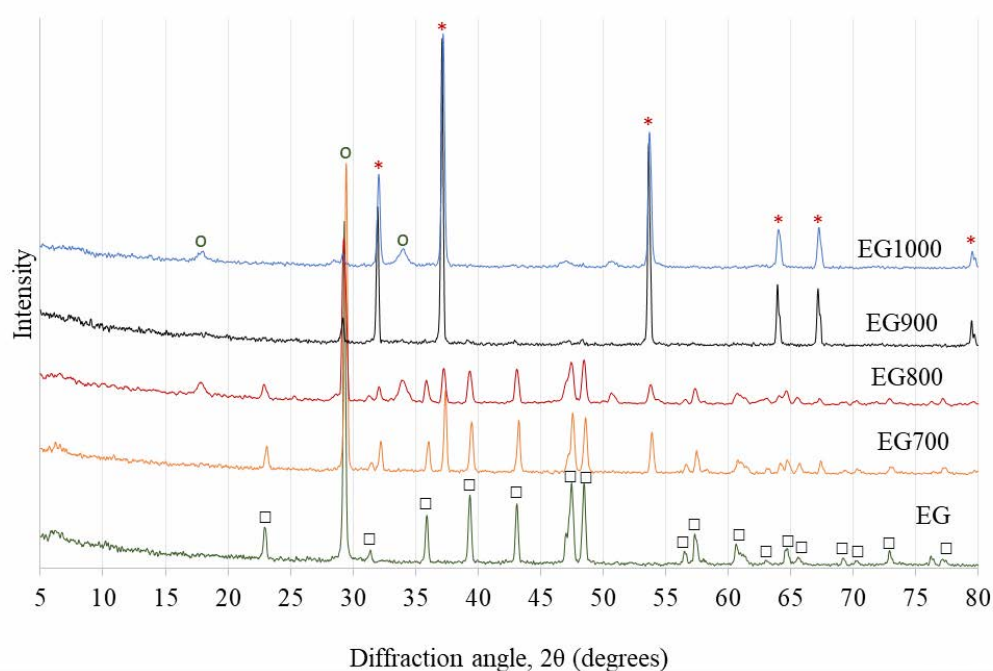


Figure 3: XRD spectra of eggshell-derived catalyst samples; Where: o = Ca(OH)_2 ; * = CaO ; □ = CaCO_3 .

Use of the eggshell-derived catalysts: EG700, EG800, EG900, and EG1000, resulted in various BTME yields. Table 1 shows the transesterification Catalytic activities of eggshell-derived catalysts. EG900 was chosen as the best and used for further studies.

Table 1: Transesterification Catalytic activities of eggshell-derived catalysts

| Catalyst | Yield/% |
|----------|---------|
| EG700 | 0 |
| EG800 | 57.13 |
| EG900 | 87.5 |
| EG1000 | 72.61 |

The SEM images of eggshell-derived catalyst samples are shown in Figure 4. The morphologies reveal gradual decomposition of larger particles of calcium trioxocarbonate (a), into interwoven strands of greater porosity than raw EG, on moving from 4a to 4i. TEM imaging of EG900 showed that the observed strands were actually agglomerated particles.

3.2. Comparison between CaO synthesized with and without membrane. Table 2 shows the catalytic activities of EG900 and EG_{nil} . The XRD patterns of Figure 3, show that CaO is the active material in the calcined catalyst powder and this was confirmed from the XRF data of EG900, which revealed

CaO content of 98.91 %, amongst TiO_2 (0.074 %), MnO (0.08 %), Fe_2O_3 (0.082 %) and some trace elements. This implies that the calcination process effectively converted all the calcium carbonates in the raw chicken eggshell to CaO as desired for transesterification catalysis. However

elemental composition of EG_{nil} , showed slightly higher material purity. The morphology of EG_{nil} was non-interwoven like that of EG900. Without membrane, quicklime of lower surface area, with just a little greater composition and catalytic activity was obtained. Even before (b4) calcination, the crushed shells with membrane gave higher BET surface area. Light-weight membranes might have acted as spacers, preventing the calciums from compacting/sintering. Inclusion or exclusion of membrane had no significant effect on crystalline composition of the material, both before and after calcination as seen

from the XRD spectra of Figure 4.

Table 2: Comparison between EG900 and EG_{nil}

| | Weight (g) | Surface area (m ² /g) | Purity (%) | Activity, Yield (%) |
|-------------------|------------|----------------------------------|------------|---------------------|
| EG900 | 1292 | 3.61 (b4: 2.98) | 98.91 | 95.94 |
| EG _{nil} | 697 | 0.58 (b4: 0.32) | 99.03 | 96.78 |

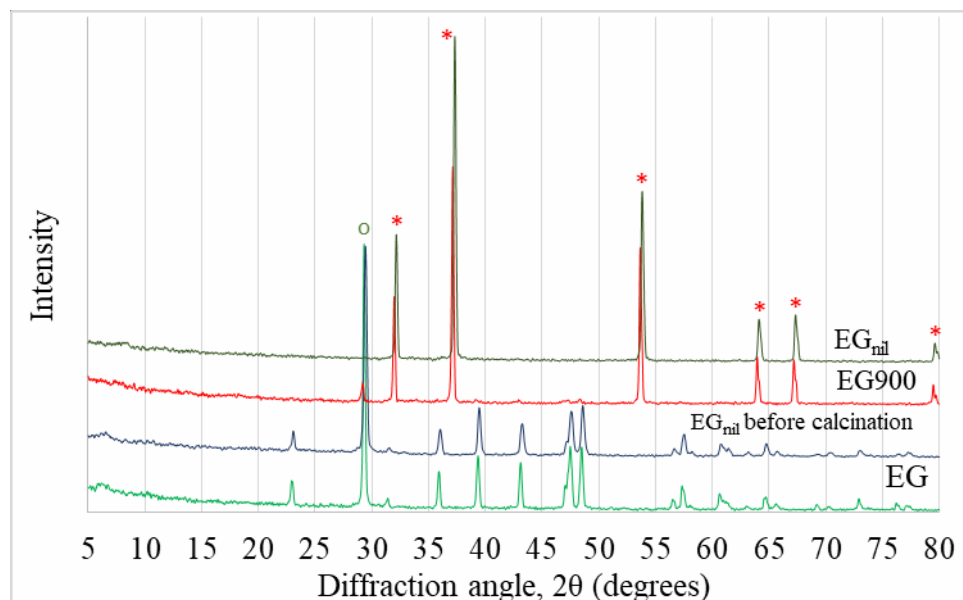
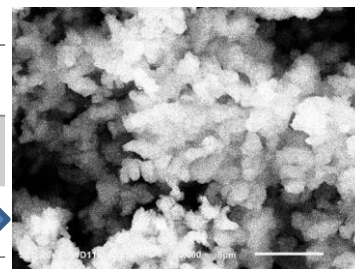


Figure 4: XRD spectra of eggshells calcined at various T, * = CaO, O = Ca(OH)₂.

Unit cell parameter = CaCO₃

4 Conclusions

Quicklime has been produced with and without egg membrane, and characterized. The membrane was found to have acted as a spacer. It can be concluded that the inclusion of egg membrane enhances material's surface area, alters the surface morphology, while only slightly tarnishing its purity and catalytic activity. Such inclusion is recommendable for high surface area applications, like in supercapacitor electrodes and adsorbents. From economic point of view, membrane removal is unnecessary for biodiesel production.

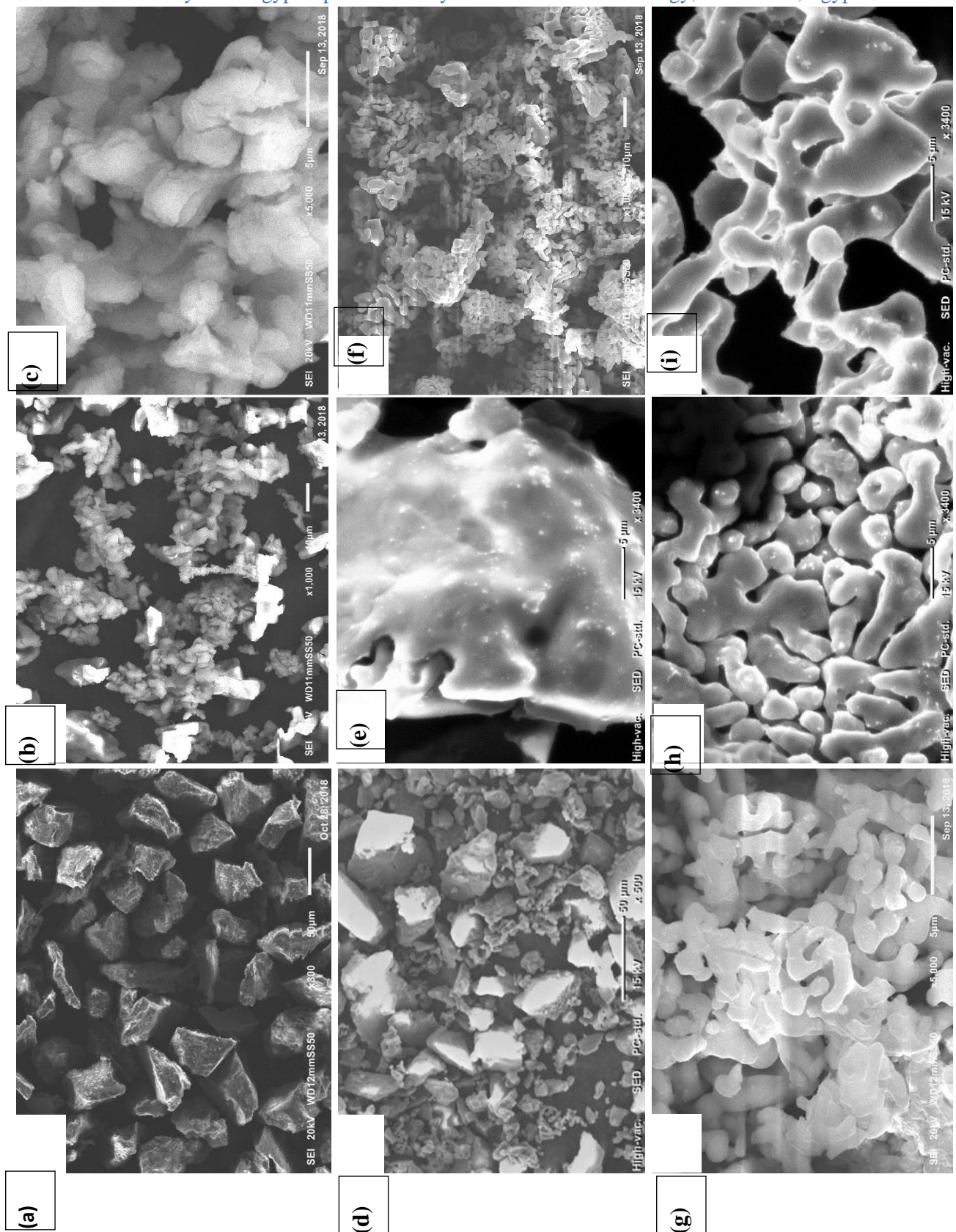


Figure 4: SEM images of eggshell-derived catalyst samples: EG (a), EG700 (b, c), EG800 (d, e), EG900 (f, g), EG1000 (h, i).

Acknowledgement

The corresponding author acknowledges full MSc. scholarship support from the Ministry of Higher Education (MOHE) at Egypt-Japan University of Science and Technology, Egypt.

References

- [1] O. Y. Ababio, *New School Chemistry for Senior Secondary Schools*, Revised Ed. Africana-FEP Publishers Limited, 1980.
- [2] N. Viriya-empikul, P. Krasae, B. Puttasawat, B. Yoosuk, N. Chollacoop, and K. Faungnawakij, "Waste shells of mollusk and egg as biodiesel production catalysts," *Bioresour. Technol.*, vol. 101, no. 10, pp. 3765–3767, 2010.
- [3] O. S. Okwundu, A. H. El-Shazly, and M. Elkady, "Comparative effect of reaction time on biodiesel production from low free fatty acid beef tallow: a definition of product yield," *SN Appl. Sci.*, vol. 1, no. 2, p. 140, Feb. 2019.
- [4] C. Ngamcharussrivichai, P. Nunthasanti, S. Tanachai, and K. Bunyakiat, "Biodiesel production through transesterification over natural calciums," *Fuel Process. Technol.*, vol. 91, no. 11, pp. 1409–1415, 2010.
- [5] T. Oates, "Lime and Limestone," in *Ullmann's Encyclopedia of Industrial Chemistry*, 7th ed., Wiley, 2007, pp. 1–32.
- [6] IndiaMART, "Powder Calcium Oxide (quick Lime), Usage: Industrial," 2018. [Online]. Available: <https://www.indiamart.com/proddetail/calcium-oxide-powder-quick-lime-powder-9379435955.html>. [Accessed: 31-Dec-2018].
- [7] E. Croddy, "Chemical warfare: A brief history," in *Chemical and Biological Warfare: A Comprehensive Survey for the Concerned Citizen*, Springer-Verlag, 2002, pp. 127–168.
- [8] M. S. Kim, Y. Jun, C. Lee, and J. E. Oh, "Use of CaO as an activator for producing a price-competitive non-cement structural binder using ground granulated blast furnace slag," *Cem. Concr. Res.*, vol. 54, pp. 208–214, 2013.
- [9] G. A. M. Ali, O. A. Habeeb, H. Algarni, and K. F. Chong, "CaO impregnated highly porous honeycomb activated carbon from agriculture waste: symmetrical supercapacitor study," *J. Mater. Sci.*, vol. 54, no. 1, pp. 683–692, 2019.
- [10] Z. Tingyu, Z. Shouyu, H. Jiejie, and W. Yang, "Effect of calcium oxide on pyrolysis of coal in a fluidized bed," *Fuel Process. Technol.*, vol. 64, no. 1, pp. 271–284, 2000.
- [11] H. Liu *et al.*, "Catalytic role of conditioner CaO in nitrogen transformation during sewage sludge pyrolysis," *Proc. Combust. Inst.*, vol. 35, no. 3, pp. 2759–2766, 2015.
- [12] S. Chen, Z. Sun, Q. Zhang, J. Hu, and W. Xiang, "Steam gasification of sewage sludge with CaO as CO₂sorbent for hydrogen-rich syngas production," *Biomass and Bioenergy*, vol. 107, pp. 52–62, 2017.
- [13] H. Faridi and A. Arabhosseini, "Application of eggshell wastes as valuable and utilizable products: A review," *Res. Agric. Eng.*, vol. 64, no. 2, pp. 104–114, 2018.
- [14] Ohio State University, "Engineered Eggshells To Help Make Hydrogen Fuel," *ScienceDaily*, 2007. [Online]. Available: www.sciencedaily.com/releases/2007/09/070926113832.htm. [Accessed: 22-Jun-2019].
- [15] SHELLBRANE, "Separating eggshell and its membrane to turn eggshell waste into valuable source materials," 2012. [Online]. Available: http://shellbrane.eu/?fbclid=IwAR34QytYeP_j_T5bNuBBg6Jgy6ZRWNaxAAwU883cD6j3U9SEBLo-iLRDiaw. [Accessed: 17-Jun-2019].
- [16] T. Zaman, M. S. Mostari, M. A. Al Mahmood, and M. S. Rahman, "Evolution and characterization of eggshell as a potential candidate of raw material," *Cerâmica*, vol. 64, no.

370, pp. 236–241, 2018.

[17] D. Cree and A. Rutter, “Sustainable Bio-Inspired Limestone Eggshell Powder for Potential Industrialized Applications,” *ACS Sustain. Chem. Eng.*, vol. 3, no. 5, pp. 941–949, 2015.

[18] A. R. Gupta and V. K. Rathod, “Waste cooking oil and waste chicken eggshells derived solid base catalyst for the biodiesel production: Optimization and kinetics,” *Waste Manag.*, vol. 79, pp. 169–178, Sep. 2018.

[19] Z. Wei, C. Xu, and B. Li, “Application of waste eggshell as low-cost solid catalyst for biodiesel production,” *Bioresour. Technol.*, vol. 100, no. 11, pp. 2883–2885, Jun. 2009.

[20] B. Aghel, M. Mohadesi, S. Sahraei, and M. Shariatifar, “New heterogeneous process for continuous biodiesel production in microreactors,” *Can. J. Chem. Eng.*, vol. 95, no. 7, pp. 1280–1287, 2017.

[21] S. Niju, K. M. Meera, S. Begum, and N. Anantharaman, “Modification of egg shell and its application in biodiesel production,” *J. Saudi Chem. Soc.*, vol. 18, no. 5, pp. 702–706, Nov. 2014.

[22] Y. C. Sharma, B. Singh, and J. Korstad, “Latest developments on application of heterogenous basic catalysts for an efficient and eco friendly synthesis of biodiesel: A review,” *Fuel*, vol. 90, no. 4, pp. 1309–1324, 2011.

[23] F. Ma, L. D. Clements, and M. A. Hanna, “The effect of mixing on transesterification of beef tallow,” *Bioresour. Technol.*, vol. 69, no. 3, pp. 289–293, Sep. 1999.

[24] O. S. Okwundu, A. H. El-Shazly, M. F. Elkady, and W. M. Shaaban, “Response surface modeling and optimization of heterogeneous methanolysis of beef tallow,” in *AIP Conference Proceedings*, 2019, vol. 2123, no. 1, p. 020003.

[25] Mr. Otter Art Studio, “How to Peel the Skin out of an Eggshell,” *YouTube Video*, 2015. [Online]. Available: <https://www.youtube.com/watch?v=FJY-p7mfByU>. [Accessed: 05- Jun-2019].

[26] Y. H. Zhao and Y. J. Chi, “Characterization of Collagen from Eggshell Membrane,” *Biotechnology*, vol. 8, no. 2, pp. 254–258, 2009.

15- Reinforcing polyhydroxybuterate-co-valerate with agriculture waste to produce a biodegradable composite for packaging application

Samir Elagamy^{1,a}, Ahmed Abd El-Fattah^{2,b}, Ahmed H. El-shazly^{3,c} and Sherif Kandil^{2,d}

¹Alexandria petroleum co. Egypt.

²Department of Materials Science, Institute of Graduate Studies and Research, Alexandria University, Alexandria, Egypt

³Chemical and Petrochemical Engineering Department, Egypt-Japan University of Science and Technology.

^a s_elagamy66@yahoo.com, ^b a_fattaho@yahoo.com ^c ahmed.elshazly@ejust.edu.eg, ^d S.Kandil@usa.net,

Abstract

Over the past century, accumulation of agriculture residues and plastics waste has raised serious concerns about their bad impact on the environment. Many attempts were applied to reuse agriculture wastes and replace synthetic plastics by biodegradable polymers to produce composites to be used in several applications. Among these available biodegradable polymers are the polyhydroxybuterate-co-valerate polymers (PHBVs). In this study, biodegradable composites were prepared using (PHBV) and rice straw (RS). Three (PHBV-RS) formulations (80/20, 70/30 and 60/40 wt/wt%) were prepared. To enhance the compatibility between the polymer and rice straw, the rice straw was treated with alkali (sodium hydroxide) to reduce the content of lignin in the rice straw that obstruct the compatibility between polymer and fiber. Then another three formulations were prepared from treated rice straw (TRS) with the polymer (PHBV) with the same previous ratios. The composites' properties (as morphological, mechanical, thermal and physical) were studied and were compared with the pure polymer PHBV without loading. A thin film sheet of the composite was prepared through mixing by two mill followed by hot compression compounding. Morphological studies of the (PHBV-RS) composites indicated that there was more entanglement between composites' constituents as the fiber loading was increased. Also the structure alignments, the thermal and mechanical properties of (PHBV-RS) composites were slightly enhanced compared to that of the pure polymer. The structural alignment and the mechanical properties of the treated composites (PHBV-TRS) were better than that of the untreated composites (PHBV-RS). The thermal properties for both composites having the treated and untreated rice straw were similar. The improvement in the mechanical properties of the treated composites (PHBV-TRS) reached nearly (70%) with (TRS) content of 40 wt % as compared to that of neat PHBV. The work proved that the rice straw could be used as eco-friendly reinforcement material for the PHBV polymer. However, the utilization of biodegradable components makes the production of PHBV-TRS composites promising for the packaging and automotive industry where the biodegradability is desirable.

keywords: rice straw, PHBV, biodegradable composites.

1-Introduction

The agriculture sector still plays an important role in the national economy of many countries. Due to the size of agricultural production, a large volume of residues is generated each year from this sector. As an example in Egypt, the total agricultural residues were estimated to be around 300 Mt/year and the rice straw constitutes about 10.7%. Open burning is the technique that is most commonly used to dispose the agricultural residues, which causes the growing of greenhouse gas emission in the world.^[1, 2]

Out of the 8300 million metric tons (Mt) of plastics that were produced between 1950 and 2015, 2500 Mt are currently in use, 800 Mt have been incinerated, and only 600 Mt have been recycled, as only 9% of the global plastics are recycled. In 2015, 42% of the primary produced plastics are used in packaging. Most of the packaging plastics turn into plastic waste within the same year in which they are produced. This means that a huge quantity of plastics wastes are increasing annually.^[3, 4]

The objectives of sustainable development and the reduction of environmental impacts may be achieved by the use of biodegradable plastics produced from renewable resources. Among the possible alternatives that are currently gaining attention is the development of composites using agro-wastes or lignocellulosic materials as reinforcing fillers and biopolymers as matrixes. Intense research efforts in the last two decades are currently focused on developing “green” composites by combining (natural/bio) fibers with suitable biopolymer matrices. For a material to be effectively used in packaging applications, it should be renewable, efficient, economically competitive, and its end products should be compostable and environmentally friendly.

The biopolymer (hydroxybutyrate-co-hydroxyvalerate) (PHBV) is widely used in many applications. However its widespread application was limited because of its narrow processing window and poor mechanical properties. The addition of natural fiber for reinforcement can markedly improve the mechanical properties of these biopolymers to be suitable for different applications including packaging and automotive industries.

In the present study, we investigated the possibility of using agricultural waste as reinforcing filler in these eco-composites and prepared a biodegradable composites of (PHBV) and rice straw. [5-10]

Treatment of the rice straw may be used to increase the compatibility between polymer and fiber through removing the hindering constituents for achieving optimal mechanical performance and producing effective transfer of stress of the fiber reinforced composites. Alkali treatment ‘mercerization’, which is an old method of cellulose fiber modification, was tried. [11]

2. Materials and methods

Polyhydroxybuterate-co-valerate (PHBV) in a fine powder form was provided by Tainan Biologic Materials co., ltd. China, under trade name ENMAT PHBV powder Y1000, with molecular weight of 400,000 Daltons and contains 3mole% of β -hydroxyvalerate. Rice straw was collected from Behaira Governorate, Egypt, and small fibers were cleaned via washing with pressurized tap water for about 30 min. then it was air dried. The air dried fiber was ground using a hammer mill and then oven dried at 80°C for 24hr to reach a constant weight, the powder was sieved on a molecular sieve of 70 mesh and stored in sealed bags. The dried powder of rice straw (RS) was treated with toluene / ethanol (2:1 v/v) in soxhelt for 8 hrs to remove any waxy materials, the dewaxed straw was treated with 2% sodium hydroxide solution at 55°C for 2hrs, then neutralized with 6M hydrochloric acid to pH 5.5 and finally washed with distilled water. The treated rice straw (TRS) was filtered and washed with distilled water followed by drying in an oven at 60°C for 24hrs. [12] The physical and chemical analysis of rice straw was carried out at Wood Testing Laboratory, Department of Forestry and Wood Technology, Faculty of Agriculture, Alexandria University, Egypt. The reagents as Isopropyl alcohol (anhydrous assay 99%), hydrochloric acid solution (analar assay 99.9%), sodium hydroxide solution (analar Assay 99.9%), toluene (analar purity 99.5%), sulphuric acid solution (analar assay 95-99%), nitric acid solution (analar assay 95-99%), phosphoric acid solution (analar assay 95-99%), ethanol solution (analar assay min 99.8%) were purchased from Sigma- Aldrich Chemical co., Germany.

2.1. Compounding and manufacturing of the composites

Poly hydroxybuterate-co-valerate (PHBV) was mixed with untreated rice straw (RS) and treated rice straw (TRS) in different ratios as illustrated in Table 1.

Table 1. Formulation of PHBV with untreated and treated rice straw composites

Untreated rice straw % (RS)

| Composite symbol | Poly hydroxybuterate-co-valerate % (PHBV) | Untreated rice straw % (RS) |
|------------------|---|-----------------------------|
| PV-RS-0 | 100 | 0 |

| PV-RS-20 | 80 | 20 |
|------------------|---|----------------------------|
| PV-RS-30 | 70 | 30 |
| PV-RS-40 | 60 | 40 |
| Composite symbol | Poly hydroxybuterate-co-valerate % (PHBV) | Treated rice straw % (TRS) |
| PV-TRS-0 | 100 | 0 |
| PV-TRS-20 | 80 | 20 |
| PV-TRS-30 | 70 | 30 |
| PV-TRS-40 | 60 | 40 |

These formulations were mixed and melted in a two-roll mill (Betol Machinery Ltd, UK) at 160 °C for 12 min. A compression molding machine (HEXA PLAST- INDIA) was used for the preparation of sheets (20 mm × 20 mm × 3 mm) through compression molding at 160 °C and pressure of 20 ton for 10 min.

2.2. Characterization techniques Fourier-transform infra red (FTIR) analysis of the prepared composites

(FTIR) spectroscopy was performed on a Perkin Elmer spectrum BX. The samples were dried completely and pressed with Potassium Bromide (KBr) to form disks. The IR spectra of neat PHBV, RS, TRS and its prepared composites were recorded.

2.3. Morphological studies by Scanning Electron Microscope (SEM)

A morphological study was done using a JEOL Scanning Electron Microscope Jeol model JSM-5300 LV instrument at the City of Scientific Research and Technology, Alexandria, Egypt. The samples were mounted directly onto aluminum specimen stubs and coated with gold-palladium in a sputter coating unit for approximately 40 s at 20 µA and 75 mTorr. Then they were placed in aluminum stubs inside the SEM chamber for viewing the surface morphology.

2.4. Mechanical testing

The tensile strength and tensile modulus for the prepared composites were performed according to ASTM D 638 and D790 respectively using the Universal Testing Machine Shimadzu AG-IS, at the City of Scientific Research and Technology, Alexandria, Egypt,

2.5. Thermal analysis

Thermogravimetric analysis (TGA) was carried out according to ASTM D3850 using a TA instrument Shimadzu TGA-50/50H and the differential scanning calorimetry (DSC) was examined according to ASTM D 3418 ^[13] using a Shimadzu DSC-60 at the City of Scientific Research and Technology, Alexandria, Egypt.

2.6. Water absorption, specific gravity and average diffusion coefficient

The water absorption test was done according to ASTM D 570. Samples were placed in a container filled with distilled water and after 24 hrs the samples were removed, wiped off and weighed. The specific gravity of the fiber composites was measured according to the ASTM D 792 standard test method. ^[13] The average diffusion coefficient (D) was calculated, that indicates the rate of moisture diffusion through all the faces of the specimen.

3. Results and Discussions

3.1. Physical and chemical characterization of untreated and treated rice straw

As we are preparing fiber reinforced polymers, we needed to characterize the fiber compositions. The physical and chemical properties of the untreated and treated rice straw illustrated that, the cellulose content has increased after the treatment process while both Hemicellulose and lignin contents have decreased as shown in table 2. This will enhance the compatibility between the rice straw and the polymer and consequently improve their mechanical properties.

Table 2. Physical and chemical characterization of untreated and treated rice straw

| Test | | | | | | |
|---------------------------|-------------------------------------|--------------------|---------------------|-------------------------|------------------|-------------------|
| Sample | Specific gravity gm/cm ³ | Moisture content % | Cellulose content % | Hemicellulose content % | Lignin content % | Residue content % |
| Untreated rice straw (RS) | 1.08 | 7.65 | 41.15 | 28.4 | 16.2 | 6.6 |
| Treated rice straw (TRS) | 1.15 | 7.94 | 74.52 | 10.57 | 4.81 | 2.16 |

3.2. Functional groups characterization of RS, TRS, PHBV and their composites

The functional groups of the reinforced composites were investigated by FTIR as shown in Figure 1.

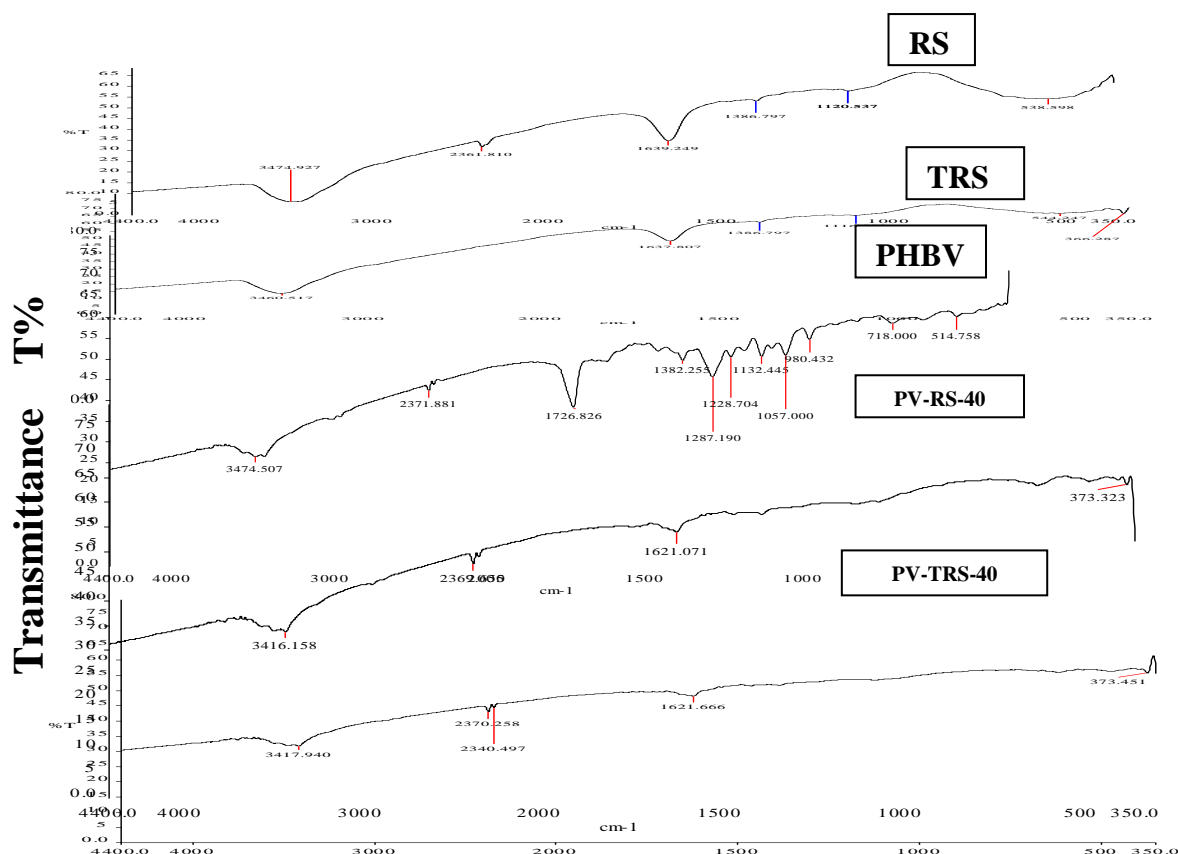


Figure 1. FTIR spectra for RS, TRS, PHBV and their composites

The FTIR spectra of PHBV revealed the presence of ester bands at 1726 cm⁻¹ (C=O stretching), 1132 cm⁻¹ (C-O stretching), and the bands at 1287–1382 cm⁻¹ were assigned to the stretching vibration of C-O-C group. [14-18] The spectra of both RS and TRS showed an absorption band at a range from

3200 to 3600 cm^{-1} that is characteristic of the OH stretching resonance. The position and shape of this OH band suggest that the hydroxyl groups of fiber and polymer were involved in hydrogen bonding. By comparing the spectra of the TRS with that of the RS, the band at 2361 cm^{-1} disappeared; this could be attributed to the effect of rice straw treatment.^[19-22] The band of the carbonyl group C = O in the PHBV, RS and TRS appeared at 1726 cm^{-1} it was shifted to 1621 cm^{-1} in the reinforced composites, which could be attributed to hydrogen bonding between the polymer and fiber. The FTIR spectra of the reinforced composites indicated that there is an interaction between the fiber and the polymer that will be reflected in their mechanical properties.

3.3. Morphology of RS, TRS, PHBV and their composites

The SEM micrograph of PHBV clearly showed homogenous, smooth, and uniform surface, while the SEM of RS indicated a random distribution for the fiber particles as shown in Figure 2.

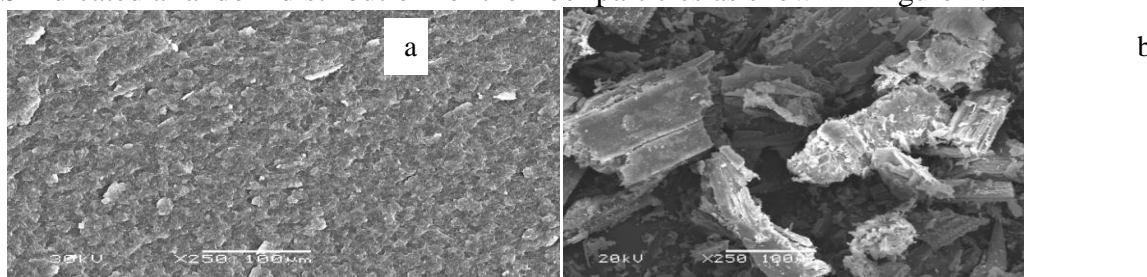


Figure 2. SEM micrographs of: (a) PHBV, (b) RS

The SEM micrographs of the untreated rice straw (RS) reinforced (PHBV) composites (PV-RS-20, PV-RS-30 and PV-RS-40) indicated that the fibers are agglomerated and appeared to be free of any matrix interactions as shown in Figure 3.

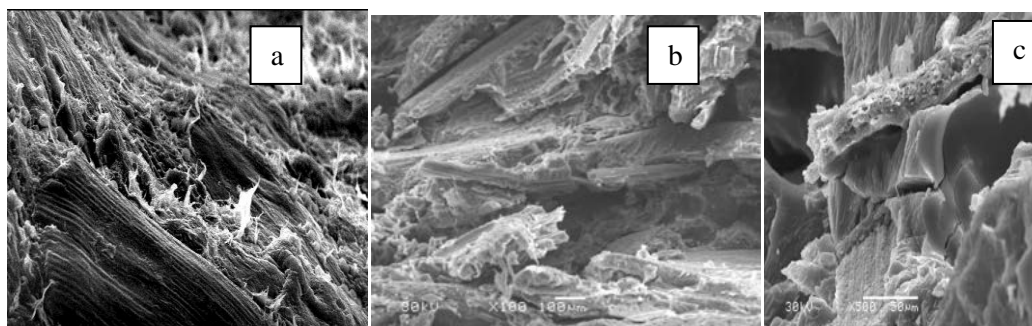


Figure 3. SEM micrographs of PHBV/RS composites (a) PV-RS-20, (b) PV-RS-30, (c) PV-RS-40.

It was clear that, as the fiber's percentage in the composites increases, the probability of agglomeration of the fiber increases leading to weakness of mechanical properties due to difficulty of transferring the stress along the composites as mentioned by Neilsen.^[23]

Singh *et al*^[24] observed similar morphology for bamboo fiber reinforced PHBV composites. The SEM micrographs of the reinforced (PHBV) polymer with treated rice straw (TRS) (PV-TRS-20, PV-TRS-30 and PV-TRS-40) showed better alignment between TRS and PHBV which is clearly noticed in Figure 4. It was concluded that, as the content of TRS in the composites increases, the number of cracks and voids decreased and the fibers are well embedded in the polymer matrix, leading to improvement in the mechanical properties.

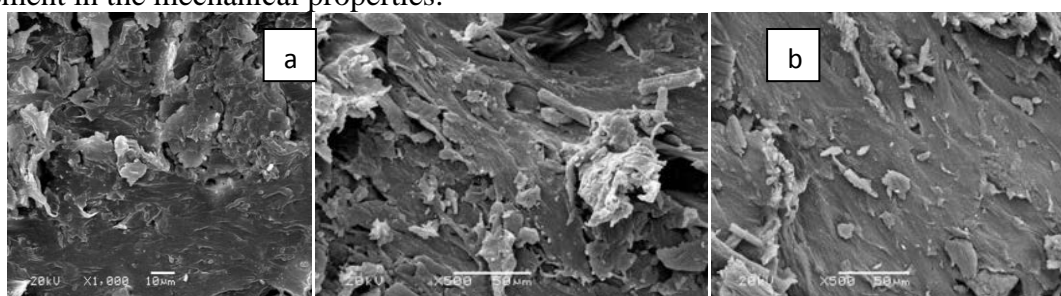


Figure 4. SEM micrographs of PHBV-TRS composites: (a) PV-TRS-20, (b) PV-TRS-30, (c) PV-TRS-40.

3.4. Mechanical properties of PHBV /RS and PHBV-TRS composites

The stress-strain deformation graphs of the tested composites showed that the reinforcing effect of the natural fibers on the elasticity of the polymer is very high compared to the unreinforced matrix. It was noticed that, the tensile strength for the untreated rice straw (RS) reinforced (PHBV) composites (PV-RS-20 and PV-RS-30) was slightly less than that of the PHBV matrix; this could be attributed to the amorphous arrangement between the fiber and the polymer and the agglomeration of fibers. According to *Rouison et al*^[25] as the dispersed phase loading increases, the effective cross-sectional area of the continuous phase is reduced, subsequently resulting in a decrease of the tensile strength. While for the composite (PV-RS-40) the tensile strength was improved, due to the flexibility of lignocellulosic fiber which is higher than that of the (PHBV) polymer.

For the PHBV-TRS composites, the tensile strength were higher than that of the PHBV-RS composites as indicated in Figure 5, this was attributed to good homogeneity and compatibility between TRS and PHBV matrix after treatment of the fiber and removal of most of lignin and Hemicellulose that were resistant somewhat to the compatibility process. Similar trends have been reported by *Rouison et al* and *Sreekumar et al*^[25, 26] for hemp fiber reinforced and sisal fiber reinforced polyester composites.

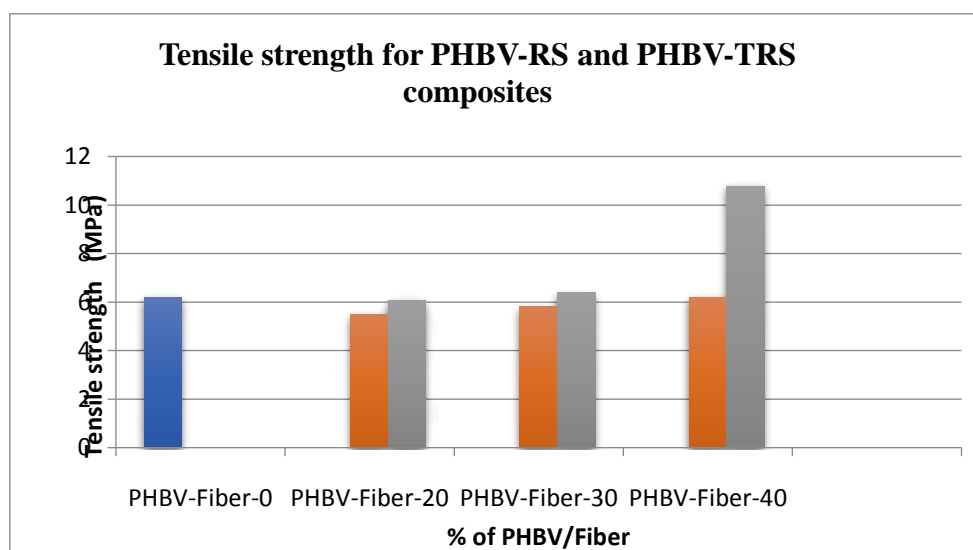


Figure 5. Tensile strength of PHBV-fiber composites in different ratios.

As the content of the TRS in PHBV-TRS composites increased from (20 to 40 wt %), the tensile strength has increased from (8 to 77.7%) respectively.

The modulus of elasticity for both PHBV-RS and PHBV-TRS composites had increased with increasing the fiber loading as shown in Figure 6.

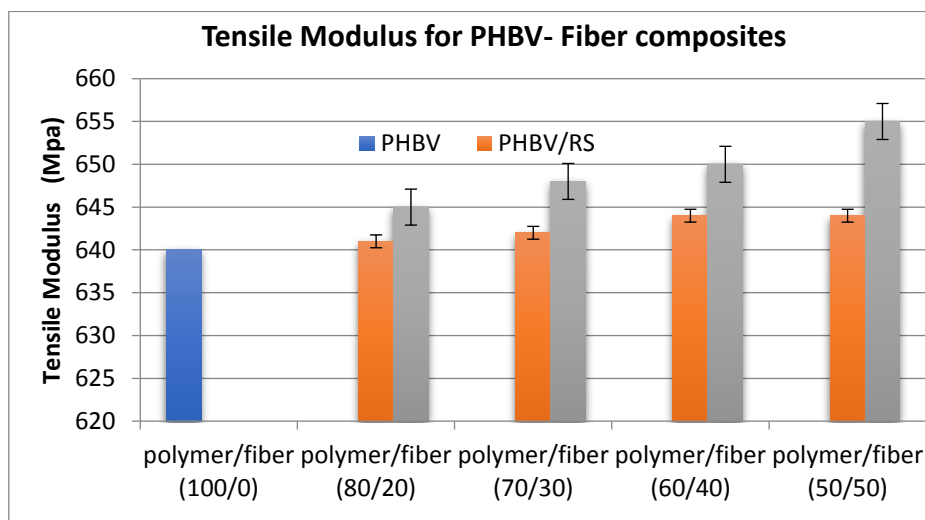


Figure 6. Tensile modulus for PHBV-fiber composites in different ratios.

3.5. Thermal analysis

a. Thermogravimetric analysis of PHBV, PHBV-RS and PHBV-TRS composites

The TGA curve of PHBV indicated that the thermal decomposition of PHBV has occurred at (270°C) in a single step of degradation with a weight loss of (96.67%). While the degradation of the RS started at (150°C), which was attributed to water vaporization^[27] then the degradation increased by increasing the temperature due to the thermal decomposition of hemicelluloses and the glycosidic links of cellulose, and the onset temperature was (238°C) as illustrated in Figure 7.

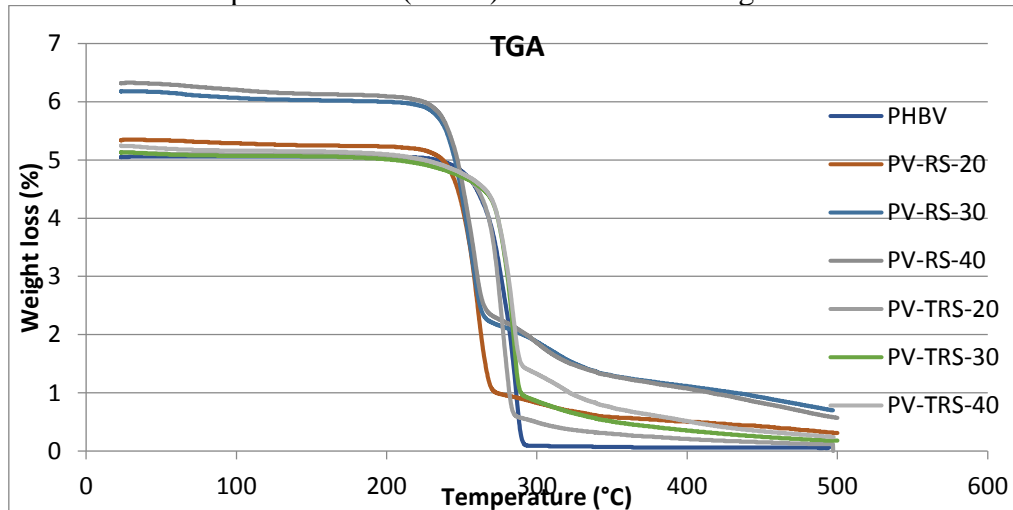


Figure 7. TGA curves for PHBV-RS and PHBV-TRS composite in different ratios of fiber

Thermal decomposition of PHBV-RS composites occurred in a two-step process. The first step occurred at (245°C) that could be attributed to the thermal decomposition of the RS fibers. The second thermal decomposition step at (309°C) that was most likely due to the thermal degradation of the polymer PHBV, which means that the reinforcement of the polymer with the RS has increased the thermal stability of the polymer as illustrated in Table 3.

The reinforcing of the polymer (PHBV) with the RS and TRS did not significantly change the thermal decompositions of all PHBV-RS and PHBV-TRS composites as their degradation temperatures are nearly the same.^[28-31]

Table 3. Thermal properties from TGA of different formulation of PHBV-RS and PHBV-TRS composites.

| Composite | First stage | | Second stage | | Final stage | |
|------------|-------------|----------|--------------|----------|-------------|----------|
| | T (°C) | Wt loss% | T (°C) | Wt loss% | T (°C) | Wt loss% |
| PHBV | 229 | 1.58 | 270 | 96.67 | 334 | 0.535 |
| PV- RS-20 | 247 | 78.91 | 309 | 7.25 | 421 | 5.32 |
| PV -TRS-20 | 248 | 86.64 | 305 | 5.12 | 421 | 3.88 |
| PV- RS-30 | 241 | 59.45 | 304 | 15.08 | 418 | 12.38 |
| PV-TRS-30 | 243 | 71.67 | 306 | 7.84 | 420 | 6.75 |
| PV-RS-40 | 245 | 63.16 | 309 | 12.66 | 423 | 8.13 |
| PV-TRS-40 | 260 | 68.37 | 310 | 7.89 | 445 | 7.11 |

b. Differential scanning calorimetry of PHBV, PHBV-RS and PHBV-TRS composites

Generally, the DSC results for PHBV/RS composites showed that, as the content of RS in the composite was increased the first and second melting temperatures changed a little. While for PHBV-TRS composites the first and the second melting temperatures were higher than that of the PHBV-RS composites as shown in Table 4. These could be attributed to the good adherence between the TRS and the PHBV polymer. Also, the probability of formation of hydrogen bonds between the functional group of the TRS fiber and the carbonyl group of the PHBV. These functional materials acted as a physical cross-linking agent, herein reducing the crystallization rate of PHBV. [32] The DSC results indicated the presence of crystallization in only the (60/40wt %) composites.

Table 4. Thermal properties from DSC of different formulation of PHBV-RS and PHBV-TRS composites.

| Composite | T _{m1} (°C) | H _{m1} (J/g) | T _{m2} (°C) | H _{m2} (J/g) | T _c (°C) | H _c (J/g) |
|------------|-------------------------|--------------------------|-------------------------|--------------------------|------------------------|-------------------------|
| PHBV | 164.4 | -20.68 | 174.19 | -80.54 | - | - |
| PV-RS-20 | 147.31 | -9.11 | 159.84 | -25.14 | - | - |
| PV -TRS-20 | 163.13 | -67.61 | 172.4 | -68.16 | - | - |
| PV- RS-30 | 145.3 | -9.86 | 155.68 | -26.83 | - | - |
| PV-TRS-30 | 162.56 | -58.88 | 172.81 | -71.6 | - | - |

| | | | | | | |
|-------------------|---------------|--------------|---------------|---------------|------------|-------------|
| PV-RS-40 | 128.61 | -2.1 | 154.2 | -36.07 | 115 | 1.59 |
| PV -TRS-40 | 162.66 | -44.4 | 173.29 | -45.36 | - | - |

3.6. Density results of PHBV, PHBV-RS and PHBV-TRS composites

Density has been proved to have a very large influence on the mechanical properties of fiber plastic composites. Therefore, changes in density would likely be a function of increased fiber dispersion or polymer penetration of the fibers. [33] Neat PHBV was found to have density of (1.25 g/cm³) while the density of rice straw (RS) and treated rice straw (TRS) were (1.08 g/cm³, 1.15 g/cm³) respectively. The density of the reinforced composites (PHBV-RS) was slightly decreased. This could be attributed to the lower density of the RS than that of the PHBV. So as the content of fiber increased in the composites the density of the composite was decreased, as shown in Table 5. The density of (PHBV-TRS) composites was lighter than that of (PHBV-RS) composites; this could be attributed to the treatment of RS, which removes most of lignin and hemicelluloses constituents from the rice straw.

Table 5. Density of PHBV, RS, TRS, Cellulose and their different composites

| Sample | Density g/cm³ |
|-------------------|---------------------------------|
| PHBV | 1.250 |
| RS | 1.080 |
| TRS | 1.150 |
| PV-RS-20 | 1.220 |
| PV-RS-30 | 1.184 |
| PV-RS- 40 | 1.194 |
| PV-TRS-20 | 1.210 |
| PV-TRS-30 | 1.182 |
| PV-TRS- 40 | 1.178 |

The low density of biocomposites is favored for lightweight composite applications. Lightweight composites are preferred by automakers and packaging industries due to potential weight savings. As for example the density of fiber is significantly lower than that of glass fiber reinforced composite counterparts. So the lignocellulosic fibers with density ranging from (1-1.5g/cm³) were preferred as reinforcement materials rather than the high density glass fibers (2.6 g/cm³) for such applications.

3.7. Water absorption of the prepared composites

One can recognize that most of the water absorption behaviors of fiber reinforced composites depend on the fiber content. Initially, all the prepared PHBV-RS composite samples showed a very rapid increase in percentage of water absorbed, as the immersion period increased. The absorption curve reached a plateau after the first week till the end of period of test (14 days), suggesting that the samples attained a saturation point and no more water could be absorbed into the composite system. It was noticed that, as the ratio of fiber increased in the composite, the uptake of water increased due to the highly hydrophilic character of fibers. The water uptake is dependent on the chemical constituents present in the individual fibers. Out of the three major constituents of the lignocellulosic fibers, cellulose and hemicelluloses are hydrophilic, while lignin is hydrophobic in nature. [33] For the PHBV-TRS composites, as the TRS content increased the water absorption decreased, as shown in Figure 8, this could be attributed to the elimination of lignin components from the RS during the treatment

process, which was considered as an aromatic structure, which acts as a hollow site inside the fiber and facilitates water absorption process to occur.

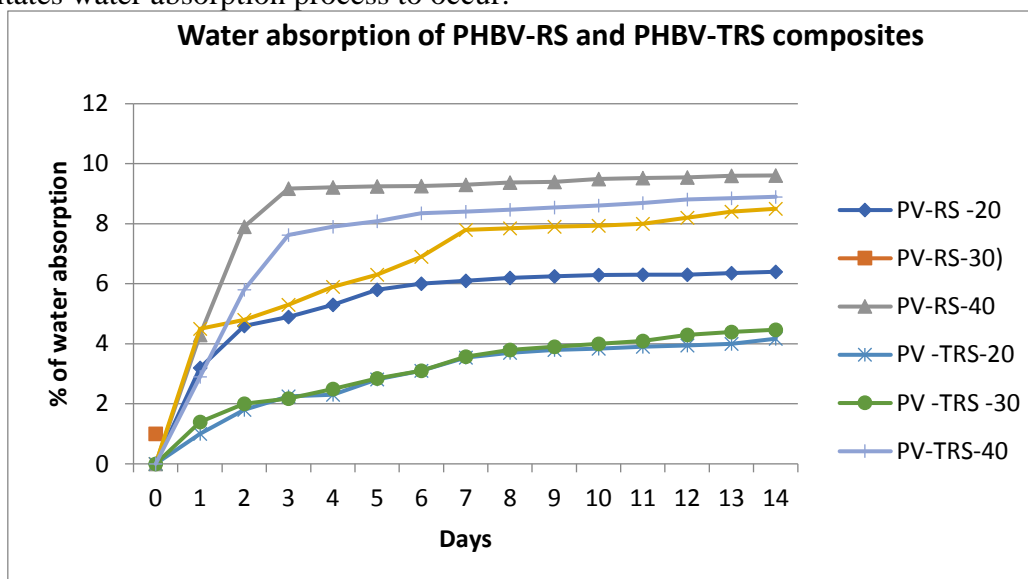


Figure 8. Water absorption behavior as a function of time for PHBV-RS and PHBV-TRS composites in different ratios.

The low water absorption of (PHBV-TRS) composites makes them favored for packaging applications.

3.8. The average diffusion coefficient (D)

The average diffusion coefficient D measures the rate of moisture diffusion through all faces of the specimen. The average diffusion coefficient (D) in table 6 showed that, the results increased for the untreated fiber reinforcement PHBV-RS composites and decreased for treated fiber reinforcement PHBV-TRS composites samples.

Table 6. The average diffusion coefficient of different composites

| Composite sample | Average diffusion coefficient (mm ² /day) |
|------------------|--|
| PV-RS-20 | 0.006 |
| PV-RS-30 | 0.005 |
| PV-RS-40 | 0.002 |
| PV-TRS-20 | 0.980 |
| PV-TRS-30 | 0.033 |
| PV-TRS-40 | 0.010 |

Conclusion

Reinforcing PHBV with cellulosic fiber can overcome its drawbacks as brittleness and low impact resistance. [33] The addition of rice straw to PHBV matrix did not affect the thermal properties of the composite. The tensile strength and modulus of elasticity for the characterized (PHBV-RS) composites showed slight improvement when compared to that of the pure polymer (PHBV). While for (PHBV-TRS) composites (40%TRS w/w), the mechanical properties has improved by nearly 70% compared to that of the pure polymer. The results of this work have showed that the rice straw waste could be used as alternative biodegradable reinforcement material and the (PHBV-TRS) composites will produce good mechanical and thermal material. However, the utilization of renewable and degradable components with decreasing the cost of the final material and eliminating of wastes make the production of (PHBV-TRS) composites promising for packaging, automotive and agriculture applications.

References

- [1] Environment and natural resources management, 2017, working paper, FAO ISSN 2226-6062
- [2] M. R. Sokele and A. Pilipović, Waste Management & Research, (2017), Vol. 35(2) 132 –140
- [3] Environmental Commission, (2017), “Measures to combat plastic pollution in water” EMUN.
- [4] S. Lambert and M. Wagner, “Environmental performance of bio-based and biodegradable plastics: the road ahead”, Chem. Soc. Rev. (2017), 46, 6855-6871
- [5] Klyosov A.A., “Wood-Plastic Composites”, (2008) Hoboken, NJ: John Wiley & Sons.
- [6] Clemons C., “Composites from wood and plastics. In: Wood and Fiber Product”, Seminar. VTT and USDA Joint Activity, Finland, September (2009) 22–23.
- [7] Summerscales J., Nilmini P.J.D., Virk A.S. and Hall W., Composites: Part A: Applied Science and Manufacturing (2010), 41: 1336–1344.
- [8] Rowell R.M., “Handbook of Wood Chemistry and Wood Composites”, (2012), Boca Raton, FL: Taylor and Francis.
- [9] Ouajai S. and Shanks R.A., , “Preparation, structure and mechanical properties of all-hemp cellulose biocomposites”, Composites Sciences and Technology (2009) ,69: 2119–2126.
- [10] Joshi S.V., Drzal L.T., Mohanty A.K. and Arora S., Composites Part A: Applied Science and Manufacturing, (2004), 35: 371–376.
- [11] Buzarovska A, Gentile G, Errico M, (2008), Australian Journal of Crop Science, 1(2):37-42.
- [12] Sarkar N. and Aikat K., (2012), J. Microbiol. Biotech. Res., 2012, 2 (5):717-726.
- [13] American society for testing and materials (ASTM), (2013), USA, 1,2,3,8.
- [14] Villegas P., Rodríguez J., Valle J. and García J., (2007), J. Anal. Appl. Pyrolysis , 80, 507-514.
- [15] Gómez-Serrano, V., Piriz-Almeida F., Durán-Valle C.J. and Pastor-Villegas J., A study by FT-IR spectroscopy”, Carbon, (1999).37, 1517 1528
- [16] Gómez-Serrano V., Pastor-Villegas J., Perez-Florindo A., Duran-Valle C. and Valenzuela-Calahorra C., “FT-IR study of rockrose and of char and activated carbon”, J. Anal. Appl. Pyrolysis , (1996), 36, 71 80 .
- [17] Pastor-Villegas J., Meneses Rodríguez J.M., Pastor-Valle J.F. and García M.G., 2007, “Changes in commercial wood charcoals by thermal treatments”, J. Anal. Appl. Pyrolysis, (2007), 80, 507514.
- [18] Peng F., Song H., Jun X., Lushi S., Tao Y., Anchao Z. and Z. Junying, “Mechanism Study of Rice Straw Pyrolysis by Fourier Transform Infrared Technique product engineering and chemical technology”, Chinese Journal of Chemical Engineering ,(2009) 17(3) 522 -529.
- [19] Liu P. and Su Z.X., “Surface-initiated atom transfer radical polymerization (SI-ATRP) of n-butyl acrylate from starch granules”, Carbohydr. Polym. 62 (2005) 159–163.
- [20] Kaewtatip K. and Tanrattanakul V., “Preparation of cassava starch grafted with polystyrene by suspension polymerization”, Carbohydr. Polym. 73 (2008) 647–655.
- [21] Nunes J.S., de Vasconcelos C.L., Dantas T.N.C., Pereira M.R. and Fonseca J.L.C., “Electrokinetic behavior of a poly(butyl acrylate-co methacrylic acid) latex”, Colloids Surf. A 275 (2006) 148–152.
- [22] Goncalves S. P. C., Martins-Franchetti S. M. and Chinaglia D. L., 2009, “Biodegradation of the Films of PP, PHBV and Its Blend in Soil”, J Polym Environ. (2009)17:280–285.
- [23] Nielsen L.E., “.Mechanical properties of polymers and composites”,(1974) vol. 2. New York: Marcel Dekker, Inc.,
- [24] Singh S., Mohanty A.K., Sugie T., Takai Y. and Hamada H., “ Renewable resource based biocomposites from natural fiber and polyhydroxybutyrate-co -valerate (PHBV) bioplastic”, Composites, Part A(2008); 39 (5): 875-886.
- [25] Rouison D., Sain M. and Couturier M., “Resin transfer molding of hemp fiber composites: optimization of the process and mechanical properties of the materials”, Composites Sci. Technol. (2006); 66 (7-8): 895 -906.

- [26] Sreekumar P.A., Joseph K., Unnikrishnan G. and Thomas S., “A comparative study on mechanical properties of sisal -leaf fiber -reinforced polyester composites prepared by resin transfer and compression moulding techniques”, *Composites Sci. Technol.* (2007); 67 (3 -4): 453 -461
- [27] Otari S.V. and Ghosh J.S., “Production and Characterization of the Polymer Polyhydroxy Butyrate-co-polyhydroxy Valerate by *Bacillus Megaterium* NCIM 2475”, *Current Research Journal of Biological Sciences*, (2009) 1(2): 23-26.
- [28] Sugama Y., Amirul A., Sipaut C. and Nasri M., “Biosynthesis of poly(3-hydroxybutyrate- co - 3-hydroxyvalerate) and characterisation of its blend with oil palm empty fruit bunch fibers”, *Bioresource Technology* 102 (2011) 3626–3628.
- [29] Liu B., Jiang L., Liu H. and Zhang J., *Ind. Eng. Chem. Res* (2010) 49:6399–6406
- [30] Rui Z, Liu H and Zhang J. , *Ind. Eng. Chem. Res*, (2011) 51:7786–7792
- [31] Wang X., Chen Z., Chen X. and Jueyu P., “Miscibility, Crystallization Kinetics, and Mechanical Properties of Poly(3-hydroxybutyrate-co-3-hydroxyvalerate)(PHBV)/Poly(3-hydroxybutyrate-co-4 hydroxybutyrate) (P3 /4HB) Blends’, Multidisciplinary Research Center, Shantou University, Guangdong 51506 3, Shantou, China, *J Appl Polym Sci.* (2010) 117: 838–848.
- [32] Nagarajan V., Misra M. and Mohanty K., “New engineered biocomposites from poly(3-hydroxybutyrate-co-3-hydroxyvalerate)(PHBV)/poly(butylenesadipate-co-terephthalate) (PBAT) blends and switchgrass: Fabrication and performance evaluation”, *Industrial Crops and Products*, (2013), 42, 461– 468.
- [33] Lim JS, Abdul Manan Z, Wan Alwi SR and Hashim H., “A review on utilization of biomass from rice industry as a source of renewable energy”, *Renewable and Sustainable Energy Reviews* (2012); 16:Pages 3084-3094.

16- Desalination of Simulated Sea Water by Emulsion Liquid Membrane Using Edible Oils as Liquid Membrane

Shaimaa G.Sadek^{†1}, A. A. Moneer², Moustafa S. Abbassy¹, Mona M.Naim³

¹Institute of Graduate Studies and Research, Alexandria, Egypt

²National Institute of Oceanography and Fisheries, Alexandria, Egypt

³Faculty of Engineering, Alexandria University Alexandria, Egypt

[†]E-mail: eng.shimal2@gmail.com

Abstract

Desalination using liquid membrane (LM) technology has been investigated using different configurations with hazardous organic solvents as LM barriers between donor phase (DP) and receptor phase (RP). However, edible oils have not yet been applied as green and safe LMs in desalination processes, to the best of our knowledge, as is clear from the literature cited. Accordingly, in this paper, the emulsion LM (ELM) technique with green edible oils was investigated in the removal of sodium chloride from aqueous solutions of different concentration as an attempt towards desalination to avoid the negative impact of hazardous organic solvent on the environment. Variables investigated included: type of LM (edible oils), treatment ratio (TR), concentration of sequestering agent in RP and initial concentration (C_i) of DP. In conclusion, the investigation showed the simplicity and adequacy of desalination of simulated seawater by the application of the ELM technique, using green edible oils reached 99% of salt extraction with high initial concentration (simulated sea water), in the absence of either MC or emulsifier.

Keywords: Desalination, Emulsion liquid membrane, Sequestering agent, Soluble starch, , edible oils.

1. Introduction

Freshwater makes up a very small fraction of all water on our planet. 94% of the water around the globe is salty water in seas and oceans while only 6% is free of salt. Of the latter, about 77% is in glaciers and 22% is underground. While salt water is important for transportation and fisheries, it is too salty to sustain human life or farming. Desalting techniques have increased the range of water resources available for use by a community ^[1].

The water level dropped while the rate of population is growing with increase in water consumption. In the near future, this point may create a serious problem, since freshwater for both drinking and irrigation will not be sufficient. Accordingly, desalination of sea or brackish waters was being a must, including Egypt (particularly with the starting of Ethiopian Dam construction on the Blue Nile that provides 85% of the Nile water to Egypt), so desalination processes for separation of salts from saline water are to be improved to achieve this aim.

Desalination technologies that are in common practice are divided mainly into two main categories which are: thermal processes (include multi-stage flash distillation, multi-effect distillation and vapor compression distillation), and membrane processes (including electro-dialysis, and reverse osmosis), and all of them are well established and applied on an industrial scale. Each technique has its merits and drawbacks. Desalination by thermal processes have numerous limitations, which include intensive energy consumption, high capital costs and corrosion problems, while membrane processes suffer from membrane fouling and high membrane cost and other problems including low water recovery, and environmental problems due to brine disposal in case of reverse osmosis ^[2].

In other hand, liquid membranes (LMs) technique was discovered in 1968, by Li ^[3]. It offers the advantages of active transport, high selectivity, easy scale-up, low energy requirements, low capital and operating costs, and no pores to be blocked or fouled like solid membranes ^[3]. LMs also known as pertraction, appeared as a new and prospective separation technique due to its advantages over solid membranes and liquid-liquid extraction, and have since then attracted the attention of many scientists and engineers. The LM itself separates two miscible phases from each other, and is insoluble in these phases. It can have a hydrophilic or a lipophilic character. An LM explores a very simple idea: two homogeneous, completely miscible liquids, which may be referred to as donor phase (DP)

and receptor phase (RP), are spatially separated by a third liquid, immiscible and practically insoluble in the former two liquids- the membrane phase. Due to the favourable thermodynamic conditions created at the interface between DP and RP, some components are extracted from DP and transported into the LM ^[4]. Simultaneously, at the second interface (LM/RP), conditions are created, which favour the reverse transport, i.e., the extraction of the above-mentioned components from the LM and their accumulation in RP ^[5]. There are three basic types of liquid membranes - the Emulsion Liquid Membrane (ELM), the Immobilized Liquid Membrane (ILM), also called Supported Liquid Membrane (SLM) and the bulk liquid membrane (BLM).

In general, no literature cites desalination of seawater by LMs, except by Naim (2001) the ELMs has been accomplished effectively for the first time, and has been investigated using a supported LM by Naim and Monir (2003)^{[6]& [7]}. Various factors that would affect the degree of desalination were studied, and these were type of organic membrane liquid (ML), thickness of ML, presence of emulsifier or MC in the ML, concentration of MC in ML, presence of polyelectrolyte (sequestant) in the RP and presence or absence of magnetic stirring. The volume ratio of DP to RP was kept constant at 4:1 and DP (simulated seawater) ranged between 36 and 39 g/L, cellophane constituted the support for the ML. The removal of NaCl using facilitated up-hill transport through BLMs containing dibenzo-18-crown-6 was investigated by Naim et al. ^[8] from solutions of different concentrations as an attempt for desalination. Variables investigated included: type and quantity of LM, quantity of MC in LM, and type and quantity of SA in RP. Results indicated that a mixture of 1:1 b.v. DCE plus chlorobenzene (CB) was a better LM than CB alone, and that DCE was almost equivalent to nitrobenzene. As to the effect of SA, soluble starch gave better complexation with NaCl than sorbitol in the RP. It was also shown that the presence of the selected MC was efficient. An optimum quantity of MC led to the highest percentage of extraction of NaCl. The smaller volume. A prototype was devised and constructed by Naim et al. ^[9] as a preliminary step for the development of an industrial scale process in which desalination by an ELM technique with CB as LM takes place. The process is intended to be a breakthrough in the field of desalination, which should compete with the currently used reverse osmosis technique. The prototype consists of three stages: emulsion formation, desalination stage, and separation of the product into two phases (desalinated water and spent emulsion). However, the LMs used were not environmentally friendly and thus posed a threat to humans, animals and aquatic life. Numerous works on the transport ability of various cations through edible oils as LMs has been done but not applied on desalination process. Ahmad et al. ^[10] studied the utilization of ELM for removal of cadmium from aqueous solution. Aliquat 336 and Span 80 were used as carrier and surfactant, respectively, whereas **corn oil** was used as an environmentally benign diluent in the membrane phase. Influence of operating conditions that affect the performance including ultra-sonic power, emulsification time, TR, stirring speed, and together with initial cadmium concentration were investigated. A kinetic study of Cu(II) transport through a **soybean** oil-based BLM containing di-2-ethylhexylphosphoric acid (carrier) and tributyl-lphosphate (phase modifier) diluted in soybean oil (diluent) was conducted by Changa et al. ^[11]. Effects of initial Cu (II) concentration in the feed phase, and temperature, were investigated, and their kinetic parameters were determined from the kinetic models of two consecutive irreversible first order reactions. Various initial Cu(II) concentrations in the feed phase (50-500 mg/L) and various temperatures (27-43°C) were found not to affect the rate of extraction process significantly. The rate-controlling steps of both extraction and stripping processes were determined and a plausible transport mechanism was proposed. The kinetics of Cu(II) transport through soybean oil-based BLM was then compared with that of a similar kerosene-based BLM, and the application of soybean oil-based BLM in real industrial wastewater was also studied. The extraction efficiency of hexavalent chromium from water has been investigated using a **vegetable oil**-based ELM technique by Norasikin et al. ^[12] and Björkegren et al. ^[13]. The main purpose of these study was to create a novel ELM formulation by choosing a more environmentally friendly and non-toxic diluent such as **palm oil**. The membrane phase so formulated includes the mobile carrier TOMAC, to facilitate the metal transport, and the hydrophilic surfactant Tween 80, to facilitate the dispersion of the ELM phase in the aqueous solution. Span 80 was used as surfactant and butanol as co-surfactant. The results demonstrated that this novel ELM formulation,

using the vegetable palm oil as diluent, is useful for the removal of Cr(VI) with an efficiency of over 99% and is thus competitive with the already existing, yet less environmentally friendly, ELM formulations. Different water qualities (deionized, distilled, or tap water) did not significantly influence the extraction rate. Kiani and Mousavi ^[14] conducted water in **oil emulsions** by using ultrasound waves and used in an ELM process in order to recover arsenic (V) ions from an aqueous medium, the effect of emulsifier concentration and composition, and also sonication time on the emulsion droplet size and the extraction efficiency in order to obtain stable emulsions with small droplets that favor the extraction. Muthuraman and Palanivelu ^[15] studied a SLM system for removal and recovery of textile dye from the aqueous solution using renewable, non-toxic, natural **vegetable oils**, never used before as a liquid membrane. A flat sheet polypropylene supported Teflon membrane impregnated with vegetable oils has been tested for transport of Astacryl golden yellow (a cationic dye). The fundamental parameters influencing the transport of dye such as pH of the feed solution, H₂SO₄ concentration in the strip solution and different type of oils, stirring speed, and initial dye concentrations have been determined. Kazemia et al. ^[16] studied the transport of phenol through SLM using TBP and **sesame oil** as LM. Factors affecting the permeation of phenol such as initial phenol concentration, carrier concentration, feed phase pH and stripping phase concentration. In addition to transport study, stability of the membrane was investigated by examination of stripping phase concentration, carrier concentration and salt concentration effects. The transport of phenol through a flat sheet SLM containing **vegetable oil** as LM has been inspected by Venkateswaran and Palanivelu ^[17]. The permeation of phenol was investigated by varying the experimental conditions like, selection of LM, support material; feed phase pH, stripping solution concentration, stirring speed and different C_i of phenol. It was found that, each LM investigated in the present study, shows the effective removal of phenol using PTFE membrane and PP membrane as a solid support. Among the various oils tested, **palm oil** was found to be the best LM with high permeability, which also confirmed by Othman et al. ^[18] to treat a simulated wastewater containing 300×10⁻⁶ of phenol solution using ELM process. The removal of phenol from wastewater, using pertraction in rotating discs contactor, was studied by Ehtasha et al. ^[19]. A preliminary equilibrium extraction study, with several organic solvents, showed that some vegetable oils such as rapeseed and **sunflower oils**, can substitute classically volatile organic solvent-extracting agents. Rapeseed oil allowed very efficient removal of phenol from acid aqueous solutions to basic aqueous solution during batch pertraction studies. In order to optimize operating conditions, the effect of rotating discs speed and initial phenol concentration in the feed phase, on phenol removal, was studied. The transport rate of phenol was found to increase with increasing rotating discs' speed, and the increase of feed phase concentration had no influence on transport rate. Jusoh et al. ^[20] investigated the outline steps for developing an ELM process for the purification of succinic acid from fermentation broth by using **palm oil** as LM. The steps included LM formulation, ELM stability and extraction of succinic acid. Several carrier, diluent and stripping agents were screened to find appropriate membrane formulation. Later, ELM stability was investigated to enhance the recovery of succinic acid. Finally, the performance of ELM was evaluated in the extraction process.

In this paper desalinate simulated sea water by a ELM technique to obtain potable water for drinking, irrigation and industrial purposes was investigated by using various edible oils as LM were selected and applied as barriers between DP and RP. These various edible oils are safe and could be totally and easily removed from the desalinated water by post treatment. The selected technique which was applied in this work was the ELM technique, since it offers very rapid mass transfer among the three phases concerned (DP, LM and RP), and is expected to give very high degrees of desalination in a single stage.

The experiments was conducted using vegetable oils of different kinds were tested as LMs, soluble starch or water as sequestering agent. Ultra-sonication was used to form the W/O emulsion between the LM phase and the RP. Different variables were studied for their effect on the degree of desalination and the extent of mass transfer from DP to RP and they were: type of LM, TR, concentration of RP, C_i of salt in DP and different power of ultrasonication to produce a successful emulsion.

2. Experimental Part

2.1. Materials

Chlorobenzene CB (LoBa Chemie, India, Analar 99.5%), Green edible oils (sesame, linseed, sunflower, olive, corn) purchased from local supermarket, were used as LMs, Soluble starch (SS) (product of Fisher Chemical, USA) was used as sequestering agent (SA) in RP. Sodium Chloride (product of Alpha Chemika, India, Analar 99.9%) was used for preparation of simulated sea water as DP and distilled water prepared in Lab.

2.2. Procedure

The work that has been carried out can be divided into main three steps;

A- Prepare Emulsion Stage

1. Prepare RP which is soluble starch solution (SSS): dissolve a known volume of SS in 20 ml of distilled water DW.
2. The LM mixed by magnetic stirrer with emulsifier and mobile carrier if they were used.
3. The emulsion was prepared by adding SSS drop wise to LM phase. For the preparation of stable emulsion, the size of internal droplets should be very tiny as small as 1 – 3 μm in diameter. It can be accomplished by high input of energy density to W/O emulsion during emulsification. For the small ELM system, high-speed mechanical agitators with stirring rates up 20,000 rpm and/or ultrasonic emulsifiers are used to prepare emulsion ^[21].

B- Extraction Stage

1. Prepare DP: a known volume of saline water in a cylindrical beaker.
2. The emulsion was added to the saline water DP all at once and dispersed emulsion to form numerous small globules with a typical size of 0.1 – 2 mm in diameter. It by using gentle mixing however, increasing the agitation speed increase shear rate and shear stress and thus, reduce the stability of emulsion, which causes breakage of emulsion liquid membranes ^[21].
3. The extraction stage set-up is as showing in figure (1), the concentration of salt in DP was traced at different time intervals by using a conductivity meter until reaching three consecutive constant concentrations.
4. The concentration ratio of NaCl in DP C_t/C_o is plotted vs. time (minutes) of experimentation and the percent of extracted salt was calculated.
5. Extraction salt from DP according to the following equation:

$$\% \text{ Extraction} = [(C_o - C_t) \div C_o] \times 100$$

where C_o is the initial concentration of sodium chloride in DP before extraction of salt, C_t represents the final concentration of sodium chloride in DP at time (t) after extraction the salt.

C- Separation Stage

1. Separation of the product into two phases (desalinated water and spent emulsion) by settling.
2. Demulsification or Breaking the emulsion: The emulsion is broken by heating it to 50°C accompanied with moderate manual stirring, in the presence of a small amount of acetone, this process is of great importance to maintain recycling of the constituents of the emulsion for further using after adjustment of the quantities of these constituents in case of loss of any of them. Hence, the separation of two immiscible liquids of oil membrane phase containing surfactant and extractant and internal aqueous phase containing highly concentrated solute is generally inevitable ^[22&23].

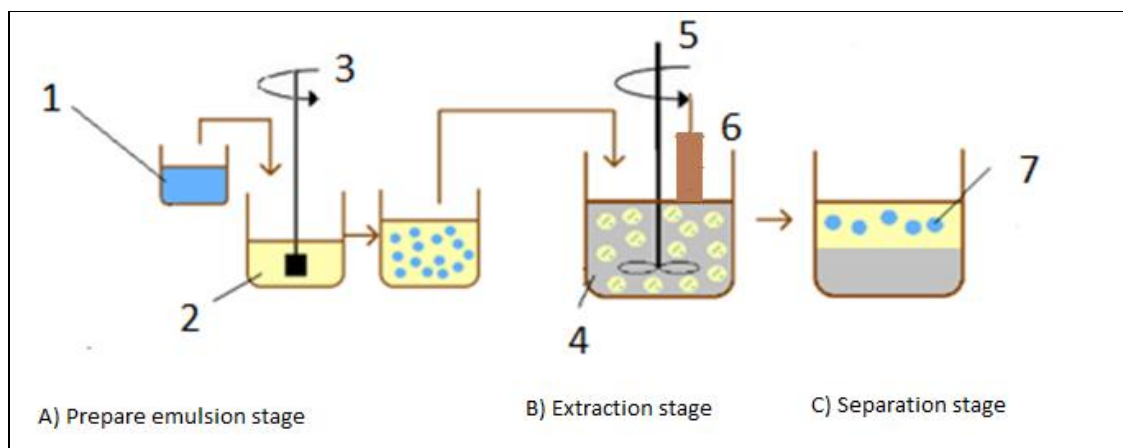


Fig.15: schematic diagram of apparatus, 1) soluble starch solution (receptor phase), 2) liquid membrane, 3) ultra-sonication, 4) saline water (donor phase), 5) gentle mixer, 6) conductivity meter, 7) spent emulsion layer.

3. Results and discussion

3.1. Effect of Types of LM

The viscosity of emulsion is directly proportional to the stability of emulsion [24 & 25]. Therefore, employing highly viscous oil as a membrane phase is able to provide more stable emulsions. However, it has been found that the increased viscosity of the membrane significantly decreases the diffusivity for Newtonian fluids [25 & 26]. Thus this remedy reduces a solute diffusivity, and consequential decrease in extraction rate has been identified as problematic in ELM process [25, & 27].

Six experiments present in figure 2 in which CB, Sesame oil (S), Corn oil (C), Sun Flower oil (SF), Linseed oil (LS) and olive oil (O) were used respectively as LM and % extraction were 30.96, 76.278, 91.987, 78.07, 26.95 and 92.4256 respectively. Accordingly, in the six experiments that follow and in which for the first time green oils were used as LM, which is expected to present a breakthrough worldwide in desalination by ELM using green technology, it was confirmed that on using saline water of $C_i = 35\text{g/l}$, without any MC or Span 80 as emulsifier added to the green edible oils. This is clarified under the figure, which shows the conditions under which the experiments were carried out. Although O oil extracted the salt 92.4256% more than C oil but it was unstable and slower rate of removing salt than C oil. Corn oil is very promising, and these results made us wonder what are the properties of C oil behind these significant degrees of desalination. So when looking up for the composition of C oil it was found C oil consists of 39-63 % linoleic fatty acid and 24 % linolenic acid and 20-42 % oleic acid. CO was the only one with high % of linoleic followed by linolenic, but the O oil consists of 4- 21 % only. Furthermore the corn oil has lower viscosity than other oil (31 mPas) [28].

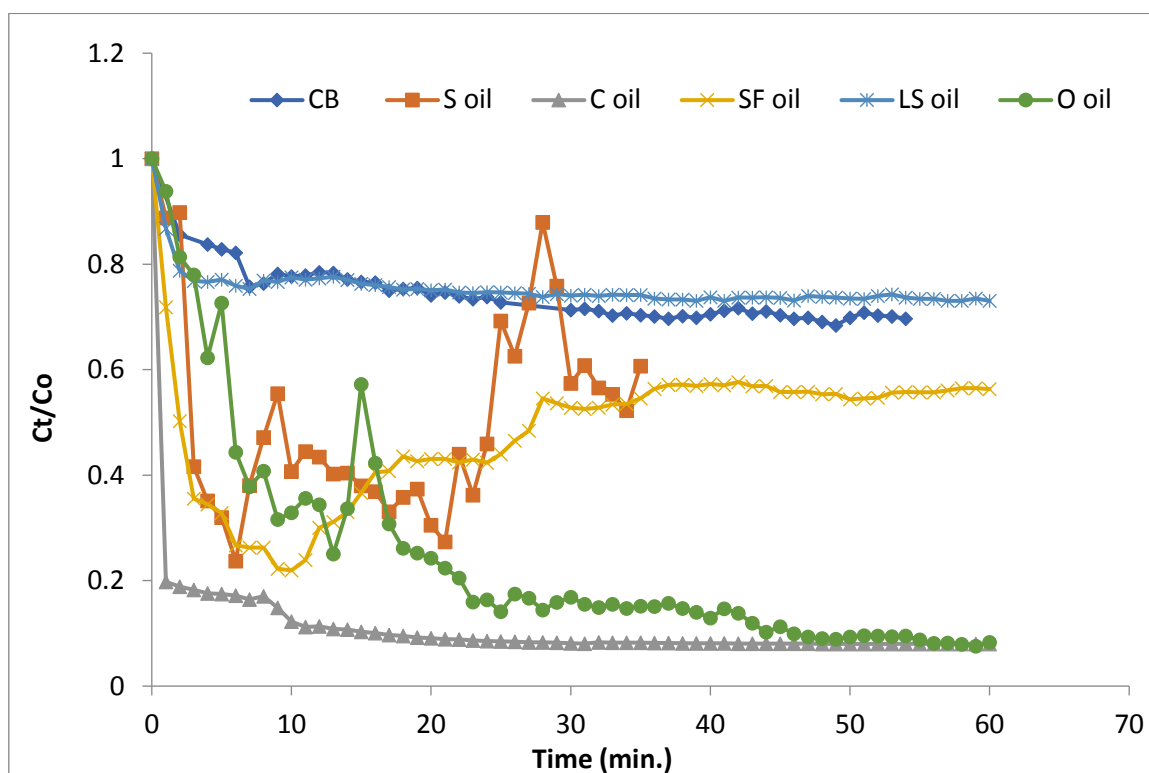


Fig. 2: Effect of type of LM, DP= 500 ml, C_i = 35g/l, 80ml of LM, RP=20ml (1%), TR= 1:5, Room Temp., No MC or emulsifier in LM, Speed of agitation for dispersion emulsion in DP = 750 rpm, ultra-sonication power= 350 Watt and Time of sonication= 15 min.

3.2. Effect of Power of Ultrasonication

Two experiments present in figure 3 in which S oil was used as LM, , in that here the emulsion was prepared by ultrasonication (US). It is observed that though the conditions were all the same in both experiments, yet when the amplitude of the ultrasonicator was decreased from 50 to 40%, percent extraction dropped to almost one third its value, from 76.278 to 27.457, which stresses the importance of adjusting the conditions during US, such that a proper and stable emulsion is formed by providing it with sufficient power during US.

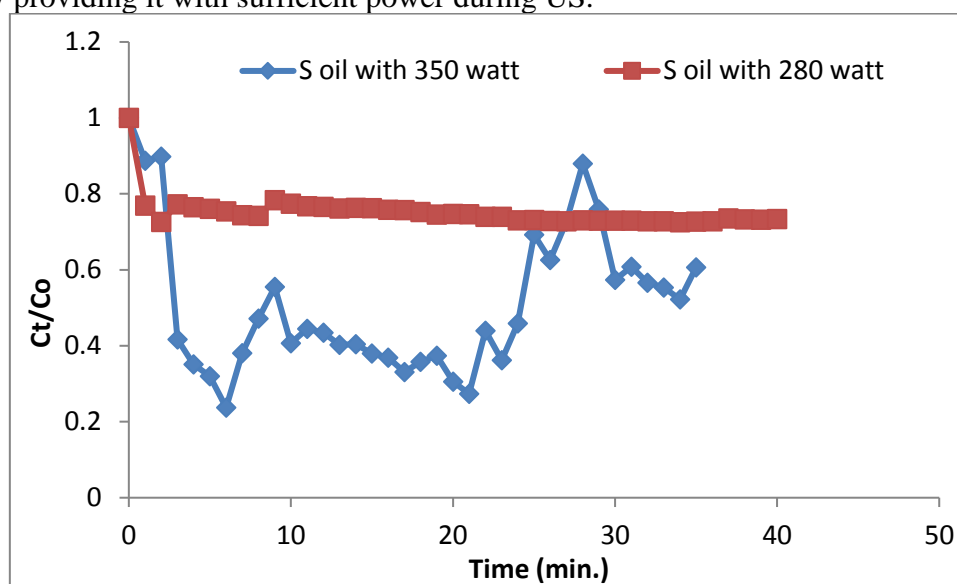


Fig. 3: Effect of power of US, DP= 500 ml, C_i = 35g/l, LM=80ml of S oil, RP=20ml (1%), TR= 1:5, Room Temp., No MC or emulsifier in LM, Speed of agitation for dispersion emulsion in DP = 750 rpm and Time of sonication= 15 min.

3.4. Effect of Initial Concentration of Salt

Accordingly, in the three experiments were confirmed that on using saline water of $C_i = 35, 10$ and 22 g/l , 91.987, 42.28 and 98.38% respectively of the salt was removed by simply using C oil without any MC or Span 80 as emulsifier added to the green edible oil with TR 1:5. The effect of C_i was investigated, and it was realized that as the latter increased from 10 to 22 up to 35 g/l , extraction increased from 42.28 to 98.38% at 22 g/l , then decreased to 91.987% at $C_i = 35 \text{ g/l}$. This result can be attributed to the following reasons: as C_i is increased from 10 to 22 g/l , the driving force for mass transfer from LM to AP increases, at the same time the amount of SS is sufficient to sequester the NaCl and retain it as a complex in the AP and prevent it from diffusing back to the LM phase. However, as C_i is increased to 35 g/l , crowding of the salt ions in the LM occurs and a traffic jam takes place as the ions compete with each other to reach their destination until they become sequestered in the LM, however the SS is seemingly insufficient to sequester all the quantity of salt, by which both reasons lead to a reduction in the percent extraction. This discussion is confirmed by the longer times (60 mins) taken for maximum extraction to take place, in the cases when C_i was either 10 or 35 g/l , whereas when C_i was 22 g/l , the time taken was only 35 mins (at which extraction was the highest (98.38%).

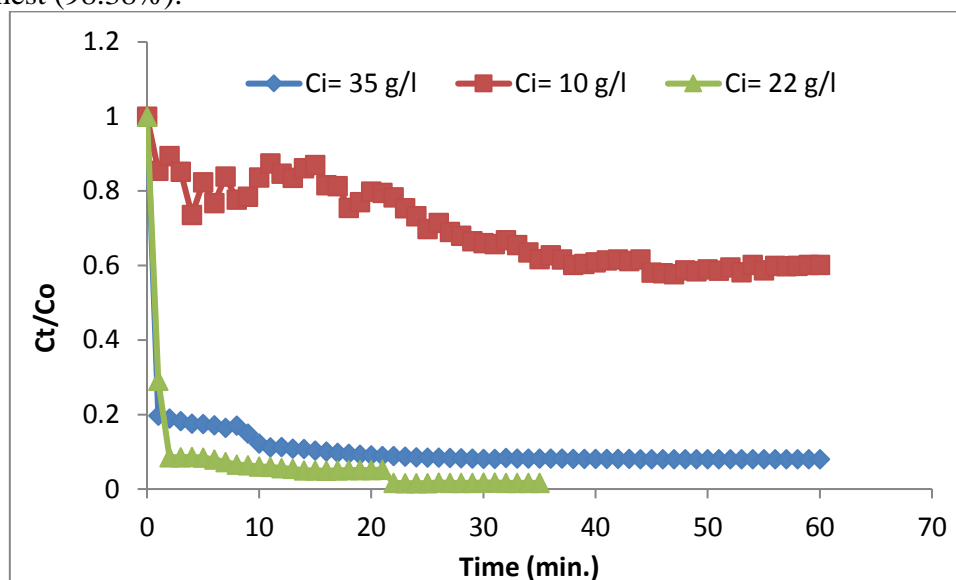


Fig. 4: Effect of C_i , DP= 500 ml, LM=80ml of C oil, RP=20ml (1%), TR= 1:5, Room Temp., No MC or emulsifier in LM, Speed of agitation for dispersion emulsion in DP = 750 rpm, ultra-sonication power= 350 Watt and Time of sonication= 15 min.

3.5. Effect of Treatment Ratio (Emulsion: DP)

In five following experiments which their TRs were 1:5, 1:10, 1:50, 1:30 and 1:20 and their % extractions were 98.38, 99.07, 25.78, 39.311 and 82.587% respectively. It is observed that when $C_i = 22 \text{ g/l}$ the extraction was greater at TR = 1:10 than at 1:5. This is probably due to the lower apparent viscosity of the whole mixture during extraction due to large fraction of water which has a low viscosity, and partly due to the lower amount of salt ions (Na^+ and Cl^-) which can be mostly sequestered. However, in both cases the percent extractions are high (99.07 and 98.38%).

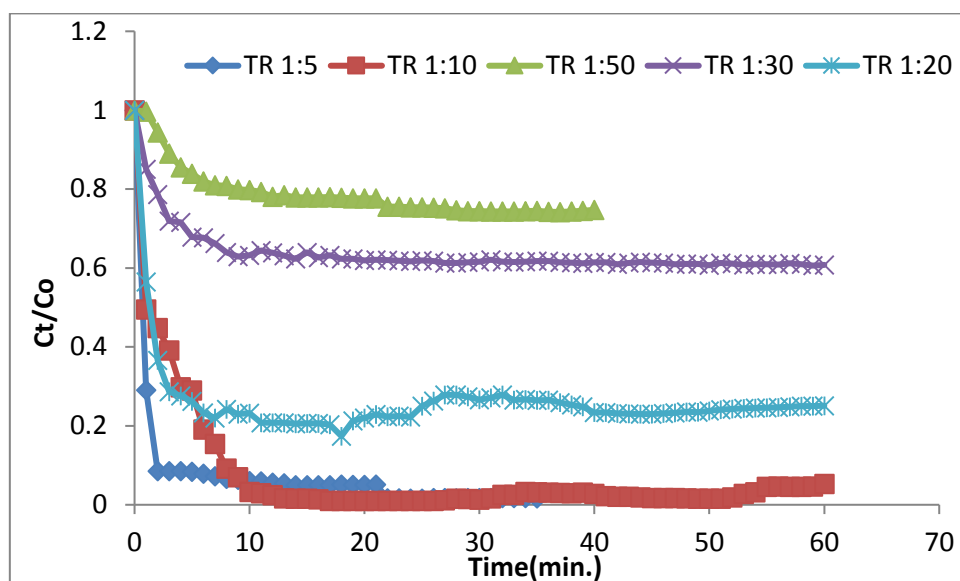


Fig. 5: Effect of TR: $C_i = 22\text{g/l}$, $LM = 80\text{ml}$ of C oil, $RP = 20\text{ml}(1\%)$, Room Temp., No MC or emulsifier in LM, Speed of agitation for dispersion emulsion in DP = 750 rpm, ultra-sonication power= 350 Watt and Time of sonication= 15 min.

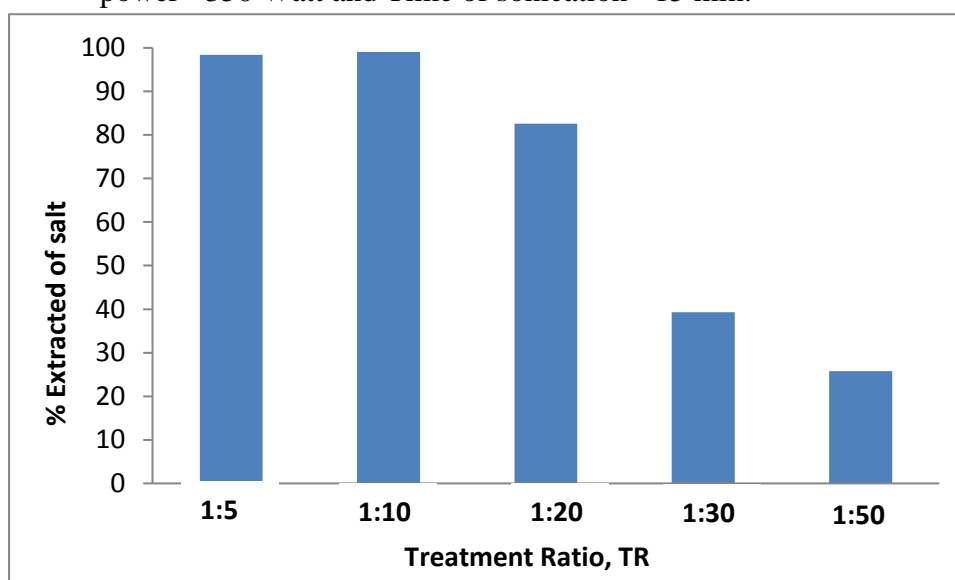


Fig.6 Comparing between % extracted of salt from DP verses treatment ratio: $C_i = 22\text{g/l}$, $LM = 80\text{ml}$ of C oil, $RP = 20\text{ml}$ of DW+0.2g of SS, Room Temp., No MC or emulsifier in LM, Speed of agitation for dispersion emulsion in DP = 750 rpm, ultrasonication power= 350 Watt and Time of sonication= 15 min.

3.5. Effect of Concentration of RP

Starch is a relatively inexpensive and biodegradable biopolymer which is expected to cause minimum pollution to the environment, was chosen in our work as a sequestering agent for sodium ion while the latter carried over chloride ions with it. It is known that starch consists of amylose (a straight chain polymer), and amylopectin (branched chain polymer) [29]. The presence of hydroxyl groups in the starch molecules is known to form a relatively stable complex with cations such as sodium ion through a coordinate bond in which the slight electronegativity of the oxygen atom renders it attracted to the positive sodium cation, concomitantly, the negative chloride ion is attracted to the electropositive hydrogen atom of the hydroxyl group. In this way, Na^+ ion is attracted to both O atom of the hydroxyl group fixed on the starch chain, plus a Cl^- ion, while, Cl^- ion is attracted to both H^+ of the hydroxyl group, and Na^+ ions, thus forming a coordinate bond [30, 31].

An SA was chosen in the present work to trap the NaCl after reaching the RP. The particular SA selected by the authors which, to the best of our knowledge, has never been investigated by any

authors before, was soluble starch, and which was used to trap the NaCl by forming a coordinate bond. Each anhydro-glucose unit contains three hydroxyl groups of which two are secondary and the third is a primary one. In this way the NaCl is trapped within the RP and does not back diffuse to the LM due to its large molecular weight together with its inability to diffuse through the LM, due to its insolubility in the organic LM, thereby allowing diffusion of NaCl from DP to RP to take place irreversibly.

Comparing between two following experiments which the conc. of RP were 1% and 2% and their % extractions were 99.07 and 65.487% in respective order. It is clear that increasing the SS in RP caused an increase in its viscosity, which hindered mass transfer, in addition to the traffic jam of the to and fro bulky starch molecules which cause steric hindrance to simple diffusion. Therefore, advantageously, 0.2g of SS is preferred to 0.4g, which means that, in this respect, the process is further economic. However, it must be mentioned that exactly 40% of C_i is extracted in exactly 1min, after which the rate drops within the next 3mins to reach slightly over 50% extraction, then slows down again and drops to slightly over 60% of C_i in further 12 mins, so that after a total of 16mins the final concentration is reached. This stepwise behavior of extraction indicates that 0.4g of SS is not recommended to be added in RP, for poorer extraction takes place (about 63%) and a longer time (16mins) is needed, simultaneously.

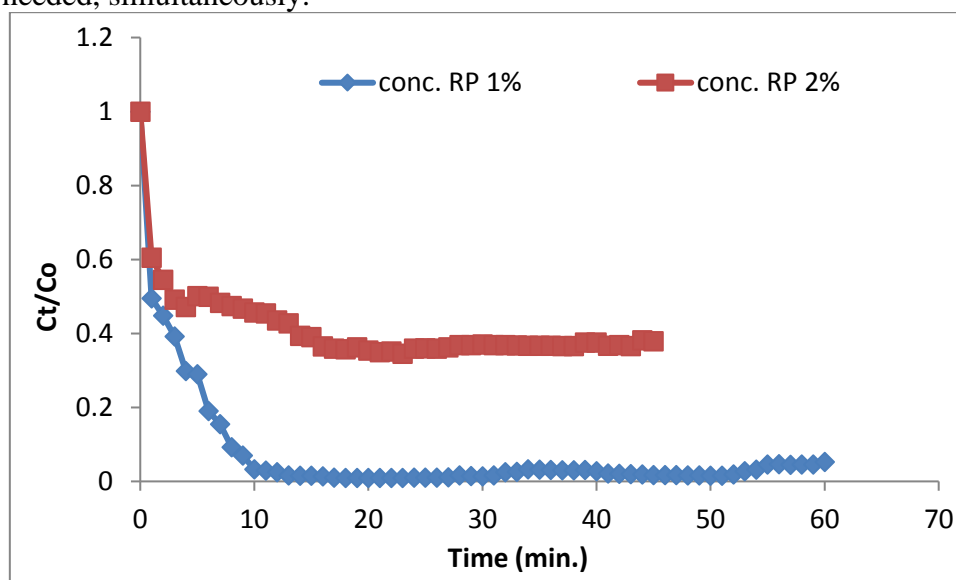


Fig.7: Effect of conc. RP, DP= 1000 ml, C_i = 22g/l, LM=80ml of C oil, RP=20ml, TR= 1:10, Room Temp., Speed of agitation for dispersion emulsion in DP = 750 rpm, ultra-sonication power= 350 Watt and Time of sonication= 15 min.

4. Conclusions

Emulsion liquid membrane technique has been applied successfully to the extraction of sodium chloride from saline water. Environmentally friendly LMs special corn oil is promising and successful technique for desalination process. It investigates very high degrees of desalination in a single stage. More than 98% was achieved. Many variables were found effect the extraction efficiency, and they were optimized in the present work to obtain the highest percent extraction.

The conclusions which deduced from the experimental work are show as following:

- The present of soluble starch in RP is essential in sequestering the NaCl.
- Optimum concentration of RP is 1%.
- Desalination increase as initial concentration of simulated sea water increase with sufficient amount of SS.
- Corn oil as LM is better than olive, sesame, linseed and sunflower oil without any additives (MC & emulsifier).
- Extraction of salt increase as treatment ratio (Emulsion: DP) increase.
- Ultasonicator gives more stable emulsion with high percent of extraction salt.

5. Recommendations

From the present work, the following recommendations for future work are:

- Other natural green oils such as palm oil and cotton seed oil should be tried.
- Studying the recycling and reusing the spent emulsion.
- Using different power of ultra-sonicator with different time.
- Testing other MCs soluble in green oils.
- Adding stabilizer to more stable emulsion during extraction and separation stage.
- Studying desalination by other LM technique such as hollow fiber contained LM (HFCLM) and electrostatic pseudo LM (ESPLM).

References

- [1] Water Resources: Distribution, Use and Management. John R. Mather. John Wiley & Sons, Inc., and V.H. Winston & Sons. (1984). IGSRLibrary SF 362.
- [2] Buros, O.K., "The ABCs of Desalting", International Desalination Association, (2000).
- [3] N.N. Li, "separating hydrocarbons with liquid membranes", U.S. Patent 3, 410, 794, (1968).
- [4] E. Makrlík, J. Hálová and M. Kyrš, "Contribution to the thermodynamics of complexes of alkali metal cations with dibenzo-18-crown-6 in water-nitrobenzene extraction system", Collection of Czechoslovak chemical communications 49, pp. 39-44, (1984).
- [5] L. Boyadzhiev and Z. Lazarova, "Liquid membranes (Liquid pertraction) in: Membrane Separations Technology: Principles and Applications", R.D. Noble, S.A. Stern (eds.), Elsevier Science B.V., Amsterdam, the Netherlands, chapter 7, pp. 283–352, (1995).
- [6] M.M. Naim, A. A. Monir, "Desalination using supported liquid membranes", Desalination 153, 361-369, (2002).
- [7] M.M. Naim, A. A. Monir, "Study on desalination by a flowing liquid membrane", 5th International Conference on Role of Engineering towards a Better Environment Alexandria, Egypt, 11-13 December, (2004).
- [8] M. M. Naim, A. A. Moneer, M. M. Elewa, "Removal of NaCl using facilitated up-hill transport through bulk liquid membranes containing dibenzo-18-crown-6", Desalination and Water Treatment, vol. 51, 4350–4358, (2013).
- [9] M. M. Naim, A. A. Moneer, A. A. El-Shafei, M. M. Elewa, "Automated prototype for desalination by emulsion liquid membrane technique", Desalination and Water Treatment, vol. 73, 164–174, (2017).
- [10] A.L. Ahmad, M.M.H. Shah Buddinb, B.S. Ooia, Adhi Kusumastuti, "Utilization of environmentally benign emulsion liquid membrane (ELM) for cadmium extraction from aqueous solution", Journal of Water Process Engineering, vol. 15, 26–30, (2017).
- [11] S. H. Changa, T. T. Tengb, I. Norlib, "Kinetic study of Cu(II) transport through soybean oil-based bulk liquid Membrane: Kinetic study", Chemical Engineering Journal, vol. 173, 352– 360, (2011).
- [12] O.Norasikin, N.M.F.Norul, P. W. Khoo, Y. Z. Ooi, "High Performance of Chromium Recovery from Aqueous Waste Solution using Mixture of Palm-oil in Emulsion Liquid Membrane", Procedia Eng. Vol.148, 765:773, (2016).
- [13] S. Björkegren, R. F. Karimi, A. Martinelli, N. S. Jayakumar, M. A. Hashim, "A New Emulsion Liquid Membrane Based on a Palm Oil for the Extraction of Heavy Metals", Membranes, vol.5, 168:179 (2015).
- [14] S. Kiani, S.M. Mousavi, "Ultrasound assisted preparation of water in oil emulsions and their application in arsenic (V) removal from water in an emulsion liquid membrane process", Ultrasonics Sonochemistry, vol. 20, 373–377, (2013).
- [15] G. Muthuraman, K. Palanivelu, "Transport of textile dye in vegetable oils based supported liquid membrane", Dyes and Pigments, vol. 70, 99-104, (2006).
- [16] P. Kazemia, M. Peydayeshb, A. Bandegib, T. Mohammadia, O. Bakhtiari, "Stability and extraction study of phenolic waste water treatment by supported liquid membrane using tri butyl phosphate and sesame oil as liquid membrane", chemical engineering research and design, vol. 92, 375–383, (2014).

- [17] P. Venkateswaran, K. Palanivelu, "Recovery of phenol from aqueous solution by supported liquid membrane using vegetable oils as liquid membrane", *Hazardous Materials B* 131,146–152, (2006).
- [18] N. Othman, N.F. Noah , L. Y. Shu, Z. Y.Ooi, N. Jusoh , M. Idroas , M. Goto, "Easy removing of phenol from wastewater using vegetable oil-based organic solvent in emulsion liquid membrane process", *Chinese Journal of Chem.Eng.* vol. 00604 (2016).
- [19] M. Ehtasha, M.-Ch. F.Salaüna, K.Dimitrov, Ph. Salaüna, A. Sabonid, "Phenol removal from aqueous media by pertraction using vegetable oil as a liquid membrane", *Chem. Eng. Journal*, vol. 250, 42–47, (2014).
- [20] N. Jusoh, N. Othman, N. A. Nasruddin, "Emulsion liquid membrane technology in organic acid purification", *Malaysian Journal of Analytical Sciences* Vol 20 No 2, 436 – 443, (2016).
- [21] Zhang, X.-J., Liu, J.-H., Fan, Q.-J., Lian, Q.-T., Zhang, X.-T. and Lu, T.-S., *Industrial application of liquid membrane separation for phenolic wastewater treatment. Separation Technology* United Engineering Trustees, New York, 190-203, **(1988)**.
- [22] Dines, M.B., "Regeneration of liquid membrane without breaking emulsion", U.S. Patent 4,337,225, **(1982)**.
- [23] Sun, D., Duan, X., Li, W. and Zhou, D., "Demulsification of water-in-oil emulsion by using porous glass membrane", *Journal of Membrane Science* 146 (1), 65-72, **(1998)**.
- [24] Kinugasa, T., Watanabe, K. and Takeuchi, H., "Effect of organic solvents on stability of liquid surfactant membranes", *Journal of Chemical Engineering of Japan* 22 (6), 593-597, **(1989)**.
- [25] Terry, R.E., Li, N.N. and Ho, W.S., "Extraction of phenolic compounds and organic acids by liquid membranes", *Journal of Membrane Science* 10 (2-3), 305-323, **(1982)**.
- [26] Skelland, A.H.P. and Meng, X., "Non-Newtonian conversion solves problems of stability, permeability, and swelling in emulsion liquid membranes", *Journal of Membrane Science* 158 (1-2), 1-15, **(1999)**.
- [27] Wang, C.C. and Bunge, A.L., "Multisolute extraction of organic acids by emulsion liquid membranes. I. Batch experiments and models", *Journal of Membrane Science* 53 (1- 2), 71-103, **(1990)**.
- [28] Basiron, Y.oils. In *Bailey's Industrial Oil and Fat Products*; Shahidi, F., Ed.; John Wiley&Sons, Inc.: Hoboken, NJ, USA, **(2005)**.
- [29] C.A. Brautlecht, *Starch-Its sources, production and uses*, Reinhold Publishing Corporation, New York, 1953.
- [30] S.J. Angyal, *Complexes of Metal Cations with Carbohydrates in Solution in: Advances in Carbohydrate Chemistry and Biochemistry*, R.S. Tipson, H. Derek (eds.), Academic Press, 1989, pp. 1-43.
- [31] J.A. Rendleman Jr, *Complexes of Alkali Metals and Alkaline-Earth Metals with Carbohydrates in: Advances in Carbohydrate Chemistry*, L.W. Melville, R.S. Tipson (eds.), Academic Press, 1967, pp. 209-271.

17- Analysis of the effectiveness of green roofs to mitigate the urban heat island effect in local outdoor spaces – A review paper

Tahani A. Elbondira¹, Mona G. Ibrahim^{1,2}

¹Egypt-Japan University of Science and Technology, Alexandria, Egypt

²Environmental Health Department, High Institute of Public Health, Alexandria University, Alexandria, Egypt

Tahani.elbondira@ejust.edu.eg

Abstract

As global temperatures rise due to climate change, the effect of urban heat island in urban areas is becoming more severe. Green spaces are believed to be one of the most successful strategies to mitigate the impact on the urban microclimate due to the cooling effect of vegetation. Considering the limited land resources of the city, green roofs promise to add more greening to the city without the need for additional space of land. The paper reviews the potential of using green roofs as part of the urban green infrastructure of the city to regulate the microclimate of outdoor spaces in the local scale. The review found that little research has been done on the effectiveness of green roofs as an urban heat mitigation strategy for the selected spatial scales. Nevertheless, the study found that such effectiveness is dependent on a number of factors, mainly: the specific characteristics of the climate in the which the site lies, the characteristics of the vegetative roof and the height of the building. The paper concludes with identifying gaps for future research that are necessary to help urban planners and designers optimize the use of green roofs for the benefit of the urban microclimate.

Keywords: urban heat island, urban microclimate, green roofs

9 Introduction

Massive emissions of greenhouse gases due to human activity and mostly from the burning of fossil fuels has led to the warming of Earth's climate. Most cities, in particular medium to high density, experience hotter climates than their rural surroundings, as the urban heat island phenomenon (UHI) explains. The wide use of hard impermeable surfaces, lack of vegetation, geometrical characteristics of urban areas and the anthropogenic heat resulting from the concentration of human activity are considered the main factors contributing to the formation of UHI. The problem is even more exacerbated as such increases in temperatures is usually met with an increase in the use of air conditioning and cooling appliances which in turn means an increase in fossil fuel combustion and greenhouse gas emissions, contributing back again to the original problem of climate change (Gartland, 2008; Levermore, Parkinson, Lee, Laycock, & Lindley, 2018; Oke, 1973, 1981).

Therefore, cities need to adopt strategies that improve the thermal conditions and fight the negative impacts of UHI on its microclimate. One of such strategies is by tackling the main source of the problem: as mentioned before, the increase of impervious surfaces that retain more solar energy and heat at the expense of vegetation that provides cooling through shading and evapotranspiration. Thus, creating more urban green spaces is believed to be one of the successful strategies to mitigate the impact on the urban microclimate (Saaroni, Amorim, Hiemstra, & Pearlmutter, 2018; Solecki et al., 2005).

However, land resources in cities are limited and since green spaces are publicly provided, they are sacrificed for other landuses that have higher monetary values and generate more revenues (Rößler, 2008; Rupprecht, 2017). As a result, other ways to increase vegetation are needed. Green roofs promise to add more greening to the city and without the need for additional space of land. Considering the fact that building roofs cover a relatively large percentage of the urban surface, 20-

25 % in the U.S. according to Akbari and Rose (2008), extensive use of green roofs can alter the thermal properties of the urban surface and contribute to the reduction in surface and air temperatures.

In fact, extensive research has been done on the benefits of green roofs for indoor microclimates and air quality (Besir & Cuce, 2018; Coutts, Daly, Beringer, & Tapper, 2013; Di Giuseppe & D'Orazio, 2015; Djedjig, Bozonnet, & Belarbi, 2015; Li, Chow, Yao, Zheng, & Zhao, 2019). For outdoor climates, most studies have been concerned with the potential influence of green roofs when implemented at the scale of a city (Berardi, GhaffarianHoseini, & GhaffarianHoseini, 2014; Santamouris, 2014). The interest to study the mitigation impact at a city scale can be mainly attributed to the fact that improving the thermal properties by changing the surface materials (e.g. more greenery and materials with higher reflectivity or albedo) is more effective when applied in larger scale.

When adopted largely at the scale of the city, Santamouris (2014) found that a reduction of 0.3 – 3 K of average ambient temperature can be achieved, while Smith and Roebber (2011) found a decrease of up to 3 °C in the city of Chicago. However, a more limited application of the technology at the city scale can still have a mitigation effect. A research report on the application of green roofs in New York city found that a 50% coverage of the city surface with green roofs has resulted in 0.1 - 0.8 °C reduction in surface temperature (Rosenzweig, Gaffin, & Parshall, 2006).

Although green roofs require a large scale application (e.g. meso or city scale) before a noticeable impact on the average temperature of the city can be observed, there is a need to understand how the application of the technology at a finer scale could influence the microclimate at that scale. In fact, the neighborhood level (local scale) is the level where local government and development plans are created and implemented (Norton, Coutts, Livesley, & Williams, 2013). However, there is still a lack of knowledge on the optimum design of the different types of urban green infrastructure at local and street canyon scales, in general, and the green roofs, in particular, at pedestrian level (Bartesaghi Koc, Osmond, & Peters, 2018).

Therefore, this paper aims to help understanding how the application of green roofs at finer spatial scales can benefit the microclimate of that area. It reviews recent research on the effects of green roofs on the microclimate of outdoor urban spaces at the local neighborhood and street canyon levels. The main objective of this review is to provide an overview of the main findings and reach conclusions on the optimum design considerations based on current literature in addition to identifying the gaps in knowledge that will help better optimize the implementation of green roofs for the benefit of urban microclimate at the local scale.

10 Methods

Due to the scarcity of research on the potential effects of using green roofs for the microclimate at small spatial scales, studies addressing the effects of green roofs at local scale are included with no exclusion criteria set for the following: date of publication, climatic zones and conditions, microclimate variables and methods of investigation. Furthermore, studies that evaluate the impact of green roofs as a part of a greening plan that includes other types of greenery are also included.

The “local scale” is considered as the middle scale between the “micro” and the “meso” scales. Micro scale is the scale of urban elements such as buildings. Meso scale pertains to the larger scales of urban areas like cities and metropolitan areas. A local scale is the scale that covers areas that extends along 100-10000 m of length and ranges from suburbs down to neighborhoods and street canyons (Grimmond & Oke, 2002). In this review, local scale includes neighborhoods, urban blocks and street canyons.

The search process used the databases of ScieinceDirect, Google Scholar and Jstor to obtain the relevant literature. The following keywords were used for the search: “green roofs”, “roof greening”, “living roofs”, “vegetative roofs”, “outdoor microclimate”, “microclimate”, “thermal comfort”, “urban heat island” and “cooling effect”. The search retrieved 19 studies that are conducted at the local scale. The papers were organized, according to the spatial scale into: street canyon, urban block and neighborhood levels, for further analysis.

The following section starts with comparing the characteristics of the different systems of green roofs that are believed to contribute to the effectiveness of the application of the roof system. Second, the mitigating effects of the green roofs at the three spatial scales are reported subsequently. Eventually, a comparison and an analysis of the reported information are made to understand the potential design considerations, climatic or technical specifications that can be considered to achieve optimum application of the technology.

11 Results and discussion

3.1 Green roofs: types and characteristics

In general terms, a typical green roof (also known as vegetative or living roof) consists mainly of a vegetation layer, a substrate (growing medium) and the roof structure in addition to the necessary insulation and waterproofing layers. Fig.1 shows a detailed cross-section of a typical green roof (Vijayaraghavan, 2016).



Fig. 1: Cross-section of a typical green roof. Source: Vijayaraghavan (2016)

Green roofs are mostly classified into extensive and intensive green roofs, with a possible third and intermediate type called a semi-intensive green roof. The classification of green roofs can be basically determined by the depth of the substrate layer (growing medium) and the plants in the vegetation layer. Generally speaking, green roofs are still an artificial habitat for the plant community that has several limitations, particularly, in relation to water availability for irrigation and the structural loads. Such limitations play a role in the selection of proper plant species and the substrate layer depth (Vijayaraghavan, 2016). The characteristics of each of the three green roof types are summarized as follows (Besir & Cuce, 2018; Oberndorfer et al., 2007; Vijayaraghavan, 2016; Wilkinson & Reed, 2009):

- Extensive green roofs, the most widely used type, have a shallow substrate layer that can range in depth from 2 – 20 cm, which makes it a relatively lightweight (approximately 60-170 kg/m²). This type prefers a plant that requires less watering and can survive under harsh climate conditions and nutrients (like Sedum and Moss). Therefore, this type requires little maintenance and irrigation and also has a lower cost than the other types.
- Conversely, intensive green roofs are heavier (180 – 970 kg/m²) and can function as a park or a garden due to its deeper substrate layer (15 – 40 cm) that can host a variety of plants including shrubs and trees. It is, hence, requires a higher maintenance and irrigation frequency and costs more than extensive roofs.
- Semi-intensive green roofs are a combination of both extensive and intensive types. They weigh from 120 – 200 kg/m² and have medium costs, substrate depth (12-25 cm), maintenance requirements and irrigation frequencies and they can grow grass and shrubs but not trees.

Fig. 2 shows examples of each of the green roof types.



Fig. 2: Extensive (left), semi-intensive (middle) and intensive (right) green roofs. Source: (Besir & Cuce, 2018; <http://www.greenroofers.co.uk/green-roofs/>)

Overall, the thermal performance of green roofs is defined by aspects related to the characteristics of the plant, the growing medium and irrigation schemes. Larger leaf area index (LAI), higher coverage ratio of plant, higher leaf thickness are all correlated positively with greater cooling effect (Fang, 2008; Wong, Chen, Ong, & Sia, 2003; Wong, Tan, & Chen, 2007). Liu and Bass (2019) found that deeper substrate with lighter colors are more effective. They also found that well irrigated green roofs have reduced air temperature in downtown Toronto by up to 2° C.

3.2 UHI mitigation effects of green roofs

a. UHI mitigation at street canyon level

In their study on the effects of greening the building envelope on the microclimate at pedestrian level in nine cities of different climates and different canyon geometries, Alexandri and Jones (2008) found that the application of both green roofs and walls can largely mitigate air temperature at canyon level. The hotter and drier the climate, the more significant the effect is. Therefore, the largest decrease was found in the desert climate of Riyadh, when maximum reduction of air temperature reached 11.3 °C and a daytime average of 9.1 °C. The study concluded with indicating that green roofs had weaker mitigating performance than green walls at canyon level, but larger impact at roof level which suggests that a wide application of green roofs are more effective at urban scale.

Djedjig, Bozonnet, and Belarbi (2013) have conducted an experimental study to examine the effect of installing green roofs and walls on outdoor environment of the Oceanic temperate climate of La Rochelle, France. An experimental model of five rows of buildings (with H: 1.24 m and W: 1.2m) used 2 types of extensive green roofs on 2 rows; one type with Sedum and the other type has a deeper substrate with a variety of grass and plants. Green walls are used on one row while 2 rows were kept in between as reference buildings. The study found that green walls were more effective reducing temperature by up to 1.5 °C while green roofs reduction was less than 1.5 °C.

Using the same previous physical model, Ouldboukhitine, Belarbi, and Sailor (2014) conducted their experiment and modeling to examine the effect of only green roofs. The difference of air temperature in streets with green roofs and without reached 0.8 °C. The study concludes with suggesting an experiment of a full scale model to compare the results with the adopted reduced scale. However, they emphasized that the use of green roofs can positively improve the microclimate at pedestrian level by cooling the air.

A study by Gromke et al. (2015) has examined the cooling effect of different types of urban greenery including green roofs in the center of Arnhem city in the Netherlands. A computational fluid dynamics (CFD) simulation was conducted on a hot summer day (July, 16th in 2003 at 15 h) on a main street and the surrounding buildings along the street in the city center. They found that the effect of installing green roofs with a 25% coverage of building rooftops along the street is negligible at 2m height, at pedestrian level (maximum reduction of 0.2 °C). However, they hypothesized that conducting the simulation with different wind directions and speed could result in a noticeable decrease of air temperature at pedestrian level.

In the humid temperate climate of Bilbao city, in Spain, Lobaccaro and Acero (2015) have performed ENVI-met simulation to test the impacts of different greening scenarios on thermal comfort at pedestrian level. Among the greening actions, a 0.5 m grass covered green roofs (100% coverage) are installed on rooftops of buildings along three types of canyons: compact low-rise (H/W:3.5), compact mid-rise (H/W: 1.5) and open-set high-rise (H/W: 1.3). The building heights were 16m, 24m and 40m, respectively, corresponding to the canyon geometry. The simulation was conducted for a hot summer day in August, 2010. The results shows that green roofs were ineffective in the compact low-rise streets (reduction of 0.13 °C), while for the compact mid-rise and the open high-rise the decrease reached 1.04 °C and 1.23 °C, respectively.

In another study, the effect of four types of extensive Sedum green roofs on a 4-story university building in Toronto was simulated in Berardi (2016). The extensive roof was assumed to only receive water from precipitation. The four types were categorized only by varying soil depth and LAI. When LAI increased from 1 to 2, the cooling effect improved from 0.2 °C to 0.4 °C. Although such effect

is slight, together with the more noticeable mitigation effect at the rooftop level, installing green roofs promises to mitigate the UHI impact. Table 1 summarizes the mitigation potential impact at street canyon scale.

Table 1. Summary of the main findings at street canyon scale

| Reference | Scale | Climate | Method | Green roof system | Results |
|--------------------------------------|---------------|---|---------------------------|--------------------------|--|
| Alexandri and Jones (2008) | Street canyon | Temperate-Subarctic-Continental cool summer-Mediterranean-Steppe- Hot desert- Humid subtropical- Rain forest- Savanna | Modeling | Extensive (Albedo: 0.94) | Lowest canyon air temperature when both green roofs and walls are used (up to 11.3 °C in desert climate of Riyadh) The mitigation effect is higher in hot and dry climates than cold climates Green roofs are not as effective as green walls at pedestrian level, but more effective at roof level and –as a result- at urban level |
| Djedjig et al. (2013) | Street canyon | Oceanic temperate | Experiment | Extensive | A reduced scale-model shows that green walls were more effective (1.5 °C max decrease in temperature) than green roofs (<1.5 °C). |
| Ouldboukhiti ne et al. (2014) | Street canyon | Oceanic temperate | Experimental and modeling | Extensive | Application of green roof in a reduced model reduced air temperature at canyon level by 0.8 °C |
| Gromke et al. (2015) | Street canyon | Oceanic temperate | Simulation | Not specified | No noticeable decrease in air temperature at pedestrian level (max. 0.2 °C at 2m height) Re-conducting simulation with different wind direction and lower wind speed can result in significant reduction of air temperature |
| Lobaccaro and Acero (2015) | Street canyon | Humid temperate (Köppen: Oceanic temperate) | Simulation | Extensive | Negligible effect for compact low-rise streets (0.13 °C). Reduction of 1.04°C and 1.23 °C, respectively, for compact mid-rise and open high-rise streets |
| Berardi (2016) | Street canyon | Warm humid continental | Simulation | Extensive | Maximum cooling effect of 0.4 °C at pedestrian level achieved by increasing LAI values |

b. UHI mitigation at urban block level

To explore the impact of roof greening at the scale of urban block (smallest unit of a building group surrounded by streets), Chen, Ooka, Huang, and Tsuchiya (2009) have simulated the effects of applying green roofs in two urban block varying in their geometrical characteristics. The first block lies in a high-rise district (Otemachi) with building heights are on average 67.4 m, while in Kyobashi, a mid-rise district, the average building heights are 28.6 m. 100% coverage of rooftops with vegetation were simulated and compared against initial state and other mitigations strategies. The results showed that the roof greening in both Otemashi and Kyobashi had a minimal impact on air temperature at pedestrian level. The authors suggested that the height of buildings could be the reason behind such slight impact.

Another study in Japan by Srivanit and Hokao (2013) has tested the potential cooling impacts of two greening strategies: trees and green roofs, at pedestrian level in the campus of Saga University. The maximum height of buildings was 24 m. 20% increase in trees amount resulted in a reduction of 2.27

°C. Adding roof greening (extensive with 0.5 m grass layer) to trees has resulted in a further decrease, although it was only by 0.02 °C. The study has not simulated the effect of green roofs separately.

Almost a similar result was reported by Zölch, Maderspacher, Wamsler, and Pauleit (2016) who conducted a simulation study in an urban block in a densely-built up area with buildings mainly range in height from 17-24 m and others from 3-10m. Extensive green roofs covering only 9% and 47% of buildings rooftops were simulated. In both scenarios, effect of roof greening was found to be negligible. The reductions in comparison to baseline scenario were 0.5 % and 0 for the 47% and 9% coverage scenarios, respectively.

Unlike the previous study, a simulation study in Colombo, Sri Lanka (tropical climate) found a significant cooling effect of green roofs comparable to a green walls scenario (Herath, Halwatura, & Jayasinghe, 2018). By applying green roofs to 100% of available roof area in a block of 4.5 ha, a maximum reduction in air temperature recorded was 1.98 °C compared to 2.03 °C when green walls were used.

Likewise, Dwivedi and Mohan (2018) found that applying green roofs over at least 50% of available rooftops in two urban blocks in Mumbai could result in a noticeable decrease in air temperature reaching a maximum of 3 °C and average of 2.1 °C. They found that increasing the coverage to 75% could achieve up to 25% reduction in air temperature.

Another study compared the cooling effects of four green types in four climates of: Cairo, Hong Kong, Tokyo and Paris using coupled simulation of EnergyPlus and ENVI-met. An urban block (1.8 ha) was modeled with building heights of 60m, 30m and 10m. The four types were: intensive (0.7m soil depth, 1m canopy height, LAI: 2), extensive (0.2m plant height, LAI:2), semi-intensive and semi-extensive. Both intensive and extensive had 100% coverage while semi-intensive (extensive) covered 50% of rooftop areas of each building. At pedestrian level, the maximum cooling achieved was 0.6 °C.

The study found that the effectiveness of green roofs influenced by climate, green roof types and building heights. Hot desert climate was impacted the most. In terms of roof type: full-intensive was as twice effective as the extensive, which even had a lower impact than the semi-intensive. Overall they found that LAI and tree canopy height was more effective than coverage ratio. Regarding the building heights, the larger temperature reduction was associated to lower building heights (Morakinyo, Dahanayake, Ng, & Chow, 2017).

A more recent study by Wang, Ni, Chen, and Xia (2019) evaluated the potential mitigating influence of greenways, green roofs and trees in the subtropical maritime climate of kwai chung in China. The study area is a dense low-rise area (24% building coverage) with an existing large urban park (16% of its area). Addition of semi-intensive green roofs (with LAI:2) to 10% of roadside buildings were simulated. The results of the simulation at 1.5m pedestrian level revealed that roof greenery has contributed to a limited reduction of air temperature by a maximum and average of 0.6 °C and 0.03 °C, respectively, at noon. Less than that of 10% greenways with 0.8 °C and 0.05 °C decreases. Table 2 summarizes the mitigation potential impact at urban block scale.

Table 2. Summary of the main findings at urban block scale

| Reference | Scale | Climate | Method | Green roof system | Results |
|-----------|-------|---------|--------|-------------------|---------|
|-----------|-------|---------|--------|-------------------|---------|

| | | | | | |
|-----------------------------------|-------------|--|--------------------------------|--|--|
| Chen et al. (2009) | Urban block | Humid subtropical- | Simulation | Not specified | Minimal impact on air temperature from a 100% green roof coverage in a high-rise (>65 m) and mid-rise (>25 m) urban blocks in Tokyo, Japan. |
| Srivaniit and Hokao (2013) | Urban block | Humid subtropical- | Field measurement & simulation | Extensive | Adding a 0.5m grass layer on rooftops in Saga University campus to a scenario of 20% increase in trees amount resulted in a further decrease in max. air temperature from 2.27 °C to 2.29 °C. |
| Zölch et al. (2016) | Urban block | humid continental | Simulation | Extensive | Negligible impact of extensive green roofs covering 9% and 47% of buildings in a 3.5ha urban block in Munich. Reductions compared to baseline scenario were 0.5% and 0% for the 47% and 9% scenarios |
| Morakinyo et al. (2017) | Urban block | Hot desert- Humid subtropical (hot)- Humid subtropical (warm)- Oceanic temperate | Simulation | Intensive- Extensive- Semi-intensive- Semi-extensive (Albedo:0.33 5) | Maximum air temperature decrease was 0.6 °C Effectiveness of intensive roofs was a twice as extensive roofs. Semi-intensive roofs were even more effective than the full extensive Lower building height (10 m) associated to more decrease than higher buildings (30m and 60m) Cooling effect of green roofs were more pronounced in hot-dry desert climates |
| Herath et al. (2018) | Urban block | Tropical rainforest | Simulation | Not specified | Applying 100% green roof coverage in a block of 4.5 ha area reduced air temperature at 1.5m street level by 1.98 °C max compared to 2.03 °C by green walls |
| Dwivedi and Mohan (2018) | Urban block | Tropical savanna | Simulation | Not specified | 50% of urban block's rooftops greenery yeiled a max of 3 °C temperature decrease. 75% could decrease temperature by up 25% |
| Wang et al. (2019) | Urban block | Subtropical maritime | Field measurement & simulation | Semi-intensive | Semi-intensive green roofs of LAI:2 over a fraction of 10% of urban block's area Maximum and average decrease of air temperature by 0.6 and 0.03 °C, respectively, at noon |

c. UHI mitigation at urban neighborhood level

Ng, Chen, Wang, and Yuan (2012) compared different greening strategies in different urban settings and building heights in a highly-dense neighborhood in Hong Kong. The study found roof greening an ineffective strategy when pedestrian level air temperature reduction is sought. They found that trees are more effective when 33% of the total area is planted, in which case a 1 °C reduction can be achieved. It has to be noted that building heights in the area range from 20m to 60m which is suggested as a reason for producing less effective results, in line with Chen et al. (2009) and Morakinyo et al. (2017).

Conversely, in Hong Kong, Peng and Jim (2013) has compared the cooling effect of both extensive and intensive green roofs in five residential neighborhoods and found that cooling effect extended to the street level, in particular, in low-rise neighborhoods ($H \leq 15$). Intensive roofs had a greater effect on canyon temperature, of 0.5 °C-1.7 °C reduction, than extensive roofs (decreased by 0.4 °C-0.7 °C). Thus, they recommend green roof application at neighborhood scale to help mitigate the local UHI.

In Melbourne, Australia, Meek, Jayasuriya, Horan, and Adams (2014) conducted a simulation study on the environmental effects of extensive green roof retrofitting in the central business district (CBD).

They found that for green-roofs that are ready for application (28%), reduction in air temperature reached up to 0.7 °C, while if total roof surface area were used (60%), a maximum of 1.5 °C decrease could be achieved.

In Los Angeles, Taleghani, Sailor, and Ban-Weiss (2016) quantified the impact of several mitigating strategies on microclimate and pedestrian thermal comfort in a neighborhood. They found that both green and cool roofs had lower impact at street level (0.2 °C reduction) compared to street trees and cool pavements. They suggested the building heights and specific geometry of the neighborhood case study leads to rooftop strategies being more effective at roof level way above street levels.

In the a Mediterranean climate of Madrid, Alcazar, Olivieri, and Neila (2016) conducted a simulation of a neighborhood with 20m high buildings where extensive green roofs of leaf area density (LAD) of 0.5 and 1.5 were compared. Temperature decrease was 0.2 °C and 1 °C for the extensive roofs of LAD of 0.5 and 1.5 respectively. They found that the effect was positively associated with calm wind and shade.

In the hot desert climate of Egypt, Fahmy, Ibrahim, Hanafi, and Barakat (2018) studied the effects of several mitigation strategies in present and in future scenarios for 2050 and 2080 in a residential neighborhood in Cairo. They found that the use of extensive green roofs and tree lines can lower air temperatures largely in present scenario (1.16 – 2.51 °C) and to a lower extent in future scenarios (up to 0.87 °C and 0.85 °C, in 2050 and 2080, respectively). They recommended the use of both greening strategies to improve the temperature at neighborhood scale. Table 3 summarizes the mitigation potential impact at neighborhood scale.

Table 3. Summary of the main findings at neighborhood scale

| Reference | Scale | Climate | Method | Green roof system | Results |
|-------------------------|--------------|---------------------------|--------------------------------|------------------------|--|
| Ng et al. (2012) | Neighborhood | Humid subtropical | Field measurement & simulation | Extensive Intensive | - Planting grass or trees on rooftops in a high dense neighborhood in Hong Kong did not result in effective reduction in air temperature due to height of buildings (20m – 60m). Decrease of 1°C could be achieved if 33% of area were trees. |
| Peng and Jim (2013) | Neighborhood | Humid subtropical | Field measurement & simulation | Extensive Intensive | - Application of green roof in low-rise neighborhoods in Hong Kong resulted in noticeable decrease in air temperature at canyon level Intensive roofs achieved reduction of 0.5 – 1.7 °C while extensive roofs were 0.4 – 0.7 °C |
| Meek et al. (2014) | Neighborhood | Oceanic temperate | Modeling | Extensive | A wide scale application of extensive green roofs of all available space in CBD in Melbourne (60%) yielded reduction of up to 1.5 °C. Application over ready rooftop space (28%) achieved a max reduction of 0.7 °C |
| Taleghani et al. (2016) | Neighborhood | Mediterranean climate | Simulation | Extensive | Negligible effect of 0.2 °C air temperature decrease at street level when extensive roof greening applied in an LA neighborhood |
| Alcazar et al. (2016) | Neighborhood | Mediterranean continental | Simulation | Extensive | In neighborhood in Madrid with 20m high buildings, green roofs with higher LAD of 1.5 reduced air by 1 °C, while LAD of 0.5 caused a 0.2 °C reduction. |

| | | | | | |
|------------------------|--------------|------------|--------------------------------------|----------------------------|---|
| Fahmy et al. (2018) | Neighborhood | Hot desert | Field measurement & simulation | Extensive (Albedo: 0.2) | The use of both extensive green roofs and tree lines in a neighborhood in Cairo, has lowered air temperature at pedestrian level by 1.16 – 2.51 °C. |
|------------------------|--------------|------------|--------------------------------------|----------------------------|---|

3.3 Discussion

By reviewing literature on the potential mitigation effects of green roofs at the local scale at pedestrian level, it can be seen that there variations in the reported results among the studies across the different scales, that are identified in this study. In some studies, green roofs proved to result in a noticeable mitigating impact (Dwivedi & Mohan, 2018; Herath et al., 2018; Lobaccaro & Acero, 2015; Meek et al., 2014; Morakinyo et al., 2017; Ouldboukhithine et al., 2014; Peng & Jim, 2013), while other studies found that green roofs are ineffective in particular compared to other strategies like façade greening (Alcazar et al., 2016; Alexandri & Jones, 2008; Chen et al., 2009; Ng et al., 2012; Srivanit & Hokao, 2013; Taleghani et al., 2016; Wang et al., 2019; Zölch et al., 2016). Furthermore, some studies did not reach a decisive conclusion, mostly due to research limitations (Berardi, 2016; Djedjig et al., 2013; Fahmy et al., 2018; Gromke et al., 2015).

Overall, it can be observed that the majority studies have employed extensive green roofs. It is worth noting that, extensive green roofs usually have less cooling potential due to the shallower soil and vegetation layers, the type of plants and the less irrigation schemes they require. In fact, extensive green roofs are believed to be principally used as a thermal insulation or a protection layer (Lundholm, Macivor, Macdougall, & Ranalli, 2010; Wilkinson & Reed, 2009). Nonetheless, many studies reported that they are ineffective in well insulated buildings. Therefore, by considering the fact that modern building construction practices well considers building insulation; this study can conclude that extensive green roofs may require further research to justify for their use, either for indoor or outdoor microclimates.

On the other hand, most studies that found green roofs less effective in lowering pedestrian level air temperature are conducted in areas where building heights exceeded 15m. In addition, studies have mainly employed simulation methods with simplified vegetation models (with several assumptions) and climate conditions (Gromke et al., 2015). Monitoring pedestrian level microclimate for real green roof cases can help understand and quantify actual mitigation effects and further help validate modeling and simulation results.

Finally, different climates appear to have an effect on the mitigation potential of the technology. For instance, hot and dry climates were found to be largely impacted by the application of green roofs. However, such conclusion was drawn based on few and fragmented research. For example, only 3 out of 19 studies reviewed in this study involved hot desert areas. Thus, more research in hot desert climates in particular, and various climates and climate conditions, need to be carefully investigated.

12 Conclusions

This paper presents a review on the effectiveness of green roofs in improving thermal environment at pedestrian level at the local scale. The local scale is further classified into: street canyon, urban block and neighborhood levels. In total, 19 studies were reviewed. The results on the effectiveness of green roofs have varied in the reviewed literature.

Overall, it can be concluded that there are several factors that can influence the effectiveness of the applying green roofs for the benefit of outdoor microclimate at pedestrian level. Building heights comes on top of the factors with many studies suggest that heights less than 10m (or 15m) can be a threshold if a noticeable reduction of air temperature at street level is sought. Climate also is another factor, with hot desert and drier climates are assumed to reap larger benefits from the application of the roof systems. Last but not least, green roof types can have a significant influence on the mitigation potential. According to reviewed studies, intensive and semi-intensive roofs can be more effective than extensive green roofs.

However, since research in this subject is scarce at this spatial scale, more studies are needed to confirm the previous results. Field measurements of real green roofs cases are specifically required to understand the actual mitigating potential and validate the simulation and modeling results.

Acknowledgements

The first author would like to thank the Egyptian Ministry of Higher Education (MoHE) for providing the financial support (Ph.D. Scholarship) for this research as well as the Egypt–Japan University of Science and Technology (E-JUST) for offering the facilities and the tools needed to conduct this work.

References

- Akbari, H., & Rose, L. S. (2008). Urban Surfaces and Heat Island Mitigation Potentials. *Journal of the Human-Environment System*, 11(2), 85-101. doi: 10.1618/jhes.11.85
- Alcazar, S. S., Olivieri, F., & Neila, J. (2016). Green roofs: Experimental and analytical study of its potential for urban microclimate regulation in Mediterranean–continental climates. *Urban Climate*, 17, 304-317. doi: <https://doi.org/10.1016/j.uclim.2016.02.004>
- Alexandri, E., & Jones, P. (2008). Temperature decreases in an urban canyon due to green walls and green roofs in diverse climates. *Building and Environment*, 43(4), 480-493. doi: <https://doi.org/10.1016/j.buildenv.2006.10.055>
- Bartesaghi Koc, C., Osmond, P., & Peters, A. (2018). Evaluating the cooling effects of green infrastructure: A systematic review of methods, indicators and data sources. *Solar Energy*, 166, 486-508. doi: <https://doi.org/10.1016/j.solener.2018.03.008>
- Berardi, U. (2016). The outdoor microclimate benefits and energy saving resulting from green roofs retrofits. *Energy and Buildings*, 121, 217-229. doi: <https://doi.org/10.1016/j.enbuild.2016.03.021>
- Berardi, U., GhaffarianHoseini, A., & GhaffarianHoseini, A. (2014). State-of-the-art analysis of the environmental benefits of green roofs. *Applied Energy*, 115, 411-428. doi: <https://doi.org/10.1016/j.apenergy.2013.10.047>
- Besir, A. B., & Cuce, E. (2018). Green roofs and facades: A comprehensive review. *Renewable and Sustainable Energy Reviews*, 82, 915-939. doi: <https://doi.org/10.1016/j.rser.2017.09.106>
- Chen, H., Ooka, R., Huang, H., & Tsuchiya, T. (2009). Study on mitigation measures for outdoor thermal environment on present urban blocks in Tokyo using coupled simulation. *Building and Environment*, 44(11), 2290-2299. doi: <https://doi.org/10.1016/j.buildenv.2009.03.012>
- Coutts, A. M., Daly, E., Beringer, J., & Tapper, N. J. (2013). Assessing practical measures to reduce urban heat: Green and cool roofs. *Building and Environment*, 70, 266-276. doi: <https://doi.org/10.1016/j.buildenv.2013.08.021>
- Di Giuseppe, E., & D'Orazio, M. (2015). Assessment of the effectiveness of cool and green roofs for the mitigation of the Heat Island effect and for the improvement of thermal comfort in

- Nearly Zero Energy Building. *Architectural Science Review*, 58(2), 134-143. doi: 10.1080/00038628.2014.966050
- Djedjig, R., Bozonnet, E., & Belarbi, R. (2013). Experimental study of the urban microclimate mitigation potential of green roofs and green walls in street canyons. *International Journal of Low-Carbon Technologies*, 10(1), 34-44. doi: 10.1093/ijlct/ctt019
- Djedjig, R., Bozonnet, E., & Belarbi, R. (2015). Analysis of thermal effects of vegetated envelopes: Integration of a validated model in a building energy simulation program. *Energy and Buildings*, 86, 93-103. doi: <https://doi.org/10.1016/j.enbuild.2014.09.057>
- Dwivedi, A., & Mohan, Buddhiraju K. (2018). Impact of green roof on micro climate to reduce Urban Heat Island. *Remote Sensing Applications: Society and Environment*, 10, 56-69. doi: <https://doi.org/10.1016/j.rsase.2018.01.003>
- Fahmy, M., Ibrahim, Y., Hanafi, E., & Barakat, M. (2018). Would LEED-UHI greenery and high albedo strategies mitigate climate change at neighborhood scale in Cairo, Egypt? *Building Simulation*, 11(6), 1273-1288. doi: 10.1007/s12273-018-0463-7
- Fang, C.-F. (2008). Evaluating the thermal reduction effect of plant layers on rooftops. *Energy and Buildings*, 40(6), 1048-1052. doi: <https://doi.org/10.1016/j.enbuild.2007.06.007>
- Gartland, L. (2008). *Heat islands : understanding and mitigating heat in urban areas*: London : Earthscan.
- Grimmond, C., & Oke, T. R. (2002). Turbulent heat fluxes in urban areas: Observations and a local-scale urban meteorological parameterization scheme (LUMPS). *Journal of Applied Meteorology*, 41(7), 792-810.
- Gromke, C., Blocken, B., Janssen, W., Merema, B., van Hooff, T., & Timmermans, H. (2015). CFD analysis of transpirational cooling by vegetation: Case study for specific meteorological conditions during a heat wave in Arnhem, Netherlands. *Building and Environment*, 83, 11-26. doi: <https://doi.org/10.1016/j.buildenv.2014.04.022>
- Herath, H. M. P. I. K., Halwatura, R. U., & Jayasinghe, G. Y. (2018). Modeling a Tropical Urban Context with Green Walls and Green Roofs as an Urban Heat Island Adaptation Strategy. *Procedia Engineering*, 212, 691-698. doi: <https://doi.org/10.1016/j.proeng.2018.01.089>
<http://www.greenroofers.co.uk/green-roofs/>.
- Levermore, G., Parkinson, J., Lee, K., Laycock, P., & Lindley, S. (2018). The increasing trend of the urban heat island intensity. *Urban Climate*, 24, 360-368. doi: <https://doi.org/10.1016/j.uclim.2017.02.004>
- Li, Z., Chow, D. H. C., Yao, J., Zheng, X., & Zhao, W. (2019). The effectiveness of adding horizontal greening and vertical greening to courtyard areas of existing buildings in the hot summer cold winter region of China: A case study for Ningbo. *Energy and Buildings*, 196, 227-239. doi: <https://doi.org/10.1016/j.enbuild.2019.05.025>
- Liu, K., & Bass, B. (2019). Performance of green roof systems.
- Lobaccaro, G., & Acero, J. A. (2015). Comparative analysis of green actions to improve outdoor thermal comfort inside typical urban street canyons. *Urban Climate*, 14, 251-267. doi: <https://doi.org/10.1016/j.uclim.2015.10.002>
- Lundholm, J., Macivor, J. S., Macdougall, Z., & Ranalli, M. (2010). Plant species and functional group combinations affect green roof ecosystem functions. *PLoS One*, 5(3), e9677. doi: 10.1371/journal.pone.0009677
- Meek, A., Jayasuriya, N., Horan, E., & Adams, R. (2014). *Environmental Benefits of Retrofitting Green Roofs to a City Block* (Vol. 20).
- Morakinyo, T. E., Dahanayake, K. W. D. K. C., Ng, E., & Chow, C. L. (2017). Temperature and cooling demand reduction by green-roof types in different climates and urban densities: A co-simulation parametric study. *Energy and Buildings*, 145, 226-237. doi: <https://doi.org/10.1016/j.enbuild.2017.03.066>
- Ng, E., Chen, L., Wang, Y., & Yuan, C. (2012). A study on the cooling effects of greening in a high-density city: An experience from Hong Kong. *Building and Environment*, 47, 256-271. doi: <https://doi.org/10.1016/j.buildenv.2011.07.014>

- Norton, B., Coutts, A., Livesley, S., & Williams, N. (2013). Urban Heat Island Report: Decision principles for the selection and placement of Green Infrastructure: Victorian Centre for Climate Change Adaptation Research.
- Oberndorfer, E., Lundholm, J., Bass, B., Coffman, R., Doshi, H., Dunnett, N., . . . Rowe, D. (2007). Green Roofs As Urban Ecosystems: Ecological Structures, Functions And Services (Vol. 57).
- Oke, T. R. (1973). City size and the urban heat island. *Atmospheric Environment* (1967), 7(8), 769-779. doi: [https://doi.org/10.1016/0004-6981\(73\)90140-6](https://doi.org/10.1016/0004-6981(73)90140-6)
- Oke, T. R. (1981). Canyon geometry and the nocturnal urban heat island: comparison of scale model and field observations. *Journal of climatology*, 1(3), 237-254.
- Ouldboukhite, S.-E., Belarbi, R., & Sailor, D. J. (2014). Experimental and numerical investigation of urban street canyons to evaluate the impact of green roof inside and outside buildings. *Applied Energy*, 114, 273-282. doi: <https://doi.org/10.1016/j.apenergy.2013.09.073>
- Peng, L. L., & Jim, Y. C. (2013). Green-Roof Effects on Neighborhood Microclimate and Human Thermal Sensation. *Energies*, 6(2). doi: 10.3390/en6020598
- Rosenzweig, C., Gaffin, S., & Parshall, L. (2006). Green roofs in the New York metropolitan region: Research report. Columbia University Center for Climate Systems Research and NASA Goddard Institute for Space Studies. New York, 1-59.
- Rößler, S. (2008). Green space development in shrinking cities: opportunities and constraints. *Urbani Izziv*, 19(2), 147-152.
- Rupprecht, C. D. D. (2017). Informal Urban Green Space: Residents' Perception, Use, and Management Preferences across Four Major Japanese Shrinking Cities. *Land*, 6(3), 59.
- Saaroni, H., Amorim, J. H., Hiemstra, J. A., & Pearlmutter, D. (2018). Urban Green Infrastructure as a tool for urban heat mitigation: Survey of research methodologies and findings across different climatic regions. *Urban Climate*, 24, 94-110. doi: <https://doi.org/10.1016/j.uclim.2018.02.001>
- Santamouris, M. (2014). Cooling the cities – A review of reflective and green roof mitigation technologies to fight heat island and improve comfort in urban environments. *Solar Energy*, 103, 682-703. doi: <https://doi.org/10.1016/j.solener.2012.07.003>
- Smith, K. R., & Roebber, P. J. (2011). Green roof mitigation potential for a proxy future climate scenario in Chicago, Illinois. *Journal of applied meteorology and climatology*, 50(3), 507-522.
- Solecki, W. D., Rosenzweig, C., Parshall, L., Pope, G., Clark, M., Cox, J., & Wiencke, M. (2005). Mitigation of the heat island effect in urban New Jersey. *Global Environmental Change Part B: Environmental Hazards*, 6(1), 39-49. doi: <https://doi.org/10.1016/j.hazards.2004.12.002>
- Srivanit, M., & Hokao, K. (2013). Evaluating the cooling effects of greening for improving the outdoor thermal environment at an institutional campus in the summer. *Building and Environment*, 66, 158-172. doi: <https://doi.org/10.1016/j.buildenv.2013.04.012>
- Taleghani, M., Sailor, D., & Ban-Weiss, G. A. (2016). Micrometeorological simulations to predict the impacts of heat mitigation strategies on pedestrian thermal comfort in a Los Angeles neighborhood. *Environmental Research Letters*, 11(2), 024003.
- Vijayaraghavan, K. (2016). Green roofs: A critical review on the role of components, benefits, limitations and trends. *Renewable and Sustainable Energy Reviews*, 57, 740-752. doi: <https://doi.org/10.1016/j.rser.2015.12.119>
- Wang, Y., Ni, Z., Chen, S., & Xia, B. (2019). Microclimate regulation and energy saving potential from different urban green infrastructures in a subtropical city. *Journal of Cleaner Production*, 226, 913-927. doi: <https://doi.org/10.1016/j.jclepro.2019.04.114>
- Wilkinson, S. J., & Reed, R. (2009). Green roof retrofit potential in the central business district. *Property Management*, 27(5), 284-301. doi: 10.1108/02637470910998456
- Wong, N. H., Chen, Y., Ong, C. L., & Sia, A. (2003). Investigation of thermal benefits of rooftop garden in the tropical environment. *Building and Environment*, 38(2), 261-270. doi: [https://doi.org/10.1016/S0360-1323\(02\)00066-5](https://doi.org/10.1016/S0360-1323(02)00066-5)

- Wong, N. H., Tan, P. Y., & Chen, Y. (2007). Study of thermal performance of extensive rooftop greenery systems in the tropical climate. *Building and Environment*, 42(1), 25-54. doi: <https://doi.org/10.1016/j.buildenv.2005.07.030>
- Zölch, T., Maderspacher, J., Wamsler, C., & Pauleit, S. (2016). Using green infrastructure for urban climate-proofing: An evaluation of heat mitigation measures at the micro-scale. *Urban Forestry & Urban Greening*, 20, 305-316. doi: <https://doi.org/10.1016/j.ufug.2016.09.011>

18- comparison among numerous numerical alternatives using ansys on open channel confluence

M. Abd EL-Mooty¹, W.Kh. El-Hamamy²

Faculty of engineering, Alexasndria university, Alexandria, Egypt

E-mail: walaa_hamamy@yahoo.com

Abstract

Study of open channel junctions has a quite interest in the hydraulics field. Due to these junctions, a main zone of separation just downstream the junction is formed. The current study concerns with the separation zone occurs as a result of open channel confluence. There are many variables and factors affecting the separation zone characteristics. These variables could be divided into two main sets; geometry variables and flow variables.

The present study introduced a CFD analysis using ANSYS in 2D approach, to simulate a confluence case with reasonable assumptions. The basic governing equations (Momentum, continuity) based on Reynolds-averaged Navier–Stokes equations “RANS”. The finite volume method was chosen to discretize the governing equations. The study used numerous viscosity models (K- ϵ), (K- ω), SST. Further, different viscosity sub-models and near wall treatment functions were involved as well, using different pressure velocity coupling alternatives; SIMPLE, SIMPLIC, COUPLED and PISO, with changing spatial discretization method for momentum, turbulent kinetic energy, specific dissipation rate schemes form second order upwind to QUICK, which makes a total number of runs equal to 104. These alternatives were validated to experimental data done by Weber et. al (2001). A comparison is done between all the possible solution scenarios (104 runs) to choose the simulation alternative with the least error for the solution according to the study limitations. In addition, a detailed analysis of the CDF analysis of results between different schemes is presented in the paper

Keywords: Open channel confluence – ANSYS - (K- ϵ), (K- ω), SST

Introduction

The open channel junctions affect the flow characteristics, causing changes as forming zones of separation, recirculation, turbulence, wide range of velocities and a shear plane which is developed between the two joining flows downstream of the confluent area.

The separation zone is an area of reduced pressure, recirculating flow and sediment, which affects hydraulic geometry, channel roughness, and so on. Fig. 1 shows the main characteristics at open channel junctions as mentioned by Weber. A set of variables affect the separation zone characteristics, these factors as; discharge ratio and width ratio between the branch channel and the main one, junction angle between the two channels, channels cross section, channels bed slope, Froude number in D.S and channels roughness. These variables make it difficult to create an accurate simulation accommodates all of the variables. Thus, the need for using CFD is being a necessity.

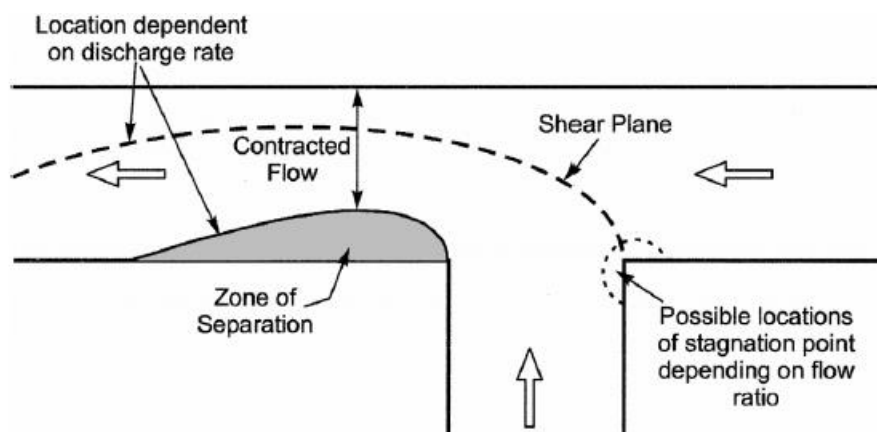


Figure 1: Flow characteristics in open channel junction - Weber, et al, 2001.

Literature review

Walaa El-Hamamy, (2019),⁽¹⁾ presented a comprehensive numerical study using different CFD scenarios (104 different scenarios), to select the closer scenario to the complete similarity with Weber's⁽²⁾ experimental data, this most appropriate model involved in this study here to investigate the effect of changing; discharge ratio, the width ratio and different confluence angles on the separation zone characteristics. Further, Walaa El-Hamamy, (2018)⁽³⁾ analyses and visualized the available experimental data and presented clear visualization. Webber e. al. (2001)⁽²⁾, compiled a data set that fully describes the complex, 3D flow conditions present in a 90 ° open-channel junction. Moreover, to provide a benchmark experimental data set for validation of future numerical models. Larry J. Weber et al (2002)⁽⁴⁾, presented a 3D numerical analysis to investigate the flow in an open channel junction. The model was validated by experimental data of 90° confluence angle "Shumate 1998- Weber's". Then, the model used to investigate the effect of changing confluence angle. M. Sivakumar, K. Dissanayake and A. Godbole (2004)⁽⁵⁾ presented a 3D numerical simulation of a horizontal-bed open-channel water flow with a 90° equal-width junction, using a commercially available CFD package PHOENICS (version 3.5) and compare it with an experimental data. Rashwan, I.M.H.1, Tarek A. Saafan (2004)⁽⁶⁾, introduced a theoretical model for division case of T-junction "right angled junction" over a horizontal bed. Subcritical steady flow through extension main and branch, with equal widths. They used to verification. Chung-Chieh's experimental data were used. Hamid Shamloo (2008)⁽⁷⁾, presented a numerical simulation of lateral intake flow using FLUENT 2D application. "Using RMS' turbulent model. Waqid Hameed Al-Mussawi (2009)^(8, 9), provides detail application of numerical solution (Finite Volume) by using FLUENT-2D and FLUENT-3D software in simulation of 90° open channel junction flows, the results compare with experimental data. G. Kesserwani et al. (2010)⁽¹⁰⁾, presented an unsteady mathematical model depends on St. Venant solutions, and apply it to investigate model for flow diversion through a right-angled open-channel junction to compare three cases of flow bifurcations (super-, trans-, and sub- critical flow) and experimental data" Hsu et al.2002; Rivière et al. (2007)" or theoretical prediction "relationships developed by Mizumura et al. (2003), Rivière et al. (2007)." Mung Dinh Thanh, Ichiro Kimura, Yasuyuki Shimizu and Takashi Hosoda (2010)⁽¹¹⁾, introduced a numerical simulation using depth average models with secondary current effects. R.Goudarzizadeh et al (2011)⁽¹²⁾, presented a numerical model, developed by Ghobadian et al (2006), which simulate the flow by the use of Reynold-stress method (RSM) to investigate the effect of both width and discharge ratios on the separation zone dimensions and the quality of bed shear stress distribution, in an open channel confluence. Mung Dinh Thanh et al (2011)⁽¹³⁾, presented the results of 3 D-simulation study using a numerical model with the linear and nonlinear K- ξ models. Q. Y. Yang, T. H. Liu, W. Z. Lu, and X. K. Wang (2013)⁽¹⁴⁾, presented a simulation using new dynamic mesh" ANSYS FLUENT". The results were compared with experimental data and with 2 turbulence models (rigid lid and volume of fluid-VOF-) to investigate the impact by tracing the free surface boundary. A. Baghlani & N. Talebbeydokhti (2013)⁽¹⁵⁾ presented a 2D numerical simulation to a right-angled channel confluence. The study focused on the main parameters: discharge ratio, width ratio and downstream F.N, and results were compared with an experimental data set. Firooz Rooniyan (2013)⁽¹⁶⁾, use FLUENT 6.3.26 numerical model to analyze and evaluate the effect of changing the confluence angle (30°, 45°, 60°) for different discharge ratios (0.083, 0.917) on the flow pattern and the separation zone dimensions. M Brito, et al, (2014)⁽¹⁷⁾, Introduced a 3D numerical simulation using different turbulence models "(k- ϵ , RNG k- ϵ , k- ω , SST k- ω , EARSM) for a 70° junction. Minoo Sharifipour, et al, (2015)⁽¹⁸⁾, used a CFD model to study the effect of changing both discharge and width ratios on the velocity distribution. STÉPHAN CREËLLE et al.(2014)⁽¹⁹⁾, presented an assessment to the effect of increasing bed friction on an open channel confluence of 90° using a 3D numerical simulation model, which depends on the shallow water equations. This model is validated using (Shumate 1998) experimental data. Amir Hossein Zaji & Hossein Bonakdari (2015)⁽²⁰⁾, presented a comparison of velocity field results in an open channel 90° junction between two numerical methods: Artificial Neural Network (ANN) & 3D CFD modeling "ANSYS – CFX". Both methods were validated with Weber's experimental data (2001), & Shumate and Weber 1998.

The previous studies depended on their comparison between 4 or 5 selected scenarios of CFD simulation schemes. However, the study here made a comprehensive investigation by comparing between the all available numerical schemes. Compares between 104 scenarios, to get the best scenario according to the applied mesh. All results obtained these scenarios were in comparison with Weber's experimental data.

3-d analysis for the experimental data

One of the main experimental works, is the work done by Webber 2001⁽²⁾, we will use his data to validate the applied ANSYS models. However, Weber's data was a comprehensive data, it needed more clear visualization. For instance, his 3-D results for velocity were presented in 2-D contours, and did not give a 3-D visualization for the 3-D velocities. The paper here analyzed intensively his data and presented his results in comprehensive visualization figures, some of them is presented here.

Weber's experimental data procedure

His experimental procedure is arranged as follows:

Combining flume with 90° sharp edged junction. The floor for all facility is horizontal, and there are 2 tanks to supply discharge to channels. A honeycomb and perforated plates were placed in the inlet to ensure properly developed flow, and a tail gate was placed to control the tail water depth. The channel width is constant for all channels $W = 0.914\text{m}$. All distances normalized with the channel width to be in dimensionless form. X^* , Y^* , Z^* , where ($x^* \rightarrow x/W$, $y^* \rightarrow y/W$, $z^* \rightarrow z/W$). The origin for all points measured was the bed at the upstream corner of the junction. The velocity measurements normalized by the downstream average velocity $V_t = 0.628\text{ m/s}$. Discharge ratio $q^* = Q_m/Q_t$ (where Q_m is the main channel discharge and Q_t the total discharge downstream the confluence). The experiments were carried for 6 values of q^* , [$q^* = 0.083, 0.25, 0.417, 0.583, 0.750, 0.917$].

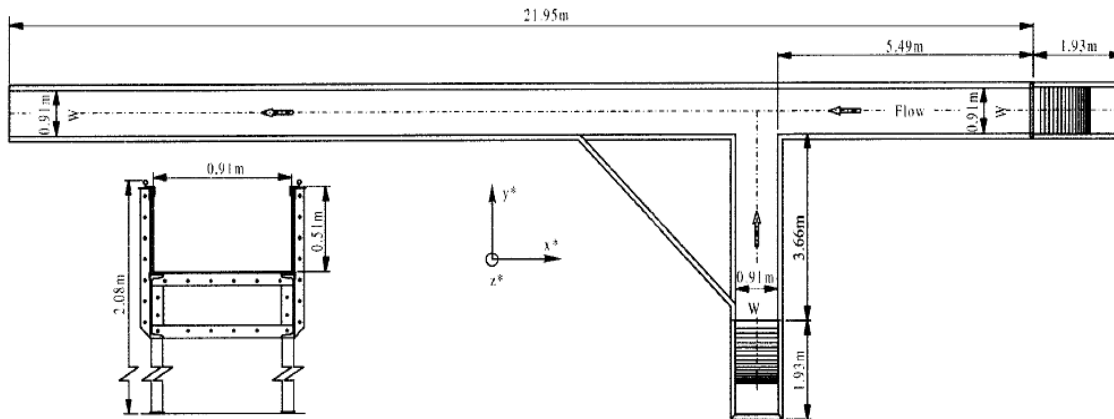


Figure 2: Experimental channel junction, Weber's, et al.

Analysis of the velocity data

For each point with (x, y, z) coordinates. Further, this data is found twice, once for the main channel, and another for the branch.

The velocity data distribution in the three dimensions x^* , y^* , z^* directions u^* , v^* , and w^* respectively are analyzed using Matlab visualization format where the velocities are normalized by dividing it by the downstream velocity $= 0.628\text{ m/sec}$. Sample of u^* , v^* and w^* velocities for $q^* = 0.25$ was as the following:

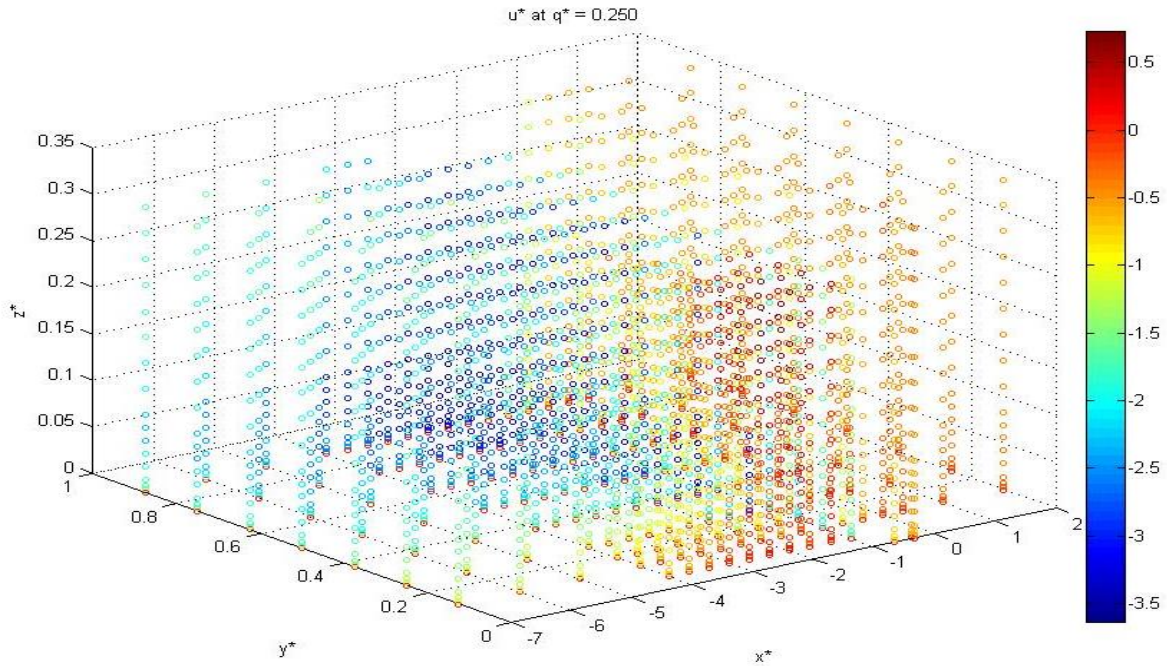


Figure 0: The relative velocity in x direction u^* at $q^* = 0.25$

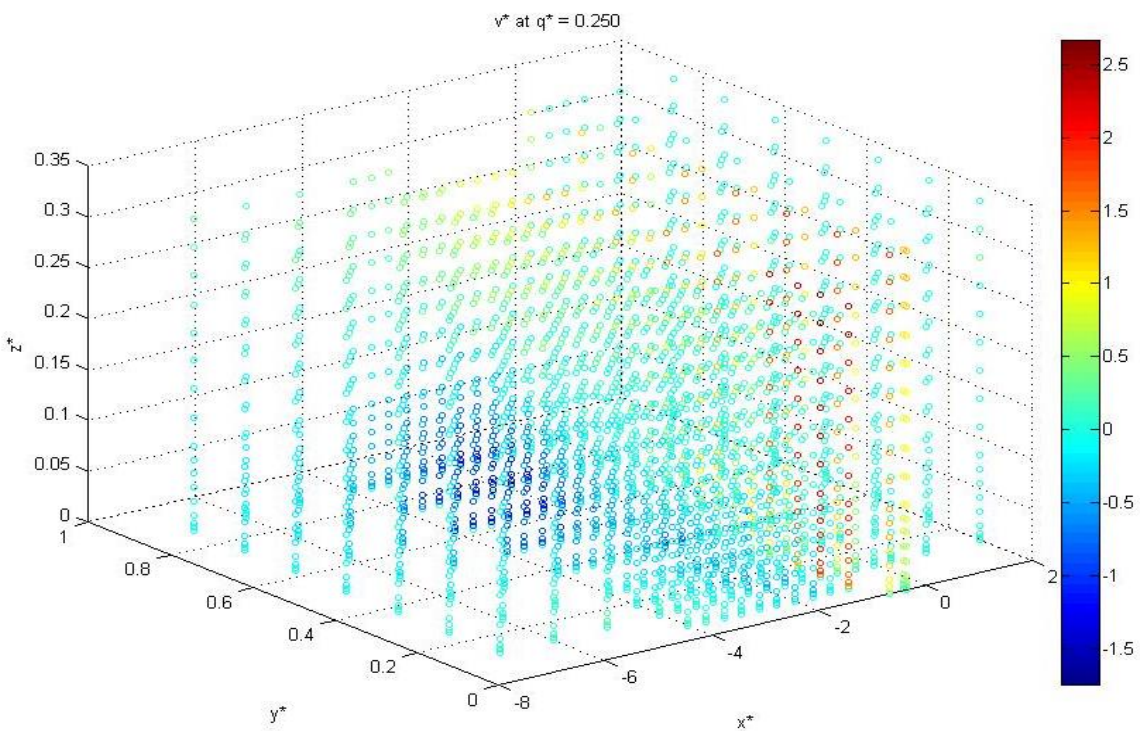


Figure 4: The relative velocity in y direction v^* at $q^* = 0.25$

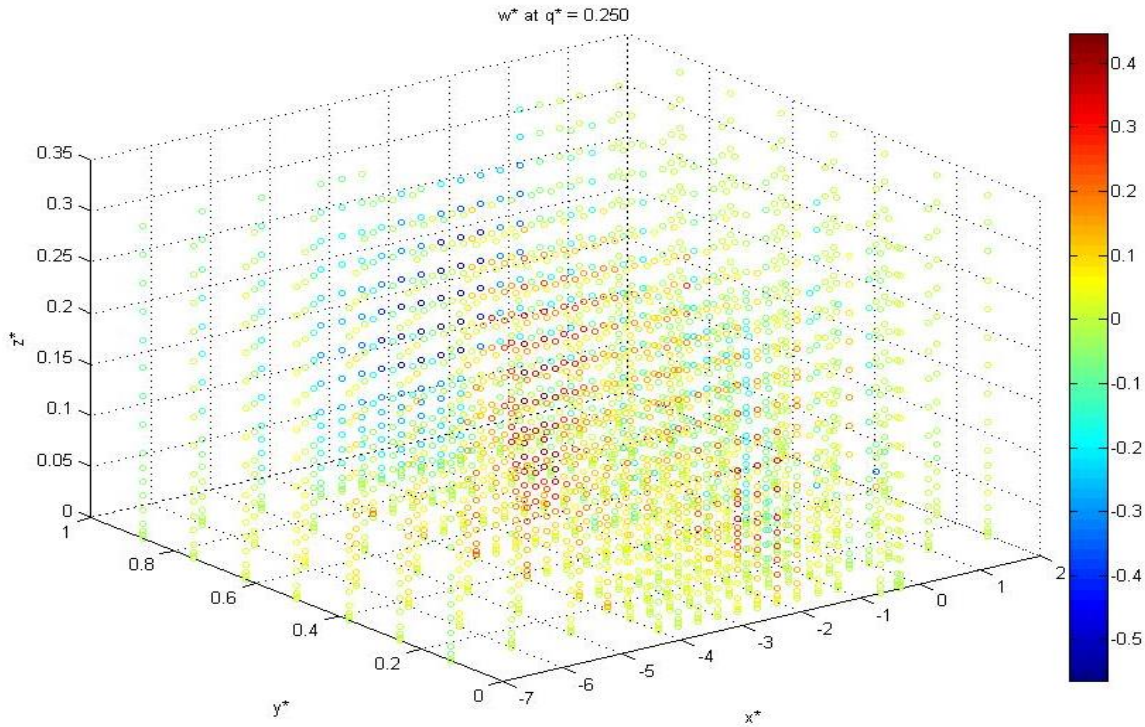


Figure 5: The relative velocity in z direction w^* at $q^* = 0.25$

Numerical simulation analysis

2-D numerical simulation using ANSYS is carried out and presented with reasonable assumptions to simulate the existing problem. The basic governing equations (Momentum, continuity) based on Reynolds-averaged Navier–Stokes equations “RANS”. The finite volume method was chosen to discretize the governing equations. The selected initialization method in the study is “Hybrid initialization”, this provides a quick approximation of the flow field, by a collection of methods. It solves Laplace's equation to determine the velocity and pressure fields. The study used numerous viscosity models (K- ϵ), (K- ω), SST. Further, different viscosity sub-models and near wall treatment functions were involved as well, using different pressure velocity coupling alternatives; SIMPLE, SIMPLIC, COUPLED and PISO, with changing spatial discretization method for momentum, turbulent kinetic energy, specific dissipation rate schemes from second order upwind to QUICK, which makes a total number of runs equal to 104. A comparison was done between all the possible solution scenarios (104 runs) to choose the simulation alternative with the least error for the solution. These alternatives were validated to experimental data done by Weber et. al (2001)⁽²⁾.

Governing equations:

Navier-Stokes equation:

$$\begin{aligned} \frac{\partial u}{\partial t} + u \frac{\partial u}{\partial x} + v \frac{\partial u}{\partial y} + w \frac{\partial u}{\partial z} &= -\frac{1}{\rho} \frac{\partial p}{\partial x} + \nu \left(\frac{\partial^2 u}{\partial x^2} + \frac{\partial^2 u}{\partial y^2} + \frac{\partial^2 u}{\partial z^2} \right) + g_x \\ \frac{\partial v}{\partial t} + u \frac{\partial v}{\partial x} + v \frac{\partial v}{\partial y} + w \frac{\partial v}{\partial z} &= -\frac{1}{\rho} \frac{\partial p}{\partial y} + \nu \left(\frac{\partial^2 v}{\partial x^2} + \frac{\partial^2 v}{\partial y^2} + \frac{\partial^2 v}{\partial z^2} \right) + g_y \\ \frac{\partial w}{\partial t} + u \frac{\partial w}{\partial x} + v \frac{\partial w}{\partial y} + w \frac{\partial w}{\partial z} &= -\frac{1}{\rho} \frac{\partial p}{\partial z} + \nu \left(\frac{\partial^2 w}{\partial x^2} + \frac{\partial^2 w}{\partial y^2} + \frac{\partial^2 w}{\partial z^2} \right) + g_z \end{aligned}$$

..... eq. 1

Where u, v, w : are the velocities in x, y, z directions respectively, ρ : is the density, p : is the pressure, t : is time, g_x, g_y, g_z : represents body accelerations acting on the continuum (in x, y, z directions respectively) and ν : the kinematic viscosity

Continuity equation:

$$\frac{\partial \mathbf{u}}{\partial x} + \frac{\partial \mathbf{v}}{\partial y} + \frac{\partial \mathbf{w}}{\partial z} = 0 \quad \text{eq. 2}$$

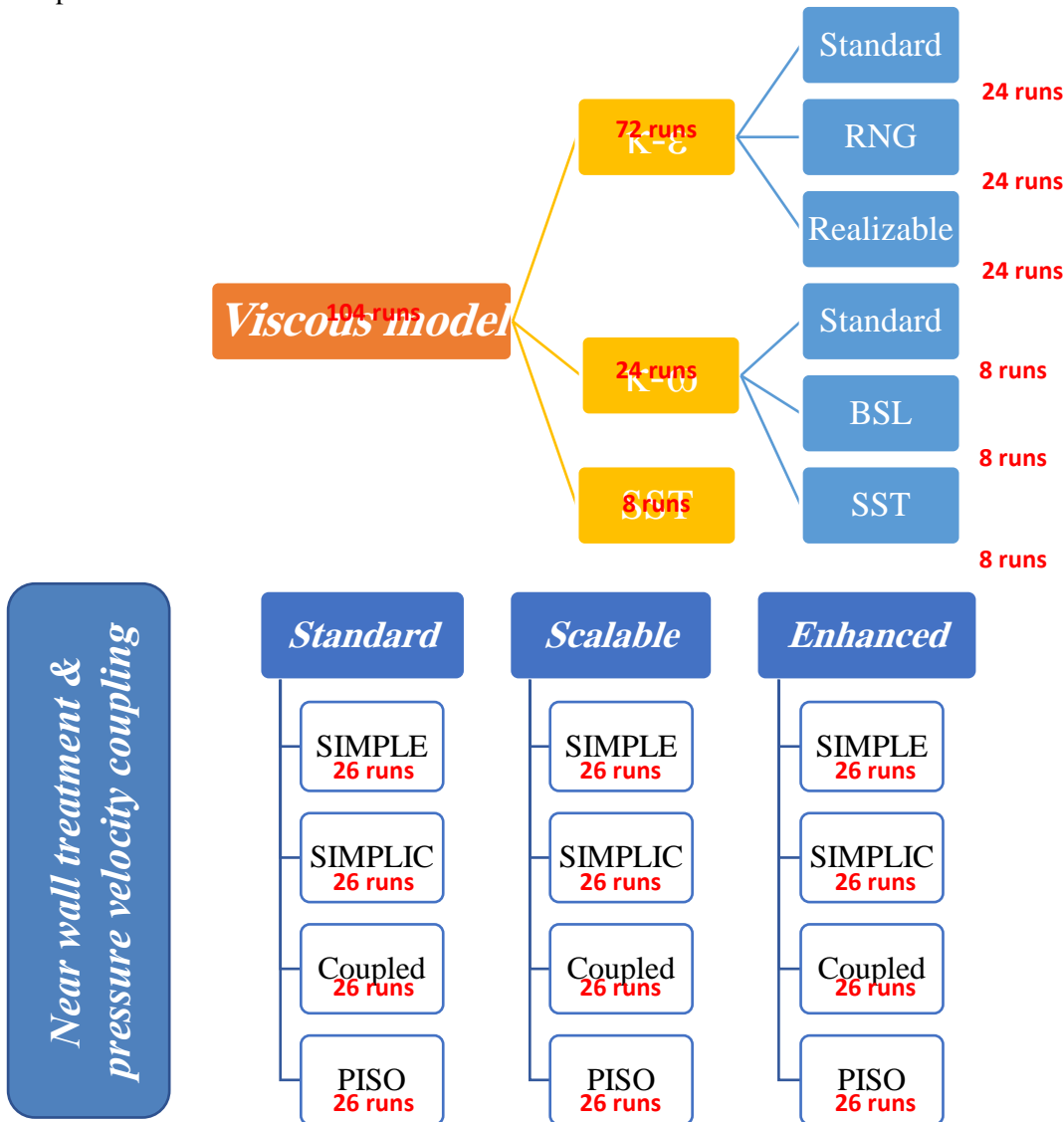
Turbulence Modelling:

Turbulence modeling is the construction and use of a model to predict the effects of turbulence. Turbulence kinetic energy k equation is used to determine the turbulence velocity scale:

$$\frac{\partial (\rho k)}{\partial t} + \frac{\partial (\rho \bar{u}_i k)}{\partial x_i} = \underbrace{-\rho \bar{u}'_i \bar{u}'_j \frac{\partial \bar{u}_i}{\partial x_j}}_{P_k} - \rho \varepsilon + \frac{\partial}{\partial x_j} \left[\left(\mu + \frac{\mu_t}{\sigma_k} \right) \frac{\partial k}{\partial x_j} \right] \quad \text{eq. 3}$$

Also, each one will be investigated according to tow spatial discretization methods, (Second order upwind and QUICK).

The flowing flow chart present the different applied scenarios (104 runs), by suing different viscosity models, different viscosity sub-models and near wall treatment functions, different pressure velocity coupling alternatives with changing spatial discretization method for momentum, turbulent kinetic energy, specific dissipation rate schemes.



Spatial discretization method for momentum, turbulent kinetic energy and specific dissipation rate

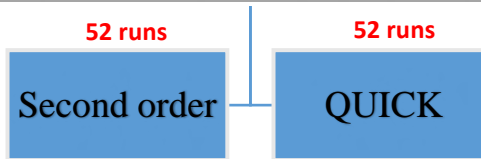


Chart 1: All applied schemes for the different scenarios (104 runs) in ANSYS

Geometry and meshing:

The geometry was set as Weber's experimental dimensions to achieve verification, the mesh nodes were 338463 the dimensions and the mesh are shown in the following figures:

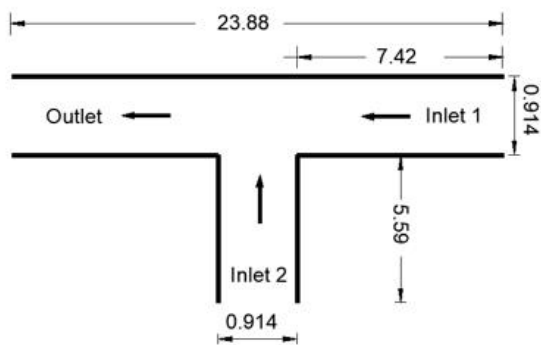


Figure 6: Weber's dimensions in meters

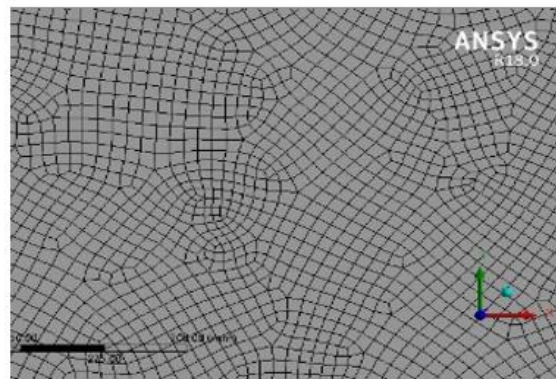


Figure 7: Mesh after the junction area

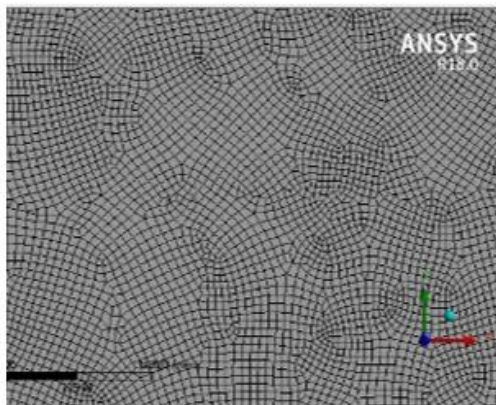


Figure 8: Mesh in the junction area

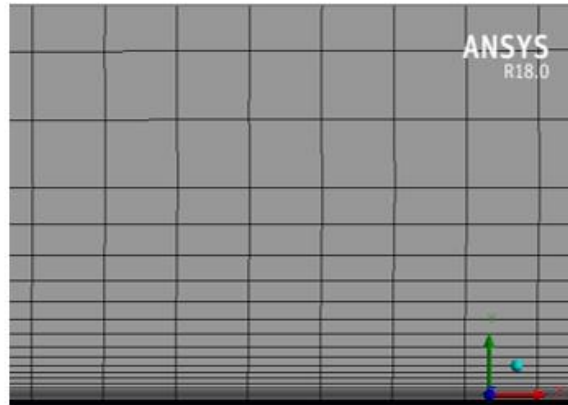


Figure 9: Mesh at boundary layer

Boundary conditions:

The boundaries were set according to weber's, the selected q^* value is 0.25,
(where $q^* = q_{\text{mainstream}} / q_{\text{tail water}}$)

- Inlet (1): velocity inlet (1) = 0.1571 m/sec. Inlet (2): velocity inlet (2) = 0.4713 m/sec. Outlet: pressure outlet = 0.0. Walls: stationary wall, no-slip, standard wall roughness model, roughness height = 0.0. The type of flow is incompressible and the time is steady.

Calculations:

Start the iteration number with 3000 iterations, and the final number differs according to the selected method of solution.

Ansyes output:

Every scenario result was compared with the experimental data at different Z^* sections, ($z^*=z/b$), where the simulation is 2-D and the available data were for different z^* sections, thus, the simulation results had to be compared with at different sections.

The selected comparison Z^* sections were those who gave closer values to the simulated results, these sections are the nearer to the water surface:

- 1- At $z^* = 0.194$ (at a depth equal 40.10% from the water surface)
- 2- At $z^* = 0.222$ (at a depth equal 31.45% from the water surface)
- 3- At $z^* = 0.25$ (at a depth equal 22.80% from the water surface)
- 4- At $z^* = 0.278$ (at a depth equal 14.16% from the water surface)
- 5- At z^* average value.

The analysis of data showed that; the simulated results are much closer for the experimental data generated at $Z^* = 0.278$.

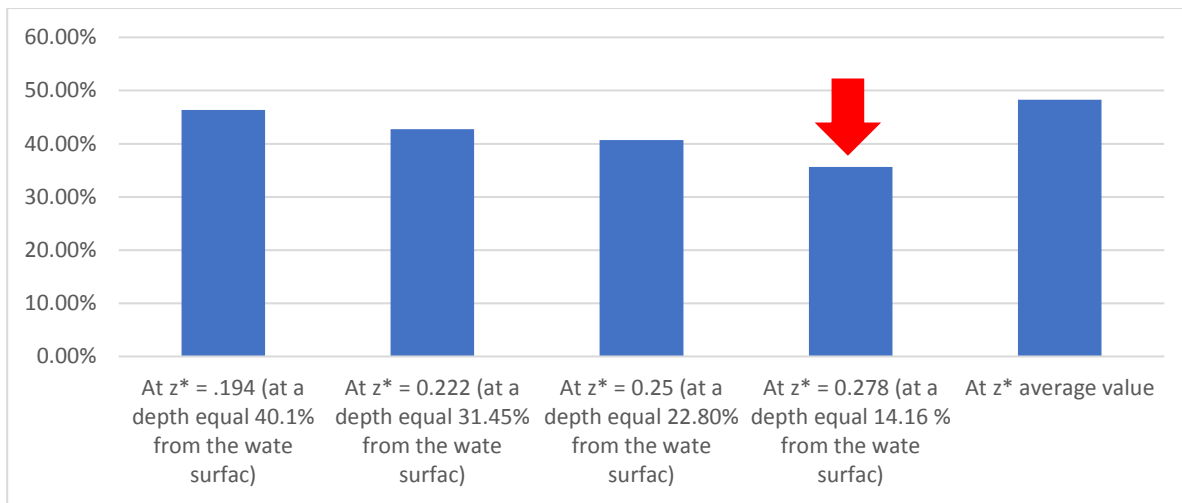


Figure 10: Conclusion of applying different simulating result scenarios, at different Z^* values for the experimental data

Moreover, the simulated results compared with different y^* sections ($y^*=y/b$). Six values of y^* were involved, at $y^* = 0.565, .125, .25, .375, .50, .75$. as shown in the following figure:

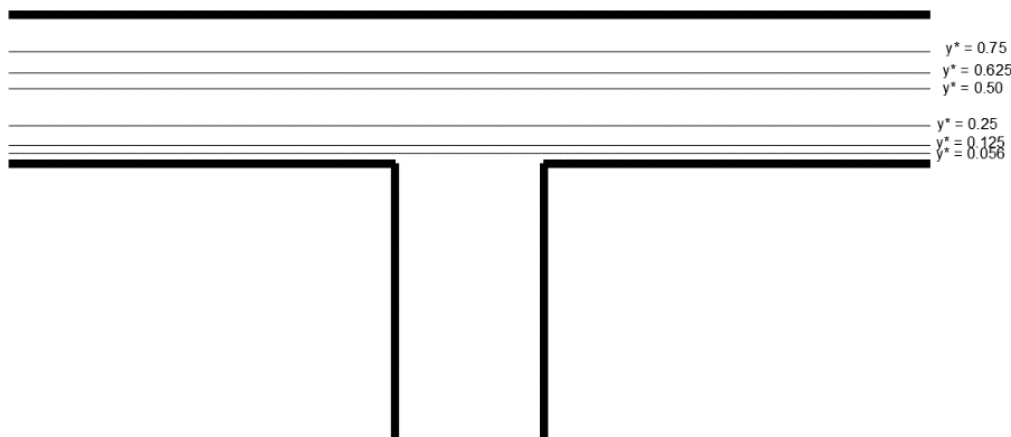


Figure11: different y^* sections involved in the study

Comparison of x_{velocity} for all alternatives proceeded in ansys

The alternatives are 104, however the runs of PISO for pressure velocity coupling does not converged, thus there are no results for them in the appendix.

The numbers of these figures are, 7, 8, 15, 16, 23, 24, 31, 32, 39, 40, 47, 48, 55, 56, 63, 64, 71, 72, 79, 80, 78, 88, 95, 96, 103, and 104.

Further, the results of all scenarios showed that; the minimum error value was for Run Number (49), it gave percentage of error as the following:

The error percentages in the separation zone dimensions were 3% for the separation zone length and 16% for the contracted zone width. The average error in x_{velocity} = 32.47%, as shown in the following table:

| | |
|--|--------|
| Average Error Value of Median % | 38.03% |
| Average Error Value of S.D % | 29.59% |
| Average Error Value of IQR % | 29.80% |

Where:

$$\text{Error \%} = \frac{\text{Simulation result} - \text{Experimental results}}{\text{Simulation results}} \%$$

Further, it gave an average correlation coefficient = 86%

This run used; κ - ε viscous model, realizable viscous sub-model, standard near wall treatment, SIMPLE pressure velocity coupling method, and Second order up-wind spatial discretization method for; momentum, turbulent kinetic energy and specific dissipation rate.

The results were as the following:

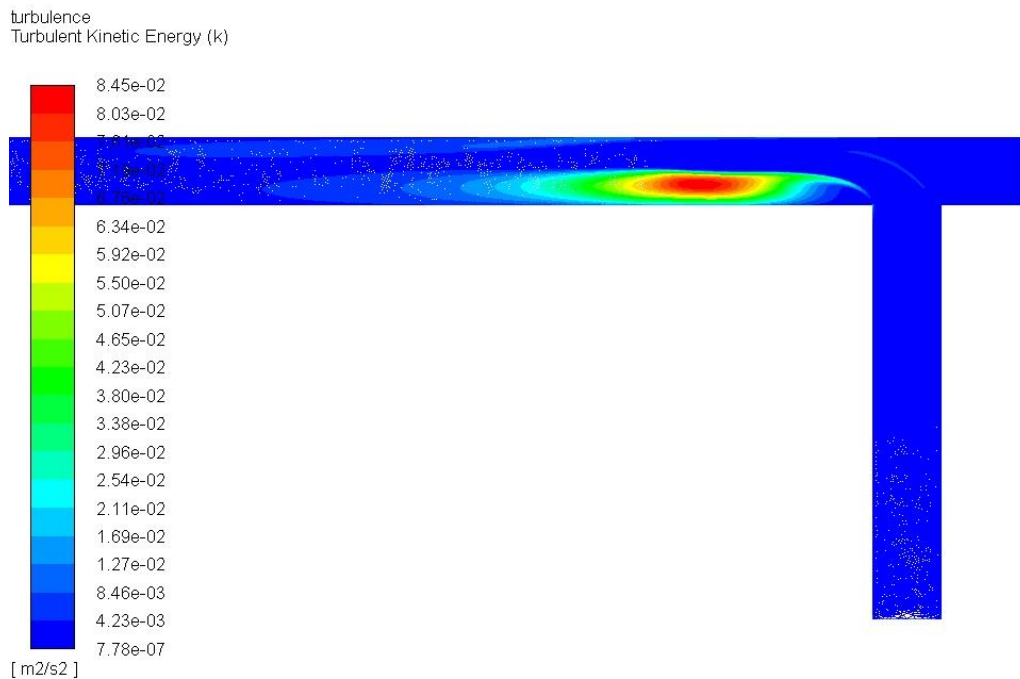


Figure 12: Contour of turbulence results (TKE)

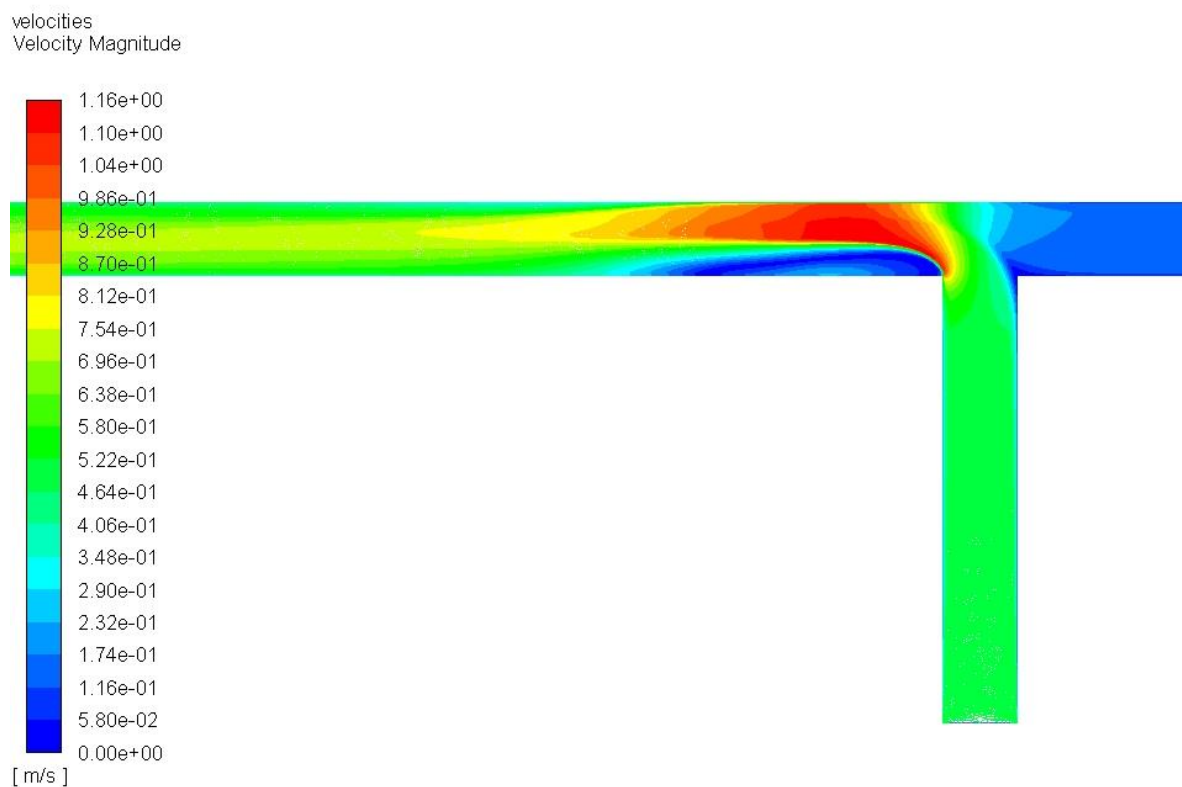


Figure 13: Contour of velocity magnitude (m/sec)

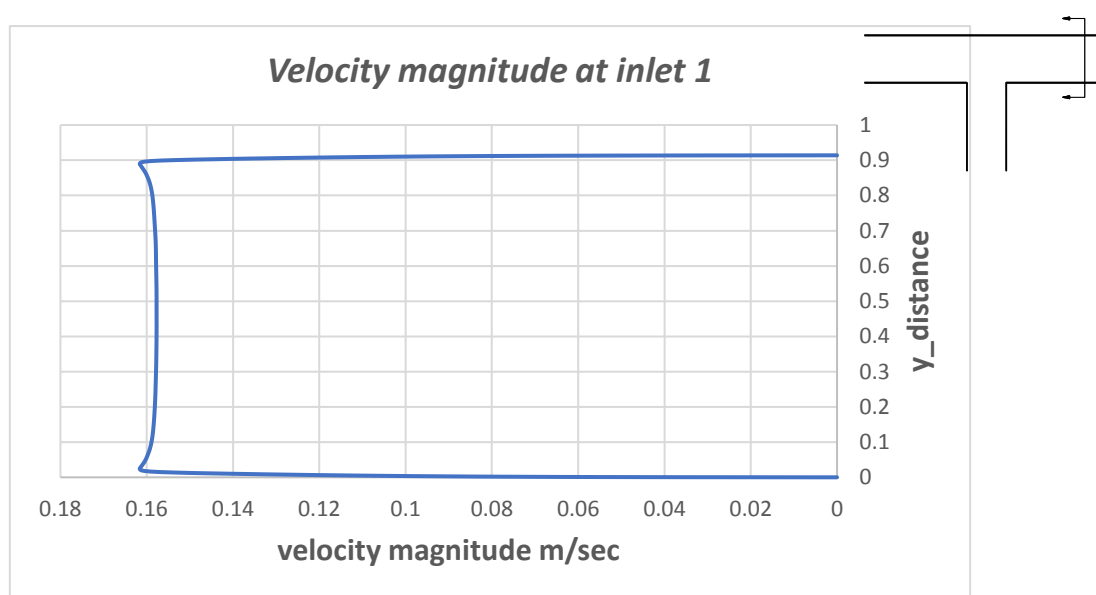


Figure 14: Velocity magnitude for inlet_1, after a distance = 0.42m from entry

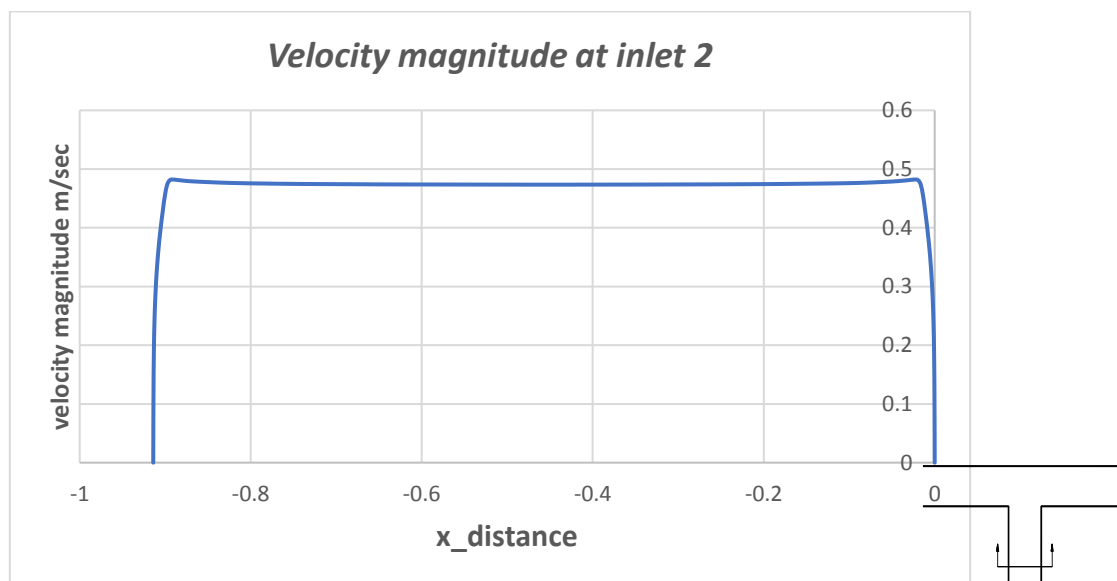


Figure 15: Velocity magnitude for inlet_2, after a distance = 0.59m from entry

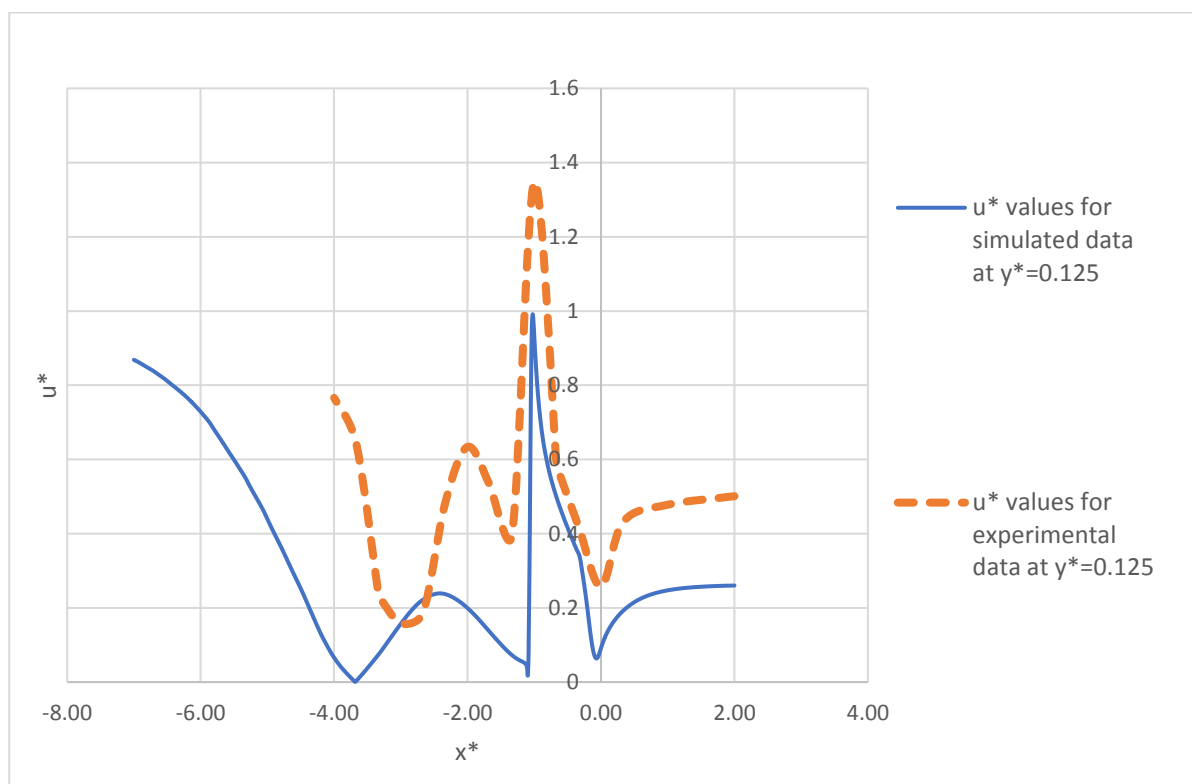


Figure 16: comparison between u^* absolute values at $y^*=0.125$ for weber's experimental data at $z^*=0.278$

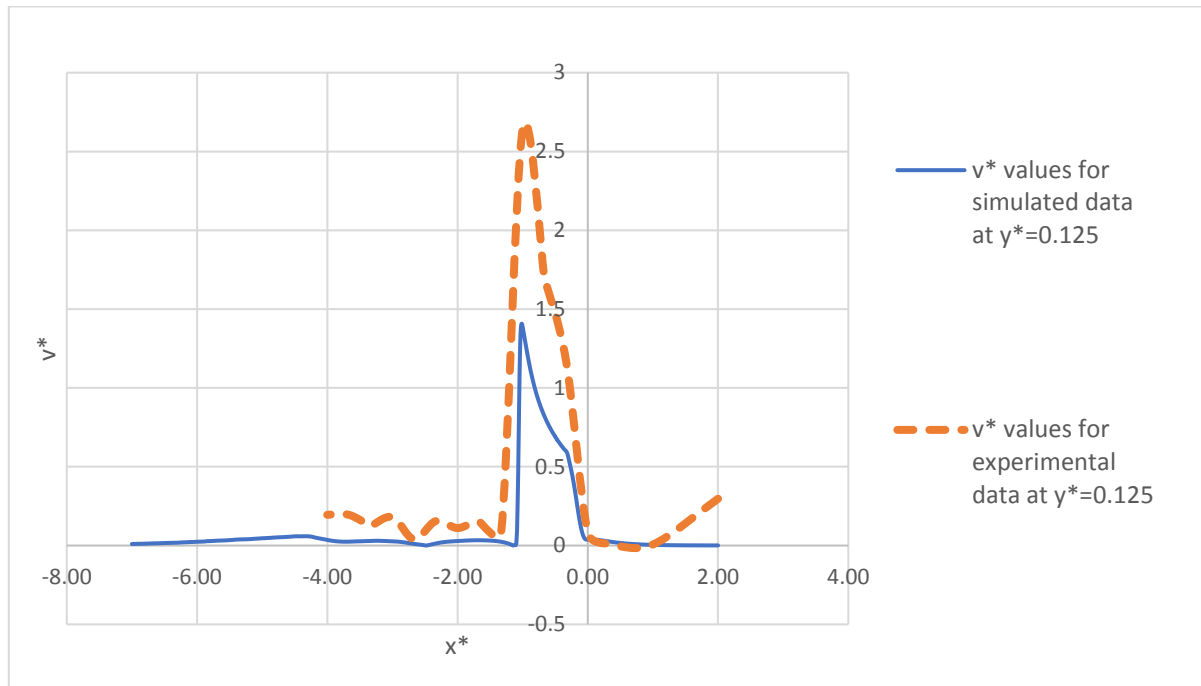


Figure 17: comparison between v^* absolute values at $y^*=0.125$ for weber's experimental data at $z^*=0.278$

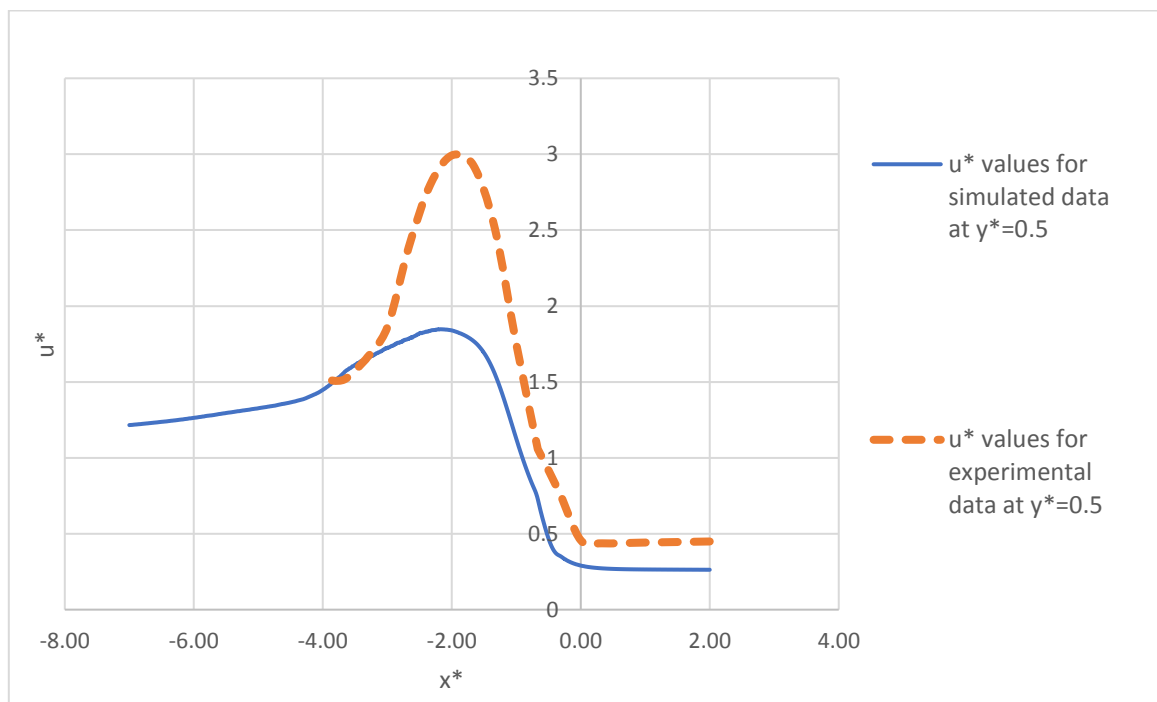


Figure 18: comparison between u^* absolute values at $y^*=0.5$ for weber's experimental data at $z^*=0.278$

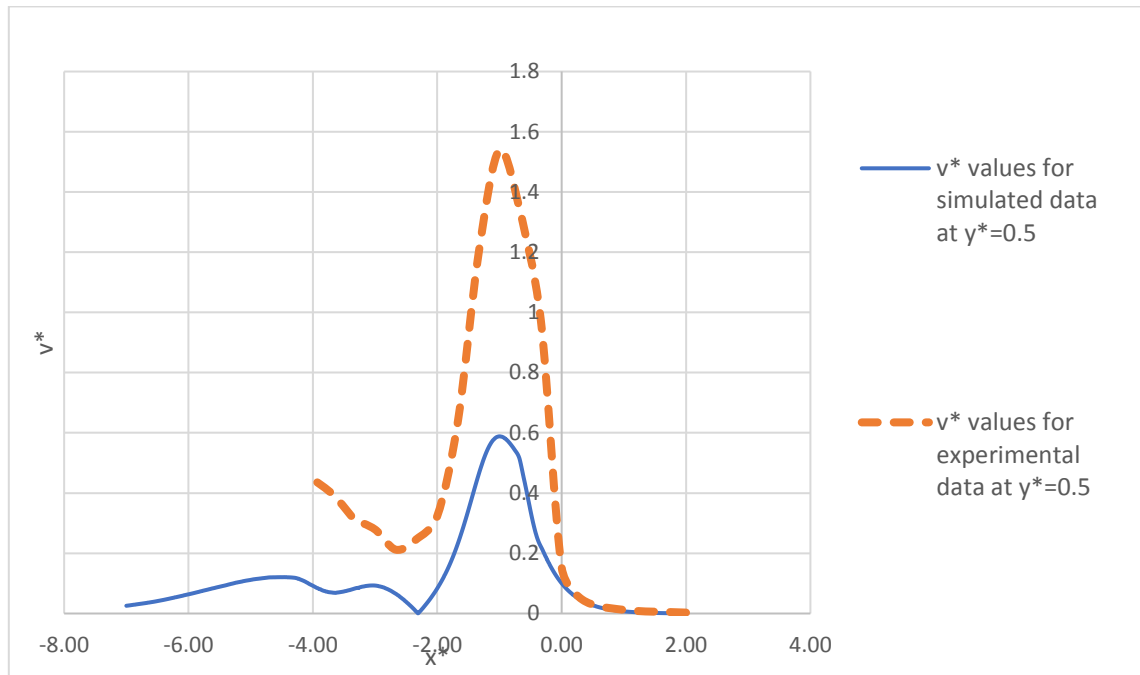


Figure 19: comparison between v^* absolute values at $y^*=0.5$ for weber's experimental data at $z^*=0.278$

Conclusion

This paper investigated the separation zone behavior occurred as a result of open channel junction existence. A comprehensive analysis for different computational schemes were proceeded by using ANSYS CFD program release 18.0, the study was proceeded in 2-D scale. Further, these different scenarios were compared with the chosen experimental data to select the closer scenario to the complete similarity. According to the study limits, the most appropriate scenario to simulate an open channel junction in 2D, is involving the following:

- Viscus model → κ - ϵ .
- Viscus sub-model → Realizable.
- Near wall treatment → Standard.
- Pressure velocity coupling method → SIMPLE.
- Spatial discretization method for; momentum, turbulent kinetic energy and specific dissipation rate → Second order up-wind.

List of references:

1. El-Hamamy WK. THE HYDRAULIC CHARACTERISTICS OF THE OPEN CHANNEL CONFLUENCE 2019.
2. Weber LJ, Schumate ED, Mawer N. Experiments on flow at a 90 open-channel junction. Journal of Hydraulic Engineering. 2001;127(5):340-50.
3. Mohamed Abd-El-Mooty RK, Walaa Khamees El-Hamamy, editor THE HYDRAULIC CHARACTERISTICS OF THE OPEN CHANNEL CONFLUENCE. RETBE'17; 2018; Alexandria, Egypt
4. Huang J, Weber LJ, Lai YG. Three-dimensional numerical study of flows in open-channel junctions. Journal of hydraulic engineering. 2002;128(3):268-80.
5. Sivakumar M, Dissanayake K, Godbole A. Numerical modeling of flow at an open-channel confluence. 2004.
6. Rashwan I, Tarek A. Dividing Flow at 90 o Open Channel Junction. Mansoura University. 2004;29(1).

7. Shamloo H, Pirzadeh B. Investigation of characteristics of separation zones in T-junctions. WSEAS transactions on Mathematics. 2008;7(5):303-12.
8. Al-Mussawi WH. Numerical Analysis Of Velocity Profile And Separation Zone In Open Channel Junctions. Al-Qadisiya Journal for Engineering Sciences. 2009;2(2):262-74.
9. Al-Mussawi WH, Al-Shammary MH, Alwan HH. Three-dimensional numerical investigation of flow at 90 open channel junction. journal of kerbala university. 2009;7(4):260-72.
10. Kesserwani G, Vazquez J, Rivière N, Liang Q, Travin G, Mose R. New approach for predicting flow bifurcation at right-angled open-channel junction. Journal of Hydraulic Engineering. 2010;136(9):662-8.
11. Thanh MD, Kimura I, Shimizu Y, Hosoda T. Numerical simulation of flow at an open-channel confluence using depth-averaged 2D models with effects of secondary currents. Journal of Applied Mechanics. 2010;15:769-80.
12. Goudarzizadeh R, Mousavi J, Hedayat N, Naghshineh M. Numerical investigation of the flow separation zone and quality of the bed shear stress distribution at open-channel confluences. World Acad Sci Eng Tech. 2011;73:968-71.
13. THANH MD, Kimura I, Shimizu Y. Three-Dimensional Simulation of Flow at AN Open-Channel Confluence with Turbulence Models. Journal of Japan Society of Civil Engineers, Ser B1 (Hydraulic Engineering). 2011;67(4):I_181-I_6.
14. Yang Q, Liu T, Lu W, Wang X. Numerical simulation of confluence flow in open channel with dynamic meshes techniques. Advances in Mechanical Engineering. 2013;5:860431.
15. Baghlani A, Talebbeydokhti N. Hydrodynamics of right-angled channel confluences by a 2D numerical model. Iranian Journal of Science and Technology Transactions of Civil Engineering. 2013;37(C2):271.
16. Rooniyan F. The Effect of Confluence Angle on the Flow Pattern at a Rectangular Open-Channel. Engineering, Technology & Applied Science Research. 2013;4(1):576-80.
17. Brito M, Canelas O, Leal J, Cardoso A. 3D numerical simulation of flow at a 70° open-channel confluence. TC. 2014;1100:0.114.
18. Sharifipour M, Bonakdari H, Zaji AH, Shamshirband S. Numerical investigation of flow field and flowmeter accuracy in open-channel junctions. Engineering Applications of Computational Fluid Mechanics. 2015;9(1):280-90.
19. Créëlle S, De Mulder T, Schindfessel L, Van Oyen T, editors. Influence of hydraulic resistance on flow features in an open channel confluence. 3rd Europe Congress (IAHR-2014); 2014.
20. Zaji AH, Bonakdari H. Efficient methods for prediction of velocity fields in open channel junctions based on the artificial neural network. Engineering Applications of Computational Fluid Mechanics. 2015;9(1):220-32.

19- Meteo-parameters variability in the equatorial rainforest

Z. Arétouyap^{†1}, D. Bisso, J.L. Méli'i, P. Njandjock Nouck, R.

Nouayou, M.L. Angue Awona, E. Ntomb Biboum, S.A. Lepatio Tchieg, P. Soppo

University of Yaounde I, Yaounde, Cameroon

[†]E-mail: aretouyap@gmail.com

Abstract

The present investigation aims at questioning any potential trend in the annual and monthly series of temperature, rainfall and standardized precipitation index (SPI) at the scale of the strategic equatorial rainforest region that constitutes the “second lung of the globe”. In fact, as the “second lung of the globe”, this rainforest stands as a major global climate regulator. Hence, practitioners and scholars working in development field may be interested in the variation of regional meteo-parameters in order to reshape their sustainable development policy. The present paper specifically addresses the variability of regional meteo-parameters, using a dataset built up from 4 localities for the half century 1960-2010. This database has been used to identify significant trends at the local scale by applying the non-parametric Mann-Kendall test, then regional interpretation has also been performed because of the natural spatial variability of the equatorial climate. Our study finds four major results: (i) there is a strong consistence between the trends observed in the 4 localities of interest and those observed at a larger scale; (ii) annual mean temperature is increasing throughout the equatorial rainforest region while annual precipitation and SPI (standardized precipitation index) exhibit a downward trend; (iii) an increasing trend for monthly temperature is observed everywhere excepted in 2 localities for several months (Station 2 in February and December, and Station 4 in January, February, March, November and December); and (iv) there is a consistence between the significant trends observed in meteo-parameters from different data sources.

Keywords: *trend detection, rainfall, temperature, climate variability, rainforest*

13 Introduction

Due to the complex nature of climate dynamics, understanding the response of the climate system is a challenging problem, involving analysis of the variations and trends in long time series of atmospheric measurements and proxy records. The global mean surface temperature is one of the most important and most discussed indicators of global change and many policy makers and the general public are more interested in whether they already feel the effects of global warming where they live (Heino et al. 1999; Beg et al. 2002; Gadgil and Dhorde 2005; Bhutiyan 2007; Aityken 2013; Capparelli et al. 2013; Wang et al. 2014). The importance of forest - and water- dominated regions is very well known due to their major role in providing fresh water to large population and dioxygen to the nature (Barnett et al. 2006; Singh and Bengtsson 2004). The enhanced warming in equatorial region may initially affect forest density, but ultimately will cause a decrease in water availability and greenhouse gas regulation in the nature since toxic gases are mainly absorbed by the equatorial forest. These changes have multiple effects on the other drivers in the society, and have large impact especially on billion of people worldwilde.

The present study aims at analysing temperature data in the region, their anomalies in terms of trend and their annual and seasonal variations. Furthermore, some statistical tests such as Mann-Kendall, Spearman Rank Correlation, Sens's Slope, Sequential Mann-Kendall test and linear regression test will be conducted. This may enable to forsee and prevent harmful impacts in various domains such as agricultural production, ocean and savanna ecosystems, coastal populations and infrastructure, human health and population movement, and social, environmental and economic systems (Giannini et al. 2008). All those impacts have direct repercussions on the development policy and can cause various conflicts. Whereas they make uncertain future water supply, storage, and hazards, like famine and malnutrition (Orlove et al. 2008). In view of the importance of temperature and of availability of a long-term temperature record in the Central African Equatorial Region, an attempt has been made to understand the warning trend in the last half century in this region. The annual and seasonal temperature variations have also been analysed in order to undersand the evolution.

2 Method and material

2.1 Study area

Central Africa is an ecologically strategic region with the second forest reserve in the world after the Amazon Forest (Sayer et al. 1992; Alpert 1993). Overall, this is an equatorial region with a mild climate, moderate temperature, abundant rainfall and has one of the wettest places in the world: Debundsha, with an annual rainfall of more than 10,000 mm (Frankham et al. 2004). However, the region shows signs of concern for climate variability, which would extend over the entire sub-region with damaging and diversified environmental and socio-economic consequences as shown in Figure 1 and table 1 (www.enchantedlearning.com 2015). The region is under the influence of the African monsoon, and is dominated by the seasonal translation of the Inter-Tropical Convergence Zone and by the Harmattan winds coming from Sahara. It can be divided into two sub-climatic areas: the sahalian zone stretching over the 8th parallel, and the sudanian (or sudano-sahalian) zone located southward.

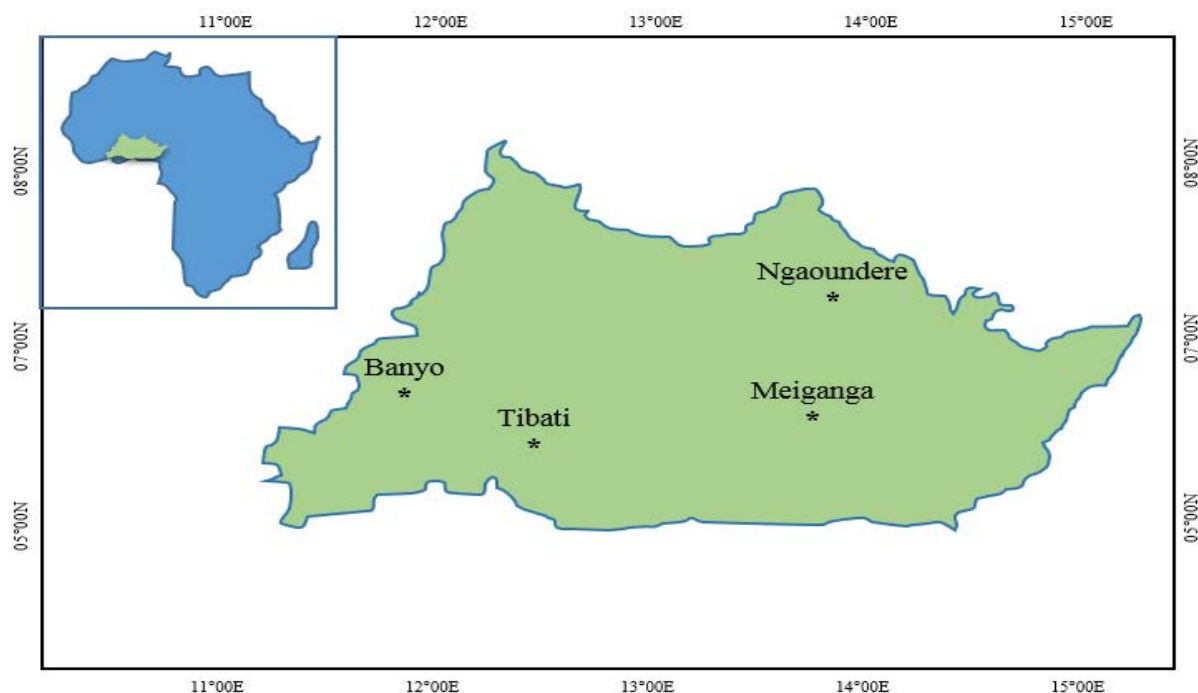


Figure 1 Zoom Rainforests after, www.enchantedlearning.com, 2015

Table1 Geographical coordonnates of the weather and parks stations

| Station | Latitude (in °) | Longitude (in °) | Name |
|---------|-----------------|------------------|------------|
| T1 | 6°44 | 11°48 | Banyo |
| T2 | 6°32 | 14°17 | Meiganga |
| T3 | 7°21 | 13°33 | Ngaoundere |
| T4 | 8°28 | 12°37 | Tibati |

2.2 Methodology and data origin

The data are provided by weather stations and parks, regional and international partner agencies like the Agency for the Safety of Air Navigation in Africa and Madagascar (ASECNA) and the World Meteorological Organization (WMO); and this for a half century (1960-2010) that constitutes the study period. Functioning periods were chosen that were common to all stations. The latter criterion was imposed to be able to perform a regional interpretation of trend detection tests. The monthly series were checked for this study, with a search for breaks resulting from a change in meteorological conditions (Mestre. 2002). Buishand's break test, Pettitt's break test and Hubert's segmentation test (Lubès-Niel et al. 1998) confirmed the consistence and the compatibility of stations used. For the seasonal analysis, the data have been divides into four season, like winter (December-February), premonsoon (March-May), monsoon (June-September), and post-monsoon (October-November).

The monthly data were averaged to provide annual and seasonal values for each year. The data were passed through the Mann-Kendall test (Mann 1945; Kendall 1975), along with few other statistical approaches for trend deduction. Assessing the quality of the data is a very important and necessary step. All the data have been checked for outliers, since outliers play a key role in parametric tests and in assessing the magnitude of the possible changes by computing means (moments) and linear regression (Grant and Leavenworth 1972; Eischeid et al. 1995; Feng et al. 2004; Peterson et al. 1998; Talkhashi et al. 2011; Darshana and Pandey 2013; Xu and Ignatov 2014). Outliers are values that are singularly greater or lower in comparison with the whole database. They can be due to a mistake when recording data. Our dataset did not contain outliers. As there were no data gaps, so the gap filling method was not required. Different statistical tools for trend detection have been applied to know the temperature pattern over the period from 1985 to 2009 (Yue et al. 2002; Modarres and da Silva 2007). As all lag 1 serial correlation coefficients were statistically not significant (Haan 2002), there was no need to pre-white the data, and all statistical tests described above are applied to the original time series (Luo et al. 2007). The lag 1 serial correlation coefficient (Wallis and O'Connell 1972) of annual temperature series was estimated using the equation (1) given at the 5% significance level for a two-tailed test.

$$r_1 = \frac{\sum (x_t - \bar{x})(x_{t+1} - \bar{x})}{\sum (x_t - \bar{x})^2} \quad (1)$$

Where $\bar{x} = \sum x_t / N$ is the overall mean of N sample sizes.

The first order autocorrelation coefficient r_1 can be tested against the null hypothesis using Anderson's (1941) limit for the two-tailed test (relations 2 and 3):

$$r_1(95\%) = \frac{-1 \pm 1.96\sqrt{N-2}}{N-1} \quad (2)$$

$$r_1(90\%) = \frac{-1 \pm 1.645\sqrt{N-2}}{N-1} \quad (3)$$

The Mann-Kendall test, also called Kendall's tau test based on the test statistics S defined in equation 4, is a rank-based non parametric test for assessing the significance of a trend and has been widely used by many researchers in meteorological and data analysis (Goossens and Berger 1986; Kadioglu 1997; Tayanc and Toros 1997; Aesawy and Hasanean 1998; Hamed and Ramachandra Rao 1998; Zhao et al. 2013; Darshana and Pandey 2013; Gocic and Trajkovic 2013).

$$S = \sum_{j=1}^{n-1} \sum_{i=j+1}^n \text{sgn}(x_j - x_i) \quad (4)$$

Where x_1, x_2, \dots, x_n represent 'n' data points and x_j the data point at time j.

A very high positive value of 'S' is an indicator of an increasing trend, whereas a very low negative value indicates a decreasing trend (equation 5):

$$\text{sgn}(x_j - x_i) = \begin{cases} 1 & \text{if } (x_j - x_i) > 0 \\ 0 & \text{if } (x_j - x_i) = 0 \\ -1 & \text{if } (x_j - x_i) < 0 \end{cases} \quad (5)$$

It has been documented that when $n \geq 10$, the statistic S is approximately normally distributed with the mean $E(S)=0$, and its variance is given in equation 6:

$$\text{Var}(x_j - x_i) = n(n-1)(2n+5) \sum_{i=1}^m t_i(t_i-1)(2t_i+5) \quad (6)$$

Where n is the number of data points, m is the number of tied groups (a tied group is a set of sample data having the same value), and t_i is the number of data points in the ith group. The standardized test statistic Z is computed using equation 7:

$$Z = \begin{cases} \frac{s-1}{\sqrt{\text{Var}(s)}} & \text{if } s > 0 \\ 0 & \text{if } s = 0 \\ \frac{s+1}{\sqrt{\text{Var}(s)}} & \text{if } s < 0 \end{cases} \quad (7)$$

The null hypothesis, H_0 , which assumes that there is no significant trend is present and will be rejected if $|Z_s|$ is greater than $Z_{\alpha/2}$, where α represents the chosen significance level. The Spearman Rank Correlation (SRC) test, also used is based on the coefficient r (equation 8):

$$r = 1 - 6 \left\{ \frac{\sum_{i=1}^n d_i^2}{n(n^2-1)} \right\} \quad (8)$$

In this relation, n is the total number of data points in the series. $d_i = RX_i - RY_i$, where RX_i is the rank of variable X_i , which is the chronological order of the observations. The series of observations Y_i is transformed into its equivalent rank RY_i by assessing the chronological order in the ranked series. For the ties, an average rank will be considered. The test statistic t is given by equation 9:

$$t = r \sqrt{\frac{(n-2)}{(1-r)^2}} \quad (9)$$

The null hypothesis implying no trend will not be rejected if $t_{v,\alpha/2} < t < t_{v,1-\alpha/2}$, where the test statistic t follows a student's t distribution with degrees of freedom $v = n - 2$ and significance level α . The method of Sen (1968) is also used to evaluate, the magnitude of the slope according to the equation 10:

$$b = \text{Median} \left[\frac{Y_i - Y_j}{i - j} \right] \text{ for all } j < i \quad (10)$$

Where Y_i and Y_j are data at time points i and j, respectively. If the total number of data points in the series is n, then there will be $n(n-1)/2$ slope estimates. Positive and negative signs of test statistics indicate increasing trend and decreasing trend, respectively. The test statistic t_j of the Sequential Mann-Kendal test (SQMK) is calculated with equation 11 (Modarres and Sarhadi 2009; Sneyers 1990):

$$t_i = \sum_i^j n_j \quad (11)$$

The mean and variance of the test statistic t_j are presented in equation 12 and 13:

$$E(t) = \frac{n(n-1)}{4} \quad (12)$$

$$\text{Var}(t_j) = \frac{j(j-1)(2j+5)}{72} \quad (13)$$

After that, $u(t_j)$ is calculated using equation 14:

$$u'(t_j) = \frac{t_j - E(t)}{\sqrt{\text{Var}(t_j)}} \quad (14)$$

In the same way $u'(t_j)$ is calculated starting from the end of the series.

3 Results

3.1 Temperature data analysis

Temperature data collected from the 4 localities between 1960-2010 were individually analysed. Different statistical factors, like mean, standard deviation, skewness, and kurtosis of the annual mean temperature have been computed. Variations of maximum, minimum and mean temperatures are for the four stations are represented in table 2. Those stations are Banyo (T1), Meiganga (T2), Ngaoundere (T3) and Tibati (T4). The skewness test is positive for 80% of the time in the case of maximum temperatures, and for 56% and 64% of the time for minimum and mean temperatures, respectively. Kurtosis, a statistic parameter describing the peakedness of a symmetrical frequency distribution varied from -1.70 to -1.21 °C, from -1.62 to -0.87 °C and from -1.58 to -1.04 °C, respectively for maximum, minimum, and mean temperatures. High skewness values can indicate the existence of outliers. Like skewness, kurtosis is a statistical measure used to describe a dataset. whereas skewness measures extreme values in one versus the other tail, kurtosis measures extreme values in each tail.

Table 2 Magnitude of variation of maximum, minimum and mean temperature over the study period in the region.

| Station | Max (°C) | Min (°C) | Mean (°C) | SD (°C) |
|---------|----------|----------|-----------|---------|
| T1 | 4.7 | 2.9 | 2.5 | 1.1 |
| T2 | 3.7 | 8.5 | 2.7 | 1.5 |
| T3 | 3.6 | 3.5 | 2.6 | 0.8 |
| T4 | 3.7 | 9.6 | 2.6 | 1.2 |

3.2 Analysis of temperature anomalies

Temperature anomalies can be defined as the difference from the normal trend (Kumar et al. 2014). In the present study, these anomalies have been analysed for a better understanding of the variations in the maximum, minimum and mean temperatures for the period extending from 1960 to 2010. The positive anomaly was found for maximum, minimum and mean temperature in T1 and T4. The same trend is observed for maximum and mean temperature in T2, while the minimum temperature in this locality is almost constant. On the other hand, a downward trend is observed in for maximum and mean temperature while the minimum temperature is constant. These change trends are shown in figures 2-5. A noticeable warming trend has been observed for the maximum temperature from all stations except in T4 where on observe nevertheless a peak of 28.5 °C in 1973. The annual minimum temperature exhibits also a upward trend except in T2 and in T4 where one recorded a minimum temperature less than 15 °C. T4 is the unique locality that shows a downward trend for the mean temperature. It is very evident from the comparisons that, night temperature is increasing at a faster rate than day temperature. This would be critical for the locations equatorial region that contains large reserves of forest and watersheds (Congo, Sanaga, etc.). This may enhance the deforestation and dryness that will adversely impact freshwater availability in the region, and the greenhouse spread worldwide. The data were also used for seasonal analysis in order to observe the impact of the season on the temperature pattern. To have a quick look at the seasonal and annual warming trend, the data are presented in graphical form (Figures 2-5). This significant trend clearly shows that annual minimum, maximum and mean temperatures are increasing in the region. Evidently, the dry season has the downward trend with negative values in T2 and T4 (Figure 6).

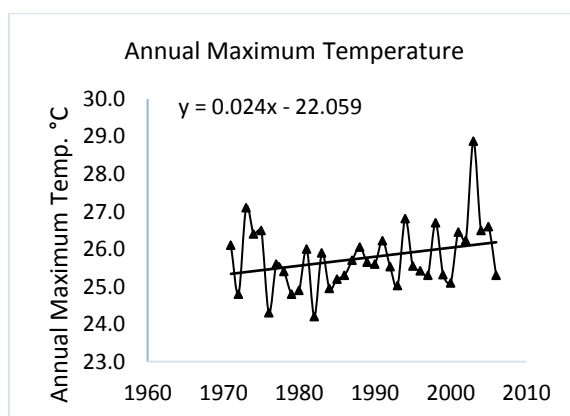


Figure 2 (a)

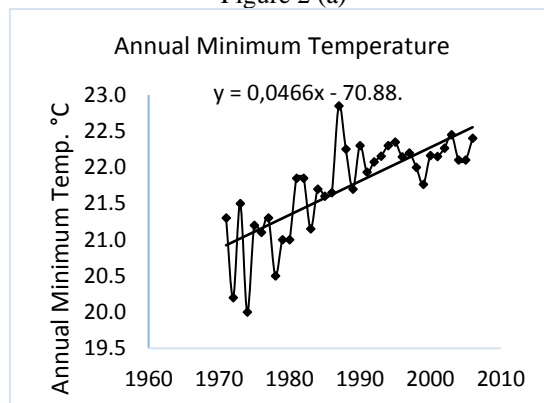


Figure 2 (b)

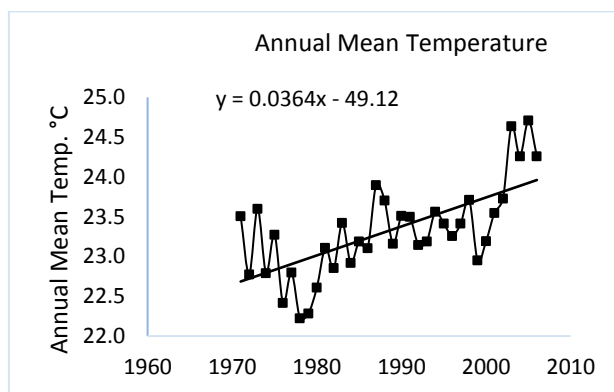


Figure 2 (c)

Figure 2 Annual temperature in T1 from 1960 to 2010 (a) max, (b) min, (c) mean.

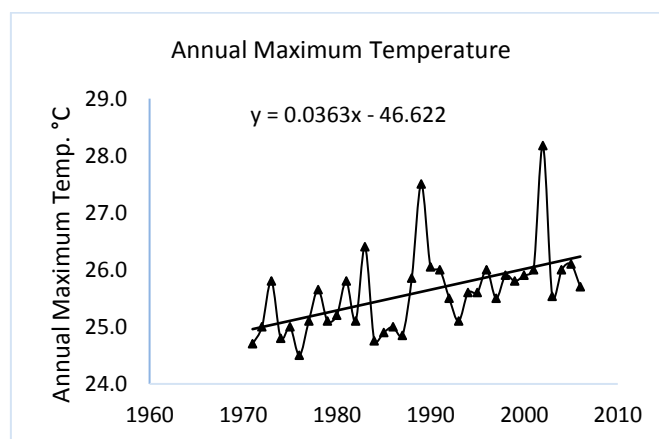


Figure 3 (a)

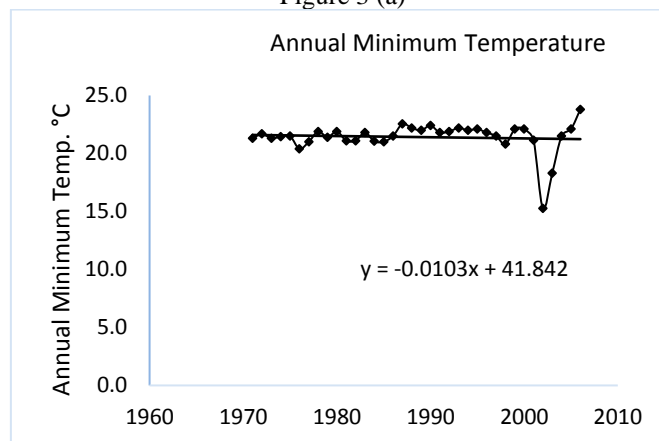


Figure 3 (b)

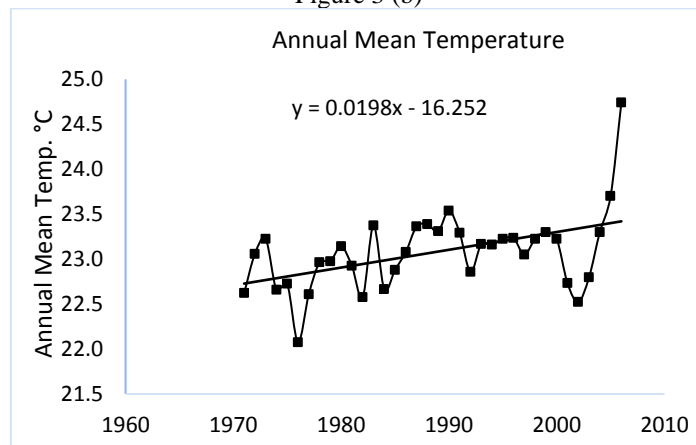


Figure 3 (c)

Figure 3 Annual temperature in T2 from 1960 to 2010 (a) max, (b) min, (c) mean.

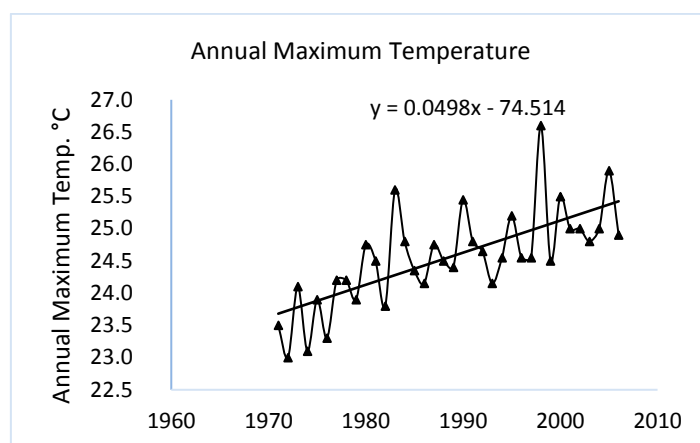


Figure 4 (a)

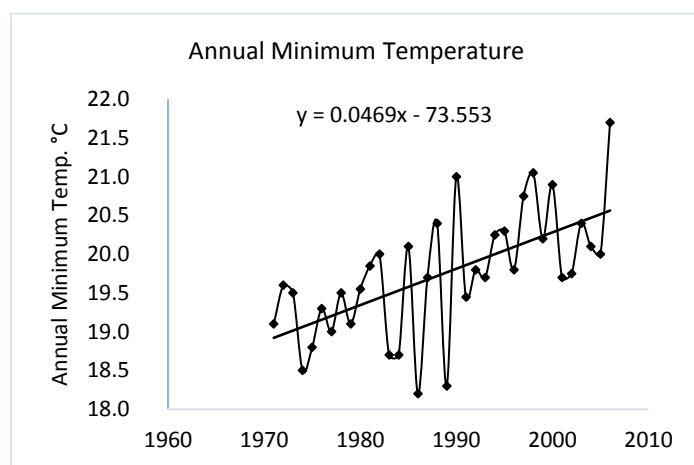


Figure 4 (b)

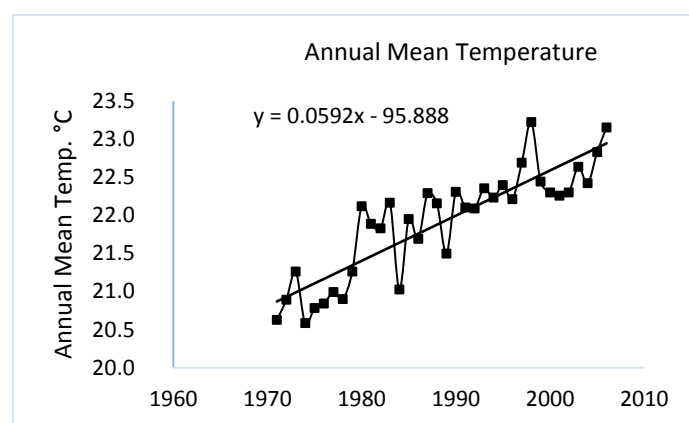


Figure 4 (c)

Figure 4 Annual temperature in T3 from 1960 to 2010 (a) max, (b) min, (c) mean.

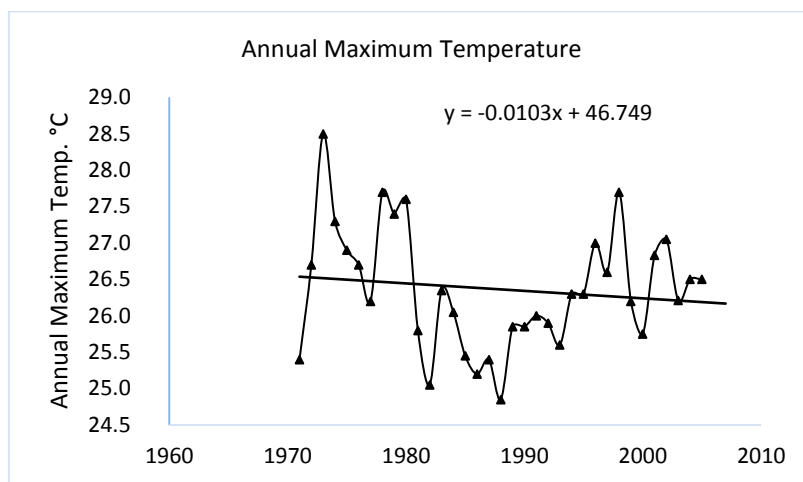


Figure 5 (a)

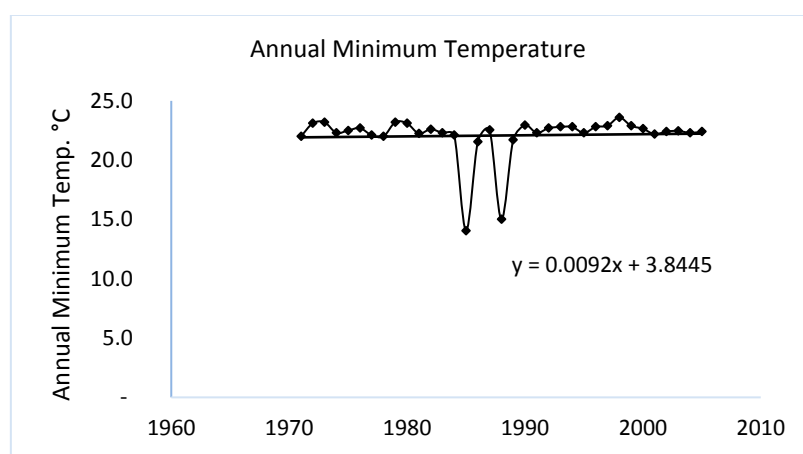


Figure 5 (b)

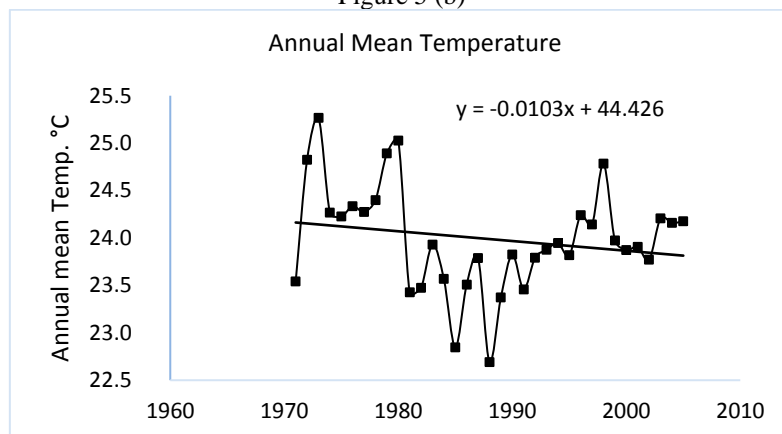
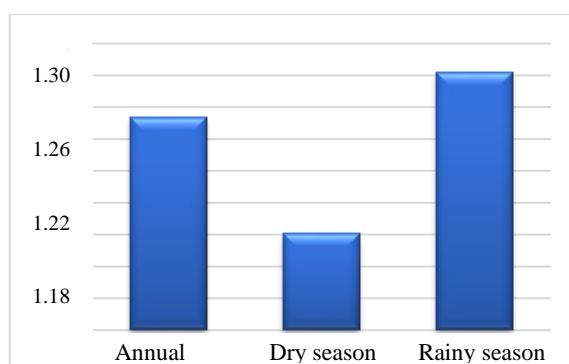


Figure 5 (c)

Figure 5 Annual temperature in T4 from 1960 to 2010 (a) max, (b) min, (c) mean.



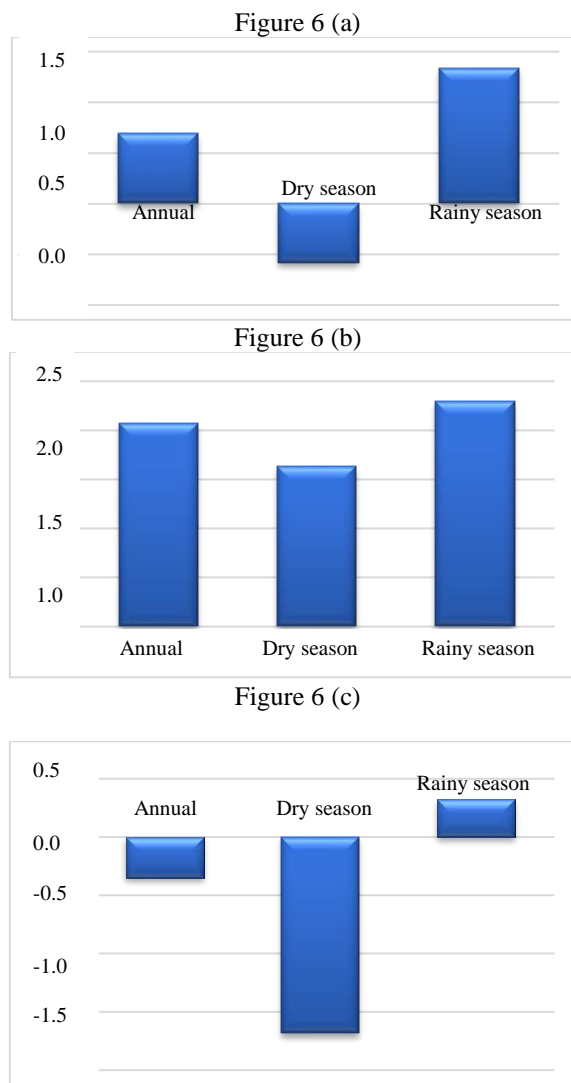
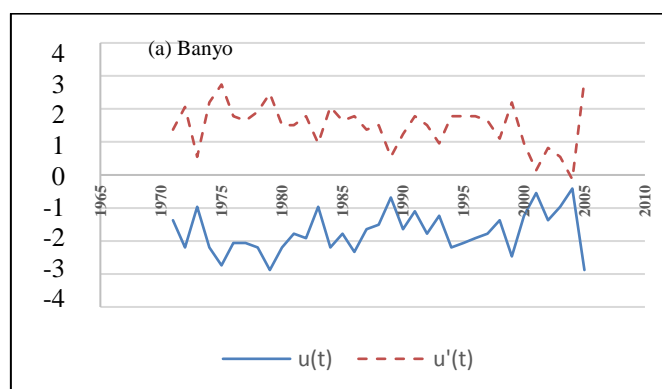


Figure 6 Annual and seasonal temperature anomaly for 1960–2010 reference period (dry season: November-Mars; rainy season: April-October) (a) T1; (b) T2; (c) T3; (d) T4.



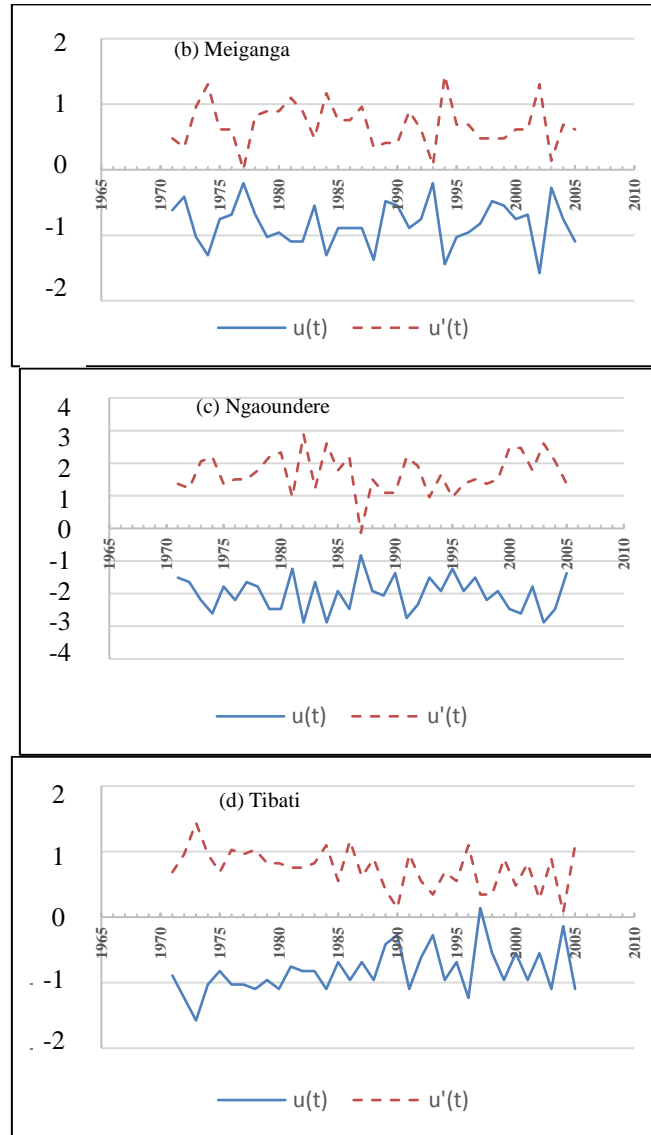


Figure 7 Progressive and retrograde sequential values of mean temperature using SQMK test statistics

3.3 Four-yearly variations of annual and seasonal temperature

To ascertain whether the warming rate was uniform for the entire period of analysis or whether there were fluctuations in the warming, the four-yearly temperature variation was analyzed on annual and seasonal bases (Table 3) and also compared with data for the entire period (1970-2010). Note that the ideal study period is 1960–2010. Unfortunately, some stations did not work properly until 1970. In T1, the variation is positive for annual and rainy season temperatures except during 1971-1980 and 1996-2000, negative for the dry season except during 1981-1985 and 2000-2010. In T2, the variation is positive for the rainy season temperature. The tendency is the same for the annual temperature except during 1971-1975 and for the dry season except during 1971-1975, 1981-1985 and 2005-2009. In T3, the variation is positive for the dry season. The tendency is the same for the annual temperature except during 1981-1985 and for the rainy season except during 1971-1975, 1981-1985 and 2005-2009. In T4, 1981-1985 and 1996-2000 exhibit negative variation for annual and rainy season temperatures while 2005-2009 shows negative variation for annual and dry season temperatures. On the whole, the anomaly for annual temperature in the region ranges from -0.43°C (in T4: 1981-1985) to 2.07°C (in T3: 2005-2009), for the dry season temperature from -1.68°C (in T4: 2005-2009) to 3.11°C (in T2: 2000-2004), and for the rainy season temperature from -0.81°C (in T4) to 2.29°C (in T3).

Table 3 Four-year variations of mean annual, dry and rainy seasons temperatures over the study area

| Interval | T1 | | | T2 | | | T3 | | | T4 | | |
|----------|-------------|----------|------------|-------------|----------|------------|-------------|----------|------------|-------------|----------|------------|
| | Annual (°C) | Dry (°C) | Rainy (°C) | Annual (°C) | Dry (°C) | Rainy (°C) | Annual (°C) | Dry (°C) | Rainy (°C) | Annual (°C) | Dry (°C) | Rainy (°C) |
| 71-75 | -0.180 | -0.130 | -0.205 | -0.077 | -0.560 | 0.175 | 0.003 | 0.110 | -0.050 | 0.323 | 0.190 | 0.390 |
| 76-80 | -0.053 | -0.050 | -0.055 | 1.000 | 0.255 | 1.372 | 1.127 | 0.730 | 1.325 | 0.800 | 0.740 | 0.830 |
| 81-85 | 0.090 | 0.095 | 0.088 | 0.000 | -0.775 | 0.388 | -0.267 | 0.095 | -0.448 | -0.427 | 0.340 | -0.810 |
| 86-90 | 0.033 | -0.140 | 0.120 | 0.345 | 0.130 | 0.452 | 0.177 | 0.755 | -0.112 | 0.084 | 0.280 | 0.010 |
| 91-95 | 0.099 | -0.196 | 0.247 | 0.067 | 0.020 | 0.090 | 0.290 | 0.165 | 0.352 | 0.348 | 0.110 | 0.482 |
| 96-00 | -0.237 | -0.178 | -0.267 | 0.093 | 0.050 | 0.115 | -0.030 | 0.070 | -0.080 | -0.363 | 0.090 | -0.590 |
| 00-04 | 0.875 | 1.318 | 0.607 | 2.010 | 3.105 | 1.515 | 0.836 | 1.813 | 0.306 | 0.370 | 1.086 | 0.012 |
| 05-09 | 1.274 | 1.201 | 1.302 | 0.693 | -0.585 | 1.341 | 2.072 | 1.628 | 2.289 | -0.350 | -1.683 | 0.312 |

3.4 Results of Mann-Kendall (MK), Spearman Rank Correlation (SRC), Sen's Slope (SS), Sequential Mann-Kendall test (SQMK) and linear regression test

MK, SRC, and SS tests have been applied from 1960 to 2010 for three categories, viz., T_{max} , T_{min} , and T_{mean} . The linear regression test was also used to evaluate the monthly, annual and seasonal long-term changes in air temperature. The linear trend fitted with the data was also tested with Student's t-test to verify the results obtained by MK and SRC tests; the results are presented in tables 4 and 5. The results of all the tests reveal the significant increasing trend of minimum, maximum and mean temperature in almost all months. In the MK test, the analysis of the maximum temperature showed a significant warming trend in all the months, except January-March and October-December in T4, from 1960 to 2010. Using the linear regression test, the highest monthly rate of change in T1 is 3.0 °C (December), 2.75 °C in T2 (April), 3.85 °C in T3 (September), and 1.00 °C in T4 (August). The rainy season exhibits an upward trend in all stations while dry season shows a slight drop in temperature change in T2 and T4. An analysis of the SRC test confirms the general upward trend observed from MK test. Results obtained from both SRC and MK tests are confirmed by Sen's Slope test as exposed in table 4. The SQMK test has been applied to annual average temperature as illustrated in Figure 7. The graphs show the trend observed in temperature variation and results of standardized test, summarized in table 5 according to the trend/no trend hypothesis (Nalley et al. 2013).

Table 4 Results of Mann-Kendall statistical tests for monthly and seasonal temperature variables over the period 1960-2010. Δ is the confidence level for the significance of the trend.

| Month | T1 | | | T2 | | | T3 | | | T4 | | |
|-------------|------|----------------------|----------|------|-----------------------|----------|------|----------------------|----------|------|-----------------------|----------|
| | Z | Linear equation | Δ | Z | Linear equation | Δ | Z | Linear equation | Δ | Z | Linear equation | Δ |
| Jan | 3.01 | $y = 0.026x - 27.5$ | 0.91 | 2.54 | $y = -0.021x + 64.3$ | 0.72 | 1.51 | $y = 0.029x - 36.4$ | 0.83 | 2.96 | $y = -0.067x + 156.8$ | 0.84 |
| Feb | 1.32 | $y = 0.003x + 18.1$ | 0.72 | 2.36 | $y = -0.008x + 40.4$ | 0.90 | 1.69 | $y = 0.028x - 33.5$ | 0.93 | 3.06 | $y = -0.050x + 125.1$ | 0.93 |
| Mar | 2.26 | $y = 0.027x - 27.9$ | 0.83 | 2.15 | $y = 0.031x - 35.5$ | 0.73 | 3.57 | $y = 0.048x - 70.5$ | 0.89 | 2.45 | $y = -0.013x + 52.5$ | 0.75 |
| Apr | 2.87 | $y = 0.03x - 34.9$ | 0.82 | 3.02 | $y = 0.056x - 85.9$ | 0.75 | 2.09 | $y = 0.068x - 111.4$ | 0.85 | 2.49 | $y = 0.013x - 0.6$ | 0.86 |
| May | 3.14 | $y = 0.023x - 22.3$ | 0.93 | 1.98 | $y = 0.029x - 34.4$ | 0.92 | 3.54 | $y = 0.062x - 100.7$ | 0.98 | 3.00 | $y = 0.007x + 11.5$ | 0.84 |
| Jun | 1.22 | $y = 0.033x - 42.9$ | 0.74 | 1.74 | $y = 0.0346x - 45.9$ | 0.81 | 3.80 | $y = 0.063x - 102.4$ | 0.74 | 2.47 | $y = 0.008x + 6.6$ | 0.82 |
| Jul | 1.98 | $y = 0.044x - 64.4$ | 0.75 | 3.45 | $y = 0.030x - 37.6$ | 0.94 | 3.59 | $y = 0.068x - 112.8$ | 0.72 | 2.40 | $y = 0.010x + 2.7$ | 0.75 |
| Aug | 2.07 | $y = 0.040x - 57.8$ | 0.82 | 2.87 | $y = 0.035x - 48.2$ | 0.86 | 2.78 | $y = 0.062x - 100.6$ | 0.85 | 3.99 | $y = 0.020x - 17.4$ | 0.94 |
| Sep | 2.56 | $y = 0.038x - 53.6$ | 0.98 | 1.79 | $y = 0.029x - 36.7$ | 0.76 | 2.16 | $y = 0.077x - 131.5$ | 0.84 | 2.64 | $y = 0.009x + 5.3$ | 0.88 |
| Oct | 1.68 | $y = 0.041x - 59.6$ | 0.96 | 2.87 | $y = 0.012x - 0.5$ | 0.92 | 2.61 | $y = 0.075x - 127.1$ | 0.75 | 2.09 | $y = -0.019x + 61.9$ | 0.92 |
| Nov | 2.22 | $y = 0.033x - 41.9$ | 0.87 | 2.04 | $y = 0.004x + 14.1$ | 0.79 | 1.98 | $y = 0.074x - 125.5$ | 0.91 | 1.33 | $y = -0.027x + 78.2$ | 0.84 |
| Dec | 2.18 | $y = 0.064x - 113.3$ | 0.84 | 2.06 | $y = -0.065x + 151.9$ | 0.85 | 1.59 | $y = 0.044x - 68.1$ | 0.94 | 1.94 | $y = -0.053x + 129.6$ | 0.76 |
| Annual | 2.78 | $y = 0.036x - 49.1$ | 0.85 | 3.05 | $y = 0.0198x - 16.3$ | 0.91 | 3.27 | $y = 0.059x - 95.9$ | 0.69 | 2.13 | $y = -0.010x + 44.4$ | 0.91 |
| Dry seas. | 3.99 | $y = 0.034x - 44.7$ | 0.92 | 3.67 | $y = -0.017x + 56.1$ | 0.82 | 3.69 | $y = 0.047x - 71.6$ | 0.91 | 2.17 | $y = -0.049x + 122.4$ | 0.75 |
| Rainy seas. | 2.36 | $y = 0.068x - 113.3$ | 0.81 | 1.87 | $y = 0.038x - 53.1$ | 0.91 | 2.37 | $y = 0.065x - 107.5$ | 0.85 | 3.06 | $y = 0.009x + 5.3$ | 0.82 |

Table 5 Results of Sen's Slope statistical tests for monthly temperature over the period 1971-2005 for each station

| Year | Station |
|------|---------|
|------|---------|

| | T1 | T2 | T3 | T4 |
|------|-----------|-----------|-----------|-----------|
| 1971 | 0.215 | 0.164 | 0.234 | 0.135 |
| 1972 | 0.300 | 0.183 | 0.176 | 0.053 |
| 1973 | 0.158 | 0.342 | 0.380 | 0.345 |
| 1974 | 0.426 | 0.235 | 0.253 | 0.363 |
| 1975 | 0.388 | 0.173 | 0.235 | 0.245 |
| 1976 | 0.214 | 0.244 | 0.293 | 0.194 |
| 1977 | 0.210 | 0.200 | 0.240 | 0.033 |
| 1978 | 0.269 | 0.165 | 0.242 | 0.247 |
| 1979 | 0.260 | 0.229 | 0.230 | 0.250 |
| 1980 | 0.257 | 0.196 | 0.375 | 0.311 |
| 1981 | 0.174 | 0.174 | 0.277 | 0.206 |
| 1982 | 0.161 | 0.273 | 0.236 | 0.145 |
| 1983 | 0.203 | 0.188 | 0.216 | 0.158 |
| 1984 | 0.252 | 0.279 | 0.263 | 0.250 |
| 1985 | 0.151 | 0.154 | 0.213 | 0.103 |
| 1986 | 0.238 | 0.272 | 0.333 | 0.230 |
| 1987 | 0.225 | 0.013 | 0.289 | 0.168 |
| 1988 | 0.238 | 0.196 | 0.245 | 0.088 |
| 1989 | 0.039 | 0.078 | 0.100 | 0.037 |
| 1990 | 0.107 | 0.116 | 0.051 | 0.058 |
| 1991 | 0.173 | 0.300 | 0.341 | 0.142 |
| 1992 | 0.156 | 0.150 | 0.231 | 0.105 |
| 1993 | 0.091 | 0.105 | 0.115 | 0.027 |
| 1994 | 0.194 | 0.141 | 0.337 | 1.370 |
| 1995 | 0.179 | 0.144 | 0.306 | 0.160 |
| 1996 | 0.166 | 0.188 | 0.306 | 0.288 |
| 1997 | 0.193 | 0.224 | 0.092 | 0.100 |
| 1998 | 0.228 | 0.235 | 0.100 | 0.164 |
| 1999 | 0.188 | 0.195 | 0.229 | 0.117 |
| 2000 | 0.090 | 0.213 | 0.185 | 0.098 |
| 2001 | 0.056 | 0.294 | 0.181 | 0.148 |
| 2002 | 0.146 | 0.201 | 0.250 | 0.147 |
| 2003 | 0.189 | 0.397 | 0.210 | 0.066 |
| 2004 | 0.214 | 0.250 | 0.046 | 0.272 |
| 2005 | 0.294 | 0.258 | 0.394 | 0.266 |

4 Discussion

Analyses from this study show that the daily maximum, minimum, average and air temperature had and increasing trend in 50 years in the Central Africa. The results obtained in this study confirm those of many other researchers worldwide. In fact, Christensen et al. (2007); Malhi and Wright (2004); Arétouyap et al. (2014) observed a decadal warming rates of 0.29 °C in Central Africa. Nevertheless, many global circulation models (GCM) addressed the issue of temperature variability in the region (IPCC 2007). More recently, Mc Sweeney et al. (2007) observed a mean temperature of 24.1 °C over the period 1970-1999 and an increasing trend of 0.15 °C per decade over the period 1960-2006. The present study conducted over the period 1960-2010 reveals an increasing rate of 1.82 °C (i.e. 0.36 °C per decade) in T1, 0.99 °C (i.e. 0.20 °C per decade) in T2, 2.96 °C (i.e. 0.59 °C per decade) in T3 and -0.52 °C (i.e. -0.10 °C per decade) in T4.

Impact of climate change in general and temperature change in particular, has been observed in the region throughout both natural and human systems. This is being modifying the environmental behavior, the agricultural practice, the economy and the human habits. Extreme hit events are more and more frequent; aridity is increasing in Chad, northern Cameroon and Central Africa Republic; sea level keeps increasing every year; undernutrition and infectious diseases are more frequent in all riparian countries (Serdeczny et al. 2016). The agricultural systems of the region, which are essentially rainfed, are particularly vulnerable to this change. The livelihoods of a large proportion of the region's population depend on such systems. As a result, the rate of rural-urban migration is increasing in main towns such as Bangui, Bongor, Brazzaville, Douala, Kinshasa, Libreville, Ndjamena, Pointe-Noire, Yaounde, etc. This movement of people into informal settlements expose

them to a variety of risks different but not different from those faced in their place of origin. Those risks include outbreaks of infectious diseases, flash flooding and food price increases.

The data collected and analyzed from each station show that, it is very important to multiply and diversify the measures in situ, helping to better define policies and strategies to better manage the impacts of climate change around the world. This work shows that, even if in general the trends are the same, there are small, highly significant details that might helped to better understand the situation in each locality given the still uncertain nature of the effects due to this change such as, floods, droughts and desertification.

5 Conclusion

A half century-long temperature records have been presented and analyzed in the Central Africa rain forest. The study demonstrates that, as in so many other regions of the world, the maximum, minimum, and mean temperatures change. The analysis indicated that there is an overall warming trend in the region. The temperature has a general upward trend over time. However, this work shows that, between two regions very close to each other, the temperature variations may have otherwise paces. This variability would produce crucial impacts on the sectors of water, agriculture, food, industry, health, diseases and deforestation since those fields are very sensitive to air temperature change. Following sectors are already experiencing those impacts: agricultural production, ocean and savanna ecosystems, coastal populations and infrastructure, human health and population movement. All those impacts have direct repercussions on the development policy and can cause various conflicts. So, further analysis is necessary to investigate factors related to the spatial and temporal temperature changes and how these changes can be effectively managing in order to protect this rain forest region. The Causes on some of these changes might be due to global climate change or more to a combination of climate and human activities.

6 References

- Aesay A. M. and H. M. Hasanean, 1998. Annual and seasonal climatic analysis of surface air temperature variations at six southern Mediterranean stations. *Theor. Appl. Climatol.* 61, 55-68.
- Aitken H., 2013. Sustainable development, climate change and challenges for India. *Int. J. Environ. Sustain.* 8 (1), 1-14.
- Alpert P., 1993. Conserving biodiversity in Cameroon. *Ambio* 20, 372-383.
- Anderson R. L., 1941. Distribution of the serial correlation coefficients. *Ann. Math. Stat.* 8 (1), 1-13.
- Arétouyap Z., P. Njandjock Nouck, D. Bisso, R. Nouayou, B. Lengué and A. LepatioTchieg, 2014. Climate variability and its possible interactions with water resources in Central Africa. *J. Appl. Sci.* 14(19), 2219–2233
- Barnett T. P., J.C. Adam and D. P. Lettenmaier, 2005. Potential impacts of a warming climate on water availability in snow dominated regions. *Nature* 438, 303-309.
- Beg N., J. C. Morlot, O. Davidson, Y. A. Okessee, L. T. Denton, Sonoka, Y. J. Thomas, P. Rovere, E. L., J. K. Parikh and K. A. Rahman, 2002. Linkages between climate change and sustainable development. *Climate Policy* 2(2-3), 129-144.
- Bhutiyan M. R., V. S. Kale and N. J. Pawar, 2007. Long-term trends in maximum, minimum and mean annual air temperatures across the northwestern Himalaya during the twentieth century. *Climate Change* 85, 159-177.
- Capparelli V., C. Franzke, A. Vecchio, M. P. Freeman, N. W. Watkins and V. Carbone, 2013. A spatiotemporal analysis of U.S. station temperature trends over the last century, *J. Geophys. Res. Atm* 118, 1–8.
- Christensen J. H., B. Machenhauer, R. G. Jones, C. Schär, P. M. Ruti, M. Castro and G. Visconti, 1997. Validation of present-day regional climate simulations over Europe: LAM simulations with observed boundary conditions. *Climate Dyn.* 13, 489–506.
- Darshana D. and A. Pandey, 2013. Statistical analysis of long term spatial and temporal trends of precipitation during 1901-2002 at Madhya Pradesh. *India. Atmos. Res.* 122, 136-149.

- Eischeid J. K., C. B. Baker, T. R. Karl and H. F. Diaz, 1995. The quality control of long-term climatological data using objective data analysis. *J. Appl. Meteorol.* 34, 2787-2795.
- Feng S., Q. Hu and W. Qian, 2004: Quality control of daily meteorological data in China, 1951-2000: a new dataset. *Int. J. Climatol.* 24, 853-870.
- Frankham R., J. D. Ballou and D. A. Briscoe, 2004: *A primer of conservation genetics*. Cambridge University Press, Cambridge, 180p.
- Gadgil A. and A. Dhorde, 2005. Temperature trends in twentieth century at Pune. India. *Atm. Environ.* 39, 6550-6556.
- Giannini A., M. Biasutti and M. M. Verstraete, 2008. A climate model-based review of drought in the Sahel: Desertification, the re-greening and climate change. *Global and Planetary Change* 64, 119-128.
- Gocic, M. and S. Trajkovic, 2013. Analysis of changes in meteorological variables using Mann-Kendall and Sens's slope estimator statistical tests in Serbia. *Global Planet. Change* 100, 172-182.
- Goossens A. H. and A. Berger, 1986. Annual and seasonal climatic variations over the northern hemisphere and Europe during the last century. *Ann. Geophysics* 4B, 385-400.
- Grant E. L. and R. S. Leavenworth, 1972. *Statistical Quality Control*. McGraw-Hill, New-York, 324p.
- Hamed K.H., 2009. Exact distribution of the Mann-Kendall trend test statistic for persistent data. *J. Hydrology* 365 (1-2), 86-94.
- Hann C.T., 2002. *Statistical Methods in Hydrology, second version*. Blackwell Publishing, Iowa State Press, Ames, 126 p.
- Hamed K. H., and A. Ramachandra Roa, 1998. A modified Mann-Kendall trend test for auto correlated data. *J. Hydrol* 30 (1-4), 182-196.
- Heino R., R. Brazdil, E. Forland, H. Tuomenvirta, H. Alexandersson, M. Beniston, C. Pfister, M. Rebetz, S. Rosenhagen and J. Wibig, 1999. Progress in the study of climatic extremes in northern and Central Europe. *Climatic Change* 42, 151-181.
- IPCC. Climate Change 2007: Synthesis Report. An Assessment of Intergovernmental Panel on Climate Change (2007) Geneva, Switzerland, <http://ipcc.ch/index.html>.
- Kadioglu M., 1997. Trends in surface air temperature data over Turkey. *Int. J. Climatol.* 17 (5), 511-520.
- Kendall M. G., 1975. Rank Correlation Methods, 4thed. Charles Griffin, London, 202 p.
- Kumar. D., E. Kodra and A. R. Ganguly, 2014. Regional and seasonal intercomparison of CMIP3 and CMIP5 climate model ensembles for temperature and precipitation. *Clim. Dyn.* 43, 2491-2518.
- Lubès-Niel H., J. M. Masson, J. E. Paturel and E. Servat, 1998. Variabilité climatique et statistique, Etude par simulation de la puissance et de la robustesse de quelques tests utilisés pour vérifier l'homogénéité de chroniques. *Rev. Sci. Eau* 3, 383-408.
- Luo Y., L. Shen, S. Fu, J. Liu, G. Wang and G. Zhou 2007. Trends of precipitation in Beigiang River Basin, Guangdong Province, China. *Hydrol. Proc.* 22 (13), 2377-2386.
- Malhi Y. and J. Wright, 2004. Spatial patterns and recent trends in the climate of tropical rainforest regions, *Philos. Trans. R. Soc. London B* 359 (1443), 311-329.
- Mann H. B., 1945. Non-parametric test against trend. *Econometrica* 13, 245-259.
- Mc Sweeney C., M. New and G. Lizanco, 2007. *Climate Change Country Profiles*. Oxford: UNDP, London, 52 p.
- Mestre O., 2002. *Méthodes statistiques pour l'homogénéisation de longues séries climatiques*. Dissertation, Université Paul-Sabatier, Toulouse, 229 p.
- Modarres R. and V. P. R. Da Silva, 2007. Rainfall trends in rid and semi-arid regions of Iran. *J. Arid Environ.* 70, 344-355.
- Modarres R. and A. Sarhadi, 2009. Rainfall trends analysis of Iran in the last half of the twentieth century. *J. Geophys. Res.* 114, D03101, <http://dx.doi.org/10.1029/2008JD010707>.
- Nalley D., J. Adamowski and B., Khalil, 2013. Trend detected in surface air temperature in Ontario and Quebec, Canada during 1967-2006 using the discrete wavelet transform. *Atm. Res.* 38, 375-398.

- Orlove B., E. Wiegandt and B. H. Luckman, 2008. *Darkening peaks, glacier retreat, science and society*. University of California Press, Berkeley, 136p.
- Peterson T. C., R. Vose and R. V. Razuvaev, 1998. Global Historical Climatology Network (GHCN) Quality Control of Monthly Temperature Data. *Int. J. Climatol.* 18, 1169-1179.
- Sayer A. J., C.S. Harcourt and N. M. Collins, 1992. *The Conservation atlas of tropical forests. Africa*. Macmillan Publishers Ltd., London, 288 p.
- Sen P. K., 1968. Estimates of the regression coefficient based on Kendall's tau. *J. Am. Stat. Assoc.* 63, 1379-1389.
- Esrdeczny O., S. Adams, F. Baarsch, D. Coumou, A. Robinson, W. Hare, M. Schaeffer, M. Perette and J. Reinhardt, 2016. Climate change impacts in Sub-Saharan Africa: from physical changes to their social repercussions. *Reg. Environ. Change*. DOI 10.1007/s10113-015-0910-2.
- Singh P. and L. Bengtsson, 2004. Hydrological sensitivity of a large Himalayan basin to climate change. *Hydrol. Proc.* 18, 2362-2385.
- Sneyers R., 1990. *On the statistical analysis of series of observations*. Tech. Note, Geneva, 192 p.
- Takahashi G., T. Suzuki and H. Kawamuru, 2011. Detection of outliers in meteorological observation data. *J. Quality* 18 (5), 393-405.
- Tayanc M. and H. Toros, 1997. Urbanization effects on regional climate change in the case of four large cities of Turkey. *Climatic Change* 35(4), 501-524.
- Wallis R. and P. E. O'Connell, 1972. Small sample estimation of ρ_1 . *Water Resour. Res.* 8 (3), 707-712.
- Wang L., Z. Li, F. Wang, H. Li and P. Wang, 2014. Glacier changes from 1964 to 2004 in the jingle river basin, Tianshan. *Cold Regions Sci. Technol.* 102, 78-83.
- Xu, F. and A. Ignatov, 2014. In situ SST Quality Monitor (iQuam). *J. Atm, Oceanic Technol.* 31, 167-180.
- Yue S., P. Pilon, B. Phinney and G. Cavadias, 2002. The influence of autocorrelation on the ability to detect trend in hydrological series. *Hydrol. Proc.* 16, 1807-1829.
- Zhao G., X. Mu, P. Tian, F. Wang and P. Gao 2013. Climate changes and their impacts on water resources in semiarid regions: a case study of the Wei River basin, China. *Hydrol. Process* 27, 3852-3863
- www.enchantedlearning.com (2015)

20- Inverse slope method for interpreting vertical electrical soundings and characterizing hydraulic and environmental properties of the Adamawa aquifer

J. Asfahani¹, Z. Arétouyap^{†2}, D. Bisso, P². Njandjock Nouck²

¹Geology Department, Atomic Energy Commission, P.O. Box 6091, Damascus, Syria

²University of Yaounde I, Yaounde, Cameroon

[†]E-mail: aretouyap@gmail.com

Abstract

Fifty vertical electrical soundings (VES) carried out in the Adamawa (Central Africa region) have been reinterpreted using the inverse slope method (ISM). This aimed at proving the applicability and the suitability of the ISM technique to interpret VES points for groundwater and hydrogeophysical purpose, and especially in the Pan-African context. The ISM used with the curve matching method (CMM) can overcome both the several limitations of the latter and the complexity of lithological sections in terms of strata numbers, thickness and resistivity. The ISM technique is simpler than CMM, and has numerous qualitative and quantitative advantages. It allows in so far to distinguish all geologic layers even thinner ones and can be used to interpret VES data collected with any electrodes array. More accuracy has been obtained in this research paper by using ISM technique, which helps in reducing water stress people from central Africa are experiencing, and in enhancing environmental management through the world. The results obtained by the ISM geoelectrical interpretation correlate well, and are in good agreements with the available lithological description logs. Resistivity, thickness and depth of the Pan-African aquifer in the Adamawa region, Central Africa have been well determined by applying the ISM method. The ISM can be therefore recommended for interpreting VES measurements in the similar Pan-African context worldwide.

Keywords: Central Africa, CMM, groundwater, ISM, Pan-African, VES

Introduction

Geoelectrical DC methods stand out in the domain of groundwater prospection, thanks to their accuracy and high efficiency in comparison with traditional methods of pumping test. Several quantitative techniques have been already proposed and discussed for interpreting DC earth-resistivity measurements. Ghosh (1971) determined inverse filter coefficients for the computation of apparent resistivity standard curves for a horizontally stratified earth. Zohdy (1985) modified Dar-Zarrouk functions for automatic interpretation of Schlumberger VES sounding curves, and improved later this technique by adding Wenner sounding curves. Koefoed (1976) presented progressive developments in the direct interpretation of the resistivity sounding. However, it is important to assess limitations regarding suitability and assets (accuracy) in relation to different subsurface conditions of each technique, for each one is based on a separate approach and methodology (Asfahani 2016). Geoelectrical DC methods have been already used to investigate groundwater in the Pan-African context of Central Africa region (Arétouyap et al. 2015). Fifty Schlumberger VESs were carried out in the Adamawa region and interpreted using a conventional curve matching method (CMM approach). It was found that the resolution of this CMM is so poor, such as thin layers buried at important depth are simply indistinguishable on the logarithmic plot. This CMM limitations encourage us to reinterpret the VESs data using the ISM approach, previously developed by Sanker Narayan and Ramanujachary (1967). ISM has been recently applied by Mohamed et al. (2014). Asfahani (2016) applied successfully ISM in exploration geophysics for characterizing phosphatic layers in Al-Sharquieh mine in Syria. This technique is simpler than CMM, and has numerous qualitative and quantitative advantages. It allows in so far to distinguish all geologic layers even thinner ones, and can be used to interpret VES data collected with any electrodes array (Mohamed et al. 2014). The ISM technique is used herein to reinterpret VES data already investigated by Arétouyap et al. (2015) for groundwater and hydrogeology purpose. The main objective of the present paper is therefore to use ISM to achieve the following points:

- Test the suitability and the applicability of the ISM in the context of Pan-African;

- Overcome major interpretation difficulties (as the eclipse of thinner layers and the sensibility to electrodes array used for VES data collection), associated with traditional curve matching methods;
- Compare results obtained from both ISM and CMM methods;
- Use the geoelectrical results of ISM for hydrogeophysical and aquifer characterization in the Pan-African context of Central Africa.

2 Geomorphology and hydrogeology of the Adamawa plateau

This research is conducted in the Adamawa-Cameroon region, located in the heart of Central Africa between 6°-8° north and 11°-16° east (Fig. 1). The study region extends over a length of about 410 km from west to east between the Federal Republic of Nigeria and the Central African Republic, with an area of 6782 km². The morphology of the region is of volcanic highlands, resulting from tectonic uplift and subsidence accompanied by intense magmatic emissions (Toteu et al. 2000). Although the average altitude is 1100 m, this region of a rugged terrain is limited at the North by a large cliff and an uneven escarpment of several hundred meters that dominates the area.

The center of the plateau is marked by soft forms barely accented and swampy valleys, dotted with mountains or/ and volcanic cones. At the East, there are massifs resulting from the former erosion and tectonic movements. In the West, the terrain is mountainous with hills. Volcanic inheritance covers the North, the East and the South areas. One notes the presence of an assembly line which occupies an important part of the region, reaching altitudes more than 2240 m. There are also plains and basins (Toteu et al. 2000).

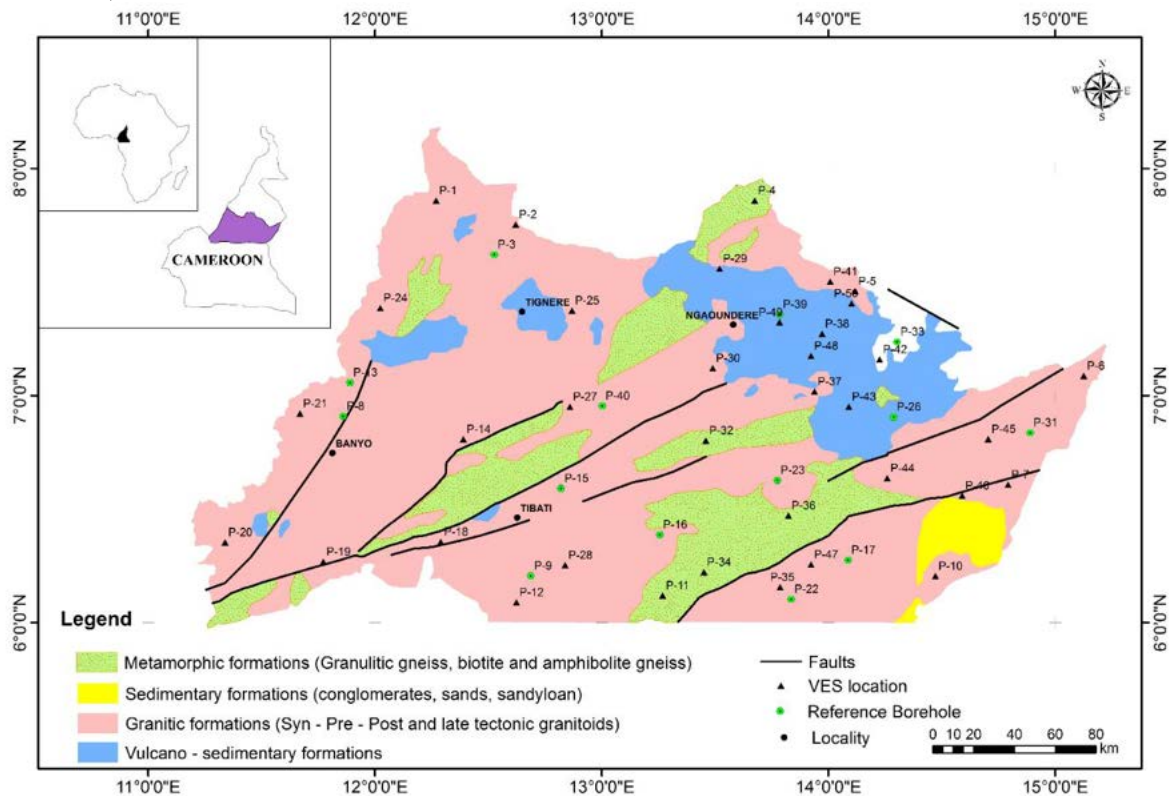


Fig. 1 Geological map of the study area, with the locations of VES measurements (Maréchal 1976) as amended

The geological history of the Adamawa-Cameroon region is marked by three major events (Toteu et al. 2000):

- A long period of continental erosion from Precambrian to Cretaceous;
- The onset of volcanism from Cretaceous to Quaternary;
- And recurrent basement tectonics that explains the horst and graben structure of the Adamawa Plateau.

An investigation of superficial formations in the region has highlighted the Pan-African granite-gneiss bedrock, represented by Ordovician granites, gneisses and Pan-African migmatites. Main geological formations encountered are basalts, trachytes and trachyphonolites based mostly on concordant calc-alkaline granites and discordant alkaline granites (Toteu et al. 2000).

Three main geological units are observed on the surface. Each type of those geological units contains some VES locations. The largest formation, made up of granite contains the majority of VES points. Metamorphic formations contain some pits such as P-11, P-34, P-36, etc. Pits P-28, P-29, etc. are located in volcano-sedimentary units.

In hydrological terms, 150 to 300 km wide, the Adamawa plateau is called “the water tower of the region” because it feeds three of the four major watersheds of the region, namely, the Lake Chad basin, the Niger basin in the North and the Sanaga Atlantic basin in the South. Indeed, many rivers such as Mayo Deo, Mayo Banyo, Mbere, Vina (tributaries of the Logone), Mbam, Kim, Djerem and Lom (tributaries of the Sanaga) divert from this region. There are also many crater lakes including Tyson, Mbalang and Vina lakes resulting from a long volcanic history in the region (Ngako et al. 2008). In addition to the existence of many lineaments in the region, this important hydrosphere may forecast the existence of aquifers located at interesting depth with significant thickness.

Geophysical survey reveals that the Pan-African belt was tectonically active and occurs many lineaments and faults (Cornacchia and Dars 1983; Dumont 1986; Robain et al. 1996; Toteu et al. 2004; Ngako et al. 2008; Njonfang et al. 2008). We assume that those lineaments constitute “high way” for groundwater. Although the groundwater productivity is directly linked to the bedrock alteration, there is no recent study aimed at locating and characterizing local aquifers. This situation justifies the interest of the present paper.

3 Methodology

3.1 VES data recording and interpretation

Schlumberger configuration is used to locate and characterize the aquifers in the study region. Electrical resistivity variations are expressed in this array as a function of depth. Fifty VES have been carried out in the study area, using the Terrameter ABEM SAS-1000 with a spacing of current electrodes varying from 1 to 600 m. This device directly measures the resistance, which enables us to calculate the apparent resistivity of the rock using the Ohm's law expressed by Eq. 1, and taking into account the geometrical factor k of the used array expressed in Eq. 2. The principle of the VES method is illustrated by Fig. 2.

$$\rho_a = k \frac{U_{MN}}{I} . \quad (1)$$

$$\text{Where} \quad k = \frac{2\pi}{\left(\frac{1}{AM} - \frac{1}{BM} - \frac{1}{AN} + \frac{1}{BN} \right)} . \quad (2)$$

I is the intensity of the electrical current injected in the ground by electrodes A and B, and U_{MN} is the voltage potential between electrodes M and N.

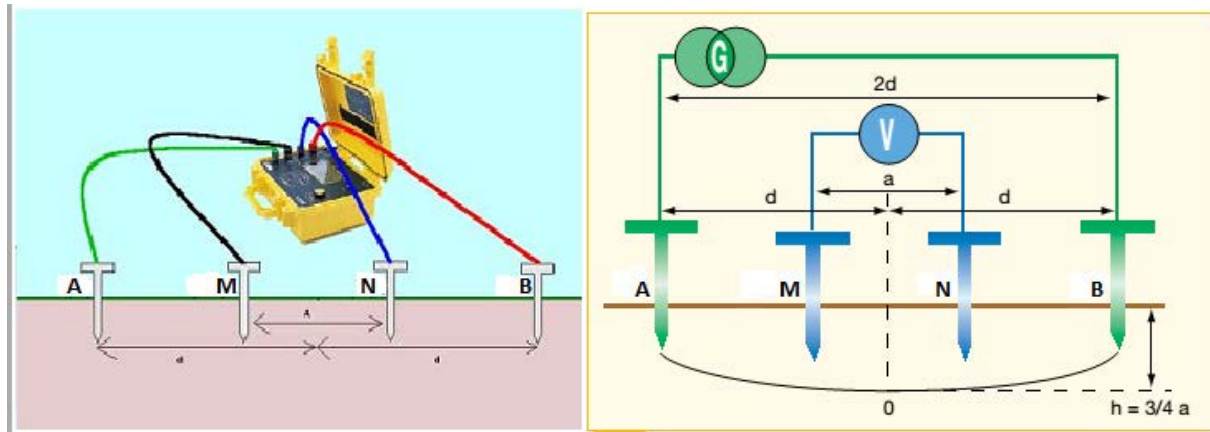


Fig. 2 Schlumberger configuration used for recording VES data

The values of the apparent resistivity ρ_a depend on several factors such as true layers resistivities and thicknesses, and electrodes location. The accuracy in their determination depends on the homogeneity of the substratum. For a heterogeneous medium, CMM interpretation does not provide enough accurate results.

However, some ambiguity problems can arise during the interpretation. A sample interpretation exercise must be carried out before each project in order to solve such encountered problems. If those ambiguity problems are too complex, further methods such as seismic and test wells are required (Asfahani 2007). Sometimes, the use of an alternative independent method is indispensable (Asfahani 2013).

The results of the CMM is used in the present paper for comparison with those of ISM. For CMM technique, an inverse technique programme fit thereafter both theoretical and field curves for each experimental VES (Zohdy 1985; Zohdy and Bisdorf 1989). This operation requires the double condition of accuracy in calculations and reasonable geological modelling. Furthermore, we assume that the medium is a one-dimensional model 1D (Dey and Morrison 1979). The 1D quantitative interpretation of the fifty VES by using CMM enabled identification of hydrogeoelectrical characteristics of the Pan-African deposits (Arétouyap et al. 2015).

3.2 Inverse Slope Method

ISM can be used to obtain directly the resistivities and the thicknesses of subsurface layers from field data (Sanker Narayan and Ramanujachary 1967). Asfahani (2016) from which the current Subsection has been extracted, methodically explained all the steps of the ISM approach. The inverse resistivity $(AB/2)/\rho_a$ was plotted against the electrode separation $(AB/2)$. Each line segment resulting from this graph represents a layer; and the intersection of the line segments, multiplied by a factor of 2/3, corresponds to the depth of a particular layer. Concretely, let $t_1 \dots t_n$ be intersection points, then $2/3 \times t_i$ is equal to the depth of the i^{th} interface.

Similarly, when $(AB/2)/\rho_a$ is plotted versus $AB/2$, the equation $\Delta x_i / \Delta y_i$ gives the resistivity of the i^{th} layer except when the segment representing the high-resistivity layer shows a negative slope. In this case, the resistivity of the layer is taken as infinity (Asfahani 2016). The application of ISM enables to decipher thin layers even if they are buried at great depths.

When applied in the context of groundwater determination, a geological layer is said to be aquifer when it meets the following conditions: it is thick enough with a resistivity quantitatively similar to that of other surrounding aquifers, and tucked between two other geological layers of higher resistivities. The aquifer depth results from summing depths of all geological layers above the aquifer.

3.3 Interpolation method

Aquifer's parameters we investigated in this paper have been measured or computed punctually (especially on VES sites). Yet, an efficient and sustainable management of groundwater resources requires an accurate and continuous determination of hydrodynamic parameters. Geostatistics has been used to assess and interpolate aquifer resistivity, depth and thickness. This technique applied herein is essentially based on the notions of semivariogram and kriging (Arétouyap et al. 2016).

3.3.1 Semiariogram

Caridad and Jury (2013) designated the variogram as a geostatistical tool used to describe the spatial continuity of a phenomenon (De Carvalho et al. 2013). Its theoretical formulation is given in Eq. 3.

$$\gamma(r) = \frac{1}{2} \text{var}[h(x) - h(x+r)]. \quad (3)$$

In this equation, *Var* is the variance applied to the difference between two observations $h(x)$ and $h(x+r)$ separated by a distance r .

3.3.2 Kriging

Kriging is very indicated for interpolating and predicting spatial data, considered as a set of some observable variables. Those observations may be spatially correlated. If applied adequately, kriging provides expected value and variance for every point within a region. Hence, this approach can be used to estimate the unknown value h^* (Eq. 4) of a variable at a point from the surrounding known values h_i , with a unique solution.

$$h^* = \sum_{i=1}^n (\lambda_i h_i). \quad (4)$$

In this relation, λ_i represent the kriging weights.

Equation 5 expresses the minimum estimation variance of the system (kriging variance).

$$\sigma_k^2 = \text{var}[h] - \sum_{i=1}^n \lambda_i \text{cov}[h, h_i] - \mu. \quad (5)$$

Determination of kriging weights, which are needed to estimate a point defined by the linear estimator is exposed in Arétouyap et al. (2014).

This approach is very important in the context of developing countries where data collected are generally sparse and irregular. We observed the three following steps to asses efficiently investigated parameters: exploratory data analysis, structural data analysis and prediction (interpolation).

3.3.3 Exploratory data analysis

Data consistency has been checked, outliers (strange values which are very high or very low compared to the dataset) removed and statistical distribution identified. Indeed, an optimal application of Kriging techniques requires normal data distribution. For this, the mean and the median values of the parameters to be estimated should be are very similar.

3.3.4 Structural data analysis

Kriging uses a scattered set of points with z -values to generate an estimated surface. The regionalized variable is the main theory used by this technique. The theory assumes a well statistically homogeneity throughout the surface of the spatial variation in the phenomenon represented by the z -values (Chilès and Delfiner 1999). The spatial variation is quantified by the semivariogram. The sample semivariogram is calculated from the sample data (Eq. 6).

$$\gamma(h) = \frac{1}{2} E[z(x) - z(x+h)]^2. \quad (6)$$

For discrete variables, this function can be written as shown in Eq. 7.

$$\gamma(h) = \frac{1}{2N(h)} \sum_{i=1}^{N(h)} [z(x_i) - z(x_i+h)]^2. \quad (7)$$

Where $z(x_i)$ is the value of the variable Z at location x_i , h the lag, and $N(h)$ the number of pairs of Vertical electrical sounding locations (VES) separated by h .

3.3.5 Prediction

The best semivariogram model (on the basis of cross validation) is selected to interpolate each parameter. Hence, various types of error were computed and compared. Those are mean error (ME), mean square error (MSE), root mean square error (RMSE), average standard error (ASE) and root mean square standardized error (RMSSE). $ME \approx 0$ when predictions are unbiased. Unfortunately, this ME strongly depends upon the scale of the data, and usually is indifferent to the wrongness of semivariogram. Because of this weaknesses, ME is generally standardized by the MSE, being ideally equal to zero.

Yet, a strong similarity between the root mean square error and the average standard error ($RMSE \approx ASE$) indicates a good assessment of prediction. Else, when $RMSE < ASE$ (or $RMSSE < 1$), the variability of predictions is overestimated; and if the $RMSE > ASE$ (or $RMSSE > 1$), then the variability of predictions is underestimated. The thematic map of each parameter to be estimated has been drawn using the best semivariogram model. Those errors are expressed by Eq. 8 to Eq. 12 below (Goovaerts 1997; Gorai and Kumar 2013).

$$ME = \frac{1}{N} \sum_{i=1}^N [Z^*(x_i) - Z(x_i)] \quad (8)$$

$$MSE = \frac{1}{N} \sum_{i=1}^N \left[\frac{Z^*(x_i) - Z(x_i)}{\sigma^2(x_i)} \right]^2 \quad (9)$$

$$RMSE = \sqrt{\frac{1}{N} \sum_{i=1}^N [Z^*(x_i) - Z(x_i)]^2} \quad (10)$$

$$ASE = \sqrt{\frac{1}{N} \sum_{i=1}^N \sigma^2(x_i)} \quad (11)$$

$$RMSSE = \sqrt{\frac{1}{N} \sum_{i=1}^N \left[\frac{Z^*(x_i) - Z(x_i)}{\sigma^2(x_i)} \right]^2} \quad (12)$$

Where $\sigma^2(x_i)$ is the Kriging variance, $Z^*(x_i)$ and $Z(x_i)$ are the estimated and the measured values of the geophysical parameter at the location x_i respectively.

4 Results and discussion

The fifty VES measurements have been interpreted by using ISM to firstly identify qualitatively different geoelectrical layers, and to secondly obtain quantitatively resistivities and thicknesses of those respective layers. Fig. 3 compares the results obtained by both ISM and CMM with the available field lithological descriptions for the VES (P-8, P-9, P-14, P-17, P-22, P-23, P-26, P-31, P-13, P-39, P-40). CMM and ISM provide for example for VES (P-17) the same results in terms of quantity (number of layers and their respective thicknesses), which are well fitted with the lithological field description. However, some significant differences are noticed between ISM and CMM results for VES (P-9, P-13 and P-14), for which one can for example observe that CMM interpretation doesn't display the clay layer. CMM interpretation gives in the other side the same results as the available field drilling descriptions for the VES (P-23, P-39 and P-40). Overall, ISM results are the ones which produce the results that are closest to geological reality as it is shown in Fig. 3. The geoelectrical ISM results are in good agreement with the available lithological descriptions for the studied VES in the region.

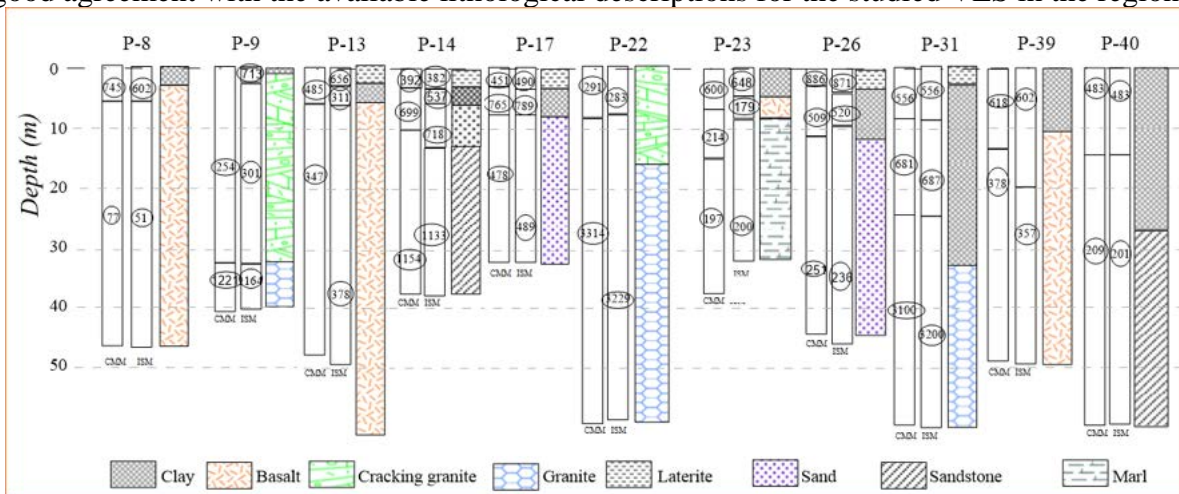


Fig. 3 Comparative results obtained respectively from left to right from CMM, ISM and lithological descriptions of some available pits

ISM provides better resolution than CMM. It allows to distinguish thinner and deeper layers. The above table 1 in which both interpretations are displayed reveals the improvement brought out by the ISM. Its suitable application to interpret VES data highlights several advantages over the CMM. This method allows to directly solve the field equation to obtain the resistivities and thicknesses of subsurface layers

from field data. The geo-electrical ISM results and the lithological logs of pits P-8, P-9, P-13, P-14 and P-23 are in good agreement as presented in Fig. 3.

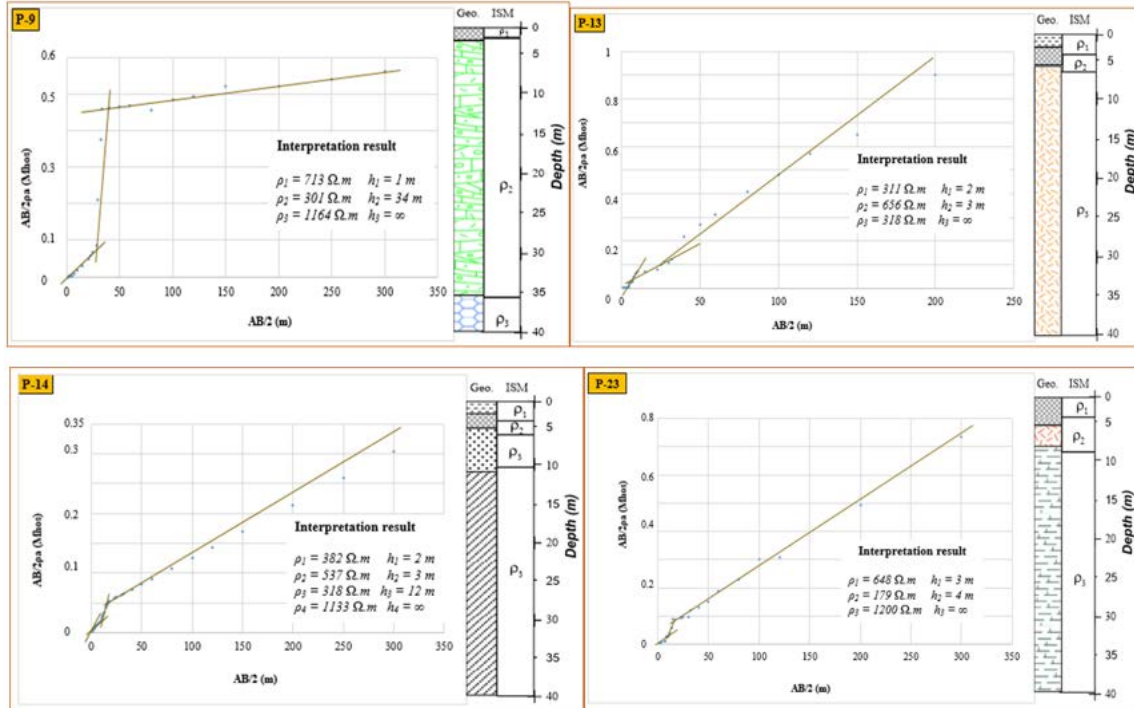


Fig. 4 Interpretation result of some pits (P-9, P-13, P-14 and P-23) using ISM

Fig. 4 is extracted from Fig. 3 to illustrate clearly the pits interpretation using inverse slope method. The interpretation of VESs P-9, P-13, P-14 and P-23 with ISM shows a good agreement with the available lithological description of those pits.

The interpretation of VES P-7 by ISM highlights the presence of three layers arranged downward as follows: laterite with a resistivity of 444 $\Omega.m$ and a thickness of 14 m, clay with a resistivity of 137 $\Omega.m$ and a thickness of 58 m and granite with a resistivity of 2500 $\Omega.m$ and an infinite depth as illustrated in Fig. 5.

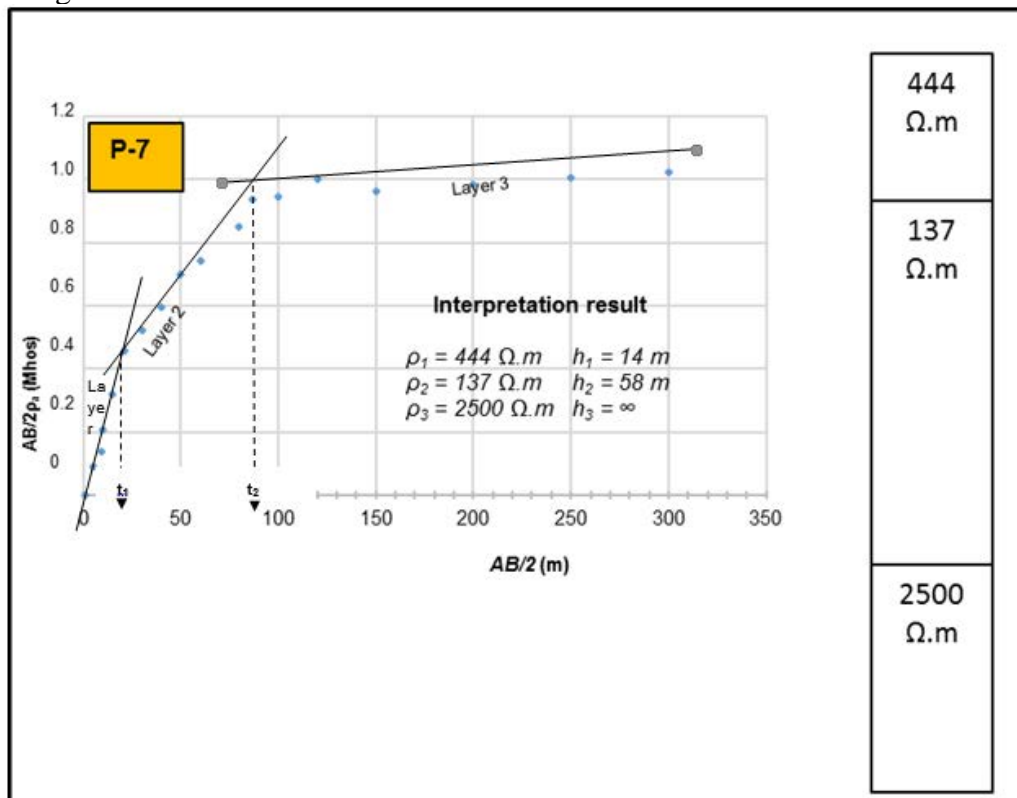


Fig. 5 Interpretation of P-7 using ISM

These ISM results are compared with the true lithological description. One can observe that both the ISM results and lithological logs have exactly the same number of layers with respective thicknesses slightly different.

It is observed for all the interpreted pits that the last segment is characterized by a very low slope, equivalent to a very high resistivity ($> 2500 \Omega.m$). This high-resistive layer corresponds to the bedrock, made of granite. It is also observed some differences in terms of layers' number and resistivities, thicknesses and depths between the ISM results and those obtained using CMM (Arétouyap et al. 2015). Table 1 compares the Pan-African aquifer characteristics obtained from both methods.

Table 1 Comparison of the Pan-African aquifer resistivity, thickness and depth obtained using CMM and ISM

| Stn. N° | CMM results | | | ISM results | | |
|---------|----------------------------|---------------|-----------|----------------------------|---------------|-----------|
| | Resistivity ($\Omega.m$) | Thickness (m) | Depth (m) | Resistivity ($\Omega.m$) | Thickness (m) | Depth (m) |
| P-1 | 565 | 40 | 18.4 | 320 | 42.1 | 21 |
| P-2 | 200 | 38 | 23 | 190 | 35 | 22 |
| P-3 | 157 | 6 | 10.7 | 210 | 8.4 | 14.5 |
| P-4 | 410 | 40 | 40.2 | 350 | 37 | 43 |
| P-5 | 640 | 30 | 44 | 751 | 39.5 | 37.4 |
| P-6 | 100 | 22 | 41.2 | 197 | 15 | 36 |
| P-7 | 114.1 | 19 | 36.5 | 137 | 58 | 14 |
| P-8 | 53 | 62 | 22.1 | 47 | 47.2 | 26 |
| P-9 | 341 | 23 | 22 | 289 | 31.6 | 21.8 |
| P-10 | 408 | 31 | 31 | 420 | 42 | 20 |
| P-11 | 446 | 43 | 17.4 | 387 | 30 | 20 |
| P-12 | 110.8 | 38 | 18.1 | 122 | 35.4 | 22 |
| P-13 | 472 | 2 | 16.0 | 382 | 4.2 | 16.6 |
| P-14 | 362.1 | 47 | 24.8 | 263 | 31.7 | 29 |
| P-15 | 61 | 93 | 29 | 11 | 15 | 6 |
| P-16 | 392.6 | 70 | 19.1 | 408 | 86 | 18 |
| P-17 | 387 | 14 | 22 | 524 | 19.8 | 24.5 |
| P-18 | 137 | 1 | 43.7 | 241 | 2 | 40 |
| P-19 | 13 | 6 | 39.4 | 25 | 11.2 | 40 |
| P-20 | 112.9 | 17 | 22 | 203 | 12.8 | 26 |
| P-21 | 4 | 21 | 69 | 11 | 32.1 | 79 |
| P-22 | 134 | 43 | 50.2 | 98 | 51.4 | 39.7 |
| P-23 | 207 | 19 | 24.1 | 196 | 33 | 30 |
| P-24 | 20 | 7 | 11 | 22 | 12 | 10 |
| P-25 | 8 | 8 | 10.8 | 16 | 9 | 13.5 |
| P-26 | 212 | 52 | 20 | 259 | 50 | 22 |
| P-27 | 422 | 28 | 9.8 | 602 | 19.2 | 14 |
| P-28 | 25 | 33 | 20.1 | 38 | 25 | 23 |
| P-29 | 47 | 85 | 14.7 | 69 | 77 | 17 |
| P-30 | 811 | 25 | 42 | 726 | 31 | 39 |
| P-31 | 502 | 6 | 39 | 717 | 10 | 41 |
| P-32 | 221.5 | 19 | 25.7 | 150 | 12 | 27 |
| P-33 | 270.4 | 32 | 32.8 | 302 | 37 | 37.45 |
| P-34 | 825 | 38 | 51.1 | 900 | 32 | 48 |
| P-35 | 10 | 11 | 41 | 14 | 17 | 43.45 |
| P-36 | 479 | 42 | 24 | 611 | 34 | 29.75 |
| P-37 | 3 | 8 | 29.4 | 20 | 12 | 24 |
| P-38 | 216.1 | 15 | 29.4 | 198 | 21 | 32 |

| | | | | | | |
|------|-------|-----|------|-----|----|-------|
| P-39 | 40 | 60 | 33 | 69 | 58 | 38 |
| P-40 | 28 | 27 | 30 | 56 | 24 | 22.9 |
| P-41 | 26 | 34 | 31 | 31 | 32 | 28.25 |
| P-42 | 46 | 46 | 35.8 | 30 | 17 | 16 |
| P-43 | 177 | 48 | 30.4 | 168 | 29 | 28 |
| P-44 | 22 | 37 | 33 | 41 | 25 | 30 |
| P-45 | 188 | 61 | 21 | 200 | 51 | 25 |
| P-46 | 608 | 20 | 35 | 618 | 26 | 37 |
| P-47 | 48 | 59 | 50.1 | 50 | 61 | 42.9 |
| P-48 | 175.7 | 48 | 27.9 | 187 | 50 | 32.5 |
| P-49 | 62 | 101 | 18.5 | 100 | 90 | 21.45 |
| P-50 | 104 | 33 | 5.1 | 47 | 85 | 17 |

The qualitative interpretation of P-15 reveals three main layers: clay, cracking granite and granite arranged downward. The quantitative interpretation allows to obtain their respective resistivities as 502 $\Omega.m$, 11 $\Omega.m$ and 2531 $\Omega.m$, and their respective thicknesses as 6 m, 15 m and infinite.

The clay resistivity for this pit VES P-15 is very high, and may be higher for the following pits. These high values are due to the non-pure character of the clay. In fact, this is a mixture of clay and laterite (Koita et al. 2013). The VES P-42 exhibits four layers with the clay (748 $\Omega.m$, 16 m) at the top and the granitic bedrock (5217 $\Omega.m$) at the bottom. Intermediary layers are basalt (104 $\Omega.m$, 33 m) and ferruginous clay (3 $\Omega.m$, 17 m). The geoelectrical interpretation of this VES according to the ISM method is shown in Fig. 6.

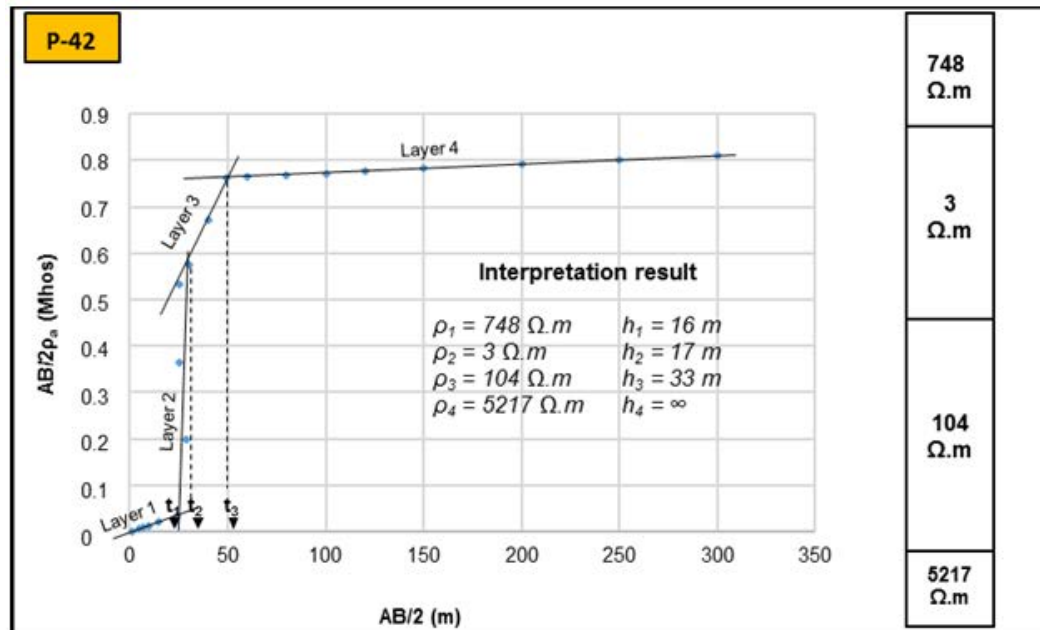


Fig. 6. Interpretation of P-42 using ISM

VES P-50 pit is another 3-layer one, with a more resistive clayey layer at the top, with a thickness of 17 m and a resistivity of 989 $\Omega.m$. The second layer is sandstone with a resistivity equal to 47 $\Omega.m$ and a thickness equal to 85 m. An infinitely thick and highly resistive granitic layer constitutes the third basement layer as shown in Fig. 7.

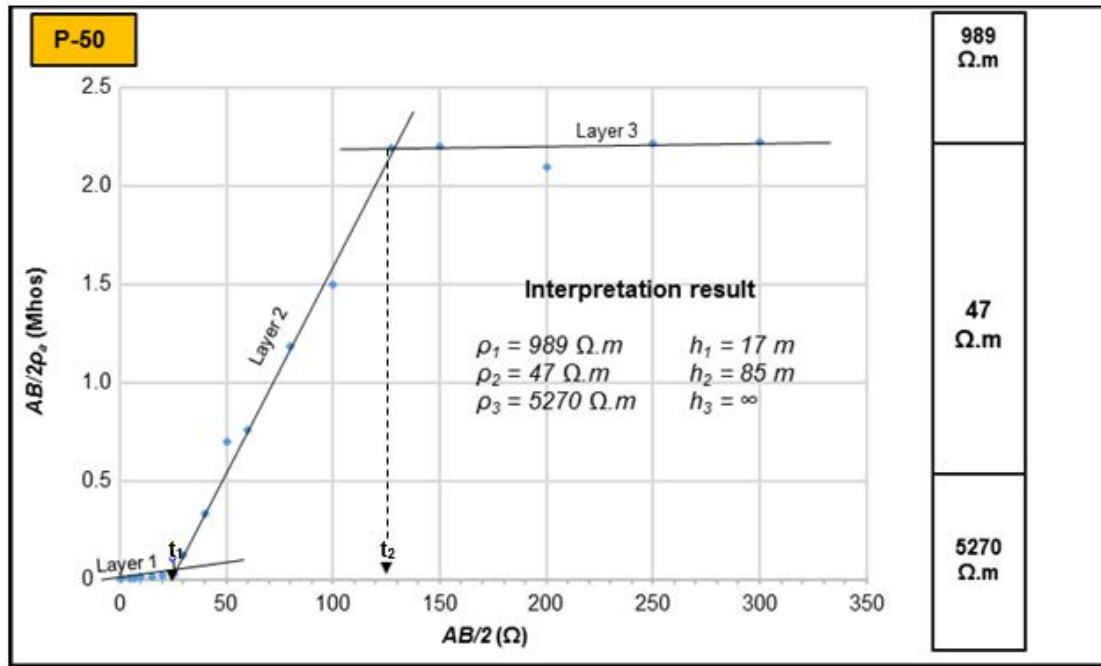


Fig. 7 Interpretation of P-50 using ISM

All of the fifty pits have been interpreted similarly by using ISM, where the local Pan-African aquifer made up of the upper weathering portion of the granitic basement has been characterized as shown in this Table 2.

Table 2 Summary of the Pan-African aquifer characteristics derived from ISM in Adamawa, Central Africa

| | Metamorphic rocks | | | | Granitic rocks | | | | Sedimentary rocks | | | | General | | | |
|----------------------------|-------------------|-----|-------|----|----------------|-----|------|----|-------------------|-----|------|----|---------|-----|------|----|
| | Min | Max | Mean | SD | Min | Max | Mean | SD | Min | Max | Mean | SD | Min | Max | Mean | SD |
| Resistivity ($\Omega.m$) | 35 | 90 | 562 | 21 | 20 | 25 | 124 | 8 | 11 | 75 | 231 | 22 | 20 | 900 | 241 | 22 |
| Thickness (m) | 0 | 0 | | 9 | 9 | | | 1 | 1 | | | 2 | 2 | 90 | 33 | 21 |
| Depth (m) | 30 | 37 | 33,25 | 3 | 12 | 85 | 43 | 24 | 2 | 90 | 32 | 23 | 2 | 90 | 33 | 21 |
| | 20 | 43 | 37 | 12 | 16 | 38 | 25 | 7 | 6 | 79 | 28 | 14 | 6 | 79 | 37 | 16 |

For some pits, numbers of layers obtained from both interpretations (CMM and ISM) are different. CMM does not split some thinner layers, where those thin layers are detected by ISM.

Furthermore, significant differences are observed in layers' thicknesses and resistivities for the aquifer. For P-1 for example, CMM interpretation provides 565 $\Omega.m$ resistivity, 40 m thickness and 18.4 depth while ISM interpretation provides respectively 320 $\Omega.m$, 42.1 m and 21 m for the same parameters as shown and compared in Table 1. Such differences are observed for almost all other VES points. Given the importance of aquifer resistivity and thickness in the groundwater productivity and management (Asfahani 2007; Arétouyap et al. 2015), these dissimilarities observed from different techniques demonstrate the necessity of using and comparing both methods in the context of accurate interpretation and efficient water resources management.

Assuming that an aquifer is probably a lower-resistive layer stuck between two higher-resistive layers, local Pan-African aquifer is predominantly made of upper weathered part of the granitic bedrock. The spatial distribution of the main aquifer parameters (resistivity, thickness and depth) obtained from ISM interpretation are represented in Figs. 8, 9 and 10. But in order to highlight differences and/or similarities between results obtained from CMM and ISM, each of those figures is made of two parts. Part (a) is the map obtained by Arétouyap et al. (2015), using CMM while Part (b) in the present result obtained from ISM. For this, geostatistical tools and parameters used to plot maps presented in Arétouyap et al. (2015) are the same used in the present manuscript. Those are semivariogram model, its sill, its range and its nugget variance.

Fig. 8 shows the distribution of the Pan-African aquifer resistivity deduced from the ISM interpretation of the fifty pits. Minimum values are observed in the northeast part of the region above VES location P-4 and maximum values are observed in the southwest part where is located P-20. Values obtained from ISM range from 20 to 860 $\Omega.m$ instead of [190–265] obtained previously using CMM. The previous and the present maps have the same trends. High gradients are observed around P-4, P-25 and P-38. Given that the local Pan-African aquifer is almost made up of weathered portion of the granitic bedrock, minimum values of the aquifer resistivity correspond to more cracked basement while maximum resistivity values correspond to less fractured basement portion. Deeper tectonic surveys are envisaged in order to check this hypothesis. One can also observe that northeast part of the region is covered of volcano-sedimentary formations (see Fig. 1). Other geological and geothermal factors as age and temperature can explain these maximum and minimum values. The resistivity map divides the area into two zones: a high-resistive zone in southwest and a low-resistive zone in northeast. Groundwater therefore may flow from northeast (where is concentrated the recharge area) to southwest.

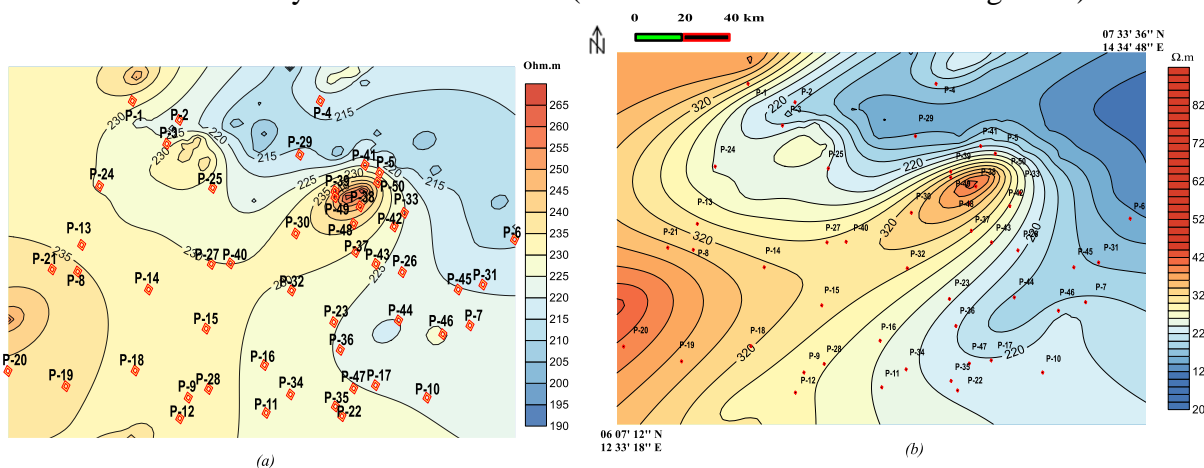


Fig. 8 Isoresistivity map of the Pan-African aquifer in the Adamawa region

Fig. 9 shows the distribution of the saturated Pan-African aquifer thickness h deduced from the use of the 50 VES points interpreted by Inverse Slope Method. The minimum thickness is observed northward above VES P-4 point and the maximum eastward at VES P-6. As for the resistivity, both maps representing the aquifer thickness exhibit several similarities, especially in terms of trends and gradient points. Differences are observed on the endpoints. In fact, for the present map, the values of the aquifer

thickness range from 2 to 86 m while they range from 20 to 58 m in Arétouyap et al. (2015). The aquifer formations correspond with the low-resistivity layers. Higher aquifer thickness is observed in the eastern part of the study area.

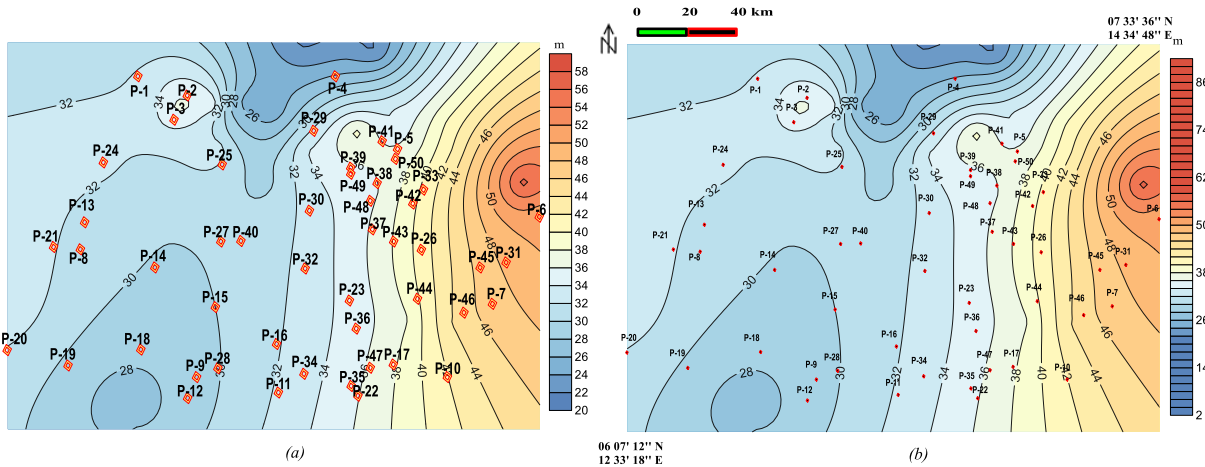


Fig. 9 Isothickness map of the Pan-African aquifer in the Adamawa region

An attentive analysis of Figs. 9 and 10 insinuates that aquifer depth and resistivity vary inversely. Indeed, highest depth values are observed south-eastward while highest resistivity values are observed north-westward. This situation has an advantage and an inconveniency. Knowing that more productive aquifers, in terms of flow or recharge, are less resistive, populations can perform productive hand-made wells in the region. But because of the shallow location of these wells, they are very vulnerable to pollution, quality alteration and climate variability. However, both results (obtained previously using CMM and obtained in this investigation using ISM) show many differences in the spatial distribution of the aquifer depth. Contrary to the previous results, the present ones almost divided the study area into two parts: a low-deep aquifer region located northwestwardly and a high-deep one on the opposite side.

Globally, ISM provides more accuracy and precision. It allows to more precisely determine the hydraulic parameters such as resistivity, thickness and depth of the aquifer. These parameters are very useful in the integrated and sustainable management of groundwater resources. Their importance is also due to the potential environmental impacts they can generate in case of poor control. Such impacts can be wetland desiccation and especially structural damage as in London and Birmingham (Biwas 1992).

In fact, Biwas (1992) stated that any groundwater project needs a good environmental impact assessment. In particular, developing countries such as Cameroon are very concerned.

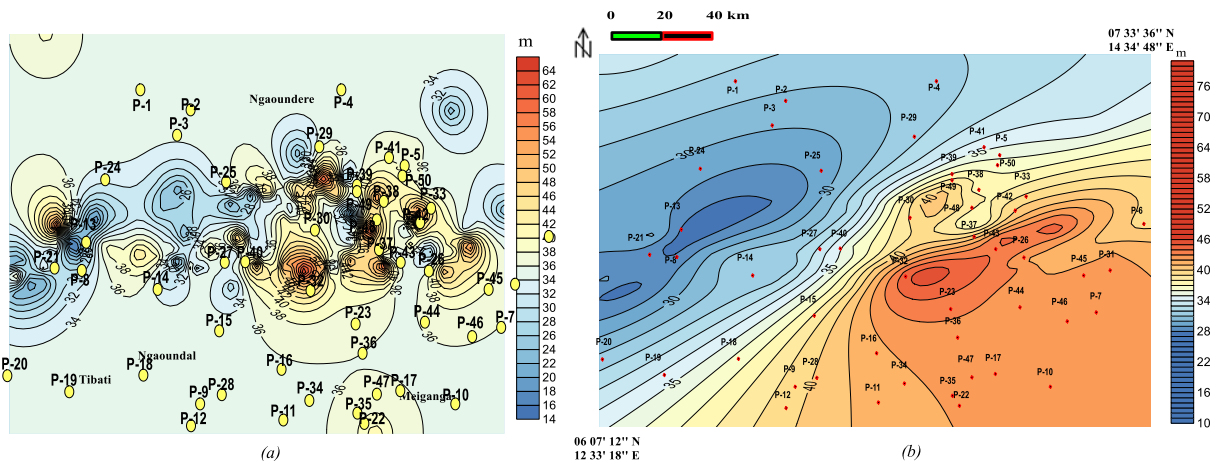


Fig. 10 Isodepth map of the Pan-African aquifer in the Adamawa region

5 Conclusion

The application of the ISM in the present paper for interpreting VES data demonstrated the suitability of this method in the Pan-African context on groundwater purpose. This method enabled to complete and overcome several difficulties encountered during quantitative interpretation of geoelectrical measurements using CMM. ISM is simpler than CMM, and has numerous qualitative and quantitative advantages. It allows in so far to distinguish all geologic layers even the thinner ones and can be used to interpret VES data collected with any electrodes array. Its application has allowed characterization and derivation of the hydrogeophysical parameters of the Pan-African aquifer in the Adamawa region, which will be useful for further groundwater modeling. The Pan-African aquifer resistivity values obtained by applying this ISM approach ranges from 20 to 900 $\Omega\cdot\text{m}$ with a mean of 241 $\Omega\cdot\text{m}$ and a standard deviation of 228 $\Omega\cdot\text{m}$. The aquifer thickness ranges from 2 to 90 m, with an average of 33 m and a standard deviation of 21 m. This aquifer is globally located at 37 m. These results improve our understanding of the uneven Pan-African terrain and may be taken into account when planning the groundwater management in the context of sustainable development.

6 Acknowledgement

The authors are very thankful to Prof. Ibrahim Othman, General Director of the Syrian Atomic Energy Commission for allowing Prof. Jamal Asfahani to take part in this investigation.

7 References

- Arétouyap Z, Njandjock Nouck P, Bisso D, Nouayou R, Lengué B, Lepatio Tchieg A (2014a) Climate change and its possible interactions with water resources in Central Africa. *J Appl Sci* 14 (19): 2219-2233. doi: 10.3923/jas.2014.2219.2233.
- Arétouyap Z, Nouayou R, Njandjock Nouck P, and Asfahani J (2015) Aquifers productivity in the Pan-African context. *J Earth Syst Sci* 124: 527–539.
- Asfahani J (2007) Neogene aquifer properties specified through the interpretation of electrical sounding data, Salamiyeh region, Central Syria. *Hydrol Process* 21: 2934-2943.
- Asfahani J (2013) Groundwater potential estimation deduced from vertical electrical sounding measurements in the semi-arid Khanasser Valley region, Syria. *Hydrol Sci J* 58: 468–482.
- Asfahani J (2016) Inverse slope method for interpreting vertical electrical soundings in sedimentary phosphatic environments in the Al-Sharquieh mine, Syria. *CIM Journal* 7: 1–12.
- Biwas AK (1992) Environmental impact assessment for groundwater management. *J Water Res Dev* 8: 113–117.
- Chilès JP, Delfiner P (1999) *Geostatistics: Modeling Spatial Uncertainty*. John Wiley and Sons Inc, New York.
- Cornacchia M, Dars R (1983) Un trait structural majeur du continent africain. Les linéaments centrafricains du Cameroun au Golfe d'Aden. *Bulletin de la Société géologique de France* 7 : 101-109.
- Dumont JF (1986) Identification par télédétection de l'accident de la Sanaga (Cameroun). Sa position dans le contexte des grands accidents d'Afrique centrale et de la limite nord du craton congolais. *Géodynamique* 1: 13-19.
- Ghosh DP (1971) Inverse filter coefficients for the computation of apparent resistivity standard curves for a horizontally stratified earth. *Geophys Pros* 19: 769–775.
- Goovaerts P (1997) *Geostatistics for natural resources evaluation*. Oxford University Press, Applied Geostatistics Series, London.
- Gorai AK, Kumar S (2013) Spatial distribution analysis of groundwater quality index using GIS: A case study of Ranchi municipal corporation (RMC) area. *Geoinfor Geostat: An Overview*. doi.org/10.4172/2327-4581.1000105.
- Koefoed O (1976) Recent developments in the direct interpretation of resistivity soundings. *Geosurveying* 14: 243–250.
- Koita M, Jourde H, Koffi KJP, Da Silveira KS, Biaou A (2013) Characterization of weathering profile in granites and volcanosedimentary rocks in West Africa under humid tropical climate conditions. Case of the Dimbokro Catchment (Ivory Coast). *J Earth Syst Sci* 122: 841–854.

- Maréchal A (1976) Géologie et géochimie des ressources thermominérales du Cameroun. Doc ORSTOM 59: 169-176.
- Mohamed HS, Senosy MM, Abdel GZ (2014) Upgrading of the inverse slope method for quantitative interpretation of earth resistivity measurements. Arab J Geosci 7 : 4059–4077.
- Ngako V, Jegouzo Nzenti JP (1991) Le Cisaillement Centre Camerounais. Rôle structural de la zone mobile panafricaine de l'Afrique Centrale au contact du craton du Congo. Compte-Rendu de l'Académie des Sciences II 303: 369–381.
- Njonfang E, Ngako V, Moreau C, Affaton P, Diot H (2008) Restraining bends in high temperature shear zones: "The Central Cameroon Shear Zone", Central Africa. J Afr Earth Sci 52: 9-20.
- Robain H, Descloitres M, Ritz M, Yene Atangana JQ (1996) A multiscale electrical survey of a lateritic soil system of the rain forest of Cameroon. J Appl Geophys 47: 237-253.
- Sanker Narayan PV, Ramanujachary KR (1967) An inverse slope method of determining absolute resistivity. Geophysics 32: 1036–1040.
- Toteu SF, Ngako V, Affaton P, Nnange JM, Njanko TH (2000) Pan-African tectonic evolution in Central and Southern Cameroon: Tranpression and transtension during sinistral shear movements. J Afr Earth Sci 36: 207-214.
- Toteu SF, Penaye J, Poudjom Djomani Y (2004) Geodynamic evolution of the Pan-African belt in central Africa with special reference to Cameroon. Can J Earth Sci 41: 73-85.
- Zohdy AAR (1989) A new method for the automatic interpretation of Schlumberger and Wenner sounding curves. Geophysics 54: 245–253.
- Zohdy AAR, Bisdorf RJ (1989) Schlumberger Sounding Data Processing and Interpretation Program. Geological Survey, Washington.

21- Living Organisms to Produce Bio-Materials Through Bio-design Strategies

Ola M. Mohammed Ahmed

Faculty of fine arts Alexandria University, Alexandria, Egypt

FA.OLA.MOHAMED@alexu.edu.eg

Abstract.

The boundaries between science and design are increasingly melting. Today, architects and designers are seeking to build sustainable and flexible buildings. The field of sustainable biotechnologies revolves around the use of renewable natural resources to produce innovative biological materials in a sustainable way. Therefore, this requires changing the way we produce energy, reducing carbon emissions and other harmful chemicals. Furthermore, we are now on the threshold of a biological revolution in which biology and material science are being integrated. Designers are constantly looking for new methods of producing materials and developing dynamic digital models based on the advanced biotechnologies. Bio-materials include the elements of medicine, biology, chemistry, tissue engineering and materials science. Meanwhile, biological materials refer to: natural materials. Organic material is a substance which originated from a living organism once or is made up of organic compounds; a chemical present or produced in an organism. So that, bio-material will change the concepts of design through integrating biological processes in nature with design and architecture to create the future structure of biomaterials. Besides, designers are increasingly turning to living organisms, in addition, they are studying bio-materials related to living tissue or microorganisms which can be used to produce biomaterials. Finally, the main concern of research is to analyze living organisms which can create innovative biotechnologies through bio-design strategies and provide a sustainable world through merging digital fabrication and biology. Consequently, the concept of bio-design is designed to allow our buildings to become one with nature.

Keywords: Bio-design, Sustainable, Bio-materials, Living Organism, Computational Design.

1. Introduction

One of the major challenges of this century is to transform our consumer-oriented economic system into an environmentally friendly and sustainable society which can reduce energy consumption, carbon emissions and waste production while minimizing production costs [1]. Climate change and increasing levels of pollution have led to an ongoing effort to make our cities greener and more sustainable, especially in the developed world. The urgency of improving the environmental quality of our cities has been urgent. So that, designers are increasingly turning to living organisms, as well as, studying biological materials related to living tissue or microorganisms which can be used to produce bio-materials. Bio-materials will change design concepts through integrating biological processes in nature with design and architecture to create a future structure for bio-materials. Designers are constantly looking for new methods of creating products and developing dynamic digital models based on the computational tools of advanced biotechnologies. In addition, biomaterial will change the way we think as biological processes have been integrated into nature with design and architecture, and new techniques have been applied to create the future architecture of bio-materials. Meanwhile, bio-materials include the elements of medicine, biology, chemistry, tissue engineering and materials science. Biological materials refer to: natural materials. Organic material is a substance which originated from a living organism once or is made up of organic compounds; a chemical or produced in an organism. Biotechnology has become an important component of sustainable development in the world of architecture design. One of the most important sources of inspiration is the manufacture of materials from living organisms, such as fungi and bacteria. The research aims to develop the concept of bio-materials in design from living organism when designers are inspired by biological objects [2].

1.1 Bio-digital Future

Inspiration extends from nature to imagination and creates new speculative worlds in architecture and design [3]. Designers look at the way things and shapes grow through analyzing biological processes in their physical aspects [4]. They are increasingly turning to living organisms

in nature to study materials related to living tissue or microorganisms and others which can be harnessed to create a biologically designed product where bio-materials will provide a sustainable alternative and new look at the use of living organisms to create innovative biotechnologies through biological design standards, which can be applied in interior design and architecture. Living organisms produce substances. So that, designers can look at materials in nature and imagine a future to reach bio-digital future using biotechnology. The use of organic materials of nature such as ivory, wood, leather, concrete, silk and building materials, for instance, brick, concrete and insulation materials. Sustainable development cannot be achieved without significant change in the way of construction, architectural design and the use of biology natural resources in construction. The research is based on a unique set of methods which will enable researchers to link innovative computational design, manufacturing and labs, with a special focus on innovative biomaterial design to explore new environmental design solutions which respond to the increasing challenges in our cities [5]. The research explores organisms as a sustainable ecosystem in the biological design of the production of biological materials in architecture [6].

1.2 Live Plant Engineering

The research analyses the role of designers and scientists in pushing boundaries to explore new materials and techniques through biotechnology. Designers are constantly looking for new ways to produce products, while the boundaries between science and design are increasingly melting. This will be useful for all fields of design and fabricating; however, the environment can benefit radically. We have seen an increase in the number of designers and architects who rely on biological philosophies, and even incorporate the use of living organism into their designs. For instance, the proposed kitchen research project for the future: a series of standard glass storage containers for food and liquids which can be automatically refilled from the outside, which can eliminate the need for packing, resulting in excessive waste (figure 1). The research project is a building of experience and performances. It embodies the new possibilities of live plant engineering, in addition, it depicts the architectural and ecological potential of Baubotanik, "the building of botany."



Fig. 1, The interior design of wall kitchen in a tower which uses trees and branches to enhance naturally in response to stress or overload, such as the natural properties of trees [7].

1.3 Biological Revolution

We are now on the threshold of a biological revolution in which the convergence of synthetic biology and nanotechnology brings together everything we do, from fashion to products to architectural design through the integration of biological processes into nature. Buildings are designed which incorporate natural structures for more environmental designs. Architects apply new and old

techniques to create the structure of the future. One of the first companies to have patented a biologically designed product, New York-based Ecovative Design, produces alternatives to plastics, as well as foam polystyrene foam. This is already used for building materials such as bricks, insulation materials, and applications in product design - all innovative examples of the advantages of using these materials. [8]. The next revolution will be the biotechnological revolution. Italian designer Maurizio Montalti imagines a world in which the traditional concept of production is replaced by a new model of growth and agriculture, where products come alive through a process resembling a kind of natural three-dimensional printing. Through the Growing Lab, its studio offers a series of mushroom-based products such as bowls and vats. As well as, the discipline of design is analyzing, creating and leading the profound transformations which characterize the age we live in, it also aims at reflecting a proposal and vision on how plastics will change in the future: Growing Lab is indeed an evolving project which seeks to engage in strong collaboration with natural systems, suggesting unprecedented paths in generating better and economically sustainable production models, transforming existing models, existing systems and networks, and proposing a shift from the traditional concept of industrial production towards a new agriculture model in bio-design [1].

1.4 Growing Object Research Project

The research team created Growing Object project (figure 2). Crop residue materials can be used as essential components for the cultivation of these fully soluble materials, which are also water-resistant and fire-resistant. So, the potential of fungus-based materials is truly incredible. Designers are increasingly turning to the laboratory to study living organisms and ecosystems which can be harnessed to improve the organisms on which we rely. Biology is the best set of tools to reach our design goals, as well as the most important resource for our long-term survival [1].



Fig. 2, The research team imagine a new world in which products are the result of a new model of growth and agriculture such as Growing Object which inspired from living organism.

2. Materials and Methods

The research depends on the descriptive approach to look at living organisms for creating innovative biotechnologies through bio-design strategies and provide a sustainable world through merging digital fabrication and biology. The paper explores the possibilities of dynamic digital models based on the advanced biotechnologies to produce bio-materials from nature such as living

organism. The aim of the research is to link the biological properties, their application in the architecture and interior design through integrating biological processes in nature with digital design.

2.1 Programming Biology in Design and Architecture

New sustainable materials are developed through programming biology. Designers and architects used living organism in their inspiration such as mycelium, the root structure of fungi, throughout the technology platforms to develop advanced materials [9]. Mycelium can build total structures. This aspect is unique to bio-manufacturing platforms in biotechnology. The research team in Fungal Mycelium project built high-performance structures against the manufacture of individual components which need to be assembled into a functional material (figure 3). Designers could control porosity, texture, strength, flexibility, fiber orientation and more in Mycelium project.

2.2 Fungal Mycelium Research Project

Ecovative is a company of materials science which is developing a new class of bio-plastic disposable home-compostable based on fungus, organism. Mushroom Materials is a high-performance, environmentally responsible alternative to traditional plastic foam packaging, insulation and other synthetic materials [9]. Ecovative used mycelium which is the vegetative growth stage of fungus. Bacteria were produced by a fruiting body or a mushroom, and researchers did not plant our material long enough to produce mushrooms or germs (figure 3).



Fig. 3, Diagram of mushroom material which consisted of agricultural waste and fungal mycelium to use in Fungal Mycelium Pavilion project.

2.3 Definition of Mycelium

Mycelium is a fast-growing vegetable portion of fungus, consisting of a narrow network of interstitial cells, called filaments. Thanks to this structure, mycelium can harvest, convert and redistribute food for its own benefit (mushroom growth) and for the larger ecosystem. In fact, it is possible to develop materials with peculiar properties, for instance with respect to strength, elasticity, thickness, homogeneity, water repelling, etc..... [1]. Mycelium is the vegetative part of the fungus consists of a network of fine white filaments. "After one to five weeks on the weed weeds, the pie leaves, or capillaries of plant fungi, to the bottom of the leg." Poisons occur in fungus. Mycelium Foundry used natural inputs to produce sophisticated high-performance materials to be compatible with the planet.

2.4 Bio-based & Sustainable design Through Living Organism

Mycelium material will decompose over time after the intended product life cycle, unlike plastic-based materials which have been around for thousands of years. The team researchers do research, development and production of all our fungus-based materials [9]. The structure of Mycelium produces 100% pure. Sponge foam provides a sustainable alternative to plastic based materials for a wide range of applications ranging from high performance shoes to leather substitutes (figure 5) [9].



Fig. 4,5, Fungal Mycelium Pavilion Research Project inspired from Mycelium material.

2.5 Carbon Dioxide and Energy Through Biotechnology Research Project

Biotechnology and synthetic biology are increasingly exploring the ability of photovoltaics to use sunlight to convert carbon dioxide into useful energy, with the ability to perform functions such as bio-filtration and air purification in the form of their by-products. However, their extensive applications for buildings and infrastructure have not been explored. This research project examines the possibility of developing self-sustaining systems through the continuous exchange of energy and nutrients with their surroundings. This system, saturated between distinct natural and synthetic environments, explores these systems through the Robotic Algae-Laden Printed Hydrogel Scaffolds (RALPHS) deposits (figure 6,7) [10].



Fig. 6,7, Bio material of Robotic Algae-Laden Printed Hydrogel Scaffolds (RALPHS) deposits.

2.6 A living Wall to Combat Pollution and Promote Biodiversity Research Project

Volvo has installed an eco-friendly wall along the Sydney Harbor coast to improve biodiversity and water quality in the region. The Volvo Living Seawall wall consists of 50 hexagonal slabs with small corners designed to simulate the root structure of the native mangrove trees - a popular habitat for marine wildlife. Marine wildlife tile consists of marine concrete reinforced with recycled plastic fibers [11]. Developed in collaboration with the Sydney Institute of Marine Science and the Reef Design Lab, this project provides an alternative to traditional linear sea walls, often associated with the loss of surrounding ecosystems. The irregular tiles designed on the surface of the current wall structure have been linked to wildlife, such as oysters and molluscs, which filter water by feeding on passing particles [11]. Sea Seawall is designed to simulate the root structure of native mangrove trees, adding complexity to the existing wall structure and providing habitat for marine life. This helps biodiversity and attracts objects which feed filters, absorb and filter contaminants - such as particles and heavy metals - to keep the water clean. Researchers will monitor the Living Seawall over the next 20 years to see how it affects biodiversity and water quality in the region [11].

Volvo has developed seawall tiles after its research found which one plastic garbage truck enters the world's oceans every minute and more than half of Sydney's coastline is made up of artificial seawalls. Rich and vibrant habitats have been replaced by sea walls and degradation due to plastic contamination (figure 8,9) [11]. By adding seawall tiles to an existing sea wall, the project aims to transform a man-made structure into a potential marine habitat. It is also a unique opportunity to look for the best designs and the architecture of the sea wall which better support the ecosystems of our oceans.

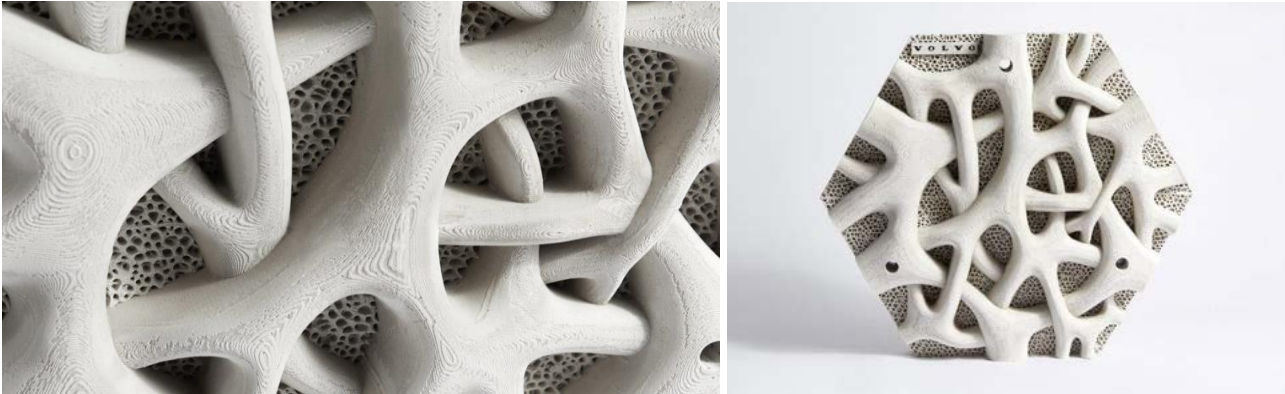


Fig. 8,9 Volvo has pledged to replace all single-use plastics with sustainable alternatives in the end of 2019. Other companies which have taken similar initiatives include IKEA, which has unveiled plans to eliminate all single-use plastics from a single group Products by 2020 [11].

2.7 Mycelium Chair Research Project

Dutch designer Eric Clarenbick explores ways of three-dimensional organisms such as mycelium, fungus-like nets and local raw materials to create negative carbon effect products. Because of his research, mycelium chair is made of a mixture of powdered straw and mycelium. This unlimited natural source of organisms is used as a living glue for organic waste (figure 10,11).



Fig. 10,11, Mycelium Chair prototype inspired from living organism.

Once it is fully grown and dried, it becomes a structural, stable and renewable substance. In addition to 3D printing, it gives designers tremendous design freedom. It is possible to create products with a negative carbon effect (figure 12). Instead of just wasting less, they absorb emissions. After use, the product is completely fully compostable and can be disposed of without damaging the environment. On the contrary, it will fertilize our surroundings [12].



Fig. 12, This chair is really a metaphor for what can be made using this technique of printing a 3D living object and then making it grow more. It can be a table, a complete interior or even a house.

3. Biodegradability & Biocompatibility and Architecture

Architecture today is static and unresponsive. However, it is time to confirm the role of biology and allow our buildings to grow and adapt with a strong focus on mycelium fungi, the research team created a bio-scaffold inspired from bio-engineering algorithm, which was designed for the growth and degradation of this organic matter. Inspired by the formation of the medical and tissue engineering industry, this bio scaffold integrated both digital and biological manufacturing. The three-dimensional structure of the cells belonged to the native cells and protein proteins to promote cell adhesion and tissue regeneration. Being a biocompatible and bioavailable substance, scaffold was designed to degrade over time [13].

3.1 Bio Scaffold research project

The research project suggested how biodegradability and biocompatibility could occur outside the human body (figure 13,14). Moreover, these properties could be extracted from the medical field and applied to an architectural context. By studying the properties of mycelium during a previous research project, fungus was found to absorb nutrients through their cell walls. Therefore, by providing them with the appropriate tissue engineering scaffold, mycelium fungi would eventually break down the substance by absorbing the nutrients. Therefore, the target of mycelium fungi was gradually replacing the cultivated tissue. By applying mycelium to various different scaffold typologies, the research team would be design and monitor the direction of growth and orientation of growth (figure 15) [13].



Fig. 13,14, 3D models of Bio Scaffold research project.



Fig. 15, Bio-material of the implanted scaffold While mycelium fungi have been previously tested on a larger scale, the research team tried in this project to control growth by focusing on the material through a small scale [13].

3.2 Biodegradable Materials and Complex Engineering

Identifying an inspiration from the medical industry, various biodegradable materials will be tested when knowing the organic substances which mycelium decomposes successfully. These digitally manufactured shapes are made of wood, bamboo and PVA (water soluble yarns) will be produced.

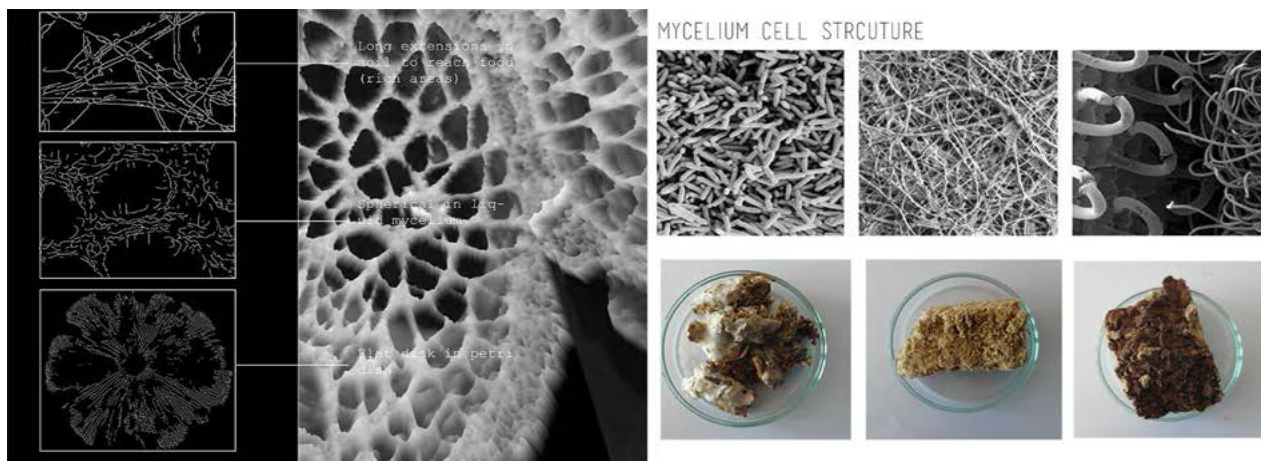


Fig. 16,17, These bio-materials will be printed three-dimensional simultaneously to produce complex geometry for diverse patterns.

3.3 Mathematical Algorithm

The research team will create complex geometric shapes and pathways to infiltrate mycelium. Through nature's inspiration of nature, this bio-emulator structure varies in porosity, materiality, scale, texture. Therefore, bio-scaffold geometry will be based on a mathematical algorithm which strategically determines the growth and form of mycelium to take advantage of the structural features of fungi which include their ability to withstand stress. Mycelium fungus will be strategically injected into tissue scaffold bio-tissue areas which need support [13].

3.4 Bio Scaffold Process

(Surgery, medicine) artificial structure, planted in the body, tissue grows in the form of missing or damaged member, etc.; a process called tissue engineering. To apply this biodegradability concept to the architectural context, the final form was printed on a 1: 1 scale as a table. After conducting various tests on the material, it was discovered which the fungus block works better in compression rather than in tension. Therefore, to take advantage of the structural features of mycelium, the table can withstand any external forces and pressure applied to the surface. Ultimately, this concept was designed to allow our buildings to become one with nature and to become living breathing organisms.

3.5 Buildings become living breathing organisms

The research team discovered fungus which absorbs nutrients through their cellular walls. Therefore, this three-dimensional wooden form was planted with mycelium cells to encourage the deterioration of its outer walls. However, to control the growth and design of the mycelium, a gradient was carried out in terms of volume, porosity and material importance to control this fossilization process. For structural purposes, the lower half of the scaffold tissue consisted of larger perforated tubes [14].

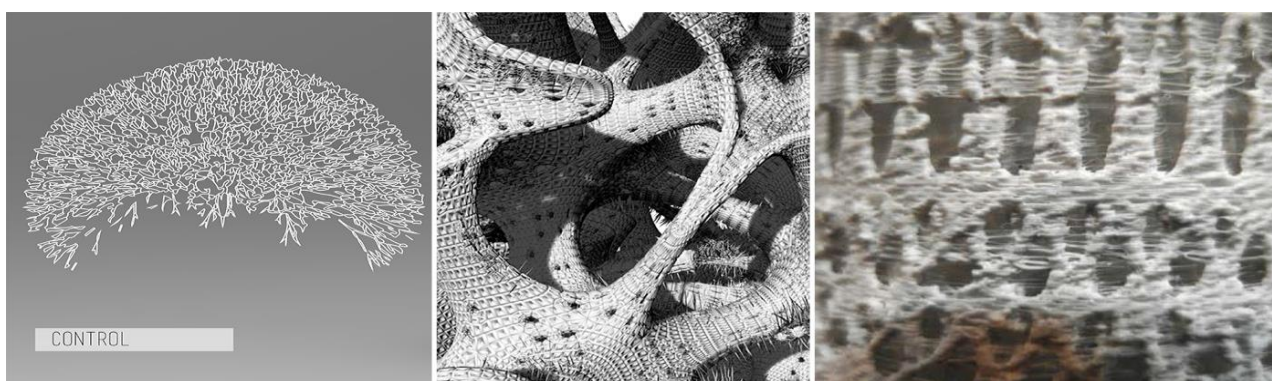


Fig. 18, The growth of the mycelium, the holes would allow the fungi to decompose the scaffold tissue successfully at a faster rate. The fungus mixture was introduced through an injection then incubated.

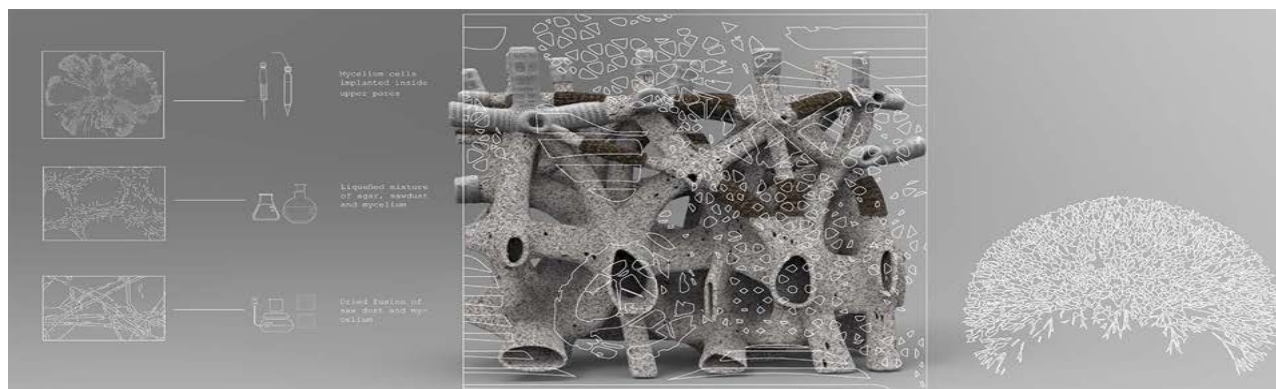


Fig. 19, Bio-digital simulation system to generate form.

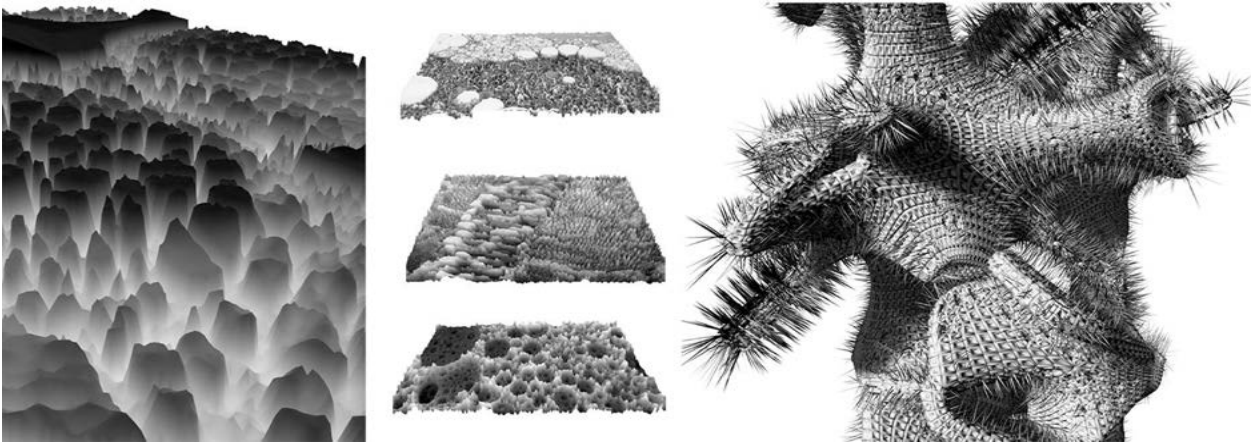


Fig. 20, Form Finding process in bio-digital design.

4. BioConcrete

People have used a variety of other materials for decades, including concrete, which is one of the most basic building materials. Concrete is another illustrative way to show how bio-processing can be used to reduce our environmental effect. Rapid urbanization in the world leads to a huge increase in the production and use of concrete. Today, there is a new and urgent need to reduce the environmental impact of human activities, including construction. The environment cannot bear this pressure and at the same time continue to maintain life [8]. Given the environmental pressures of building for an increasing population, Professor Henk Junkers of the Delft University of Technology has developed BioConcrete with the help of bacteria. These biologically integrated materials can extend the life of the concrete service, while also reducing the cost of maintenance, reducing the carbon effect of one of the most common building materials in the world. BioConcrete uses specialized microbes for making self-healing concrete. If this material can be mastered and widely adopted, this alone can represent a huge step towards reducing the impact of human activities on the environment [8].

4.1 Bioreceptive Concrete Facade Panels Research Project

The computational seeding of biological materials receiving Bio-Receptive Materials is a multidisciplinary research proposal which combines a design team with highly experienced architecture, biology and engineering (figure 21,22) [15].

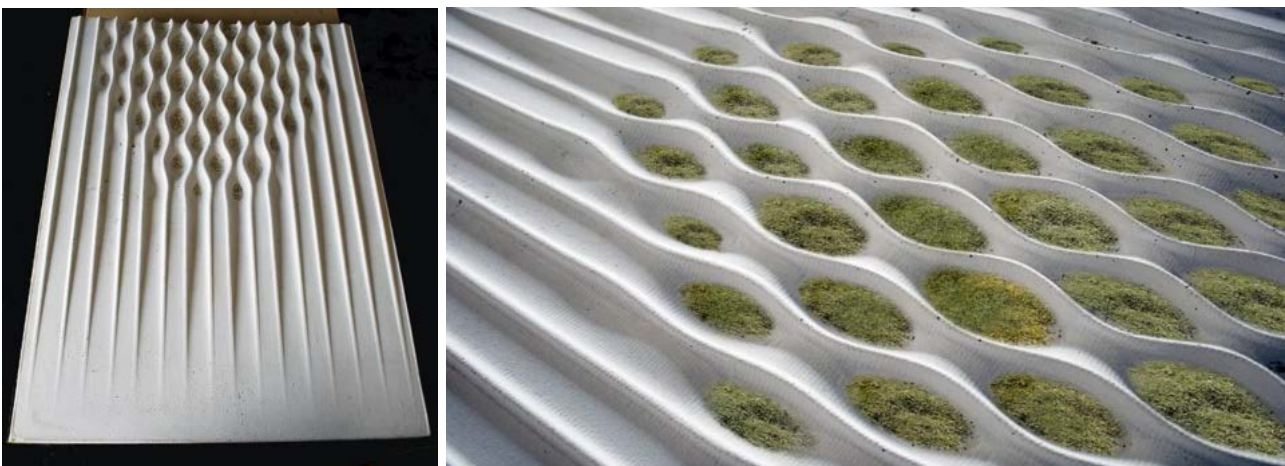


Fig. 21,22, The adoption of biologically accepted concrete as a means of promoting green growth has the potential to become the building's own facade as the biological substrate for the growth of photosynthetic systems.

The research project aims to develop an innovative wall panel system capable of growing microorganisms directly on its surface. By using new engineering techniques in design, the project seeks to improve interface performance by implementing a new type of biologically receptive

concrete. This system aims to overcome many of the restrictions on existing green walls, especially the need for expensive mechanical irrigation systems and maintenance. This proposal responds to the urgent need to improve the environmental quality of our cities. Climate change, increasing levels of pollution, and loss of previous surfaces in the urban fabric have led to an ongoing effort to make our cities greener and more sustainable, especially in the developed world (figure 23) [15].



Fig. 23, Biologically receptive cementitious materials were studied and chemically changed to provide pH levels, porosity values and water retention properties which are conducive to microorganisms for their establishment and spread.

5. Bioceramics and Bioglasses

A porous bioceramic granule of an orthobiologic calcium composition manufactured by Cam Bioceramics. Bioceramics and bioglasses are biocompatible ceramic materials [16]. Bioceramics are an important subset of bio-materials. Bio-ceramics vary in bio-compatibility from chemical oxides, which are inert in the body, to the other end of absorbable materials, which are eventually replaced by the body after they have helped in the repair. Bio-ceramics are used in many types of medical procedures (figure 24,25,26) [16].



Fig. 24,25,26, Bio-ceramics are usually used as solid materials in surgical implants, although some bio-ceramics are flexible. The ceramic material used is not the same as ceramic material of ceramic type. Instead, bio-ceramics are closely related either to body materials or to extremely solid metal oxides [17].

6. Bioplastics

Ecovative is a company of material science which is developing a new class of bioplastics accessible to home-compostable compost based on mycelium, a living organism. Mushroom

Materials are high performance, environmentally responsible alternatives to traditional foam packaging, foam insulation, and other synthetic materials (figure 28,29,30,31) [18].

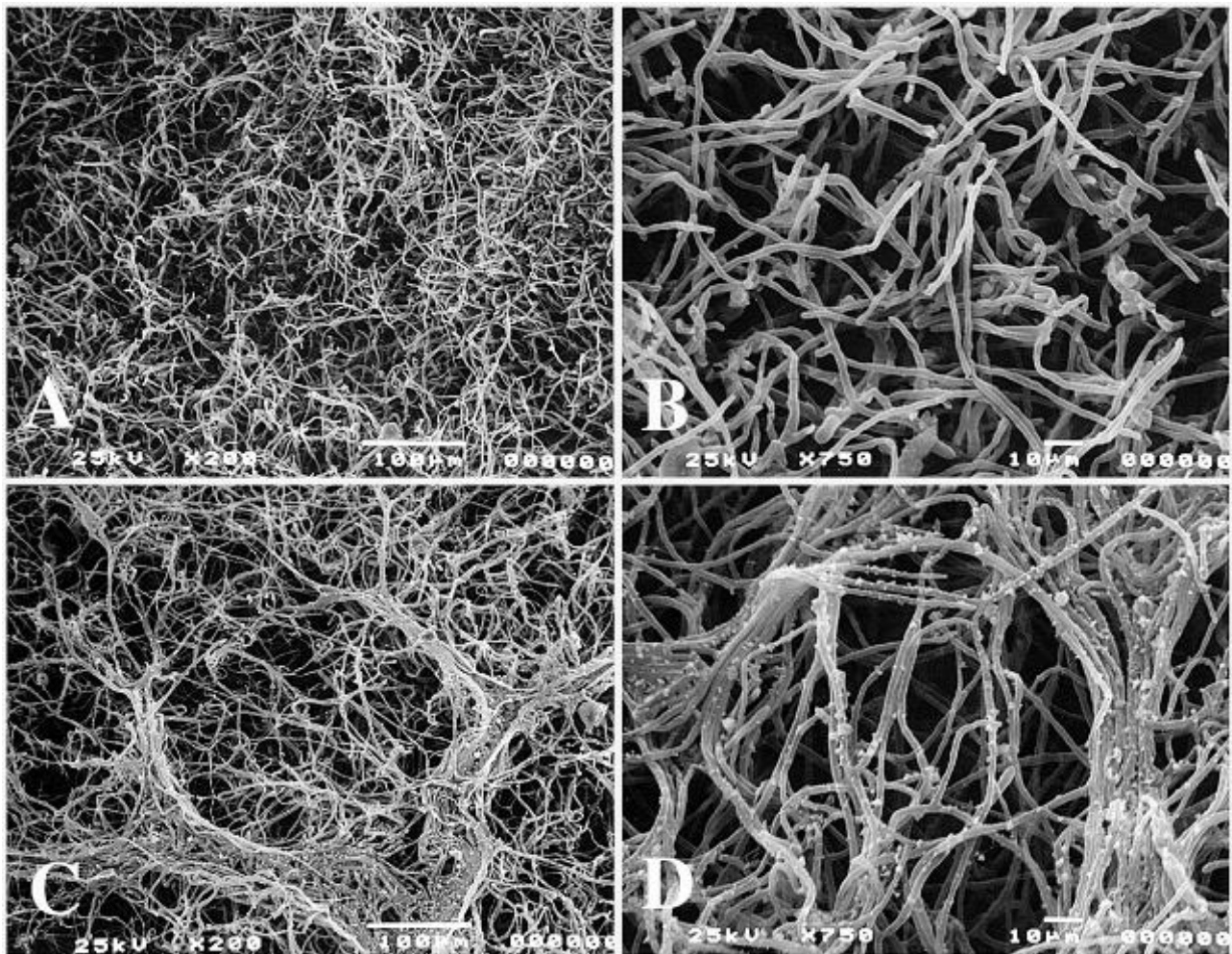


Fig. 27, Mushroom Materials cells.



Fig. 28,29, Ecovative use mycelium, the vegetative growth stage of fungus. Germs are produced by a fruiting body or fungus and we do not plant our materials long enough to produce mushrooms or germs [18].



Fig. 30,31, Bio-material compounds of mycelium.

7. BIQ – The Algae House Research Project

The Algae House project features the world's first algae bioreactor interface, held at the Hamburg International Building Show in 2012 and 2013. As Smart Material House, it combines intelligent materials and technologies with new types of living [19]. The project is a multi-story residential building which uses a typical method of energy production, light regulation and sun shading.

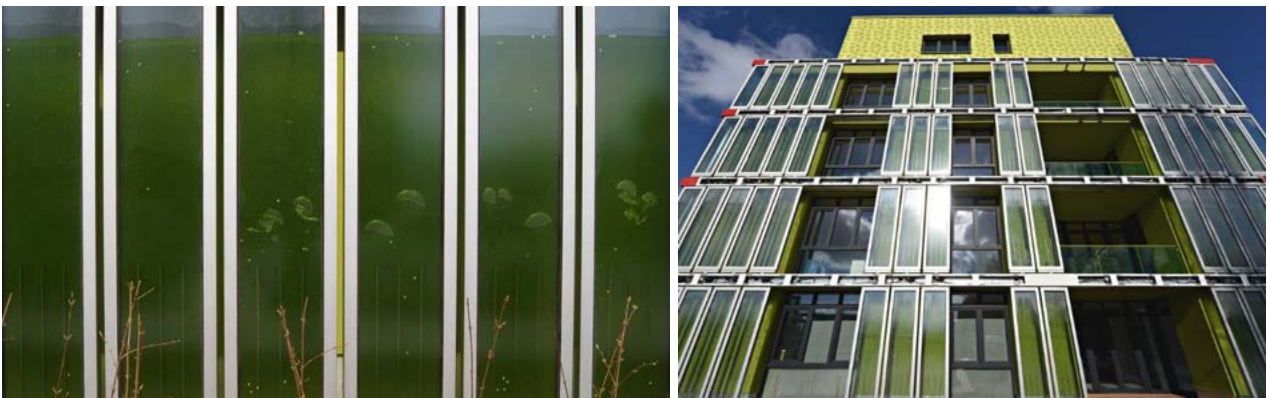


Fig. 32,33, From close range, the façades, which oscillate from afar through growing algae, begin to move; the bubbles formed by the supply of carbon dioxide and nitrogen, as well as the permanently necessary circulation of water containing aerosol-like algae -like microalgae, suggest which biomass production can be a solar-powered installation, constantly rising [19].

7.1 Energy hybrid

The mixed function of its algae façade, this building combines the various processes of renewable energy production to create a sustainable circulation system: solar heat, geothermal energy which forms energy, biomass and fuel cell together three energy sources which can be stored in the form of heat and electricity and biogas (figure 34,35) [19].



Fig. 34,35, The façade performs all the expected functions of traditional building cladding: it not only acts as a thermal and sound insulator, but also as a ray of sunlight. 130 translucent glass containers - called plate-shaped glass containers - consist of two structurally linked glass panels. The outer glass pane is manufactured as a photovoltaic glass module [19].

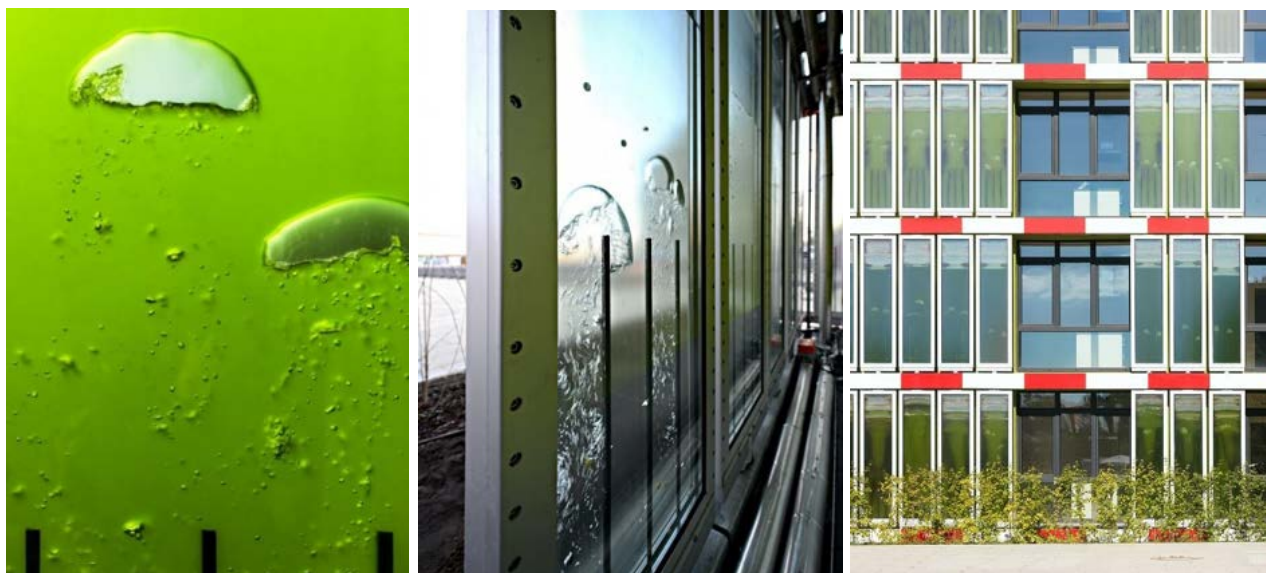


Fig. 36,37,38, In the same container, microalgae are grown in the middle of a water culture then processes photosynthesis by absorbing natural light, and then produces biomass when supplied with carbon dioxide, nitrogen and phosphorus. They can store carbon dioxide and produce biogas in an internal fuel cell which generates 4500 kWh 4,500 kWh per year. In addition, the solar thermal function of bioreactors produces about 32 megawatts of heat (MW) of heat per year that can be used directly at home or inserted into the local power grid or alternatively stored underground [19].

8. Alga(e)zebo by marcosandmarjan Research Project

The project Alga (e) zebo is one of several temporary pavilions exhibited in the city. It sets in Euston Square Gardens; this complex feature is a large structure decorated with a Gazebo. The concept of Gazebo follows the English tradition in which this tiny structure becomes a gem which intersects the landscape, creating a small gathering point or view which also regulates the surrounding natural surroundings. The steel structure also fits the traditions of exposed steel tools - gates, fences, fountains, pipe works, etc. - which distinguish and enrich many UK cities. The intricate patterns of the surface create a unique decorative structure which evokes elegance, with the ever-changing effect of light and shadows [20]. The internal space functions as a sitting facility for visitors to rest and gather or just think about the surroundings. The permeable limits of the structure also allow an endless operation of the framed scenes through it. Gazebo also launches links to dynamism, indeterminateness, transparency, cheerfulness, celebration and community, in addition to recyclable material and enhanced structure biotechnology, making it a landmark in the London Olympics [20].

Alga (e) beads intertwine between a human artifact and a natural environment. This is achieved in three different styles which vary in size and effect. Gazebo allows the growth of trees or taller shrubs between the structure. Multifaceted patterns create scaffold tissue for smaller plants to grow as pergola. The three cases reflect complex boundary negotiations between architecture and nature in our contemporary cities. There is an aspiration to overlap and integrate these situations; architecture behaves and looks more like biological construction, while nature is manipulated through human intervention [20]. Installation makes a statement to use the latest technologies along with multidisciplinary work methodologies with its intricate geometry and perforated decoration. The design results in the implementation of complex digital media processes. Scripting and algorithms allow Bollinger-Grohmann-Schneider to optimize the design of two-dimensional processes

(interfacing scripting) and structural integrity in three dimensions (topological projections) (figure 39,40,41) [20].

The world's leading Formstaal / CSI company ensures the construction of double-curved welded steel panels from recycled steel. Then laser panels are cut off by CNC machines (which are controlled by the computer). Process of perforated double steel curvature in Formstaal / CSI, Stralsund in Germany. Separate columns, made up of different size bioreactors, contain a variety of micro-organisms. Carbon dioxide is consumed by the carbon dioxide from the surrounding bacterium. The columns represent a real and unique test of the world, specifically looking at how this technology can be adapted to work in the complexity of a non-uniform environment which is inevitably inhabited by architecture [20].



Fig. 39,40,41, Vertical columns include algae tubes with different strains of locally bred algae, which differ in texture and color. It refers to Alga (e) zebo.

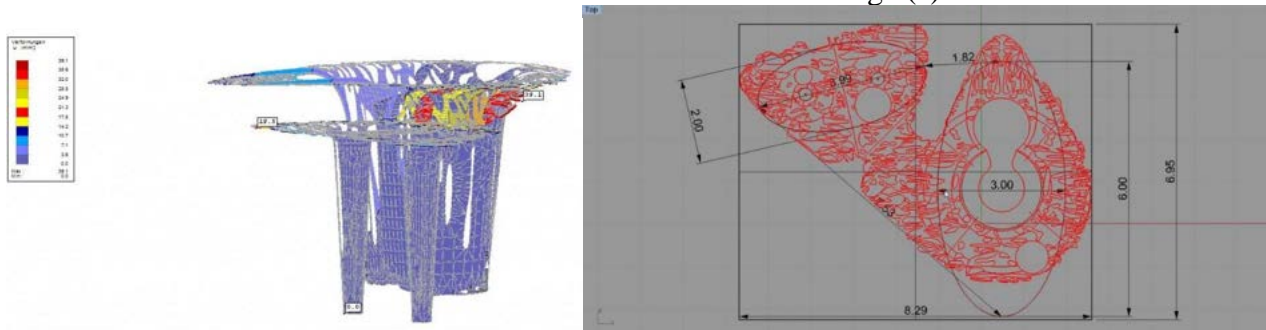


Fig. 42,43, Calculation of ornamental pattern by Bollinger-Grohmann-Schneider, Vienna Austria.



Fig. 44,45, Testing of algae insertion into different thicknesses of growth medium, Carbon-impregnation of 3D prints, which work as a scaffold to attracts the growth of algae.

9. Urban Algae Folly Research Project

An interactive exhibition integrates living micro-algal cultures, a combined example of bio-digital future. Microalgae, in this case Spirulina, are photosynthetic machines exceptional. They

contain essential nutrients for the human body, such as minerals and plant proteins; microscopic algae microalgae oxygenate also oxygenate air and can absorb CO₂ from the urban air ten times more effectively than large trees (figure 46,47) [21].



Fig. 46,47, Alge Folly's innovative architecture stems from the evolution of the ETFE system, the skin system; in this case it can provide a habitat to spur the growth of Spirulina's growth and ensure the comfort of visitors.

In sunny summer days, microscopic algae grow rapidly, increasing the potential of the shading of the architectural envelope and improving human comfort. Visitors, in their presence, will activate the digital regulatory system which stimulates algal oxygenation, solar insolation and growth. At any given moment, the transparency, color, reflectivity, sound and effective productivity of Urban Algae Folly are the result of the symbiotic relationship of climate, micro algae, humans and digital control systems [21]. The Future Food District, designed by Carlo Ratti Associate for the COOP supermarket series, is one of the thematic areas of the Expo 2011 "Feeding the Planet, Energy for Life." FFD consists of a 2,500 square meter Market) and a public square area of 4500 square meters.

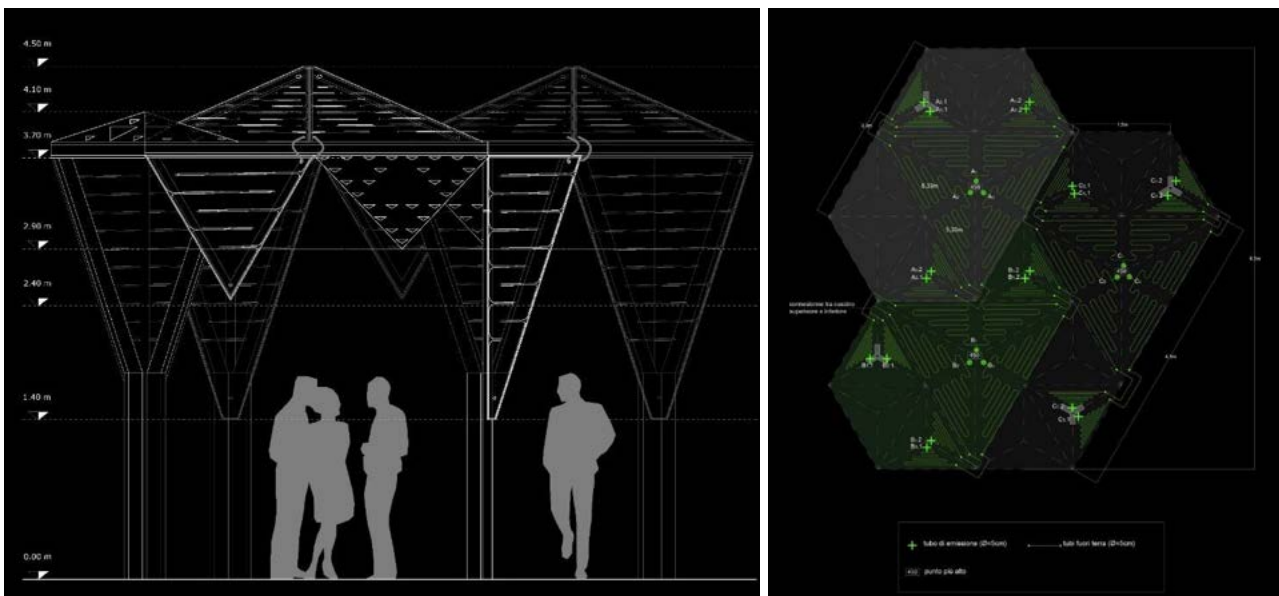


Fig. 48,49, Drawings of an interactive exhibition project which explore new forms of interactions between people and products to re-imagine the future supermarket as a place for free exchange where everyone can be productive and consumer. Visitors from FFD are invited to interact with the Urban Algae Folly; they can join events interacting with the structure with their smartphones [21].

10. Urban Algae Canopy Research Project

Algae is the unlikely term which is being discussed at the heart of Expo Milano 2015. As part of the future food zone project, sponsored by Carlo Ratti Associati at the central crossroads of the

EXPO, a new vision for digital bioengineering in the future Powered by microalgae microorganisms' organisms which were proposed by London-based ecoLogicStudio. This vision is about to become a reality where a large umbrella roof and vertical facades, designed by ecoLogicStudio [Claudia Pasquero and Marco Bolito] were unveiled with local architect Cesare Griffa. These prototypes represent a revolution in the concept of integrated agriculture and urban agriculture. The principle of prototyping depends on the exceptional properties of microalgae organisms, which are more than ten times more effective than photosynthesis compared to trees and grasses (figure 50,51) [22].



Fig. 50,51, Once completed as part of the EXPO2015 Future Food Zone, Urban Algae Canopy will produce an equivalent oxygen equivalent of 4 hectares of forest and up to 150 kg of biomass daily, 60% of which are natural plant proteins.

Based on ecologic Studio's six-year research on building integrated digital biological systems, the Urban Algae Canopy has been presented with a prototype of 1: 1 of the world's first digital biosphere featuring micro algae cultures and real-time digital farming protocols Unique architectural system. The exceptional properties of algal organisms are enhanced by cultivating them within the specially designed three-layer ETFE cladding system. Developed with close collaboration between ecoLogicStudio and Taiyo Europe, this system represents a radically new interpretation of the potential of the traditional ETFE coating system. The special CNC welding technology is at its core and enables ecoLogicStudio to design and control the shape of pillows under pressure as well as the fluid dynamic behavior of the waterway during transition [22].

Therefore, the flow of energy, water and carbon dioxide is regulated to respond and adapt to weather patterns and visitor movements. When the sun rises intensively, algae will enjoy photosynthesis and grow, thus reducing the transparency of the canopy and increasing its shading ability. Because this process is driven by the biology of algae, it is naturally responsive and adaptable; visitors will benefit from this natural shading feature while they can influence. It will activate the electric valves to change the speed of algae flow through the canopy, resulting in an emergency differentiation across space. At any given time, the transparency, colors and actual shading of the umbrella will be in this complex set of relationships between climate, micro-algae, visitors and digital control systems. "It is now time to overcome the separation of technology and the typical nature of the mechanical age, to adopt a systematic understanding of architecture" - Claudia Pasquero of ecoLogicStudio concludes in this prototype. The boundaries between physical, spatial and technological dimensions have been carefully defined for efficiency, flexibility and beauty [22].

11. Results and Discussion

Climate change and increasing levels of pollution have led to an ongoing effort to make our cities greener and more sustainable. We need to change the way we produce energy, reducing carbon emissions and other harmful chemicals. The research enhanced a new vision for digital

bioengineering in the future inspired from living organism to produce bio-materials through biotechnology. Bio-materials include the elements of medicine, biology, chemistry, tissue engineering and materials science, in addition they will change the concepts of design through integrating biological processes in nature with design and architecture to create bio-digital future. Finally, the research encompassed living organisms to create innovative biotechnologies through bio-design strategies such as scripting and algorithms, as well as it provided a sustainable world through merging digital fabrication and biology.

12. Conclusions

In conclusion, biotechnology and bio-digital processes provided many design possibilities. The research inspired architects to build a greener future. The results of the study could inspire from living organism to create an innovative bio-material. Therefore, designers could contribute in the development of new materials for sustainable production and they were increasingly turning to living organisms through bio-materials related to living tissue or microorganisms. Consequently, the concept of bio-design was designed to allow our buildings to become one with nature.

References

- [1] U. U. Maurizio Montalti (OC), "Growing object," 2018. [Online]. Available: <http://www.corpuscoli.com/projects/the-growing-lab/>.
- [2] S. Camere and E. Karana, "Fabricating materials from living organisms: An emerging design practice," *J. Clean. Prod.*
- [3] S. Pickersgill, *Super Architects and Dream Factories*, vol. 17. 2017.
- [4] F. Cvrčková, D. Oulehlová, and V. Žárský, "On growth and formins," *Plant Signal. Behav.* 11, 2016.
- [5] "living organisms," 2016. [Online]. Available: <http://marcoscruzarchitect.blogspot.com.eg>.
- [6] J. C. L. J. and S. M., "Organisms as Ecosystem Engineers," *Oikos* 69, 373, 1994.
- [7] "Baubotanik Tower," 2015. [Online]. Available: <https://studiomegan.nl/bibi/bookshelf/ffo/OPS/3tbc1a.xhtml>.
- [8] "Biological revolution," 2017. [Online]. Available: <https://studiomegan.nl/bibi/bookshelf/ffo/OPS/3tbc1a.xhtml>.
- [9] "Programming biology," 2018. [Online]. Available: <https://ecovatedesign.com/>.
- [10] "biological materials," 2018. [Online]. Available: http://www.biota-lab.com/?page_id=3178.
- [11] "A living wall," 2019. [Online]. Available: <https://www.dezeen.com>
- [12] "Mycelium Chair," 2019. [Online]. Available: <http://www.ericklarenbeek.com/>.
- [13] N. Almina, "Bio Scaffold," 2015. [Online]. Available: <http://syndebio.com/bio-scaffold/>.
- [14] "Mycelium," 2015. [Online]. Available: <http://materiability.com/portfolio/bio-scaffold/>.
- [15] "Bioreceptive Concrete Facade," 2015. [Online]. Available: <http://syndebio.com/>
- [16] G. W. H. P. Ducheyne, "CRC metal and ceramic biomaterials," *CRC Met. Ceram. Biomater.*, vol. 1, 1984.
- [17] K. S. H. Oonishi, H. Aoki, "Bioceramics," *Bioceramics*, vol. 1, 1988.
- [18] "Bioplastics," 2014. [Online]. Available: <http://syndebio.com/ecovative-muchroom-materials/>.
- [19] "Algae House," 2014. [Online]. Available: http://www.niggli.ch/en_ch/the-algae-house.html.
- [20] "Alga(e)zebo," 2014. [Online]. Available: <http://syndebio.com/>.
- [21] "Bio-digital future," 2015. [Online]. Available: <http://syndebio.com/urban-algae-folly/>.
- [22] "Urban Algae Canopy," 2014. [Online]. Available: <http://syndebio.com>

22- Electrochemical synthesis of silicon and gallium arsenide photovoltaic thin films: A critical review and a novel approach

Ashraf Bakkar^{1,2,a}

¹ Metallurgical & Materials Engineering Department, Faculty of Petroleum & Mining Engineering, Suez University, Egypt

² Department of Environmental Engineering, College of Engineering at Al-Lith, Umm Al-Qura University, Corniche Road, Al-Lith City, Saudi Arabia

^a ashrafbakkar@yahoo.com

Abstract

This paper presents, firstly, an overview of results arisen worldwide on semiconductive thin films used in photovoltaic (PV) cells as a function of time and efficiency. Secondly, the paper demonstrates electrodeposition of silicon and gallium arsenide films suggested for PV cells, with a focus on electrodeposition from ionic liquids. Ionic liquids, due to their wide electrochemical window, are used for electrodeposition of elements and compounds impossible to be electrodeposited from aqueous solutions. Finally, a new approach referred to a recent patent by the author, is illustrated to facilitate the practical electrodeposition of semiconductors from ionic liquids to be suggested for industrial applications.

Keywords: PV cells, Semiconductors, Electrodeposition, Ionic liquids.

1. Introduction

Renewable energy sources are urgently being searched and deeply researched for replacing petroleum because of the crisis of petroleum shortage. Among these energy sources, the thin film photovoltaic (PV) cells are promising candidate. There are some materials, e.g. silicon (Si), cadmium telluride (CdTe), cadmium selenide (CdSe), gallium arsenide (GaAs), copper indium selenide (CuInSe₂), and copper indium gallium selenide (CuInGaSe₂), can be applied in a thin film to a supporting substrate such as glass or ceramics [1-3]. At present there is concurrent research in all of the aforementioned thin film materials, see Fig.1.

The first generation of photovoltaic (PV) cells, named also solar cells, is synthesized from massive silicon wafers, which achieves energy payback of 5-7 years. Till now the most of commercial production of PV cells is of silicon wafers. Production of silicon wafers consumes high energy exhausted in high temperature processes [1]. Thin film technology reduces the energy involved in these high temperature processes, and thus reduces the production costs.

There are many types of PV thin films, as shown in Fig. 1, which can be classified according to their efficiencies. Much of current research is focused on bringing down the cost of photovoltaic electricity by increasing the efficiency (generation of more electricity per incident solar power unit "watt/watt") and decreasing the cost of the solar cells per generated unit of power. These thin films are deposited, as single layers or multilayers, by complicated and expensive methods based on sputtering and vapour deposition. For example, silicon thin films are mainly deposited by plasma-enhanced chemical vapour deposition (PE-CVD) from silane gas [4]. Another example, copper indium gallium selenide (CIGS) thin films have been grown by physical vapour deposition (PVD) in a three-stage co-evaporation process. In this process In, Ga and Se are evaporated in the first step; it is followed by Cu and Se co-evaporation in the second step; and the last step is terminated by evaporation of In, Ga and Se again [5].

In general, PV thin films can be deposited by a large range of expensive and complicated techniques including pulsed laser deposition, sputtering, e-beam evaporation, chemical vapour deposition (CVD), physical vapour deposition (PVD), molecular beam epitaxy and spray pyrolysis [6]. Solution methods include sol-gel synthesis [7], chemical solution deposition [8] and electrodeposition [3,9,10] can also be used for the synthesis of PV thin films. Electrochemical synthesis of the PV thin films is of great interest and is superior over all aforementioned techniques. In addition to significantly lower

cost and being easily scaled up, electrodeposition technique gives the possibility to deposit elements, alloys and compounds with versatile compositions, microstructures and properties [11].

Some of semiconducting films such as gallium (Ga) [12], zinc oxide (ZnO) [13], and chalcopyrite (Cu(In,Al)Se₂) [14] can be electrodeposited from aqueous solutions. However, ionic liquids are superior to aqueous solutions for at least two properties. On the one hand, the electrochemical windows of ionic liquids are much wider so that side reaction during electrodeposition can easily be prevented. The gallium, for example, electrodeposited from aqueous solutions is often complicated by hydrogen evolution, which results in poor current efficiency rather than brittle deposits [15]. Pure ZnO layers free of metal hydroxide, normally deposited in aqueous solutions, can be electrodeposited in ionic liquids [9,16]. On the other hand, the temperature can be varied over a wide range leading to a great effect on the crystalline size of the deposit, which is of a particular importance for photoluminescence [9]. Moreover, ionic liquids give the possibility to electrodeposit the elements impossible to be deposited from aqueous solutions. Silicon and germanium can only be deposited from non-aqueous solutions.

Although the successful electrodeposition of reactive semiconductors from ionic liquids has been scientifically issued, standard industrial procedures have not yet been established. The electrodeposition process and handling of chemicals must be performed inside an inert gas-filled glove box. Thus, the importance of a novel approach, invent by Bakkar & Neubert [17,18], that aims at the introduction of a breakthrough technology with the potential to transform the electrodeposition of reactive metals and semiconductors in ionic liquids from the laboratory experimentation to be applicable in industry. Electrodeposition of reactive elements from ionic liquids has been, for the first time, conducted successfully in air [19]. The procedure of this novel method will be demonstrated in section 4 below.

The present paper focuses on the synthesis of semiconductive thin films utilized in PV cells via electrodeposition in different types of ionic liquids, which are demonstrated in the next section. This technique is adoptive because some elements (e.g. Si and Ge) could not be deposited from aqueous solutions. Also, other semiconductive thin films, even are deposited in aqueous solutions, can be deposited with versatile novel properties in ionic liquids.

2. Background

Electrodeposition of semiconductor films in aqueous solutions is limited by hydrogen evolution. Instead, ionic liquids are superior electrolytes for electrochemical deposition of semiconductor films with versatile microstructures and properties. Because electrodeposition studies in ionic liquids are relatively recent and not yet as well-known as in aqueous solutions, we give below explanations of some particular questions may be asked in this subject.

What are ionic liquids and what is the motivation to use in electrochemical deposition?

Ionic liquids are— as the name indicates— composed solely of ions. They are distinguished from classical molten salts as systems with melting points below 100°C [20]. Many of the most interesting systems have melting points around or below the room temperature. In contrast to the aqueous solutions, ionic liquids have wide *electrochemical windows*, and the problems associated with hydrogen evolution can be eliminated.

The electrochemical window determines the electrochemical stability of an electrolyte, which is a key criterion for its application in the electrochemical deposition of metals and semiconductors. The electrochemical window of an electrolyte is defined as the voltage range between which the electrolyte does neither get oxidized nor reduced [21]. The electrochemical window of water is only about 1.2 V, and subsequently the electrodeposition of many elements and compounds is restricted by hydrogen evolution. Therefore, aqueous-based solutions limit the electrodeposition industry to Cr, Zn, Cu, Ni, Ag, Au, Sn and Pb. Also, some of these solutions contain toxic and corrosive chemicals. Ionic liquids have significantly larger electrochemical windows, up to 6 V. Consequently, these liquids have enabled to deposit reactive elements, such as Al, Ta, Si, Ge, and their alloys, impossible to be deposited in aqueous solutions. Ionic liquids exhibit good electrical conductivity, low volatility and very low to no toxicity [20-23].

Ionic liquid systems can be historically classified into four generations which indicates the order of

which each became explored. At present there is concurrent research into all four generations.

First generation. Chloroaluminate ionic liquid systems based on AlCl_3 and different organic salts like for example 1-ethylpyridinium chloride or 1-ethyl-3-methylimidazoliumchloride ($[\text{EMIm}]^+\text{Cl}^-$) were discovered in 1951 by Hurley and Wier [24], and developed in 1970s by Osteryoung et al [25,26] and in 1980s by Hussey et al [27-29] for electrochemical deposition of aluminium. Although these ILs are extremely hygroscopic, they are still today the best understood systems.

Second generation. Systems based on organic cations like in first generation and tetrafluoroborate $[\text{BF}_4]^-$, hexafluorophosphate $[\text{PF}_6]^-$, or hexafluoroantimonate $[\text{SbF}_6]^-$ as anion. These systems, synthesized by Wilkes & Zaworotko in 1992 [30], can be regarded as the first air and water stable ionic liquids. Nevertheless, their physicochemical properties are changed by exposure to moisture for long time due to slow hydrolysis of $[\text{BF}_4]^-$ and $[\text{PF}_6]^-$ liberating HF [31].

Third generation. Systems based on the aforementioned organic cations and different hydrolysis-resistant anions like for example tosylate, bis-(trifluoromethylsulfonyl)imide and others were developed in 1996 [20,32]. These systems are classified as hydrophobic ionic liquids and have large electrochemical windows, up to 6 V.

Fourth generation. Deep eutectic systems formed by the reaction of amine salt such as choline chloride (ChCl), with a metallic halide such as ZnCl_2 , with a hydrated salt such as $\text{CrCl}_3 \cdot 6\text{H}_2\text{O}$, or with hydrogen bonders such as urea were invented by Abbott et al [33-35]. These liquids are stable in air and water. Bakkar & Neubert [36] determined high water contents, up to few percentages, in some examples thereof. This, in addition to their relatively narrower electrochemical windows, may hinder their use for electrodeposition of very reactive metals and semiconductors. However, their low cost and easy preparation enable their use in large-scale applications for deposition of less active metals and semiconductors [37].

It is worth noting that the above groups can be classified according to their sensitivity to water, thereby indicating higher air and water stability increasing from the first generation to the fourth generation.

Is the electrodeposition of reactive metals and semiconductors possible in air?

Air and water stable ionic liquids can be handled and processed in the ambient atmosphere. Nevertheless, reactive metals and semiconductors till today, apart from our pioneered method [17-19], can not be deposited outside inert-gas filled glove box. Cation bearing salts, for example AlCl_3 , SiCl_4 , etc., are strongly hygroscopic and absorb water rapidly and quantitatively, and consequently HCl with different reactive halides form in the liquid. Kinetic and thermodynamic reasons associated with the complications of reactive halides seem to prevent an electrodeposition [31].

3. State of the art

This section reviews the update advancement in electrodeposition of silicon (Si) and gallium arsenide (GaAs) semiconductive thin films. The Si and GaAs PV thin films are widely researched. Si thin films is already used in synthesis of practical PV cells. GaAs films showed higher energy efficiency. These films- revealed in Fig. (1)- are synthesized by other approaches, apart from electrodeposition, mostly by high vacuum techniques. The electrodeposition of numerous semiconductors has been demonstrated by old and recent review papers and books (e.g. Refs. [10,11,38-41]). This section focuses on the development of the electrodeposition of Si and GaAs thin films, with highlighting the electrodeposition in ionic liquids.

3.1. Silicon

Silicon is the most abundant element in the earth's crust. Silicon wafers were used in the conventional PV cells. Silicon thin-film PV cells were developed after Si films had been deposited by chemical vapor deposition (CVD) techniques. Controlling CVD parameters yielded polycrystalline, nanocrystalline, and amorphous Si films [4]. National Renewable Energy Laboratory (NREL) reported an energy conversion efficiency of about 21.2 %, as maximum laboratory efficiency, for Si thin-film cells (See Fig. 1).

Electrodeposition of Si must run in non-aqueous electrolytes because of its highly negative reduction potential and the high reactivity of most of its compounds to water. Schlesinger et al [11] presented a survey of several papers on Si electrodeposition from molten salts at elevated temperatures. Si

deposited from molten salts is not expected to be utilized in PV cells because of consumption of large quantities of energy required to keep the electrolytes molten at high temperatures.

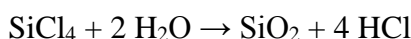
Organic solvents are reported as inexpensive electrolytes for Si electrodeposition [42]. Examples of these organic solvents which have been used as non-aqueous solvents for silicon halides since 1980s are: propylene carbonate [43], acetonitrile [44], and tetrahydrofuran [45]. Best results were obtained by Agrawal & Austin [43] using propylene carbonate as a solvent for SiHCl₃. Tetrabutylammonium chloride was added as a supporting electrolyte. Amorphous silicon was electrodeposited at temperatures of 35-145°C [43]. Thicker Si films were deposited with increasing the Si concentration in the electrolyte and increasing temperature. Annealing at 470 °C as a post heat treatment released bonded hydrogen in the Si films. Amorphous Si films synthesized by this approach were reported as a possible inexpensive material for PV cell applications [11,43].

Nishimura & Fukunaka [46] electrodeposited amorphous silicon from SiCl₄ dissolved in propylene carbonate containing tetrabutylammonium chloride. Porous Si film was deposited with a thickness of 50 µm, and oxidized when exposed to air. In similarity to another study by Nicholson [47], it was postulated that the oxidation is due to the porous morphology of Si deposits. This paper [46] can be distinguished with studying the electrodeposition mechanism in terms of chronopotentiometry and chronoamperometry along with microstructure observations. Also, cyclic voltammetry showed that Si deposition was accompanied by reductive decomposition of the electrolyte ingredients. However, there was no development in the Si film deposited in comparison with previous studies.

Munisamy & Bard [48] described electrodeposition of Si in a helium-filled glove box from SiCl₄ and SiHCl₃ dissolved in acetonitrile and tetrahydrofuran, respectively; Tetrabutylammonium chloride was added to the two electrolytes. Amorphous Si films were deposited but contained C, N, O and Cl impurities and oxidized on contact with air. Annealing of amorphous Si films in argon atmosphere reduced impurities concentrations and led to partial crystallization. Eventually, the electrochemical techniques used in the study postulated a mechanism for nucleation and growth of Si. However, the Si films deposited did not show the desired photoelectrochemical behaviour.

Bechelany et al [49] studied electrodeposition of amorphous silicon from SiCl₄ dissolved in two non-oxygenated organic solvents, acetonitrile and dichloromethane, under argon atmosphere. In both solvents, tetraethylammonium chloride was used as a supporting electrolyte. A highly dense Si film was deposited using acetonitrile solvent. Heat treatment in hydrogen atmosphere followed by HF etching increased the stability of Si deposits. However, the cyclic voltammetry measurements, included in the study [49], demonstrated that Si reduction takes place simultaneously with dissociation of tetraethylammonium chloride. Vichery et al [50] reported on stabilization of amorphous Si films, electrodeposited in tetrahydrofuran, against oxidation. Electrodeposited samples were successively annealed in argon atmosphere in the same glove box used for the electrodeposition. Stabilization of Si films has been achieved through the breaking of Si-H bonds and formation of Si-Si bonds, leading to higher oxidation resistance of Si films, even exposed to air for prolonged times [50]. Recently, Link et al [51] investigated the electrodeposition of Si from sulfolane-based electrolyte. Thin Si layers were deposited but with incorporation of organic contaminants.

Finally, it can be stated that Si electrodeposition in organic solvents is not a straightforward process. It has to be performed in inert gas-filled glove box with using anhydrous and pure chemicals. Traces of water, if found in either the solvent or the supporting electrolyte, will react with silicon halide (eg. SiCl₄) according to the reaction:



Consequences of the above reaction are: - Si is deposited at more negative potentials beyond the background of water reduction, - a decrease in current efficiency, and - deposition of Si oxide instead of elemental Si. Moreover, the organic solvents-based electrolytes have narrow electrochemical windows, and dissociation of organic solvent and/or supporting electrolyte, occurs along with Si deposition [46,49]. The gas evolution was actually observed at more negative potentials [46,49]. In the same context, as a consequence, impurities of C, N, O and Cl are co-deposited with silicon [46-50].

Ionic liquids are always superior alternative to organic solvents for electrodeposition of reactive elements. In the last three decades, the ionic liquids prevailed upon the research on Si electrodeposition. Katayama et al [52] electrodeposited Si from 1-ethyl-3-methylimidazolium hexafluorosilicate at 90 °C. However, the film deposited oxidized by moisture and air to form SiO₂. Endres and co-workers [53,54] succeeded to deposit Si film from SiCl₄ dissolved in one of the third generation of ionic liquids, namely 1-butyl-1-methylpyrrolidinium bis(trifluoromethylsulfonyl)amide ([BMP]Tf₂N). Although the ionic liquid used is categorized as an air and water-stable ionic liquid, the electrolyte was dried to water content below 1 ppm and the electrodeposition was processed in dry inert gas. The Si film deposited had nanostructure morphology with a band gap of 1.1±0.2 eV. The maximum thickness of Si film was 100 nm on highly oriented pyrolytic graphite (HOPG) substrate [53] and 1000 nm on gold substrate [53]. The same hydrophobic ionic liquid ([BMP]Tf₂N), having a wide electrochemical window up to 6 V, was again researched by Endres group [55] to prove reproducibility of nanostructure Si electrodeposition onto gold substrate. Furthermore, Si_xGe_{1-x} films were electrodeposited at room temperature when GeCl₄ was dissolved into the electrolyte.

Less successful trials were reported by Martinez et al [56] on Si electrodeposition from the oxygen and water-stable N-butyl-N-methyl-pyrrolidinium bis(trifluoromethyl-sulfonyl)amide ionic liquid dissolving SiCl₄ or SiBr₄. Reactive, rough and porous Si films were deposited in slow rates on Al and Ni substrates. Park et al [57] found that the cathodic reduction of Si in the ionic liquid ([BMP]Tf₂N) is strongly dependent on the working electrode material. Elemental Si thin film was deposited on Au electrode. Komadina et al [58] investigated electrodeposition of Si from ionic liquid trimethyl-n-hexyl ammonium bis-(trifluoromethylsulfonyl) imide (TMHATFSI). Si film with non-uniform thickness of 75-100 nm was deposited with high contents of C, F, and N. The Si film oxidized to SiO₂ upon exposure to air. Endres group [59] reported a comparison study on Si electrodeposition in three hydrophobic ionic liquids, namely [Py_{1,4}]TfO, [Py_{1,4}]TFSA, and [Py_{1,4}]FAP, in which only the anion was varied. The results showed that the anion type has a slight influence on the deposition process. The silicon films deposited from the three ionic liquids were amorphous with a band gap of 1.1 eV [59].

Zhang et al [60] electrodeposited crystalline Si from SiCl₄ dissolved in the ionic liquid [N₄₄₄₁][TFSI] at 100 °C onto Ga electrode. The growth mechanism of Si onto liquid-metal Ga was proposed. Si layers were also deposited from SiCl₄ in the ionic liquid ([BMP][TFSI]), and the effect of micro-defects on the frequency and damping response was in situ observed during deposition [61]. Recently, Thomas et al [62] electrodeposited Si from SiCl₄ in the presence of the ionic liquid Py_{1,4}[TFSI]. The electrodeposition parameters were optimized to grow Si film with appropriate structural properties.

Electrodeposition of Si in ionic liquids is less successful than electrodeposition of other reactive elements like Al. Very high hygroscopic nature of Si precursor (SiCl₄ or SiBr₄) necessitates performing the deposition in dry inert gas atmosphere with O₂ concentration ≤ 1 ppm. The electrolyte has to be vacuum-dried at 100 °C for long times. Reactants used have to be anhydrous and highly pure. Although these precautions were applied in successful studies mentioned above, the maximum thickness of continuous Si film deposited was about 1 μm. The high electrical resistivity of Si at low temperatures complicates transfer of electrons through the deposited film and thus hinders further electrodeposition. Also, Si films in most cases were active and oxidized by air. Furthermore, the studies did not prove the reproducibility of uniform, dense and easily scalable Si films. In addition, there is no research to date dealt with the photoactivity of Si films deposited from ionic liquids.

Limited success in Si electrodeposition from ionic liquids makes returning of research on molten salts in 2010s is reasonable. Bieber et al [63,64] electrodeposited Si films on Ag, Si, and C substrates from Na₂SiF₆ dissolved in molten mixture of NaF-KF (40-60 mol%) under argon atmosphere in the temperature range 820-950 °C. The Si films were smoother and had higher purity up to 99 wt.% with increasing the temperature and decreasing the current density [64]. Photoactive crystalline Si film with higher purity (99.9 wt.%) was deposited from SiO₂ nanoparticles in CaCl₂ molten salt at 850 °C by Cho et al [65]. Lower temperature molten salt (600 °C) of LiF-NaF-Kf was used by Sakanaka & Goto [66] to deposit crystalline Si film on Ag electrode from SiO₂. Recently, Zou et al [67,68]

reported on successful electrodeposition of robust Si thin films from silicate/silicon oxide-based molten salt.

In conclusion, Si film deposition by electrochemical routes is still less competitive to its synthesis via vacuum deposition processes. Until now, there is concurrent research on Si electrodeposition from molten salts, organic solvents, and ionic liquids. Ionic liquids are distinguished by their low temperature, wide electrochemical window, and high stability. Furthermore, Ionic liquids can be used for electrodeposition outside glove box after innovation discussed in section 4. Thus, the only challenge for this technology will be how to overcome the high resistivity of deposited Si layer at room temperature, which limits the film thickness. Facilitating the electrodeposition procedure from ionic liquids, in addition to the quest for reducing the cost of synthesis of PV silicon, may encourage researchers to develop untraditional ideas to increase the thickness of Si films deposited and to improve their photovoltaic grades.

3.2. Gallium Arsenide

Gallium arsenide (GaAs) is a well-known semiconducting compound possessing optical band gap of about 1.5 eV at room temperature. Due to having a band gap energy close to the solar spectrum value in addition to high mobility of its charge carriers, GaAs was reported to have a high energy efficiency in the range of 23-26 % [69]. Recent reports by NREL reported energy efficiency up to ~ 30 % for GaAs thin films (Fig. 1). In 1987, Murali et al [69] reviewed and described the techniques used for fabrication of GaAs thin films, including chemical vapour deposition (CVD), molecular beam epitaxy (MBE), vapour phase epitaxy (VPE), liquid phase epitaxy (LPE), hot wall epitaxy (HWE), and electrodeposition.

Electrodeposition of GaAs has advantages of easy control of the film thickness, microstructure, and composition through varying the current density and the electrolyte composition and temperature. In addition, electrodeposition of GaAs avoids the use of dangerous volatile materials used in the other techniques, such as AsCl_3 and AsH_3 [11]. The first trials for electrodeposition of GaAs were at 750 °C from molten salt of $\text{B}_2\text{O}_3\text{-NaF-Ga}_2\text{O}_3\text{-NaAsO}_2$ [70] and at 300 °C from molten salt of AsI-KGaCl_4 [71].

Starting conditions of trials for electrodeposition of GaAs from aqueous solutions were revealed by Chandara et al [72-74] based on Pourbaix diagrams of Ga and As and polarization studies on aqueous solution of HCl dissolving Ga and As_2O_3 . Quasi-stoichiometric GaAs films were deposited in the pH range 0.3-0.7 at potential of - 0.7 V_(vs. NHE) [74].

Mahalingam et al [75] studied the electrodeposition of GaAs from acidic aqueous solution containing GaCl_3 and As_2O_3 . Layers of GaAs were successfully deposited within a narrow window of electrodeposition conditions; namely: deposition potential = - 0.7 ± 0.1 mV, pH = 2.0 ± 0.1, and temperature = 60 °C. Post annealing of the GaAs film improved its crystallinity. However, the authors neither disclosed the complete composition of the electrolyte, nor measured the thickness of the films deposited. The deposited GaAs film revealed an efficiency of only 0.81 %. The authors expected that the efficiency can be improved through optimization of the post annealing treatment and surface modification [75]. However, the final results of this relatively recent study [75] did not differ from that reported about two decades ago by Gao et al [76]; in which GaAs deposited from acidic solution on SnO_2 -coated glass recorded an efficiency of 0.51%. Gallium arsenide films prepared by electrodeposition from alkaline aqueous solutions were pulverulent and having relatively poor adhesion to the substrate [77].

Lajnef et al [78] succeeded to electrodeposit GaAs films with maximum thickness of 340 nm on porous silicon substrate from acidic solution with pH 1. The acidic electrolyte was composed of concentrated HCl dissolving equimolar amounts of Ga and As_2O_5 . The crystallinity of GaAs film increased with increasing the deposition current density and with annealing at 300 °C for 1 h in nitrogen atmosphere. The obtained film was n-type semiconductor. Kozlov et al [79] synthesized GaAs films by heat treatment of individually deposited Ga and As layers. The single layers were electrodeposited from alkaline Ga and acidic As solutions. Post heating for 2 h at 190 °C formed GaAs phase revealed by XRD pattern.

Ionic liquids were used, for the first time, for electrodeposition of GaAs by Wicelinski & Gale [80]. A Lewis acidic chloroaluminate ionic liquid composed of AlCl_3 and 1-butylpyridinium chloride was used to dissolve GaCl_3 and AsCl_3 at 40 °C. GaAs film was potentiostatically deposited. The film was contaminated with Al, which is co-deposited through underpotential phenomenon. Another approach by Carpenter & Verbrugge [81,82] avoided Al contamination using a chlorogalate ionic liquid composed of GaCl_3 and 1-methyl-3-ethylimidazolium chloride, in which AsCl_3 was dissolved. GaAs film was deposited at room temperature and then thermally annealed. However, although new ionic liquids have been developed and researched for deposition of many semiconductors, GaAs electrodeposition has not yet been experimented in these new ionic liquids.

Recently, Fahrenkrug et al [83] presented a new approach for synthesis of crystalline GaAs, through electrodeposition of As from an alkaline aqueous solution onto a liquid gallium electrode at temperatures above 80 °C. The as-deposited film resulted was solid crystalline GaAs. The liquid gallium served simultaneously as a cathodic electrode for crystal growth of As and as a co-reactant alloying element for the synthesis of polycrystalline GaAs semiconductor.

4. A novel approach

Electrodeposition of semiconductors in ionic liquids has overcome upon the challenge of electrodeposition of reactive elements impossible to be deposited in aqueous solutions. Also, ionic liquids have enabled electrodeposition of semiconductors depositable in aqueous solutions but with more better microstructure properties. However, scaling-up of semiconductors electrodeposition in ionic liquids has not yet been established due to the difficulties associated with the electrodeposition in closed system filled with inert gas.

We suggest a novel approach for electrodeposition of semiconductive thin films from ionic liquids in open-to-air conditions [18,18]. Our pioneer method was applied for electrodeposition of aluminum in highly hygroscopic ionic liquid outside glove box [19]. This new approach has been also approved in various ionic liquids by other authors [84,85]. The new method includes preparation of ionic liquid electrolyte inside an inert gas-filled glove box and covering the IL electrolyte with a non-water-absorbable hydrocarbon layer of decane that is stable and has no reaction with the ionic liquid. Thus, insulating of the electrolyte from air enables conducting the electrodeposition procedure outside the glove box in ambient atmosphere. More details for application of this novel approach for electrodeposition of semiconductors from ionic liquids in ambient atmosphere are illustrated in our current research under publication [86]. Fig. 2 shows a schematic diagram illustrating potentiostatic electrodeposition of Ga in the ionic liquid AlCl_3 /1-ethyl-3-methylimidazolium chloride (EMIC) under ambient atmosphere after protecting the ionic liquid with a hydrocarbon layer of decane ($\text{C}_{10}\text{H}_{22}$) [86].

Summary

Electrodeposition is a superior technique for synthesis of semiconductive PV thin films. It overcomes the complications involved in high vacuum techniques used at present. Moreover, the electrodeposition technique is of lower price with easy scalability, and gives the possibility to deposit semiconductors with desired microstructure and appropriate properties.

We presented a literature survey on synthesis of two PV thin films with higher energy efficiency, namely Si and GaAs, via electrodeposition in different types of non-aqueous electrolytes particularly ionic liquids. Electrodeposition in ionic liquids is adoptive because some elements (e.g. Si and Ge) could not be deposited in aqueous solutions. Also, other semiconductive thin films, even are deposited in aqueous solutions, can be deposited with better and novel properties in ionic liquids.

A suggested novel approach has been demonstrated for electrodeposition of semiconductive thin films from ionic liquids in open-to-air conditions after covering the ionic liquid with an inert hydrocarbon layer of decane. The electrodeposition of semiconductive thin films in ionic liquids under ambient atmosphere has the potential to transform the electrochemical synthesis of PV thin films from the laboratory scale to the industrial procedure.

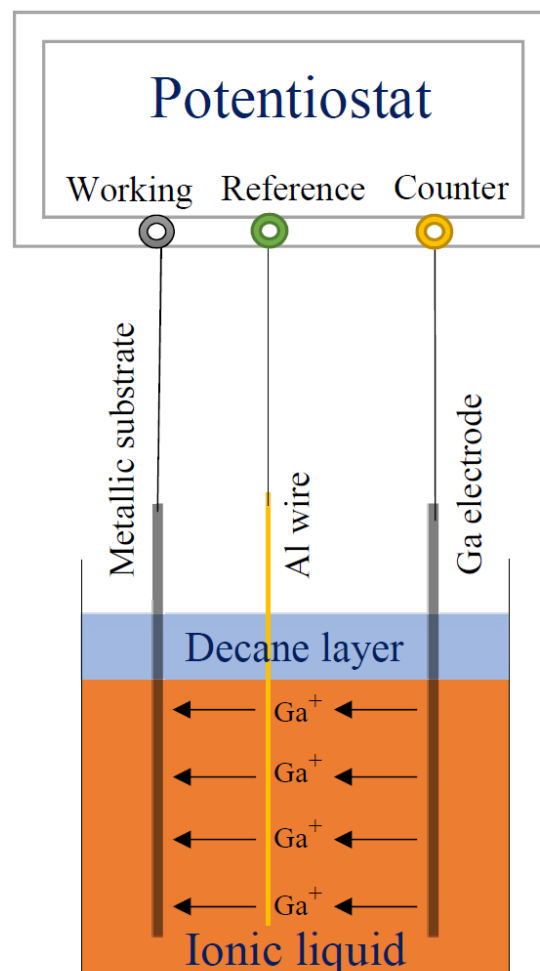


Fig. 2: A schematic diagram illustrating potentiostatic electrodeposition of Ga from EMIC ionic liquid in a three-electrode cell under ambient atmosphere after protecting the ionic liquid with a decane layer [86].

References

- [1] Information on http://en.wikipedia.org/wiki/Solar_cell, 30.05.2019.
- [2] F. Endres, *ChemPhysChem* 3, 2 (2002) 144-154.
- [3] W.-L. Liu, S.-H. Hsieh, W.-J. Chen, P.-I. Wei, and J.-H. Lee, *Int. J. Minerals, Metallurgy & Materials* 16, 1 (2009) 101–107.
- [4] R.W. Collins, A.S. Ferlauto, G.M. Ferreira, C. Chen, J. Koh, R.J. Koval, Y. Lee, J.M. Pearce, C. R. Wronski, *Solar Energy Materials and Solar Cells*, 78(1-4), (2003) 143.
- [5] Information on <http://www.nrel.gov> by National Renewable Energy Laboratory (NREL), USA, 30.05.2019.
- [6] M. Ohring, D. Gall, S.P. Baker, *Materials Science Thin Films : Deposition and structure*, 3rd edition, Academic Press, 2014.
- [7] S.S. Alias, A.A. Mohamad, *Synthesis of Zinc Oxide by Sol–Gel Method for Photoelectrochemical Cells*, *Springer Briefs in Materials*, 2014.
- [8] G. Hodes, *Chemical solution deposition of semiconductor films*, 1st Edition, CRC Press, 2002.
- [9] R. Jayakrishnan, G. Hodes, *Thin Solid Films* 440 (2003) 19-25.
- [10] D. Lincot, *Thin Solid Films* 478 (2005) 40-48.
- [11] T.E. Schlesinger, K. Rajeshwar, N.R.D. Tacconi, *Electrodeposition of semiconductors*, in Ed. M. Schlesinger, M. Paunovic, *Modern Electroplating*, 5th Edition, John Wiley & Sons, Inc. 2010, 383-411.
- [12] D.O. Flamini, S.B. Saidman, J.B. Bessone, *J. Appl. Electrochem.* 37 (2007) 467-471.
- [13] A.B. Moghaddam, T.N.J. Badraghi, M. Kazemzad, *Int. J. Electrochem. Sci.* 4 (2009) 247-257.

- [14] K.G. Deepa, N.L. Shruthi, M.A. Sunil, J. Nagaraju, Thin Solid Films 551 (2014) 1–7.
- [15] P.-Y. Chen, Y.-F. Lin, I.-W. Sun, J. Electrochem. Soc. 146 (1999) 3290-3294.
- [16] M. Harati, D. Love, W.M. Lau, Z. Ding, Materials Letters 89 (2012) 339–342.
- [17] A. Bakkar, V. Neubert, Deutsche Patent DE102011055911B3, 29.11.2012.
- [18] V. Neubert, A. Bakkar, European Patent EP2599896A2, 05.05.2013.
- [19] A. Bakkar, V. Neubert, Electrochem. Commun. 51 (2015) 113-116.
- [20] P. Wasserscheid, T. Welton, editors. Ionic Liquids in Synthesis. VCH-Wiley; 2002.
- [21] H. Ohno, editor. Electrochemical Aspects of Ionic Liquids. New Jersey: John Wiley; 2005.
- [22] T. Welton, Chemical Reviews 99 (1999) 2071-2084.
- [23] K.R. Seddon, j. Chem. Technol. Biotechnol. 68 (1997) 351-356.
- [24] F.H. Hurley, T.P. Wier, J. Electrochem. Soc. 98 (1951) 207-212.
- [25] H.L. Chum, V.R. Koch, L.L. Miller, R.A. Osteryoung, J. Am. Chem. Soc. 97 (1975) 3264-3265.
- [26] J. Robinson, R.A. Osteryoung, J. Am. Chem. Soc. 101 (1979) 323-327.
- [27] J.S. Wilkes, J.A. Levisky, R.A. Wilson, C.L. Hussey, Inorg. Chem. 21 (1982) 1263-1264.
- [28] C.L. Hussey, Adv. Molten Salt Chem. 5 (1983) 185.
- [29] D. Appleby, C.L. Hussey, K.R. Seddon, J.E. Turp, Nature 323 (1986) 614-616.
- [30] J.S. Wilkes, M.J. Zaworotko, *J. Chem. Soc. Chem. Comm.* (1992) 965-967.
- [31] F. Endres, Z. Phys. Chem. 218 (2004) 255-283.
- [32] P. Bonhote, A.P. Dias, N. Papageorgiou, K. Kalyanasundaram, M. Grätzel, Inorg. Chem. 35 (1996) 1168-1178.
- [33] A.P. Abbot, G. Capper, D.L. Davies, R. Rasheed, V. Tambyrajah, U.K. Patent PCT/GB00/01090, 1999.
- [34] A.P. Abbot, G. Capper, D.L. Davies, R. Rasheed, V. Tambyrajah, U.K. Patent PCT/GB01/04300, 2000.
- [35] A.P. Abbot, G. Capper, D.L. Davies, R. Rasheed, V. Tambyrajah, U.K. Patent PCT/GB01/04306, 2000.
- [36] A. Bakkar, V. Neubert, Electrochem. Commun. 9 (2007) 2428-2435.
- [37] A.P. Abbott, G. Frisch, K.S. Ryder, Annual Review Matter. Res. 43 (2013) 335-338.
- [38] R.C. DeMattei, R.S. Feigelson, Electrochemical Deposition of Semiconductors. In: McHardy J., Ludeig F. (eds.) Electrochemistry of Semiconductors and Electronics. New Jersey: Noyes Publications; 1992. p1-52.
- [39] R.K. Pandey, S.N. Sahu, S. Chandra, Handbook of Semiconductor Electrodeposition. New Yourk: Marcel Dekker; 1996.
- [40] N. Borisenko, S. Zein El Abedin, F. Endres, Electrodeposition of Semiconductors in Ionic Liquids. In F.Endress, D.MacFarlane, A. Abbott, Electrodeposition from Ionic Liquids. Weinheim: Wiley; 2008. p147-166.
- [41] L.M. Peter, Electrochem. Commun. 50 (2015) 88-92.
- [42] B.D. Falola, I.I. Suni, Current Opinion in Solid State and Materials Science 19 (2015) 77-84.
- [43] A.K. Agrawal, A.E. Austin, J. Electrochem. Soc. 128 (1981) 2292-2296.
- [44] C.H. Lee, F.A. Kroger, J. Electrochem. Soc. 129 (1982) 936-942.
- [45] J. Gobet, H. Tannenberger, J. Electrochem. Soc. 135 (1988) 109-112.
- [46] Y. Nishimura, Y. Fukunaka, Electrochim. Acta 53 (2007) 111-116.
- [47] J.P. Nicholson, J. Electrochem. Soc. 152, 12 (2005) C795-C802.
- [48] T. Munisamy, A.J. Bard, Electrochim. Acta 55 (2010) 3797-3803.
- [49] M. Bechelany, J. Elias, P. Brodard, J. Michler, L. Philippe, Thin solid films 520 (2012) 1895-1901.
- [50] C. Vichery, V. Le Nader, C. Frantz, Y. Zhang, J. Michler and L. Philippe, Phys.Chem.Chem.Phys 16 (2014) 22222-22228.

- [51] S. Link, S. Ivanov, A. Dimitrova, S. Krischok, A. Bund, *Electrochem. Commun.* 103 (2019) 7–11.
- [52] Y. Katayama, M. Yokomizo, T. Miura, T. Kishi, *Electrochemistry* 69 (2001) 834-836.
- [53] S.Z. El Abedin, N. Borissenko, F. Endres, *Electrochemistry Communications* 6 (2004) 510-514.
- [54] N. Borissenko, S.Z. El Abedin, F. Endres, *J. Phys. Chem. B* 110 (2006) 6250-6256.
- [55] R. Al-Salman, S.Z. El Abedin, F. Endres, *Phys. Chem. Chem. Phys.* 10 (2008) 4650-4657.
- [56] [A.M. Martineza](#), [K.S. Osen](#), [O.E. Kongsteina](#), [E. Sheridana](#), [A.G. Ulyashina](#), [G.M. Haarbergb](#), *ECS Transactions* 25, 27 (2010) 107-118.
- [57] J. Park, C.K. Lee, K. Kwon, H. Kim, *Int. J. Electrochem. Sci.* 8 (2013) 4206-4214.
- [58] J. Komadina, T. Akiyoshi, Y. Ishibashi, Y. Fukunaka, T. Homma, *Electrochim. Acta* 100 (2013) 236-241.
- [59] G. Pulletikurthi, A. Lahiri, T. Carstens, N. Borisenko, S. Z. El Abedin, F. Endres, *J. Solid State Electrochem.* 17 (2013) 2823-2832.
- [60] J. Zhang, S. Chen, H. Zhang, S. Zhang, X. Yao, Z. Shi, *RSC Adv.* 6 (2016) 12061–12067.
- [61] S. Ivanov, C. Vlaic, A. Bund, I. Efimov, *Electrochim. Acta* 219 (2016) 251–257.
- [62] S. Thomas, D. Kowalski, M. Molinari, J. Mallet, *Electrochim. Acta* 265 (2018) 166-174
- [63] A.L. Bieber, L. Massot, M. Gibilaro, L. Cassayre, P. Chamelot, P. Taxil, *Electrochim. Acta* 56 (2011) 5022-5027.
- [64] A.L. Bieber, L. Massot, M. Gibilaro, L. Cassayre, P. Taxil, P. Chamelot *Electrochimica Acta* 62 (2012) 282-289.
- [65] S.K. Cho, F.R.F. Fan, A.J. Bard. *Angew. Chem. Int. Ed.* 51 (2012) 12740-12744.
- [66] Y. Sakanaka, T. Goto, *Electrochim. Acta* 164 (2015) 139-142.
- [67] X. Zou, L. Ji, X. Yang, T. Lim, E.T. Yu, A.J. Bard, *J. Am. Chem. Soc.* 139 (2017) 16060-16063.
- [68] L. Ji, X. Zou, A.J. Bard, E.T. Yu, *IEEE* (2018) 0325-0327.
- [69] K.R. Murali, M. Jayachandran, N. Rangarajan, *Bull. Electrochem.* 3 (1987) 261-265.
- [70] R. C. DeMattei, D. Elwell and R.S. Feigelson, *J. Cryst. Growth* 43 (1978) 643-644.
- [71] I.G. Dioum, J. Vedel and B. Tremillion, *J. Electroanalytical Chem.* 139 (1982) 329-333.
- [72] S. Chandra, N. Khare, *Semicond. Sci. Technol.* 2, 4 (1987) 214-219.
- [73] S. Chandra, N. Khare, *Semicond. Sci. Technol.* 2, 4 (1987) 220-225.
- [74] S. Chandra, N. Khare, H.M. Upadhyaya, *Bull. Mater. Sci.* 10, 4 (1988) 323-332.
- [75] T. Mahalingam, S. Lee, H. Lim, H. Moon, Y.D. Kim, *Solar Energy Materials & Solar Cells* 90 (2006) 2456-2463.
- [76] Y. Gao, A. Han, Y. Lin, , Y. Zhao, J. Zhang, *J. Appl. Phys.* 75, 1 (1994) 549-552.
- [77] C. Gheorghies, L. Gheorghies, G. Fetecau, *J. Optoelectron. Adv. Mater.* 9 (2007) 2795-2798.
- [78] M. Lajnef, R. Chtourou, H. Ezzaouia, *Appl. Surf. Sci.* 256 (2010) 3058-3062.
- [79] V.M. Kozlov, B. Bozzini, L.P. Bicelli, *J. Alloys Comp.* 379 (2004) 209-215.
- [80] S.P. Wicelinski, R.J. Gale, in eds: M.-L. Saboungi, D.S. Newman, K. Johnson, D. Inman, *Fifth International Symposium on Molten Salts*, (PV 86-1), the Electrochemical Society Softbound Proceedings Series, 1986, Pennington, NJ, p. 144.
- [81] M.K. Carpenter, M.W. Verbrugge, *J. Electrochem. Soc.* 137 (1990) 123-129.
- [82] M.W. Verbrugge, M.K. Carpenter, *AIChE J.* 36 (1990) 1097-1106.
- [83] E. Fahrenkrug, J. Gu, S. Maldonado, *J. Am. Chem. Soc.* 135, 1 (2013) 330-339.
- [84] A.P. Abbott, R.C. Harris, Y.-T. Hsieh, K.S. Rydera, I.W. Sun, *Phys. Chem. Chem. Phys.* 16 (2014) 14675–14681.
- [85] Y. Hou, R. Li, J. Liang, *Appl. Surf. Sci.* 434 (2018) 918–921.
- [86] A. Bakkar, V. Neubert, *Electrodeposition of semiconductive thin films from ionic liquids in ambient atmosphere: Gallium from a chloroaluminate ionic liquid, under publication.*

23- Performance of a Two Stage Modified Air Heating HDH System

I. Toor^a, M. Faizan^b and M. A. Antar^c

Mechanical Engineering Department, KFUPM, Saudi Arabia

^ag201806480@kfupm.edu.sa, ^bg201806460@kfupm.edu.sa, ^cantar@kfupm.edu.sa

Abstract.

Humidification-Dehumidification Systems (HDH) are among thermal desalination systems characterized by low-grade energy requirements and ease to build and operate. Many layouts of the HDH system that were demonstrated lately include the modified air heated system that showed a thermodynamic superiority over the conventional air heated system. Moreover, improvements in system performance occur by incorporating certain modifications in the operating and design parameters. One such modification is through using multistage heating and humidification. This work aims at comparing various HDH systems with different number of heat addition/humidification options. Open-air cycle with single heater and single humidification unit is considered as a baseline for comparison sake. It is compared with modified HDH system with multiple heaters and humidification sections. Then, the study is extended to compare an open modified air heated HDH system with its closed air circuit counterpart. It is observed that modified system performs better than base line system in terms of Gained Output Ratio (GOR). However, when comparing open and closed modified air heated HDH systems, the closed system had better performance with a GOR of 2.1.

Keywords: Desalination, Humidification dehumidification, HDH, model, multistage.

Introduction

The effect of continuously increasing population and change in people's lifestyle, resources for pure consumable water become limited in addition to climate change are the reasons that accelerate the demand of pure water. The common methods for obtaining fresh water from saline water are membrane desalination and thermal desalination. These are very intensive energy techniques. That's why they need considerable improvement in many manners, especially in the area of energy consumptions for small to large scale production, specific area required for producing fresh water and durability of systems towards fouling and scaling due to high salinity of water.

The shortage of fresh water leads to desalinate the seawater. For this purpose, we always seek to produce fresh water not compromising the water quality and making it able to be produced on commercial and domestic level. There are many systems that can produce millions of gallons per day. However, the basic aim of this work to focus on energy efficiency. Evaporation of saline water by thermal energy followed by condensation of the vapor to fresh water, which is free from salt is a basic and useful method to obtain fresh water. Humidification dehumidification (HDH) systems are useful to produce fresh water for small to medium scale. There are many investigations carried out by researchers throughout the world to produce fresh water using limited resources. It is interesting to note that HDH systems do not require sophisticated technical skills or expertise and can operate using low-cost heat source (such as solar energy) for heating and humidification of air.

Literature Review

HDH systems are classified generally based on heating fluid (air, water or both). A second major classification is based on fluid streams that flow through open and/or closed loop system. Various combination that are tested to achieve maximum GOR as well as minimum specific area have been considered. The study of HDH system start from thermodynamics analysis of its constituents taking in to consideration energy and mass balance of each component or a

whole system. One of the advantages of the HDH desalination systems is that it is made of three different processes, represented by three different components; the humidifier, the dehumidifier and the heater. This allows to separately design each component for better system performance.

The review presented by Narayan et al. [1] summarizes different components performance. As a matter of fact, HDH has received considerable attention during the last two to three decades. Bourouni et al. [2] studies HDH systems to show their attractive technique to produce distilled water. This study showed the advantages related to easy installation, less initial and operating cost, flexibility in producing fresh water capacity, its simplicity, possibility against using low energy (low temperature operation) such as geothermal, solar energy, waste energy or cogeneration.

Ettouney [3] showed interesting features of HDH such as operating at low top temperature and the ability to produce freshwater on small scale, coupling with various energy sources, especially sustainable or renewable like solar and geothermal energy. This study investigated several layouts for HDH system characteristics with special attention to the dehumidification technique. Orfi et al. [4] developed a system that can also operate on solar energy to produce 40 liter of fresh water per day per square meter of solar collector surface.

Water heated HDH systems were investigated by several researchers such as Al-Hallaj et al. [5], Muller-Holst et al. [6], Al-Hallaj and Selman [7], Dai et. al.[8], Orfi et al. [4], Shaobo et al. [9], Aburub et al. [10], and Lawal et al. [11]amongmany others. On the other hand, air heated cycles (or both) were analyzed by Chafik et al. [12-14], Fath and Ghazy [15], Nafey et al. [16] and Yamali and Solmus [17,18] and Antar and El-Sharqawy [19].

It is important, however to state that a modified heated cycle has been first proposed by Narayan et al. [20] who showed thermodynamic superiority of this cycle over the conventional air heating cycle. The air heater is placed after the humidifier such that humid air is heated sensibly before it flows to the dehumidifier. Sharqawy et al. [21] provided guidelines to design a water heated cycle as well as a modified air heated cycle and showed the optimum mass flow rate ratio that may result in the best cycle GOR. They provide step-by-step design procedure for both cycles based on energy balance.

Maximum GOR is found by decreasing maximum water temperature or increasing inlet temperature of water to the dehumidifier (bottom temperature). However, in case of air heated HDH cycle, this maximum GOR leads to the requirement of higher system size. In other words, high initial cost.

Qasem et al. [22] extended this work for other top and bottom cycle temperature. Lately, Lawal et al. [23, 24] considered both water heated cycle and air heated HDH cycles operated by a heat pump and showed high values of GOR for the modified air heated cycle.

It is important to state that the modified air heated cycle has received little attention in spite of the fact that the thermodynamic analysis shows it has a potential as a promising layout of the HDH desalination system. This work is aimed at investigating the modified air heated HDH system with two stage humidification in order to load the air with more vapor such that more product can be condensed in the dehumidifier. To the best of the author knowledge, multi stage modified air heated systems have not been investigated in the literature.

Mathematical Model

Consider the two stage modified air heated HDH system shown in Fig 1, the mass and energy balance equations for various components are given as follows:

Dehumidifier

Mass balance:

$$m_w + m_a \cdot \omega_3 = m_w + m_a \cdot \omega_5 + m_d \quad (1)$$

$$m_d = m_a \cdot (\omega_3 - \omega_5) \quad (2)$$

Energy balance:

$$m_w \cdot h_{w,0} + m_a \cdot h_{a,4} = m_w \cdot h_{w,1} + m_a \cdot h_{a,5} + m_d \cdot h_d \quad (3)$$

$$m_w \cdot (h_{w,1} - h_{w,0}) + m_d \cdot h_d = m_a \cdot (h_{a,4} - h_{a,5}) \quad (4)$$

First Humidifier (Simple humidifier)

Mass balance:

$$\alpha \cdot m_w + m_a \cdot \omega_0 = m_b + m_a \cdot \omega_1 \quad (5)$$

$$\alpha \cdot m_w - m_b = m_a(\omega_1 - \omega_0) \quad (6)$$

Energy balance:

$$\alpha \cdot m_w \cdot h_{w,2} + m_a \cdot h_{a,0} = m_b \cdot h_{w,b} + m_a \cdot h_{a,1} \quad (7)$$

$$m_b \cdot h_{w,b} - \alpha \cdot m_w \cdot h_{w,2} = m_a \cdot (h_{a,0} - h_{a,1}) \quad (8)$$

Second Humidifier (Bubble column humidifier)

Mass balance:

$$(1 - \alpha) \cdot m_w + m_a \cdot \omega_1 = m_{b1} + m_a \cdot \omega_3 \quad (9)$$

$$(1 - \alpha) \cdot m_w - m_{b1} = m_a(\omega_3 - \omega_1) \quad (10)$$

Energy balance:

$$(1 - \alpha) \cdot m_w \cdot h_{w,2} + m_a \cdot h_{a,2} = m_{b1} \cdot h_{w,b1} + m_a \cdot h_{a,3} \quad (11)$$

$$m_{b1} \cdot h_{w,b1} - (1 - \alpha) \cdot m_w \cdot h_{w,2} = m_a \cdot (h_{a,2} - h_{a,3}) \quad (12)$$

Heaters:

Water Heater-1

$$Q_1 = m_w \cdot (h_{w,2} - h_{w,1}) \quad (13)$$

Air Heater-2

$$Q_2 = m_a \cdot (h_{a,2} - h_{a,1}) \quad (14)$$

Air Heater-3

$$Q_3 = m_a \cdot (h_{a,4} - h_{a,3}) \quad (15)$$

Effectiveness of dehumidifier:

$$\varepsilon_d = \frac{\Delta H}{\Delta H_{max}} = \max \left\langle \frac{m_a \cdot (h_{a,4} - h_{a,5})}{m_a \cdot (h_{a,4} - h_{ideal,Tw0})}, \frac{m_w \cdot (h_{w,1} - h_{w,0})}{m_w \cdot (h_{ideal,Ta4} - h_{w,0})} \right\rangle \quad (16)$$

Effectiveness of first humidifier:

$$\varepsilon_{h1} = \frac{\Delta H}{\Delta H_{max}} = \max \left\langle \frac{m_a \cdot (h_{a,1} - h_{a,0})}{m_a \cdot (h_{ideal,Tw2} - h_{a,0})}, \frac{\alpha \cdot m_w \cdot h_{w,2} - m_b \cdot h_{w,b}}{\alpha \cdot m_w \cdot h_{w,2} - m_b \cdot h_{ideal,Ta0}} \right\rangle \quad (17)$$

Effectiveness of second humidifier:

$$\varepsilon_{h2} = \frac{\Delta H}{\Delta H_{max}} = \max \left\langle \frac{m_a \cdot (h_{a,2} - h_{a,3})}{m_a \cdot (h_{a,2} - h_{ideal,Tw2})}, \frac{(1 - \alpha) \cdot m_w \cdot h_{w,2} - m_{b1} \cdot h_{w,b1}}{(1 - \alpha) \cdot m_w \cdot h_{w,2} - m_{b1} \cdot h_{ideal,Ta2}} \right\rangle \quad (18)$$

The current system is a two stage humidification one. Therefore, it is suitable to keep the air temperature leaving the humidifier high such that air maintains the ability to carry more water vapor. For this reason, a water heater is used to keep water temperature high enough so as not to cool the air in the humidifier. See Fig. 2. In this system, the air heaters are distributed such that a heater would be placed after each humidifier to sensibly heat humid air. The first humidifier is packed-bed whereas the second is a bubble column humidifier, this is interpreted in the value of the effectiveness given for both.

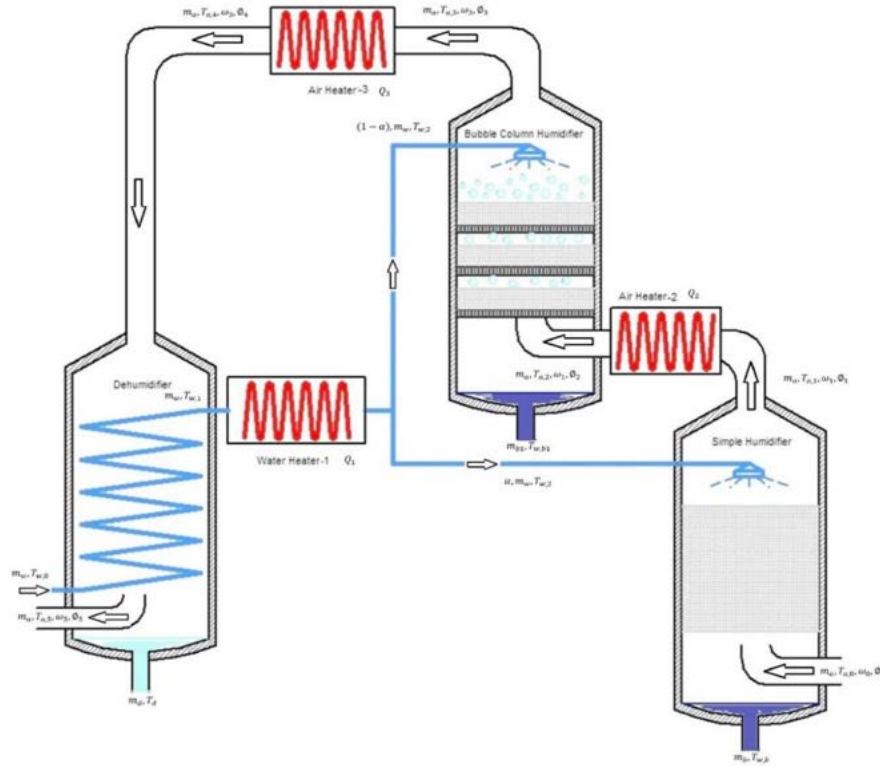


Figure 1: Schematic of the two-stage modified air heated HDH system

The following assumptions are considered while solving the governing equations using Engineering Equation Solver, EES:

- Inlet air has 50% saturated for open air cycle.
- Efficiency of simple humidifier, bubble column humidifier and dehumidifier set to 80%, 95% and 85% respectively.
- Inlet air and water temperature are 35⁰C and 28⁰C respectively.
- Air leaves first humidifier with saturation of 90% and after second humidifier its saturation increase up to 95%. Same 95% saturation when it blows out from dehumidifier.

Results and Discussion

It is important to state that the current analysis has been expanded to consider a single stage modified air heated system, a double stage modified air heated systems for both layouts of open air cycle (air to the first humidifier is obtained from ambient condition) and closed air cycle (where the air stream leaving the dehumidifier is admitted to the first humidifier). A comparison of the performance in terms of the Gained Output ratio (GOR) is shown in Table 1.

Table 1: Comparison of GOR between the systems considered in this study

| SYSTEM | No. OF HEATERS | GOR |
|---|----------------|------|
| Open Air Heated Cycle | 1 | 0.97 |
| Modified Open Air Heated Cycle | 3 | 1.4 |
| Modified Closed Air Heated Cycle | 3 | 2.2 |

Detailed performance analysis is presented in Figures 2,3 and 4. Fig. 2 shows the effect of the mass flow rate ratio on the system GOR for both open-air cycle (Fig. 2a) and closed air cycle (Fig. 2b). It is generally observed that there exists an optimum value of the GOR that corresponds to a certain mass flow rate ratio. This result is in-line with the analyses reported in the literature about an optimum mass flow rate ratio [21]. The reason is that in case of too small

water flowrate, air is still capable of absorbing more water vapor in the humidifier(s), thus increasing water flowrate for a given air flow rate increases productivity and hence GOR. On the other hand, too much water exceeds the saturation limit of air and results in higher energy consumption (Q_{in}) to heat the higher flowrate of water in the humidifier, thus decreasing the GOR.

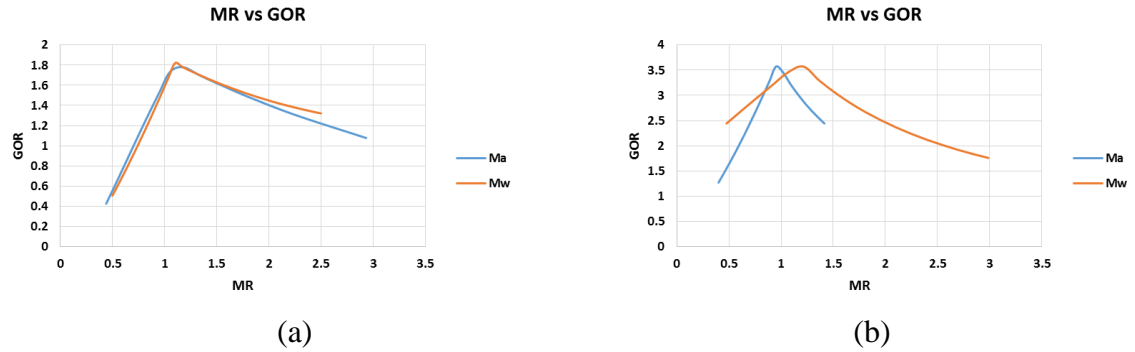


Fig 2.: Variation of GOR with inlet air and cooling water mass flow rates for modified HDH cycles with (a) open and (b) closed air flow paths

Figure 3 shows the change in GOR with Q_{in} for both cycles. It is observed that closed modified air heated cycle has a better performance than closed air cycle. This is partly due to the fact that the air rejected from the open-air system is close to saturation and is at higher temperature. This means that energy is needed to make the air saturated with water vapor and hot has not been recovered back by the system in case of an open air system. The closed system includes a sort of regeneration within the system where rejected air at high humidity and high temperature is again reused by the system. This not only improves the distillate mass flow rate, but also the system GOR. However, it needs to be highlighted that closed systems are relatively harder to fabricate and operate owing to the difficulties associated with making the system leak proof for air.

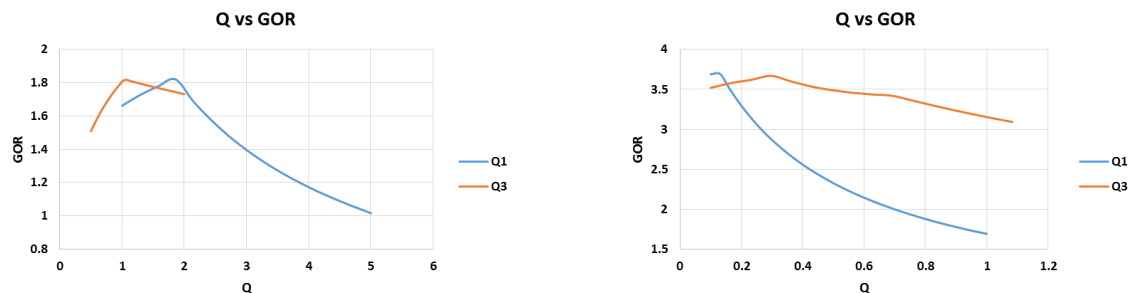


Fig.3: Variation of GOR with input heat to system for modified HDH cycles with (a) open and (b) closed air flow paths

Once again, it is observed that system performance (GOR) increases to a maximum value with varying air and water mass flow rates and then starts to decrease. This trend is similar but has different values for different heat input rates.

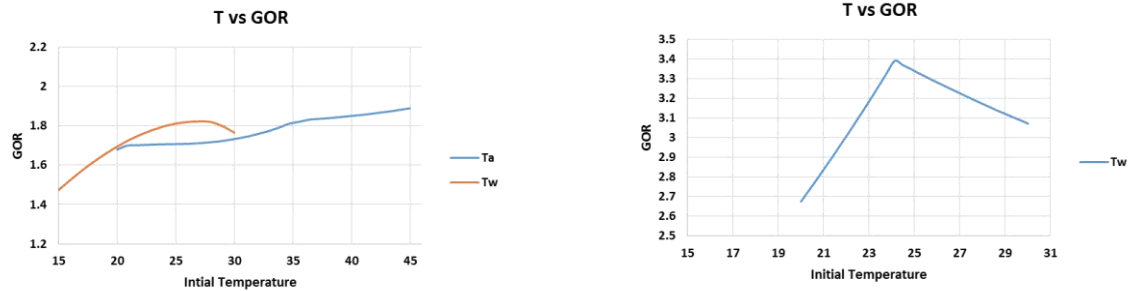


Fig. 4: Variation of GOR with inlet air and cooling water temperatures for modified HDH cycles with (a) open and (b) closed air-flow paths

We can see in Fig. 4 that increasing initial temperature increases the system GOR for the open air system since higher air temperature is associated with better humidification due to the ability of air to absorb more moisture as its temperature increases. It is not an independent parameter in case of closed air cycle since the outlet air temperature relies on both inlet water temperature and dehumidifier effectiveness. There appears to be an optimum water temperature as shown in Fig. 4b at which the GOR is maximized. Too low temperature would require additional heat to the cycle to reach top cycle temperature. On the other hand, too high temperature affects the condensation adversely since it results in reduced motive for condensing humid air in the humidifier due to lower temperature difference between hot humid air and colder water stream.

Acknowledgement: the authors acknowledge the support provided by KFUPM to carry out this work through project # IN151012.

Conclusion

In light of the analytical model carried out for a new two-stage modified air heated cycle with heated humidification water flow, the modified air heated cycle has a higher GOR compared to simple air heated Cycle. Moreover, Closed air modified cycle has higher GOR than open air cycle. Furthermore, there exists an optimum mass flowrate ratio where the GOR reaches a maximum value. Increasing the ambient air temperature improves the system performance for an open air cycle while an optimum inlet water temperature exists for closed air systems.

Nomenclature

| | | |
|----------------|------------------------------------|--------------------------------------|
| A | Surface area | m ² |
| sA | Specific area | m ² /kg · s ⁻¹ |
| h | Specific enthalpy | kJ/kg |
| m | Mass flow rate | kg/s |
| P _a | Ambient Pressure | kPa |
| Q | Heat input | kW |
| T | Temperature | K |
| U | Overall heat transfer co-efficient | kW/m ² · K |

Greek symbols

| | | |
|---|-------------------------|-------|
| α | Alpha (mass ratio) | |
| ω | Specific humidity ratio | kg/kg |
| ø | Relative humidity | kg/kg |
| ε | Effectiveness | |

Abbreviations

| | |
|------|---|
| GOR | Gain Output Ratio = $\dot{m}_a h_{fg}/Q_{in}$ |
| MR | Mass-flow-rate ratio = \dot{m}_w/\dot{m}_a |
| PR | Performance ratio |
| LMTD | Log mean temperature difference |

Subscripts

| | |
|-----|--|
| a | humid air |
| w | saline water |
| d | distilled water |
| b | rejected brine water |
| b1 | rejected brine water from bubble column humidifier |
| h1 | simple humidifier |
| h2 | bubble column humidifier |
| d | dehumidifier |
| lmd | litters-per-day |

References

- [1] G.P. Narayan, M.H. El-Sharqawy, E.K. Summers, J.H. Lienhard, S.M. Zubair and M.A. Antar, : Renewable and Sustainable Energy Reviews, Vol. 14 (4), (2010) p. 1187.
- [2] K. Bourouni, M. T. Chaibi, and L. Tadrist, *Desalination*, vol. 137(1-3), (2001), p. 167.
- [3] H. Ettouney, *Desalination*, Vol. 183(1-3), (2005), p. 341.
- [4] J. Orfi, M Laplante, H Marmouch, N Galanis, B. Benhamou, S. Ben Nasrallah, and C.T. Nguyen, *Desalination*, Vol. 168(1-3), (2004), p. 151.
- [5] S. Al-Hallaj, M.M. Farid, and A.R. Tamimi, *Desalination*, Vol. 120(3), (1998), p 273.
- [6] H. Muller-Holst, M. Engelhardt, and W. Scholkopf, *Desalination*, Vol 122, (1999), p. 255.
- [7] S. Al-Hallaj, and J.R. Selman, Middle East Desalination Research Center Report 98-BS-032b (2002).
- [8] Y.J. Dai, R. Z., Wang, and H.F. Zhang, *Desalination*, Vol. 142, (2002), pp. 107.
- [9] H. Shaobo, Y. Shengquan and H. Zhang, *Desalination*, Vol. 183 (1–3), (2005), p. 143.
- [10] A. Aburub, M. Aliyu, D. U. Lawal and M. A. Antar, *Int. Water Tech. Journal*, Vol. 7(3), (2017) p. 198.
- [11] Dahiru U. Lawal, Mohamed A. Antar, Abdelrahman Aburub and Mansur Aliyu, *Desalination and Water Treatment*, Vol. 104, (2018), p. 28.
- [12] E. Chafik, *Desalination*, Vol. 153, (2002), p. 25.
- [13] E. Chafik, *Desalination*, Vol. 156, (2003), p. 333.
- [14] E. Chafik, *Desalination*, Vol. 168, (2004), p. 55.
- [15] H.E.S. Fath and A. Ghazy, *Desalination*, Vol. 142, (2002), p. 119.
- [16] A.S. Nafey, H.E.F. Fath, S.O. El-Helaby, and A.M. Soliman, *Energy Conversion and Management*, Vol.45, (2004), p. 1243.
- [17] C. Yamali, and I. Solmus, *Desalination*, Vol. 205, (2007), p. 163.
- [18] C. Yamali, and I. Solmus, *Desalination*, Vol. 220(1-3), (2008), p. 538.
- [19] M. A. Antar and M. H. Sharqawy, *Desalination and water Treatment*, Vol. 51 (4-6), (2013) p. 837.
- [20] G.P. Narayan, M.H. El-Sharqawy, J.H. Lienhard V, and S.M. Zubair, *Desalination and Water Treatment*, Vol. 16, (2010), p. 339.
- [21] M. H. El-Sharqawy, M. A. Antar, S. M. Zubair and A. M. Al-Basheer, *Desalination*, Vol. 349 (2014), p. 10.
- [22] N. Qasem, B. Imteyaz and M. A. Antar, *Proc. of ASME 2016 IMECE*, November 11-17, 2016, Phoenix, AZ, USA.
- [23] Dahiru U. Lawal, Mohamed A. Antar, Atia Khalifa, Syed Zubair and Fahad Al-Sulaiman, *Energy Conversion and Management*, Vol. 161, (2018), p. 128.
- [24] Dahiru U. Lawal, Syed. M. Zubair, M. A. Antar, *Desalination*, Vol. 443, (2018), p. 11.

24-Theoretical study of influence of the geometric parameters on the performance of Solar Chimney Power Plants

I. MOUSA^{1*}, T. Mekhail¹, M. Sadik¹, M. Shaban¹

¹ Mechanical Power Engineering, Faculty of Energy Engineering, Aswan University, Egypt

*email: islammmohammed@energy.aswu.edu.eg

Abstract

The Solar Chimney Power Plant (SCPP) is a new technology for utilizing the free solar energy to generate electrical power, which needs to be investigated to enhance the performance. It consists of three simple components, chimney, collector and turbine. The objective of this study is to evaluate the performance of Solar Chimney Power Plants affected by varying the geometric parameters, such as chimney height, chimney diameter, collector diameter, and collector height. The geometric parameters are modeled theoretically, and an iterative technique is carried out to solve the performed mathematical model. The basic dimensions used in the model that the variable dimensions referred to them are for the Solar Chimney Power Plant installed in Aswan (Egypt). The study showed that the generated power increases considerably with the increase of the chimney height and slightly with the increase of the collector diameter. Thus, the same generated power can be obtained with different combinations of collector diameter and chimney height. Furthermore, the output power has a negative relationship with the collector height. In addition, the results found that the chimney diameter has an optimum range for the maximum output power. The Optimal geometric can be determined only by including the cost of the individual components (chimney, collector and mechanical parts) at a particular site.

Keywords: Solar chimney, Solar collector, Geometric parameters, SCPP

1. Introduction

The rapid depletion of conventional energy resources and increasing energy demand in Egypt stimulated the need to consider renewable energy as an alternative to imported power. The solar chimney power plant (SCPP) is a clean power generation technology utilizing the concept of converting the solar energy to power generation, the typical one consists of a solar collector, a chimney and a turbine. The solar collector is a relatively horizontal roof made from a transparent material, elevated above the ground and opened at its periphery. The chimney is supported exactly at the center of the collector and at the base of the chimney, and inside the collector, there is the location of the turbine or the generator (see Fig. 1). A large amount of hot air is produced when the solar radiation lands on the collector roof, rises the chimney, due to the air density difference between the chimney base and the surroundings. The rising air is used to drive the installed turbine at the chimney base to generate electricity. The first (SCPP) prototype was installed in Manzanares (Spain), designed by Schlaich, who is the first to propose solar chimney as a means to harness energy from the sun [1].

Even though the technology is quite simple, considerable insights concerning many aspects are required before designing the plant for optimal performance. Two of these aspects are the effects of geometric parameters and the solar radiation on the plant performance, and they have been examined by several researchers. The study of Haaf et al. showed that an increase in the collector diameter increased output power but reduced plant efficiency [2]. On the other hand, efficiency increased with the tower height, and mass flow rate increased with the chimney diameter while the flow velocity remained constant. Pasumarthi and Sherif reported that increase of chimney height resulted in higher velocity and mass flow rate; and when the solar radiation was fixed, an increase in the mass flow rate was accompanied by a lower air temperature at the collector outlet [3]. Chitsomboon (2000) found that the plant

efficiency was invariant with respect to the insolation, the size of the collector cover and the tower diameter. He also found that the functional relationships between the generated power and the efficiency with the tower height were linear [4]. Dai et al. (2003) demonstrated that the generated power increased nonlinearly with the size of the plant, rapidly when the size was small and at a slower rate when the size was larger [5].

This study presents a Theoretical model that can predict how the power output of a solar chimney power plant may be affected by varying the geometrical dimensions, basically chimney height, chimney diameter, collector height, and collector diameter. The basic dimensions used in the model that the variable dimensions referred to them are for the Solar Chimney Power Plant installed in Aswan (Egypt).

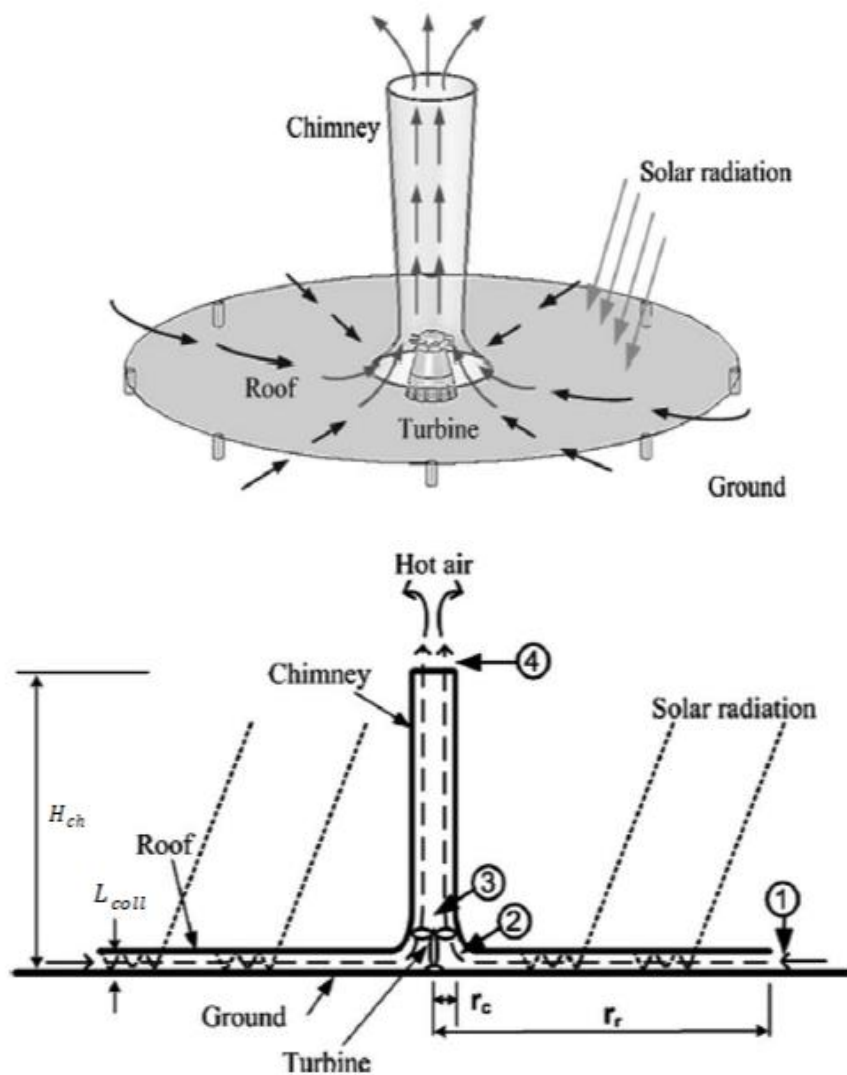


Fig. 1. Schematic layout of the solar chimney power plant [6].

2. Mathematical modeling

The Schematic diagram of the solar chimney power plant is presented in Fig.1. A mathematical model has been developed to predict the performance of the solar chimney thermal power generating equipment for different geometric parameters, which including the major components, the solar collector, the chimney and the wind turbine. The mathematical

model is developed by using (MAT LAP) software code and an iterative technique is carried out to solve the performed mathematical model. The following assumptions are made:

1. Air is an incompressible fluid and follows the ideal gas law.
2. A steady state condition and one-dimensional flow.
3. There is no leakage or friction considered in the system and only the buoyancy force is considered in the chimney.

2.1. The mathematical model of the collector

The incident solar radiation on the collector glass S is given by:

$$S = I \alpha \tau \quad (1)$$

Where I is the solar incidence on the collector cover, α is the glass absorptivity and τ is the glass transmittance. To evaluate collector performance, it is necessary to know the heat transfer Coefficients in the collector as shown in Fig. 2.

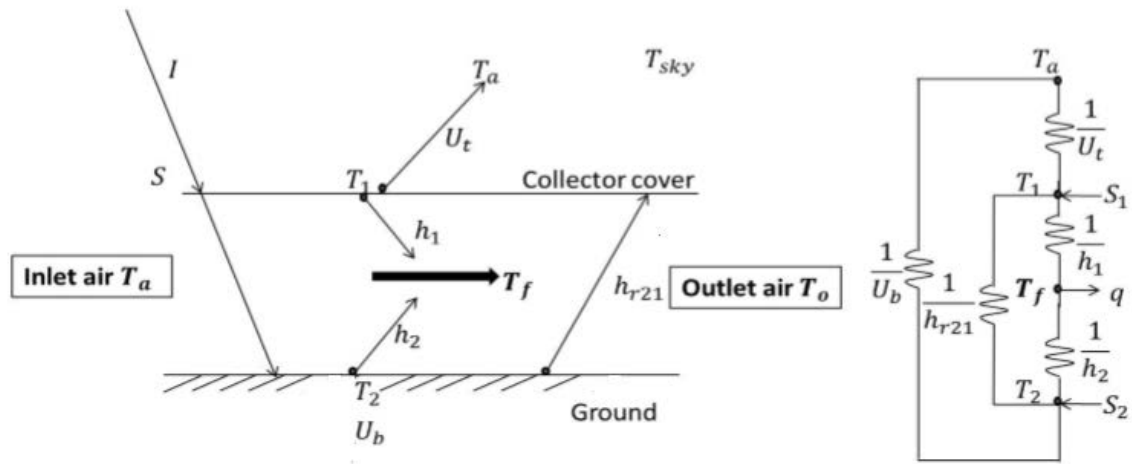


Fig. 2. Airflow, energy interactions, and equivalent thermal resistance in the collector [7].

The overall heat loss coefficient for the top of the collector U_t , is a result of convection and radiation phenomena [8]:

$$U_t = h_{rs} + h_w \quad (2)$$

The convective heat transfer due to the wind blowing over the glass h_w and the radiation heat transfer coefficient between the collector cover h_{rs} and the sky are as follows [3, 9]:

$$h_w = 5.67 + 3.86(V) \quad (3)$$

$$h_{rs} = \sigma \varepsilon_1 (T_1 + T_2) (T_1^2 + T_2^2) \left(\frac{T_1 - T_{sky}}{T_1 - T_a} \right) \quad (4)$$

Where T_2 is the ground temperature and T_1 is the collector cover temperature, V is the local wind speed, ε_1 and is the emissivity of the collector cover, T_a is the ambient air temperature and T_{sky} is the sky temperature expressed as:

$$T_{sky} = 0.552(T_a)^{1.5} \quad (5)$$

The radiation heat transfer coefficient between the glass and the ground can be estimated by [10]:

$$h_{r21} = \frac{\sigma \varepsilon_1 (T_1 + T_2)(T_1^2 + T_2^2)}{\frac{1}{\varepsilon_1} + \frac{1}{\varepsilon_2} - 1} \quad (6)$$

Where ε_2 is the emissivity of the ground, The free convection heat transfer coefficient between the collector glass and the air flow h_1 can be expressed as [11]:

$$h_1 = N_u \frac{k}{L_c} \quad (7)$$

Where N_u is the Nusselt number, k is the thermal conductivity of the air and L_c is the characteristic length. For an approximately uniform heat flux condition, the Nusselt number which is valid for large Rayleigh numbers [12]:

$$N_u = 0.14(R_a)^{1/3} \quad \text{for} \quad R_a < 2 \times 10^8 \quad (8)$$

Where R_a is the Rayleigh number and can be evaluated as a product of the Prandtl P_r and the Grashof numbers G_r :

$$R_a = G_r P_r = \frac{g \beta (\Delta T_{c-f}) L_c^3}{\nu^2} P_r \quad (9)$$

Where ΔT_{c-f} is the temperature difference between the collector glass and the air flow, g is the gravitational acceleration, β is the volumetric thermal expansion coefficient of the air. Similarly, the free convection heat transfer coefficient between the ground and the air flow h_2 can be expressed as [11, 13]:

$$h_2 = N_u \frac{k}{L_c} \quad (10)$$

Where the Nusselt number for a heated isothermal surface facing upward and a cold surface facing downward can be expressed as [14]:

$$N_u = 0.54(R_a)^{1/4} \quad \text{for} \quad 2 \times 10^4 < R_a < 8 \times 10^4 \quad (11)$$

$$N_u = 0.15(R_a)^{1/3} \quad \text{for} \quad 8 \times 10^4 < R_a < 8 \times 10^6 \quad (12)$$

$$R_a = G_r P_r = \frac{g \beta (\Delta T_{g-f}) L_c^3}{\nu^2} P_r \quad (13)$$

Where ΔT_{g-f} The temperature difference between the ground and the air flow. Bernardes et al. presented the ground loss coefficient U_b as [13]:

$$U_b = 2 \left(\frac{k \rho c_p}{\pi t} \right)^{0.5} \quad (14)$$

Where ρ the density of the air is c_p is specific heat capacity and t is the hour from the midnight.

The air is modeled as an ideal gas; therefore, the properties of air are only a function of temperature. By using the following empirical equations we can estimate the specific heat capacity

air density ρ and, thermal conductivity k , which are valid for the temperature range 280 K to 470 K [1].

$$c_p = 1002.5 + 27510^{-6}(T - 200)^2 \quad (15)$$

$$\rho = 3.9147 - 0.016082T + 2.9013 \times 10^{-5}T^2 - 1.9407 \times 10^{-8}T^3 \quad (16)$$

$$k = (0.0015215 + 0.097459T + 3.3322 \times 10^{-5} \times T^2)T^{-6} \quad (17)$$

The collector overall loss coefficient U_L , obtained from the equation [8]:

$$U_L = \frac{(U_b + U_t)(h_{r21}h_1 + h_2h_{r21} + h_2h_1) + U_b U_t(h_1 + h_2)}{h_{r21}h_1 + h_2h_{r21} + h_2h_1 + U_t h_2} \quad (18)$$

The collector efficiency factor \hat{F} , the collector heat removal factor F_R and the collector flow factor found respectively from the equations [8],

$$\hat{F} = \frac{h_1 h_{r21} + h_2 U_t + h_2 h_{r21} + h_2 h_1}{(U_t + h_{r21} + h_1)(U_b + h_{r21} + h_2) - h_{r21}^2} \quad (19)$$

$$F_R = \frac{\dot{m} c_p}{A_c U_L} \left[1 - e^{-\left(\frac{A_c U_L \hat{F}}{\dot{m} c_p}\right)} \right] \quad (20)$$

$$\hat{F} = \frac{F_R}{\dot{m}} \quad (21)$$

Where \dot{m} is the mass flow rate of the air and A_c is the collector area. The actual useful energy gain of the hot air in the collector can be calculated by the equation below [8]:

$$Q_u = A_c F_R [S - U_L \Delta T] \quad (22)$$

Where Q_u is actual useful energy and ΔT is the temperature difference between the outlet temperature T_{out} and the inlet temperature T_{in} of the collector assumed to be equal to the ambient temperature. The ground temperature, the collector cover temperature, the mean temperature of the airflow and the collector outlet temperature, will be obtained from Duffie and Beckman, respectively [8]:

$$T_2 = T_{in} + \frac{Q_u}{F_R A_c U_L} (1 - F_R) \quad (23)$$

$$T_1 = \frac{U_t(T_2 - T_a)}{h_{c21} + h_{r21}} \quad (24)$$

$$T_{fm} = T_{in} + \frac{Q_u}{F_R A_c U_L} (1 - \hat{F}) \quad (25)$$

$$T_{fm} = T_{in} + \frac{Q_u}{\dot{m} c_p} \quad (26)$$

The solar collector efficiency can be expressed as a ratio of the heat output of the collector as heated air Q_u and the solar radiation I times A_c .

$$\eta_{coll} = \frac{Q_u}{A_c I} \quad (27)$$

2.2. The Mathematical Model of the Chimney

The chimney converts the heat-flow Q_u product by the solar collector into kinetic energy (convection current) and potential energy (pressure drop at the turbine). Thus, the density difference of the air caused by the temperature rise in the collector works as a driving force. Schlaich et al. estimated the inlet velocity to the chimney V_{ch} and the mass flow rate as follows [1]:

$$V_{ch} = \sqrt{\frac{2 g H_{ch} \Delta T}{T_a}} \quad (28)$$

Where H_{ch} is the chimney height and A_{ch} is the chimney cross-sectional area. The chimney efficiency is given as:

$$\eta_{ch} = \frac{P_{tot}}{Q_u} = \frac{g H_{ch}}{c_p T_a} \quad (29)$$

This simplified representation explains one of the basic characteristics of the solar chimney, which is that the chimney efficiency is fundamentally dependent only on chimney height.

2.3. Turbine model

The axial wind turbine located at the base of the chimney which converts the kinetic energy of the air flow into useful mechanical rotary work. The Efficiency of the turbine can be expressed as [15]:

$$\eta_t = 1 - \frac{V_{ch}^2}{2 c_p \Delta T \eta_{ch}} \quad (30)$$

Turbine electrical power (output power) can be calculated as follows [11]:

$$P_e = Q_u \eta_t \eta_{ge} = A_c I \eta_{coll} \eta_{ch} \eta_t \eta_{ge} \quad (31)$$

Where η_t is the turbine efficiency, and η_{ge} is the generator efficiency and they are considered to equal to (0.8) as widely reported in SCPP literature [9, 16]. The total efficiency (plant efficiency) η_{tot} is determined here as a product of the individual component efficiencies:

$$\eta_{tot} = \eta_{coll} \eta_{ch} \eta_t \quad (32)$$

3. Solution procedure

According to the above formulation, at a known or assumed ambient temperature and solar radiation which is a function on time, date and geographical location, then the plant power output can be attained. A flowchart of this procedure is illustrated in Fig. 3.

4. Results and discussion

The parameters investigated in this paper were: collector diameter, chimney height, chimney diameter. The prototypical power plant is the Solar chimney power plant in Aswan – Faculty of Energy Engineering shown if Fig. 4 and has the dimension shown in Table 1. The parameters used in the calculation of the system performance at the constant condition of solar irradiance (900 W/m^2) and ambient temperature (310 K).

Table 1: Dimensions of the modeled power plant

| Parameter | Chimney height | Chimney diameter | Collector diameter | Collector height |
|-----------|----------------|------------------|--------------------|------------------|
| Value | 20m | 1m | 32.218 m | 1.25m |

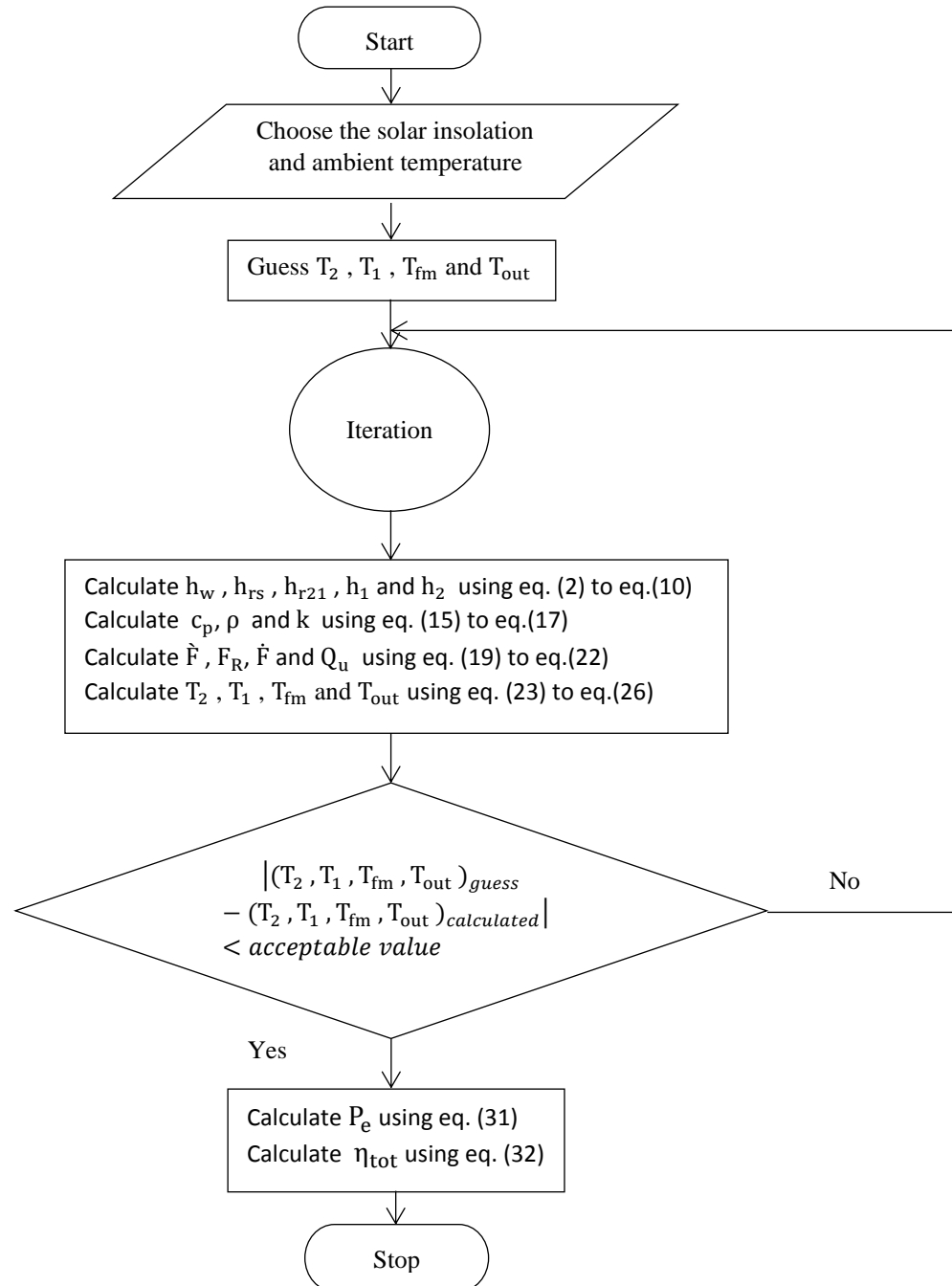


Fig. 3. Flowchart of solution procedures.



Fig. 4. Aswan solar chimney power generation.

The effect of different parameters presented in Figs. 5-10 respectively. The first parameter is chimney height as shown in Fig. 5. That the higher chimney height the greater power output will be. Increasing chimney height means increase in the driving force which is the buoyancy difference led to increasing the velocity and mass flow rate, and that is the flow energy which is needed for the wind turbine. Similar to the variation in the output power, as shown in Fig. 5, efficiency increased from 0.07% at a chimney height of 21m to 0.5% at a chimney height of 150m.

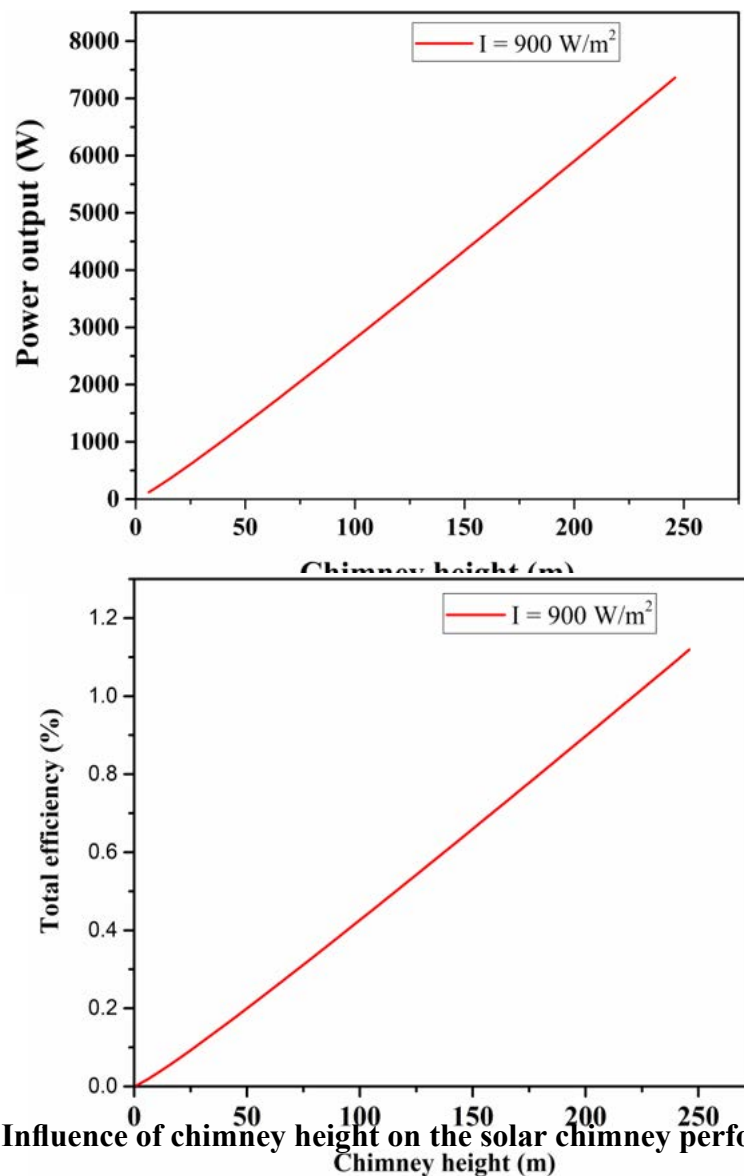


Fig. 5. Influence of chimney height on the solar chimney performance.

It can be seen from Fig. 6 that by increasing the chimney diameter, the air pressure decreases and the velocity and mass flow rate increases. Augmentation in mass flow rate causes increment in output power, but with increasing the chimney diameter to a critical value (5m) causes the mass flow rate through the collector to increase, the temperature rises through the collector decreases led to decreasing in the useful energy gained.

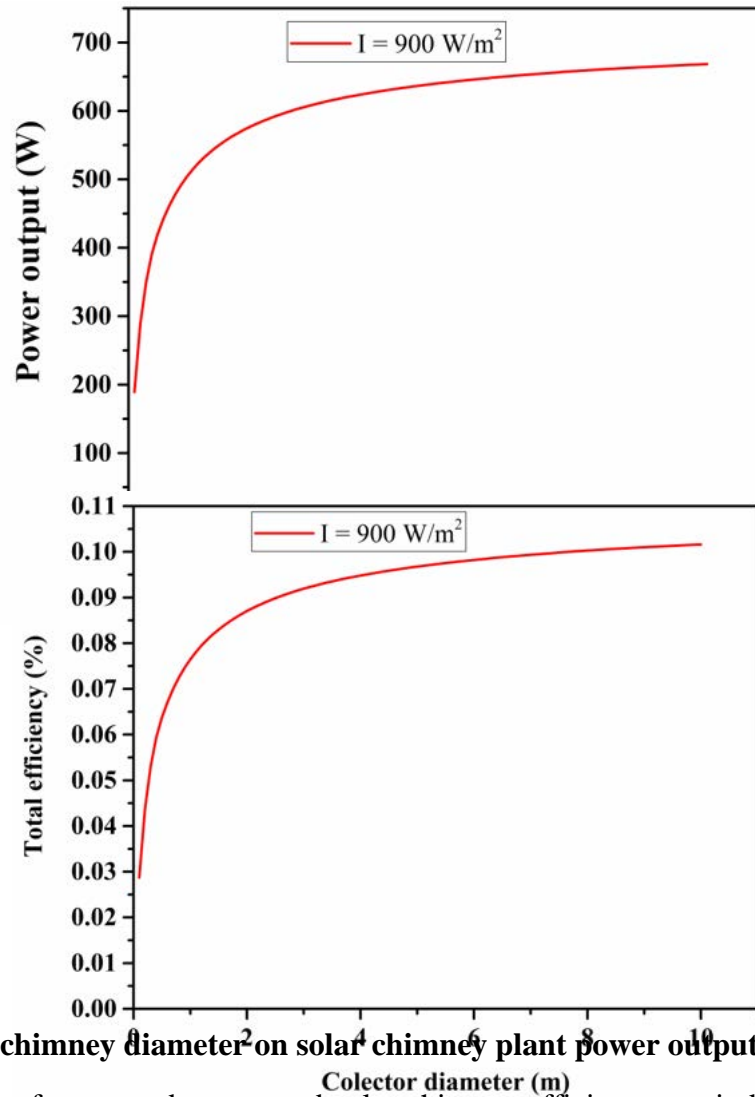
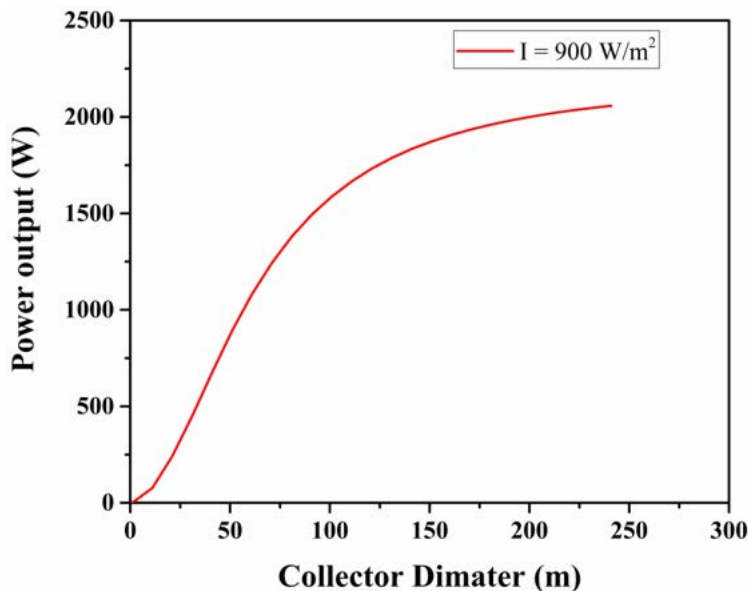


Fig. 6. Effect of chimney diameter² on solar chimney plant power output and efficiency.

In Fig. 7, changes of generated power and solar chimney efficiency are indicated where the value of collector diameter varies from 30m to 250 m, which means that flow power would be greater at more values while it is inverted with efficiency. By increasing the collector area, the area of heat transfer increased, which caused the temperature and mass flow to increase but with respect to the constant heat flux, collector efficiency decreased causing to decrease the total efficiency.



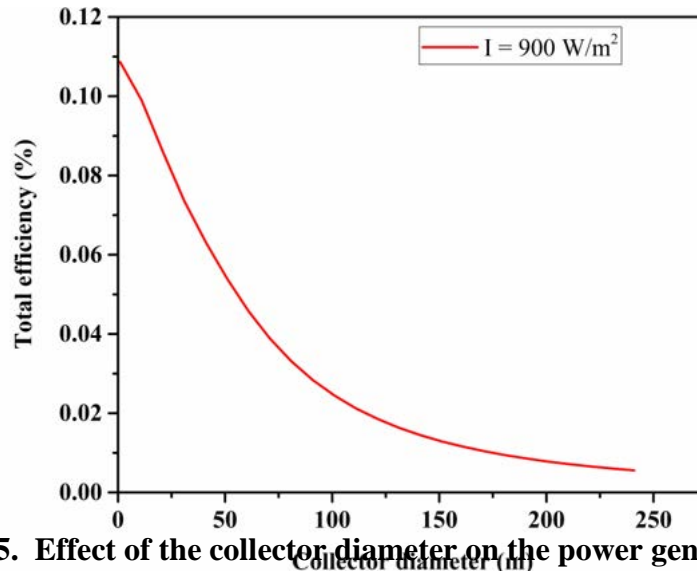


Fig. 5. Effect of the collector diameter on the power generation.

5. Conclusion

The influences of the geometric parameters, mainly the collector diameter, chimney height, and chimney diameter, on solar chimney power plant performance have been studied by using a theoretical model. The capacity of power generation is dependent on the ambient conditions and structural dimensions such as solar insolation, ambient temperature, chimney height, and collector diameter, etc. The results indicated that the power generation from this type of power plant increases with the increase in solar chimney height and solar collector area. The larger the solar collector size and the higher the solar chimney height is, the greater the power will be. By the analysis, it was found that the chimney diameter parameter had an optimum range with maximum values for the efficiency and output power.

References

1. Schlaich, J., *The solar chimney: electricity from the sun*. 1995: Edition Axel Menges.
2. Haaf, W., et al., *Solar chimneys part I: principle and construction of the pilot plant in Manzanares*. International Journal of Solar Energy, 1983. **2**(1): p. 3-20.
3. Pasumarthi, N. and S. Sherif, *Experimental and theoretical performance of a demonstration solar chimney model—Part II: experimental and theoretical results and economic analysis*. International Journal of Energy Research, 1998. **22**(5): p. 443-461.
4. Chitsomboon, T., *Potential and efficiency of solar chimney in the production of electrical energy*. Research and Development Journal of the Engineering Institute of Thailand, 2000. **11**(3): p. 38-44.
5. Dai, Y., H. Huang, and R. Wang, *Case study of solar chimney power plants in Northwestern regions of China*. Renewable Energy, 2003. **28**(8): p. 1295-1304.
6. Koonsrisuk, A. and T. Chitsomboon, *Accuracy of theoretical models in the prediction of solar chimney performance*. Solar Energy, 2009. **83**(10): p. 1764-1771.
7. Okoye, C.O. and O. Taylan, *Performance analysis of a solar chimney power plant for rural areas in Nigeria*. Renewable energy, 2017. **104**: p. 96-108.
8. Duffie, J.A. and W.A. Beckman, *Solar engineering of thermal processes*. 2013: John Wiley & Sons.
9. Larbi, S., A. Bouhdjar, and T. Chergui, *Performance analysis of a solar chimney power plant in the southwestern region of Algeria*. Renewable and Sustainable Energy Reviews, 2010. **14**(1): p. 470-477.

10. Ong, K., *A mathematical model of a solar chimney*. Renewable energy, 2003. **28**(7): p. 1047-1060.
11. Duffie, J.A., W.A. Beckman, and W. Worek, *Solar engineering of thermal processes*. Vol. 3. 2013: Wiley Online Library.
12. Fujii, T. and H. Imura, *Natural-convection heat transfer from a plate with arbitrary inclination*. International Journal of Heat and Mass Transfer, 1972. **15**(4): p. 755-767.
13. Bernardes, M.d.S., A. Voß, and G. Weinrebe, *Thermal and technical analyses of solar chimneys*. Solar Energy, 2003. **75**(6): p. 511-524.
14. McAdams, W.H., *Heat transmission*. 1954.
15. Nizetic, S. and B. Klarin, *A simplified analytical approach for evaluation of the optimal ratio of pressure drop across the turbine in solar chimney power plants*. Applied Energy, 2010. **87**(2): p. 587-591.
16. Nizetic, S., N. Ninic, and B. Klarin, *Analysis and feasibility of implementing solar chimney power plants in the Mediterranean region*. Energy, 2008. **33**(11): p. 1680-1690.

25- Experimental investigation of a two-bed adsorption cooling system

A.T. Abd El-Hamid^a, M.B. Elsheniti^b, O.A. El-samni^c and S. M. Elsherbiny^d

Mechanical Engineering Department, Faculty of Engineering, Alexandria University, El-Chatby,
Alexandria 21455, Egypt

^aahmedatm2010@gmail.com, ^bmelsheniti@gmail.com, ^celsamni@gmail.com,

^dsamymelsherbiny@yahoo.com

Abstract.

A lab-scale two- bed adsorption chiller was designed, constructed and evaluated experimentally in Thermal Engineering Lab, Alexandria University, Egypt. Isotherms characteristic of silica gel that was packed in the two beds were determined depending on the experimental DVS (dynamic vapor sorption) analyzer results. To visualize the sorption phenomena in the two beds and in the evaporator during the adsorption and desorption cycle, a special transparent glass was used as the upper cover for these components. The time variations for the temperatures and pressures at each component are measured, simulated and analysed. The system performance was experimentally investigated under various operating conditions. The results showed that the specific cooling capacity (SCC) was about 37 W/kg while the coefficient of performance (COP) was 0.38, when the hot water inlet temperature is 80 °C, the cooling water inlet temperature is 25 °C, and the chilled water inlet temperature is 18 °C.

Keywords: Adsorption chiller, Solar cooling, Silica gel isotherms, COP, Packed bed.

Introduction

In recent years, increasing greenhouse gases concentration and climate changes are widely recognized as a serious potential threat. Therefore, utilizing environmentally friendly equipment has a great interest worldwide. Adsorption cooling systems (ADS) that can be driven by low grade energy and use safe refrigerants is one of the promising technologies to replace the traditional vapor compression refrigeration systems (VCS). VCS contribute to global warming, ozone layer depletion and consume excessive electrical power [1-3]. Silica gel-water adsorption cooling systems with two-bed have been investigated analytically and experimentally by many researchers [4-6]. This pair features with low regeneration temperature about 70-85 °C for silica-gel. In such case, a number of evacuated tube solar collector can be used to supply the heating water as reported by Elsheniti et al. [7]. Besides, water has zero global warming potential (GWP) and ozone depletion potential (ODP), and high latent heat of vaporization. Saha et al. [8] experimentally investigated a new two-stage non-regenerative adsorption chiller, which uses low temperature solar/waste heat (40–75 °C) as the heating source. With a 55 °C driving source in combination with a 30°C cooling temperature, the COP of the two-stage chiller is 0.36. Liu et al.[9] developed an adsorption water chiller powered by low heat source with the temperature as low as 70 °C and the test results show that cooling power of 6.3 kW with a COP of about 0.4 can be produced using silica gel–water as working pair. Wang et al. [10] designed a novel silica gel–water adsorption chiller and found that with hot water temperature of 85 °C, cooling water temperature of 31 °C and the chilled water inlet temperature of 20 °C, the COP was 0.65 even the cooling capacity was 12.6 kW .Elsheniti et al. [11] evaluated numerically the effect of geometrical parameters of fins on a two-bed adsorption chiller. They concluded that fins' height and spacing should be optimized to enhance the system performance. Saha et al. [6] investigated analytically the performance of the thermally driven, advanced three-stage adsorption chiller utilizing low-grade waste heat of 50 °C and lower temperatures as the driving heat source, in combination with a heat sink of 30 °C, a COP of 0.15 can be obtained. Chua et al. [12,13] analytically presented a transient

distributed-parameter model for a two-bed, silica gel–water adsorption chiller and compared with previous lumped-parameter model and cyclic steady-state model, respectively. The results showed better agreement between the model prediction and experimental data. Chua et al. [14] also analytically performed a multi-bed regenerative adsorption chiller aiming to extract the most enthalpy from the low-grade waste heat and to minimize the chilled water temperature fluctuation. The results indicate that a four-bed chiller generates 70% more cooling capacity than a typical two-bed chiller and a six-bed chiller generates 40% more cooling capacity than a typical four-bed chiller.

Çağlar [15] studied the effect of the fins in the adsorbent beds and compared between the finless and finned tube adsorbent beds in terms of heat transfer inside the bed. He found that temperatures decreased by 10–17 K by increasing the fin radius while the heat transfer significantly enhanced by increasing the number of fins. Sharafian et al. [16] experimentally studied the effects of fin spacing on the temperature distribution in a two copper finned tube adsorber beds with 6.35 mm and 9.5 mm fin spacing. They found that the optimum fin spacing is about 6 mm for silica gel beads size 2–4 mm.

In this study, silica gel–water has been selected as the adsorbent–adsorbate pair and packed in rectangular finned tube beds which associated into evaporator and condenser in a lab-scale adsorption chiller. The introduced experimental work utilized the parametric studies developed by Elsheniti et al. [11] in assigning the bed geometrical parameters. Nevertheless, this paper reports the design and the fabrication procedure for the two-bed silica gel –water adsorption cooling system. In addition, the performance of the system is experimentally investigated under different operating conditions and different adsorption/desorption cycle times.

Theory of Operation

This adsorption cycle consists of four steps: Adsorption- evaporation, Preheating-pressurization, desorption- condensation, and precooling-depressurization. The water is first charged into the evaporator and a vacuum is applied to the entire system. Referring to Fig. 2, in the first step (Adsorption- evaporation), Valve 2 is then opened to allow the water to evaporate at T_{evap} and travel as a vapour into Bed I where is adsorbed on the silica gel at that time heat is removed from the chilled water Q_{chilled} . The heat generated during adsorption Q_{ads} is removed by cold water circulating in Bed 1, while Bed II is in the desorption phase. Once the silica in Bed 1 is saturated with water, Valve 2 is closed to start the second step (Preheating-pressurization). The water circulating through Bed I is then switched to hot water to bring the bed pressure up to the condenser pressure P_{cond} . Valve 1 is then opened to start the third step (desorption- condensation) and allow the adsorbed water in Bed I to pass into the condenser while continuously circulating the hot water at T_{des} . Water vapor desorbed from Bed I by Q_{des} is then condensed in the condenser by removing heat Q_{cond} . and then passes through the expansion valve to the evaporator. Valve 1 is then closed to start the final step (precooling-depressurization) and cold water is circulated through Bed 1 to reduce its pressure to the evaporator pressure P_{evap} . Valve 2 is then opened to start the following cycle. These processes are carried out continually and alternately in Bed I and Bed II by controlling the actuated valves on time.

Description of the Lab-scale chiller

A pictorial view of the main components of test facilities that we have successfully prototyped in our laboratory is shown in Fig. 3. All main components are combined in one movable carriage. The prototype is designed to be a full-automated device using a control system with its measuring instruments and electrically actuated valves. In addition, it is essential to observe the sorption phenomena during the adsorption and desorption cycle, thus

a special transparent glass with a standard O-rings is fabricated to visualize the sorption phenomena in the two beds and in the evaporator. Furthermore, the working pressures are very low pressures (near to absolute vacuum between 1 to 7 kPa absolute), so that special considerations have been taken during the bed fabrication and assembly. Moreover, a commercially available silica gel in Egypt was selected and studied by measuring its characteristics using the DVS analyzer, and grinded to a very fine granules (0.3 – 0.5 mm in diameters), so specific packing procedures and mesh fixing have been considered to facilitate entering and leaving the adsorptive vapor from the adsorbent space. Four vacuum pressure sensors are installed in each component (the 2 beds, evaporator and condenser) to measure the vacuum pressure during the operation, *PXM319-0.35AI* Omega UK sensor type with a full range 0-350 mbar absolute with 4-20 mA output and accuracy about $\pm 0.25\%$ FS. *DS18B20* sealed digital temperature probe is used to precisely measure temperatures in wet environments with temperature range from -55°C to $+125^{\circ}\text{C}$ and $\pm 0.5^{\circ}\text{C}$ accuracy from -10°C to $+85^{\circ}\text{C}$ with 3.0-5.5V input voltage. To record the data during operation, both temperatures and pressures are connected to computer through a microcontroller kit called Arduino. The detailed description of the main components will be discussed in the following sections.

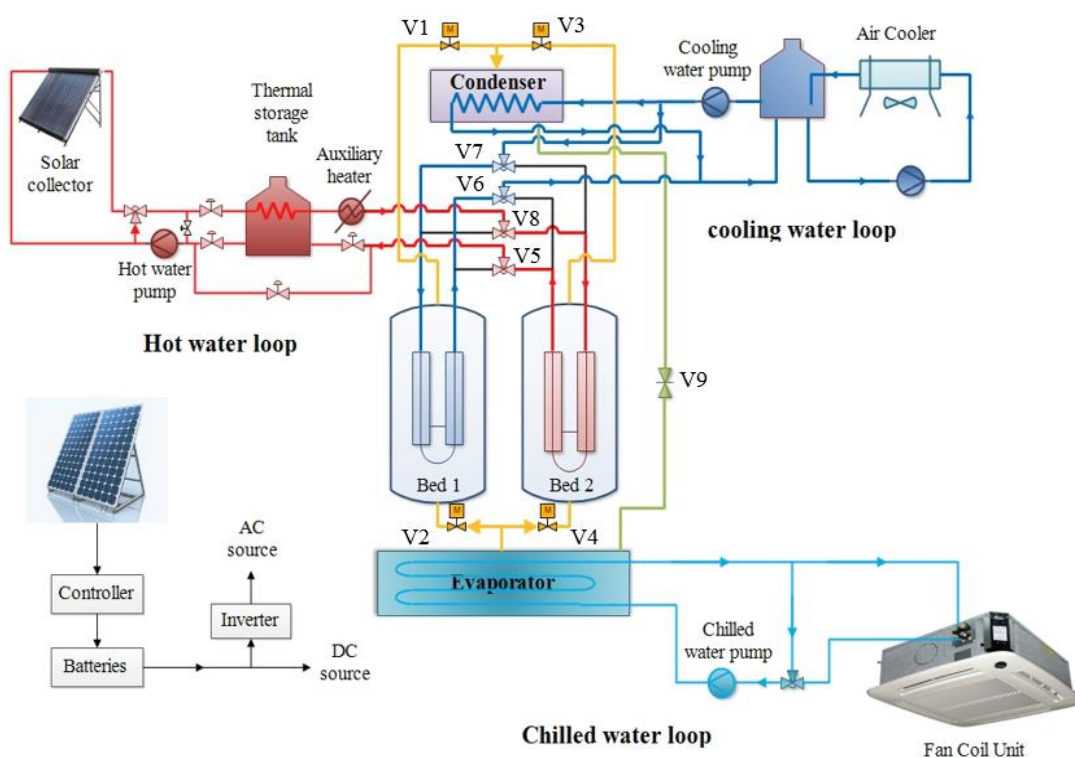


Fig. 2 Schematic diagram of all the adsorbent test facilities

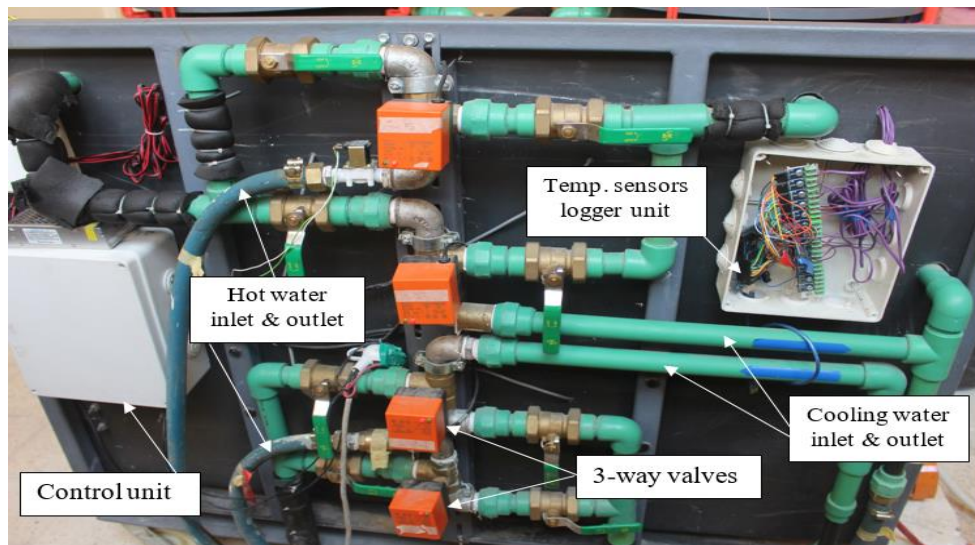


Fig. 3 Pictorial view of the main component test facilities

Design of the main components.

Adsorber beds. The system composed of two adsorber beds, each of them contains five heat exchangers. The selection of the heat exchanger has been studied to choose the most adequate layout design to have the highest specific heat transfer area, low weight, compact size and the ability to host high amount of the adsorbent material. Aluminum finned tube heat exchangers have been proved good performance with the previous requirements [17-19]. Circular tube heat exchanger with corrugated aluminum fins as shown in Fig. 4 is used as the adsorber bed. Main features of each heat exchanger with its containers are shown in Table 5.

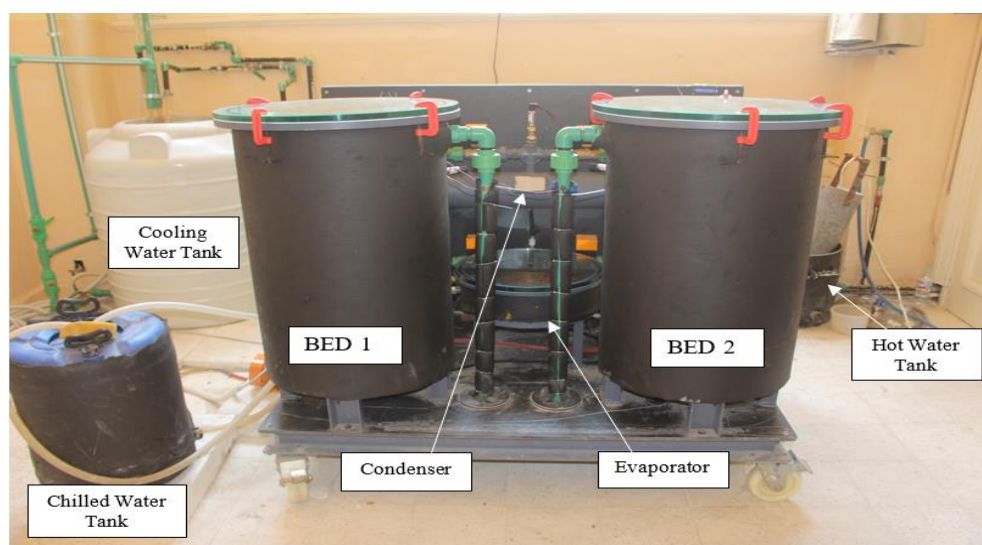


Table 5: Main features of the adsorber bed

| | | | |
|---------------|---|--------------------|--|
| Module | <ul style="list-style-type: none"> • $(L \times W \times t)$: 680×280×28 [mm] | Header | <ul style="list-style-type: none"> • Copper material • Thickness: 1.2 [mm] • Outer diameter: 28.0[mm] |
| Tubes | <ul style="list-style-type: none"> • Copper material • Thickness of tube: 0.5 [mm] • Outside diameter: 9.53 [mm] • Tube length: 290 [mm] • Tube spacing: 25 [mm] | Casing | <ul style="list-style-type: none"> • (Height*ID): 835*495 [mm] • Flange diameter: 605 [mm] • Thickness: 8.0 [mm] |
| Fins | <ul style="list-style-type: none"> • Aluminum material • Thickness: 0.2 [mm] • Height: 6.0 [mm] • 12 fins per inch | Glass Cover | <ul style="list-style-type: none"> • Thickness: 18.0 [mm] • Diameter: 600 [mm] |

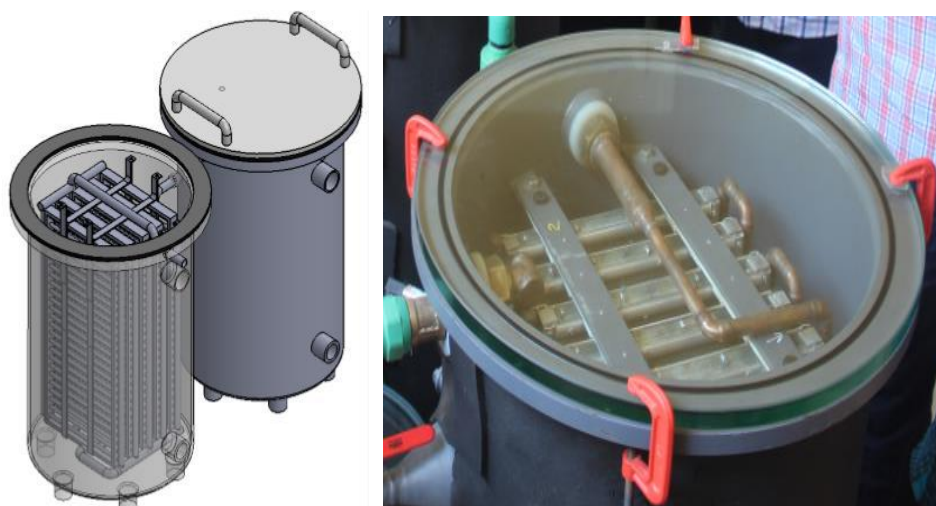
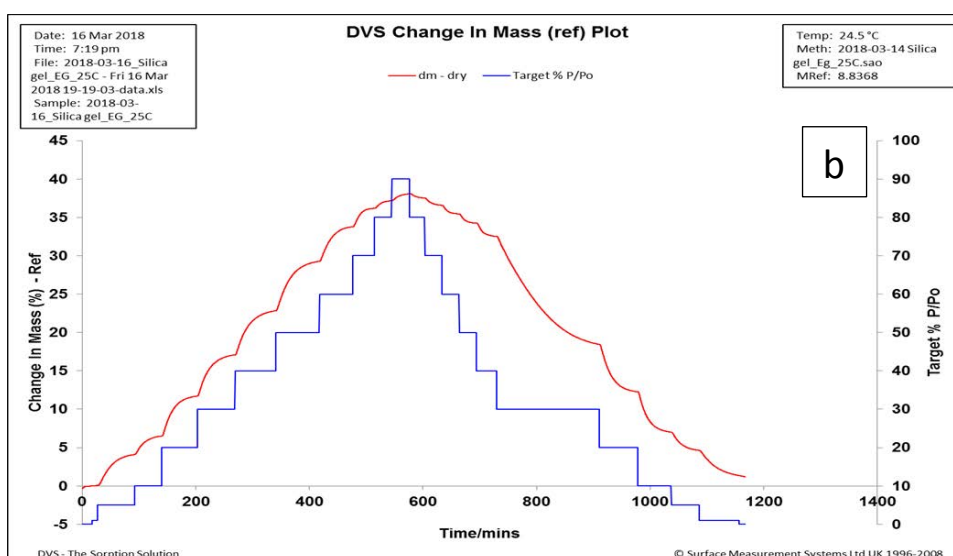
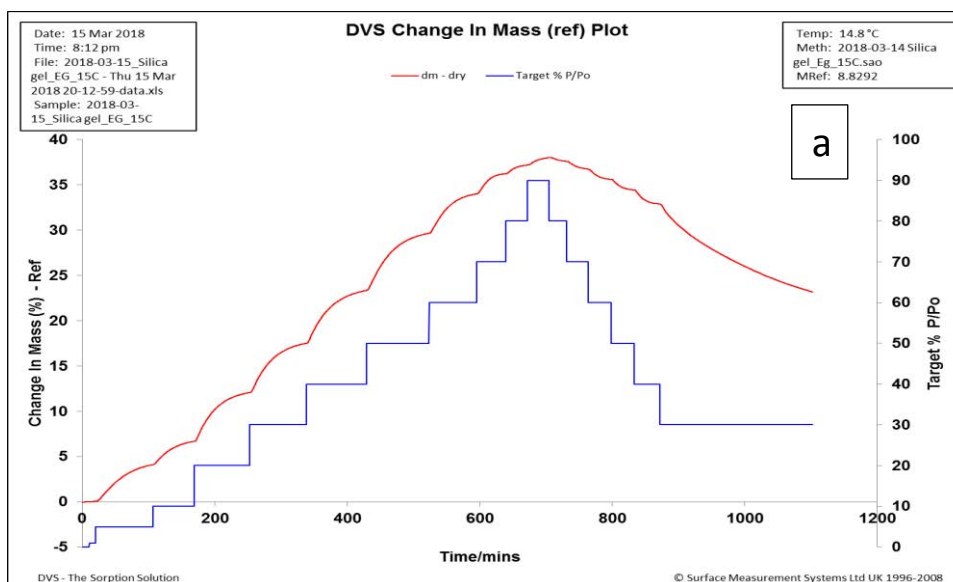


Fig. 4 The five heat exchangers in the adsorber bed

Adsorbent material nature and characteristics. Common types of silica gel used in adsorption systems such as Fuji Davison ‘A’, ‘3A’ and ‘RD’ silica gel are well known and investigated by many researchers Ng et al. [20] and X. Wang et al. [21]. The type of the silica gel used in this study is an unknown type and selected due to the commercial availability in local market in Egypt, so a sample was sent to Birmingham University in UK to measure its characteristics using the DVS analyser, besides another sample was sent to the faculty of science, Alexandria University, Egypt to perform scanning analysis using SEM device. The adsorption characteristics that affect the chiller performance are adsorption isotherms, isosteric heat of adsorption and adsorption kinetics. Tested samples of 9.3745 mg each has been allowed to undergo through adsorption / desorption tests at various partial pressures using the DVS analyzer at three different temperatures 15, 25 and 35 °C. The sample mass is recorded every 20 seconds at different vapor pressure values to determine the adsorption kinetics, Fig. 5(a, b, c). Tests showed that at temperature 35 °C, the change in mass reached its maximum value of

38.65 % in 498.33 min., which is higher than the values at 25 and 15 °C (38.09% and 38.02 % respectively). The sample isotherm is measured at each value of vapor pressure at the point of no change in adsorbent mass by measuring the adsorbent uptake.



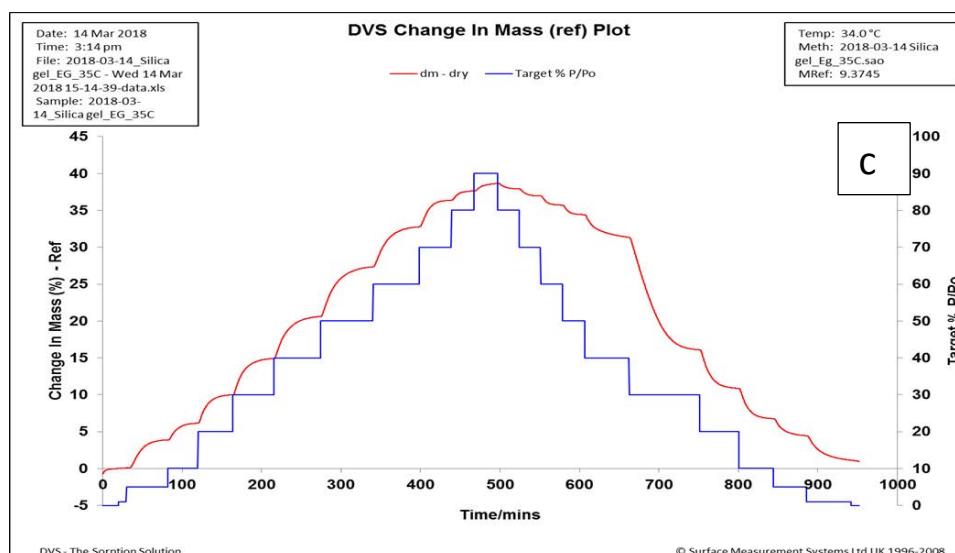


Fig. 5 Change of mass and pressure over time at different temperatures during adsorption and desorption processes using DVS analyzer a) at 15 °C , b) at 25 °C , c) at 35 °C

Fig. 6 presents the experimental adsorption isotherms for our silica gel at temperatures 15 °C, 25 °C and 35 °C. It is shown that silica gel isotherms behave as *type-IV* adsorbents, according to the IUPAC classification [22, 23]. It's shown that silica gel at T=35 °C adsorbs more water vapor about 38.64 Kg_w/kg_{ads} which is higher than the values in other temperatures, so our silica gel exhibited type A adsorption isotherm compared with Wang et al. [21] isotherms which have a maximum uptake of 0.4 Kg_w/kg_{ads}.

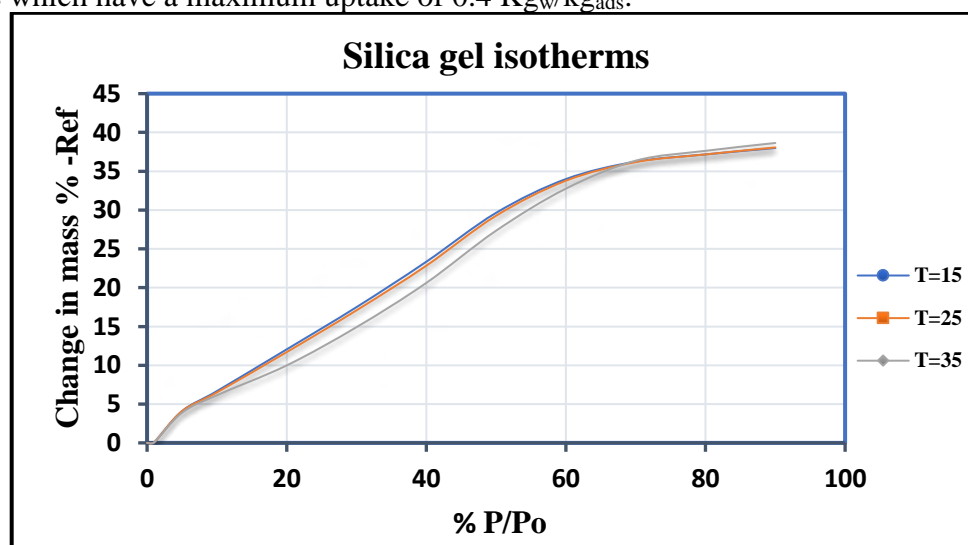


Fig. 6 Adsorption isotherms for different temperatures

Additionally, the surface morphology of the silica gel had been studied using SEM device model *JEOL JSM-5300LV* and the results are presented in Fig. 7. Two tests were conducted, the first one is Scanning Electron Microscopy (SEM), which provides detailed high resolution images of the sample by rostrering a focused electron beam across the surface and detecting secondary or backscattered electron signal. The second is Energy Dispersive X-Ray Analysis (EDX) which was also used to provide elemental identification and quantitative compositional information. Fig. 7a shows SEM image of the crystal size and size distribution of the sample with a magnification scale X150. In addition, by increasing the scale, the surface pores appear

as shown in Fig. 7b. Random measurements were performed on some pours, which indicate a variety of the pour sizes Fig. 7b and 5c.

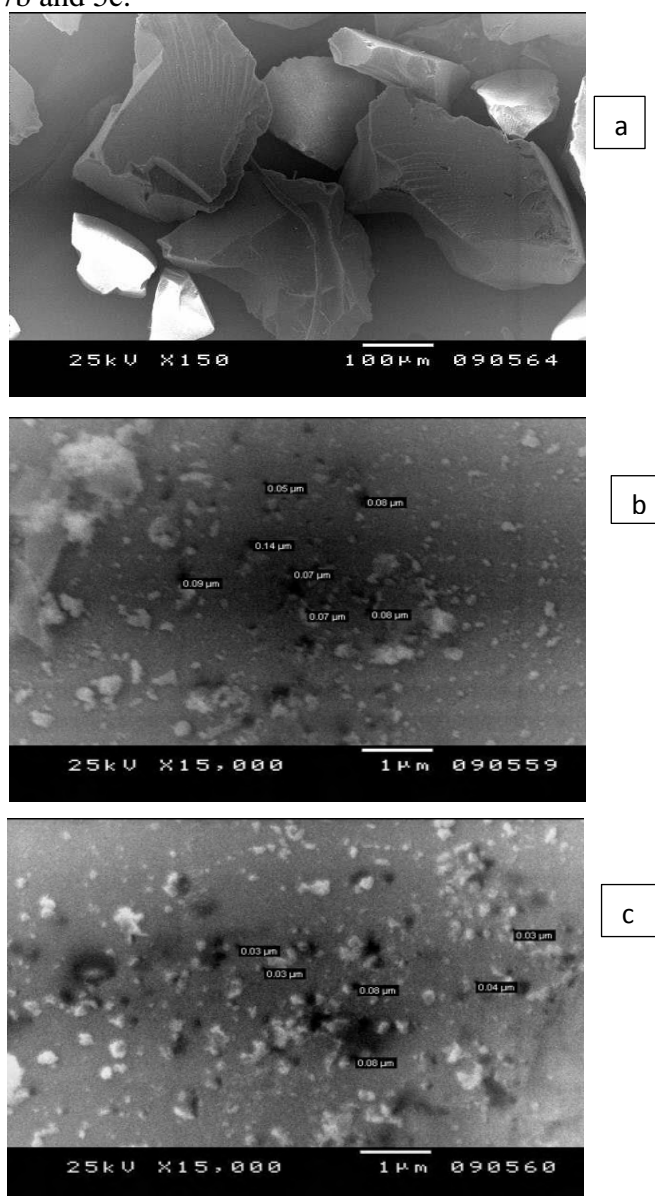


Fig. 7 Scanning electron microscope (SEM) images with a magnification scale X150 and X15000 with pours dimensions.

EDX analysis was carried out on a thin layer of the sample. The layer contained small amounts of Calcium, Copper, Potassium and sulfur in addition to the silica, which has the major percentage of the mixture about 98.7 % as shown in Fig. 8. The composition of the sample is shown in **Error! Reference source not found.**

Table 6 Composition of the sample

| Label | Range [keV] | Gross | Net | % total |
|-----------|----------------|-------|-------|---------|
| Si | 1.607 to 1.867 | 58176 | 40851 | 98.7 |
| S | 2.168 to 2.447 | 1390 | 93 | 0.2 |
| K | 3.168 to 3.467 | 1321 | 153 | 0.4 |
| Ca | 3.547 to 3.848 | 1233 | 169 | 0.4 |
| Cu | 7.867 to 8.227 | 767 | 121 | 0.3 |

About 3.8 kg of silica gel is grinded from beads with diameters around 3-4 mm to be in diameters between 0.5 -0.15 mm, then packed in each module and specific consideration have been carried out to keep the silica gel between the copper heat-transfer-tube and the aluminum fins, so a fine mesh made of stainless steel is used for this purpose and fixed with the bed by using aluminum bars.

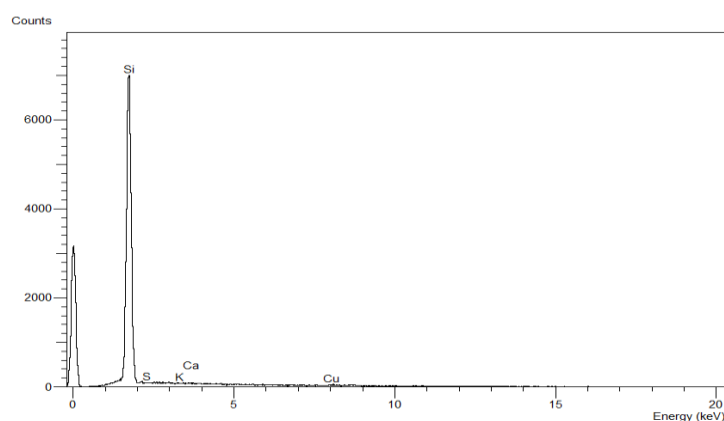
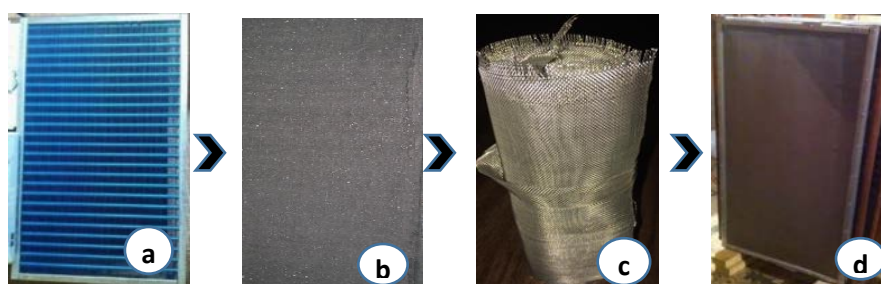


Fig. 8 EDX spectra of the tested sample

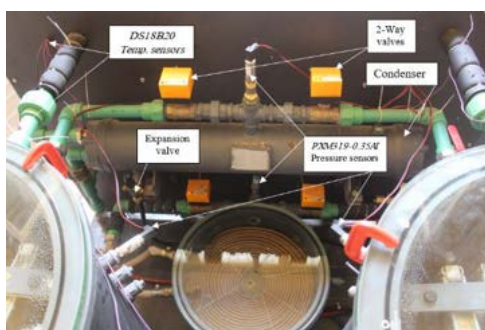
Fig. 9 Silica gel packing. (a) Single module before packing. (b) Module during packing. (c) Wire mesh. (d) Packed module. shows the manufacturing procedure of adsorbers where it is possible to see



the silica gel grains laying between the heat exchanger fins.

Fig. 9 Silica gel packing. (a) Single module before packing. (b) Module during packing. (c) Wire mesh. (d) Packed module.

Evaporator and condenser. The condenser is a simple shell and tube heat exchanger with four passes 1'' copper tubes with helical fins on the outer surface with 830 mm shell length and 145 mm outer diameter. The evaporator composed of two layers spirally coiled copper tubes in order to enhance the mass transfer performance. The evaporator is made of an insulating material PVC with a thermal insulation material on the outer surface to reduce the loss of refrigeration capacity. The two heat exchangers are connected each other through the adsorption beds by electrically operated valves. Fig. 10 shows a view of the evaporator and condenser as well as the electrically operated valves. Main features of the evaporator are



reported in Table 7.

Fig. 10 View of the evaporator and condenser with the electrically operated valves

Table 7 Physical parameters of the evaporator

| Parameter | Data |
|---------------------|---|
| Container | Inner diameter: 400 [mm] |
| | Height: 135 [mm] |
| | Thickness: 1.22 [mm] |
| Copper coils | Two rows copper coils Tube outer diameter 9.525 [mm] Thickness: 0.61 [mm] length: 30 [m] |
| Glass cover | Diameter: 460 [mm] Thickness: 18 [mm] |

Isotherms Equation and Performance Indicators.

Many correlations have been studied to describe the adsorption isotherms for selected material such as langmuir, Freundlich, Henry and Tóth equation. In this study, we find that Tóth equation Eq. 1 could fit the adsorption experimental data very well, but both the Henry equation and Freundlich equation could not fit the experimental data over the active region. Therefore, Tóth equation can be used here to find the isotherm parameters and the isosteric heats of adsorption. Wang et al. [21, 24] used the form of Tóth equation that we used in the present work as given:

$$q^* = K_0 \exp[\Delta H_{ads}/(RT)] P / \{ 1 + [K_0/q_m \exp(\Delta H_{ads}/(RT))] P \}^{1/t} \quad (1)$$

Where q^* is the amount of adsorbate in the adsorbent under equilibrium conditions, q_m denotes the monolayer capacity, P , T are the equilibrium pressure and temperature of the adsorbate in the gas phase respectively, R is the universal gas constant, ΔH_{ads} is the isosteric enthalpy of

adsorption, K_0 is a pre-exponential constant, and t is the dimensionless Tóth constant. The isotherm parameters and isosteric heats of adsorption have been obtained from Tóth equation as shown in Table 8.

Table 8 Tóth equation parameters

| Parameter | Value | Unit |
|------------------|----------|--|
| K_0 | 1.92E-02 | [kg kg ⁻¹ kPa ⁻¹] |
| ΔH_{ads} | 2.72E+03 | [kJ/kg] |
| q_m | 0.38 | [kg kg ⁻¹] |
| t | 8.7 | - |

The COP and SCP of the system should be calculated to evaluate the system performance. Eq. 2 is used to calculate the coefficient of performance (COP) where Q_{chill} and Q_{des} represent the cooling output power and heating input power, respectively. Q_{chill} and Q_{des} are calculated from the measured flow rates, the isobaric specific heat capacities, and inlet and outlet temperatures of the chilled water and hot water as shown in Eq. 3 and Eq. 4 below, respectively:

$$COP = \frac{\int_0^{t_{cycle}} \left(\frac{Q_{chill}}{Q_{des}} \right) dt}{\int_0^{t_{cycle}} dt}. \quad (2)$$

$$Q_{chill} = m_{chill}^{\circ} C_{p_{chill}} (T_{chill,in} - T_{chill,out}). \quad (3)$$

$$Q_{des} = m_{hot}^{\circ} C_{p_{hot}} (T_{hot,out} - T_{hot,in}). \quad (4)$$

Where $C_{p_{chill}}$ (J/kg/K) and $C_{p_{hot}}$ are the specific heat of water under the temperature $(T_{chill,in} - T_{chill,out})/2$ and $(T_{hot,out} - T_{hot,in})/2$, respectively. m_{chill}° (kg/s) is mass flow rate of cold water and m_{hot}° (kg/s) is mass flow rate of hot water. $T_{chill,in}$ and $T_{chill,out}$ are inlet and outlet temperature of cold water, respectively. $T_{hot,in}$ and $T_{hot,out}$ are inlet and outlet temperature of hot water, respectively, and t_{cycle} (s) is cycle time of the system. (SCC) the specific cooling capacity of the adsorption cooling systems is calculated from Eq. 5 where M (kg) is adsorbent total mass inside the two adsorbers.

$$SCC = \frac{Q_{chill}}{M}. \quad (5)$$

Results and discussion

The standard operating conditions of the heating and cooling fluid inlet temperatures to the adsorber beds and the cooling and chilled water inlet temperatures to the condenser and evaporator were set at the desired operating conditions as shown in Table 9.

Table 9 Standard operating conditions for the adsorption

| | |
|-------------------------------------|-------------------|
| Hot water inlet temperature. | 75-80 [°C] |
|-------------------------------------|-------------------|

| | |
|---|--|
| Cooling water inlet temperature. | 25 [°C] |
| Chilled water inlet temperature. | 14[°C] |
| Hot water flow rate. | 15.2[L/min] |
| Chilled water flow rate. | 8.2 [L/min] |
| Cycle time | Adsorption 600 [sec.] Desorption 600 [sec.] |
| Isosteric heating duration | 60 [sec.] |
| Isosteric cooling duration | 60 [sec.] |

Temperature profile of the heat transfer fluid (water). In the following, a several tests are conducted under the operating conditions reported in Table 9. The cooling water inlet temperature is 25 °C while the hot water temperature ranging from 75-80 °C and the chilled water inlet temperature is 14 °C.

Fig. 11 shows the temperature profiles during the experiment carried out under above detailed conditions. In details, the figure shows the inlet and outlet heat transfer fluid temperatures for the two beds and the inlet and outlet water temperature for the condenser and the evaporator for 7 cycles. It indicates that the system has a stable operating repeatability along the operating time. The chilled water inlet temperature at the beginning was about 18 °C and from the second cycle it was kept stable at 14 °C with a small variation about 0.4 °C. The chilled water outlet temperature was varied from 12.3 °C to 14 °C at the end of the adsorption cycle, at the beginning of the adsorption cycle the temperature dropped to the lowest value quickly due to the high adsorption capability of the adsorber then increased gradually to reach its maximum value 14 °C at the end of the cycle due to the weakness of the adsorber at the end of the phase. At the preheating and precooling phases, there is no change in the chilled water temperature as there is no refrigeration in the evaporator in these phases.

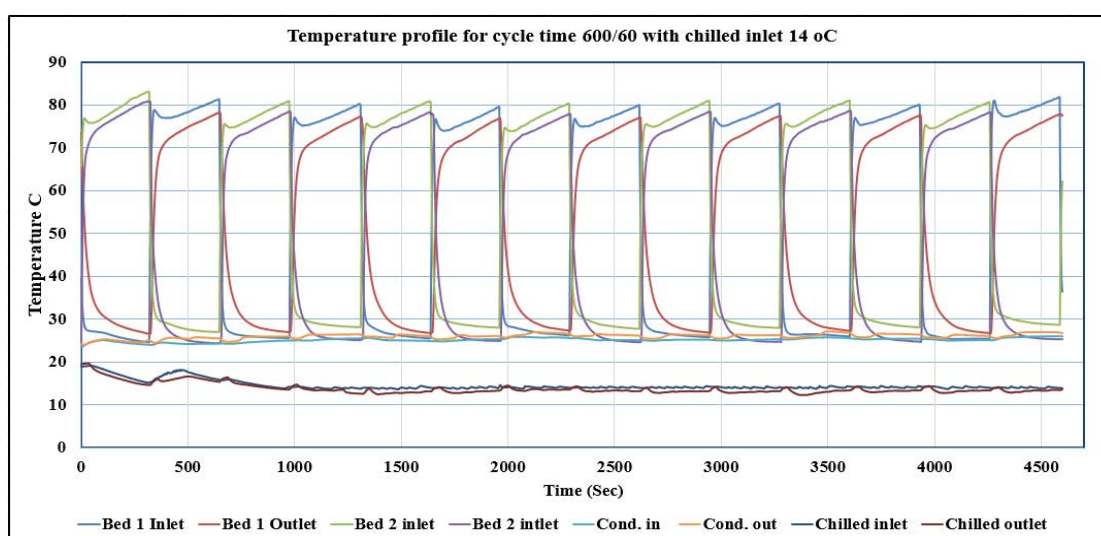


Fig. 11 Temperature profile for cycle time 600/60 with chilled inlet 14 °C

The cooling water inlet temperature and a single bed inlet and outlet temperature during the adsorption and desorption phases are shown in Fig. 12. The cooling water temperature was controlled to be about 25 °C with a small variation about 0.6 °C while the hot water temperature was varied from 75 °C to 80 °C along the desorption phase. The outlet temperature of the cooling and heating water is varying largely during the adsorption and desorption phases and the average temperature difference for the heating and cooling water is about 3.5 and 2.5 °C, respectively. During the preheating process, there is a noticeable change in the hot water inlet temperature, the temperature decreased first then increased again along the desorption phase. This is because the bed in that time is subjected to the cooling water from the previous adsorption phase so, during the beginning of preheating phase the bed temperature was low then increases gradually along the desorption phase. In contrast, during the precooling phase, the cooling water increased first then decreased along the adsorption phase to reach the cooling water tank temperature because the bed temperature was high from the previous desorption phase. In the adsorption phase, it can be seen that the cooling water temperature difference is high at the starting then reduces gradually along the whole time of this phase because the adsorber has high adsorption capacity, so it releases much heat to adsorb more at the beginning then decreases gradually at the end of the phase. Finally, during the desorption process the desorber will adsorb much heat to desorb more at the beginning of the phase; so, the hot water temperature difference reduces along the desorption phase.

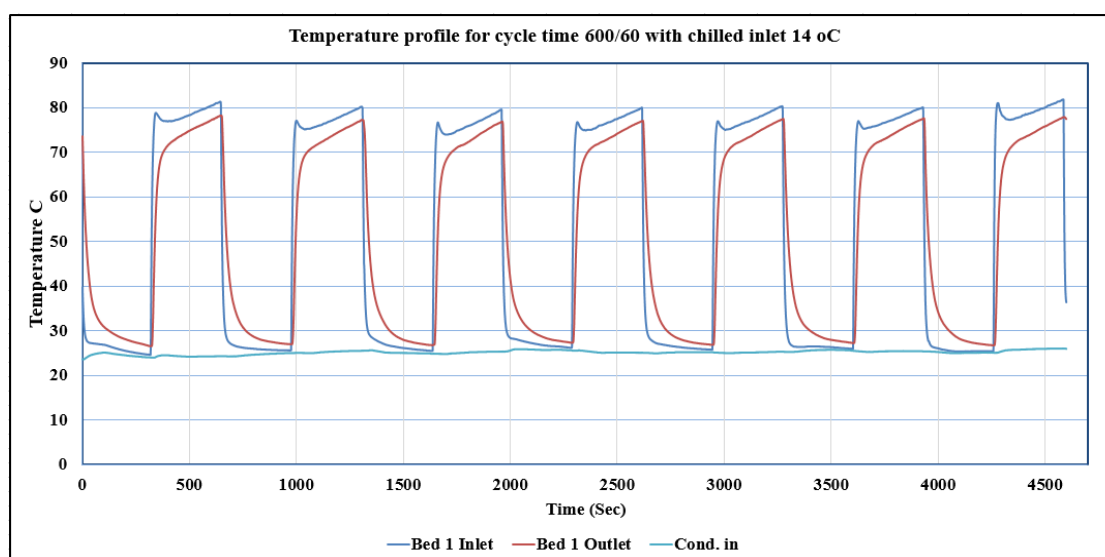


Fig. 12 Inlet and outlet bed temperature profile for single bed

Pressure profile of the main components. Fig. 13 shows the pressure profile during the chiller operation. It can be seen that the pressure of the evaporator reaches its minimum value about 9 mbar while Beds pressure are about 7 mbar.

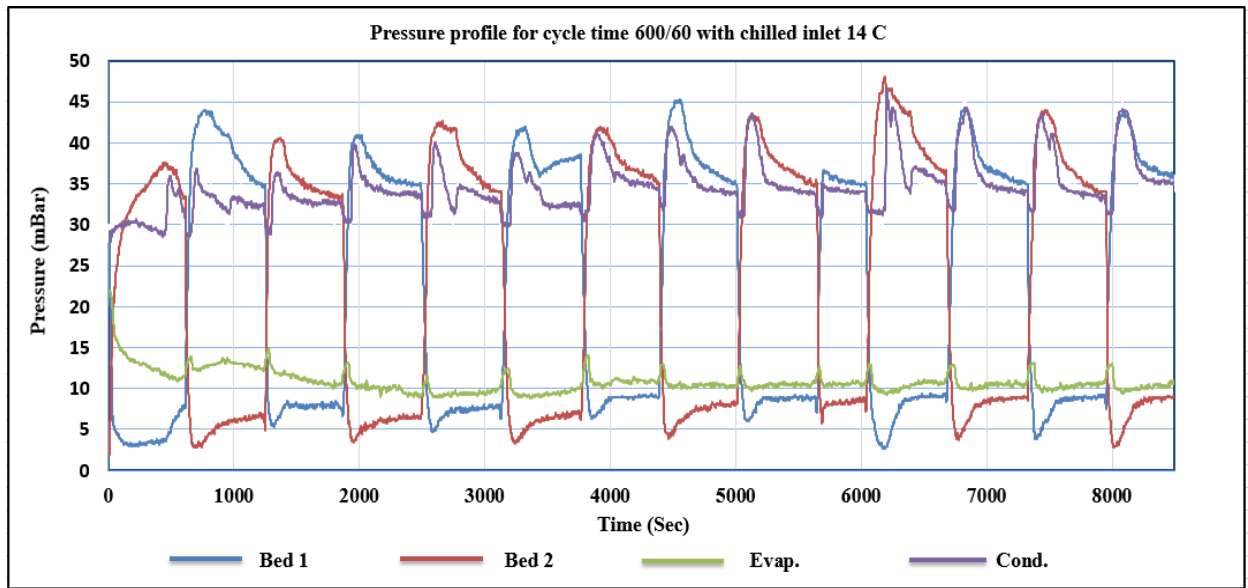


Fig. 13 Pressure profile for cycle time 600/60 with chilled inlet 14 °C

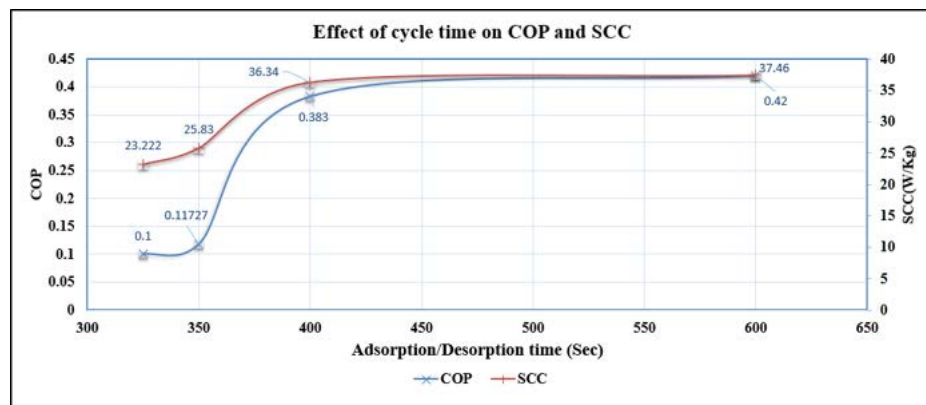


Fig. 14 Effect of adsorption/desorption phase time on the SCC and COP

Effect of adsorption/desorption phase time on adsorption performance.

Fig. 14 shows the effect of adsorption/desorption phase time on the SCP and COP performance of the adsorption

cooling system. It is noticed that the COP increases continuously with the increasing of phase time. The operating conditions are same as the values specified in Table 9 except the phase time since it is being discussed here and the chilled water inlet temperature is 18 °C. The COP is almost stable below 360 sec. then both COP and SCC increase dramatically with the phase time till 400 sec. The growth rate then slows down to be stable above 460 sec. For shorter adsorption/desorption phase times, liquid will remain filled to the larger pore radius until an equilibrium vapor pressure that satisfies the smaller pore radius is reached and the non-uniformity of pore geometries as shown in Fig. 7 yields a hysteresis which in role makes the desorption process incomplete. This hysteresis restricts the adsorption capacity of silica gel adsorbent. As a result, the SCP and COP are low at a shorter phase time. To conclude, it is obvious that the optimum adsorption/desorption phase time for this prototype is 460 sec.

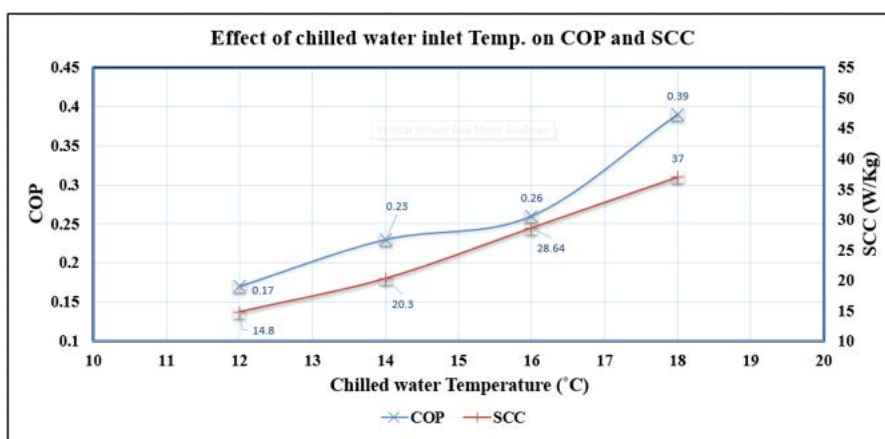


Fig. 15 Effect of chilled water inlet temperature on the SCP and COP

Effect of chilled water temperature on adsorption performance. The variations of COP and SCC with different chilled water inlet temperature to the evaporator are shown in

Fig. 15. It is found that both COP and SCC increase with the increase of chilled water inlet temperature. This is because higher chilled water temperature leads to higher evaporation pressure which in turn increases the cycle adsorbate mass and then a larger amount of water vapour is adsorbed by the silica gel adsorbent. As a result the cooling capacity increases with increasing chilled water inlet temperature.

Conclusions

Adsorption cooling has been considered as an important way to utilize low-grade thermal energy replacing the traditional vapor compression refrigeration units. A lab-scale two-bed adsorption chiller with silica gel-water as the adsorbent-adsorbate pair was designed, constructed and the system performance was experimentally evaluated under various operating conditions and the conclusions are drawn as follows.

- The system performance has a stable operating repeatability along the full operating time under various adsorption / desorption phase times.
- The optimal half cycle time is 460 sec. under the conditions of 80 °C hot water temperature, 25°C cooling water temperature, 18°C chilled water temperature. The COP and SCP can reach 0.38, 36.34 W/kg.
- The COP and SCP increase with the increasing of hot water temperature, the decreasing of cooling water temperature, the increasing of chilled water temperature.

Acknowledgement

This work is funded by the Science and Technology Development Fund (STDF) under the National Challenge Program NCP Grants, project ID 10519. We would like to thank Birmingham University in UK for their support in analysing silica gel used in this research.

References

- [1] M. Verde, K. Harby, J.M. Corberán, Optimization of thermal design and geometrical parameters of a flat tube-fin adsorbent bed for automobile air-conditioning, *Appl. Therm. Eng.* 111 (2017) 489–502.
- [2] I. Girnik, et al., Dynamic optimization of adsorptive chillers: compact layer vs. bed of loose grains, *Appl. Therm. Eng.* 125 (2017) 823–829.
- [3] M.B. Elsheniti, O.A. Elsamni, R.K. Al-dadah, S. Mahmoud, E. Elsayed, K. Saleh, Adsorption refrigeration technologies, in: *Sustainable Air Conditioning Systems*, IntechOpen, 2018, pp. 71-95.
- [4] H.T. Chua, K.C. Ng, A. Malek, T. Kashiwagi, A. Akisawa, B.B. Saha, Modeling the performance of two-bed silica gel– water adsorption chillers, *Int J Refrig* 22 (1999) 194–204.
- [5] H.T. Chua, K.C. Ng, W. Wang, C. Yap, X.L. Wang, Transient modeling of a two-bed silica gel–water adsorption chiller, *Int J Heat Mass Transfer* 47 (2004) 659–669.
- [6] B.B. Saha, E.C. Boelman, T. Kashiwagi, Computational analysis of an advanced adsorption-refrigeration cycle, *Energy* 20 (10) (1995) 983–994.
- [7] M.B. Elsheniti, A. Kotb, O. Elsamni, Thermal performance of a heat-pipe evacuated-tube solar collector at high inlet temperatures, *Applied Thermal Engineering*, 154 (2019) 315-325.
- [8] B.B. Saha, A. Akisawa, T. Kashiwagi, Silica gel water advanced adsorption refrigeration cycle, *Energy* 22 (4) (1997) 437–447.
- [9] Y.L. Liu, R.Z. Wang, Z.Z. Xia, Experimental performance of a silica gel–water adsorption chiller, *Appl Therm Eng* 2 (2005) 3359–3375.
- [10] Wang DC, Wu JY, Xia ZZ, et al., Study of a novel silica gel-water adsorption chiller: part I. Design and performance prediction. *Int J Refrig*;28(7): (2005) 1073–83.
- [11] M.B. Elsheniti, M.A. Hassab, A.-E. Attia, Examination of effects of operating and geometric parameters on the performance of a two-bed adsorption chiller, *Applied Thermal Engineering*, 146 (2019) 674-687.
- [12] H.T. Chua, K.C. Ng, W. Wang, C. Yap, X.L. Wang, Transient modeling of a two-bed silica gel–water adsorption chiller, *International Journal of Heat and Mass Transfer* 47 (2004) 659–669.
- [13] H.T. Chua, K.C. Ng, A. Malek, T. Kashiwagi, A. Akisawa, B.B. Saha, Modeling the performance of two-bed gel–water adsorption chiller, *International Journal of Refrigeration* 22 (1999) 194–204.
- [14] H.T. Chua, K.C. Ng, A. Malek, T. Kashiwagi, A. Akisawa, B.B. Saha, Multi-bed regenerative adsorption chiller—improving the utilization of waste heat and reducing the chilled water outlet temperature fluctuation, *International Journal of Refrigeration* 24 (2001) 124–136.
- [15] A. Çağlar, The effect of fin design parameters on the heat transfer enhancement in the adsorbent bed of a thermal wave cycle, *Appl. Therm. Eng.* 104 (2016) 386–393.
- [16] A. Sharafian, C. McCague, M. Bahrami, Impact of fin spacing on temperature distribution in adsorption cooling system for vehicle A/C applications, *Int. J. Refrig.* 51 (2015) 135–143.
- [17] Sapienza A, Santamaria S, Frazzica A, Freni A. Influence of the management strategy and operating conditions on the performance of an adsorption chiller. *Energy* 2011;36:5532–8.
- [18] Aristov YuI, Sapienza A, Ovoshchnikov DS, Freni A, Restuccia G. Reallocation of adsorption and desorption times for optimisation of cooling cycles. *Int J Refrig* 2012;35:525–31.
- [19] Santamaria Salvatore, Sapienza Alessio, Frazzica Andrea, Freni Angelo, Girnik Ilya S, Aristov Yuri I. Water adsorption dynamics on representative pieces of real adsorbers for adsorptive chillers. *Appl Energy* 2014;134:11–9.

- [20] K. C. Ng, H. T. Chua, C. Y. Chung, C. H. Loke, T. Kashiwagi, A. Akisawa and B. B. Saha, Experimental investigation of the silica gel-water adsorption isotherm characteristics, Applied Thermal Engineering 21, (2001)1631-1642.
- [21] X. Wang, W. Zimmermann, K. C. Ng, A. Chakraborty and J. U. Keller, Investigation of the isotherm of silica gel + water systems : TG and volumetric methods, Journal of Thermal Analysis and Calorimetry 76, (2004) 659-669.
- [22] IUPAC Recommendations Pure Awl. Chem. 1985, 57, 603.
- [23] IUPAC Recommendations Pure Awl. Chem. 1994, 66, 1739.
- [24] Wang, X.L., H.T. Chua, and L.Z. Gao, A thermogravimetric analyzer for condensable gas adsorption under subatmospheric conditions. Journal of Thermal Analysis and Calorimetry, 2007. 90: p. 935-940.

26- NiCo alloy/carbon nanofibers composite as effective non-precious electrocatalyst for PEMFCs and hydrogen production

Nasser A. M. Barakat^{1,*}, Wael Abdelmoaz¹ and Marwa M. Abdelati¹

¹Chemical Engineering Department, Minia University, El-Minia, Egypt
nasbarakat@mina.edu.eg (N.A.M. Barakat)

Abstract

The successful commercialization of the proton exchange membrane fuel cells (PEMFCs) is quite dependent on the cost, activity and durability of the electrocatalysts. Alloy structure generates special characteristics for the nano-metallic compounds which makes this interesting class of materials promising candidates for many application fields. Moreover, the performance of the nanostructural catalysts is strongly influenced by the morphology; nanofibers reveal distinct catalytic activity compared to the nanoparticles. Because of its surface oxidation properties, nickel reveals good performance as an electrocatalyst. Many materials involving nickel as a component in their manufacture could be used as catalysts in fuel cells. Accordingly, Ni-based alloys were investigated; NiCu, NiCr and NiMn. Although, among the transition metals, cobalt has a well-known catalytic activity in many chemical reactions, it was not used as a main catalyst in the PEMFCs due to the low performance. As it is considered a chemical reaction/adsorption combination process, carbon was invoked as a support for many functional materials. In this study, novel nanofiber composite from Ni_xCo_{1-x} alloy nanoparticles incorporated in carbon nanofibers are investigated as electrocatalysts for oxidation of the most popularly used fuels in the PEMFCs; methanol urea and ethanol.

Keywords: PEMFCs, Nanofibers, Electrode, Electropisnning, Alcohol electrolysis

Introduction

Expected depletion of the fossil fuels provides the fuel cells great attentions as promised candidates for energy producing devices. Among the introduced cells, direct alcohol fuel cells (DAFCs) have received much attention during the last decade because the alcohols are inexpensive, readily available, and easily stored and transported liquid fuels [1, 2]. DAFCs do not have many of the fuel storage problems typical of some fuel cells because the alcohols have a higher energy density than hydrogen—though less than gasoline or diesel fuel. The successful commercialization of the fuel cells is quite dependent on the cost, activity and durability of the electrocatalysts [3, 4]. Alloy structure generates special characteristics for the nano-metallic compounds which makes this interesting class of materials promising candidates for many application fields. Moreover, the performance of the nanostructural catalysts is strongly influenced by the morphology; nanofibers reveal distinct catalytic activity compared to the nanoparticles. Because of its surface oxidation properties, nickel reveals good performance as an electrocatalyst. Many materials involving nickel as a component in their manufacture could be used as catalysts in fuel cells [5-7]. Accordingly, Ni-based alloys were investigated; NiCu, NiCr and NiMn [8-10]. Although, among the transition metals, cobalt has a well-known catalytic activity in many chemical reactions, it was not used as a main catalyst in the direct alcohols fuel cells (DAFCs) due to the low performance [11]. As it is considered a chemical reaction/adsorption combination process, carbon was invoked as a support for many functional materials. In this study, novel nanofiber composite from Ni_xCo_{1-x} ($x = 0.0, 0.1, 0.3, 0.5, 0.7, 0.9$ and 1.0) alloy nanoparticles incorporated in carbon nanofibers are investigated as electrocatalysts for methanol and ethanol oxidation.

Methods

Cobalt (II) acetate tetra-hydrate (CoAc) and nickel (II) acetate tetrahydrate (NiAc) aqueous solutions were first prepared and then mixed with poly(vinyl alcohol) (PVA) aqueous solution (10 wt %). Several solutions were prepared to study the effect of composition of the metallic counterpart; typically, the composition of the solutions was adapted to produce nanofibers having $\text{Ni}_x\text{Co}_{1-x}$ where $x = 0.0, 0.1, 0.3, 0.5, 0.7, 0.9$ and 1.0 . Generally, the polymer content in the final solutions was 7.5 wt%; this polymer content reveals the optimum viscosity for the electrospinning process. The solutions were vigorously stirred at 50 °C for 5 h. The electrospinning process has been carried out under DC voltage of 20 kV. The formed nanofiber mats were initially dried for 24 h at 80 °C under vacuum, and then calcined at 800 °C for 5 h in argon atmosphere with a heating rate of 2.3 °C/min.

Results and discussion

Interestingly, due to the polycondensation characteristics of the utilized metal precursors, calcination of the prepared electrospun nanofiber mats did not affect the nanofibrous morphology for all formulations. As example, Fig. 1 displays the FE SEM images for the nanofibers obtained after calcination of $\text{Ni}_{0.5}\text{Co}_{0.5}$, as shown good morphology nanofibers were obtained.

Figure 2 shows the XRD analysis results for three formulations of the sintered nanofibers. The strong diffraction peaks indicate the formation of both cobalt and nickel metals with FCC crystal structure.

Fig. 3 shows the electrocatalytic activity of the proposed nanofiber composites toward methanol and ethanol. As shown, a strong influence for the cobalt content on the electrocatalytic activity of the proposed nanofibers toward both of methanol and ethanol can be observed. Moreover, addition of cobalt does not only affect the produced current, but it also impacts the electrooxidation onset potentials of the two alcohols as shown in the figures.

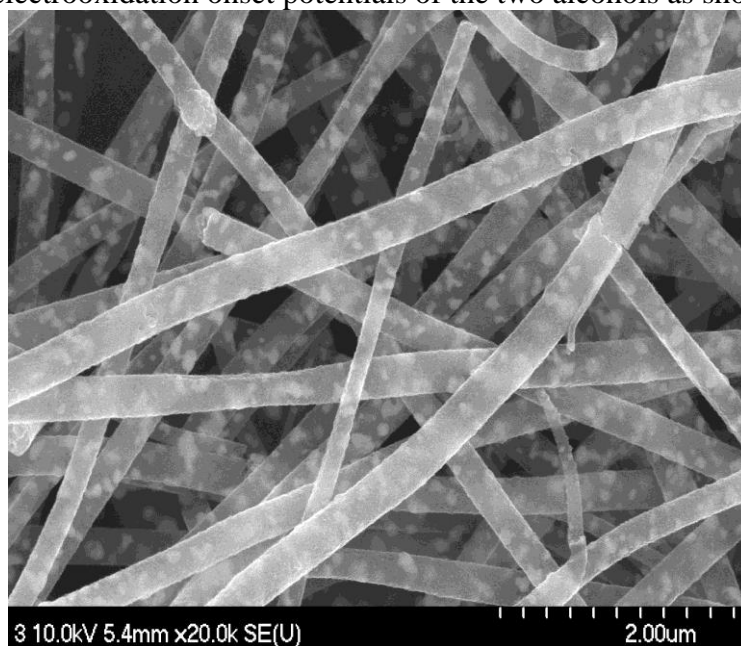


Fig. 1 FE SEM image for the $\text{Ni}_{0.5}\text{Co}_{0.5}$ sample

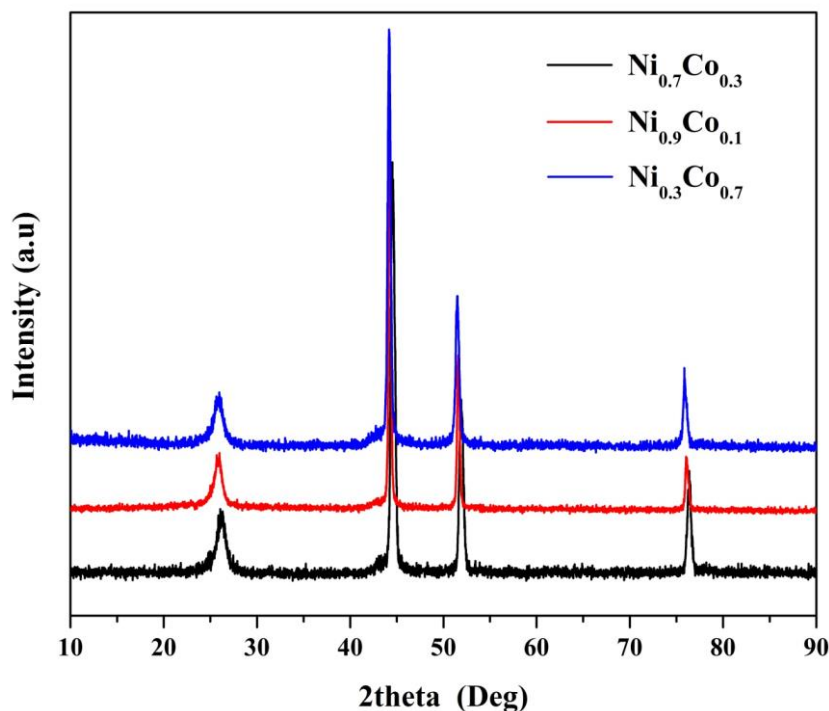


Fig. 2 XRD spectra for three prepared samples after calcination; $\text{Ni}_{0.7}\text{Co}_{0.3}$, $\text{Ni}_{0.9}\text{Co}_{0.1}$ and $\text{Ni}_{0.3}\text{Co}_{0.7}$.

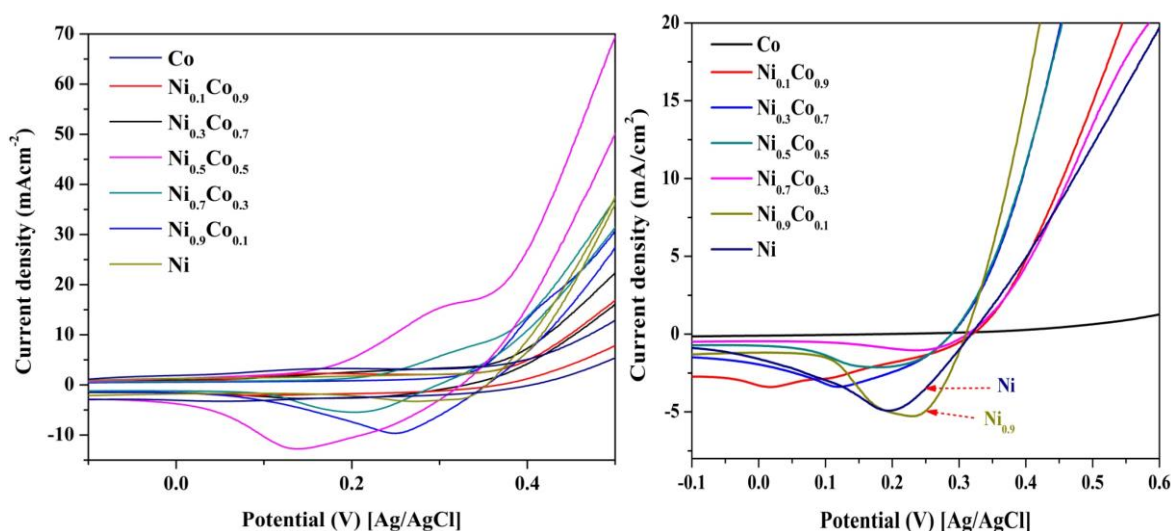


Fig. 3 Electrocatalytic activities of the prepared nanofiber composites toward methanol and ethanol.

14 Conclusions

Exploiting the abnormal thermal decomposition of nickel and cobalt acetates in the inert atmosphere can be utilized to produce nickel/cobalt alloy nanoparticles incorporated in carbon nanofibers. Briefly, calcination of electrospun nanofibers composed of nickel acetate tetrahydrate, cobalt acetate tetrahydrate and poly(vinyl alcohol) in argon atmosphere at 800 °C leads to produce metallic alloy-doped carbon nanofibers. Composition of the metallic counterpart strongly affects the electrocatalytic activity of the synthesized nanofibers toward methanol oxidation. The nanofibrous morphology and the supporting on carbon matrix have also considerable influences on the electrocatalytic activity. Therefore, it can be concluded that carbon nanofibers having $\text{Ni}_{0.5}\text{Co}_{0.5}$ alloy nanoparticles are the optimum electrocatalyst due to the corresponding high current density and low onset potential. Overall, it can be claimed

that the metallic alloys nanoparticles-doped carbon nanofibers might be new promised non precious electrocatalysts for fuel cells applications.

References

- [1] J. Prakash, D.A. Tryk, E.B. Yeager, Kinetic investigations of oxygen reduction and evolution reactions on lead ruthenate catalysts, *JOURNAL-ELECTROCHEMICAL SOCIETY*, 146 (1999) 4145-4151.
- [2] N.A. Barakat, M.A. Abdelkareem, A. Yousef, S.S. Al-Deyab, M. El-Newehy, H.Y. Kim, Cadmium-doped cobalt/carbon nanoparticles as novel nonprecious electrocatalyst for methanol oxidation, *Int. J. Hydrogen Energy*, 38 (2013) 183-195.
- [3] J. Shen, Y. Hu, C. Li, C. Qin, M. Ye, Pt–Co supported on single-walled carbon nanotubes as an anode catalyst for direct methanol fuel cells, *Electrochim. Acta*, 53 (2008) 7276-7280.
- [4] Y. Shao, J. Sui, G. Yin, Y. Gao, Nitrogen-doped carbon nanostructures and their composites as catalytic materials for proton exchange membrane fuel cell, *Appl. Catal., B*, 79 (2008) 89-99.
- [5] A. Rahim, R. Abdel Hameed, M. Khalil, Nickel as a catalyst for the electro-oxidation of methanol in alkaline medium, *J. Power Sources*, 134 (2004) 160-169.
- [6] C. Fan, D. Piron, A. Sleb, P. Paradis, Study of Electrodeposited Nickel-Molybdenum, Nickel-Tungsten, Cobalt-Molybdenum, and Cobalt-Tungsten as Hydrogen Electrodes in Alkaline Water Electrolysis, *J. Electrochem. Soc.*, 141 (1994) 382-387.
- [7] I.A. Raj, K. Vasu, Transition metal-based hydrogen electrodes in alkaline solution—electrocatalysis on nickel based binary alloy coatings, *J. Appl. Electrochem.*, 20 (1990) 32-38.
- [8] J.M. Marioli, P.F. Luo, T. Kuwana, Nickel—chromium alloy electrode as a carbohydrate detector for liquid chromatography, *Anal. Chim. Acta*, 282 (1993) 571-580.
- [9] J.M. Marioli, T. Kuwana, Electrochemical detection of carbohydrates at nickel-copper and nickel-chromium-iron alloy electrodes, *Electroanalysis*, 5 (1993) 11-15.
- [10] I. Danaee, M. Jafarian, A. Mirzapoor, F. Gobal, M. Mahjani, Electrooxidation of methanol on NiMn alloy modified graphite electrode, *Electrochim. Acta*, 55 (2010) 2093-2100.
- [11] N.A.M. Barakat, M.A. Abdelkareem, H.Y. Kim, Ethanol electro-oxidation using cadmium-doped cobalt/carbon nanoparticles as novel non precious electrocatalyst, *Applied Catalysis A: General*, 455 (2013) 193-198.

24-Life cycle assessment of three high-performance glazing systems

Youssef O. Elkhayat^{†1}, Mona G. Ibrahim¹, A. AbdelMonteleb M. Ali^{2,3}

¹Egypt-Japan University of Science and Technology, Alexandria, Egypt

²Assiut University, Assiut, Egypt

³Qassim University, Qassim, Kingdom of Saudi Arabia

[†]E-mail: youssef.elkhayat@ejust.edu.eg

Abstract

This study focuses on conducting comparative energy and environmental life cycle assessment (LCA) of three widely commercial high-performance glazing systems (HPGS) namely are Low-E, Electrochromic, and PV. The system boundry of this study is from the resource extraction stage to the stage of factory gate which is before transportation to the consumer in which it is entitled from cradle-to-gate in the LCA concept. There are cut-off phases; the use phase and disposal phase of the product. The paper aims to provide integrated study between the energy and environmental LCA tool to help specialists to select the most environment-friendly glazing system. A conventional clear double-glazing system (CDGS) is used as a basic case for benchmarking and compared to the three HPGS cases. For life cycle inventory (LCI) data, the study relied on Ecoinvent V3.5 database as a primary source besides secondary sources such as; publications, interviews, literature, and technical reports. The life cycle impact assessment (LCIA) measured six important categories; (Acidification, Eutrophication, Global warming potential, Non-renewable energy, Ozone layer depletion, and Terrestrial acid/nutria) by openLCA V1.7 software. The results of the comparison of the integrated assessment method between energy and environmental life cycle assessments show that; the PV glazing system (PVGS) consumed 166% life cycle energy of that of the CDGS and had the highest environmental impacts among the other cases, followed by the Electrochromic glazing system (ECGS). The research also shows that the melting process is the primary contributor to life cycle energy and environmental impact categories for all scenarios.

Keywords: High-performance glazing systems, Comparative life cycle assessment, Low-E glazing, Electrochromic glazing, PV glazing.

1 Introduction

Nowadays, glazing is one of the largest building's components and plays a major role in energy consumption and comfort parameters, besides affecting the environment [1,2]. The facade's design is responsible for 40% of the building's cooling loads [3]. Therefore, use of high-performance glazing systems (HPGS) has become an urgent necessity for its effectiveness in blocking the external environmental effects and improving the indoor environment with minimum energy consumption when compared with the conventional glazing systems [4]. As a possible result, applying the HPGS in buildings with air conditioning is estimated to reduce CO₂ emissions which the achieved reduction will outweigh those created in the glass production during the glass life cycle [5]. There are three widely commercial passive, active and BIPV HPGS; Low-E glazing system (LEGS) as a passive system which does not need external power to work, Electrochromic and PV glazing as active systems. Low-E glazing is coated by layers of selective coatings which reflect the infra-red radiation without any significant loss in visible light transmission. Electrochromic glazing system (ECGS) can adjust the optical properties through running voltage [6]. PV glazing system (PVGS) reduces light transmission, provides sun shading and generates electricity [7]. However, these systems can save energy and indoor comfort, it is expected that the HPGS have materials could affect negatively on the environment. Therefore, environmental factor such as emissions and waste need to be considered carefully when specifying the glazing systems for buildings.

Furthermore, analyzing the environmental impacts of the building components in the first stages of its life cycle is one of the requirements to design a sustainable building.

The study investigates the environmental impact of these HPGS according to the life cycle assessment (LCA) method and compares its impacts to that of a conventional clear double glass facade system (CDGS). In this paper, the energy consumption and CO₂ emissions have been addressed and investigated analytically by LCA tool. LCA is a widely applied technique which can be used in comparing building components alternatives to help architects in choosing the most environmentally-friendly alternative [8]. The LCA study aims to compare the environmental impacts of three types of HPGS and that of CDGS. The study investigates systems' environmental impacts from cradle-to-gate, then compares between them to determine which system has the lowest energy use and environmental impacts. Because of the high temperature for melting glass raw materials and energy consumption, the manufacturing of float glass has many environmental impacts. Emissions (i.e. carbon dioxide, sulfur dioxide, and nitrogen oxides) result from the high-temperature oxidation of atmospheric nitrogen. Furthermore, emissions from the furnace which contain dust and traces of chlorides, fluorides, and metals present in the raw materials as scums. As general, float glass should not present water pollution as water is used mainly for cooling and cleaning which can be reused or treated [9].

2 Methods

To quantify, evaluate, and compare the energy use and environmental impacts of glazing systems; energy and environmental LCA is the strongest quantitative technique which can be used for these analyses. The most widely used method of LCA in the built environment is environmental process-based LCA. This method identifies, quantifies and aggregates the input (raw materials, energy) and outputs (solid waste, air emissions) associated with the product's life cycle. Then, the inputs and outputs are classified according to their impacts. Finally, they are converted to indicators which represent several categories of environmental impacts [10].

To produce the clear float glass which is the main element of manufacturing the three types of HPGS, as in Fig. 1, the extracted raw materials are mixed in the first stage of the float glass manufacturing process. The mixing process contains raw materials (silica, soda ash, lime, feldspar, and dolomite) which are added with 15% recycled glass (cullet) and other compounds depending on the desired properties. The second stage is melting in a furnace the raw materials at 1,550°C. Then, the forming stage where the molten glass is fed into a bath of molten tin. The fourth stage is cooling in annealing lehr where the glass is passed through a controlled cooling tunnel measuring more than 100 meters in length. After cooling, the glass exits the lehr at room temperature to be automatically cut in the final stage to be ready for the next stage of coating and assembling the insulating glazing unit (IGU) [11].

The present study relies on openLCA V1.7 which an open source software for life cycle and sustainability assessment is [12]. According to ISO 14040 Environmental management [13], the LCA study consists of four phases; goal and scope definition, life cycle inventory (LCI) analysis, life cycle impact assessment (LCIA) and life cycle interpretation. Ecoinvent V3.5 database [14] is the primary source of the LCI data besides secondary sources such as; publications, interviews, literature, and technical reports.

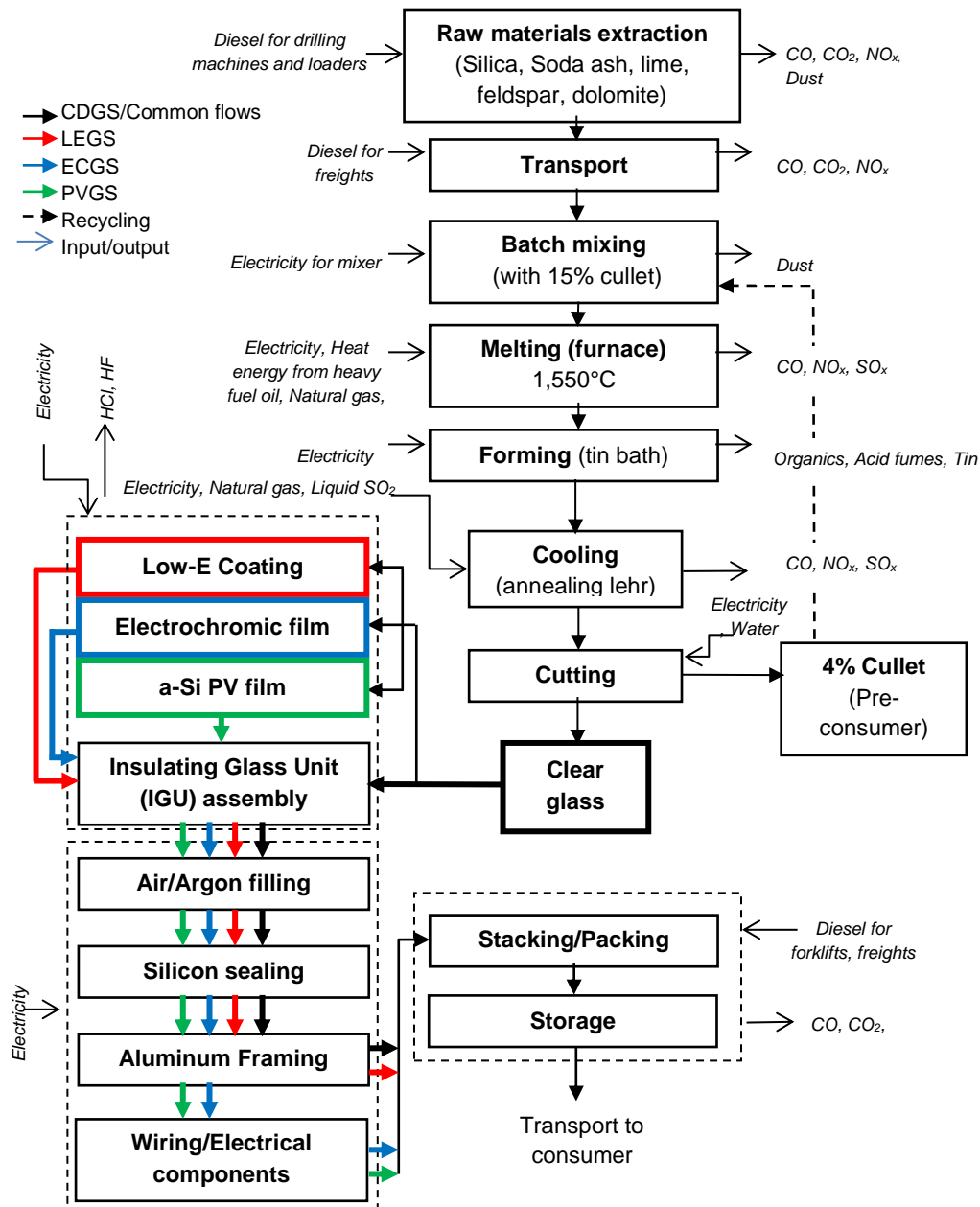
2.1 Goal and scope definition

The first phase of the LCA which defines the application of the LCA to the audience including; system boundaries, functional unit, assumptions, and limitations.

2.1.1 Goal and scope

The goal of this comparative LCA study is investigating and comparing between the environmental impacts of three HPGS (LEGS, ECGS, and PVGS) and that of the CDGS to comprehend which glazing system's life cycle has the lowest energy use and environmental

impacts. Accordingly, it will help in finding methods to reduce the environmental impact caused by glazing systems. The life cycle inventory data and analysis results are expected to assist architects and decision makers in choosing the most sustainable glazing system for buildings. To achieve this goal, the scope of this LCA study includes; Life cycle inventory


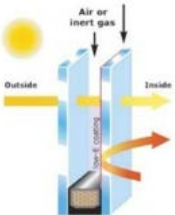
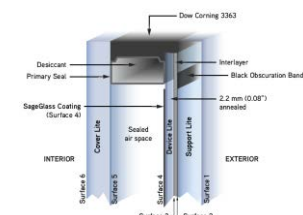
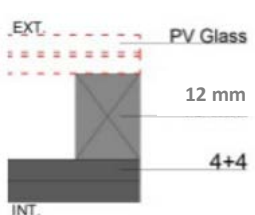


analysis (LCI) and Life cycle impact assessment (LCIA). The LCA investigated the environmental impacts during the pre-use phase of the glazing system. The inventory data associated with material extraction and production stages were obtained from Ecoinvent V3.5 database.

Fig. 1 The life cycle flow chart of the three HPGS [Author]

The selection of HPGS scenarios was based on comparing the most widely commercial passive, active and BIPV systems in the market for building façades. Each case was represented by a type which had the lowest SHGC or U-value (Table 1). A conventional CDGS was used as a basic scenario for benchmarking and comparing to the three HPGS.

Table 1 Basic and HPGS scenarios' specifications

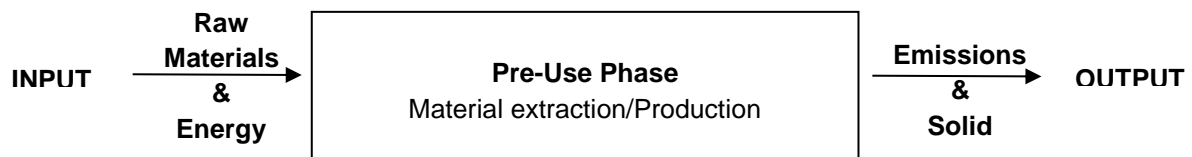
| Scenarios Type | Basic CDGS [a] | Passive LEGS [b] | Active ECGS [c] | BIPV PVGS [d] |
|----------------|---|---|---|---|
| Cross-Section |  |  |  |  |
| Specifications | 6mm clear glass pane + 16mm Sealed air + 6mm clear glass pane | 6mm (Dual-coated) glass + 16mm 90% argon cavity + (Low-E) coating + 6mm glass | 6mm clear glass + 0.89mm SentryGlass + 2.2mm SageGlass + 10mm air space with 90% Argon fill + 6mm clear glass | (6+3+6) mm amorphous silicon photovoltaic glass with a transparency 20% + 12mm air chamber + (4+4) mm clear glass |

Source: a. Saint-Gobain Glass EG - SGG PLANILUX®, b. Saint-Gobain Glass UK Ltd - SGG PLANITHERM® 4S II, c. SAGE® Electrochromics, Inc., d. Onyx Solar® Energy S.L.

2.1.2 System boundaries

ISO 14040 defined the system boundary as “a set of criteria specifying which unit processes are part of a product system” [19]. In Fig. 2, the pre-use life cycle phase was considered in this study. The pre-use phase of glazing systems includes processes (i.e. material extraction and production). The researcher is interested in studying (Acidification, Eutrophication, Global warming potential, Non-renewable energy, Ozone layer depletion, and Terrestrial acid/nutria) impact categories because of their importance.

Fig. 2 The LCA system boundaries



2.1.3 Functional unit

In ISO 14040, the International Organization of Standards has defined the functional unit as “quantified performance of a product system for use as a reference unit” [19]. To make a meaningful comparison, the functional unit for this comparative LCA study was determined to be 1 m² of the glazing system.

2.1.4 Assumptions and limitations

The comparative LCA study makes assumptions to facilitate the assessment of environmental impacts and to directly compare the three HPGS. The extraction of materials was assumed to occur within a radius of 1600 km from the manufacturing site. The LCA study limitations were related to the scope of the study and the system boundaries. The emissions associated with transportation were assessed based on the traveling distance and the weight of materials, neglecting its volume.

2.2 Life cycle inventory

Considering the functional unit, system boundaries and assumptions, the second phase of LCA - Life Cycle Inventory (LCI) - identifies and quantifies the environmental inputs and outputs associated with HPGS scenarios. The amount of input energy, raw materials, output emissions and solid waste from pre-use phase of the three HPGS life cycle were inventoried. The LCI data were obtained from Ecoinvent V3.5 database as a primary source and also from other sources such as; publications, interviews, literature, and technical reports.

In this research, openLCA V1.7 software is used for both LCI and LCIA. It is a LCA tool which is capable of addressing the entire life cycle of a glazing system from raw material extraction to production process. The tool depends mainly on Ecoinvent V3.5 database to model and analyze the environmental performance of glazing systems. The LCI results include; raw

| | CDGS | LEGS | ECGS | PVGS |
|-------------------------------------|------|------|--------|--------|
| Pre-use phase energy (MJ/FU) | 646 | 938 | 1016.7 | 1074.7 |

materials, energy inputs, emissions to air and the generated waste.

2.2.1 Material inputs

The scenarios' life cycle was modeled from resource extraction 'cradle' to factory gate (cradle-to-gate) via openLCA tool. The scenarios participate in the beginning processes of manufacturing the 6 mm clear float glass. After that, each sc of the three HPGS has specialized manufacturing processes to produce its isolated glass unit (IGU) which is installed on the office building façade (Fig. 1). Due to the comparative purpose, the materials which could not affect the results of LCA were not modeled in the tool. Table 3 shows the material inputs of the four scenarios of glazing systems, as developed by openLCA, as a part of the study LCI modeling.

Table 3 Material inputs and their quantities in (kg/FU) for the four scenarios

2.2.2 Pre-use phase energy inputs

The energy inputs in the pre-use phase consist of energy consumption in material extraction, processing, transportation, and on-site installation. The total embodied and transportation energy of each glazing system was calculated by the total mass input per functional unit and the total traveling distance of 1600 km respectively. Table 4 shows that the PVGS has the highest pre-use energy consumption (166%) of that of the CDGS due to the process of coating the a-Si layer between two 6 mm clear glass panels and consumes 7% of the total pre-use phase energy. In the second place, the ECGS which consumed 157% energy of that of the CDGS due to the coating process of electrochromic layers with Tungsten trioxide (WO₃) which consumes

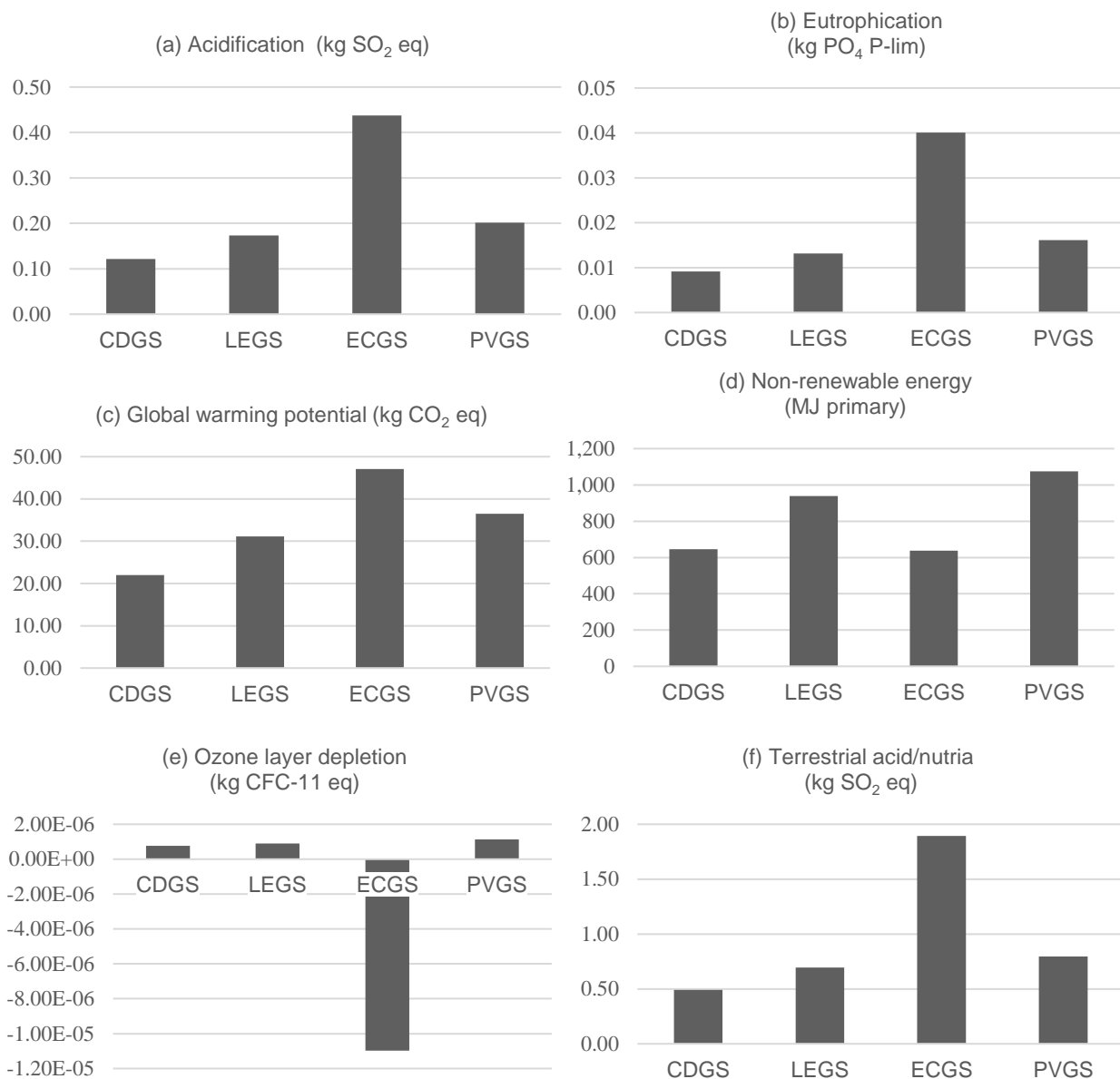
| Materials | CDGS | LEGS | ECGS | PVGS |
|------------------------|-------|---------|---------|--------|
| Clear glass (6 mm) | 30 | 30 | 30 | 30 |
| SentryGlass (0.89 mm) | - | - | 2.225 | - |
| SageGlass (2.2 mm) | - | - | 5.5 | - |
| Clear glass ((4+4) mm) | - | - | - | 20 |
| PV film | - | - | - | 7.4E-3 |
| WO ₃ layer | - | - | 7.47E-3 | - |
| Low-E coating | - | 2.75E-3 | - | - |
| Air | 0.02 | 2.06E-3 | 1.29E-3 | 0.0156 |
| Argon | - | 1.86E-2 | 0.012 | - |
| Aluminum | 0.31 | 9.01E-5 | 0.193 | 0.232 |
| Silicone sealant | 0.015 | 4.49E-6 | 0.0386 | 0.077 |
| Copper wire | - | - | 0.1 | 0.199 |

approximately 28% of the total pre-use phase energy. These results are in line with Citherlet's previous study [12] which concluded that the pre-use energy increases when the glazing system becomes more advanced with many components.

Table 4 Total pre-use phase energy for the four scenarios

2.3 Life cycle impact assessment

To classify the environmental inputs and outputs of the scenarios based on their impacts on the environment, the LCIA accumulates them into indicators to represent those impacts. In the classification step, the environmental LCI results are assigned to appropriate impact categories. Then, the characterization step which multiplies the quantity of each environmental input/output by its equivalent characterization factor for that impact category to convert quantities to environmental measures representing the environmental category of interest [16].



In openLCA V1.7, the Impact +2002 methodology is used for the impact assessment of the present study. The impacts of the four scenarios were assessed in six impact categories of (acidification, eutrophication, global warming potential, non-renewable energy, ozone layer depletion, and terrestrial acid/nutria). The impact results generated by openLCA involve the pre-use phase of glazing system life cycle as well as the transportation share associated with the pre-use phase.

3 Results and discussion

The summary of the impact assessment results is shown in Fig. 3. The following sections explain in detail the results of the impact assessment phase.

Fig. 3 Environmental impacts of the scenarios

3.1 Acidification and Eutrophication

Acidification accrues when the air pollutants transform into acids, which makes the pH-value of rainwater lower. Acidification is measured in a kilogram of equivalent sulfur dioxide (SO₂) which contributes certainly in acidification over its life cycle. Eutrophication is measured in kilogram PO₄ P-lim, reports the contribution of algae growth in water which results obstruction

of sunlight [15]. In both acidification and eutrophication impact categories, the lowest impacts are caused by CDGS scenario followed by LEGS (Fig. 3a, 3b), while ECGS contribute the most.

3.2 Global warming potential (GWP) and non-renewable energy (NRE)

Greenhouse gases are the main contributor to GWP. It is measured in a kilogram of CO₂ equivalent. The emissions of fossil fuels consumption during the melting process has a major source of contribution to GWP. Furthermore, fossil fuels are non-renewable source for energy. Therefore, both GWP and NRE impact categories are affected by the energy consumption in the pre-use phase. Although the GWP of ECGS is the highest (Fig. 3c), the NRE of it is the lowest. However, the NRE of PVGS is the highest (1075 MJ/FU) because of the energy-intensive PV film coating process. The ECGS saved 1.3% of the pre-use phase energy when compared with the base scenario (Fig. 3d).

3.3 Ozone layer depletion (OD)

The release of CFCs mainly causes ozone layer depletion. There are also other emissions such as HCFCs can cause OD. The results of OD impact category show that the PVGS scenario has the highest OD (150%) of that of the basic scenario. However, the ECGS have the lowest impact (Fig. 3e) with negative value (-1.096E-5).

3.4 Terrestrial acid/nutria

Atmospheric deposition of acidifying compounds is the main contributor in terrestrial acid/nutria. It is a global threat to plant diversity [16]. Low pH soil with low acid neutralizing capacity is generally categorized by increased toxicity of metals and decreased nitrification and organic matter decomposition rates [17]. In this impact category, the lower impacts are caused by LEGS (140%) of that of CDGS scenario, while the ECGS contributes the most (367%) (Fig. 3f).

4 Conclusion

The study investigated three scenarios which represent the most commercially used HPGS. The CDGS was considered as a base case “benchmark” for the comparison between the three types. The comparative analysis was done concerning the energy consumption and environmental life cycle impacts of the glazing systems. Therefore, the interpretation of results is important in light of present research assumptions and limitations.

In table 5, the scenarios were ranked according to their energy and environmental life cycle impacts. The ranking of scenarios exposes that the lowest energy and environmental life cycle impacts in all scenarios are caused by the CDGS, followed by the LEGS. Conversely, PVGS represent the highest environmental impacts comparing with the ECGS and LEGS. This refers to the low energy saving during the pre-use phase. In all environmental impact categories, the melting process represents the main contributor to overall scenarios life cycle.

Table 5 The ranking of scenarios based on their energy use and environmental impacts. (1 =

| Scen. | Ranks | Pre-use LC energy | Pre-use LC environmental impacts | | | | | |
|-------|----------|-------------------------|----------------------------------|-------|-----|-----|----|-------|
| | | | Acid. | Eutr. | GWP | NRE | OD | Terr. |
| CDGS | 1 | 1 | 1 | 1 | 1 | 2 | 2 | 1 |
| LEGS | 2 | 2 | 2 | 2 | 2 | 3 | 3 | 2 |
| ECGS | 3 | 3 | 3 | 3 | 3 | 1 | 1 | 4 |
| PVGS | 4 | 4 | 4 | 4 | 4 | 4 | 4 | 3 |

lowest; 4 = highest)

For all HPGS scenarios, the total pre-use phase life cycle is higher than that of CDEG. This emphasizes the importance of choosing eco-friendly materials and manufacturing methods to reduce the environmental impacts in the pre-use phase of the HPGS. Finally, the results present

an example of how the integrated energy and environmental life cycle analysis can affect the selection decision of the glazing systems especially in the early stage of the design process.

5 Limitations and recommendations

The limitations were related to resources; the study focused on just three scenarios of HPGS. Moreover, the LCI data has been collected via interviews with the manufacturers in various countries. Besides, Ecoinvent V3.5 which was used as the tool for LCI modeling and openLCA V1.7 for LCIA has a limited materials database which made the addition of more details in scenarios is impossible. The last limitation was the present study ignores both; the cost and social aspects of life cycle sustainability. Future research is recommended to especially focus on an integrated life-cycle cost (LCC) and environmental analysis of the glazing systems.

Acknowledgements

This paper is a part of the first author's Ph.D. thesis work, so he would like to thank the Egyptian Ministry of Higher Education (MoHE) for providing a fund for this Ph.D. research at the Egypt–Japan University of Science and Technology (E-JUST) where offered the required facilities and software to conduct this work. Furthermore, the authors would like to thank GreenDelta GmbH for the free openLCA V1.7 license and Ecoinvent database for academically free access.

References

- [1] IEA, Technology Roadmap: Energy-efficient Building Envelopes, International Energy Agency, 2013
- [2] G. Manioglu, Z. Yilmaz, Economic evaluation of the building envelope and operation period of heating system in terms of thermal comfort, *Energy and Buildings* 38 (3) (2006) 266–272
- [3] Hamza, N. A (2004), The Performance of Double Skin Facades in Office Building refurbishment in Hot Arid Areas, Ph.D. Thesis. University of Newcastle upon Tyne School of Architecture
- [4] A. Aksamija, Sustainable facades: Design methods for high-performance building envelopes: John Wiley & Sons, 2013
- [5] B. Scalet, M. Garcia Muñoz, A. Sissa, S. Roudier, and L. Delgado Sancho, “Best available techniques (BAT) reference document for the manufacture of glass,” *Institute for prospective technological studies. Seville: Joint Research Centre, European Commission*, 2013
- [6] R. J. Mortimer, D. R. Rosseinsky, and P. M. Monk, Electrochromic materials and devices: John Wiley & Sons, 2015
- [7] N. Skandalos, and D. Karamanis, “PV glazing technologies,” *Renewable and Sustainable Energy Reviews*, vol. 49, pp. 306-322, 2015
- [8] H. Babaizadeh, N. Haghighi, S. Asadi, R. Broun, and D. Riley, Life cycle assessment of exterior window shadings in residential buildings in different climate zones, *Building and Environment*, vol. 90, pp. 168-177, 2015
- [9] Pilkington.com, ‘Frequently Asked Questions about Sustainability’, 2018. [Online]. Available: <https://www.pilkington.com/europe/sweden/swedish/about+pilkington/sustainability/h%C3%83%C2%A5lbarhet+faqs.htm> (accessed: 23 December 2018).
- [10] R. Heijungs, S. Suh, Computational Structure of Life Cycle Assessment, Kluwer Academic Publishers, Dordrecht, 2002
- [11] A. Grané Anglarill, “Life cycle assessment of a conventional float glass production and comparison with regenerative alternatives,” Universitat Politècnica de Catalunya, 2018.

- [12] GreenDelta GmbH. openLCA. Available online: <http://www.openlca.org> (accessed: 06 March 2019).
- [13] International Organization of Standards, ISO 14040: 2006 Environmental Management—Life Cycle Assessment—Principle and Framework, National Standard Authority of Ireland, Geneva, 2006.
- [14] Ecoinvent (2018) Ecoinvent-center. Ecoinvent database v3.2; Swiss Centre for Life Cycle Inventories: 2010. www.ecoinvent.org/database/ (accessed 20 February 2019).
- [15] P. Eyerer, M. Weller, S. Hubner, J.A. Agnelli, Polymers—Opportunities and RisksII: Sustainability, Product Design and Processing, Springer, New York, 2010
- [16] Dentener et al., 2006a. Nitrogen and sulfur deposition on regional and global scales: a multi-model evaluation. Global Biogeochemical Cycles 20, GB4003
- [17] Bobbink et al., 2010; 2010. Global assessment of nitrogen deposition effects on terrestrial plant diversity: a synthesis. Ecological Applications 20, 30-59

25-Effect of the PV Position and Orientation on Improving Thermal Comfort

Lucienne G. Basaly^{1,3, a}, Mona G. Ibrahim^{1,2,b} and Mohammad Refaat M. Abdelaal^{3,c}

¹Egypt-Japan University of Science and Technology, Alexandria, Egypt

²Environmental Health Department, High Institute of Public Health, Alexandria University

³Suez Canal University, Ismailia, Egypt

^alucienne.basaly@ejust.edu.eg, ^bmona.gamal@ejust.edu.eg, ^cmrefaatm@hotmail.com

Keywords: Photovoltaic, optimum direction, thermal comfort, hot arid region, urban landscape

Abstract. The installation of photovoltaic systems is concentrated in the South direction as the most energy productive orientation, but in term of improving thermal comfort in the outdoor spaces, this relationship is still under study. In this paper, the effect of the photovoltaic (PV) position and orientation on improving thermal comfort in the outdoor spaces, in hot arid regions, has been modeled and analyzed. Three cases of PV positions on the rooftop of a shading device have been considered: PV in the South direction, South West, and South East direction. The results show that PV at the South direction has the highest energy production followed by the South West direction then the South East with a percentage of 109.37%, 102.43% and 96.89% respectively. Moreover, The PV at South direction is more efficient in improving thermal comfort followed by the South East. The results show that the optimum direction of photovoltaic installation on the rooftop of a shading device, in term of energy production and the improvement of thermal comfort, is the South direction.

Introduction

The orientation of photovoltaic and its tilt angle are the main parameters that affect the PV module performance. The amount of solar energy received by the surface of the PV module is changed due to these parameters. The optimum positions are these which register the maximum power and the maximum value of solar intensity [1]. It is generally known that the optimum collector orientation, in the northern hemisphere, is the South direction and that the optimum tilt depends on the day of the year and the latitude [2]. The final aspect concerning the PV orientation is the incorporation in the support structure. For different applications, the PV orientation is also determined by the nature of the building roof in which it is to be incorporated, as the aesthetic issues must be considered [3]. Also for photovoltaic installations in the outdoor spaces the aesthetic issues are important, as people prefer to see the PV integrated with the landscape [4].

Thermal comfort is an important factor in enhancing the utilization of urban spaces [5, 6]. Therefore, optimising the thermal condition of outdoor spaces is crucial to the success of landscape design and urban design [7]. "Outdoor landscape design can aim to maintain the thermal environment within the locally derived acceptable temperature range to optimize the quality and utilization rate of the public space" [8]. Therefore, a shading devise can be selected as a landscape element that can maintain the thermal environment as it offers more shades in the outdoor spaces. The integration of photovoltaic systems on the rooftop of a shading devise improved the thermal comfort and the functional performance of the outdoor spaces [9].

Evaluating the thermal comfort improvement by different photovoltaic orientations, in hot-arid regions, is discussed in this paper through the installation of PV on the rooftop of a shading devise in different orientations; South, South-East, and South-West, to indicate the optimum orientation concerning the improvement of thermal comfort and energy production. This paper pursues to explore the relationship between PV orientation and the improvement of thermal comfort in the outdoor spaces using a 3D simulation model.

Relying on a previous survey studying students' needs in the outdoor spaces, in addition to their behaviour and their rate of use in the case study area [9, 10]. Two solar panels were

installed on the South, South-East, and South-West directions alternately on the model using a DesignBuilder software to analyze the impact of changing the photovoltaic orientation on thermal comfort improvement. This study determined that PV modules oriented towards the South gives the highest value of electrical energy and thermal comfort improvement. After comparing these results with a previous case study, it is concluded that to get better values of thermal comfort, regarding the shape of the case study, is to install the PV in the South, South-East and the South-West directions.

Methodology

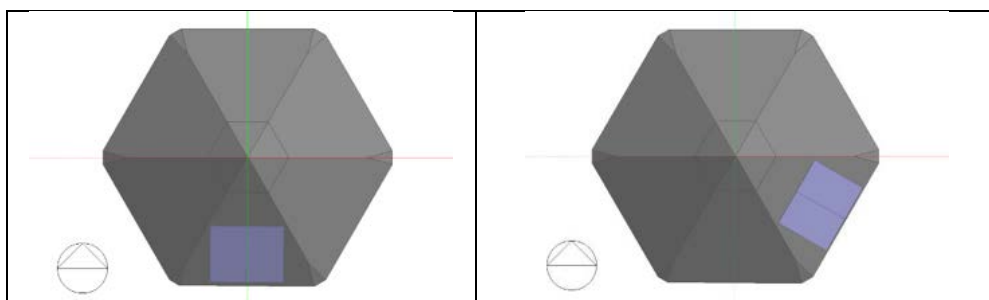
The methodology is based on the evaluation of the improvement of thermal comfort in a shading devise through the installation of PV systems on the rooftop in different orientations. The steps are as follow:

- The selected shading devise is located in the Egypt-Japan University of Science and Technology campus, the residential zone, New Borg El-Arab City, Alexandria, Egypt, where the latitude is 30.10, and the longitude is 31.18.
- Calculate the annual Fanger PMV [11] which is one of the comfort simulation outputs, in each orientation, using a model created in the DesignBuilder software and the results obtained were compared to a previously studied case study. [9]
- The main strategy is calculating the energy production of PV systems at each orientation and the Fanger PMV to indicate PV orientation and its influence on improving thermal comfort.
- The use of mounted PV modules “monocrystalline silicon 255W” in equal areas on the rooftop of the shading device with an air gap of 16.5 cm in the South, South East, and South West direction respectively, as shown in Table 1, considering that the roof tilt angle is 30°.

Table 1: Photovoltaic characteristics.

| | | |
|---------------------|-------------------------|---------------------------|
| Photovoltaic | Type | Monocrystalline 255 Watt |
| PV modules | Module Dimension | (L*W*T) 1650mm*992mm*46mm |
| | Angle | 30° |

This paper will discuss the variation in PV orientations and their impact on thermal comfort in different scenarios. Three scenarios were simulated; two solar panels were installed at the South direction, two at the South-East, and two at the South-West, as in Fig. 1.



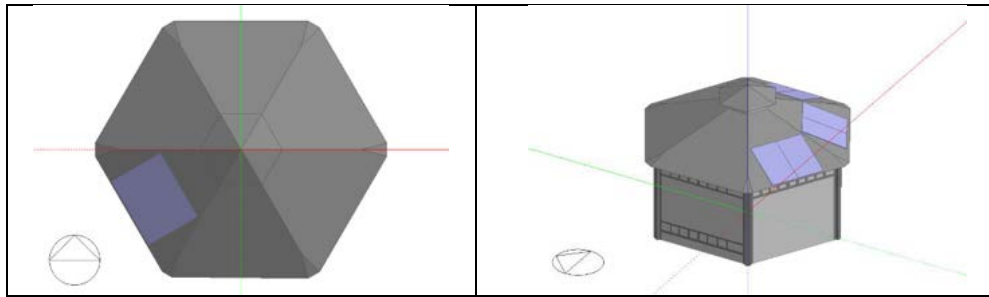


Figure 1: PV installation scenarios. (The researcher)

Case study description

The main objective of this study is to improve thermal comfort depending on PV orientation. The researcher relied on a previous survey about students' behaviour, occupancy, students' needs in the outdoor spaces concerning power outlets for different electronic devices, lighting unit and a Wi-Fi hot spot [9] with total annual site energy of 861.62 kWh.

Results and Discussion

This paper investigated the relationship between the PV orientation and the improvement of thermal comfort in the outdoor spaces, through the installation of the PV in the South, South-East and the South-West directions and studying its effect on thermal comfort and energy production. For the South-West and the South-East directions, the annual simulation results showed an inverse relationship between energy production and thermal comfort in contrast to the South direction which revealed the highest results in the simulation output, as shown in Table 2 and Table 3.

Effect on Energy production. The simulation results showed that the difference in the amount of the energy produced in the three directions was 6.94 % and 12.48%. As the PV installed in the South direction produced 109.37% of the annual consumed powered, followed by the South West with 102.43% then the South East direction with 96.89%, as in Table 2.

Table 2: PV power generation.

| PV Orientation | Annual |
|--------------------------------|-------------|
| PV in the South direction | 942.315 kWh |
| PV in the South East direction | 834.842 kWh |
| PV in the South West direction | 882.600 kWh |

Effect on thermal comfort. Based on Simple ASHRAE 55-2004, the PV orientation affects the improvement of the thermal comfort, which revealed to be the better in the South direction followed by the South-East then the South-West as the "Time Not Comfortable" is decreased after installing the panels in the South West direction by 17 hours, and after installing the panels in the South direction by 20 hours, as shown in Table 3.

Table 3: Time Not Comfort.

| | Without PV | PV at South | PV at South East | PV at South West | Three orientation |
|-----|--------------|---------------|------------------|------------------|-------------------|
| TNC | 3212.5 Hours | 3192.50 Hours | 3194 Hours | 3195.50 Hours | 3155 Hours |

Fig. 2 shows the PMV results before the installation of PV and after being installed in different directions (South, SE, and SW). The hourly annual PMV results show that the South direction performed the best in decreasing the thermal comfort along the day.

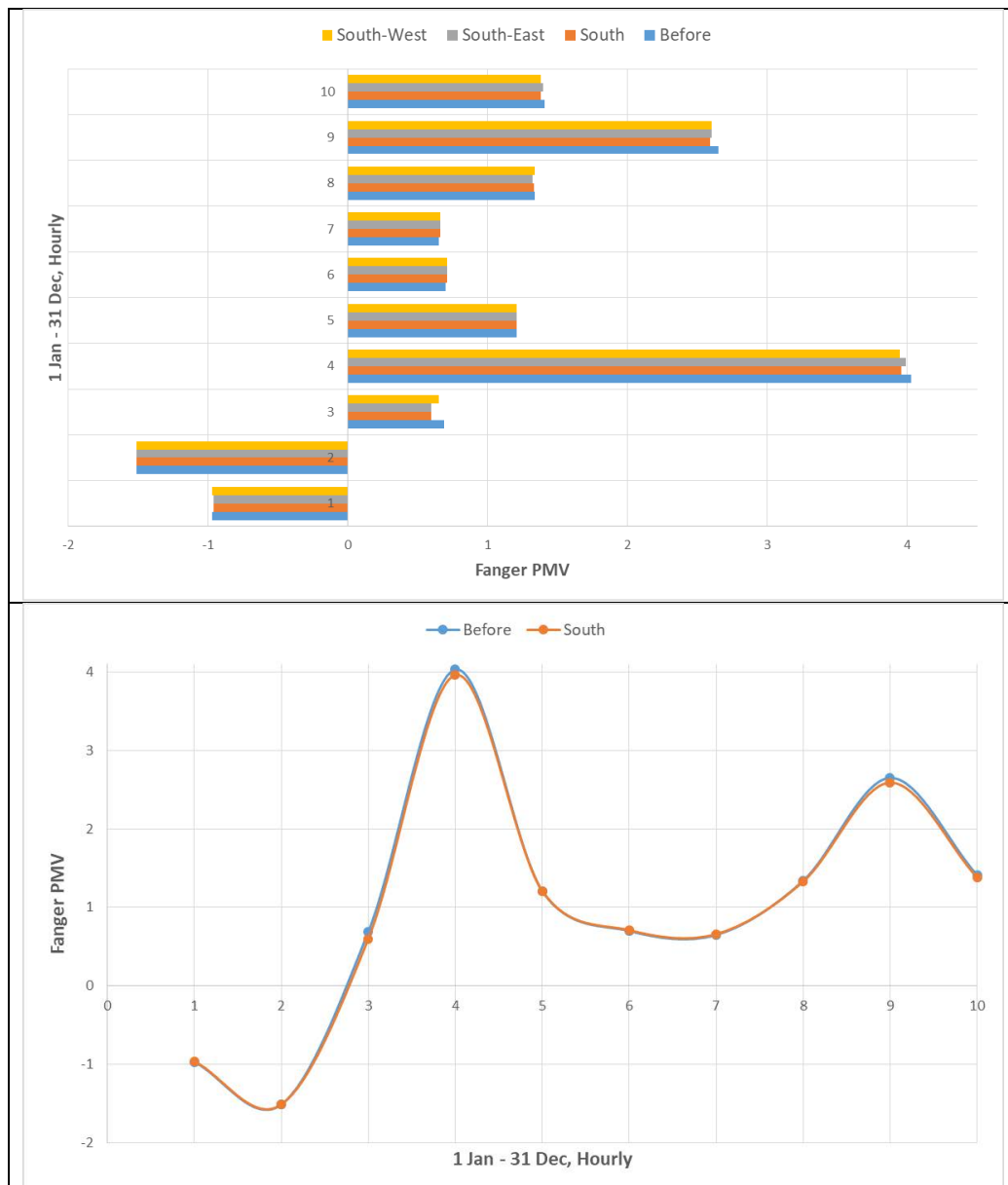


Figure 2: the difference between the PMV results

Conclusion

This paper discussed the idea of PV orientation effect on improving the thermal comfort in a shading device in the outdoor spaces. A 3D model was studied in the DesignBuilder software in three scenarios of PV orientation. The first scenario was installing two panels on the rooftop in the South direction. The second one was installing the two panels in the South East direction, and the third one was through installing two panels in the South West direction. The following results were concluded based on the study:

- The PV installed in the South West direction produced 93.66% of the total power produced by the PV installed in the South direction.
- The panels oriented to the South and the South West direction generated more than the total consumed power along the year.

- The improvement in thermal comfort after installing the PV in different orientations was the highest in the south direction followed by the South East and the South West in the range from 0.5% to 0.62% while installing the panels in the three orientation South, SE, and SW improved the thermal comfort by 1.63%.
- The optimum direction of a PV installation on the rooftop of a shading device, in term of higher energy production and the improvement of thermal comfort, is the South direction.
- Since the PV orientation affected the thermal comfort and energy production positively, so it is recommended to install the PV in the three directions South, SE, and SW to get the maximum results of improvement and the extra generated power can be used for outdoor cooling and other needs.

Acknowledgement

The first author would like to thank the Egypt–Japan University of Science and Technology (E-JUST) for offering the facility and tools needed to conduct this work.

Literature References

- [1] T. Pavlović, Z. Pavlović, L. Pantić, and L. Kostić, "determining optimum tilt angles and orientations of photovoltaic panels in niš, serbia," *Contemporary Materials I*, vol. 2, pp. 151-156, 2010.
- [2] D. Ibrahim, "Optimum tilt angle for solar collectors used in Cyprus," *Renewable energy*, vol. 6, pp. 813-819, 1995.
- [3] N. M. Pearsall and R. Hill, "Photovoltaic modules, systems and applications," *Clean Electricity from Photovoltaics*, vol. 1, pp. 1-42, 2001.
- [4] M. Lu, A. Lin, and J. Sun, "The Impact of Photovoltaic Applications on Urban Landscapes Based on Visual Q Methodology," *Sustainability*, vol. 10, p. 1051, 2018.
- [5] N. Kántor and J. Unger, "Benefits and opportunities of adopting GIS in thermal comfort studies in resting places: an urban park as an example," *Landscape and Urban Planning*, vol. 98, pp. 36-46, 2010.
- [6] D. Lai, C. Zhou, J. Huang, Y. Jiang, Z. Long, and Q. Chen, "Outdoor space quality: A field study in an urban residential community in central China," *Energy and Buildings*, vol. 68, pp. 713-720, 2014.
- [7] K. Blazejczyk, Y. Epstein, G. Jendritzky, H. Staiger, and B. Tinz, "Comparison of UTCI to selected thermal indices," *International journal of biometeorology*, vol. 56, pp. 515-535, 2012.
- [8] P. K. Cheung and C. Y. Jim, "Improved assessment of outdoor thermal comfort: 1-hour acceptable temperature range," *Building and Environment*, vol. 151, pp. 303-317, 2019.
- [9] L. G. Basaly, M. G. Ibrahim, N. M. Badawy, M. R. M. Abdelaal, and A. A. M. Ali, "Improving the functional performance of outdoor spaces in hot arid region using photovoltaics systems," in *2019 Advances in Science and Engineering Technology International Conferences (ASET)*, 2019, pp. 1-5.
- [10] L. G. Basaly, "The Functional Efficiency of Open Spaces in Universities' Campuses: An Analytical Study," Master Thesis, Architectural Engineering, Cairo University, December 2015.
- [11] P. O. Fanger and J. Toftum, "Prediction of thermal sensation in non-air-conditioned buildings in warm climates," *Indoor Air*, vol. 15, p. 48, 2002.

26-Different Methods of Water Distribution Network Analysis

Mohammed Magdy Hamed^{1,a}, Wael Hamdy Khadr^{2,b}, Sameh Youssef Mahfouz^{3,c}, Mohamed Ashraf Elsayad^{4,d}

¹Arab Academy for Science, Technology and Maritime Transport, Cairo, Egypt

²Arab Academy for Science, Technology and Maritime Transport, Cairo, Egypt

³Arab Academy for Science, Technology and Maritime Transport, Cairo, Egypt

⁴Arab Academy for Science, Technology and Maritime Transport, Cairo, Egypt

^aeng.mohammedhamed@aast.edu, ^bwkhadr@aast.edu, ^csymahfouz@hotmail.com,

^dMohamed_elsayaad@hotmail.com

Keywords: Pressure Driven Analysis, Demand Driven Analysis, Water distribution network, Extended period simulation.

In literature, there are two categories for the analysis of Water Distribution Networks (WDN). The first is Demand Driven Analysis (DDA) at which engineers satisfies the demand at each node and then calculate the pressure in the design of new networks. Softwares like EPANET and other commercial ones comprises the DDA methodologies. Normally, engineers do not take into consideration the sudden events (i.e excessive firefighting demand, excessive demand in some junctions, pipe failure, or pump failure). These events may produce negative pressure problems to the network leading to deficient nodes. In the second category named Pressure Driven Analysis (PDA), researchers attempted to solve the negative pressure problem. Indeed, the PDA methods are treated into three different ways. (i) Modifying the hydraulic solver source code by introducing a new PDA method, or (ii) adding artificial elements like check valve, internal dummy node, flow control valve, reservoir or emitter to network demand nodes, or (iii) adding some of the previous explained artificial elements to demand nodes which are suffering from pressure deficiency. Many researchers try to take into consideration the extended period simulation (EPS) in the water network. Until now, there are many challenges facing researchers to come over the problem of deficient nodes. In this paper, a comparison between results (Demand & Pressure) of a case study when using different PDA methods.

Introduction

Since 1936, Demand Driven Analysis (DDA) methods was used to simulate Water Distribution Networks (WDN) [1]. At each demand node (DN), the demand will be satisfied, and then the available pressure will be calculated. Many demand driven analysis methods exists since Cross till Rossman [1–6]. At normal condition all methods of DDA work well as the required pressure equals the available one.

In some cases pressure could be fall substantially, such as excessive firefighting demand, excessive demand in some junctions, pipe bursts, and pump failure. Under these conditions, DDA solvers fails to predict the pressure and the flow in any demand node. Hence, some demand nodes will be deficient nodes and maybe the pressure will be negative at these nodes which is physically impossible [7].

At these deficient nodes, the available pressure will be calculated depending on the available flow. For that reason, a relationship called node head flow relationship (NHFR) should be exist between the pressure and the flow at any demand node. When solving the water network, the analysis of NHFR must be satisfied with conservation of mass and energy equations, continuity equation, and loop-head loss equation at any demand node.

It is necessary to predict the performance of the WDN under failure conditions for simulation-based consistency analysis and design of WDN. These methods predict a relation between head and flow (discharge) at any demand node as shown in Fig. 1 **Error! Reference source not found..**

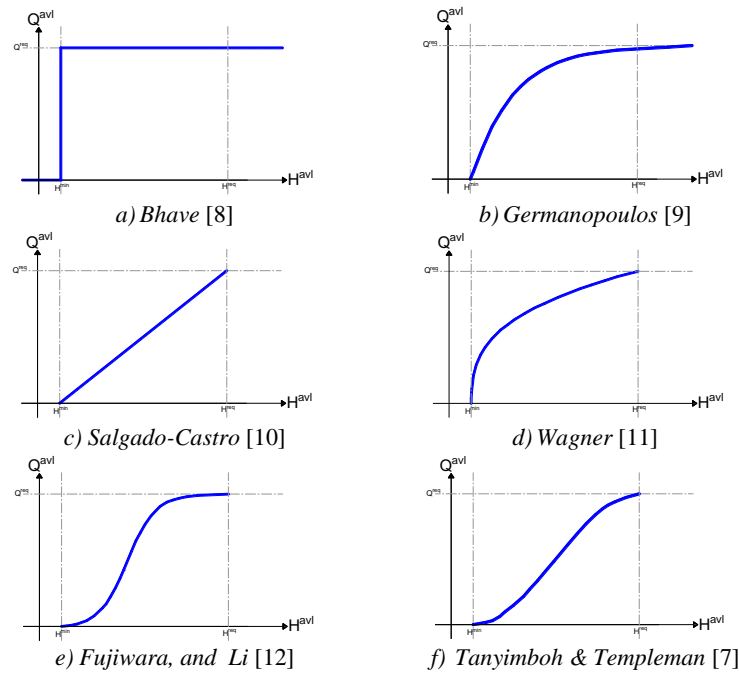


Fig. 1 Different head-flow relationships used in PDA

Many Researchers attempt to make a comparison between different nodal head flow relationships. Bhave, Sayyed & Gupta, and Herman [13–15] highly recommend the function that uses parabolic relationship proposed by Wagner [16] for matching the best experimental data, and well prediction of deficient network performance. A comparison between different

Table 4 Comparison between different node head flow relationships

| Name | Participation |
|---------------------------|--|
| Bhave [8] | Assume that nodal flow will occur depends only on the minimum required head. |
| Germanopoulos [9] | Define the minimum head for flow to occur at node, and the required head at required demand. |
| Salgado-Castro [10] | Presume a linear relation from minimum head to head required for the NHFR. |
| Wagner [11] | Define the model partial flow by using a continuous quadratic relationship. |
| Fujiwara, and Li [12] | Presume a smooth transition for the partial flow between minimum and required head. |
| Tanyimboh & Templeman [7] | Define the model partial flow by using a logit function-based formulation. |

NHFR was described in Table 4.

Pressure Driven Analysis (PDA) or Node Flow Analysis (NFA) as known by Bhave [8,17] was considered the network as it is. In this method, the available flow at each demand node will be calculated according to the available pressure. Some of PDA methods used NHFR directly and

others not. Many researchers tried to categorize the pressure driven analysis methods. Sayyed, and Gupta [14] have categorized the PDA methods into two groups according to direct and indirect approaches with the calculation of available head and flow in NHFR. While [15] Herman categorizing the PDA methods into (1) modifying the hydraulic solver source code by introducing a new PDA method, or (2) adding artificial elements like (check valve, internal dummy node, flow control valve, reservoir, emitter) to the network demand nodes. In this paper, a third category was added to Herman [15] categorization which is adding some of artificial elements to demand nodes which are suffering from pressure deficiency.

Methods

EPANET 2 [6] and other hydraulic softwares work with DDA solver. However, these softwares can be used to solve pressure deficient conditions in WDNs, which can be done in three different ways.

The first way is changing the solver source code, which introduces a new PDA method that gives a relation between head and discharge at demand node. Many researchers described this approach such as:

1- Rossman [18] extended the use of EPANET by introducing a flow emitter at a demand node to simulate NHFR. The author defined the emitter using emitter coefficient, and simulate it as an orifice in which its discharge equals a power function of nodal head as $Q_j = (H_j)^m$.

2- Ackley [19] presented optimization procedures that maximized nodal discharge under failure scenarios. The equations consists of one objective function and eight constrains. The technique is based on mathematical programming. They demonstrate their work on one WDN with two different examples. No general solution was developed for practical uses.

3- Cheung [20] changed the data structure and algorithms EPANET by using object oriented toolkit (OOTEN) to include PDA in the model. They modify the emitter state in EPANET to directly include NHFR functions. The PDA model was compared with two WDNs and three different NHFR. According to [15] the model fails to solve highly looped WDN with low discharge state and extended period simulation.

4- Liu [21,22] developed an EPANET extension using C#. The extension was implemented with EPANET Toolkit and C# to iteratively modify discharge. Their extension was called "EPANET-MNO". A comparison between four different NHFR was done in their paper. Their concern was on a technique that corrects the nodal heads only in EPANET.

5- Giustolisi [23] developed an excel based add-in called WDNXL that can deal with DDA and PDA simulations. It involves both steady state and extended period simulation (EPS).

6- Also Siew [24], introduced a technique that corrects the nodal heads only in EPANET without considering the flow. They produced an extension called "EPANET-PDX". The used a Tanyimboh [7] NHFR. The extension was tested on six networks including steady state, and EPS.

7- Yoo [25] introduced a Subsystem Based Pressure Dependent Demand (SPDD) analysis which uses the concept of effective demand to exclude the doubts caused by the NHFR. In addition, it uses the optimization techniques to maximize water demand to satisfy the nodal head under failure condition. Like Ackley [19], no general solution was developed for practical uses.

8- Morley [26] introduced an extension for EPANET called EPANETpdd. The authors made a modification for the emitters by introducing an empirical exponent to each emitter. In fact, this extension failed when applied to large or complex networks.

9- Sylvan [27] used Goldstein's algorithm to upgrade global gradient algorithm (GGA). Two optimization problems named Weighted Least Squares (WLS) and Co-content Function are satisfying the theory condition. EPS was not considered in this theory.

The second way was adding artificial elements like (check valve, internal dummy node, flow control valve, reservoir, emitter) to network demand nodes and solving the WDN as DDA. Many researchers described this approach like:

1. Hayuti [28] introduced a simple iterative method known as the Sequential Solution Seeking DDA based HDA (SSS) to reduce the number of solving iterations. The head driven analysis routine uses the computational ability of EPANET2 to solve the hydraulics while the SSS modifies the nodal flow of the pressure deficient nodes.
2. Jinesh Babu [29] proposed an algorithm called modified pressure deficient network (M-PDNA) that use DDA solver in EPANET. This algorithm addresses the limitations of Ang [30]. An artificial reservoirs (AR), and an artificial flow control valve (AFCV) were connected to all demand node. The partial flow between the minimum and the desired pressure head levels would not be simulated in this study as it works when ($H < H_{\min}$).
3. Gorev [31] discussed a simple technique that uses the square root relationship between the nodal demand and the nodal pressure. The procedure was done using EPANET2 tools and allows a WDN with pressure-dependent demands to be solved in a single run. In this procedure, artificial elements consists of a FCV, a pipe with a check valve, and a reservoir are connected to the DN. The NHFR used by the author was fixed as it is specific, parabolic type of NHFR Wagner [16].
4. Sivakumar [32,33] addressed the restriction of Ang [30] technique by adding AFCV and CV to all demand nodes. The authors simplified the (M-PDNA) technique proposed by Jinesh Babu [29]. The major function of artificial elements is to assure that the flow did not exceed the required demand. This technique uses DDA solver of EPANET directly without using the toolkit in a single simulation run, which is better than Ang [30] for the smaller number of iterations. On the other hand, the AR still could not simulate the important partial flow between the minimum and the desired pressure levels.
5. Sayyed [34,35] connect a set of artificial elements like CV, FCV, and emitter to all demand nodes. The emitter replaced the artificial reservoir. These elements are connected using a pipe with no losses. According to Herman [15], the algorithm delivered good results under steady-state analysis. However, it did not consider the effect of minimum pressure head level for a head value higher than zero.

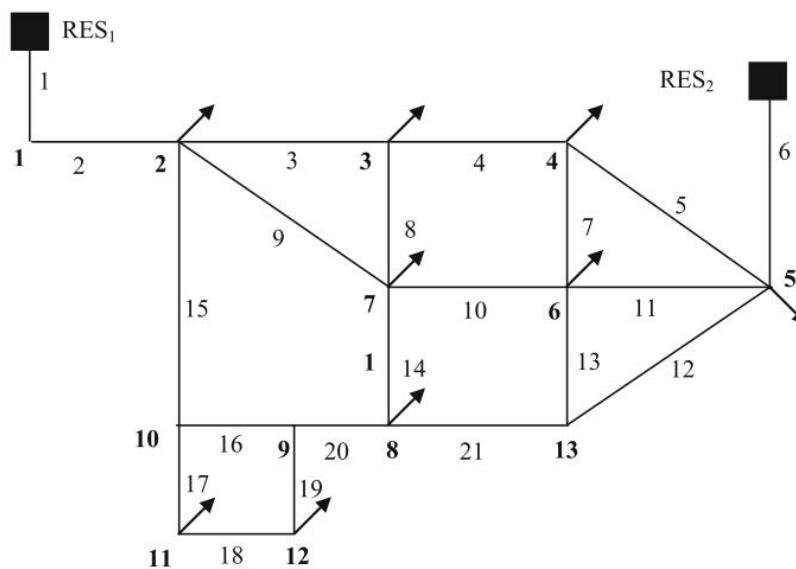
In this paper, a third category was added to Herman [15] categorization which is adding some of artificial elements to demand nodes which are suffering from pressure deficiency. These methods are described as:

1. Ozger [36] proposed a method called the Demand Driven Available Demand Fraction (DD-ADF). In this method, you should first execute a DDA run. Secondly, modify pressure deficient node properties. Next, add an AR with CV pipe to only deficient demand node. It can be very difficult to apply this method to large networks, because adding and removing AR is not an easy task, mainly under EPS analysis.
2. Todini [37] tried to solve looped networks in extended period simulations by adding AR in the deficient demand nodes. After adding the AR and running DDA, three different basic considerations were taken. It is very difficult to apply in highly looped networks.
3. Ang [30] introduce Pressure Deficient Network Algorithm (PDNA). The authors suggests connecting artificial reservoirs (AR) to nodes suffering from pressure deficient after performing a DDA simulation run with zero demand. It requires a large number of iterations (multiple hydraulic simulations) until the minimum nodal pressure head is satisfied. Extended period simulation (EPS) cannot be handled with PDNA, as well as dynamic addition and removal of ARs is very difficult task.
4. Herman [15] proposed a single-iteration PDA approach (SIPDA) which connects a set of artificial elements (check valve, an internal dummy node, a flow control valve, and an

emitter) to each pressure deficient demand node ($Q_j^{req} > 0, H_j^{avl} < H_j^{req}$). The author used Wagner [16] equation as a NHFR. They claimed that SIPDA could simulate the WDN under steady state and extended period simulations and under both normal and pressure deficient conditions.

Bench Mark Example

A looped WDN discussed in Ozger [36] was tested in more than five research papers. The network consists of 13 demand nodes and 21 pipes as shown Fig. 2. **Error! Reference source not found..** Pipes information's and nodes specification are discussed in Table 5. The minimum required head was taken as the node elevation shown in column 4 in the same table. The required head was taken as the summation of the node elevation and the required pressure. The required residual pressure at all nodes is 15 m. The emitter exponent is $\gamma = 2/3$, which is depending on the secondary network consumer's location and the losses in the pipes of secondary network. The results are compared in Table 3 & 4 for closure of pipe 3.



| Demand Driven Analysis | | | | Pipe 3 Failure | | | | | |
|------------------------|---------------|--------------|--------------|------------------------|--------------|---------------|--------------|---------------|--------------|
| | | | | Demand Driven Analysis | | DD-ADF [36] | | [29] | |
| DN | Elevation (m) | Demand (CMH) | Pressure (m) | Demand (CMH) | Pressure (m) | Demand (CMH) | Pressure (m) | Demand (CMH) | Pressure (m) |
| 1 | 27.43 | 0 | 32.28 | 0 | 32.96 | 0 | 33.16 | 0 | 33.16 |
| 2 | 33.53 | 212.40 | 25.67 | 212.40 | 26.62 | 212.40 | 26.91 | 212.40 | 26.908 |
| 3 | 28.96 | 212.40 | 27.12 | 212.40 | 5.77 | 212.40 | 17.91 | 212.40 | 17.909 |
| 4 | 32.00 | 640.80 | 22.99 | 640.80 | 2.76 | 165.77 | 15.00 | 165.11 | 15.00 |
| 5 | 30.48 | 212.40 | 24.6 | 212.40 | 11.83 | 212.40 | 19.97 | 212.40 | 19.966 |
| 6 | 34.39 | 684.00 | 15.46 | 684.00 | 0.40 | 497.97 | 15.00 | 499.05 | 12.00 |
| 7 | 29.56 | 640.80 | 20.39 | 640.80 | 6.67 | 640.80 | 17.01 | 640.80 | 17.005 |
| 8 | 31.39 | 327.60 | 17.56 | 327.60 | 4.77 | 274.74 | 15.00 | 274.56 | 15.00 |
| 9 | 32.61 | 0 | 19.62 | 0 | 16.39 | 0 | 20.94 | 0 | 20.941 |

| | | | | | | | | | |
|--------------------|-------|---------|-------|---------|--------------|--------------|--------------|--------------|--------------|
| 10 | 34.14 | 0 | 19.4 | 0 | 17.34 | 0 | 20.87 | 0 | 20.873 |
| 11 | 35.05 | 108.00 | 13.93 | 108.00 | 11.40 | 108.00 | 16.48 | 108.00 | 16.477 |
| 12 | 36.58 | 108.00 | 12.17 | 108.00 | 9.35 | 66.25 | 15.00 | 66.24 | 15.00 |
| 13 | 33.53 | 0 | 18.61 | 0 | 5.32 | 0 | 14.83 | 0 | 14.83 |
| RES ₁ | 60.96 | - | 0 | - | 0 | - | 0 | - | 0 |
| | | 2253.29 | | 1480.75 | | 1168.45 | | 1168.55 | |
| RES ₂ | 60.96 | -893.11 | 0 | - | 0 | - | 0 | - | 0 |
| | | | | 1665.65 | | 1222.28 | | 1222.41 | |
| Total Supply (CMH) | | 3146.40 | | 3146.40 | | 2390.73 | | 2390.96 | |

Table 5: Nodes & pipes characteristics

| Source Node (SN) | Head (m) | Demand Node (DN) | Elevation (m) | Demand (m^3/h) | Required Pressure (m) | n_j | Pipe ID | Length (m) | ϕ (mm) | C (H-W) |
|------------------|----------|------------------|---------------|--------------------|-----------------------|-------|---------|------------|-------------|---------|
| RES ₁ | 60.96 | 1 | 27.43 | 0.0 | | | 1 | 609.60 | 762 | 130 |
| RES ₂ | 60.96 | 2 | 33.53 | 212.4 | | | 2 | 243.80 | 762 | 128 |
| | | 3 | 28.96 | 212.4 | | | 3 | 1524.00 | 609 | 126 |
| | | 4 | 32.00 | 640.8 | | | 4 | 1127.76 | 609 | 124 |
| | | 5 | 30.48 | 212.4 | | | 5 | 1188.72 | 406 | 122 |
| | | 6 | 34.39 | 684.0 | | | 6 | 640.08 | 406 | 120 |
| | | 7 | 29.56 | 640.8 | 15 | 1.5 | 7 | 762.00 | 254 | 118 |
| | | 8 | 31.39 | 327.6 | | | 8 | 944.88 | 254 | 116 |
| | | 9 | 32.61 | 0.0 | | | 9 | 1676.40 | 381 | 114 |
| | | 10 | 34.14 | 0.0 | | | 10 | 883.92 | 305 | 112 |
| | | 11 | 35.05 | 108.0 | | | 11 | 883.92 | 305 | 110 |
| | | 12 | 36.58 | 108.0 | | | 12 | 1371.60 | 381 | 108 |
| | | 13 | 33.53 | 0.0 | | | 13 | 762.00 | 254 | 106 |
| | | | | <u>3146.4</u> | | | 14 | 822.96 | 254 | 104 |
| | | | | | | | 15 | 944.88 | 305 | 102 |
| | | | | | | | 16 | 579.00 | 305 | 100 |
| | | | | | | | 17 | 487.68 | 203 | 98 |
| | | | | | | | 18 | 457.20 | 152 | 96 |
| | | | | | | | 19 | 502.92 | 203 | 94 |
| | | | | | | | 20 | 883.92 | 203 | 92 |
| | | | | | | | 21 | 944.88 | 305 | 90 |

Table 6: No of deficient nodes in each method

| Method | No. of deficient nodes |
|------------------------|------------------------|
| Demand Driven Analysis | 9 |
| DD-ADF [36] | 5 |
| [29] | 5 |
| [31] | 8 |
| (Sayyed, 2015) | 8 |
| SIPDA [15] | 9 |

Table 7: Example Results continue

| DN | Pipe 3 Failure | | | | | |
|--------------------|----------------|---------------|----------------------|--------------|---------------|--------------|
| | [31] | | (Sayyed, 2014, 2015) | | SIPDA [15] | |
| | Demand (CMH) | Pressure (m) | Demand (CMH) | Pressure (m) | Demand (CMH) | Pressure (m) |
| 1 | 0 | 33.07 | 0 | 33.08 | 0 | 33.32 |
| 2 | 212.40 | 26.78 | 212.40 | 26.795 | 212.4 | 27.14 |
| 3 | 193.06 | 12.393 | 193.27 | 13.02 | 108.56 | 24.66 |
| 4 | 506.92 | 9.387 | 489.54 | 10.01 | 271.69 | 21.65 |
| 5 | 212.40 | 16.343 | 212.40 | 16.77 | 111.70 | 25.23 |
| 6 | 558.58 | 7.003 | 543.71 | 7.63 | 232.53 | 19.28 |
| 7 | 588.00 | 12.63 | 587.73 | 13.17 | 516.8 | 24.06 |
| 8 | 277.52 | 10.764 | 271.54 | 11.32 | 146.17 | 22.36 |
| 9 | 0 | 18.747 | 0 | 18.987 | 0 | 25.28 |
| 10 | 0 | 19.148 | 0 | 19.333 | 0 | 24.4 |
| 11 | 103.87 | 13.875 | 103.80 | 14.13 | 48.24 | 22.39 |
| 12 | 96.89 | 12.074 | 94.97 | 12.37 | 42.61 | 20.76 |
| 13 | 0 | 10.722 | 0 | 11.23 | 0 | 21.15 |
| RES ₁ | -1315.32 | 0 | - 1298.65 | 0 | -850.74 | 0 |
| RES ₂ | -1434.33 | 0 | - 1410.70 | 0 | -839.97 | 0 |
| Total Supply (CMH) | 2749.64 | | 2709.36 | | 1690.70 | |

Conclusions

The author recommend the solution discussed by Sayyed (Sayyed, 2014, 2015) as it is fast enough for regular use compared with other solutions. Table 6 illustrate the number of deficient nodes produced by each method. On the other hand, the solution by Jinesh Babu [29] does not model partial flow as it is based on H_j^{min} only. And In the explanation discussed by Gorev [31] the the NHFR is fixed. According to Gupta [38] the technique used by Herman [15] was originally formulated by Sayyed [35] which was generalized the work of Gorev [29,31]. The procedure done by Herman [15] was more complicated as it required multiple executions of EPANET 2.

References

- [1] H. Cross, "Analysis Of Flow In Networks Of Conduits Or Conductors," *Eng. Exp. Stn.*, Vol. XXXIV, No. 22, (1936).
- [2] D. W. Martin and G. Peters, "The application of Newton's method to network analysis by digital computer," *J. Inst. Water Engrs.*, Vol. 17, (1963), p. 115–129.
- [3] D. J. Wood and O. A. Charles, "Hydraulic network analysis using linear theory," *J. Hydraul. Div.*, Vol. 96, No. 7, (1970), p. 1221–1234.
- [4] L. T. Isaacs and K. G. Mills, "Linear theory methods for pipe network analysis," *J. Hydraul. Div.*, Vol. 106, No. 7, (1980), p. 1191–1201.
- [5] E. Todini and S. Pilati, "A gradient method for the analysis of pipe networks," (1987).
- [6] L. A. Rossman, *EPANET 2 Users Manual*. (2000).
- [7] T. T. Tanyimboh and A. B. Templeman, "Seamless pressure-deficient water distribution system model," (2010), Vol. 163, No. 8, p. 389–396.
- [8] P. R. Bhawe, "Node flow analysis of water distribution systems," *Transp. Engrg.*, *ASCE*, Vol. 107, No. 4, (1981), p. 457–467.
- [9] G. Germanopoulos, "A technical note on the inclusion of pressure dependent demand and leakage terms in water supply network models," *Civ. Eng. Syst.*, Vol. 2, No. 3, (1985), p. 171–179.
- [10] R. O. Salgado-Castro, "Computer modelling of water supply distribution networks using the gradient method," UNIVERSITY OF NEWCASTLE-UPON-TYNE, (1988).
- [11] B. J. M. Wagner, U. Shamir, and D. H. Marks, "Water Distribution Reliability: Analytical Methods," Vol. 114, No. 3, (1988), p. 253–275.
- [12] O. Fujiwara and J. Li, "Reliability analysis of water distribution networks in consideration of equity, redistribution, and pressure-dependent demand," *Water Resour. Res.*, Vol. 34, No. 7, (1998), p. 1843–1850.
- [13] B. R. Gupta and P. R. Bhawe, "Reliability-Based Design Of Water-Distribution Systems," Vol. 122, No. January, (1996), p. 51–54.
- [14] A. Sayyed and R. Gupta, "Predicting Deficient Condition Performance of Water Distribution Networks," *Civ. Eng. Infrastructures J.*, Vol. 46, No. 2, (2013), p. 161–173.
- [15] M. Herman A., S. Dragan, and K. Zoran, "New Pressure-Driven Approach for Modeling Water Distribution Networks," *J. Water Resour. Plan. Manag.*, Vol. 143, No. 8, (2017), p. 04017031.
- [16] B. J. M. Wagner, U. Shamir, and H. Marks, "Water Distribution Reliability: Simulation Methods," *J. Water Resour. Plan. Manag.*, Vol. 114, No. 3, (1988), p. 276–294.
- [17] P. R. Bhawe, "Node Flow Analysis," in *Analysis of flow in water distribution networks*, Lancaster, Pennsylvania 17604 U.S.A.: Technomic Publishing Company, Inc., (1991), p. 353–384.

- [18] L. A. Rossman, *EPANET2 and programmer's toolkits, Risk Reduction*. Engineering Laboratory, U.S. Environmental Protection Agency, Cincinnati., (2000).
- [19] J. R. L. Ackley, T. T. Tanyimboh, B. Tahar, and A. B. Templeman, "Head-Driven Analysis of Water Distribution Systems," (2001), Vol. 1, No. September, p. 183–192.
- [20] P. Cheung, J. E. Van Zyl, and L. F. R. Reis, "Extension of EPANET for pressure driven demand modeling in water distribution system," (2005), p. Vol. 1.
- [21] J. Liu, G. Yu, and D. Savic, "Deficient-Network Simulation Considering Pressure-Dependent Demand," *ICPTT 2011*. p. 886–900, (2011).
- [22] J. Liu and G. Yu, "Iterative Methodology of Pressure-Dependent Demand Based on EPANET for Pressure-Deficient Water Distribution Analysis," *J. Water Resour. Plan. Manag.*, Vol. 139, No. 1, (2013), p. 34–44.
- [23] O. Giustolisi, D. A. Savic, L. Berardi, and D. Laucelli, "An Excel- based solution to bring water distribution network analysis closer to users," (2011).
- [24] C. Siew and T. T. Tanyimboh, "Pressure-Dependent EPANET Extension," *Water Resour Manag.*, Vol. 26, (2012), p. 1477–1498.
- [25] D. G. Yoo, M. Y. Suh, J. H. Kim, H. Jun, and G. Chung, "Subsystem-Based Pressure Dependent Demand Analysis in Water Distribution Systems Using Effective Supply," *Civ. Eng.*, Vol. 16, No. 3, (2012), p. 457–464.
- [26] M. S. Morley and C. Tricarico, "Pressure driven demand extension for EPANET (EPANETpdd)," Exeter, U.K., (2014).
- [27] E. Sylvan, P. Olivier, D. Jochen, and S. A. R., "A Robust, Rapidly Convergent Method That Solves the Water Distribution Equations for Pressure-Dependent Models," *J. Water Resour. Plan. Manag.*, Vol. 142, No. 2, (2016), p. 4015047.
- [28] M. Hayuti, D. Naga, Y. Zhang, and R. Burrows, "An Evaluation of the Robustness of the Sample UK Water Distribution System Configurations to Operational Stresses," (2008), p. 1–19.
- [29] K. S. Jinesh Babu and S. Mohan, "Extended Period Simulation for Pressure-Deficient Water Distribution Network," *Comput. Civ. Eng.*, Vol. 26, No. August, (2012), p. 498–505.
- [30] W. K. Ang and P. W. Jowitt, "Solution for Water Distribution Systems under Pressure-Deficient Conditions," *Water Resour. Plan. Manag.*, Vol. 132, No. 3, (2006), p. 175–182.
- [31] N. B. Gorev and I. F. Kodzhesspirova, "Noniterative Implementation of Pressure-Dependent Demands Using the Hydraulic Analysis Engine of EPANET 2," Vol. 27, No. 10, (2013), p. 3623–3630.
- [32] P. Sivakumar and R. K. Prasad, "Simulation of Water Distribution Network under Pressure-Deficient Condition," *Water Resour. Manag.*, Vol. 28, No. 10, (2014), p. 3271–3290.
- [33] P. Sivakumar and R. K. Prasad, "Extended Period Simulation of Pressure-Deficient Networks Using Pressure Reducing Valves," *Water Resour Manag.*, Vol. 29, No. 5, (2015), p. 1713–1730.
- [34] A. Sayyed, R. Gupta, and T. T. Tanyimboh, "Modelling pressure deficient water distribution networks in EPANET," (2014), Vol. 89, p. 626–631.
- [35] A. Sayyed, R. Gupta, and T. T. Tanyimboh, "Noniterative Application of EPANET for Pressure Dependent Modelling Of Water Distribution Systems," *Water Resour. Manag.*, Vol. 29, No. 9, (2015), p. 3227–3242.
- [36] S. S. Ozger and L. W. Mays, "A SEMI-PRESSURE-DRIVEN APPROACH TO RELIABILITY ASSESSMENT OF WATER DISTRIBUTION NETWORKS," (2003), p. 345–352.

- [37] E. Todini, “Towards Realistic Extended Period Simulations (EPS) in Looped Pipe Network,” (2006), p. 27–30.
- [38] R. Gupta, M. A. H. Abdy Sayyed, and T. T. Tanyimboh, “Discussion of ‘New Pressure-Driven Approach for Modeling Water Distribution Networks’ by Herman A. Mahmoud, Dragan Savi’c, and Zoran Kapelan,” *J. Water Resour. Plan. Manag.*, Vol. 144, No. 6, (2017), p. 07018006.

27-Effect of window Orientation and Glass Type on Energy Consumption and Interior Conditions in a Facility

Rania Elghamry^{1,2}, Hamdy Hassan^{1,3*} Abbas ElZafarany³

¹Energy Resources Eng. Depart., Egypt-Japan University of Science and Technology (E-JUST), Alexandria, Egypt

²Architecture Eng. Depart., Faculty of Eng., Tanta University, Tanta, Egypt

³Mech. Eng. Depart., Faculty of Eng., Assiut University, Assiut, Egypt

³ Department of Urban Design, Faculty of Planning Regional and Urban, Cairo University
rania.elghamry@ejust.edu.eg, hamdyaboali@ejust.edu.eg elzafarany@hotmail.com

Abstract

Energy efficiency in buildings is today a prime objective for energy policy at regional, national and international levels. This energy can be considerably reduced with the development of passive energy buildings. The main concept toward using building elements to save energy, protect environment, and recycle the materials. So, in this paper, the Effect of window orientation with the glazing type on energy consumption in buildings under the tropical climatic conditions of New Borge Alarab city, Alexandria, Egypt has been modelled and analysed. Three glazing types option have been considered, i) clear glass type and ii) low e clear glass type iii) Gery glass. In addition, building orientation at 90° in residential room at different facility walls (South, North, East and West). Two cases are studied for the double glazing thickness on the facades; 3mm and 6mm. It has been observed that for three cases, the south façade is the effective orientation and the lowest energy consumption, while south-east 75° the effective and lowest lighting loads. the optimum glass types is double 3 mm with air that mean increasing glass thickness not save energy and prevent daylight. saving energy depend on gas insulation between double glass not the increasing the thickness.

Keywords: *passive energy, effect, glass type, orientation, daylight*

1 Introduction

The world energy demand is growing with increasing of population and growing economy. Egypt faces a continuous increase of energy demand and a decrease of available resources to expand the generation system. Saving energy consumption directly affects national economy. The shortage in the traditional energy sources and the early stages in using the renewable energy sources motivated the design of energy saving buildings. Saving Energy Design aims to minimize the negative environmental impact of buildings by using less energy and fewer limited resources, eliminating pollution, employing reusable materials and efficient use of space. Concepts, many passive strategies for energy saving are employed to enhance the efficiency of cooling, heating, ventilation and lighting in building [1]. Windows are essential components of buildings which provide vision, air ventilation, passive solar gain, day-lighting and the opportunity to leave the building in extreme situations. However, they play an important role in total energy consumed in buildings due to their remarkably higher U-values compared to other components of building envelope. Window design, sizes, position, orientation and window wall ratio (WWR) play a significant role regarding the total energy balance of buildings and interior comfort conditions. The building envelope is the most important element regarding the total energy balance of buildings, especially in developing countries where the building sector accounts for around 40-50 % of the energy consumed [2]. Glazing area percentage, type, and thickness of insulation material play an important role in heating and cooling of buildings in terms of energy consumption [3].

Research has focused on studying the design strategies and techniques that lead to reduce energy consumption by controlling the building envelope and takes into account the relationship between the building and its components. The main concept to reduce energy in

these type of building is using passive techniques "optimal solar gain by controlling building orientation and the building opening" . where is window design plays important role in .saving energy on building One of the essential parts of window is the glazing,selecting a window glazing is complicated when energy saving and daylighting aspects of abuilding are considered concurrently.Optimization techniques offer abalance solution for the contradictions in selecting awindow glazing of energy-efficient building. Such as ,S.sekar,K.lim cher toon [4] deals with smart window wich it's mechanism made by combinaing double glazing unit and other coated with low-emissivity (low-e) coating. Smart windows in a can save annual operating costs and this combination of glazing provides optimum energy efficiency and a high level of daylight transmission. Bojić, Milorad and Yik, Francis [5] evaluated the energy saving that can be achieved by applying advanced glazing by calculate the yearly electricity consumption for cooling loads for five different glazing types to a standard public housing block design in Hong Kong.the study result found the achievable saving depend on orientation of building, type and location of rooms. A.Gasparella,G.pernigotto et al ,[6] introduce whole study to evaluate the impact of different kinds of glazing systems (two double and two triple glazings) ,window size (from 16% to 41% of window to floor area ratio), orientation of the main windowed facade and internal gains on winter and summer energy need .this result summarize that the solar transmittance appears to be more important for winter and summer energy needs and the windows surface appears to be of minor importance for winter energy needs.And the use of large glazings and the south orientation enhances winter performance. A.Ebrahimpour, M.Maerefat,[7] evaluated the solar energy transmitted into or lost from the room through the fenestration areas by summarize the effect of advanced glazing and overhangs for typical residential buildings in Tehran .The study concluded that using appropriate overhang or side fin form the single clear pane glazing is more useful for any direction of window than the advanced glazing windows. M.Arici,H.Karabay,[8] determined the optimum air layer thickness of double-glazed window for different climate zones by calculating the heating costs . the study reveal that the optimum air layer thickness of double-glazed window varies between about from 12.2 to 14.6mm. Up to 60% energy saving can be achieved by a well-optimized double-glazed window. M.Bojic,F.yik,P.Sat [9] describe the investigations on the thermal behavior of two differently sized residential apartments by studing the effect of changing glazing types and building orientation on the cooling loads.data analysis reveal that the highest decrease in cooling loads of approximately 10% in case of replacing clear glass with reflective ,tinted glass for west direction. P.Tavares,A.Gaspar,A.Martins et al [10] making comparison between three glazing options and evaluated energy needs for heating and coolingby modeling the EC window dynamic behavior and the different control strategies . It is concluded that the EC in the west façade are the more effective . M.Thalfeldt,E.Pikas,J.Kurnitski et al ,[11] optimized façade parameters including window properties, external wall insulation, window-to-wall ratio (WWR) and external shading were determined with energy and daylight simulations for the lowest life cycle cost for the best achievable energy performance. The study found triple glazing with slightly larger size (WWR=37.5%) resulted in best energy performance and very large windows showed worse results compared to more reasonable sizes. While, J.Lee , H.Jung et al [12] present and optimizes the annual energy consumption associated with applying different types and properties of window systems in a building envelope by evaluating different window wall ratios and orientations in five typical Asian climates.the simulation study reveal that optimal window performance properties vary as climate change and the relative window size must be minimized. Moreover, W.Hee, M.Alghoul et al[13], reveal the impacts of window glazing on the energy and daylighting performances of building. Dynamic glazing,it is more suitable to be installed in th building which offering abalance between visual and energy aspects.

So this research objective is to study Effect of window Orientation and glazing Type on Energy Consumption and Interior Conditions in a Facility. the Effect of window orientation with the glass type on energy consumption in buildings under the tropical climatic conditions of New Borge Alarab city, Alexandria, Egypt has been modelled and analysed. Three glass type option have been considered, i) clear glass type and ii) low e clear glass type iii) Gery glass. In addition, building orientation at 90° in residential room at different facility walls (South, North, East and West). Two cases are studied for the glass thickness on the facades; 3mm and 6mm with 13mm air because this two thickness the more efficient and single glass play against saving energy and the effect of triple glass is similar to the double but more expensive.



Fig.1. indicated the room plane

2 Methods

The methodology is based on the evaluation of energy performance in buildings by the integration of architectural solutions for openings design with changing the window glass types and its thickness to reduce energy consumption in buildings. By the elevation of influence of the changes in the building orientation, the properties of the selected facility are shown in table 1, and the solution of the model, the considered assumptions of the model and the steps of the solution are as follow:


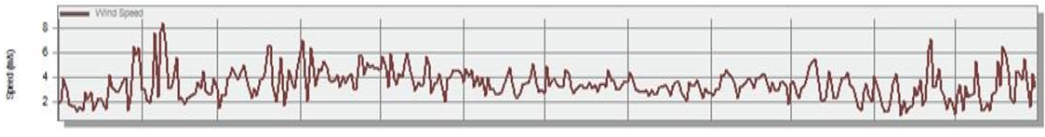
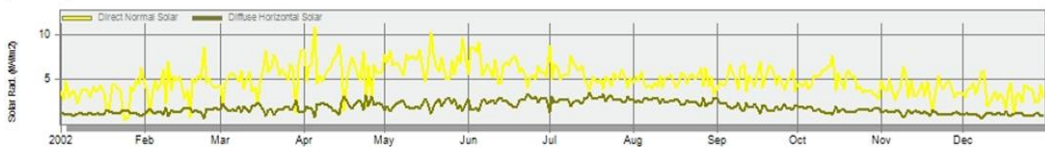
- Calculate energy consumption in buildings by using the simulation program "DESIGN BUILDER" every day annually.
- The impact of different orientations on the study model(standard residential room"6*3.6*3.5" with one façade ,all walls adiabatic and opening with window wall ratio 20% "The accepted ratio in the study area", the type of main walls of the building material is modified by those embedded in the customs of local buildings in Egypt. As indicated in table 1.
- The selected study location is the New Borg El-Arab City, Alexandria, Egypt which has the climate conditions as shown in table 2.
- The main strategy is calculate lighting and HVAC loads"heating setpoint 15 and the colling set point 24" to indicate the energy behaviour.
- The physical model of the building has no internal heat source and the activities within the facility are considered in table 1.
- Daylight and natural ventilation are mixed with HVAC system.

Table 1: Research sample characteristics

| Room dimension | | 6*3.6 m2 | |
|---------------------------------|-----------------|------------------------|--|
| Layers of the building envelope | Lighting energy | intensity | M2 – 100lux/ 5w |
| | HVAC | Control type | Suspended |
| | | Mechanical ventilation | (min fresh air (sum per person+ per area-4 |
| | | type | Split + Separate Mechanical Ventilation |
| | | Natural ventilation | 3ac /h |
| U-value (w/m2-°k) | External wall | 0.704 | Whites perlite plaster board 2 cm + Cement \plaster\mortar-cement 2 cm + brick wall thickness of 25 cm + Cement \plaster\mortar-cement 2 cm + Plastic paint white color 2 cm. |
| | Internal wall | 0.662 | Whites perlite plaster board 2 cm + Cement \plaster\mortar-cement 2 cm + brick wall thickness of 12 cm + Cement \plaster\mortar-cement 2 cm + Plastic paint white color 2 cm. |
| | floor | 0.658 | Carpets 1 cm + Ceramics Port Celine 2 cm + mortar thickness of 2 cm + Sand settlement 4 cm + reinforced concrete 12 cm + 3 cm thickness of the epithelium layer + Plastic paint white color 2 cm |
| | roof | 0.658 | Slanting slab 2 cm + mortar 2 cm + Sand settlement 4 cm + Concrete 7 cm + isolate moisture 2 cm + heat isolating 2 cm + reinforced concrete 12 cm + Plastic paint white color 2 cm. |

| | |
|------------------------------|--|
| <i>Glass type</i> | Dbl Clear 3mm and 6mm/13mm Air Dbl lowe clear 3mm and 6mm /13mm Air Dbl Gery 3mm and 6mm/13mm Air Wight |
| <i>Room - Painting color</i> | |
| <i>window wall ratio</i> | 20% |

Table 2: Climate location characteristics

| | | | |
|----------------------------------|--|---------------------------------|----------------------|
| Latitude | 30.10 | Longitude | 31.18 |
| Elevation above sea level | 74 m | Sky \ background texture | Granulated gray 453m |
| Temperature c |  <p>Temperatures rise significantly during summer months</p> | | |
| Wind speed(m/s) |  <p>Alexandria sometimes exposed to the Khamaseen winds during the period between March and June</p> | | |
| Solar radiation |  <p>Exposure to direct solar radiation is strong and the proportion of high surfaces in the summer</p> | | |
| Relative Humidity | Relative humidity is relatively high and ranging between 50-70% | | |

3 Results and discussion

Reduction of energy consumption in buildings is a major objective in the world so the world is moving towards sustainable buildings design. The building's components, especially the envelope the first energy consumer, and have large surface area of walls and window opening which could be useful. Structural features of windows, such as width, height, glass type and its thickness affect the amount of incoming solar radiation and thus affect the amount of buildings thermal and lighting energy consumption. So the methodology is based on the evaluation of energy performance in buildings by the changing the window glass type and the glass thickness to reduce energy consumption in buildings.

a) Effect of window glass type and thickness in heating loads.

The effect of each variable parameter on the amount of energy consumption for heating, cooling and lighting energy consumption was investigated separately. Fig.4. shows Average annually required heating energy for all cases of window glass types and thickness. The findings show that south orientation represents the lowest heating energy consumption which north is the highest in all winows cases . as indicated in fig.2 the case of using Dbl Clr 3mm is represent the lowest required heating loads that is because the glass clear and using 3mm glass thickness allow the solar radiation to inter the room to save the sun energy .While the Dbl Grey 6mm recored the highest heating loads consumption that is because the glass color and thickness prevent the solar radiation to heat the room . Fig.2 reveal that the clearness of glass and minimum thickness represented the most effective case in winter to acquire the sun energy.

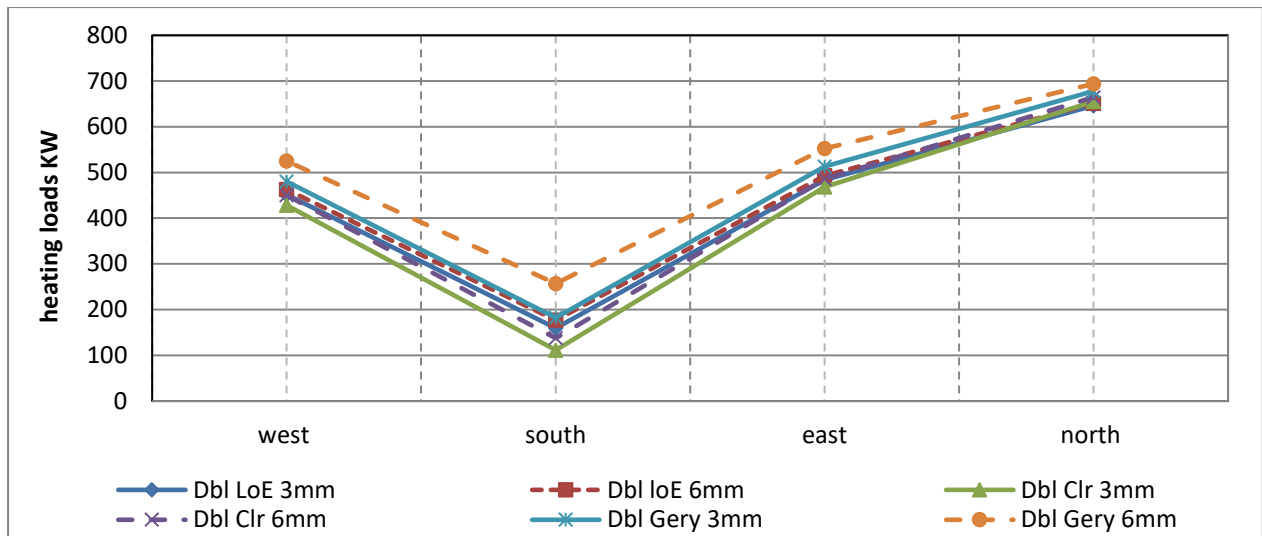


Fig.2-a.indicate required heating energy in different window glass type and thickness and orientation annually

b) Effect of window glass type and thickness in cooling loads.

Fig.3. illustrate average annually required cooling energy in different window glass type and thickness and orientation. that north orientation followed by south represents the lowest cooling energy consumption which west is the highest in all winows cases . As showed in fig.3 Dbl Gery 6mm case recored the minimum cooling loads in all orientation . This decrease was due the glass color and thickness prevents heat transfer from inside to outside . On the other hand, Dbl Clr 3mm case represented the maximum cooling loads required in all orientation . The effect of orientation is the same trend in four directions in different cases of window glass types and thickness. Fig.3 reveal that the decrease ratio between the maximum and minimum required cooling energy 2000KW . Using the Dbl Grey 6mm in window glass reduce cooling energy by 20% .

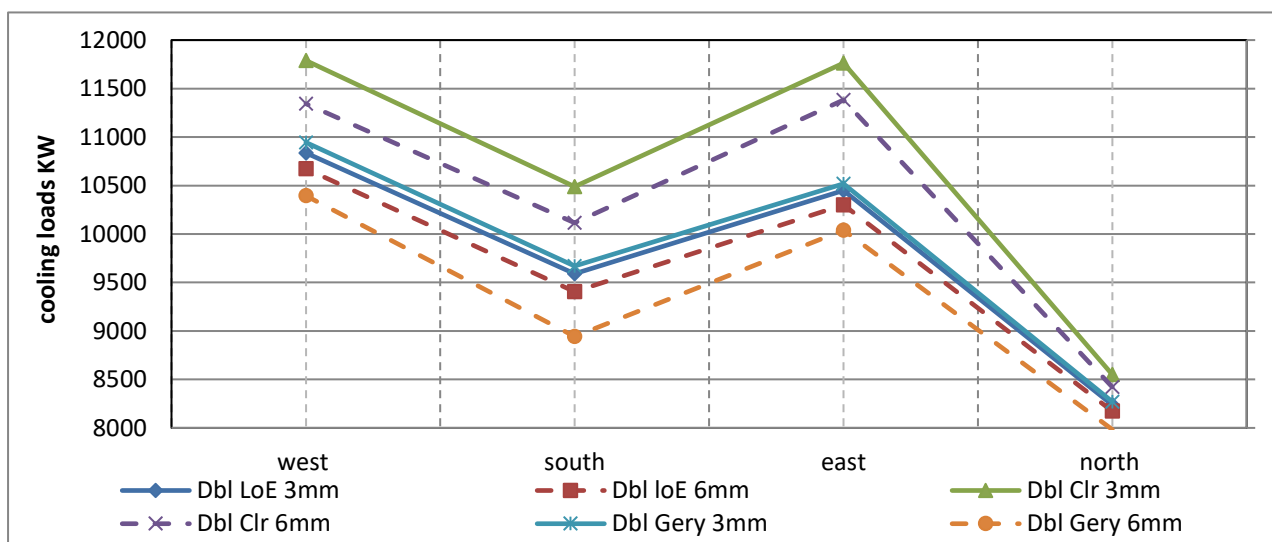


Fig.3.indicate required cooling energy in different window glass type and thickness and orientation annually

c) Effect of window glass type and thickness in Lighting required energy.

Lighting energy consumption is actually considered the main factor for determining the window glass properties; lighting depends on the opening position, direction and glass type and thickness. Window design plays important role in building architect. So when the impact of changing window glass type and thickness on building energy consumption and lighting loads, the amount of inlet lighting to the building changes producing a change of the required power of the lighting. Fig.4 present the effect of changing window glass type, glass thickness and orientation on lighting required energy. As indicated in fig.4 the Dbl Clr 3mm, Dbl Cle 6mm, Dbl loE 3mm and Dbl LoE 6mm cases recored the same amount of lighting loads and represent the nimum required lighting loads. While, the Dbl Grey6mm is the hieghest lighting loads required. The difference between the lowest and hieghest case is about 30 KW.

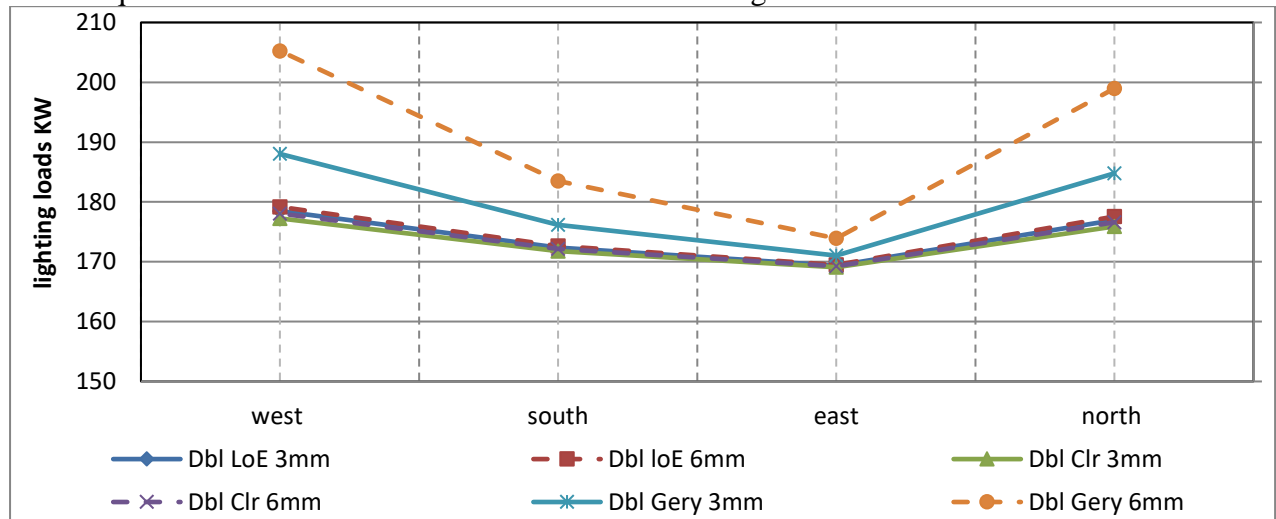


Fig.4.indicate required lighting loads in different window glass type and thickness and orientation annually

d) Effect of window glass type and thickness in required energy consumption. Figure 5 illustrates the annually energy consumptions in different window glass type and thickness and orientation annually. Figure 5 shows that the facility has the maximum energy consumption during the summer and has the minimum value at winter time for window glass type and thickness. The findings show that maximum energy consumption at weast direction different window glass type and thickness. when, the north direction represent the minimum energy consumption in all cases.

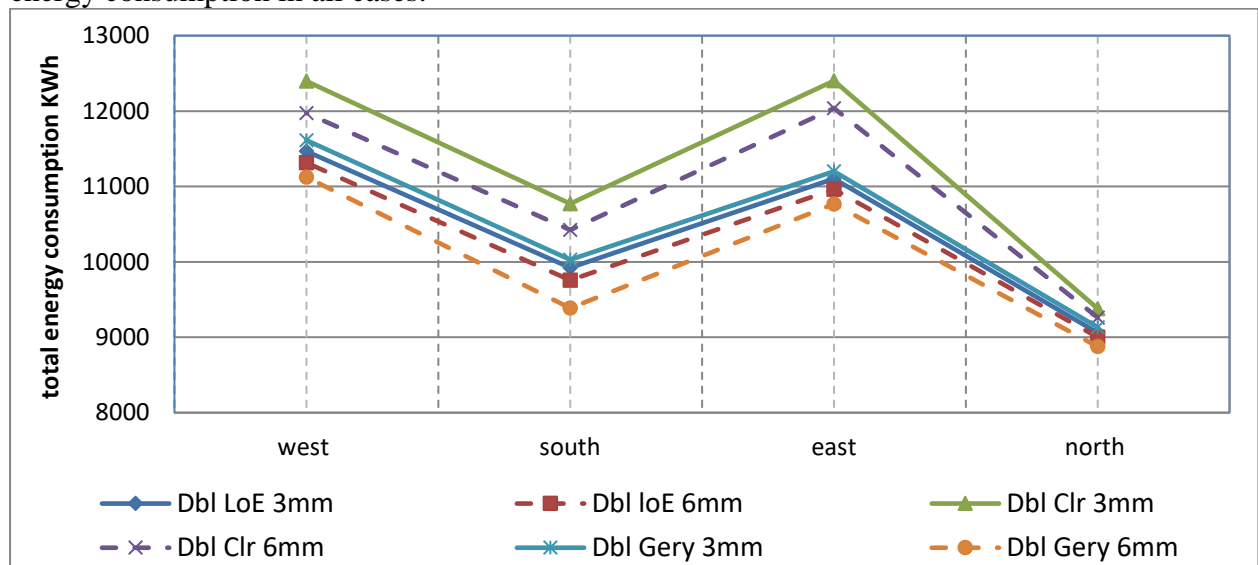


Fig.5.indicate total energy consumption in different window glass type and thickness and orientation annually

4 Conclusions

The study concludes that the north direction is the lowest of the main energy consumption trends by about 30 % of the total energy consumed , followed by south direction by 13% in all cases of the study .The required energy in building reduces by increasing the glass thickness and using glass color in range of 3525KWh. Changing window glass type reduced energy consumption in north and south by 28%,12% form the east and west orientation.Double glazing grey 6mm achieve energy decrease by 30% , while making increase in heating and lighting load by 38%,33% respectively. When double clear 3mm making decrease in heating and lighting but these decrease can neglect compare with the huge increase in cooling loads.

Acknowledgements

It is a pleasure to acknowledge Ministry of Higher Education (MoHE) of Egypt for providing a scholarship to conduct this study as well as the Egypt Japan University of Science and Technology (E-JUST) and Japan International Cooperation Agency (JICA) for offering the facility, tools, and equipment needed to conduct this research work.

References

- [1] K. Vats, G.N. Tiwari, Energy and exergy analysis of a building integrated semitransparent photovoltaic thermal (BISPV) system, Appl. Energy. 96 (2012) 409–416. doi:10.1016/j.apenergy.2012.02.079.
- [2] R. Yin, P. Xu, P. Shen, Case study: Energy savings from solar window film in two commercial buildings in Shanghai, Energy Build. 45 (2012) 132–140. doi:10.1016/j.enbuild.2011.10.062.
- [3] D.B. Özkan, C. Onan, Optimization of insulation thickness for different glazing areas in buildings for various climatic regions in Turkey, Appl. Energy. 88 (2011) 1331–1342. doi:10.1016/j.apenergy.2010.10.025.
- [4] S.C. Sekhar, K. Lim Cher Toon, On the study of energy performance and life cycle cost of smart window, Energy Build. 28 (1998) 307–316. doi:10.1016/s0378-7788(98)00026-7.
- [5] M. Bojić, F. Yik, Application of advanced glazing to high-rise residential buildings in Hong Kong, Build. Environ. 42 (2007) 820–828. doi:10.1016/j.buildenv.2005.09.021.
- [6] A. Gasparella, G. Pernigotto, F. Cappelletti, P. Romagnoni, P. Baggio, Analysis and modelling of window and glazing systems energy performance for a well insulated residential building, Energy Build. 43 (2011) 1030–1037. doi:10.1016/j.enbuild.2010.12.032.
- [7] A. Ebrahimpour, M. Maerefat, Application of advanced glazing and overhangs in residential buildings, in: Energy Convers. Manag., 2011: pp. 212–219. doi:10.1016/j.enconman.2010.06.061.
- [8] M. Arici, H. Karabay, Determination of optimum thickness of double-glazed windows for the climatic regions of Turkey, Energy Build. 42 (2010) 1773–1778. doi:10.1016/j.enbuild.2010.05.013.
- [9] M. Bojic, F. Yik, P. Sat, Energy performance of windows in high-rise residential buildings in Hong Kong, Energy Build. 34 (2002) 71–82. doi:10.1016/S0378-7788(01)00079-2.
- [10] P.F. Tavares, A.R. Gaspar, A.G. Martins, F. Frontini, Evaluation of electrochromic windows impact in the energy performance of buildings in mediterranean climates, Energy Policy. 67 (2014) 68–81. doi:10.1016/j.enpol.2013.07.038.
- [11] M. Thalfeldt, E. Pikas, J. Kurnitski, H. Voll, Facade design principles for nearly zero

- energy buildings in a cold climate, *Energy Build.* 67 (2013) 309–321. doi:10.1016/j.enbuild.2013.08.027.
- [12] J.W. Lee, H.J. Jung, J.Y. Park, J.B. Lee, Y. Yoon, Optimization of building window system in Asian regions by analyzing solar heat gain and daylighting elements, *Renew. Energy.* 50 (2013) 522–531. doi:10.1016/j.renene.2012.07.029.
- [13] W.J. Hee, M.A. Alghoul, B. Bakhtyar, O. Elayeb, M.A. Shameri, M.S. Alrubaih, K. Sopian, The role of window glazing on daylighting and energy saving in buildings, *Renew. Sustain. Energy Rev.* 42 (2015) 323–343. doi:10.1016/j.rser.2014.09.020.

28-Optimization of design Parameters of Solar Chimney: A case study in Egypt

Y. A. Attai, K. F. Megalaa and M. M. Abd Elbaset[†]

Mechanical Power Engineering Dept., Faculty of Engineering, Helwan University, Cairo, Egypt.

[†] **Corresponding Author:** Mahacen1@hotmail.com

Abstract

The solar chimney power plant converts solar thermal energy into kinetic energy to generate electricity. The main parts of solar chimney plant are collector, chimney tower and turbine. There are many factors affected on solar plant performance as solar intensity radiation, air pressure drop, temperature, velocity and mass flow rate. The produced output power depends on the design parameters of the solar chimney as well as its dimensions. Therefore; this study focused on how to optimize a solar chimney through a mathematical model to predict and estimate the optimum dimensions of any proposed solar chimney power plant by knowing the required output power and the ambient conditions. Q-basic program was used to develop such mathematical model for obtaining the optimum plant dimensions for a known output power plant. The developed mathematical model results were validated by measurements of an actual physical plant. In addition, the study proposes that the most suitable plant, affordable by local government standards to respond to the electricity demand of a typical village in Aswan. Also the developed model enables the prediction of the performance parameters of any solar chimney power plant during 24 hours a day.

Keywords: Solar chimney; Mathematical model; Optimum design; Aswan

1. Introduction

World aims to provide clean and renewable energy. Therefore, the solar chimney station is considered one of the promising facilities to achieve this, with a little maintenance cost. The solar chimney power plant (SCPP) consists mainly of three main parts shown in figure (1). The first part is the collector that is considered to be as a green house, where air is heated at the entrance of the collector and causes densities variations. As a result, buoyancy arises and hot air is directed to the second part, known as the chimney. The chimney is a tall building, located in the center of the collector. The third part is the turbine, which is located at the entrance to the chimney and is used to convert the kinetic energy of hot air into electrical energy. The main defects of SCPP are summarized in its high cost of construction; therefore, all trends lead to a mathematical calculation to reduce the cost. The optimum design of the solar chimney is the key input in economic growth and there is a close link between the availability of energy and the growth of a nation.

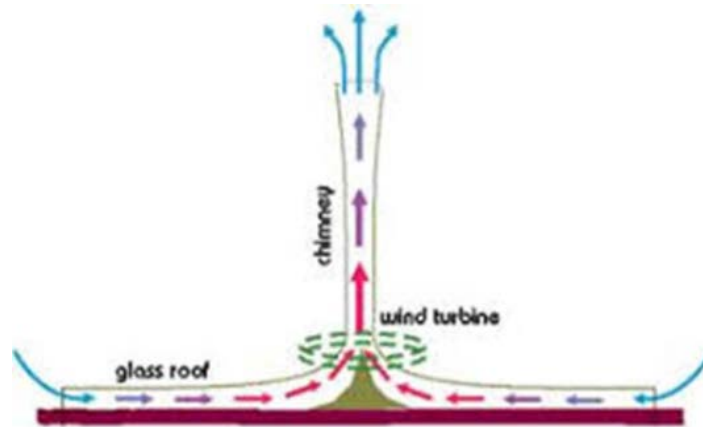


Figure (1) schematic diagram of solar chimney power plant component

Haff W et al. [1] and Haff W. [2] were the first researchers in innovation and studying solar chimneys. They made a small prototype in Manzanares, Spain. EL-sebaili et al. [3] presented a significant study on solar radiation types (direct and diffuse) in vertical and horizontal plane and applied a comprehensive investigation using the climatic conditions of Saudi Arabia. Notton et al. [4] calculated the amount of diffuse solar radiation from global data over the course of daylight hours for the horizontal plane. The amount of solar radiation over the day was determined on the horizontal surface using the available online statistics [5].

Various studies have found that the optimum driving pressure indicated by the symbol ($x = p_{\text{tur}} / p_{\text{tot}}$) equals $2/3$ based on the results of the practical experiments [1], in contrast many researchers took its value equals to 0.8 without using references [6]. Otherwise, its value ranges from 0.8 - 0.9 based on mathematical equations [7]. In the presented article, the calculated value of x depends on the practical experiment [1] and mathematical equations [8] leading to an optimum value of driving pressure equals to $2/3$ that available only for constant driving pressure Δp_{tot} and steady increase in air temperature, knowing that this value decreases throughout the day. The increase in the production capacity and the efficiency of the solar plant is mainly based on the low cost of construction, which includes the cost of the main dimensions such as collector diameter, chimney height and diameter [9, 10].

Many researchers have been and are being, devoted to study the relationship between shape of collector and its dimension with output power. This also led to the calculation of the ratio between height and radius of collector at high air flow rate [11 -15]. However, as reported by Pretorius and Kroger [16] their analytical investigation revealed that the height of the collector and its shape have a noticeable effect on the produced electrical energy. Their results proved the direct relationship between them. In contrast, Dehghani and Mohammadi [17] have used various techniques to optimize the dimensions of solar chimney power plant according to capital cost. Gholamalizadeh and Kim [18] were developed the electric power and overall efficiency of SCPP, using three different methods, have led to assess the capital cost. In addition, Sangi [19] proposed a mathematical model for SCPP with its collector diameter of 1000 meters and a chimney height of 350 meters to calculate the value of the output electric power, the results of that model showed an analysis of its performance at different solar radiation ranging from $(400 \text{ to } 750) \text{ W/m}^2$ and ambient temperature ranging from $(270 \text{ to } 315 \text{ K})$.

Numerous researchers have examined, with numerical simulations, the performance of SCPP according to Iran weather and verified its validity by comparing their results with that of Manzanares pilot plant [20]. The evaluation of heat transfer by convection with collector material and soil types on performance of large scale of SCPP have been stated by [21]. Investigation by using numerical equations under strong and weak weather to study its

influence on collector inlet and chimney output on the electric power and performance was also carried out [22]. The optimal ratio for driving pressure drop which varying between (0.66 : 0.97) was achieved to calculate the optimum output power [23]. Guo et al. [24] analyzed the performance of SCPP and the performance of their station during every hour and it was affected by the incident angle of sun rays. Kasaeian et al. [25] conducted a prototype of the solar chimney at the University of Iran and revealed that the optimal dimension of the chimney was achieved. Prediction of the temperature and velocity of the air inside the chimneys by studying the amount of solar radiation at the horizontal plane was achieved by [26]. In addition, performance prediction for different models of SCPP, by solving integrated algebraic equations, was performed to obtain the output power and efficiency of each model [27]. Moreover, Dimension Parameters and economic calculation of SCPP was analyzed by Okoye et al. [28]. Modifying numerical models to calculate static pressure, output power, driving force and efficiency, then assess the results using initial Manzanares model have been demonstrated by [29]. Pastohr et al. [30] have solved the main equations of thermodynamics using CFD for different models to improve efficiency.

From the previous literature, it can be seen that a little interest was given to the prediction and optimization of SCPP based on the Egyptian weather conditions, although Egypt has solar radiation don't less than 90%, especially at south region. Therefore, the current study objectives are to investigate how to optimize the main parameters of a solar chimney station to achieve the desired output power in a location in the southern region in Egypt. A mathematical model will be prepared to predict and estimate the optimum dimensions of any proposed solar chimney power plant by knowing its required output power and the ambient conditions. Q-basic program was used to develop such mathematical model for obtaining the optimum plant dimensions for any required output power.

Five stations were selected in Beban village (Aswan) as a case study, in which the solar radiation reaches up to 2500 kW / m² per year. All stations are considered to have the same weather conditions with different output power of each. The present model is established to predict the basic dimensions of each station. Also, this location was chosen because of the low cost compared to the European cost due to the availability of raw materials, manpower and proper weather. The optimal design of solar chimney is one of the main entry points for economic growth, and there is a close relation between energy availability and output power. In the current study, the amount of solar radiation over the day is determined on the horizontal surface using the website [5] which depends on location determination of Beban village on the map, its latitude is 24.4415 and altitude 93, and then determine the month and day to be studied. Here was chosen mid-July at 12:00 O'clock.

Maximum solar radiation at day 200 = 1046 W/m²

Solar radiation at day 200 at 12:00 = 1046 W/m².

The results appeared as curves as shown in figure (2) and figure (3).

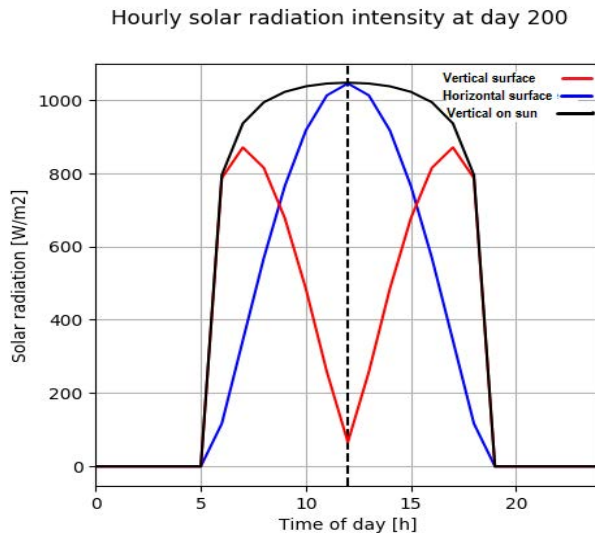


Figure (2) Hourly solar radiation intensity in Beban village in July 2019

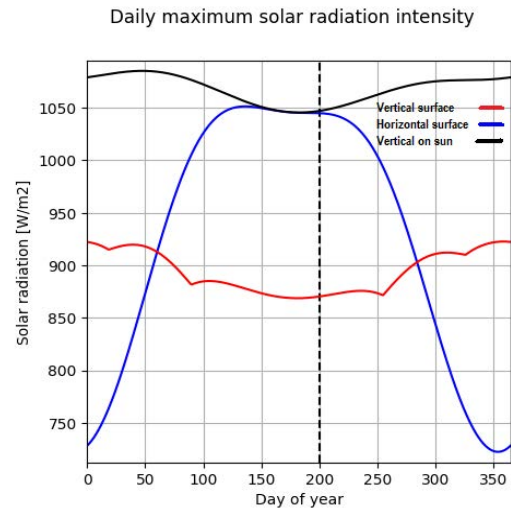


Figure (3) Daily maximum solar radiation intensity in July 2019

The previous figures (1) and (2) illustrate the intensity of solar radiation on a horizontal surface, a vertical surface and on a vertical surface on the sunlight; where figure (1) shows the intensity of solar radiation per hour and figure (2) shows the daily maximum solar radiation in July for Beban village.

2. Mathematical model and methodology

According to the concept of running hot air inside the solar chimney, it depends heavily on the change of air density. That led to a difference in pressures [1] that can be seen in figure (4). First, by knowing the value of the required electrical power from the solar chimney station that will design and determine the appropriate generator efficiency for the resulting energy [8, 9, 10, 16] then calculate the maximum energy symbolized by the P_{\max} from equation (1):

$$P_{\max} = P_{\text{ele}} / \eta_g \quad (1)$$

Where η_g is the generator efficiency

Second, calculate two types of air velocity [26]. The first velocity of the air is affected by the turbine movement (V_T) and appears on the figure (4) at point 3. This velocity is calculated from the following equation:

$$V_T = (2 * P_{\max} * 1000)^{0.5} / \dot{m} \quad (2)$$

The second velocity of the air, before being affected by the movement of the turbine (V_{noT}) [26] and shown on the figure (4) before point 2, hence can be estimated from the following equation:

$$V_{\text{noT}} = V_T / (1-x)^{0.5} \quad (3)$$

Where:

x , as mentioned before, is the ratio of the pressure drop across the turbine to the total available driving pressure of the system. Then, the maximum power can be obtained when the turbine extract pressure $x = 2/3$ of the available driving pressure [1, 2, 8]

The air mass flow rate (\dot{m}) can be assumed [1] or can be calculated from following equations:

$$P_{\text{ele}} = (16/27) * (1/2 * \rho_1 * V_T^3 * A_{\text{ch}}) \quad (4)$$

Since;

$$\dot{m} = \rho_2 * A_{\text{ch}} * V_T \quad (5)$$

By compensating by equations (3) and (5) in the equation (4) get the air mass flow rate as follows

$$\dot{m} = ((27/8) * P_{\text{ele}}) / ((V_{\text{noT}})^2 * (1-x)) \quad (6)$$

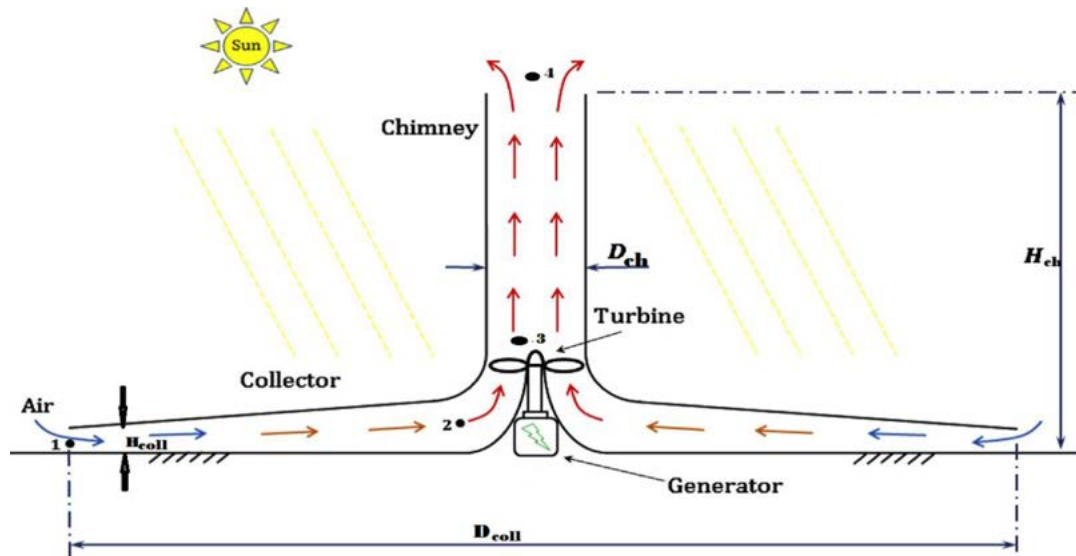


Figure (4): The drawing of air flow in solar chimney power plant

The buoyancy phenomenon occurred through differing air density and movement, which would lead to calculate the available driving pressure and its effect on air movement within the collector [11]. This can be achieved by calculating the total pressure drop within the SCPP [29] from equation:

$$\Delta p_{tot} = (0.5 * \rho_1 * V_{noT}^2) \quad (7)$$

By knowing Δp_{tot} , pressure can be computed after the effect of the turbine, which is at point 3 in figure (4) as:

$$p_3 = p_1 - \Delta p_{tot} \quad (8)$$

Therefore from the V_T value, that calculated previously, the dynamic pressure drop, proven by [29], can be calculated from:

$$\Delta p_{dyn} = (0.5 * \rho_1 * V_T^2) \quad (9)$$

Calculating the turbine pressure drop of equation (10) has been proved by [8] as follows:

$$\Delta p_{tur} = \Delta p_{tot} - \Delta p_{dyn} \quad (10)$$

However, the pressure can be computed before the effect of the turbine, which is at point 2 in figure (4) as:

$$p_2 = \Delta p_{tur} + p_3 \quad (11)$$

Although it is possible to calculate the values of the amount of solar radiation in practice or from many different sites as mentioned earlier [3, 4, and 5], furthermore, it can be mathematically calculated from the following equations [8] by selecting $\eta_{coll} = 0.32$ as reported by [1-4] using the following equation:

$$q = \eta_{coll} * I \quad (12)$$

$$\text{Also, } q = (\alpha * I) - (U * \Delta T) \quad (13)$$

Thus, the difference in temperature between points 2 and 1, specified in figure 4, can be calculated as follows [2-1]:

$$\Delta T = ((\alpha * I) - q) / U \quad (14)$$

By replacing q from equation (12) we get the following equation

$$\Delta T = (\alpha - \eta_{coll}) * (I / U) \quad (15)$$

Furthermore, the values of α , η_{coll} and U , which are constant for the same designed solar chimney station, can be compensated for each value based on the type of collector

$$\Delta T = 0.02 * I \quad (16)$$

Note that the constant (0.02) in equation (16) differs from one station to another depending on the type of collector.

Then calculate the temperature after the turbine at point 3 as:

$$T_3 = T_2 * (p_3/p_2)^{(\gamma-1/\gamma)} \quad (17)$$

The density of the air at points 2 and 3 was then estimated by thermodynamic equations used [30]:

$$\rho_2 = p_2 / (R * T_2) \quad (18)$$

$$\rho_3 = p_3 / (R * T_3) \quad (19)$$

Finally, after knowing the required electrical power, the intensity of the solar radiation and calculations of (V , Δp , q'' , ΔT and ρ), the collector dimensions can be calculated from the following equations [8]. First calculate the area of collector from its equation:

$$A_{coll} = \Delta T * (\dot{m} * c_p) / q \quad (20)$$

Then, from area can be calculated collector diameter from equation:

$$d_{coll} = (4 * A_{coll} / \pi)^{0.5} \quad (21)$$

Hence, the collector height can be calculated as follows:

$$h_{coll} = \dot{m}_{cal}^{1.5} / (\rho_2 * \pi * d_{coll} * (2 * P_{max})^{0.5}) \quad (22)$$

The dimensions of the chimney are calculated as follows [1, 8]. The diameter of chimney can be calculated from the following equation:

$$d_{ch} = ((13.5 * P_{ele}) / G)^{0.5} \quad (23)$$

While the height of chimney is calculated from following equation:

$$h_{ch} = (P_{max} * \rho_2 * 1000) / (\dot{m} * G * (\rho_1 - \rho_2) * (1-x)^{0.5}) \quad (24)$$

it can be calculated also from following equation, based on the ambient temperature and efficiency of chimney:

$$h_{ch} = (\eta_{ch} * c_p * T_1) / (G * 100) \quad (25)$$

To correct the value of assumed mass flow rate of air and efficiency of collector

$$\dot{m}_{cal} = (3.14 * h_{coll} * d_{coll} * \rho_1 * (2 * P_{max})^{0.5})^{2/3} \quad (26)$$

Then from eq.(11)

$$\eta_{coll} = \alpha - (U * \Delta T / I) \quad (27)$$

3. Results and discussion

3.1 Validation of the model with experimental data

To validate the current theoretical data of the model, compared it with the experimental results of the prototype (Manzanares, Spain), whose data were recorded in table (1). The measured data was approved on September 2, 1982 from Reference. [1]. the comparison between the empirical data and the current theoretical predictions are recorded in Table (2). Based on the data provided in the reference article, instead, the values (T_1 , P_1 , I) were calculated theoretically for the area to be studied using the designated websites [4-3].

Table (1): Main parameters and data of proto type plant in Manzanares, Spain [1].

| | |
|---|---------------------------|
| Ambient temperature (T_1) | 302 (K) |
| Ambient pressure (P_1) | 100000 (pa) |
| Collector absorption coefficient (α) | 0.65 |
| Collector losses coefficient (U) | 15 (W/ m ² .k) |
| Turbine efficiency ($\eta_{tur.}$) | 0.83 |
| Collector efficiency (η_{coll}) | 0.32 |
| Global solar radiation | 1017 (W/m ²) |
| Output power (P_{ele}) | 50 (kW) |
| Height of chimney (h_{ch}) | 194.6 (m) |
| Diameter of chimney (d_{ch}) | 5.08 (m) |
| Diameter of collector (d_{coll}) | 244 (m) |
| Height of collector (h_{coll}) | 1.85 (m) |

While the value of q is calculated from equation (12) and the value of the air velocity V_{noT} can also be measured or calculated from equation (3). Also, the value of \dot{m} is calculated by equation (6) or assumed then corrected by equation (26). Choose the value of the driven pressure ratio x at optimum output based on the calculation and references [1, 8]. Therefore, the comparison between the measured data for the Manzanares prototype and the theoretical data from current study shown in Table (2) indicate a good relationship among them to apply the proposed model to other stations.

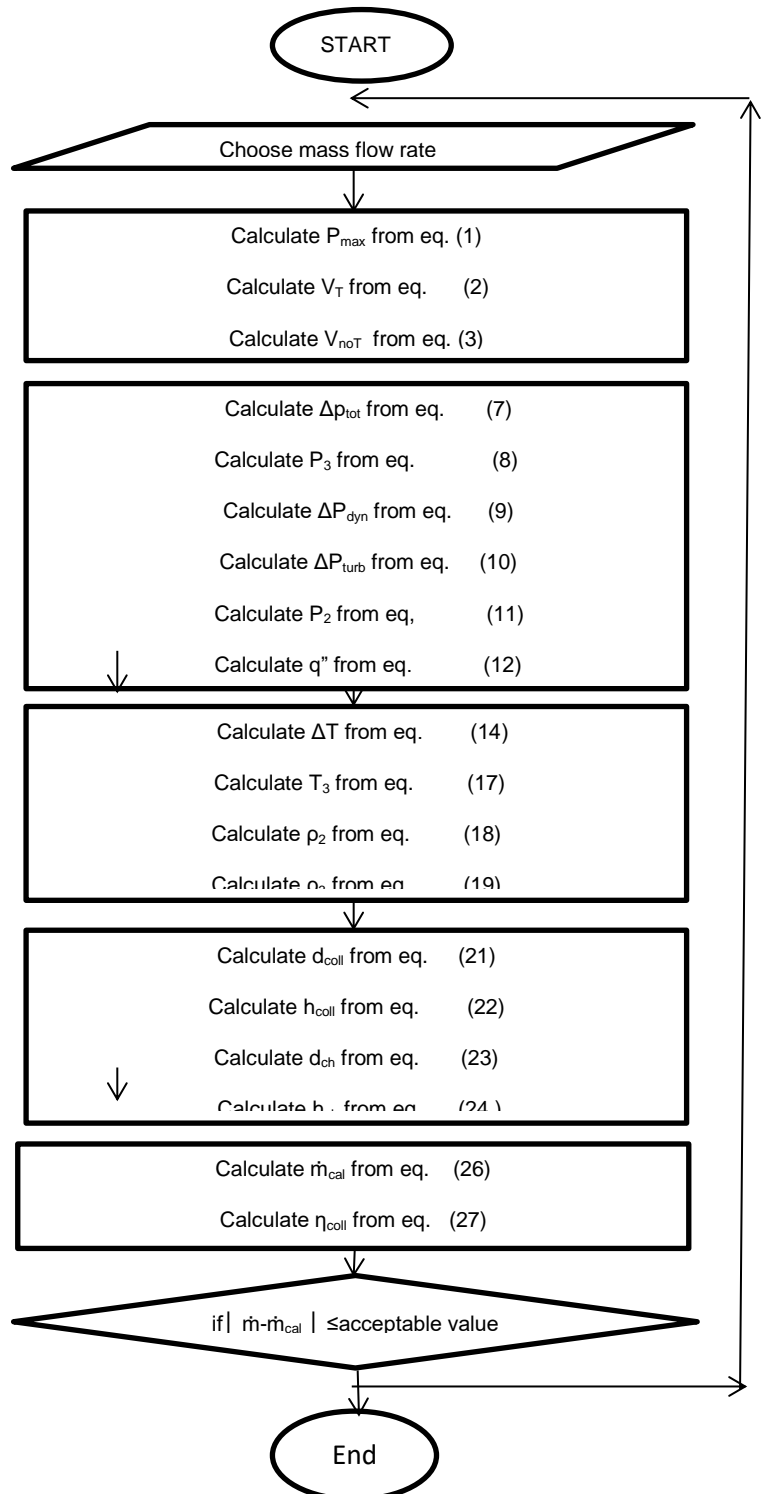
Figure (5): flowchart of solution procedures

Table (2) Comparison between measured data for Manzanares plant and theoretical results (Data of reference in 1st September (1983))

| Parameter (m) | Measured (m) | Theoretical (m) |
|-----------------------------------|--------------|-----------------|
| Collector Diameter (d_{coll}) | 244 | 242.76 |
| Collector height (h_{coll}) | 1.85 | 2.01 |
| Chimney height (h_{ch}) | 194.6 | 187.29 |
| Chimney Diameter(d_{ch}) | 10.16 | 8.27 |

3.2 Performance and characteristics of Solar Chimney System

Five different stations were selected in terms of output power and sizes required to demonstrate their characteristics as shown in Figures 6, 7, 8 and 9 according to the cost of the model



described in [1]. These five stations were selected in Beban (Aswan - Egypt) as a case study to simulate with Manzanares prototype [8] which is affordable by the local government standards to respond to the electricity demand of a typical village in Aswan. Where different electrical powers were selected for each plant under constant weather conditions, where an electric power of 100 kW was selected for the first station, while the second station 150 kW, the third station 200kW, the fourth station 250kW, and finally the fifth station 300 kW. Also the developed model enables the prediction of the performance parameters of any solar chimney power plant during 24 hours a day

3.3 Influence of electric power on characteristics SSPP

Figures (6) and (7) show the relation between electric power and air mass flow rate in two cases with calculations of solar radiation with losses and another calculation neglecting losses of solar radiation. From figure (6), the case of solar radiation with loss calculation can be observed; such calculations are performed using equation (12). The obtained trend clarifies that there is a direct relationship between the power and the amount of the mass flow rate of the air entering the collector which agrees with the previously obtained results [11], when the collector efficiency is less than 100%.

From this, it can be noted that the maximum electric power value is located near the minimum mass flow rate value. This means that increased buoyancy increases the air mass and consequently increases the kinetic energy of the turbine, which transforms it into an electric power. Both the power and mass flow rate of air were directly affected by changing the dimensions of the plant, especially the diameter of the collector and the height of the chimney.

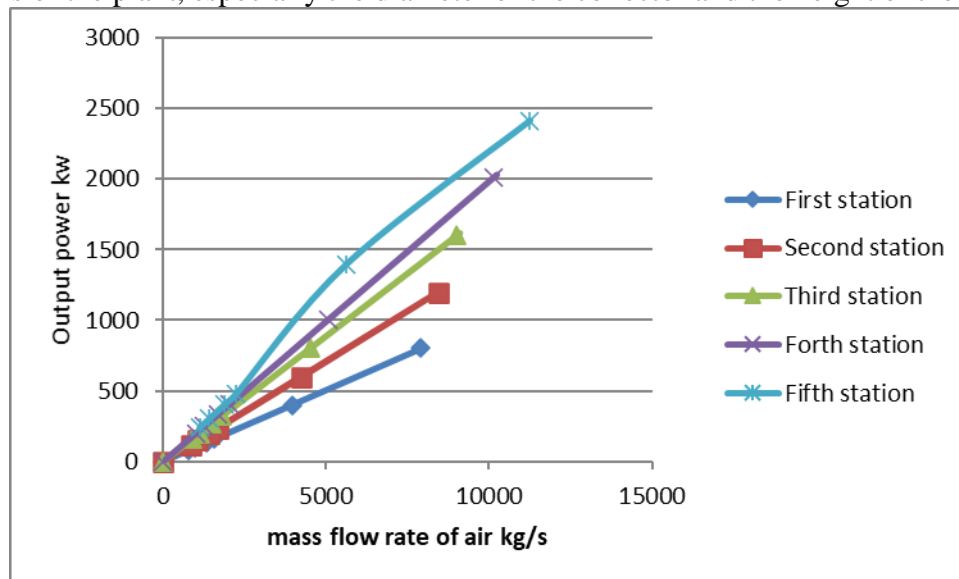


Figure (6) Effect of mass flow rate on output power for solar radiation 1046 W/m² (with losses)

It can be seen, from figure (7) that when the collector efficiency equals 100 % and no heat radiation losses, the maximum power is located between the minimum and maximum values of the air mass flow rate. As previously mentioned in Figure (6), there is direct relation between output power and amount of mass of air. Noting that the value of the mass of air in figure (7) (Solar radiation without loss) is greater than its value in figure (6) (Solar radiation with losses). On the other hand, it is clear that the amount of airflow is not constant during different hours of the day due to the difference in the intensity of solar radiation

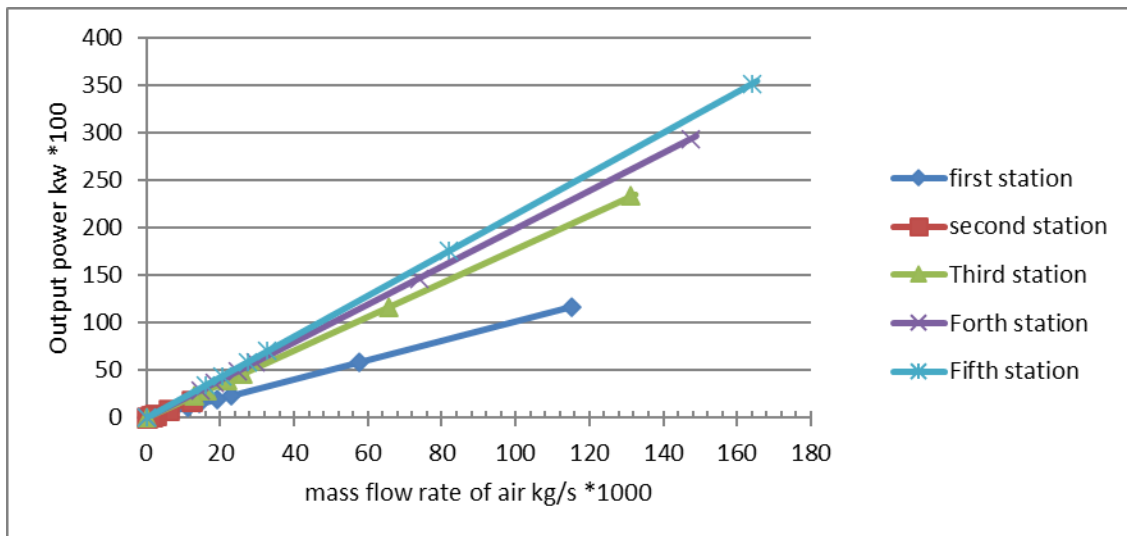


Figure (7) Effect of mass flow rate on output power for solar radiation 1046 W/m^2 (with no losses)

3.4 Influence of pressure ratio on the electric power

Figure (8) illustrates this effect at collector coefficient absorption of $(\alpha) = 0.65$, and collector losses coefficient $(U)=15$. The optimum pressure ratio is not equal to $2/3$ and its value is not constant at all hours of the day as a result of changing the intensity of solar radiation every hour. So the assumption of x value at current study was only valid for constant pressure drop and constant increase in temperature under the collector in addition, it has proven previously by [1, 8].

As a result, the value of the output power of each plant is not fixed per year and is not fixed in months or even in daytime. The analysis indicated that the optimum pressure ratio depends only on the solar radiation, and it affects the mass flow rate of the air and the output power values produced from the same station. Also note from the figure (8) that all X values resulting from mathematical calculations are decimal values. The values are slightly different due to the mathematical approximation and this explains the trend of the second station seems different from other trends, so at the power 400 value $X = 0.47$, and by the mathematical approximation $X = 0.5$. In both cases the value is practically acceptable.

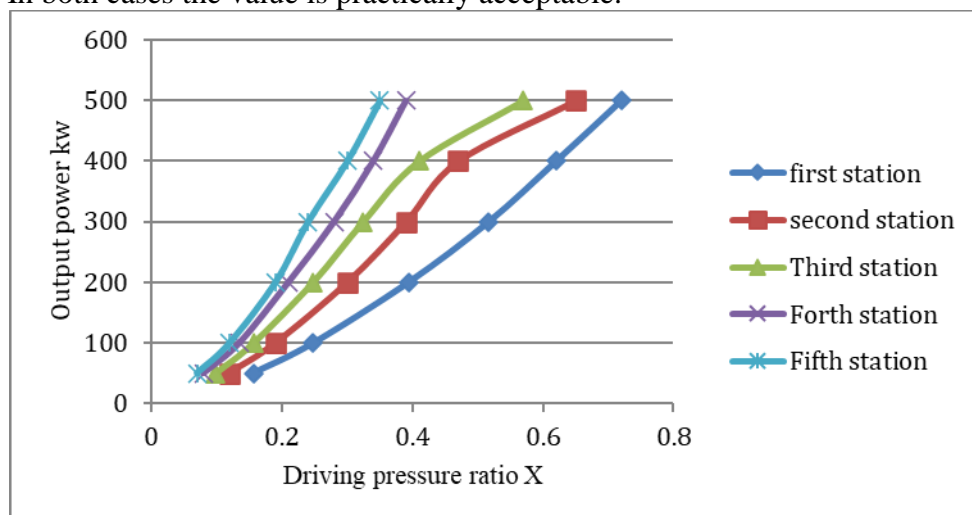


Figure (8) Effect of pressure ratio on power output for solar radiation 1046 W/m^2

3.5 Influence of temperature rises on mass flow rate of air

This effect is illustrated in Figure (9). When the collector diameter increases the difference in temperature increases while the amount of air entering the collector decrease. This is consistent

with equation (28). Also, it can be shown that the difference in temperature within the collector depends only on the diameter of the collector.

$$\Delta T = q'' \cdot A_{\text{coll}} / \dot{m} \cdot c_p \quad (28)$$

Thus, the difference temperature of the air inside and outside the collector is an important factor affecting the buoyancy and mass of air entering the collector. This means that the efficiency of the collector is determined by the value of ΔT on the basis of equation (27).

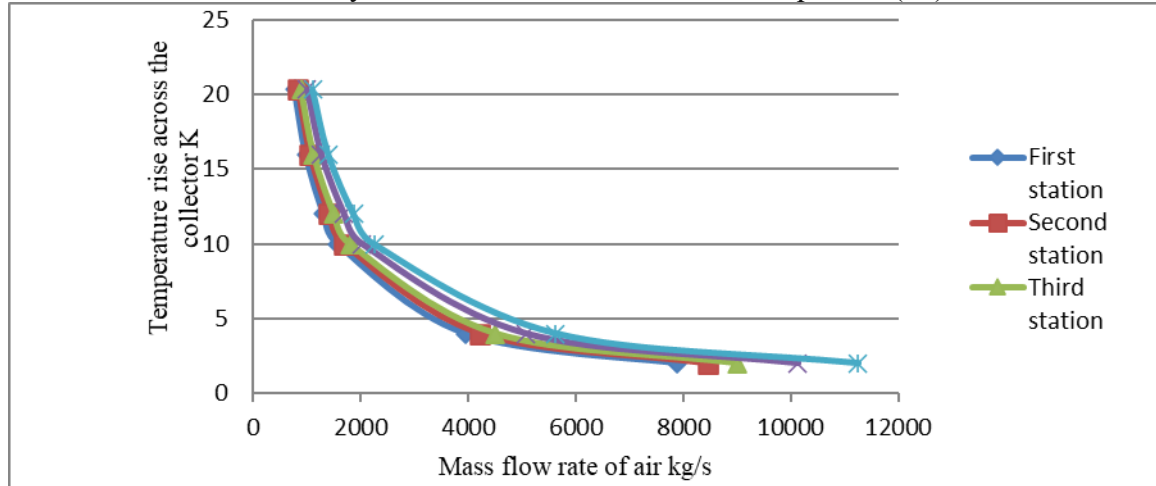


Figure (9) Effect of mass flow rate on collector temperature rises for solar radiation 1046 W/m²

3.6 Influence of pressure drop on power and mass flow rate of air

Figure (10) shows that pressure drop is actually one of the main factors responsible for changing the amount of electric power throughout the day. Its value is equal to the sum of both turbine pressure drop and dynamic pressure drop. It is clear from the graph that the relationship between them is a direct relationship.

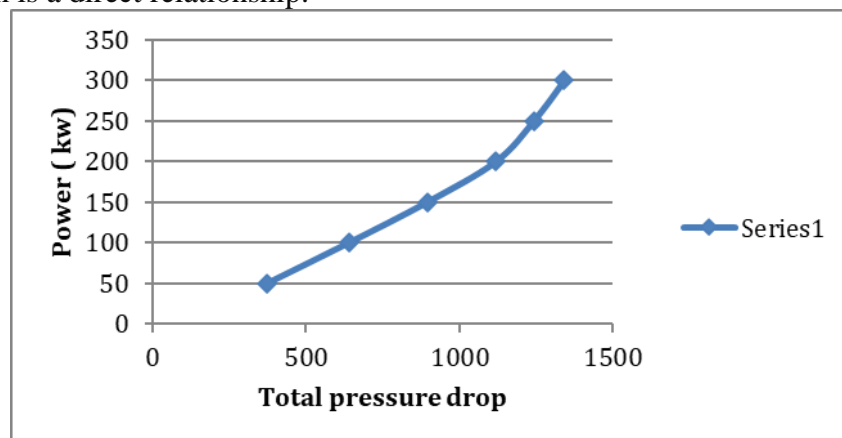


Figure (10) Relation between output power and Total pressure drop

The total pressure drop also controls the amount of airflow inside the station, see figure (11) where the buoyancy force inside the station is caused. This means that the mass flow rate is not constant during each hour of the day. Note that with the increase of the total pressure drop, the flow rate of the mass increases and vice versa.

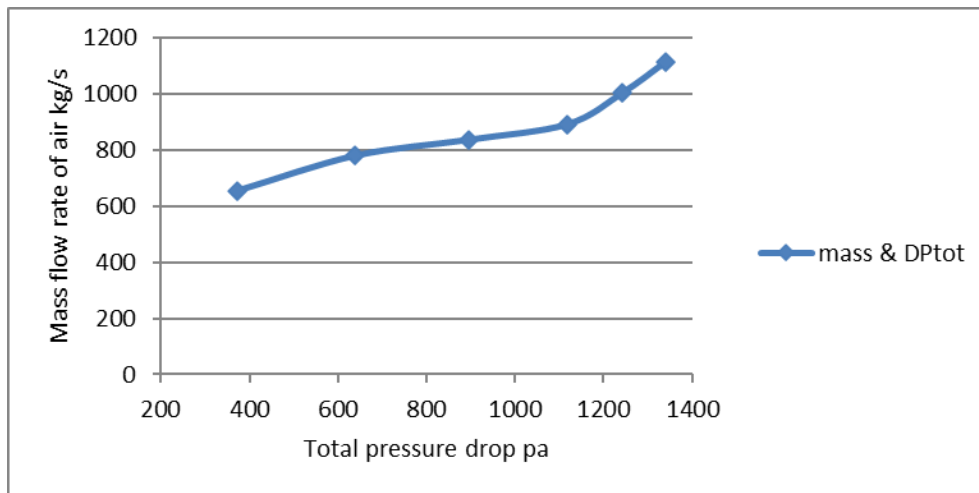


Figure (11) Effect of Total pressure drop on mass flow rate of air

3.7 Influence of main parameters of SSCP on the output power

It should be noted that the optimum design of the SSCP depends on the maximum output power. Figures 12, 13 and 14 show the relationship between output power and the main parameters D_{coll} and H_{ch} of SSCP. Figure (12) shows the relationship between electric power and chimney height. This relationship is based on Equation (24), which shows that when chimney height increases, in the studied five theoretical plants, greater driving force than friction losses is obtained, as a result of which electric power increases.

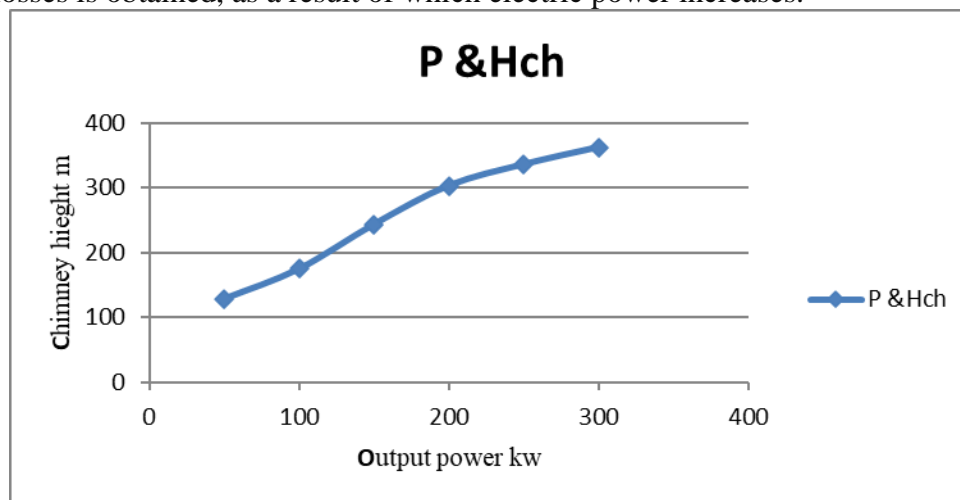


Figure (12) Relation between output power and chimney height

Figure (13) illustrates the relationship between the output power and the collector diameter. Where it was observed, using mathematical equations, that by increasing the area of the collector in the five theoretical stations, the output power also increased. Because increasing the area of the collector increases the amount of hot air inside and thus increases the driving force, which it turns to the electric power in the turbine.

The relationship between collector diameter and chimney height this effect is illustrated in figure (14) and solved by equation (26) in equation (24) and as a result, they proportional directly together. This means that when the collector area increases, the air temperature increases and therefore the driving force increases. As a result, we need to increase the chimney height to reduce friction losses and to harvest the electric power.

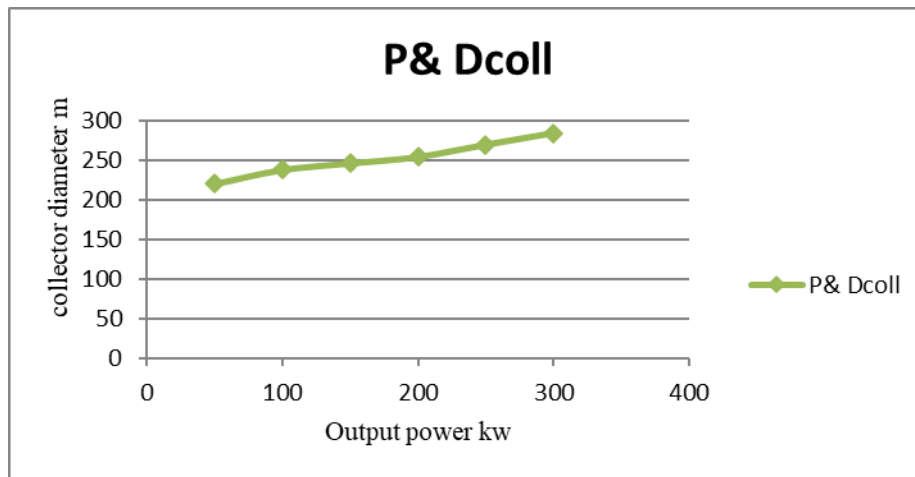


Figure (13) Relation between output power and collector diameter

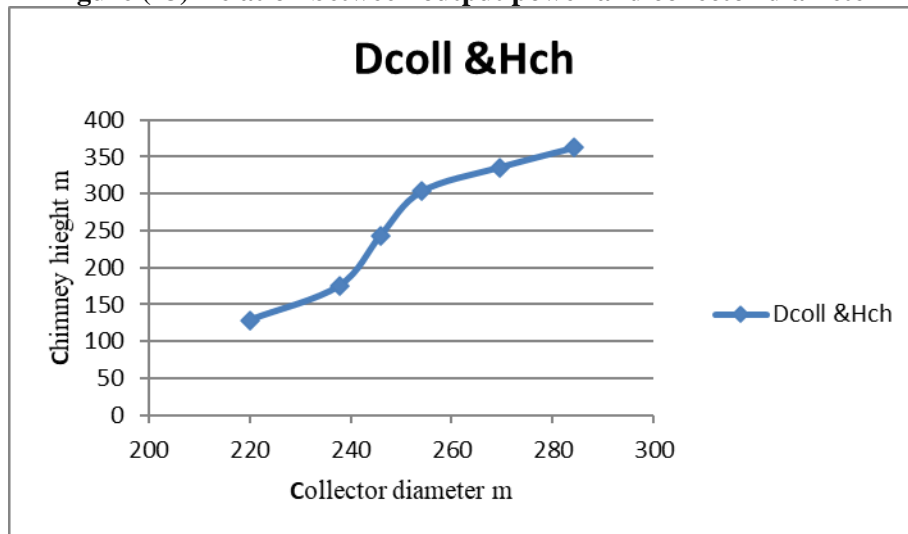


Figure (14) the relation between collector diameter and chimney height

3.8 Influence of mass flow rate of air on collector efficiency

Figure (15) shows this effect, which shows that its collector efficiency does not depend primarily on solar radiation but depends on the dimensions of the collector.

$$\eta_{coll} = (\dot{m} * c_p * \Delta T_{1-2}) / (q * A_{coll}) \quad (29)$$

This conclusion is based on equation (29) which shows that the relationship between the collector efficiency and its area is inverse relationship. As mentioned earlier from equation (20), the increasing area of the collector reduces the heat gained.

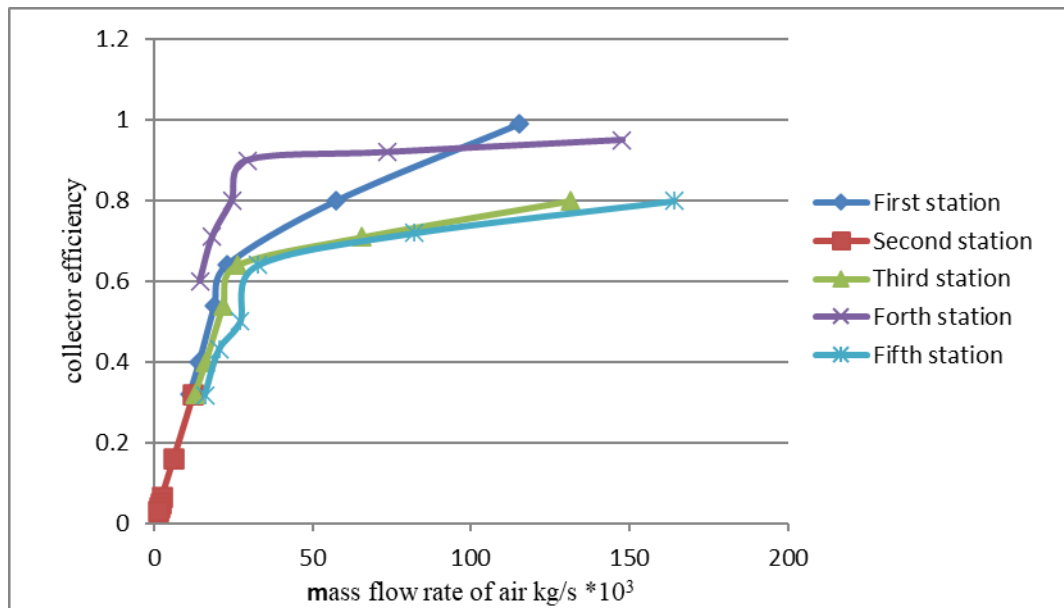


Figure (15) Effect of mass flow rate on collector efficiency with no losses of solar radiation

This theoretical simulation, to evaluate the performance of solar chimney power plants, examined the relationship between the power and the temperature across the collector, the relationship between the mass flow rate and the pressure ratio.

Current results indicate that the optimum pressure ratio x , as mentioned earlier, is not actually equal to $2/3$ and its value is not constant at all hours of the day, which is given theoretically $2/3$ at optimum power output and under continuous driving pressure [1]. However, in the case of instability, the value of x depends on the solar radiation and station size, which effect on the output power.

The paper also presented a simple mathematical model to calculate the dimension of the plant through knowledge of the output power. This calculation predicts the dimensions of five stations at ambient temperature of 318K and the maximum solar radiation of 1046 W / m^2 , selected here in mid-July at 12:00 noon and recorded the results in table (3).

To improve this model, a simple mathematical model was used for the solar power plant. Therefore that concluded that the mathematical model presented in current paper is appropriate to improve a particular station while changing the operating conditions of the entire system.

Table (3): the main parameters of five stations in Aswan taken stations at 318K and the maximum solar radiation of 1046 W / m^2

| Parameters | First station | Second station | Third station | Forth station | Fifth station |
|-----------------------|---------------|----------------|---------------|---------------|---------------|
| Output power (kW) | 100 | 150 | 200 | 250 | 300 |
| h_{coll} (m) | 1.53 | 1.34 | 1.24 | 1.25 | 1.26 |
| d_{coll} (m) | 237.72 | 246.07 | 254.14 | 269.55 | 284.13 |
| h_{ch} (m) | 175.11 | 243.7 | 303.20 | 335.96 | 362.05 |
| d_{ch} (m) | 11.73 | 14.36 | 16.59 | 18.5 | 20.31 |

4. Conclusions

This paper used a numerical model to predict the dimensions of different solar chimney stations. Such model provided a good agreement with the experimental plant. Of the above results, some important points in design should be taken:

- 1- The intensity of solar radiation is variable, so the assumption that the flow is steady is used only to calculate the total solar effect on station dimensions.
- 2- In the chimneys, the flow is incompressible, and as a result the buoyancy forces increase as well as the velocity of the airflow, neglecting the loss of friction inside the chimney.

- 3- The heat transfer equation is applied to the collector only, because the area of the collector is larger than the chimney area
- 4- The efficiency of turbines was taken from 80% or higher.
- 5- The heat transfer from the ambient to the collector is considered and calculated, however, the heat transfer from the system to the ambient is ignored.
- 6- As a result of problems arising from the cost, restrictions usually arise in the application for example high chimneys cannot be more than about 1000 m.
- 7- The values of the main geometrical parameters resulting for the five stations (d_{coll} , d_{ch} and h_{ch}) differ from one to the other according to the output power change. But h_{coll} value at all stations is approximately 1.5 meters.
- 8- When the output power exceeds 150 kW, the optimum ratio between the collector diameter and chimney device is less than 0.8.
- 9- The resulting parameters may vary in the optimization process; however, when power output is greater than 100 kW, each parameter is usually required to be within a reasonable range as follows:
 $d_{coll} > 200 \text{ m}$, $h_{ch} > 170 \text{ m}$, $d_{ch} > 11 \text{ m}$

References

- [1] Haaf W, Friedrich K, Mayr G, Schlaich: J. Solar chimneys: part I, principle and construction of the pilot plant in Manzanares, Int J Sol Energy; 2:3-20. (1983). <http://dx.doi.org/10.1080/01425918308909911>.
- [2] Haaf W: Solar chimneys, part II, preliminary test results from the Manzanares plant. Int J Sol Energy; 2:141-61.(1984) <http://dx.doi.org/10.1080/01425918408909921>.
- [3] El-sebaai, A.A., F.S. AL-H azmi, A.A. AL-Ghamdi and S.J. Yahmour: Global, direct and diffuse solar radiation on horizontal and tilted surfaces in Jeddah, Saudi Arabia ,Appl. Energy, 87(2):568-76 (2010)
- [4] Notton, G., C. Cristofari, M. Muselli and P. Poggi: Calculation on an hourly basis of solar Diffuse irradiances from global data for horizontal surfaces, In Ajaccio Energy conversion and management 45:2849-2866 (2004)
- [5] Information on <http://www.Cablizer.com>
- [6] Von Backström TW, Gannon AJ: The solar chimney air standard thermodynamic cycle. SAIMEchE R&D J; 16(1):16-24(2000)
- [7] Nizetic S, Ninic N, Klarin B: Analysis and feasibility of implementing solar chimney power plants in the Mediterranean region. Energy; 33(11): 1680-90 (2008).
- [8] A. Koonsrisuk, T. Chitsomboon: Mathematical modeling of solar chimney power plant, Int. J. Energy Res. 51, 341-322(2013) <http://dx.doi.org/10.1016/j.energy.2012.10.038>.
- [9] Mullett, L.B.: The solar chimney-overall efficiency, design and performance. Int. J. Ambient Energy 8, 35–40 (1987)
- [10] Schlaich, J., Bergemann, R., Schiel, W., Weinrebe, G: Design of Commercial solar updraft tower systems-utilization of solar induced convective flows for power generation. J. Sol. Energy Eng. 127, 117–124 (2005)
- [11] Zhou, X.P., Yang, J.K., Xiao, B., Hou, G.X.: Simulation of pilot solar chimney power equipment, Renew. Energy 32, 1637–1644 (2007)
- [12] Zhou, X.P., Yang, J.K., Xiao, B., Hou, G.X., Xing, F.: Analysis of chimney height for solar chimney power plant. Appl. Therm. Eng. 29, 178–185 (2009)
- [13] Maia, C.B., Ferreira, A.G., Valle, R.M., Cortez, M.F.B.: Theoretical evaluation of the influence of geometric parameters and materials on the behavior of the airflow in a solar chimney. Compute. Fluids 38, 625–636 (2009)

- [14] Hamdan, M.O.: Analysis of solar chimney power plant utilizing chimney discrete model. *Renew. Energy* 56, 50–54 (2013)
- [15] Koonsrisuk, A., Chitsomboon, T.: Effects of flow area changes on the potential of solar chimney power plants. *Energy* 51, 400–406 (2013)
- [16] Pretorius, J.P., Kröger, D.G.: Solar chimney power plant performance. *J. Sol. Energy Eng.* 128, 302–311 (2006).
- [17] Dehghani, S., Mohammadi, A.H.: Optimum dimension of geometric parameters of solar chimney power plants - a multi-objective optimization approach. *Sol. Energy* 105, 603–612 (2014).
- [18] Gholamalizadeh, E.; Kim, M.-H. Three-dimensional CFD analysis for simulating the greenhouse effect in solar chimney power plants using a two-band radiation model. *Renew. Energy* 63, 498–506 (2014).
- [19] Sangi, R.: Performance evaluation of solar chimney power plants in Iran. *Renew. Sust. Energy Rev.* 16, 704–710 (2012).
- [20] Gholamalizadeh, E., Mansouri, S.H.: A comprehensive approach to design and improve a solar chimney power plant: a special case – Kerman project. *Appl. Energy* 102, 975–982 (2013).
- [21] Pretorius, J.P., Kroger, D.G.: Thermo economic optimization of a solar chimney power plant. *J. Sol. Energy Eng.* 130, 021015 (2008).
- [22] Ming, T.Z., Wang, X.J., de Richter, R.K., Liu, W., Wu, T.H., Pan, Y.: Numerical analysis on the influence of ambient crosswind on the performance of solar updraft power plant system. *Renew. Sustain. Energy Rev.* 16, 5567–5583 (2012).
- [23] Guo, P.H., Li, J.Y., Wang, Y., Liu, Y.W.: Numerical analysis of the optimal turbine pressure drop ratio in a solar chimney power plant. *Sol. Energy* 98, 42–48 (2013).
- [24] Guo, P.H., Li, J.Y., Wang, Y., Liu, Y.W.: Numerical study on the performance of a solar chimney power plant. *Energy Convers. Manage.* 105, 197–205 (2015).
- [25] Kasaeian, A., Ghalamchi, M., Ghalamchi, M.: Simulation and optimization of geometric parameters of a solar chimney in Tehran. *Energy Convers. Manage.* 83, 28–34 (2014).
- [26] Sakonidou, E.P.; Karapantsios, T.D.; Balouktsis, A.I.; Chassapis, D.: Modeling of The optimum tilt of a solar chimney for maximum air flow. *Sol. Energy* 82, 80–94 (2008).
- [27] Padki, M.M.; Sherif, S.A. On a simple analytical model for solar chimneys. *Int. J. Energy Res.* 23, 345–349 (1999).
- [28] Okoye, C.O.; Atikol, U. A: parametric study on the feasibility of solar chimney power plants in North Cyprus conditions. *Energy Convers. Manag.* 80, 178–187(2014).
- [29] Tingzhen, M.; Wei, L.; Guoliang, X. Analytical and numerical investigation of the solar chimney power plant systems. *Int. J. Energy Res.* 30, 861–873 (2006)
- [30] Pastohr, H.; Kornadt, O.; Gürlebeck, K.: Numerical and analytical calculations of the temperature and flow field in the upwind power plant. *Int. J. Energy Res.* 28, 495– 510 (2004).

Nomenclature

Abbreviation

P = output power (kW)
 \dot{m} = mass flow rate of air (kg/s)
 q = Global solar radiation (W/m^2)
 I = heat transfer intensity (W/m^2)
 T = temperature (K)
 p = pressure (Pa)
 U = collector losses coefficient ($W/m^2 \cdot K$)

V =velocity of air (m/s)

C_p =specific heat capacity at constant pressure J/ (kg .K)

X =pressure ratio

d=diameter (m)

h =height (m)

A =area (m²)

G = gravitational force (m/s²)

R= ideal gas constant (J / kg. K)

Subscript

coll =collector

ch =chimney

tur = turbine

T =with turbine

noT=with no turbine

1 =ambient condition

2, 3, 4 =location condition

g =generator

tot =total

dyn =dynamic

max= maximum value

cal = calculated

ele = electric

g = generator

Greek symbols

ρ =density of air (kg/m³)

α =collector absorption coefficient

η = efficiency

Δ =difference, drop

γ=thermal conductivity (W/m.K)

π = pi (3.14)

Acronym

SCPP =solar chimney power plant

29-NiCo alloy/carbon nanofibers composite as effective non-precious electrocatalyst for PEMFCs and hydrogen production

Nasser A. M. Barakat^{1,*}, Wael Abdelmoaez¹ and Marwa M. Abdelati¹

¹Chemical Engineering Department, Minia University, El-Minia, Egypt

nasbarakat@mina.edu.eg (N.A.M. Barakat)

Abstract

The successful commercialization of the proton exchange membrane fuel cells (PEMFCs) is quite dependent on the cost, activity and durability of the electrocatalysts. Alloy structure generates special characteristics for the nano-metallic compounds which makes this interesting class of materials promising candidates for many application fields. Moreover, the performance of the nanostructural catalysts is strongly influenced by the morphology; nanofibers reveal distinct catalytic activity compared to the nanoparticles. Because of its surface oxidation properties, nickel reveals good performance as an electrocatalyst. Many materials involving nickel as a component in their manufacture could be used as catalysts in fuel cells. Accordingly, Ni-based alloys were investigated; NiCu, NiCr and NiMn. Although, among the transition metals, cobalt has a well-known catalytic activity in many chemical reactions, it was not used as a main catalyst in the PEMFCs due to the low performance. As it is considered a chemical reaction/adsorption combination process, carbon was invoked as a support for many functional materials. In this study, novel nanofiber composite from Ni_xCo_{1-x} alloy nanoparticles incorporated in carbon nanofibers are investigated as electrocatalysts for oxidation of the most popularly used fuels in the PEMFCs; methanol urea and ethanol.

PEMFCs, Nanofibers, Electrode, Electropisnning, Alcohol electrolysis

5 Introduction

Expected depletion of the fossil fuels provides the fuel cells great attentions as promised candidates for energy producing devices. Among the introduced cells, direct alcohol fuel cells (DAFCs) have received much attention during the last decade because the alcohols are inexpensive, readily available, and easily stored and transported liquid fuels [1, 2]. DAFCs do not have many of the fuel storage problems typical of some fuel cells because the alcohols have a higher energy density than hydrogen—though less than gasoline or diesel fuel. The successful commercialization of the fuel cells is quite dependent on the cost, activity and durability of the electrocatalysts [3, 4]. Alloy structure generates special characteristics for the nano-metallic compounds which makes this interesting class of materials promising candidates for many application fields. Moreover, the performance of the nanostructural catalysts is strongly influenced by the morphology; nanofibers reveal distinct catalytic activity compared to the nanoparticles. Because of its surface oxidation properties, nickel reveals good performance as an electrocatalyst. Many materials involving nickel as a component in their manufacture could be used as

catalysts in fuel cells [5-7]. Accordingly, Ni-based alloys were investigated; NiCu, NiCr and NiMn [8-10]. Although, among the transition metals, cobalt has a well-known catalytic activity in many chemical reactions, it was not used as a main catalyst in the direct alcohols fuel cells (DAFCs) due to the low performance [11]. As it is considered a chemical reaction/adsorption combination process, carbon was invoked as a support for many functional materials. In this study, novel nanofiber composite from $\text{Ni}_x\text{Co}_{1-x}$ ($x = 0.0, 0.1, 0.3, 0.5, 0.7, 0.9$ and 1.0) alloy nanoparticles incorporated in carbon nanofibers are investigated as electrocatalysts for methanol and ethanol oxidation.

6 Methods

Cobalt (II) acetate tetra-hydrate (CoAc) and nickel (II) acetate tetrahydrate (NiAc) aqueous solutions were first prepared and then mixed with poly(vinyl alcohol) (PVA) aqueous solution (10 wt %). Several solutions were prepared to study the effect of composition of the metallic counterpart; typically, the composition of the solutions was adapted to produce nanofibers having $\text{Ni}_x\text{Co}_{1-x}$ where $x = 0.0, 0.1, 0.3, 0.5, 0.7, 0.9$ and 1.0 . Generally, the polymer content in the final solutions was 7.5 wt%; this polymer content reveals the optimum viscosity for the electrospinning process. The solutions were vigorously stirred at 50 °C for 5 h. The electrospinning process has been carried out under DC voltage of 20 kV. The formed nanofiber mats were initially dried for 24 h at 80 °C under vacuum, and then calcined at 800 °C for 5 h in argon atmosphere with a heating rate of 2.3 °C/min.

7 Results and discussion

Interestingly, due to the polycondensation characteristics of the utilized metal precursors, calcination of the prepared electrospun nanofiber mats did not affect the nanofibrous morphology for all formulations. As example, Fig. 1 displays the FE SEM images for the nanofibers obtained after calcination of $\text{Ni}_{0.5}\text{Co}_{0.5}$, as shown good morphology nanofibers were obtained.

Figure 2 shows the XRD analysis results for three formulations of the sintered nanofibers. The strong diffraction peaks indicate the formation of both cobalt and nickel metals with FCC crystal structure.

Fig. 3 shows the electrocatalytic activity of the proposed nanofiber composites toward methanol and ethanol. As shown, a strong influence for the cobalt content on the electrocatalytic activity of the proposed nanofibers toward both of methanol and ethanol can be observed. Moreover, addition of cobalt does not only affect the produced current, but it also impacts the electrooxidation onset potentials of the two alcohols as shown in the figures.

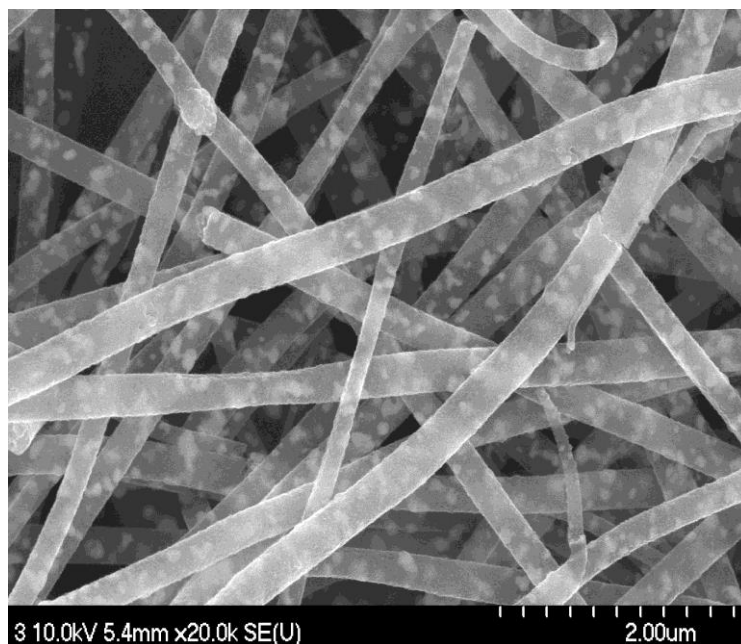


Fig. 1 FE SEM image for the Ni_{0.5}Co_{0.5} sample

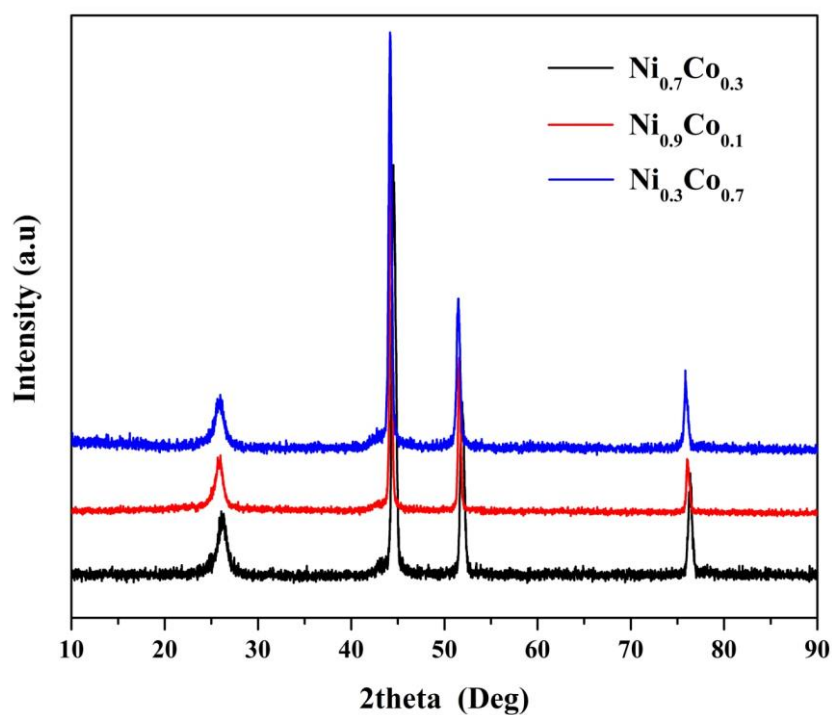


Fig. 2 XRD spectra for three prepared samples after calcination; Ni_{0.7}Co_{0.3}, Ni_{0.9}Co_{0.1} and Ni_{0.3}Co_{0.7}.

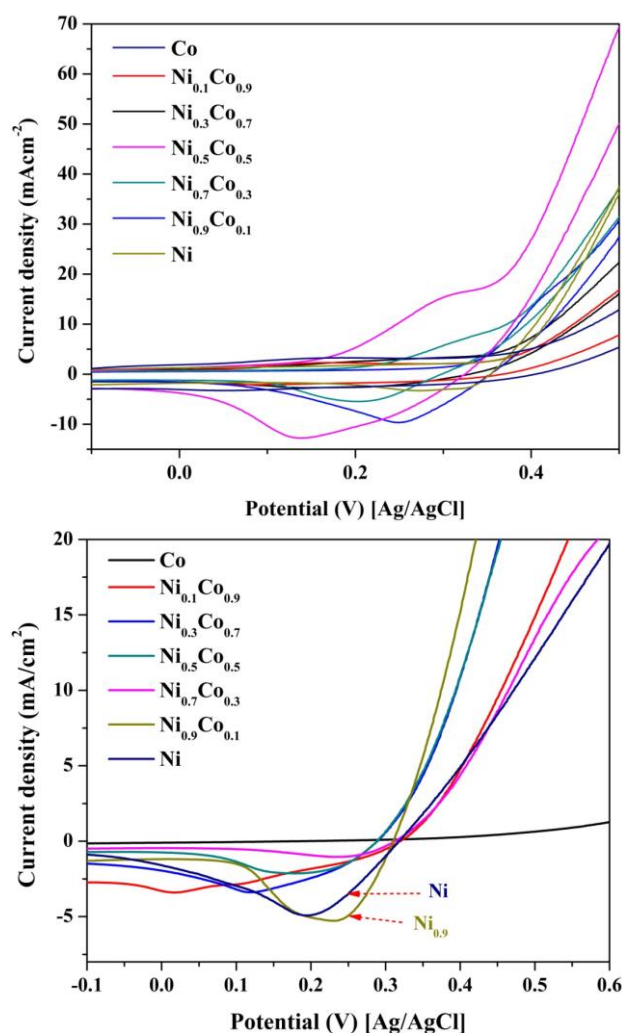


Fig. 3 Electrocatalytic activities of the prepared nanofiber composites toward methanol and ethanol.

8 Conclusions

Exploiting the abnormal thermal decomposition of nickel and cobalt acetates in the inert atmosphere can be utilized to produce nickel/cobalt alloy nanoparticles incorporated in carbon nanofibers. Briefly, calcination of electrospun nanofibers composed of nickel acetate tetrahydrate, cobalt acetate tetrahydrate and poly(vinyl alcohol) in argon atmosphere at 800 °C leads to produce metallic alloy-doped carbon nanofibers. Composition of the metallic counterpart strongly affects the electrocatalytic activity of the synthesized nanofibers toward methanol oxidation. The nanofibrous morphology and the supporting on carbon matrix have also considerable influences on the electrocatalytic activity. Therefore, it can be concluded that carbon nanofibers having Ni_{0.5}Co_{0.5} alloy nanoparticles are the optimum electrocatalyst due to the corresponding high current density and low onset potential. Overall, it can be claimed that the metallic alloys nanoparticles-doped carbon nanofibers might be new promised non precious electrocatalysts for fuel cells applications.

5. References

- [1] J. Prakash, D.A. Tryk, E.B. Yeager, Kinetic investigations of oxygen reduction and evolution reactions on lead ruthenate catalysts, *JOURNAL-ELECTROCHEMICAL SOCIETY*, 146 (1999) 4145-4151.
- [2] N.A. Barakat, M.A. Abdelkareem, A. Yousef, S.S. Al-Deyab, M. El-Newehy, H.Y. Kim, Cadmium-doped cobalt/carbon nanoparticles as novel nonprecious electrocatalyst for methanol oxidation, *Int. J. Hydrogen Energy*, 38 (2013) 183-195.
- [3] J. Shen, Y. Hu, C. Li, C. Qin, M. Ye, Pt–Co supported on single-walled carbon nanotubes as an anode catalyst for direct methanol fuel cells, *Electrochim. Acta*, 53 (2008) 7276-7280.
- [4] Y. Shao, J. Sui, G. Yin, Y. Gao, Nitrogen-doped carbon nanostructures and their composites as catalytic materials for proton exchange membrane fuel cell, *Appl. Catal., B*, 79 (2008) 89-99.
- [5] A. Rahim, R. Abdel Hameed, M. Khalil, Nickel as a catalyst for the electro-oxidation of methanol in alkaline medium, *J. Power Sources*, 134 (2004) 160-169.
- [6] C. Fan, D. Piron, A. Sleb, P. Paradis, Study of Electrodeposited Nickel-Molybdenum, Nickel-Tungsten, Cobalt-Molybdenum, and Cobalt-Tungsten as Hydrogen Electrodes in Alkaline Water Electrolysis, *J. Electrochem. Soc.*, 141 (1994) 382-387.
- [7] I.A. Raj, K. Vasu, Transition metal-based hydrogen electrodes in alkaline solution—electrocatalysis on nickel based binary alloy coatings, *J. Appl. Electrochem.*, 20 (1990) 32-38.
- [8] J.M. Marioli, P.F. Luo, T. Kuwana, Nickel—chromium alloy electrode as a carbohydrate detector for liquid chromatography, *Anal. Chim. Acta*, 282 (1993) 571-580.
- [9] J.M. Marioli, T. Kuwana, Electrochemical detection of carbohydrates at nickel-copper and nickel-chromium-iron alloy electrodes, *Electroanalysis*, 5 (1993) 11-15.
- [10] I. Danaee, M. Jafarian, A. Mirzapoor, F. Gobal, M. Mahjani, Electrooxidation of methanol on NiMn alloy modified graphite electrode, *Electrochim. Acta*, 55 (2010) 2093-2100.
- [11] N.A.M. Barakat, M.A. Abdelkareem, H.Y. Kim, Ethanol electro-oxidation using cadmium-doped cobalt/carbon nanoparticles as novel non precious electrocatalyst, *Applied Catalysis A: General*, 455 (2013) 193-198.

30-Theoretical study of influence of the geometric parameters on the performance of Solar Chimney Power Plants

I. MOUSA^{1*}, T. Mekhail¹, M. Sadik¹, M. Shaban¹

¹ Mechanical Power Engineering, Faculty of Energy Engineering, Aswan University,
Egypt

*email: islammohammed@energy.aswu.edu.eg

Keywords: Solar chimney, Solar collector, Geometric parameters, SCPP

Abstract

The Solar Chimney Power Plant (SCPP) is a new technology for utilizing the free solar energy to generate electrical power, which needs to be investigated to enhance the performance. It consists of three simple components, chimney, collector and turbine. The objective of this study is to evaluate the performance of Solar Chimney Power Plants affected by varying the geometric parameters, such as chimney height, chimney diameter, collector diameter, and collector height. The geometric parameters are modeled theoretically, and an iterative technique is carried out to solve the performed mathematical model. The basic dimensions used in the model that the variable dimensions referred to them are for the Solar Chimney Power Plant installed in Aswan (Egypt). The study showed that the generated power increases considerably with the increase of the chimney height and slightly with the increase of the collector diameter. Thus, the same generated power can be obtained with different combinations of collector diameter and chimney height. Furthermore, the output power has a negative relationship with the collector height. In addition, the results found that the chimney diameter has an optimum range for the maximum output power. The Optimal geometric can be determined only by including the cost of the individual components (chimney, collector and mechanical parts) at a particular site.

1. Introduction

The rapid depletion of conventional energy resources and increasing energy demand in Egypt stimulated the need to consider renewable energy as an alternative to imported power. The solar chimney power plant (SCPP) is a clean power generation technology utilizing the concept of converting the solar energy to power generation, the typical one consists of a solar collector, a chimney and a turbine. The solar collector is a relatively horizontal roof made from a transparent material, elevated above the ground and opened at its periphery. The chimney is supported exactly at the center of the collector and at the base of the chimney, and inside the collector, there is the location of the turbine or the generator (see Fig. 1). A large amount of hot air is produced when the solar radiation lands on the collector roof, rises the chimney, due to the air density difference between the chimney base and the surroundings. The rising air is used to drive the installed turbine at the chimney base to generate electricity. The first (SCPP) prototype was installed in Manzanares (Spain), designed by Schlaich, who is the first to propose solar chimney as a means to harness energy from the sun [1].

Even though the technology is quite simple, considerable insights concerning many aspects are required before designing the plant for optimal performance. Two of these aspects

are the effects of geometric parameters and the solar radiation on the plant performance, and they have been examined by several researchers. The study of Haaf et al. showed that an increase in the collector diameter increased output power but reduced plant efficiency [2]. On the other hand, efficiency increased with the tower height, and mass flow rate increased with the chimney diameter while the flow velocity remained constant. Pasumarthi and Sherif reported that increase of chimney height resulted in higher velocity and mass flow rate; and when the solar radiation was fixed, an increase in the mass flow rate was accompanied by a lower air temperature at the collector outlet [3]. Chitsomboon (2000) found that the plant efficiency was invariant with respect to the insolation, the size of the collector cover and the tower diameter. He also found that the functional relationships between the generated power and the efficiency with the tower height were linear [4]. Dai et al. (2003) demonstrated that the generated power increased nonlinearly with the size of the plant, rapidly when the size was small and at a slower rate when the size was larger [5].

This study presents a Theoretical model that can predict how the power output of a solar chimney power plant may be affected by varying the geometrical dimensions, basically chimney height, chimney diameter, collector height, and collector diameter. The basic dimensions used in the model that the variable dimensions referred to them are for the Solar Chimney Power Plant installed in Aswan (Egypt).

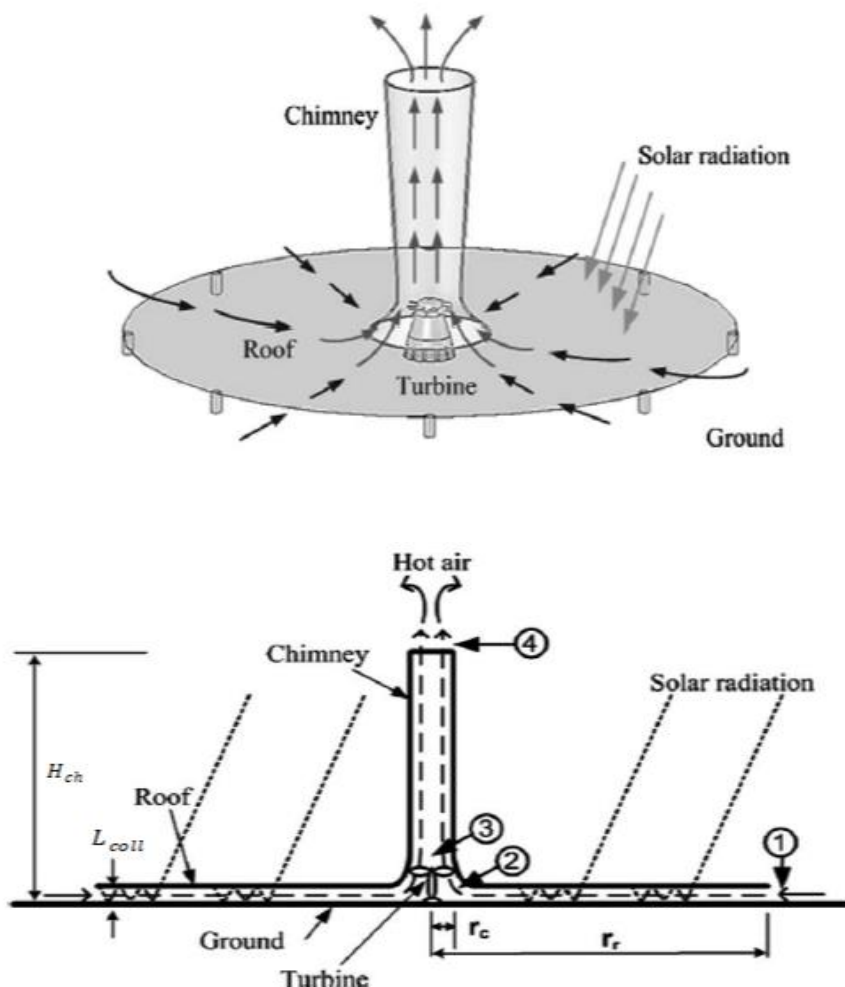


Fig. 1. Schematic layout of the solar chimney power plant [6].

2. Mathematical modeling

The Schematic diagram of the solar chimney power plant is presented in Fig.1. A mathematical model has been developed to predict the performance of the solar chimney thermal power generating equipment for different geometric parameters, which including the major components, the solar collector, the chimney and the wind turbine. The mathematical model is developed by using (MAT LAP) software code and an iterative technique is carried out to solve the performed mathematical model. The following assumptions are made:

1. Air is an incompressible fluid and follows the ideal gas law.
2. A steady state condition and one-dimensional flow.
3. There is no leakage or friction considered in the system and only the buoyancy force is considered in the chimney.

2.1. The mathematical model of the collector

The incident solar radiation on the collector glass S is given by:

$$S = I \alpha \tau \quad (1)$$

Where I is the solar incidence on the collector cover, α is the glass absorptivity and τ is the glass transmittance. To evaluate collector performance, it is necessary to know the heat transfer Coefficients in the collector as shown in Fig. 2.

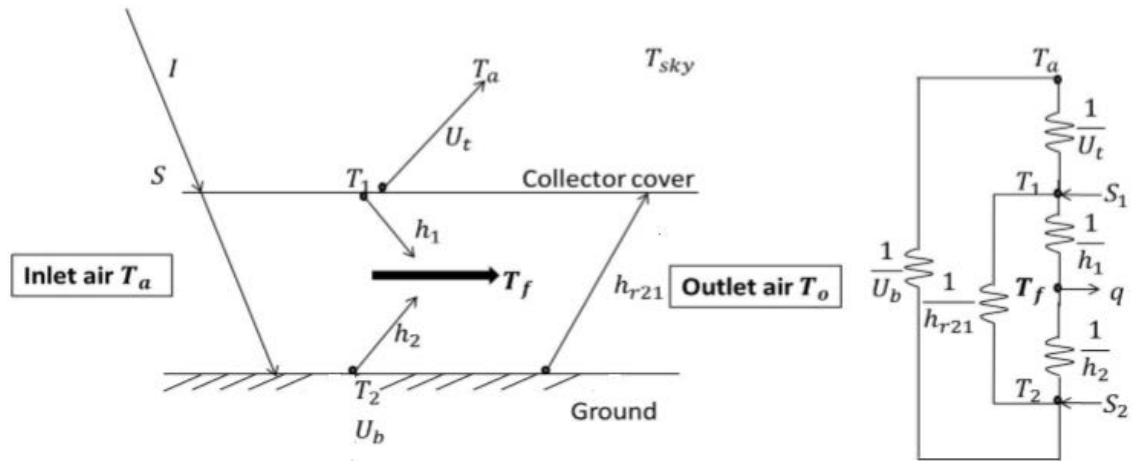


Fig. 2. Airflow, energy interactions, and equivalent thermal resistance in the collector [7].

The overall heat loss coefficient for the top of the collector U_t , is a result of convection and radiation phenomena [8]:

$$U_t = h_{rs} + h_w \quad (2)$$

The convective heat transfer due to the wind blowing over the glass h_w and the radiation heat transfer coefficient between the collector cover h_{rs} and the sky are as follows [3, 9]:

$$h_w = 5.67 + 3.86(V) \quad (3)$$

$$h_{rs} = \sigma \epsilon_1 (T_1 + T_2) (T_1^2 + T_2^2) \left(\frac{T_1 - T_{sky}}{T_1 - T_a} \right) \quad (4)$$

Where T_2 is the ground temperature and T_1 is the collector cover temperature, V is the local wind speed, ε_1 and is the emissivity of the collector cover, T_a is the ambient air temperature and T_{sky} is the sky temperature expressed as:

$$T_{sky} = 0.552(T_a)^{1.5} \quad (5)$$

The radiation heat transfer coefficient between the glass and the ground can be estimated by [10]:

$$h_{r21} = \frac{\sigma \varepsilon_1 (T_1 + T_2)(T_1^2 + T_2^2)}{\frac{1}{\varepsilon_1} + \frac{1}{\varepsilon_2} - 1} \quad (6)$$

Where ε_2 is the emissivity of the ground, The free convection heat transfer coefficient between the collector glass and the air flow h_1 can be expressed as [11]:

$$h_1 = N_u \frac{k}{L_c} \quad (7)$$

Where N_u is the Nusselt number, k is the thermal conductivity of the air and L_c is the characteristic length. For an approximately uniform heat flux condition, the Nusselt number which is valid for large Rayleigh numbers [12]:

$$N_u = 0.14(R_a)^{1/3} \quad \text{for} \quad R_a < 2 \times 10^8 \quad (8)$$

Where R_a is the Rayleigh number and can be evaluated as a product of the Prandtl P_r and the Grashof numbers G_r :

$$R_a = G_r P_r = \frac{g \beta (\Delta T_{c-f}) L_c^3}{\nu^2} P_r \quad (9)$$

Where ΔT_{c-f} is the temperature difference between the collector glass and the air flow, g is the gravitational acceleration, β is the volumetric thermal expansion coefficient of the air. Similarly, the free convection heat transfer coefficient between the ground and the air flow h_2 can be expressed as [11, 13]:

$$h_2 = N_u \frac{k}{L_c} \quad (10)$$

Where the Nusselt number for a heated isothermal surface facing upward and a cold surface facing downward can be expressed as [14]:

$$N_u = 0.54(R_a)^{1/4} \quad \text{for} \quad 2 \times 10^4 < R_a < 8 \times 10^4 \quad (11)$$

$$N_u = 0.15(R_a)^{1/3} \quad \text{for} \quad 8 \times 10^4 < R_a < 8 \times 10^6 \quad (12)$$

$$R_a = G_r P_r = \frac{g \beta (\Delta T_{g-f}) L_c^3}{\nu^2} P_r \quad (13)$$

Where ΔT_{g-f} The temperature difference between the ground and the air flow. Bernardes et al. presented the ground loss coefficient U_b as [13]:

$$U_b = 2 \left(\frac{k \rho c_p}{\pi t} \right)^{0.5} \quad (14)$$

Where ρ the density of the air is c_p is specific heat capacity and t is the hour from the midnight.

The air is modeled as an ideal gas; therefore, the properties of air are only a function of temperature. By using the following empirical equations we can estimate the specific heat capacity

$$c_p = 1002.5 + 27510^{-6}(T - 200)^2 \quad (15)$$

$$\rho = 3.9147 - 0.016082T + 2.9013 \times 10^{-5}T^2 - 1.9407 \times 10^{-8}T^3 \quad (16)$$

$$k = (0.0015215 + 0.097459T + 3.3322 \times 10^{-5} \times T^2)T^{-6} \quad (17)$$

The collector overall loss coefficient U_L , obtained from the equation [8]:

$$U_L = \frac{(U_b + U_t)(h_{r21}h_1 + h_2h_{r21} + h_2h_1) + U_b U_t(h_1 + h_2)}{h_{r21}h_1 + h_2h_{r21} + h_2h_1 + U_t h_2} \quad (18)$$

The collector efficiency factor \hat{F} , the collector heat removal factor F_R and the collector flow factor found respectively from the equations [8],

$$\hat{F} = \frac{h_1 h_{r21} + h_2 U_t + h_2 h_{r21} + h_2 h_1}{(U_t + h_{r21} + h_1)(U_b + h_{r21} + h_2) - h_{r21}^2} \quad (19)$$

$$F_R = \frac{\dot{m} c_p}{A_c U_L} \left[1 - e^{-\left(\frac{A_c U_L \hat{F}}{\dot{m} c_p}\right)} \right] \quad (20)$$

$$\hat{F} = \frac{F_R}{\hat{F}} \quad (21)$$

Where \dot{m} is the mass flow rate of the air and A_c is the collector area. The actual useful energy gain of the hot air in the collector can be calculated by the equation below [8]:

$$Q_u = A_c F_R [S - U_L \Delta T] \quad (22)$$

Where Q_u is actual useful energy and ΔT is the temperature difference between the outlet temperature T_{out} and the inlet temperature T_{in} of the collector assumed to be equal to the ambient temperature. The ground temperature, the collector cover temperature, the mean temperature of the airflow and the collector outlet temperature, will be obtained from Duffie and Beckman, respectively [8]:

$$T_2 = T_{in} + \frac{Q_u}{F_R A_c U_L} (1 - F_R) \quad (23)$$

$$T_1 = \frac{U_t (T_2 - T_a)}{h_{c21} + h_{r21}} \quad (24)$$

$$T_{fm} = T_{in} + \frac{Q_u}{F_R A_c U_L} (1 - \hat{F}) \quad (25)$$

$$T_{fm} = T_{in} + \frac{Q_u}{\dot{m} c_p} \quad (26)$$

The solar collector efficiency can be expressed as a ratio of the heat output of the collector as heated air Q_u and the solar radiation I times A_c .

$$\eta_{coll} = \frac{Q_u}{A_c I} \quad (27)$$

2.2. The Mathematical Model of the Chimney

The chimney converts the heat-flow Q_u product by the solar collector into kinetic energy (convection current) and potential energy (pressure drop at the turbine). Thus, the density difference of the air caused by the temperature rise in the collector works as a driving force. Schlaich et al. estimated the inlet velocity to the chimney V_{ch} and the mass flow rate as follows [1]:

$$V_{ch} = \sqrt{\frac{2 g H_{ch} \Delta T}{T_a}} \quad (28)$$

Where H_{ch} is the chimney height and A_{ch} is the chimney cross-sectional area. The chimney efficiency is given as:

$$\eta_{ch} = \frac{P_{tot}}{Q_u} = \frac{g H_{ch}}{c_p T_a} \quad (29)$$

This simplified representation explains one of the basic characteristics of the solar chimney, which is that the chimney efficiency is fundamentally dependent only on chimney height.

2.3. Turbine model

The axial wind turbine located at the base of the chimney which converts the kinetic energy of the air flow into useful mechanical rotary work. The Efficiency of the turbine can be expressed as [15]:

$$\eta_t = 1 - \frac{V_{ch}^2}{2 c_p \Delta T \eta_{ch}} \quad (30)$$

Turbine electrical power (output power) can be calculated as follows [11]:

$$P_e = Q_u \eta_t \eta_{ge} = A_c I_{ncoll} \eta_{ch} \eta_t \eta_{ge} \quad (31)$$

Where η_t is the turbine efficiency, and η_{ge} is the generator efficiency and they are considered to equal to (0.8) as widely reported in SCPP literature [9, 16]. The total efficiency (plant efficiency) η_{tot} is determined here as a product of the individual component efficiencies:

$$\eta_{tot} = \eta_{coll} \eta_{ch} \eta_t \quad (32)$$

3. Solution procedure

According to the above formulation, at a known or assumed ambient temperature and solar radiation which is a function on time, date and geographical location, then the plant power output can be attained. A flowchart of this procedure is illustrated in Fig. 3.

4. Results and discussion

The parameters investigated in this paper were: collector diameter, chimney height, chimney diameter. The prototypical power plant is the Solar chimney power plant in Aswan – Faculty of Energy Engineering shown in Fig. 4 and has the dimension shown in Table 1. The parameters used in the calculation of the system performance at the constant condition of solar irradiance (900 W/m^2) and ambient temperature (310 K).

Table 1: Dimensions of the modeled power plant

| Parameter | Chimney height | Chimney diameter | Collector diameter | Collector height |
|-----------|----------------|------------------|--------------------|------------------|
| Value | 20m | 1m | 32.218 m | 1.25m |

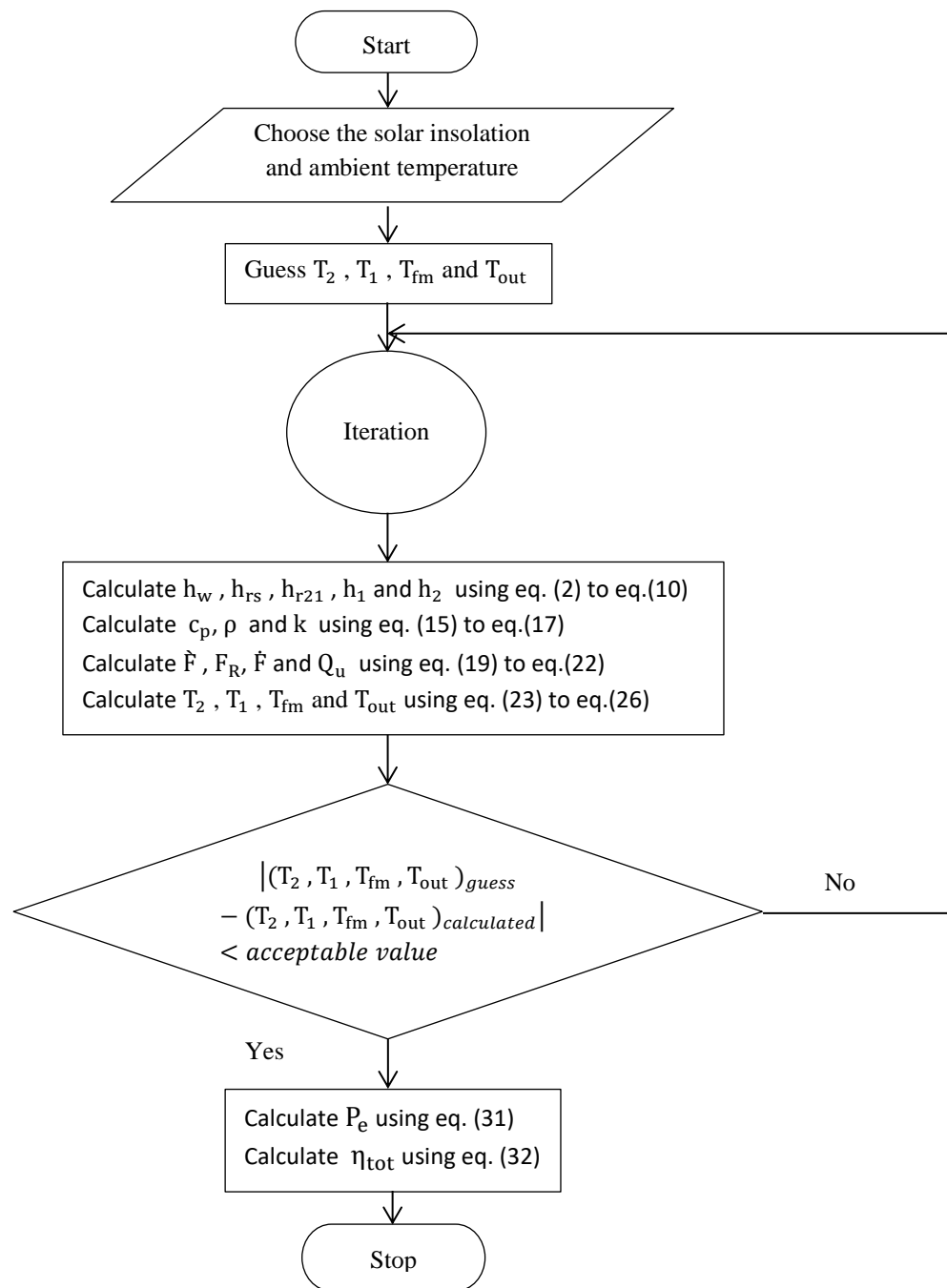


Fig. 3. Flowchart of solution procedures.



Fig. 4. Aswan solar chimney power generation.

The effect of different parameters presented in Figs. 5-10 respectively. The first parameter is chimney height as shown in Fig. 5. That the higher chimney height the greater power output will be. Increasing chimney height means increase in the driving force which is the buoyancy difference led to increasing the velocity and mass flow rate, and that is the flow energy which is needed for the wind turbine. Similar to the variation in the output power, as shown in Fig. 5, efficiency increased from 0.07% at a chimney height of 21m to 0.5% at a chimney height of 150m.

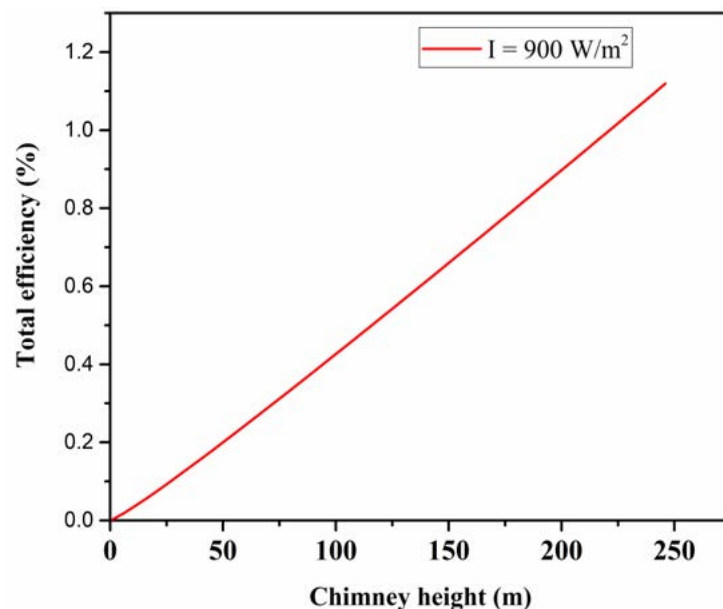
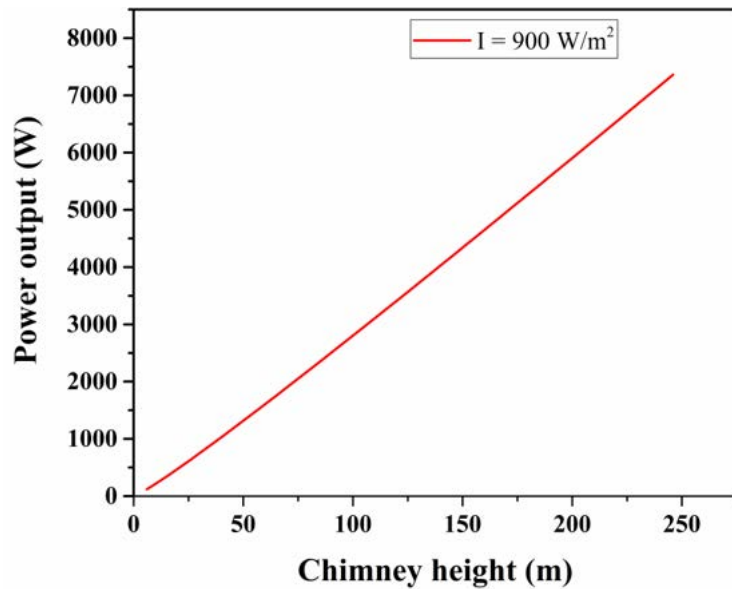


Fig. 5. Influence of chimney height on the solar chimney performance.

It can be seen from Fig. 6 that by increasing the chimney diameter, the air pressure decreases and the velocity and mass flow rate increases. Augmentation in mass flow rate causes increment in output power, but with increasing the chimney diameter to a critical value (5m) causes the mass flow rate through the collector to increase, the temperature rises through the collector decreases led to decreasing in the useful energy gained.

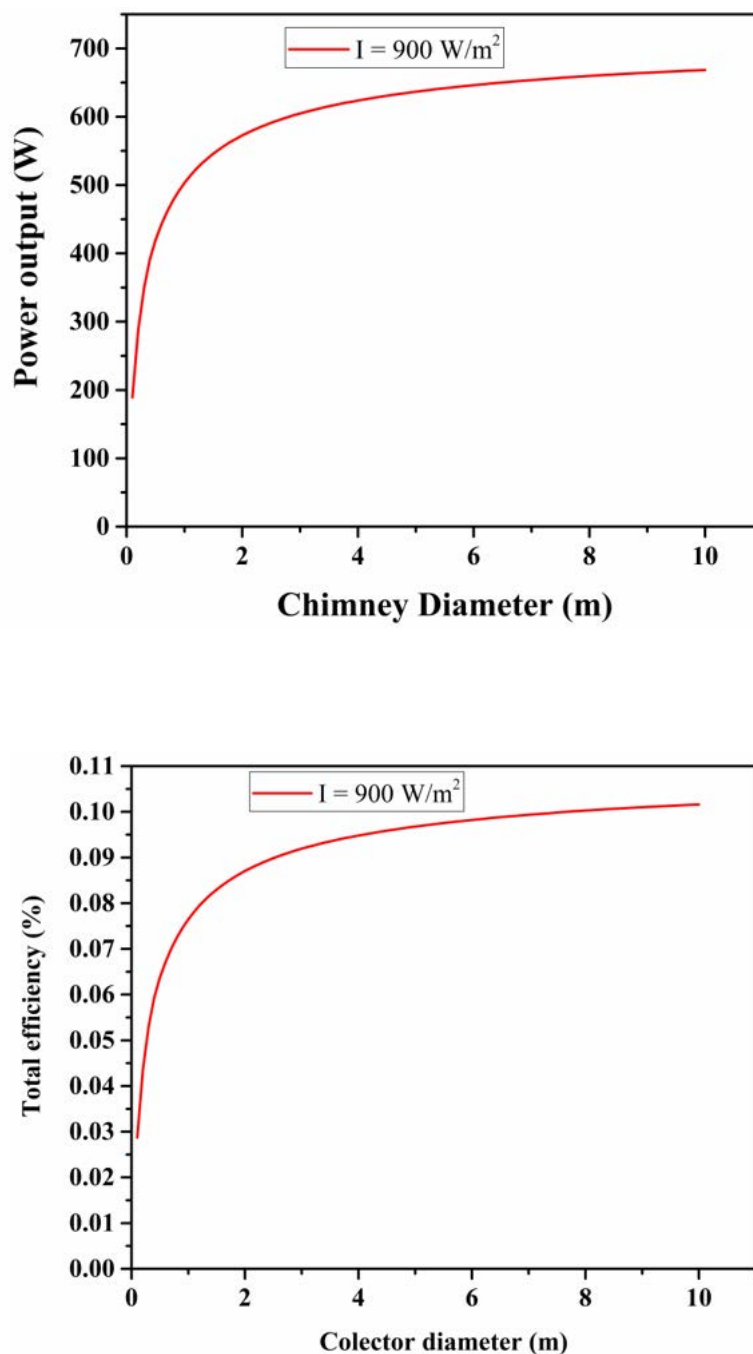


Fig. 6. Effect of chimney diameter on solar chimney plant power output and efficiency.

In Fig. 7, changes of generated power and solar chimney efficiency are indicated where the value of collector diameter varies from 30m to 250 m, which means that flow power would be greater at more values while it is inverted with efficiency. By increasing the collector area, the area of heat transfer increased, which caused the temperature and mass flow to increase but with respect to the constant heat flux, collector efficiency decreased causing to decrease the total efficiency.

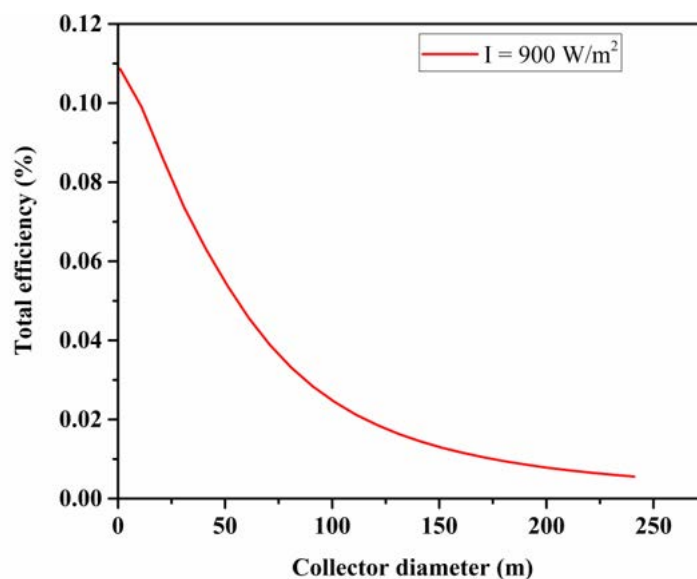
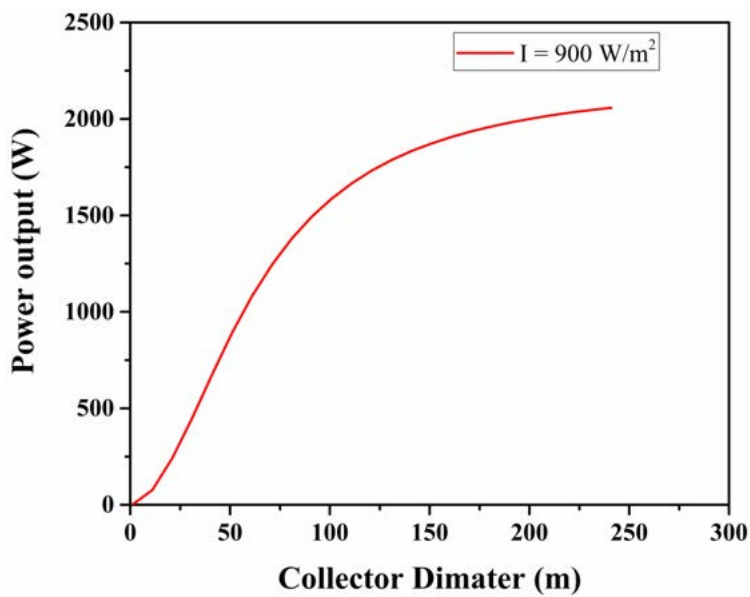


Fig. 5. Effect of the collector diameter on the power generation.

5. Conclusion

The influences of the geometric parameters, mainly the collector diameter, chimney height, and chimney diameter, on solar chimney power plant performance have been studied by using a theoretical model. The capacity of power generation is dependent on the ambient conditions and structural dimensions such as solar insolation, ambient temperature, chimney height, and collector diameter, etc. The results indicated that the power generation from this type of power plant increases with the increase in solar chimney height and solar collector area. The larger the solar collector size and the higher the solar chimney height is, the greater the power will be. By the analysis, it was found that the chimney diameter parameter had an optimum range with maximum values for the efficiency and output power.

References

1. Schlaich, J., *The solar chimney: electricity from the sun*. 1995: Edition Axel Menges.
2. Haaf, W., et al., *Solar chimneys part I: principle and construction of the pilot plant in Manzanares*. International Journal of Solar Energy, 1983. **2**(1): p. 3-20.
3. Pasumarthi, N. and S. Sherif, *Experimental and theoretical performance of a demonstration solar chimney model—Part II: experimental and theoretical results and economic analysis*. International Journal of Energy Research, 1998. **22**(5): p. 443-461.
4. Chitsomboon, T., *Potential and efficiency of solar chimney in the production of electrical energy*. Research and Development Journal of the Engineering Institute of Thailand, 2000. **11**(3): p. 38-44.
5. Dai, Y., H. Huang, and R. Wang, *Case study of solar chimney power plants in Northwestern regions of China*. Renewable Energy, 2003. **28**(8): p. 1295-1304.
6. Koonsrisuk, A. and T. Chitsomboon, *Accuracy of theoretical models in the prediction of solar chimney performance*. Solar Energy, 2009. **83**(10): p. 1764-1771.
7. Okoye, C.O. and O. Taylan, *Performance analysis of a solar chimney power plant for rural areas in Nigeria*. Renewable energy, 2017. **104**: p. 96-108.
8. Duffie, J.A. and W.A. Beckman, *Solar engineering of thermal processes*. 2013: John Wiley & Sons.
9. Larbi, S., A. Bouhdjar, and T. Chergui, *Performance analysis of a solar chimney power plant in the southwestern region of Algeria*. Renewable and Sustainable Energy Reviews, 2010. **14**(1): p. 470-477.
10. Ong, K., *A mathematical model of a solar chimney*. Renewable energy, 2003. **28**(7): p. 1047-1060.
11. Duffie, J.A., W.A. Beckman, and W. Worek, *Solar engineering of thermal processes*. Vol. 3. 2013: Wiley Online Library.
12. Fujii, T. and H. Imura, *Natural-convection heat transfer from a plate with arbitrary inclination*. International Journal of Heat and Mass Transfer, 1972. **15**(4): p. 755-767.
13. Bernardes, M.d.S., A. Voß, and G. Weinrebe, *Thermal and technical analyses of solar chimneys*. Solar Energy, 2003. **75**(6): p. 511-524.
14. McAdams, W.H., *Heat transmission*. 1954.

15. Nizetic, S. and B. Klarin, *A simplified analytical approach for evaluation of the optimal ratio of pressure drop across the turbine in solar chimney power plants*. Applied Energy, 2010. **87**(2): p. 587-591.
16. Nizetic, S., N. Ninic, and B. Klarin, *Analysis and feasibility of implementing solar chimney power plants in the Mediterranean region*. Energy, 2008. **33**(11): p. 1680-1690.

31-Impact of Hydro Energy upon Multi-Area Interconnected Power Systems via Optimal Fuzzy Logic Load Frequency Controllers

Alaaeldin M. Abdelshafy¹, Farag K. Abo-Elyousr², Hamdy HASSAN^{1,3},
Abdelfatah M. Mohamed¹, Jakub Jurasz⁴

1 Energy Resources Eng. Department, Egypt-Japan University of Science and
Technology, Alexandria, Egypt.

2 Elect. Eng. Department, Faculty of Eng., Assiut University, Assiut, Egypt.

2 Mechanical Eng. Department, Faculty of Eng., Assiut University, Assiut, Egypt.

4 Department of Eng. Management, Faculty of Management, AGH University of Science
and Technology, Cracow, Poland.

Abstract: - The main target of this research is to allow hydro energy plants to participate effectively within decentralized thermal power units. In this research, the simulated annealing algorithm for optimal tuning of fuzzy logic load frequency controllers design is introduced. The results are compared with simulated annealing and genetic algorithms optimal tuning of proportional integral (PI) controllers. In order to tune the parameters of the controllers without considering the complexity associated with the power system identification, a time-domain based objective function was formulated. A three-area interconnected power system is investigated under different loading conditions in order to verify the effectiveness of the proposed algorithm. Simulation results show that the developed fuzzy logic controller overweighs the conventional fuzzy and the other PI algorithms in terms of transient and steady state performance.

Keywords: Simulated annealing, fuzzy logic controller, genetic algorithm load frequency control, objective function.

1. Introduction

The main objective of any load frequency control (LFC) is to minimize the transient deviations in the area frequency and the tie-line powers interchanges [1-3]. The deviations between the generation and load demands cause the system frequency to deviate from the nominal value. High Frequency deviations may lead to power system partial or full collapse [2]. Optimal transient response with zero steady state errors of frequency deviations in multi-area interconnected power networks are the main targets of the LFC [4-7].

Among the various algorithms of load frequency controllers are the conventional proportional integral (PI) controllers. Although PI and PID controllers are simple for implementation and can give better dynamic response, however their response deteriorates when the complexity of the system increases due to disturbances such as the boiler load variations dynamics [2,8]. Various intelligent algorithms were implemented to LFC. In [9,10], poles shaping techniques were presented. The sliding mode control is introduced in [11]. The robust control [12,13], and decentralized aspect [14-16] are employed for LFC. Artificial neural networks (NN) and adaptive neuro-fuzzy (ANFIS) were introduced in [2,17-21]. Generally, neural networks are trained by a well-known data. In addition to that, the NN based controllers suffer from the unknown number of hidden layers, neurons, and they require plant identifications and training.

Genetic algorithm is considered one of the pioneering evolutionary algorithms [22]. In [23-25], genetic algorithm can help along the optimization to find an appropriate tune for the PI or PID controller gains. The human brain emotional learning algorithm was introduced in load frequency control within interconnected microgrids [26]. The particle swarm optimization, bacteria foraging, and ant colony were discussed for the LFC [27-32]. The cuckoo search algorithm is treated in LFC in [3,33-36]. Although the cuckoo search algorithm is recommended in [3], however all these algorithms suffer from slow convergence. In addition, they are weak in the local search ability.

On the other hand, the performance of fuzzy logic controllers (FLCs) gives much better response than (PI) controllers [37-39]. Fuzzy logic-based controllers can efficiently enhance the closed loop performance of PI/PID controllers [40,41]. Also, FLCs can handle the changes in the operating conditions or in the system parameters [42]. In other words, FLCs can online update the controller parameters performance. The most outstanding feature of the fuzzy logic technique is that they do not require description or model identification of the control systems [1].

In this paper, the simulated annealing optimization algorithm is used for optimal tuning of the PI and fuzzy-PI logic controller (FLC) gains. Another simulated annealing optimized FLC based on the previous fuzzy-PI rules is proposed and tested in this paper. The proposed simulated annealing optimized fuzzy controller is functionally equivalent the conventional FLC. The system responses results are compared with responses obtained by the conventional PI controller gains optimized by the genetic algorithm.

2. Investigated Power System

The generators constitute a coherent group in each area. From LFC design procedures, the frequency and the tie-line power flow are controlled for each area. Frequency control is done by two control actions in hydro-thermal power system as shown in Fig. 1: primary speed control and secondary control. The primary speed control loop takes the action of the initial frequency changes adjustments through the regulation constant (R). With this action, the various generators share the load variations according to their capacities. The speed of response of each machine depends on the time constants of the turbine, re-heater, and the power system itself. The secondary loop takes into account the fine adjustments of the frequency deviations to zero through a controller. The response of this loop depends on the design of the controller itself.

In the three-area hydro-thermal power system shown in Fig. 1, areas 1 and 2 are reheat thermal power systems. The third area is a hydraulic machine power system [43]. The system data and parameters are given in the Appendix. The area control error (ACE) of each area is considered as a linear combination of frequency and tie-line power errors as in (1)-(3).

$$ACE_1 = \sum \Delta P_{12} + B_1 \Delta f_1 \quad (1)$$

$$ACE_2 = \sum \Delta P_{23} + B_2 \Delta f_2 \quad (2)$$

$$ACE_3 = \sum \Delta P_{31} + B_3 \Delta f_3 \quad (3)$$

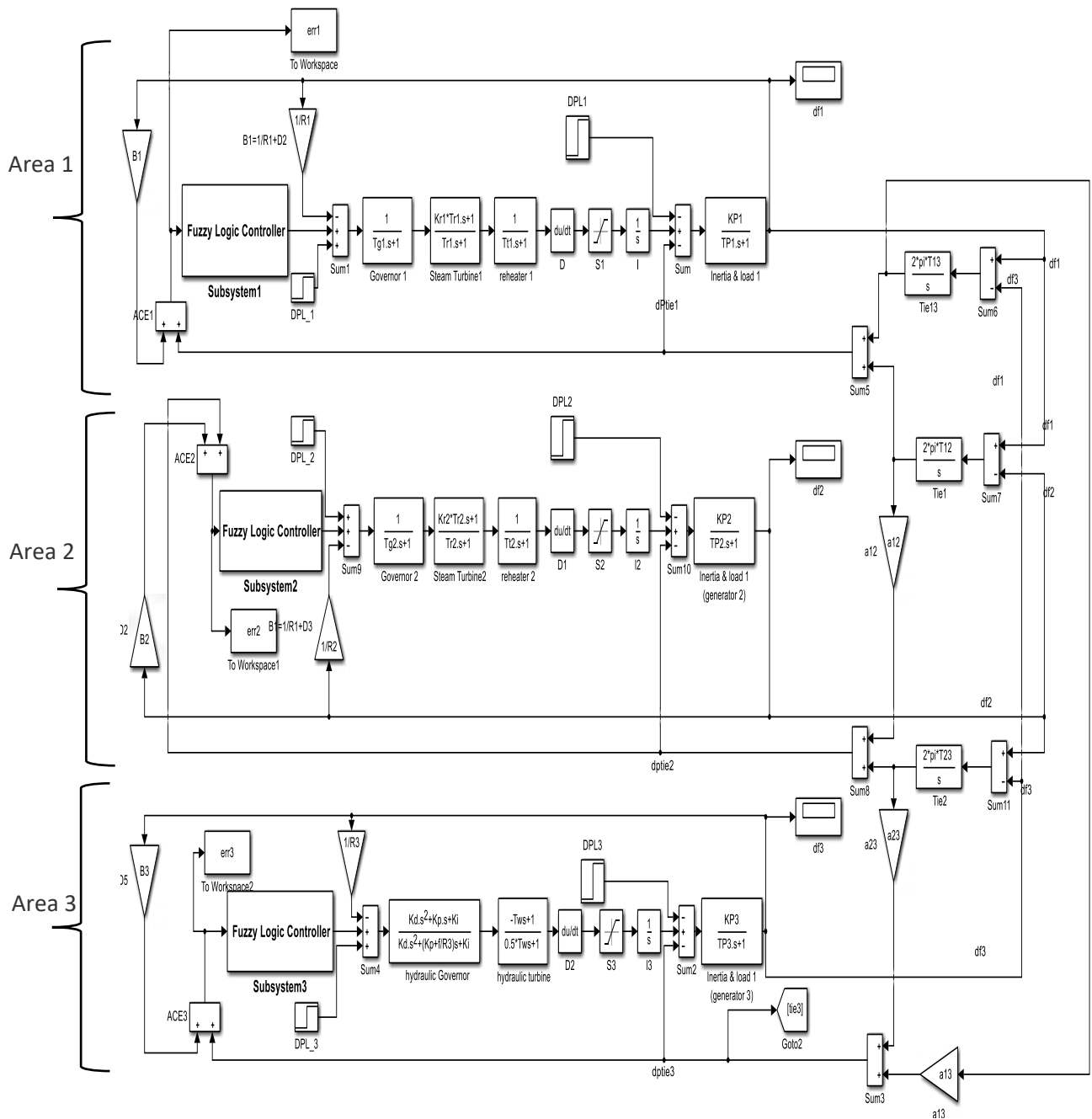


Fig. 1 Matlab/Simulink model of the system under study

Fig. 2 shows a single line diagram of three-area interconnected power system. To design a load frequency controller of each area, fuzzy logic controller approach is utilized. The gains or scaling factors of the fuzzy logic controllers are determined using an optimization technique called simulated annealing. In the next preceding sections, the control methodologies and the optimization problem will be introduced.

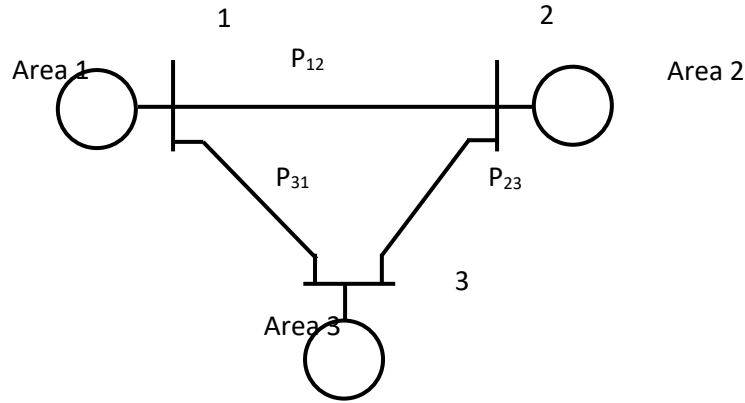


Fig. 2 Schematic diagram of the three-area power system.

3. Optimization Problem

The objective of LFC is to generate a control signal $U(s)$ that can keep the frequency deviations and the tie-line power changes at predetermined values as shown in Fig. 3. The control signal of the i^{th} area signal is defined as in (10).

$$U(s) = -G_i(s) ACE_i(s) \quad (10)$$

Where, $G_i(s)$ is related to the controller output of each area. A time formulated fitness function is defined as the sum of squares in the ACE of all areas as in (11).

$$J = \sum_{i=1}^N \sqrt{\int ACE_i^2 dt} \quad (11)$$

Where, N is the total number of the areas under study. The design procedures are to minimize J by considering the constraints of the optimization problem.

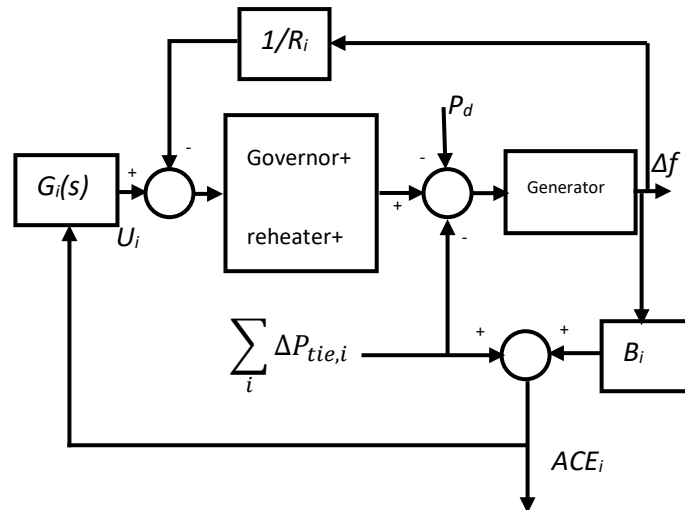


Fig. 3 Block diagram of the i^{th} area

3.1 Fuzzy-PI Logic Control Description

Fuzzy interference systems consist of input block, output block, and their membership functions. The Fuzzy rules are framed according to the frequency deviations requirements. Normalized values of two inputs: ACE deviation and the changes in the ACE deviations are considered. Normally, Fuzzy logic systems include three process: normalization, fuzzification, and defuzzification. The output is obtained by using the incremental signal generated by a discrete-time Fuzzy-PI as given by (12).

$$u(kT) = u((k-1)T) + K_u \Delta u(kT) \quad (12)$$

Where, T is the sampling time. In this paper, the simulated annealing- will be described in the next section- is used to determine optimal values of the scaling factors. The corresponding fuzzy control rules are illustrated in Table 1.

Table 1 Fuzzy logic control rules

| ACE _i | d (ACE _i) | | |
|------------------|-----------------------|----|----|
| | N | Z | P |
| N | NL | NM | Z |
| Z | NM | Z | PM |
| P | Z | PM | PL |

Where,

NL: Negative large

NM: negative medium

Z: zero

PM: positive medium

PL: positive large

3.2 Proposed Fuzzy Controller for Load Frequency Control System

The proposed fuzzy uses the same fuzzy rules and membership functions features of the previous fuzzy-PI introduced in section 3.1. However, the input of this fuzzy is the ACE error deviation and the discrete time integration of the ACE deviation of the i^{th} area as shown in Fig. 4. In this fuzzy control system, the output is obtained directly from the defuzzification stage.

Therefore, simulating annealing algorithm is employed with the objective function J given in (11) to determine optimal values for the scaling factors K_p and K_i of the i^{th} area as shown in Fig. 4. The corresponding Matlab/Simulink developed model is shown in Fig. 5. The membership functions frames of the ACE of the i^{th} area and its integration are chosen to be identical with triangular waveforms. The horizontal axis takes various values because of the controller optimization as depicted in Fig. 6.

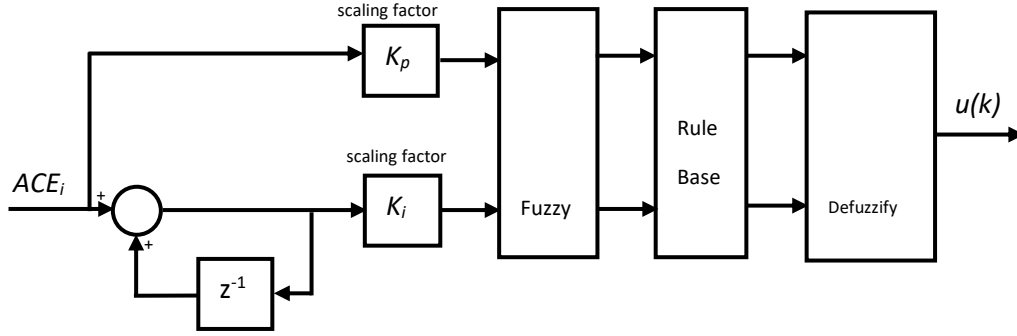


Fig. 4 Proposed fuzzy control system

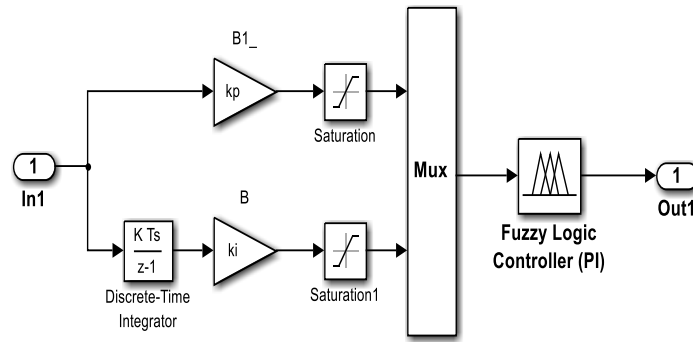


Fig. 5 Matlab/Simulink implementation of the proposed file of the i^{th} area

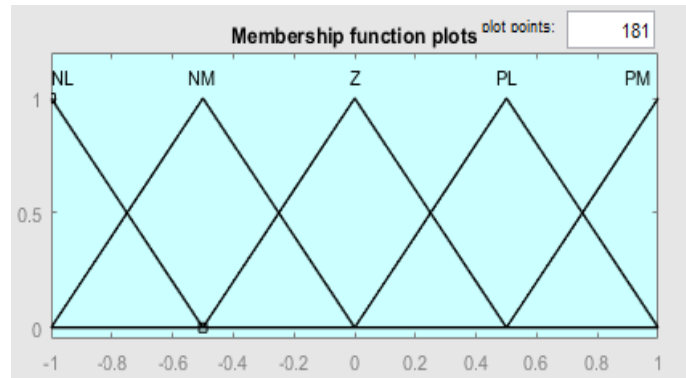


Fig. 6 The membership functions features of the output signal

3.3 Design of PI Controller for Load Frequency Control System

The proportional plus integral control technique is shown in (13).

$$G_i(s) = K_{p_pi} + \frac{K_{i_pi}}{s} \quad (13)$$

The constraints for the PI gains are given in (14) and (15) respectively.

$$K_{p_pi}^{min} \leq K_{p_pi} \leq K_{p_pi}^{max} \quad (14)$$

$$K_{i_pi}^{min} \leq K_{i_pi} \leq K_{i_pi}^{max} \quad (15)$$

The limits of the optimized gains are -2 and 2 respectively [30,44]. In this study, such constraints limits are extended to the other investigated controllers. The PI gains are optimized using the simulated annealing. The system output responses are compared with the responses obtained with using PI controller gains optimized by the genetic algorithm, as a well-known optimization algorithm for researchers.

4. Results and Discussions

A proposed simulated annealing optimized fuzzy automatic generation control is designed according to the procedures presented above. Several scenarios are investigated in order to verify the robustness of the proposed controller. The parameters or scaling factors used in this study are given in the Appendix. Four controllers using fuzzy-PI based optimal SAA, proposed fuzzy based optimal SAA, PI optimized by GA, and PI optimized by SAA are developed. Matlab/Simulink 2015b is used in the developing procedures.

Frequency deviations and tie-line power plots for the thermal and hydro-thermal power system areas obtained for 5% step load change in the power demand at the hydraulic power system area are shown in Figs. 7-13. The settling time constants are given in Table 1. The simulation response and the settling time constants reveal that developed fuzzy controller reduces the steady state error with minimal frequency peak overshoot. The proposed controller is more powerful in enhancing the damping behavior of the power system compared to fuzzy-PI, GA-PI, and SA-PI controllers. Thus, the proposed fuzzy gives better results than other controllers.

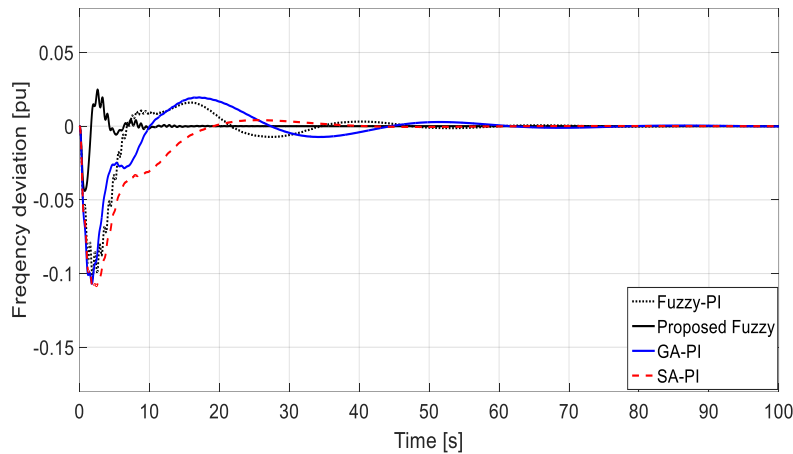


Fig. 7 Variation of frequency (f_1) under 0.05pu disturbance at the hydraulic area

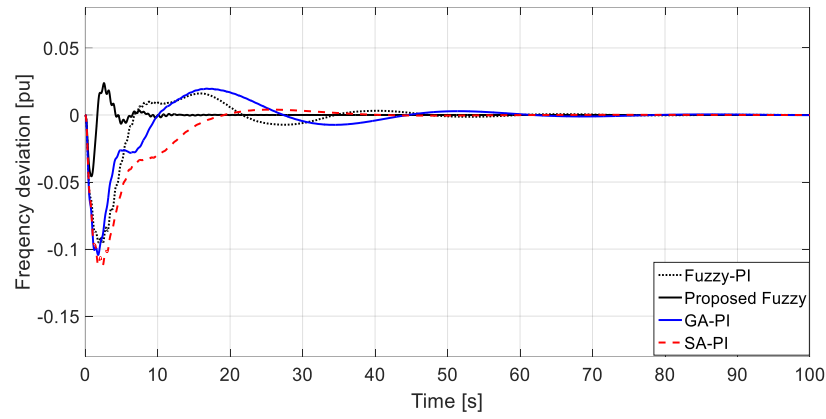


Fig. 8 Variation of frequency (f_2) under 0.05pu disturbance at the hydraulic area

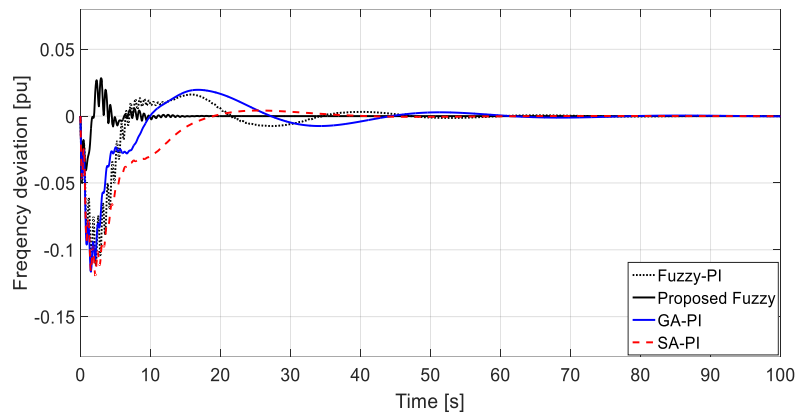


Fig. 9 Variation of frequency (f_3) under 0.05pu disturbance at the hydraulic area

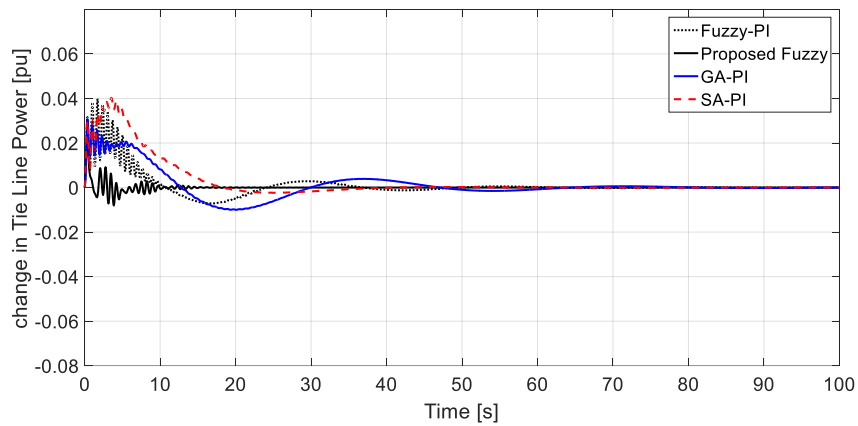


Fig. 10 Variation of tie-line power (P_{12}) under 0.05pu disturbance at the hydraulic area

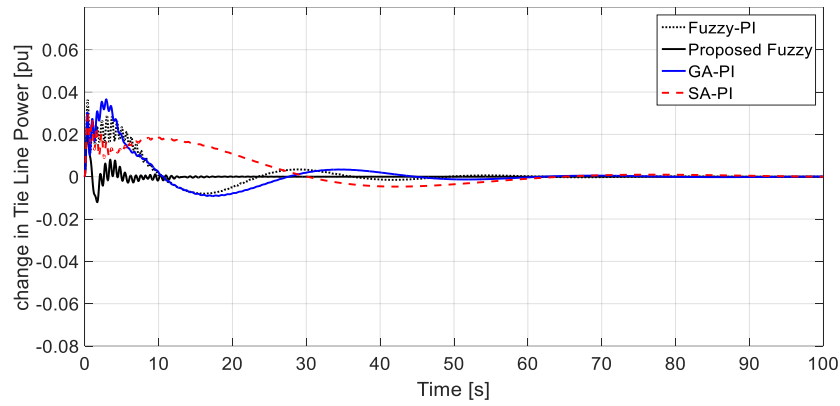


Fig. 11 Variation of tie-line power (P_{23}) under 0.05pu disturbance at the hydraulic area

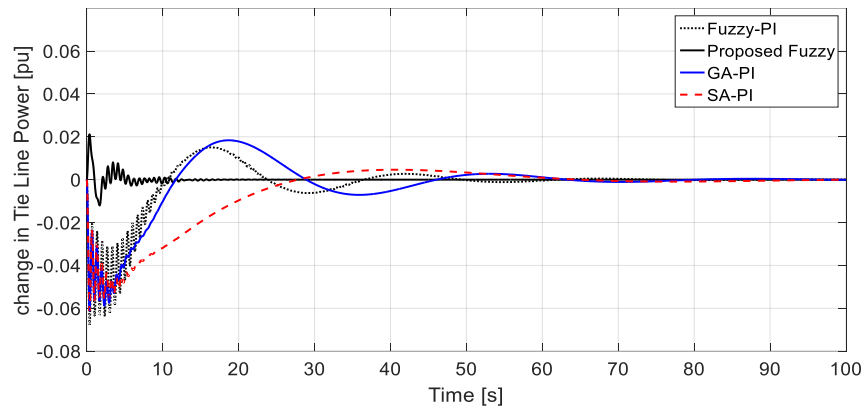


Fig. 12 Variation of tie-line power (P_{31}) under 0.05pu disturbance at the hydraulic area

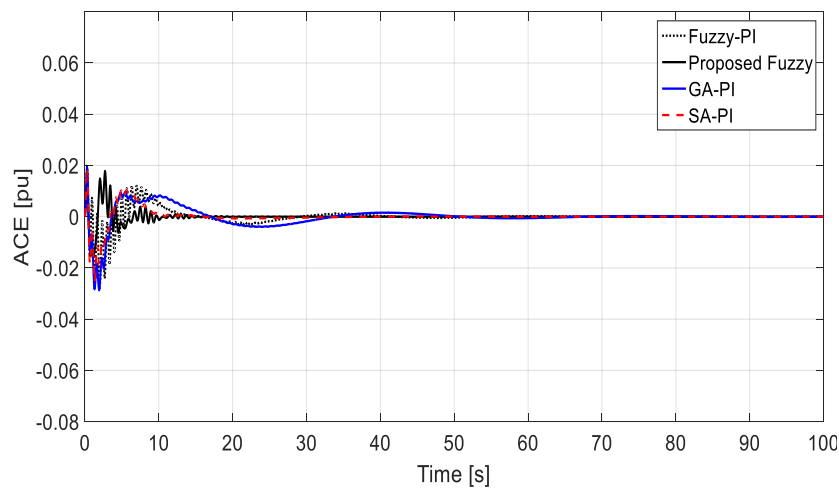


Fig. 13 ACE of area#1 variation for 0.05pu disturbance at the hydraulic area

Table 1 Settling time of some selected states in sec.

| | Δf_1 | Δf_2 | Δf_3 | ΔACE_1 | ΔACE_1 | ΔACE_3 |
|--|--------------|--------------|--------------|----------------|----------------|----------------|
| 0.05pu disturbance at the hydraulic machines | | | | | | |
| SA-PI | 33 | 33 | 33 | 85 | 58 | 55 |
| GA-PI | 56 | 56 | 55 | 25 | 27 | 59 |
| Fuzzy-PI | 44 | 44 | 44 | 37 | 39 | 46 |
| Proposed fuzzy | 10 | 11 | 13 | 15 | 14 | 13 |
| 0.01pu disturbance at all machines | | | | | | |
| SA-PI | 32 | 32 | 32 | 14 | 41 | 25.6 |
| GA-PI | 23 | 33 | 23 | 24 | 13 | 40 |
| Fuzzy-PI | 40 | 40 | 40 | 33 | 34 | 44 |
| Proposed fuzzy | 21.5 | 21.5 | 21.6 | 21.5 | 21 | 22 |

The second scenario is done with 0.01pu step change in the power demand at all areas. Frequency deviations and tie-line power plots for the thermal and hydro-thermal areas are given in Figs. 14-19. The system oscillations take long time to be attenuated by the conventional fuzzy-PI. In Table 1, the proposed fuzzy controller has lower settling time constants in most simulated signals compared to SA-PI and GA-PI based controllers. With the proposed fuzzy, the system response reaches steady state rapidly. Also, the capability of the developed controller is proven in solving the LFC stabilizing problem.

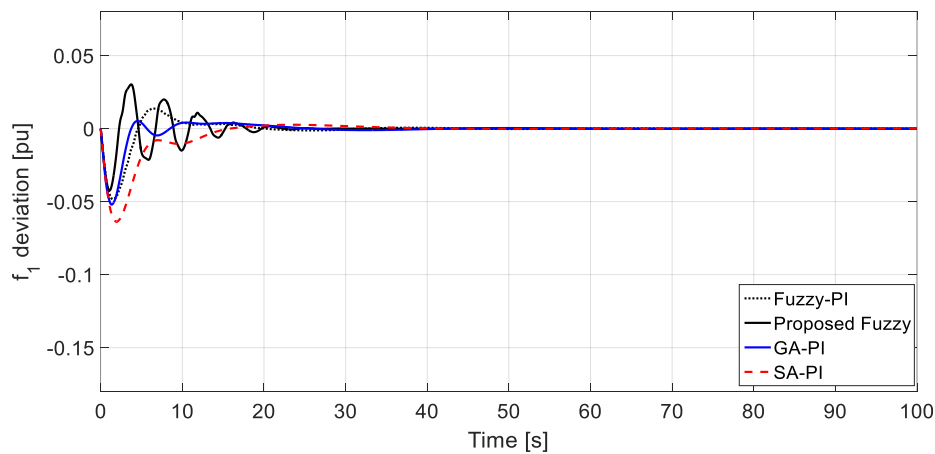


Fig. 14 Variation of frequency (f_1) under 0.01pu disturbance at all areas

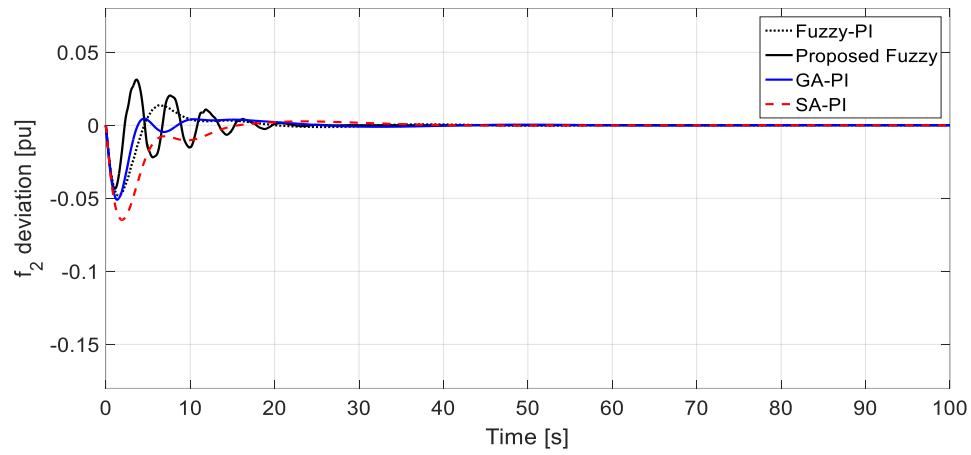


Fig. 15 Variation of frequency (f_2) under 0.01pu disturbance at all areas

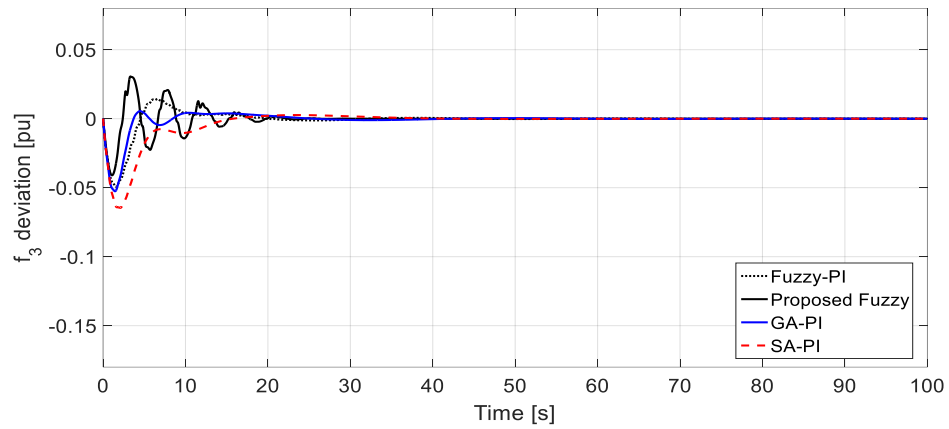


Fig. 16 Variation of frequency (f_3) under 0.01pu disturbance at all areas

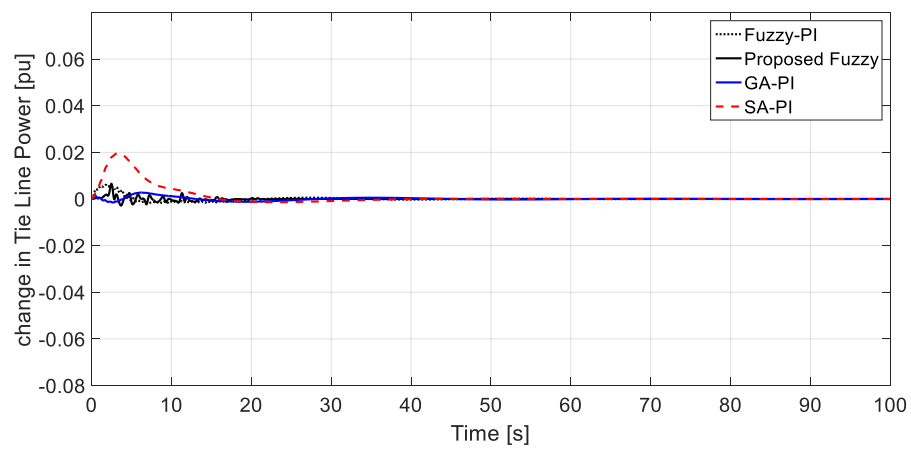


Fig. 17 Variation of tie-line power (P_{12}) under 0.01pu disturbance at all areas

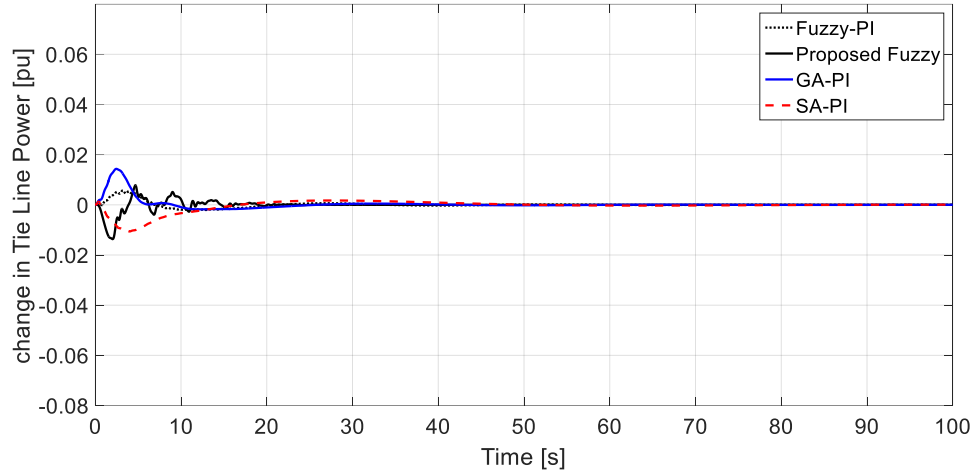


Fig. 18 Variation of tie-line power (P_{23}) under 0.01pu disturbance at all areas

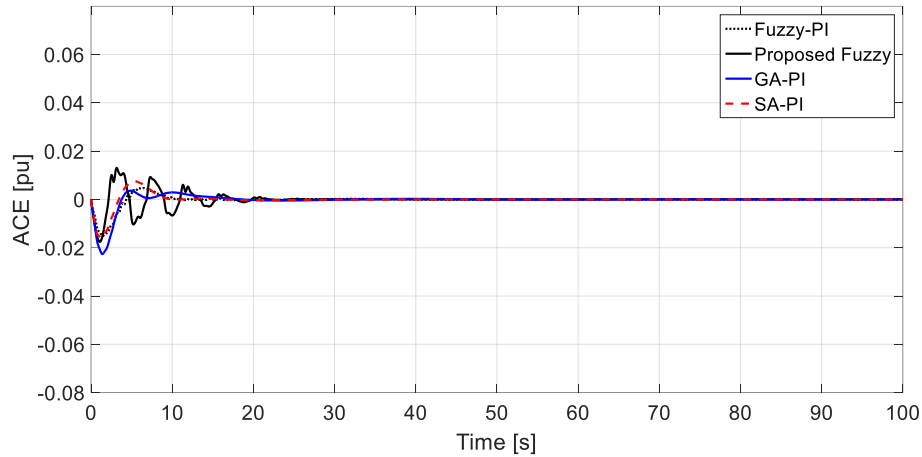


Fig. 19 ACE variation of area 1 for 0.01pu disturbance at all areas

5. Conclusions

In this article, the simulated annealing based optimal tuning of fuzzy-PI and a proposed fuzzy is introduced. The results are compared with PI controllers based optimal genetic and simulated annealing algorithms. The square root of the integral squared error (ISE) is selected to tune the PI and scaling factors parameters and improve the system response. Governor dead band nonlinearity with generation rate constraints are considered in order to confirm the effectiveness and robustness of the proposed fuzzy controller over the other investigated controllers. The proposed fuzzy is considered simple and time effective as it has a small number of fuzzy rules. The superiority and robustness of the proposed approach is clarified through various disturbances, settling time constants and parameters variation.

References

- [1] M. K. El-Sherbiny, G. El-Saady, A. M. Youssef, "Efficient Fuzzy Logic Load-Frequency", *Energy Conversion & management Journal*, Vol. 43, PP. 1853-1863, 2002.
- [2] S. Prakash, S. K. Sinha, "Simulation Based Neuro-Fuzzy Hybrid Intelligent PI Control Approach in Four-Area Load Frequency Control of Interconnected Power System", *Applied Soft Computing Systems*, Vol. 23, PP. 152-164, 2002.

- [3] A. Y. Abdelaziz, E. S. Ali, "Load Frequency Controller Design via Artificial Cuckoo Search Algorithm", *Elect Power Components and Systems*, Vol. 44(1), PP. 90-98, 2016.
- [4] G. Gross, J. W. Lee, "Analysis of Load Frequency Control Performance Assessments Criteria", *IEEE Trans. Power Sys.* Vol. 16(3), PP. 520-525, 2001.
- [5] O. I. Elgerd, "Electric Energy Systems Theory", New Delhi, Tata, Mc-Graw-Hill, 2006.
- [6] Y. Wang, R. Zhou, C. Wen, "Robust Automatic Generation Control", *Proc. Generat. Trans. Distribut.*, Vol. 140(1), PP. 11-16, 1993.
- [7] H. Saadat, "Power System Analysis", 3rd ed., PSA Publishing, 2010.
- [8] B. M. Mohan, A. Sinha, "Analytical Structure and Stability Analysis of a Fuzzy PID Controller", *Applied Soft Computing*, Vol. 8, PP. 749-758, 2008.
- [9] C. M. Liaw, "A Modified Optimal Load-Frequency Controller for Interconnected Power Systems", *Optimal Control Appl. Meth.*, Vol. 12, No. 3, PP. 197-204, 1994.
- [10] N. Hassan, "Design and Analysis of Pole-Placement Controller for Interconnected Power Systems", *Int. J. Emerging Technol. Adv. Eng.*, Vol. 2, No. 8, PP. 212-217, 2012.
- [11] K. Vrdoljak, N. Peri'c, I. Petrovi's, "Sliding Mode Based Load-Frequency Control in Power Systems", *Elect. Power Syst. Res.*, Vol. 80, PP. 514-527, 2010.
- [12] M. Mandour, E. Ali, M. Lotfy, "Robust Load Frequency Controller Design via Genetic Algorithm and H_{∞} ", *Modern Electric Power Systems (MEPS'10)*, Vol. 1(16), Wroclaw, Poland, PP. 20-22, 2010.
- [13] H. J. Lee, J. B. Park, Y. H., "Robust Load-Frequency Control for Uncertain Nonlinear Power Systems: A Fuzzy Logic Approach", *Int. J. Inform. Sci.*, Vol. 176(23), PP. 3520-3537, 2006.
- [14] W. Tan., H. Zhou, "Robust Analysis of Decentralized Load Frequency Control for Multi-Area Power Systems", *Int. J. Elect. Power Energy. Syst.*, Vol. 43 (1), PP. 996-1005, 2015.
- [15] A. I. Chidambaram, B. Paramsivam, "Genetic Based Decentralized Controller for Load-Frequency Controller of Interconnected Power systems with RFB considering TCPS in the Tie-line", *Int. J. Electron. Eng. Res.*, Vol. 1(4), PP. 299-312.
- [16] S. Selvakumaran, S. Parthasarathy, R. Karthigaivel, V. Rajasekaran, "Optimal Decentralized Load Frequency Control in a Parallel AC-DC Interconnected Power System through HVDC link using PSO algorithm", *Energy Procedia*, Vol. 14, PP. 1849-1854, 2012.
- [17] S. Parkash, S. Sinha, "Load Frequency of Three Area Interconnected Hydro-Thermal Reheat Power System Using and PI Controllers", *Int. J. Eng., Technol.*, Vol. 4, No. 1, pp. 23-37, 2011.
- [18] S. B. Shree, N. Kamaraj, "Hybrid Neuro Fuzzy Approach for Automatic Generation Control in Restructured Power Systems", *Elect. Power and Energy Syst.*, Vo. 74, PP. 274-285, 2016.
- [19] R. Francis, I. A. Chidambaram, "Applications of Modified Dynamic Neural Networks for Load Frequency Control of a Two Area Thermal Reheat Power System", *Int. Rev. Automat. Control*, Vol. 6(1), PP. 47-53, 2013.
- [20] H. Shyeghi, H. A. Shayanfar, A. Jalili, "Load Frequency Control Strategies: A State-of-the-Art Survey for Researcher", *Energy Convers. Manage*, Vol. 50, PP. 344-353, 2009.
- [21] S. R. Khunta, S. Panda, "Simulation Study for Automatic Generation Control of a Multi-Area Power System by ANFIS Approach", *Appl. Soft Comput.*, Vol. 12, PP. 333-341, 2012.
- [22] H. Bevrani, F. Habibi, P. Babahajyani, M. Watanabe, Y. Mitani, "Intelligent Frequency Control in an ac Microgrid: online PSO-Based Fuzzy Tuning Approach", *IEEE Trans Smart Grid* 2012, Vol. 3(4), PP. 1935-1944, 2012.

- [23] A. E. Milani, B. Mozari, "Genetic Algorithm Based Optimal Load Frequency Control in Two Area Interconnected Power System", *Global J. Technol Optim.*, Vol. 2, PP. 6-10, 2011.
- [24] V. Jeyalakshmi, P. Subburaj, " Load Frequency Control in Two Area Multi Units Interconnected Power System Using Multi Objective Genetic Algorithm", *WEAS Trans. Power Syst.*, Vol. 10, PP. 35-45, 2015.
- [25] H. Abbas, H. Werner, "LPV Design of Charge Control for an SI Engine Based on LFT Neural State-Space Models", *Proc. of the 17th World Congress the International Federation of Automatic Control*, Vol. 1, PP. 1-6, Seoul, Korea, July 2007.
- [26] M. R. Khalghani, M. H. Khooban, E. M. Moghaddam, N. Vafamand, M. Goodarzi, "A Self-Tuning Frequency Control Strategy for Microgrids: Human Brain Emotional Learning", *Electric Power and Energy Syst.* Vol. 75, PP. 311-319, 2016.
- [27] S. P. Ghoshal, "Optimizations of PID Gains by Particle Swarm Optimizations in Fuzzy Based Automatic Generation Control", *Electr. Power Syst. Res.*, Vol. 72(3), PP. 203-212, 2004.
- [28] R. Hooshmand, M. Ataei, A. Zargari, "A New Fuzzy Sliding Mode Controller for Load Frequency Control of Large Hydropower Plant Using Particle Swarm Optimization Algorithm and Kalman Filter Estimator", *Eur. Trans. Electr. Power*, Vol. 22(6). PP. 812-830, 2012.
- [29] V. G. Babu, B. Hemanth, T. S. Kumar, B. V, Prasanth, " Single Area Load Frequency Problem Using Particle Swarm Optimization", *Int. J. Eng. Sci.*, Vol. 3(6), PP. 33-40, 2014.
- [30] E. S. Ali, S. Abd-Elazim, "Bacteria Foraging Optimization Algorithm Based Load Frequency Controller for Interconnected Power Systems", *Int. J. Electr. Power Energy Syst.*, Vol. 33(3), PP. 633-638, 2011.
- [31] P. Dhanalakshmi, K. Mahadevan, "Assessment of Optimal PID Tuning Controllers for Load Frequency", *WEAS Trans. Power Syst.*, Vol. 10, PP. 116-122, 2015.
- [32] M. Omar, M. Soliman, A. A. Ghany, F. Bendary, "Ant Colony Optimization Based PID for Single Area Load Frequency Control", *Proc. of Int. Conference on Modeling, Identification & Control*, Vol. 1, PP. 119-123, Cairo, Egypt, Aug. 2013.
- [33] R. Rajabioun, "Cuckoo Optimization Algorithm", *Appl. Soft Comput.*, Vol. 11(8), PP. 5508-5518, 2011.
- [34] A. Bindu, M. Reddy, "Economic Load Dispatch Using Cuckoo Search Algorithm", *Int. J. Eng. Res. Appl.*, Vol. 3(4), PP. 498-502, 2013.
- [35] A. B. Mohamad, A. M. Zain, N. E. N. Bazin, "Cuckoo Search Algorithm for Optimization Problems- a Literature Review and its Applications", *Appl. Art. Intell. J.*, Vol. 28(5), PP. 419-448, 2014.
- [36] M. H. Sulaiman, M. R., "Solving Economic Dispatch Problems Utilizing Cuckoo Search Algorithm", *IEEE 8th Int. Conference on Power Engineering and Optimization*, Vol. 1, PP. 24-25, Langkawi, Malaysia, March 2014.
- [37] S. Parkash, S. K. Sinha, "Impact of Slider Gain on Load Frequency Control Using Fuzzy Logic Controller", *ARNP J. Eng. Appli. Sci.*, Vol. 4(7), PP. 20-27, 2009.
- [38] S. Parkash, S. K. Sinha, "Load Frequency Control of Three Area Interconnected Hydro-Thermal Reheat Power System Using Artificial Intelligence and PI Controllers", *Int. J. Eng. Sci. Technol.* 4(1), PP. 23-37, 2011.
- [39] J. Yen, R. Langari, "Fuzzy Logic: Intelligence, Control, and Information", 1st ed., Prentice Hall, 1998.
- [40] K. R. Mudi, R. N. Pal, "A Robust Self-Tuning Scheme for PI- and PD-Type Fuzzy Controllers", *IEEE Trans. Fuzzy Syst.*, Vol. 7(1), PP. 2-16, 1999.

- [41] K. R. Mudi, R. N. Pal, "A Self-Tuning Fuzzy PI Controller, Fuzzy Sets Syst. 115 (2), PP. 327-388.
- [42] R. K. Sahu, S. Panda, N. K. Yegireddy, "A Novel Hybrid DEPS Optimized Fuzzy PI/PID Controller for Load Frequency Control of Multi-Area Interconnected Power Systems", Vol. 24, PP. 1596-1608, 2014.
- [43] S. Khuntai, S. Panda, "Simulation Study for Automatic Generation Control of a Multi-Area Power System by ANFIS Approach", Int. J. Appl. Soft Comput., Vol. 12, PP. 333-341, 2012.
- [44] E. S. Ali, S. Abd-Elazim, "BFOA Based Design of PID Controller for of PID Controller for Two Area Load Frequency Control with Nonlinearities", Int. J. Elect. Power Energy Syst., Vol. 51, PP. 224-231, 2013.

Appendix

(a) The constants of the investigated system are [43]: Sampling time (T) = 0.001sec, $f = 60$ Hz, $T_{P1} = T_{P2} = T_{PI} = 20$ sec, $K_{P1} = K_{P2} = K_{PI} = 120$, $T_{i1} = T_{i2} = T_{iI} = 0.3$ sec, $T_{r1} = T_{r2} = T_{rI} = 10$ sec, $T_{12} = T_{23} = T_{31} = 0.545$ pu, $T_{g1} = T_{g2} = T_{gI} = 0.08$ sec, $B_1 = B_2 = B_3 = 0.425$ pu MW/Hz, $a_{12} = a_{23} = a_{31} = -1$, $R_1 = R_2 = R_3 = 2.4$ Hz/pu MW, $T_w = 1$ sec, $K_{r1} = K_{r2} = 0.5$ pu MW, $K_d = 4$, $K_i = 5$, $K_p = 1$.

(b) The following Tables give the tuned parameters of controllers for various algorithms.

Table b1 Simulated annealing and genetic algorithms controllers scaling factors

| | K_{p1} | K_{i1} | K_{p2} | K_{i2} | K_{p3} | K_{i4} |
|----------------|-------------------------------|-------------------------------|--------------------------|-------------------------------|---------------------------|-------------------------------|
| SA | - 0.044 2 | - 1.006 2 | 0.715 4 | - 0.06 4 | 0.037 92 | - 0.059 2 |
| G A | 0.278 5 | - 0.346 8 | 0.099 6 | - 1.65 25 | 0.387 4 | - 0.152 9 |

Table b2 Fuzzy-PI and proposed fuzzy controllers scaling factors

| | Fuzzy-PI | Proposed Fuzzy |
|----------------|-----------------|-----------------------|
| Area 1 | | |
| K_p | 0.8289 | 0.3773 |
| K_v or K_i | 0.2847 | -1.9919 |
| K_u | -0.8697 | ----- |
| Area 2 | | |
| K_p | 1.8918 | 1.1552 |

| | | |
|-----------------------|---------|---------|
| $K_v \text{ or } K_i$ | -1.47 | -0.8349 |
| K_u | -0.5538 | ----- |
| Area 3 | | |
| K_p | -0.9405 | 1.28 |
| $K_v \text{ or } K_i$ | 0.9405 | -1.5408 |
| K_u | 0.5595 | ----- |

32-Optimization of different Parameters of Solar Chimney

K. F. Megalaa, Youssef A. Attai and M. M. Abd Elbaset[†]

[†]E-mail: khairymegalaaa@hotmail.com, joo_attai@yahoo.com,
mahacen1@hotmail.com.

Department of Mechanical Power Engineering, Faculty of Engineering, El-Mattaria, Helwan
University, Cairo, Egypt.

Keywords: Solar chimney power plant; Mathematical model; Optimum design; solar energy

Abstract. The solar chimney power plant converts solar thermal energy into kinetic energy to generate electricity. The main parts of solar chimney plant are collector, chimney tower and turbine. There are many factors affected on solar plant performance as solar intensity radiation, air pressure drop, temperature, velocity and mass flow rate. The produced output power depends on the design parameters of the solar chimney as well as its dimensions. Therefore; this study focused on how to optimize a solar chimney through a mathematical model to predict and estimate the optimum dimensions of any proposed solar chimney power plant by knowing the required output power and the ambient conditions. Q-basic program was used to develop such mathematical model for obtaining the optimum plant dimensions for a known output power plant. The developed mathematical model results were validated by measurements of an actual physical plant. In addition, the study proposes that the most suitable plant, affordable by local government standards to respond to the electricity demand of a typical village in Aswan. Also the developed model enables the prediction of the performance parameters of any solar chimney power plant during 24 hours a day.

1 Introduction

World aims to provide clean and renewable energy. Therefore, the solar chimney station is considered one of the promising facilities to achieve this, with a little maintenance cost. The solar chimney power plant (SCPP) consists mainly of three main parts shown in figure (1).

The first part is the collector that is considered to be as a green house, where air is heated at the entrance of the collector and causes densities variations. As a result, buoyancy arises and hot air is directed to the second part, known as the chimney. The chimney is a tall building, located in the center of the collector. The third part is the turbine, which is located at the entrance to the chimney and is used to convert the kinetic energy of hot air into electrical energy. The main defects of SCPP are summarized in its high cost of construction; therefore, all trends lead to a mathematical calculation to reduce the cost. The optimum design of the solar chimney is the key input in economic growth and there is a close link between the availability of energy and the growth of a nation.

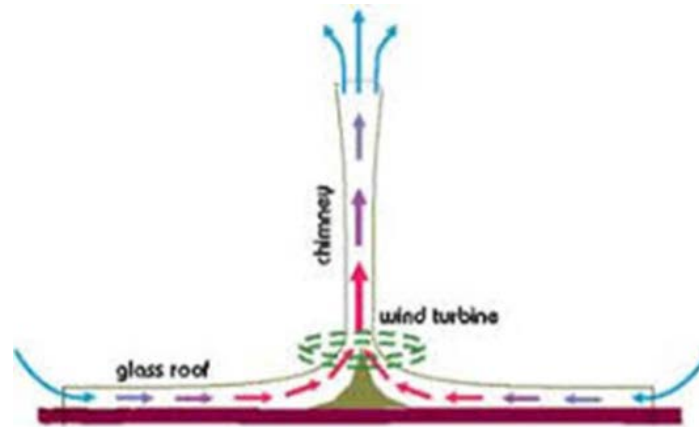


Figure (1) schematic diagram of solar chimney power plant component

Haff W et al. [1] and Haff W. [2] were the first researchers in innovation and studying solar chimneys. They made a small prototype in Manzanares, Spain. EL-sebaili et al. [3] presented a significant study on solar radiation types (direct and diffuse) in vertical and horizontal plane and applied a comprehensive investigation using the climatic conditions of Saudi Arabia. Notton et al. [4] calculated the amount of diffuse solar radiation from global data over the course of daylight hours for the horizontal plane. The amount of solar radiation over the day was determined on the horizontal surface using the available online statistics [5]

Various studies have found that the optimum driving pressure indicated by the symbol ($x = p_{\text{tur}} / p_{\text{tot}}$) equals $2/3$ based on the results of the practical experiments [1], in contrast many researchers took its value equals to 0.8 without using references [6]. Otherwise, its value ranges from 0.8 - 0.9 based on mathematical equations [7].

In the presented article, the calculated value of x depends on the practical experiment [1] and mathematical equations [8] leading to an optimum value of driving pressure equals to $2/3$ that available only for constant driving pressure Δp_{tot} and steady increase in air temperature, knowing that this value decreases throughout the day. The increase in the production capacity and the efficiency of the solar plant is mainly based on the low cost of construction, which includes the cost of the main dimensions such as collector diameter, chimney height and diameter [9, 10].

Many researchers have been and are being, devoted to study the relationship between shape of collector and its dimension with output power. This also led to the calculation of the ratio between height and radius of collector at high air flow rate [11 -15]. However, as reported by Pretorius and Kroger [16] their analytical investigation revealed that the height of the collector and its shape have a noticeable effect on the produced electrical energy. Their results proved the direct relationship between them.

In contrast, Dehghani and Mohammadi [17] have used various techniques to optimize the dimensions of solar chimney power plant according to capital cost. Gholamalizadeh and Kim [18] were developed the electric power and overall efficiency of SCPP, using three different methods, have led to assess the capital cost. In addition, Sangi [19] proposed a mathematical model for SCPP with its collector diameter of 1000 meters and a chimney height of 350 meters to calculate the value of the output electric power, the results of that model showed an analysis of its performance at different solar radiation ranging from $(400 \text{ to } 750) \text{ W/m}^2$ and ambient temperature ranging from $(270 \text{ to } 315 \text{ K})$.

Numerous researchers have examined, with numerical simulations, the performance of SCPP according to Iran weather and verified its validity by comparing their results with that of Manzanares pilot plant [20]. The evaluation of heat transfer by convection with collector

material and soil types on performance of large scale of SCPP have been stated by [21]. Investigation by using numerical equations under strong and weak weather to study its influence on collector inlet and chimney output on the electric power and performance was also carried out [22]. The optimal ratio for driving pressure drop which varying between (0.66 :0.97) was achieved to calculate the optimum output power [23]. Guo et al. [24] analyzed the performance of SCPP and the performance of their station during every hour and it was affected by the incident angle of sun rays. Kasaeian et al. [25] conducted a prototype of the solar chimney at the University of Iran and revealed that the optimal dimension of the chimney was achieved. Prediction of the temperature and velocity of the air inside the chimneys by studying the amount of solar radiation at the horizontal plane was achieved by [26].

In addition, performance prediction for different models of SCPP, by solving integrated algebraic equations, was performed to obtain the output power and efficiency of each model [27]. Moreover, Dimension Parameters and economic calculation of SCPP was analyzed by Okoye et al. [28]. Modifying numerical models to calculate static pressure, output power, driving force and efficiency, then assess the results using initial Manzanares model have been demonstrated by [29]. Pastohr et al. [30] have solved the main equations of thermodynamics using CFD for different models to improve efficiency.

From the previous literature, it can be seen that a little interest was given to the prediction and optimization of SCPP based on the Egyptian weather conditions, although Egypt has solar radiation don't less than 90%, especially at south region. Therefore, the current study objectives are to investigate how to optimize the main parameters of a solar chimney station to achieve the desired output power in a location in the southern region in Egypt. A mathematical model will be prepared to predict and estimate the optimum dimensions of any proposed solar chimney power plant by knowing its required output power and the ambient conditions. Q-basic program was used to develop such mathematical model for obtaining the optimum plant dimensions for any required output power.

Five stations were selected in Beban village (Aswan) as a case study, in which the solar radiation reaches up to 2500 kW / m² per year. All stations are considered to have the same weather conditions with different output power of each. The present model is established to predict the basic dimensions of each station. Also, this location was chosen because of the low cost compared to the European cost due to the availability of raw materials, manpower and proper weather. The optimal design of solar chimney is one of the main entry points for economic growth, and there is a close relation between energy availability and output power.

In the current study, the amount of solar radiation over the day is determined on the horizontal surface using the website [5] which depends on location determination of Beban village on the map, its latitude is 24.4415 and altitude 93, and then determine the month and day to be studied.

Here was chosen mid-July at 12:00 O'clock

Maximum solar radiation at day 200 =1046 W/m²

Solar radiation at day 200 at 12:00 =1046 W/m²

The results appeared as curves as shown in figure (2) and figure (3).

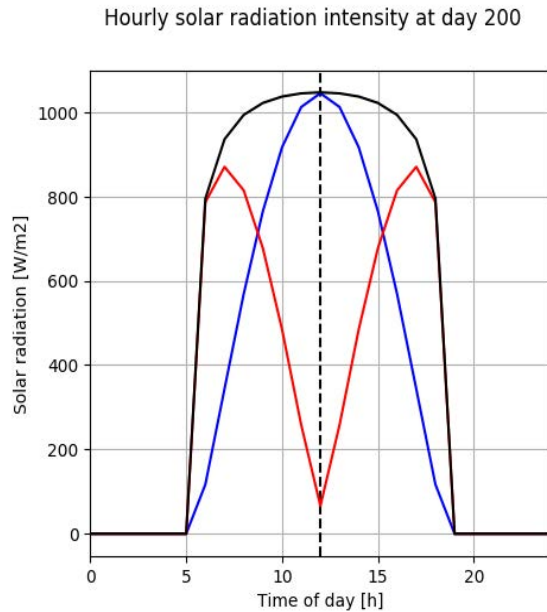


Figure (2) Hourly solar radiation intensity in radiation

Beban village in July 2019

The previous figures (1) and (2) illustrate the intensity of solar radiation on a horizontal surface (blue), on a vertical surface (red), and on a vertical surface on the sunlight (black). Figure (1) show the intensity of solar radiation per hour and figure (2) show daily maximum solar radiation in July for Beban village.

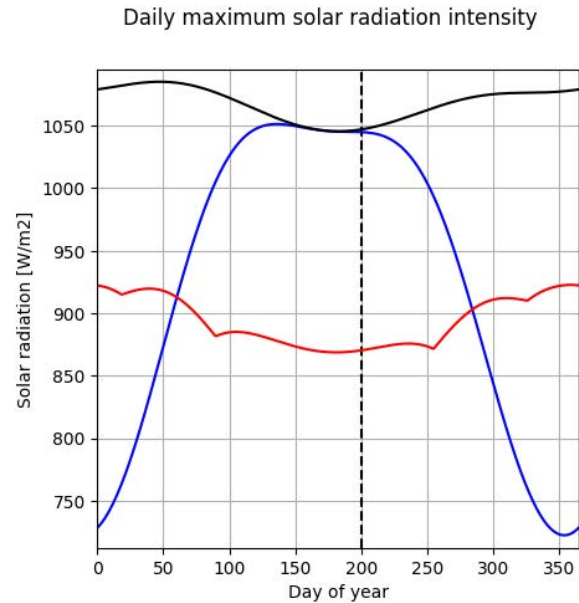


Figure (3) Daily maximum solar

intensity in July 2019

2 Mathematical model and methodology

According to the concept of running hot air inside the solar chimney, it depends heavily on the change of air density. That led to a difference in pressures [1] that can be seen in figure (4). First, by knowing the value of the required electrical power from the solar chimney station that will design and determine the appropriate generator efficiency for the resulting energy [8, 9, 10, 16] then calculate the maximum energy symbolized by the P_{\max} from equation (1):

$$P_{\max} = P_{\text{ele}} / \eta_g \quad (1)$$

Where η_g is the generator efficiency

Second, calculate two types of air velocity [26]. The first velocity of the air is affected by the turbine movement (V_T) and appears on the figure (4) at point 3. This velocity is calculated from the following equation:

$$V_T = (2 * P_{\max} * 1000)^{0.5} / \dot{m} \quad (2)$$

The second velocity of the air, before being affected by the movement of the turbine (V_{noT}) will be affected by the movement of the turbine [26] and shown on the figure (4) before point 2, hence can be estimated from the following equation:

$$V_{\text{noT}} = V_T / (1-x)^{0.5} \quad (3)$$

Where:

x , as mentioned before, is the ratio of the pressure drop across the turbine to the total available driving pressure of the system. Then, the maximum power can be obtained when the turbine extract pressure $x = 2/3$ of the available driving pressure [1, 2, 8]

The air mass flow rate (\dot{m}) can be assumed [1] or can be calculated from following equations:

$$P_{ele} = (16/27) * (1/2 * \rho_1 * V_T^3 * A_{ch})$$

(4)

Since;

$$\dot{m} = \rho_2 * A_{ch} * V_T$$

(5)

By compensating by equations (3) and (5) in the equation (4) get the air mass flow rate as follows”

$$\dot{m} = ((27/8) * P_{ele}) / ((V_{noT})^2 * (1-X))$$

(6)

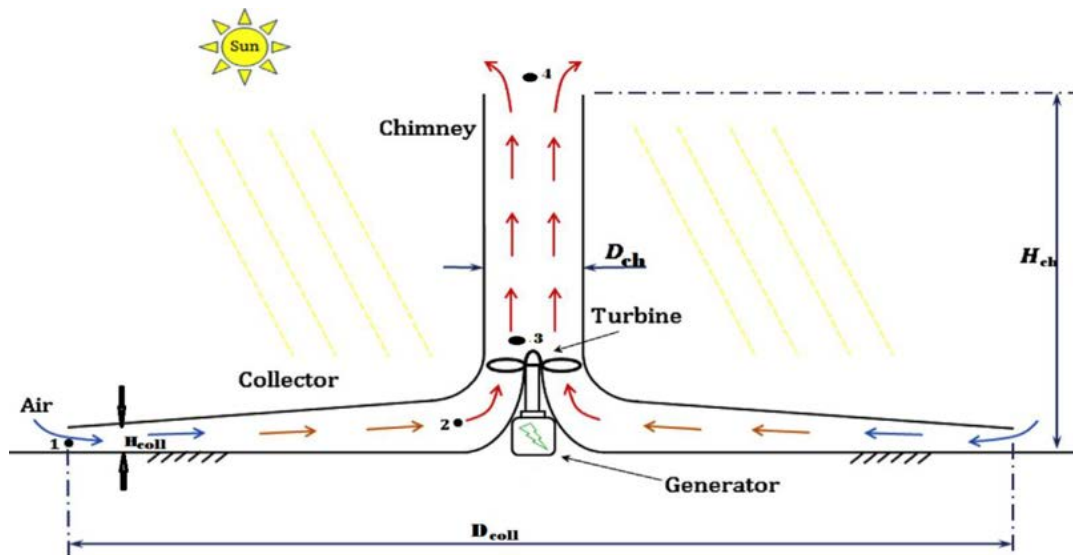


Figure (4): The drawing of air flow in solar chimney power plant

The buoyancy phenomenon occurred through differing air density and movement, which would lead to calculate the available driving pressure and its effect on air movement within the collector [11]. This is can be achieved by calculating the total pressure drop within the SCPP [29] from equation:

$$\Delta p_{tot} = (0.5 * \rho_1 * V_{noT}^2)$$

(7)

By knowing Δp_{tot} , pressure can be computed after the effect of the turbine, which is at point 3 in figure (4) as:

$$p_3 = p_1 - \Delta p_{tot}$$

(8)

Therefore from the V_T value, that calculated previously, the dynamic pressure drop, proven by [29], can be calculated from:

$$\Delta p_{dyn} = (0.5 * \rho_1 * V_T^2)$$

(9)

Calculating the turbine pressure drop of equation (10) has been proved by [8] as follows:

$$\Delta p_{tur} = \Delta p_{tot} - \Delta p_{dyn}$$

(10)

However, the pressure can be computed before the effect of the turbine, which is at point 2 in figure (4) as:

$$p_2 = \Delta p_{tur} + p_3$$

(11)

Although it is possible to calculate the values of the amount of solar radiation in practice or from many different sites as mentioned earlier [3, 4, and 5], furthermore, it can be

mathematically calculated from the following equations [8] by selecting $\eta_{\text{coll}} = 0.32$ as reported by [1-4] using the following equation:

$$q = \eta_{\text{coll}} * I$$

(12)

$$\text{Also, } q = (\alpha * I) - (U * \Delta T)$$

(13)

Thus, the difference in temperature between points 2 and 1, specified in figure 4, can be calculated as follows [2-1]:

$$\Delta T = ((\alpha * I) - q'') / U$$

(14)

By replacing q'' from equation (12) we get the following equation

$$\Delta T = (\alpha - \eta_{\text{coll}}) * (I / U)$$

(15)

Furthermore, the values of α , η_{coll} and U , which are constant for the same designed solar chimney station, can be compensated for each value based on the type of collector

$$\Delta T = 0.02 * I$$

(16)

Note that the constant (0.02) in equation (16) differs from one station to another depending on the type of collector.

Then calculate the temperature after the turbine at point 3 as:

$$T_3 = T_2 * (p_3/p_2)^{(\gamma-1/\gamma)} \quad (17)$$

The density of the air at points 2 and 3 was then estimated by thermodynamic equations used [30]:

$$\rho_2 = p_2 / (R * T_2)$$

(18)

$$\rho_3 = p_3 / (R * T_3) \quad (19)$$

Finally, after knowing the required electrical power, the intensity of the solar radiation and calculations of (V , Δp , q'' , ΔT and ρ), the collector dimensions can be calculated from the following equations [8]. First calculate the area of collector from its equation:

$$A_{\text{coll}} = \Delta T * (\dot{m} * c_p) / q$$

(20)

Then, from area can be calculated collector diameter from equation:

$$d_{\text{coll}} = (4 * A_{\text{coll}} / \pi)^{0.5}$$

(21)

Hence, the collector height can be calculated as follows:

$$h_{\text{coll}} = \dot{m}_{\text{cal}}^{1.5} / (\rho_2 * \pi * d_{\text{coll}} * (2 * P_{\text{max}})^{0.5})$$

(22)

The dimensions of the chimney are calculated as follows [1, 8]. The diameter of chimney can be calculated from the following equation:

$$d_{\text{ch}} = ((13.5 * P_{\text{ele}}) / G)^{0.5} \quad (23)$$

While the height of chimney is calculated from following equation:

$$h_{\text{ch}} = (P_{\text{max}} * \rho_2 * 1000) / (\dot{m} * G * (\rho_1 - \rho_2) * (1-x)^{0.5})$$

(24)

it can be calculated also from following equation, based on the ambient temperature and efficiency of chimney:

$$h_{\text{ch}} = (\eta_{\text{ch}} * c_p * T_1) / (G * 100)$$

(25)

To correct the value of assumed mass flow rate of air and efficiency of collector

$$\dot{m}_{cal} = (3.14 * h_{coll} * d_{coll} * \rho_1 * (2 * P_{max})^{0.5})^{2/3}$$

(26)

Then from eq.(11)

$$\eta_{coll} = \alpha - (U * \Delta T / I)$$

(27)

Solution procedures

By knowing the required output power, the mass flow rate is calculated from the equation (6) above or assumed it [1]. The following steps to calculate station dimensions are:

- 1-choose mass flow rate
- 2-calculate P_{max} from eq. (1)
- 3-Calculate V_T from eq. (2)
- 4- Calculate V_{noT} from eq. (3)
- 5-Calculate Δp_{tot} from eq. (7)
- 6-Calculate p_3 from eq. (8)
- 7-Calculate Δp_{dyn} from eq. (9)
- 8-Calculate Δp_{tur} from eq. (10)
- 10- Calculate q from eq. (12)
- 11- Calculate ΔT from eq. (14)
- 12-Calculate T_3 from eq. (17)
- 13-Calculate p_2 from eq. (18)
- 14-Calculate p_3 from eq. (19)
- 15- Calculate d_{coll} from eq. (21)
- 17-Calculate h_{coll} from eq. (22)
- 18-Calculate d_{ch} from eq. (23)
- 19-Calculate h_{ch} from eq. (24)
- 20- Calculate \dot{m}_{cal} from eq. (26)
- 21-Calculate η_{coll} from eq. (27)

By calculating the new mass flow rate (\dot{m}_{cal}) and compare its value with the assumed value (\dot{m}). If the result not less than or equal an acceptable value then iteration process should be performed until achieve its accepted value with low error. A flowchart for these steps is illustrated in Figure (5).

Results and discussion:

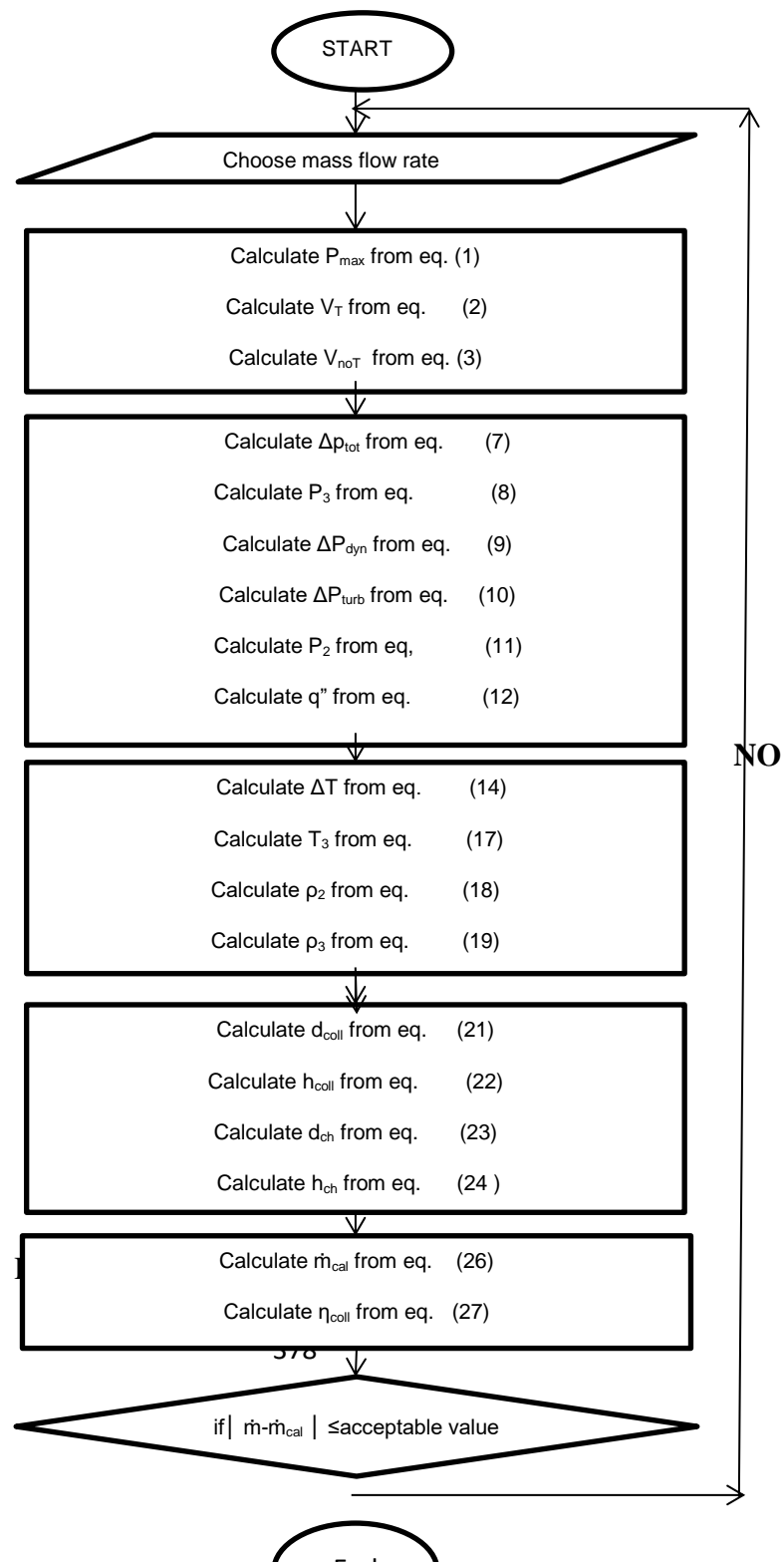
Validation of the model with experimental data

To validate the current theoretical data of the model, compared it with the experimental results of the prototype (Manzanares, Spain), whose data were recorded in table (1). The measured data was approved on September 2, 1982 from Reference. [1]. The comparison between the empirical data and the current theoretical predictions are recorded in Table (2). Based on the data provided in the reference article, instead, the values (T_1 , P_1 , I) were calculated theoretically for the area to be studied using the designated websites [4-3].

Table (1): Main parameters and data of proto type plant in Manzanares, Spain [1].

| | |
|---|-------------------------|
| Ambient temperature (T_1) | 302 K |
| Ambient pressure (P_1) | 100000 pa |
| Collector absorption coefficient (α) | 0.65 |
| Collector losses coefficient (U) | 15 W/ m ² .k |
| Turbine efficiency ($\eta_{tur.}$) | 0.83 |
| Collector efficiency (η_{coll}) | 0.32 |
| Global solar radiation | 1017 W/m ² |

| | |
|--------------------------------------|--------|
| Output power (P_{ele}) | 50 kW |
| Height of chimney (h_{ch}) | 194.6m |
| Diameter of chimney (d_{ch}) | 5.08m |
| Diameter of collector (d_{coll}) | 244m |
| Height of collector (h_{coll}) | 1.85 m |



While the value of q is calculated from equation (12) and the value of the air velocity V_{noT} can also be measured or calculated from equation (3). Also, the value of \dot{m} is calculated by equation (6) or assumed then corrected by equation (26). Choose the value of the driven pressure ratio x at optimum output based on the calculation and references [1, 8].

Therefore, the comparison between the measured data for the Manzanares prototype and the theoretical data from current study shown in Table (2) indicate a good relationship among them to apply the proposed model to other stations.

Table (2) Comparison between measured data for Manzanares plant and theoretical results (Data of reference in 1st September 1983)

Table (2) Comparison between measured data for Manzanares plant and theoretical results (Data of reference in 1st September 1983)

| Parameter (m) | Measured | Theoretical |
|-----------------------------------|----------|-------------|
| Collector Diameter (d_{coll}) | 244 | 242.76 |
| Collector height (h_{coll}) | 1.85 | 2.01 |
| Chimney height (h_{ch}) | 194.6 | 187.29 |
| Chimney Diameter(d_{ch}) | 10.16 | 8.27 |

Performance and characteristics of Solar Chimney System

Five different stations were selected in terms of output power and sizes required to demonstrate their characteristics as shown in Figures 6, 7, 8 and 9 according to the cost of the model described in [1].

These five stations were selected in Beban (Aswan - Egypt) as a case study to simulate with Manzanares prototype [8]. Affordable by local government standards to respond to the electricity demand of a typical village in Aswan. Where different electrical powers were selected for each plant under constant weather conditions, where an electric power of 100 kW was selected for the first station, while the second station 150 kW, the third station 200kW, the fourth station 250kW, and finally the fifth station 300 kW.

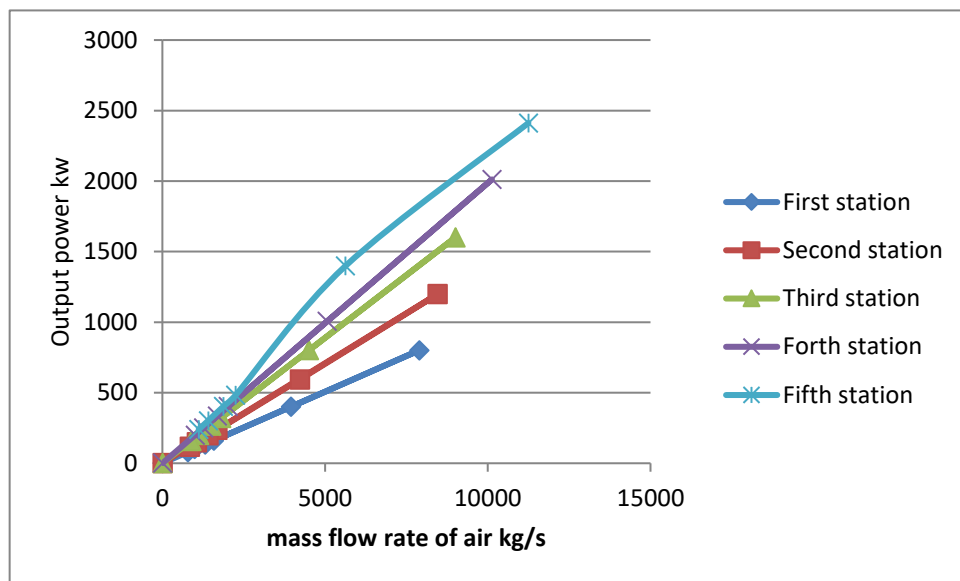
Also the developed model enables the prediction of the performance parameters of any solar chimney power plant during 24 hours a day.

Influence of electric power on characteristics SSPP

Figure (6) and (7) show the relation between electric power and air mass flow rate in two cases with calculations of solar radiation with losses and another calculation neglecting losses of solar radiation.

From figure (6), the case of solar radiation loss calculation can be observed; such calculations are performed using equation (12). The obtained trend clarifies that there is a direct relationship between the power and the amount of the mass flow rate of the air entering the collector which agrees with the previously obtained results [11], when the collector efficiency is less than 100%.

From this, it can be noted that the maximum electric power value is located near the minimum mass flow rate value. This means that increased buoyancy increases the air mass and consequently increases the kinetic energy of the turbine, which transforms it into an electric power. Both the power and mass flow rate of air were directly affected by changing the dimensions of the plant, especially the diameter of the collector and the height of the chimney.



Figure(6) Influence of mass flow rate on output power for solar radiation 1046 W/m^2 (with losses)

. It can be seen, from figure (7) that when the collector efficiency equals 100 % and no heat radiation losses, the maximum power is located between the minimum and maximum values of the air mass flow rate. As previously mentioned in Figure (6), there is direct relation between output power and amount of mass of air. Noting that the value of the mass of air in figure (7) (Solar radiation without loss) is greater than its value in figure (6) (Solar radiation with losses). On the other hand, it is clear that the amount of airflow is not constant during different hours of the day due to the difference in the intensity of solar radiation

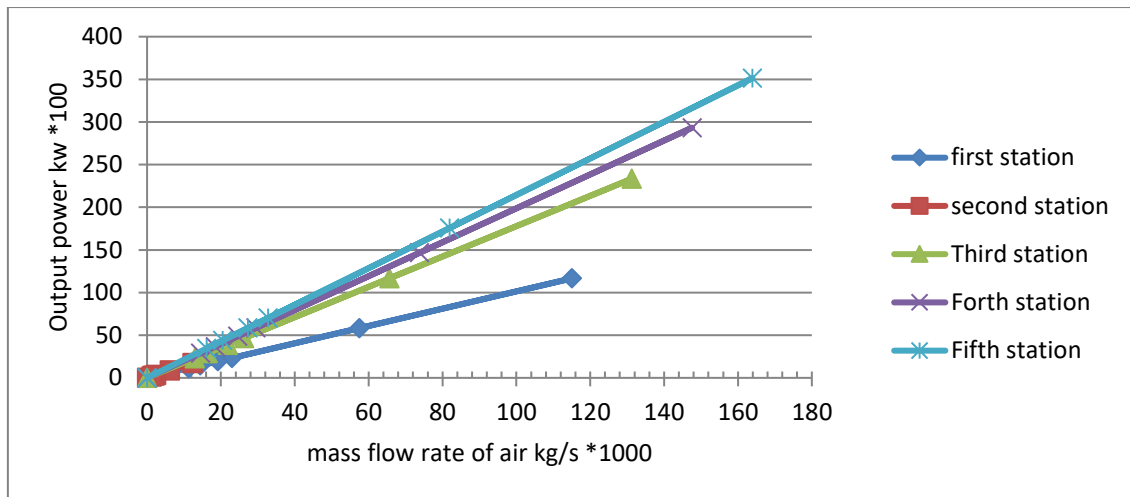
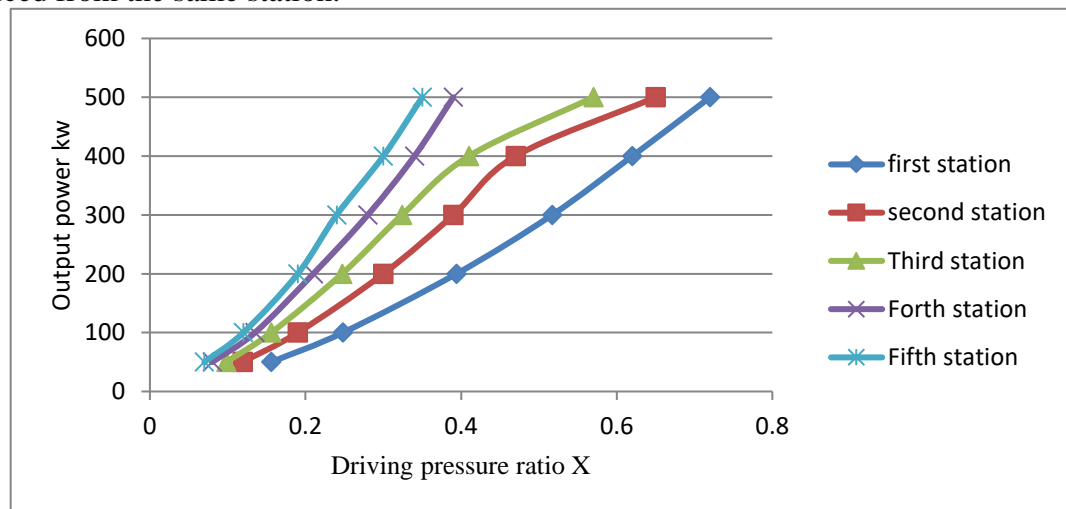


Figure (7) Effective of mass flow rate on output power for solar radiation 1046 W/m^2 (with no losses)

Influence of pressure ratio on the electric power

Figure (8) illustrates this effect at collector coefficient absorption of $(\alpha) = 0.65$, and collector losses coefficient $(U)=15$. The optimum pressure ratio is not equal to $2/3$ and its value is not constant at all hours of the day as a result of changing the intensity of solar radiation every hour. So the assumption of x value at current study was only valid for constant pressure drop and constant increase in temperature under the collector in addition, it has proven previously by [1, 8].

As a result, the value of the output power of each plant is not fixed per year and is not fixed in months or even in daytime. The analysis indicated that the optimum pressure ratio depends only on the solar radiation, and it affects the mass flow rate of the air and the output power values produced from the same station.



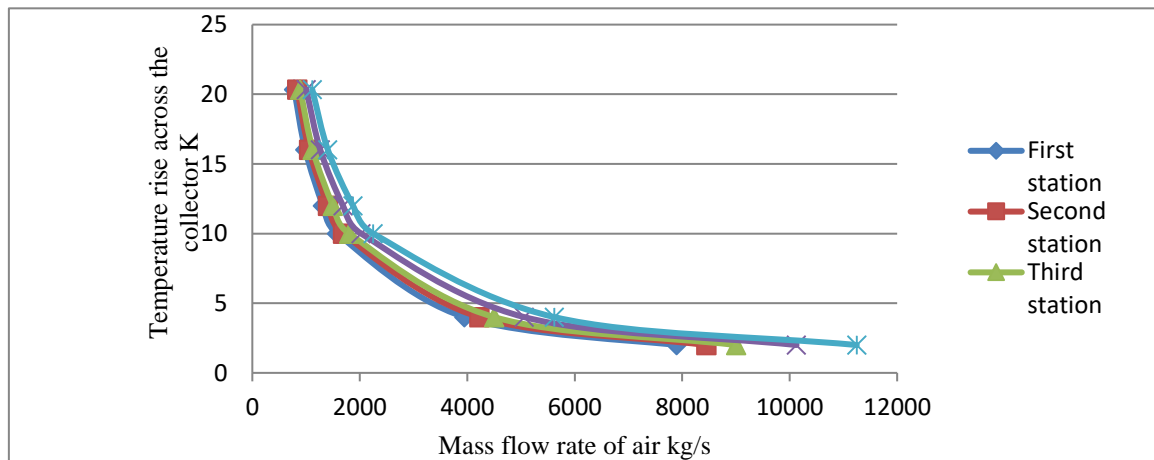
Figure(8) effective of pressure ratio on power output for solar radiation 1046 W/m^2

Influence of temperature rises on mass flow rate of air

This effect is illustrated in Figure (9). When the collector diameter increases, the difference in temperature increases and the amount of air entering the compound decreases. This is consistent with equation (28). Also, it can be shown that the difference in temperature within the complex depends only on the diameter of the collector.

$$\Delta T = q'' \cdot A_{\text{coll}} / \dot{m} \cdot c_p \quad (28)$$

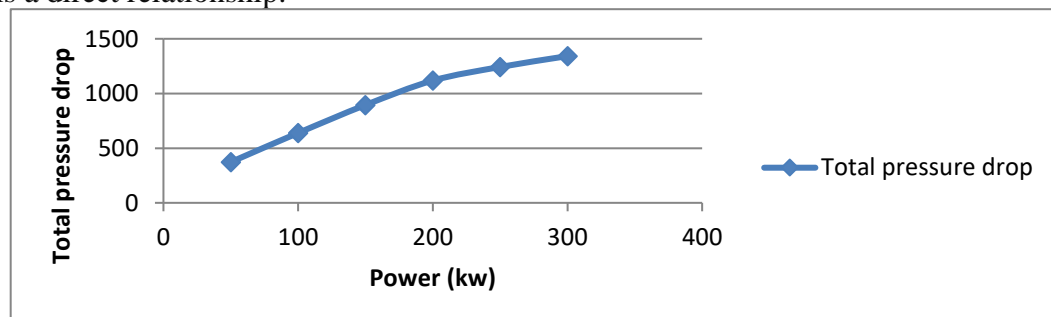
Thus, the difference temperature of the air inside and outside the collector is an important factor affecting the buoyancy and mass of air entering the collector. This means that the efficiency of the collector is determined by the value of ΔT on the basis of equation (27).



Figure(9) effective of mass flow rate on collector temperature rises for solar radiation 1046 W/m^2

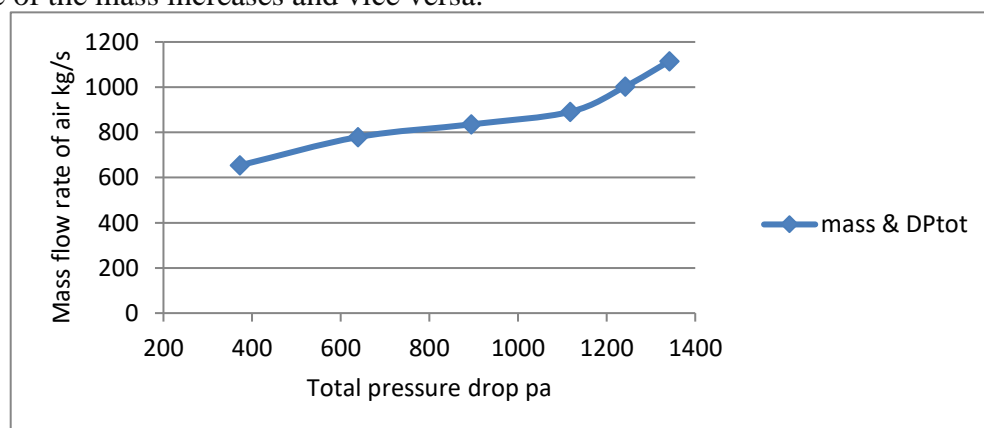
Influence of pressure drop on power and mass flow rate of air

Figure (10) shows that low pressure is actually one of the main factors responsible for changing the amount of electric power throughout the day. Its value is equal to the sum of both turbine pressure drop and dynamic pressure drop. It is clear from the graph that the relationship between them is a direct relationship.



Figure(10) the relation between output power and Total pressure drop

The total pressure drop also controls the amount of airflow inside the station, see figure (11) where the buoyancy force inside the station is caused. This means that the mass flow rate is not constant during each hour of the day. Note that with the increase of the total pressure drop, the flow rate of the mass increases and vice versa.



Figure(11) Influent of Total pressure drop on mass flow rate of air

Influence of main parameters of SSCP on the output power

It should be noted that the optimum design of the SSCP depends on the maximum output power. Figures 12, 13 and 14 show the relationship between output power and the main parameters D_{coll} and H_{ch} of SSCP. Figure (12) shows the relationship between electric power and chimney height. This relationship is based on Equation (24), which shows that when chimney height increases, in the studied five theoretical plants, greater driving force than friction losses is obtained, as a result of which electric power increases.

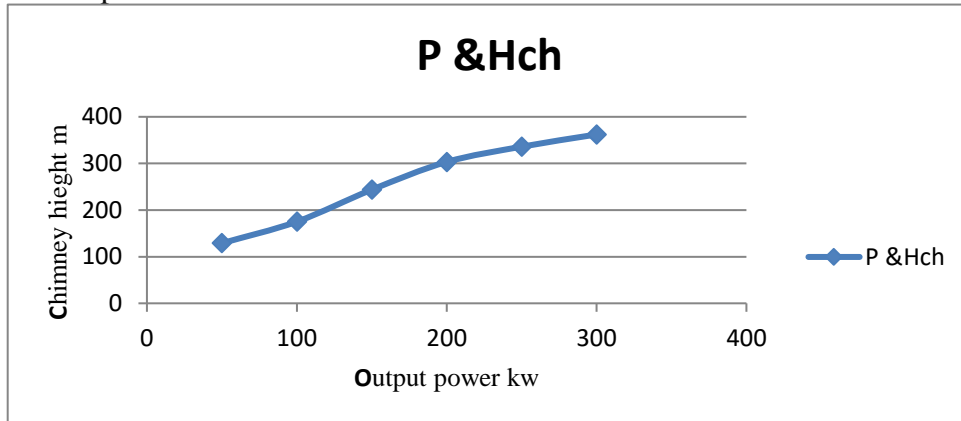


Figure (12) The relation between output power and chimney height

Figure (13) illustrates the relationship between the output energy and the collector diameter. Where it was observed using mathematical equations that by increasing the area of the collector in the five theoretical stations, the output capacity also increased. Because increasing the area of the collector increases the amount of hot air inside and thus increase the driving force, which it turns to the electric power in the turbine .

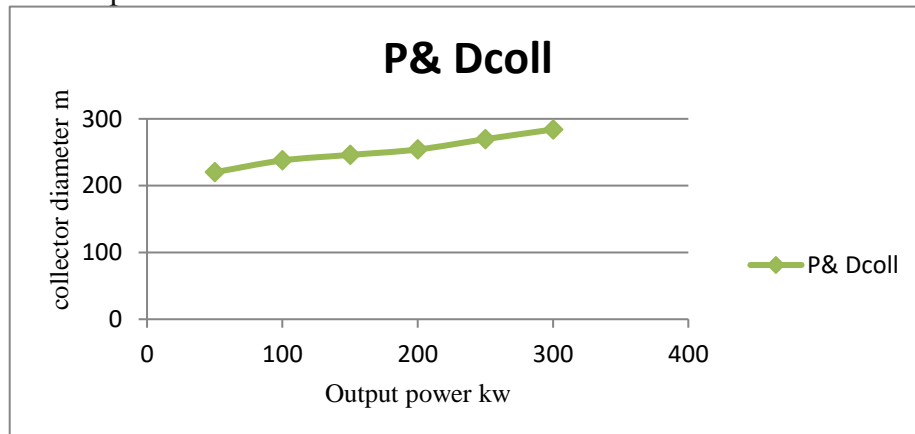


Figure (13) the relation between output power and collector diameter

The relationship between collector diameter and chimney height this effect is illustrated in figure (14) and solved by equation (26) in equation. (24). And as a result, they proportional directly together. This means that when the collector area increases, the air temperature increases and therefore the driving force increases. As a result, we need to increase the chimney height to reduce friction losses and to harvest the electric power.

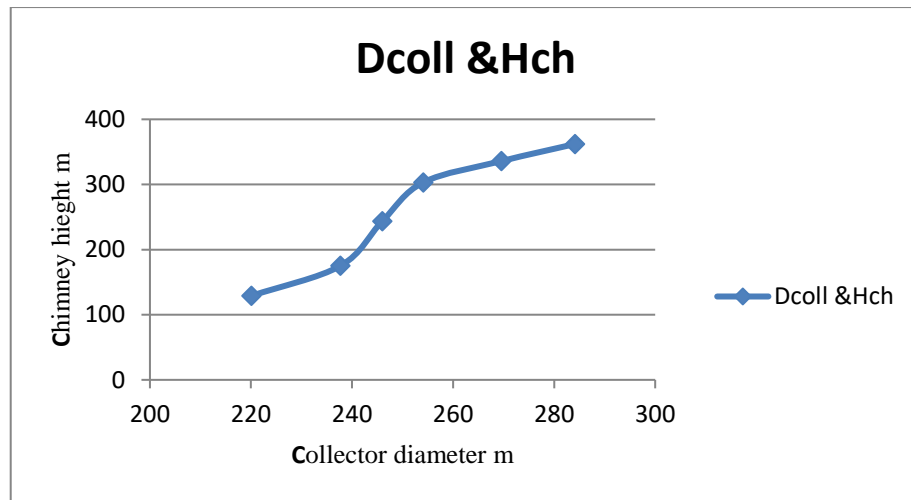


Figure (14) the relation between collector diameter and chimney height

Influence of mass flow rate of air on collector efficiency

Figure (15) shows this effect, which shows that its collector efficiency does not depend primarily on solar radiation but depends on the dimensions of the collector.

$$\eta_{\text{coll}} = (\dot{m} \cdot c_p \cdot \Delta T_{1-2}) / (q \cdot A_{\text{coll}}) \quad (29)$$

This conclusion is based on equation (29) which shows that the relationship between the collector efficiency and its area is inverse relationship. As mentioned earlier from equation (20), the increasing area of the collector reduces the heat gained.

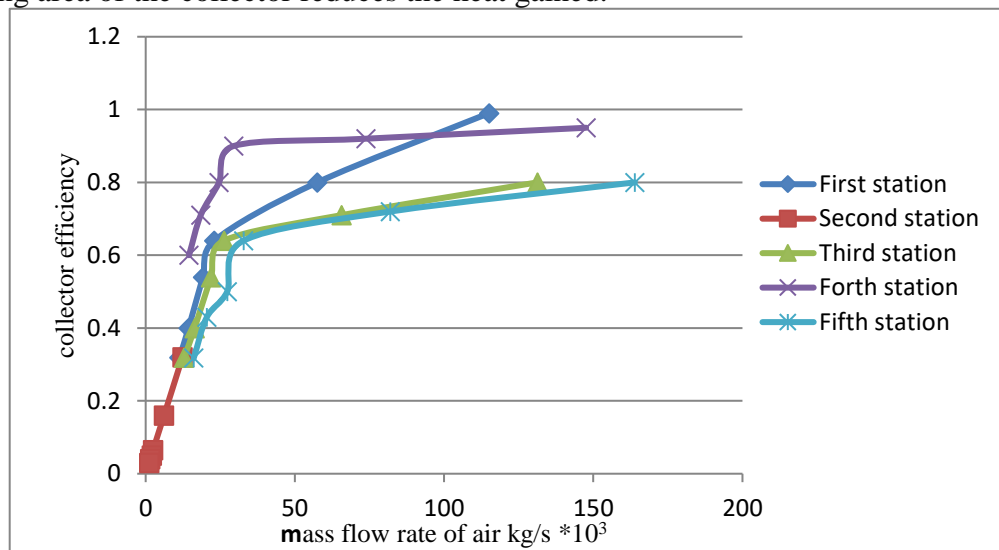


Figure (15) effect of mass flow rate on collector efficiency with no losses of solar radiation

This theoretical simulation to evaluate the performance of solar chimney power plants. That examined the relationship between the power and the temperature across the collector, the relationship between the mass flow rate and the pressure ratio.

Current results indicate that the optimum pressure ratio x , as mentioned earlier, is not actually equal to $2/3$ and its value is not constant at all hours of the day, which is given theoretically $2/3$ at optimum power output and under continuous driving pressure [1]. However, in the case of instability, the value of x depends on the solar radiation and station size, which effect on the output power.

The paper also presented a simple mathematical model to calculate the dimension of the plant through knowledge of the output power. This calculation predicts the dimensions of five stations

at ambient temperature of 318K and the maximum solar radiation of 1046 W / m², selected here in mid-July at 12:00 noon and recorded the results in Table (3).

To improve this model, a simple mathematical model was used for the solar power plant. Therefore that concluded that the mathematical model presented in current paper is appropriate to improve a particular station while changing the operating conditions of the entire system.

Table (3): the main parameters of five stations in Aswan taken stations at 318K and the maximum solar radiation of 1046 W / m²

| Parameters | First station | Second station | Third station | Forth station | Fifth station |
|-------------------|---------------|----------------|---------------|---------------|---------------|
| Output power (kw) | 100 | 150 | 200 | 250 | 300 |
| h_{coll} (m) | 1.53 | 1.34 | 1.24 | 1.25 | 1.26 |
| d_{coll} (m) | 237.72 | 246.07 | 254.14 | 269.55 | 284.13 |
| h_{ch} (m) | 175.11 | 243.7 | 303.20 | 335.96 | 362.05 |
| d_{ch} (m) | 11.73 | 14.36 | 16.59 | 18.5 | 20.31 |

4-conclusions

This paper used a numerical model to predict the dimensions of different solar chimney stations. Such model provided a good agreement with the experimental plant. Of the above results, some important points in design should be taken:

- 1- The intensity of solar radiation is variable, so the assumption that the flow is steady is used only to calculate the total solar effect on station dimensions.
- 2- In the chimneys, the flow is incompressible, and as a result the buoyancy forces increase as well as the velocity of the airflow, neglecting the loss of friction inside the chimney.
- 3- The heat transfer equation is applied to the collector only, because the area of the collector is larger than the chimney area
- 4- The efficiency of turbines was taken from 80% or higher.
- 5-The heat transfer from the ambient to the collector is considered and calculated, however, the heat transfer from the system to the ambient is ignored.
- 6-As a result of problems arising from the cost, restrictions usually arise in the application for example high chimneys cannot be more than about 1000 m.
- 7- The values of the main geometrical parameters resulting for the five stations (d_{coll} , d_{ch} and h_{ch}) differ from one to the other according to the output power change. But h_{coll} value at all stations is approximately 1.5 meters.
- 8- When the output power exceeds 150 kW, the optimum ratio between the collector diameter and flue device is less than 0.8.
- 9- The resulting parameters may vary in the optimization process; however, when power output is greater than 100 kW, each parameter is usually required to be within a reasonable range as follows:

$$d_{coll} > 200 \text{ m} , \quad h_{ch} > 170 \text{ m} , \quad d_{ch} > 11 \text{ m}$$

Reference

- [1] Haaf W, Friedrich K, Mayr G, Schlaich: J. Solar chimneys: part I, principle and construction of the pilot plant in Manzanares, Int J Sol Energy; 2:3-20. (1983). <http://dx.doi.org/10.1080/01425918308909911>.
- [2] Haaf W: Solar chimneys, part II, preliminary test results from the Manzanares plant. Int J Sol Energy; 2:141-61.(1984) <http://dx.doi.org/10.1080/01425918408909921>.
- [3] El-sebaili,AA.,F.S.AL-H azmi,A.A.AL-Ghamdi and S.J.Yahmour: Global, direct and diffuse solar radiation on horizontal and tilted surfaces in Jeddah, Saudi Arabia ,Appl.Energy,87(2):568-76 (2010)

- [4] Notton, G., Cristofari, M., Muselli, P. and Poggi, P.: Calculation on an hourly basis of solar Diffuse irradiations from global data for horizontal surfaces, In *Ajaccio Energy conversion and management* 45:2849-2866 (2004)
- [5] Information on <http://www.Cablizer.com>
- [6] Von Backström TW, Gannon AJ: The solar chimney air standard thermodynamic cycle. *SAIMEchE R&D J*;16(1):16-24(2000)
- [7] Nizetic S, Ninic N, Klarin B: Analysis and feasibility of implementing solar chimney power plants in the Mediterranean region. *Energy*; 33(11): 1680-90 (2008).
- [8] A.koonsrisuk, T.Chitsomboon: Mathematical modeling of solar chimney power plant, *Int. J. Energy Res.* 51, 341-322(2013)
<http://dx.doi.org/10.1016/j.energy.2012.10.038>.
- [9] Mullett, L.B.: The solar chimney-overall efficiency, design and performance. *Int. J. Ambient Energy* 8, 35–40 (1987)
- [10] Schlaich, J., Bergemann, R., Schiel, W., Weinrebe, G: Design of Commercial sola updraft tower systems-utilization of solar induced convective flows for power generation. *J. Sol. Energy Eng.* 127, 117–124 (2005)
- [11] Zhou, X.P., Yang, J.K., Xiao, B., Hou, G.X.: Simulation of pilot solar chimney power equipment, *Renew. Energy* 32, 1637–1644 (2007)
- [12] Zhou, X.P., Yang, J.K., Xiao, B., Hou, G.X., Xing, F.: Analysis of chimney height for solar chimney power plant. *Appl. Therm. Eng.* 29, 178–185 (2009)
- [13] Maia, C.B., Ferreira, A.G., Valle, R.M., Cortez, M.F.B.: Theoretical evaluation of the influence of geometric parameters and materials on the behavior of the airflow in a solar chimney. *Compute. Fluids* 38, 625–636 (2009)
- [14] Hamdan, M.O.: Analysis of solar chimney power plant utilizing chimney discrete model. *Renew. Energy* 56, 50–54 (2013)
- [15] Koonsrisuk, A., Chitsomboon, T.: Effects of flow area changes on the potential of solar chimney power plants. *Energy* 51, 400–406 (2013)
- [16] Pretorius, J.P., Kröger, D.G.: Solar chimney power plant performance. *J. Sol. Energy Eng.* 128, 302–311 (2006).
- [17] Dehghani, S., Mohammadi, A.H.: Optimum dimension of geometric parameters of solar chimney power plants - a multi-objective optimization approach. *Sol. Energy* 105,603–612 (2014).
- [18] Gholamalizadeh, E.; Kim, M.-H. Three-dimensional CFD analysis for simulating the greenhouse effect in solar chimney power plants using a two-band radiation model. *Renew. Energy* 63, 498–506 (2014).
- [19] Sangi, R.: Performance evaluation of solar chimney power plants in Iran. *Renew. Sust. Energy Rev.* 16, 704–710 (2012).
- [20] Gholamalizadeh, E., Mansouri, S.H.: A comprehensive approach to design and improve a solar chimney power plant: a special case – Kerman project. *Appl. Energy* 102, 975–982 (2013).
- [21] Pretorius, J.P., Kroger, D.G.: Thermo economic optimization of a solar chimney power plant. *J. Sol. Energy Eng.* 130, 021015 (2008).
- [22] Ming, T.Z., Wang, X.J., de Richter, R.K., Liu, W., Wu, T.H., Pan, Y.: Numerical analysis on the influence of ambient crosswind on the performance of solar updraft power plant system. *Renew. Sustain. Energy Rev.* 16, 5567–5583 (2012).
- [23] Guo, P.H., Li, J.Y., Wang, Y., Liu, Y.W.: Numerical analysis of the optimal turbine pressure drop ratio in a solar chimney power plant. *Sol. Energy* 98, 42–48 (2013).

- [24] Guo, P.H., Li, J.Y., Wang, Y., Liu, Y.W.: Numerical study on the performance of a solar chimney power plant. *Energy Convers. Manage.* 105, 197–205 (2015).
- [25] Kasaeian, A., Ghalamchi, M., Ghalamchi, M.: Simulation and optimization of geometric parameters of a solar chimney in Tehran. *Energy Convers. Manage.* 83, 28–34 (2014).
- [26] Sakonidou, E.P.; Karapantsios, T.D.; Balouktsis, A.I.; Chassapis, D.: Modeling of The optimum tilt of a solar chimney for maximum air flow. *Sol. Energy* 82, 80–94 (2008).
- [27] Padki, M.M.; Sherif, S.A. On a simple analytical model for solar chimneys. *Int. J. Energy Res.* 23, 345–349 (1999).
- [28] Okoye, C.O.; Atikol, U. A: parametric study on the feasibility of solar chimney power plants in North Cyprus conditions. *Energy Convers. Manag.* 80, 178–187(2014).
- [29] Tingzhen, M.; Wei, L.; Guoliang, X. Analytical and numerical investigation of the solar chimney power plant systems. *Int. J. Energy Res.* 30, 861–873 (2006)
- [30] Pastohr, H.; Kornadt, O.; Gürlebeck, K.: Numerical and analytical calculations of the temperature and flow field in the upwind power plant. *Int. J. Energy Res.* 28, 495– 510 (2004).

Nomenclature

Abbreviation

P = output power (kW)

\dot{m} = mass flow rate of air (kg/s)

q = Global solar radiation (W/m²)

I = heat transfer intensity (W/m²)

T = temperature (K)

p = pressure (Pa)

U = collector losses coefficient (W/m². K)

V = velocity of air (m/s)

C_p = specific heat capacity at constant pressure J/ (kg .K)

X = pressure ratio

d = diameter (m)

h = height (m)

A = area (m²)

G = gravitational force (m/s²)

R = ideal gas constant (J / kg. K)

Subscript

coll =collector

ch =chimney

tur = turbine

T =with turbine

noT=with no turbine

1 =ambient condition

2,3,4 =location condition

g =generator

tot =total

dyn =dynamic

max= maximum value

cal = calculated

ele = electric

g = generator

Greek-symbols

ρ =density of air (kg/m³)

α =collector absorption coefficient

η = efficiency

Δ =difference, drop

γ =thermal conductivity (W/m.K)

π = pi (3.14)

Acronym

SCPP =solar chimney power plant

33-Estimation of groundwater level changes using finite differences and GIS before and after the operation of New Assiut Barrage

Mohammed M.khoudary^{1,a}, Shenouda Ghaly^{2,b}, Kamal Ali^{3,c}, and Gamal Abozaid^{4,d}

¹ Civil Engineering Department, Aswan University, Aswan, Egypt

² Associate professor, Civil Engineering Department, Aswan University, Aswan, Egypt

³ Associate professor, Civil Engineering Department, Aswan University, Aswan, Egypt

⁴ Professor, Civil Engineering Department, Assiut University, Assiut, Egypt

^amohammed.khoudary@aswu.edu.eg , ^beng_noda@yahoo.com ,

^ckamalabbas90@yahoo.com, ^dgamal.abozaid@eng.au.edu.eg

Keywords: New Assiut Barrage (NAB), Finite Difference Method (FDM), GIS, Groundwater levels.

Abstract. Construction of Barrages on the River Nile is a double-bladed weapon action. Although, it contributes in increasing the agriculture lands and generating hydro-power, on the other hand its construction is accompanied with increasing of the groundwater levels in the vicinity of the new Barrage. As a result, various problems arise causing a decline in the crop productivity due to the increase of the groundwater levels. Furthermore, an inevitable damage of the foundations of the near residential buildings due to the fluctuations of the groundwater levels. In this research paper, a numerical model using Finite Difference Method to solve Darcy Equation which implemented on New Assiut Barrage located 400 m downstream of the Old Barrage, was constructed to supply irrigation water in the Middle Egypt to serve 1.65 Million Feddans in 5 Governorates and helping greatly in generating hydro-power about 32 Mega Watt. this model was performed to predict the groundwater levels after the Barrage construction. To validate the model, a verification step using the old groundwater levels before the Barrage construction was performed. On the other hand, GIS is used to obtain the ground levels to compare it with the previous obtained groundwater levels to determine the locations that are prone to submergence. It was found that an increase in groundwater levels by about 1.5 m (compared to pre-construction) occurs due to the barrage construction. Also, a submersion of 240 Feddans is noticed in the northern bank of the study area with a length of 4.5 km.

Introduction

The increment of Groundwater Levels (GWL) is an important issue that should be taken into consideration by the responsables for water resources managements. Monitoring of Groundwater Levels (GWL) changes due to man-made structures (especially, barrage construction on rivers) in Egypt is considered one of the main sources for the integrated water resource management implementation plan in this country [1]. The increase of Ground Water Levels has a bad effect on the building's foundations [2,3,4]. [5] discussed how groundwater effects on quality of surrounding soil, thus the growing of crops, and they debated the use of Groundwater in Agriculture in Egypt.

Finite Differences model (FD model) and GIS are widely used in monitoring the ground water variations[6]. The finite differences method (FDM) in groundwater modeling was used by many researchers {e.g. [7,8,9,10,11]}. Many Egyptian researchers presented papers related to the impact of barrages in Egypt (especially Assiut barrage) on groundwater variations {e.g. [12,13,14,15,16,17]}. The main target of this research is to monitor the ground water levels

changes via predicting the spatial distribution of the ground water levels in study area, after the New Assiut barrage (NAB) operation. Then the impacts of these changes on the study area were detected. The growth and use of GIS in groundwater investigations is increasing tremendously. It is used for groundwater potential [18] and vulnerability assessment [19], groundwater modelling [20,21] and management [22].

Finite Differences

The finite difference method is considered as the most viable and easily comprehend methods of obtaining numerical solutions to problems of steady and unsteady groundwater flow, there are a many of groundwater flow simulation programs based on this method. The general method be Consisting of superimposing a finite deference network of nodes upon the solution domain. Actually, a global identification number is given to each node, also the each of surrounding nodes about it, where the dependent variable is approximated with a finite – degree polynomial whose coefficients are written in formula of the unknown values of the dependent variable at the surrounding nodes. So, this polynomial is used to obtain an algebraic approximation for the partial differential equation for each internal nodes beside an algebraic approximation for boundary condition at each node site upon or near the solution domain boundary[23].

Laplace's equation is used in the finite difference approximation operation for such a mish is given by aquifer, we get a single second-order partial differential equation [24]:

$$\frac{\partial^2 h}{\partial^2 x} + \frac{\partial^2 h}{\partial^2 y} + \frac{\partial^2 h}{\partial^2 z} = 0 \quad (1)$$

When x, y, z directions and h is head of groundwater.

This is Laplace's equation which governs the flow of groundwater under steady state conditions, through an isotropic and homogeneous aquifer . This equation simply states that the sum of partial derivate of head (h) with respect to x , y , and z is zero (in 2D state). The solution of Laplace's equation requires specification of boundary conditions in study area, such as Dirichlet conditions and Neumann conditions [25]. Because the ground water flow in two dimensions, the Laplace's equation reduces to:

$$\frac{\partial^2 h}{\partial^2 x} + \frac{\partial^2 h}{\partial^2 y} = 0 \quad (2)$$

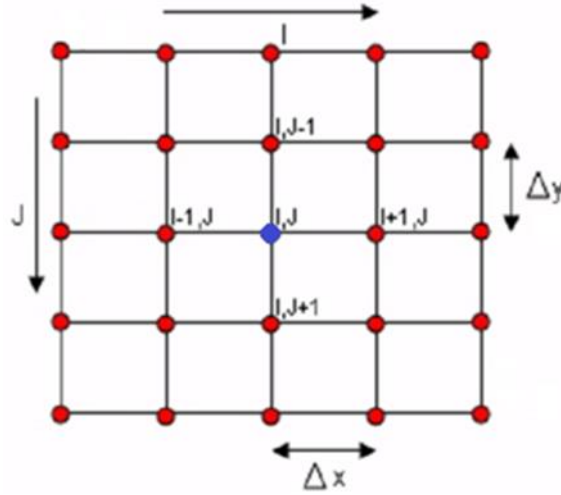


Fig. 1. Finite difference grid of nodes.

As shown in fig.1., consider a spaced grid of nodes represented by i columns and j rows, horizontally and vertically spaced by distances Δx and Δy respectively, the head at node i, j is h_{ij} .

discretization of the equation terms as follows:

$$\frac{\partial^2 h}{\partial^2 x} = \frac{h_{i-1,j} - 2h_{i,j} + h_{i+1,j}}{(\Delta x)^2}, \quad \frac{\partial^2 h}{\partial^2 y} = \frac{h_{i,j-1} - 2h_{i,j} + h_{i,j+1}}{(\Delta y)^2} \quad (3)$$

Generally, in case of:

$$\Delta x_{i \rightarrow i-1} \neq \Delta x_{i \rightarrow i+1} \text{ and } \Delta y_{j \rightarrow j-1} \neq \Delta y_{j \rightarrow j+1}$$

$$\frac{h_{i-1,j} - h_{i,j}}{(\Delta x_{i \rightarrow i-1})^2} + \frac{h_{i+1,j} - h_{i,j}}{(\Delta x_{i \rightarrow i+1})^2} + \frac{h_{i,j-1} - h_{i,j}}{(\Delta y_{j \rightarrow j-1})^2} + \frac{h_{i,j+1} - h_{i,j}}{(\Delta y_{j \rightarrow j+1})^2} = 0 \quad (4)$$

In case of equal grid:

$$\Delta x_{i \rightarrow i-1} = \Delta x_{i \rightarrow i+1} \text{ and } \Delta y_{j \rightarrow j-1} = \Delta y_{j \rightarrow j+1}$$

$$\frac{h_{i-1,j} - 2h_{i,j} + h_{i+1,j}}{(\Delta x)^2} + \frac{h_{i,j-1} - 2h_{i,j} + h_{i,j+1}}{(\Delta y)^2} = 0 \quad (5)$$

If, $\Delta x = \Delta y$

$$h_{i-1,j} + h_{i+1,j} + h_{i,j-1} + h_{i,j+1} - 4h_{i,j} = 0 \quad (6)$$

The above Eq. 4, Eq. 5 and Eq. 6 are the most widely used in finite difference solutions of steady-state flow problems. It is iteratively used in the form of a Laplacian operator for computation of heads at each node in the mesh [26].

Data Collection and Methods

The study area is located in Assiut Governorate (27° N and 30° L) with area (13.3 km²), which is bordered to the north, west and east by the Nile River, and the south by the Al-Ibrahimiya Canal, the Al-Waleediyah Canal passes through inside it, as shown fig.1 . On the eastern side (next to the Al-Walidiyah district) is the NAB, which is 400 meters north of the Old Assiut Barrage. Walidiyah district is crowded with important structures and has a large population density. Because it is near the NAB, they will be significantly affected by changes in surface water levels in U.S and D.S of the NBA.

The data collected in this study represent all data about the GWL and the levels of surface water in boundary conditions, before and after New Assiut barrage (NAB) construction. To reach the target of the present study, a Finite Differences Model (FD model) is formulated and programmed, using ArcGIS program as shown in Fig. 3. The methodology of the current study is divided into two categories, the first is to build an FD model using the data before constructing the NAB, secondly, this model is used to predict the ground water levels after the construction of the NAB in order to detect the variations in the ground water levels. The Excel program is used to create a simple program for inserting data and equations for each point in the model grid, which are processed to obtain groundwater levels for the whole area.

The ArcGIS program is used to create a layer of groundwater levels from the obtained results, as well as a layer of earth levels. An analysis of the two layers is carried out to obtain a third layer, which expresses the immersion locations of the banks and the sites of appearance of the groundwater inside the study area.

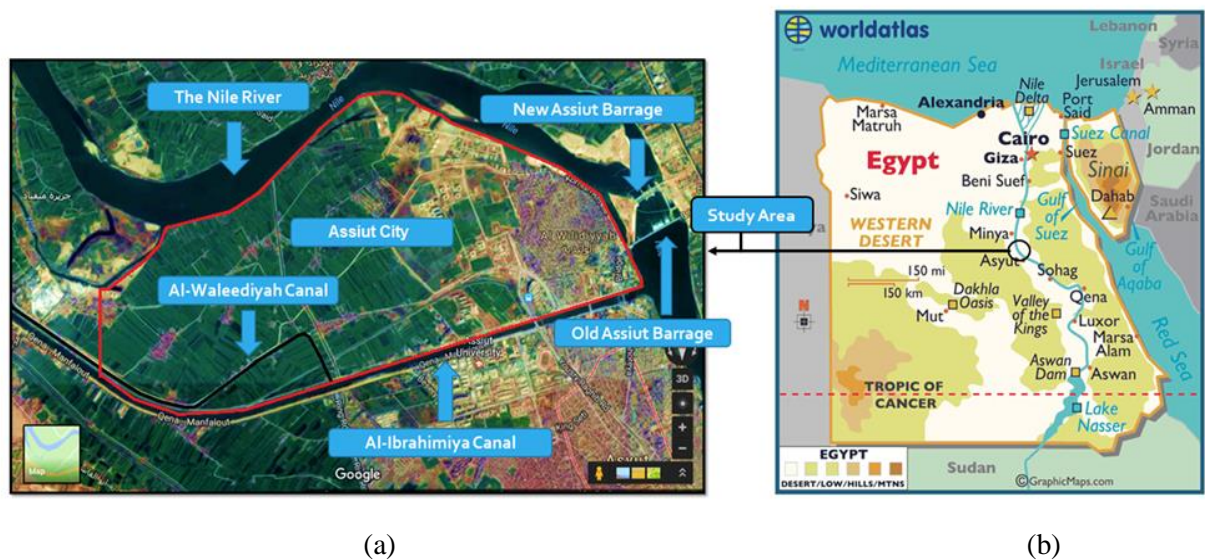


Fig. 2. Map of the study area with the boundary conditions [27].

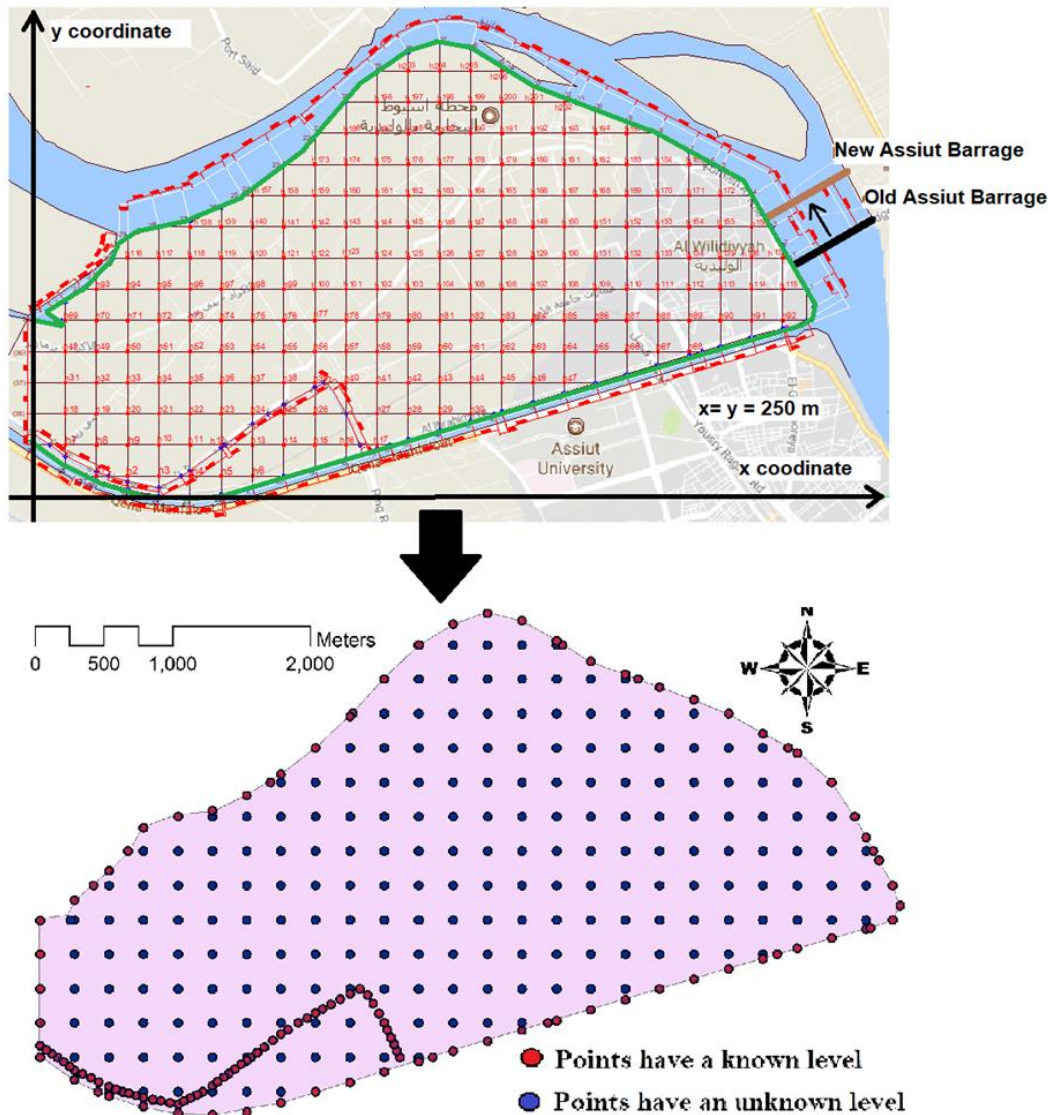
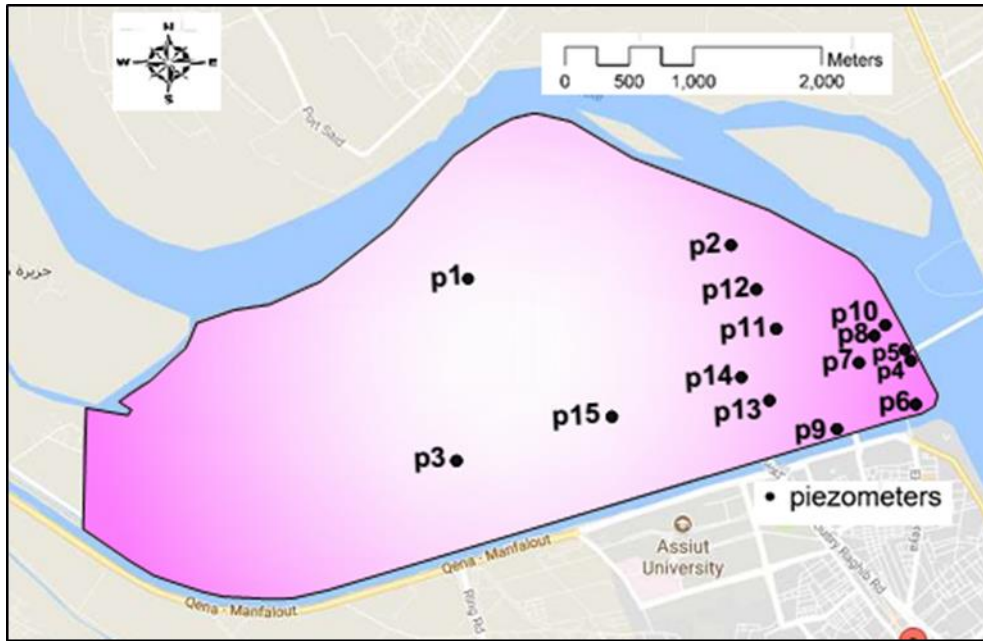


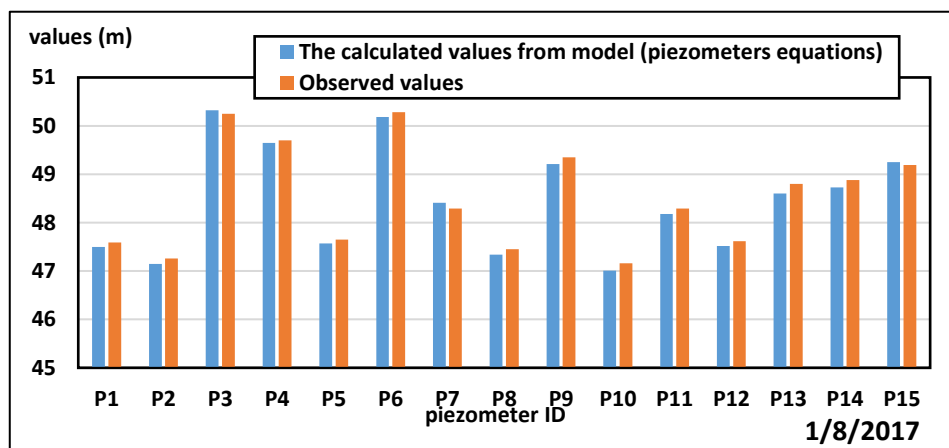
Fig. 3. Map of model's mesh.

Results and discussion

Firstly, the FD model is calibrated using the obtained data before barrage construction. It is found that there is an acceptable agreement between observed and estimated GWLs in the chosen piezometers in the study area (average correlation coefficient is about 95.6% and average root mean square error equal 10.37 %). The model was validated for one of the study years prior to the operation of the NAB. For the validity of the model, equations were made between, the values are obtained from the model and the observed values, in this stage, the model was used to calculate the values obtained, then the equations were used to derive the corrected values to be compared to the observed values, as shown in Fig. 4., the validity result was acceptable (correlation coefficient is about 0.987). Secondly, Confident with the obtained results, the model is then used to predict the ground water levels after NAB construction in order to estimate the highest ground water.



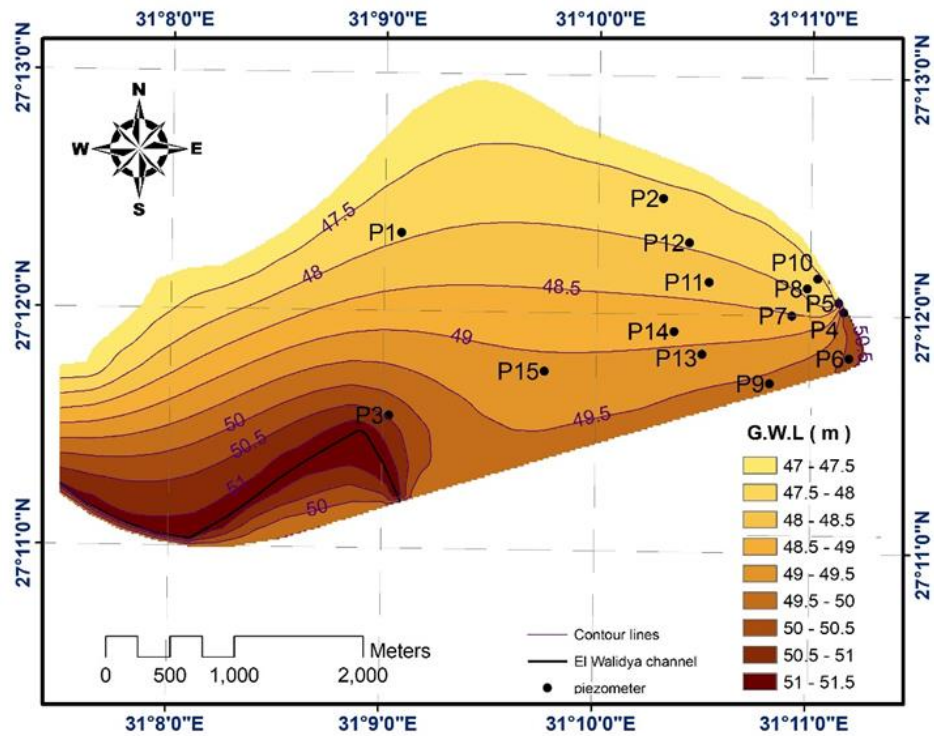
(a)



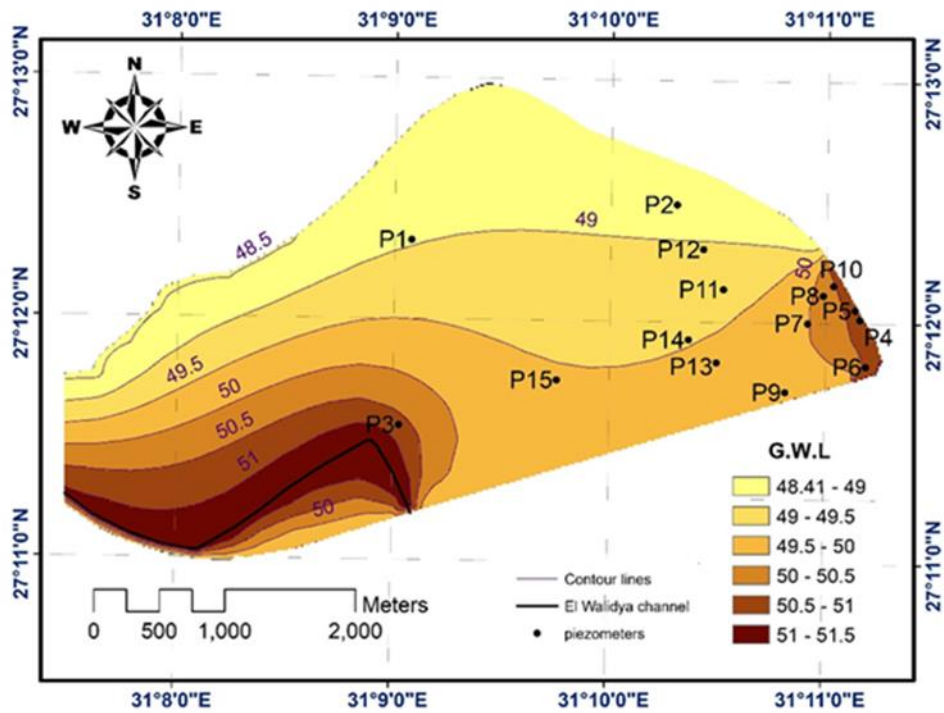
(b)

Fig. 4. (a) Map of Piezometers locations in Study Area, (b) Chart of calculated and observed values of piezometers (year 2017).

Finally, the spatial distribution map of the study area GWL after barrage operation, at maximum water level in boundary conditions, is estimated and presented in Fig.5., that shows the map (a) with the largest groundwater levels in all year before NBA construction (in year 2015), map (b) which is produced after the operation of the NAB from the forecasting process in maximum case, which showing an average increase in groundwater levels by about 1.5 meters for each study area.



(a)



(b)

Fig. 5. (a) Spatial distribution map of GWL for study for year 2015 (August). (b) Spatial distribution map of GWL for study after barrage operation.

Fig. 6. shows the map generated from the subtraction process of the groundwater layer from the ground levels layer (by ArcGIS program), which reflects the locations of groundwater appearance, and

Immersion that occurs to the study area banks which exposed to increase of the surface water levels next to it. Notable from the fig. 6., an increase in the immersion ratio of the northern bank of the study area with a length of 4.25 km (60%) and the extent of about 240 feddan (7.6% from total area) and doesn't occurs any appearance of groundwater in internal area.

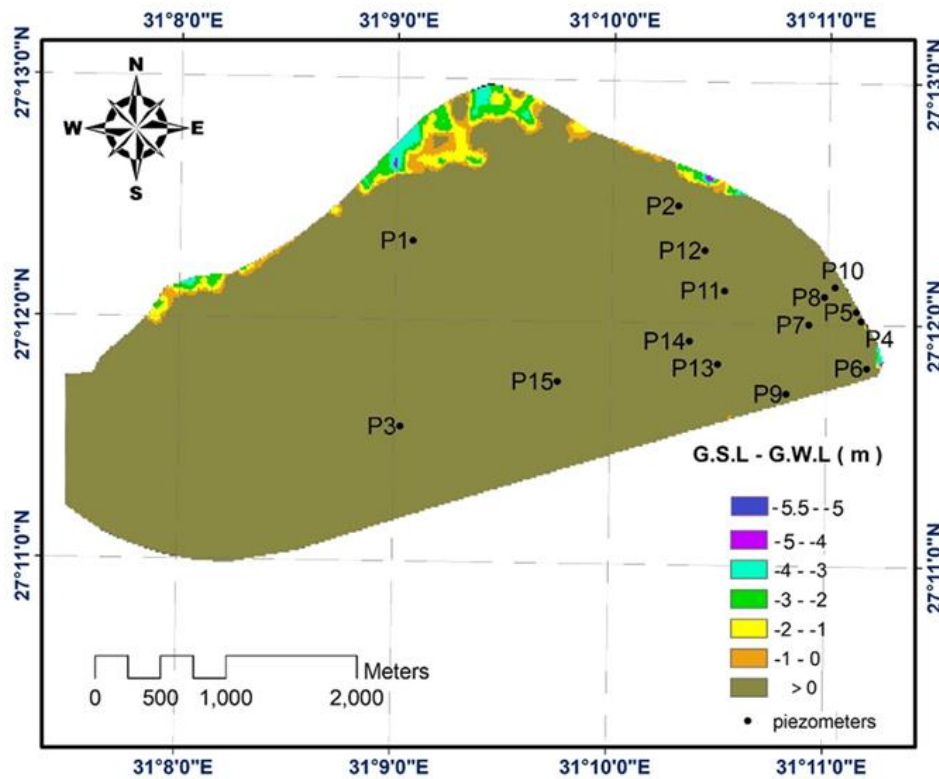


Fig. 6. Spatial distribution map of immersion area for study after barrage operation

comparing this map with the places of residential blocs distribution maps, we found that, there is no superficially damage or any appearance of groundwater in this sites, but there is an industrial zone that will be submerged (see Fig. 7.), which, located at north of the study area (317751.00 m E, 3011590.31 m N), which is illustrated by a circle in Fig.(7-b).

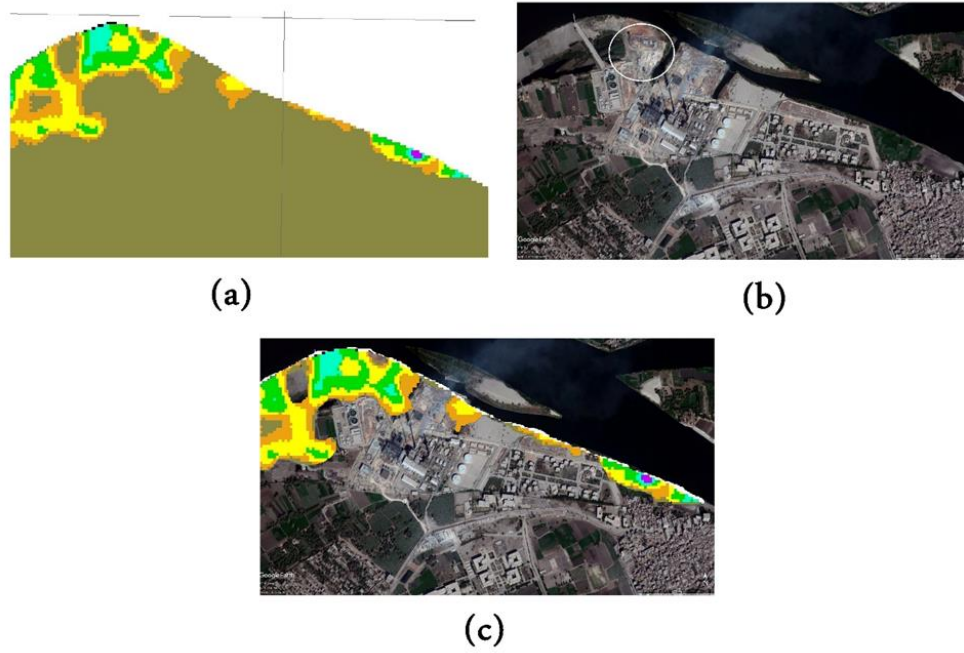
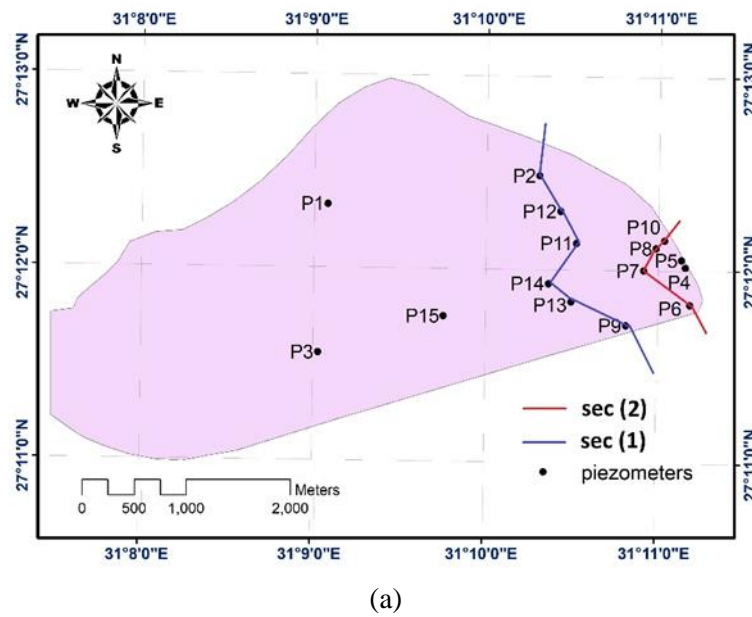


Fig. 7. (a) Part of the immersion map of the North bank in Fig. 6., (b) residential blocs distribution map [28], (c) Image of overlapping two maps together.



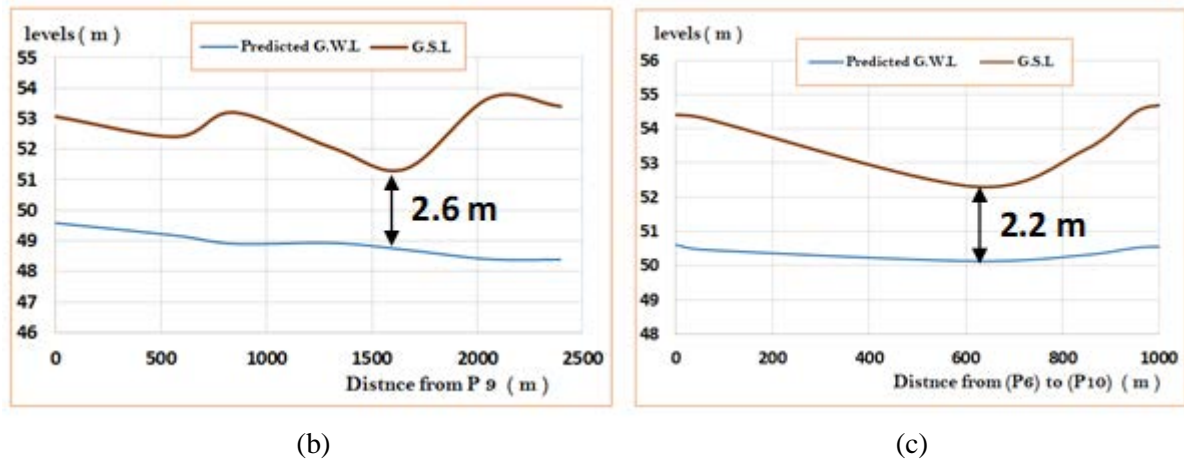


Fig. 7. (a) locations of sections, (b) sec (1), (c) sec (2)

because it is the densely populated area and also contains most of the structures in the study area, i.e. it is the most region vulnerable to problems, in the case of GWLs are raised after NAB operation. As shown in Fig. 7., there is an increase in the levels of groundwater, which was previously at the very least in these sections are 3.67 m and 4.25 m respectively, but now become 2.6 m and 2.2 m, an average increase of about 1.5 m.

Conclusions

This study presents and discusses the spatial distribution prediction of the GWL due to New Assiut barrage construction, using a Finite Differences model (FD model) and GIS. The results indicate that, the GWL in the study area were increased by about 1.5 m, this will be led to submerge of one of the industrial zones, that located at north of the study area, but without any appearance of groundwater in the locations of residential blocs. Accordingly, it can be concluded that the use of FD modeling and GIS can help to monitor ground water level changes due to man

Acknowledgements

The 1st author is very grateful for *Eng. Abdul Rahim Ahmed Ali*, (previous Director General of Environmental Studies for the New Assiut Barrage Project, Ministry of Irrigation), for his fruitful cooperation with us to reach these important results.

References

- [1] A. Negm, S. Sakr, ... I. A.-E.-G. in the N., and undefined 2018, "An Overview of Groundwater Resources in Nile Delta Aquifer," *Springer*.
- [2] V. D. Pokrovsky, E. M. Dutova, K. I. Kuzevanov, D. S. Pokrovsky, and N. G. Nalivaiko, "Hydrogeological Conditions Changes of Tomsk, Russia," *IOP Conf. Ser. Earth Environ. Sci.*, vol. 27, no. 1, 2015.
- [3] T. Phi, L. S.-R.-E. Technologies, and undefined 2015, "Prediction maps of land subsidence caused by groundwater exploitation in Hanoi, Vietnam," *Elsevier*.
- [4] Y. Medovar, I. Yushmanov, E. B.-W. Resources, and undefined 2018, "Changes in the Ecological Condition of a Territory at the Construction of Buildings with a Deep Foundation under Various Geological Conditions in Moscow," *Springer*.
- [5] N. M.-G. in the N. Delta and undefined 2017, "Use of Groundwater in Nile Alluvial Soils and Their Fringes," *Springer*.
- [6] B. Galluzzo, "A finite-difference based approach to solving the subsurface fluid flow equation in heterogeneous media2011",.

- [7] X. Xu, G. Huang, Z. Qu, L. P.-W. resources management, and undefined 2011, "Using MODFLOW and GIS to assess changes in groundwater dynamics in response to water saving measures in irrigation districts of the upper Yellow River basin," *Springer*.
- [8] Q. Yang, W. Lun, Y. F.-P. Engineering, and undefined 2011, "Numerical modeling of three dimension groundwater flow in Tongliao (China)," *Elsevier*.
- [9] C. Kumar, S. S.-I. Science, E. & Technology, and undefined 2015, "Concepts and Modeling of Groundwater System," *angelfire.com*.
- [10] M. Anderson, W. Woessner, and R. Hunt, "Applied groundwater modeling: simulation of flow and advective transport 2015",.
- [11] F. Jafari, S. Javadi, G. Golmohammadi, ... N. K.-E. E., and undefined 2016, "Numerical simulation of groundwater flow and aquifer-system compaction using simulation and InSAR technique: Saveh basin, Iran," *Springer*.
- [12] M. Dawoud, N. El Arabi, ... A. K.-J. of A. E., and undefined 2006, "Impact of rehabilitation of Assiut barrage, Nile River, on groundwater rise in urban areas," *Elsevier*.
- [13] A. El-Tuhami, H. M.-T. international water technology, and undefined 2008, "Groundwater levels estimation at areas affected by new Naga Hammadi barrages using ANN method," *academia.edu*.
- [14] Z. El-Fakharany, A. F.-W. Science, and undefined 2014, "Assessment of New Esna barrage impacts on groundwater and proposed measures," *Elsevier*.
- [15] F. Abdalla and M. Shamrukh, "Quantification of River Nile/Quaternary aquifer exchanges via riverbank filtration by hydrochemical and biological indicators, Assiut, Egypt," *J. Earth Syst. Sci.*, vol. 125, no. 8, pp. 1697–1711, Dec. 2016.
- [16] R. Abdellatif, M. Ramadan, and M. Kamel, "Groundwater Evaluation for Drinking and Domestic Uses in Diruot District, Assiut City, Egypt 2016",.
- [17] A. S. Noureldeen, S. Ghaly, K. Ali, and G. Abozaid, "Ground water Spatial distribution," pp. 853–856, 2018.
- [18] J. Krishnamurthy, N. Venkatesa Kumar, V. Jayaraman, and M. Manivel, "An approach to demarcate ground water potential zones through remote sensing and a geographical information system," *Int. J. Remote Sens.*, vol. 17, no. 10, pp. 1867–1884, 1996.
- [19] F. Laurent *et al.*, "Cartographic Modelling with Geographical Information Systems for Determination of Water Resources Vulnerability," *J. Am. Water Resour. Assoc.*, 1998.
- [20] D. W. Watkins, D. C. McKinney, D. R. Maidmen, and M.-D. Lin, "Use of Geographic information systems in groundwater flow modeling," *J. Water Resour. Plan. Manag.*, vol. 122, no. April, pp. 88–96, 1996.
- [21] G. Pinder, "Groundwater modeling using geographical information systems 2002",.
- [22] H. P. Patra, S. K. Adhikari, and S. Kunar, *Geophysical Prospecting for Groundwater*. 2016.
- [23] B. J. Galluzo, "A finite-difference based approach to solving the subsurface fluid flow equation in heterogeneous media," p. 156, 2011.
- [24] M. McDonald and A. Harbaugh, "A modular three-dimensional finite-difference ground-water flow model 1988",.
- [25] S. P. Neuman, "Calibration of distributed parameter groundwater flow models viewed as a multiple-objective decision process under uncertainty," *Water Resour. Res.*, vol. 9, no. 4, pp. 1006–1021, Aug. 1973.
- [26] M. Gulraiz Akhter, Z. Ahmad, and K. A. Khan, "Excel based finite difference modeling of ground water flow," *J. Himal. Earth Sci.*, vol. 39, pp. 49–53, 2006.
- [27] part (a) is modified from Google Earth pro. Program in period (7/12/2017), part (b) from <https://www.worldatlas.com/webimage/countrys/africa/lgcolor/egcolor.htm>

2nd International conference of Chemical, Energy and Environmental Engineering
16-18 July 2019 Egypt Japan University of Science and Technology, Alexandria, Egypt.

(28/4/2019).

[28] from Google Earth pro. Program (11/11/2018).